Strong Ground Motion Seismology

edited by Mustafa Özder Erdik and M. Nafi Toksöz

Springer-Science+Business Media, B.V.

Strong Ground Motion Seismology

NATO ASI Series

Advanced Science Institutes Series

A series presenting the results of activities sponsored by the NATO Science Committee, which aims at the dissemination of advanced scientific and technological knowledge, with a view to strengthening links between scientific communities.

The series is published by an international board of publishers in conjunction with the NATO Scientific Affairs Division

A Life Sciences B Physics	Plenum Publishing Corporation London and New York
C Mathematical and Physical Sciences	D. Reidel Publishing Company Dordrecht, Boston, Lancaster and Tokyo
D Behavioural and Social Sciences E Engineering and Materials Sciences	Martinus Nijhoff Publishers Dordrecht, Boston and Lancaster
F Computer and Systems Sciences G Ecological Sciences H Cell Biology	Springer-Verlag Berlin, Heidelberg, New York, London, Paris, and Tokyo

Series C: Mathematical and Physical Sciences Vol. 204

Strong Ground Motion Seismology

edited by

Mustafa Özder Erdik

Earthquake Engineering Research Center,
Middle East Technical University, Ankara, Turkey

and

M. Nafi Toksöz

Earth Resources Laboratory,
Massachusetts Institute of Technology,
Cambridge, Massachusetts, U.S.A.

Springer-Science+Business Media, B.V.

Proceedings of the NATO Advanced Study Institute on
Strong Ground Motion Seismology
Ankara, Turkey
June 10-21, 1985

Library of Congress Cataloging in Publication Data

NATO Advanced Study Institute on Strong Ground Motion Seismology (1985: Ankara, Turkey)
Strong ground motion seismology.

(NATO ASI series. Series C, Mathematical and physical sciences; vol. 204)
"Proceedings of the NATO Advanced Study Institute on Strong Ground Motion Seismology, Ankara, Turkey, June 10–21, 1985"— verso of t.p.
Includes index.
1. Seismology—Congresses. I. Erdik, Mustafa. II. Toksöz, M. N., 1934– III. Title. IV. Series: NATO ASI series. Series C, Mathematical and physical sciences; vol. 204.
QE31.N375 1985 551.2'2 87–12819
ISBN 978-90-481-8440-8 ISBN 978-94-017-3095-2 (eBook)
DOI 10.1007/978-94-017-3095-2

All Rights Reserved
© 1987 by Springer Science+Business Media Dordrecht
Originally published by D. Reidel Publishing Company, Dordrecht, Holland in 1987
and copyrightholders as specified on appropriate pages within.
No part of the material protected by this copyright notice may be reproduced or utilized in any form or by any means, electronic or mechanical, including photocopying, recording or by any information storage and retrieval system, without written permission from the copyright owner.

TABLE OF CONTENTS

Preface vii

List of Participants ix

SECTION 1: EARTHQUAKE SOURCE

K. Aki / Strong Motion Seismology 3

M. N. Toksöz, A. M. Dainty and J. Nabelek / Earthquake Source Mechanisms: Case Studies 41

G. De Natale, R. Madariaga, R. Scarpa and A. Zollo / Source Parameters of Some Friuli Earthquakes (1976-1977) From Strong Motion Data 85

F. Abramovici and J. Baumgarten / The Seismic Inverse Problem For a Flat Structure 99

SECTION 2: PREDICTION OF STRONG GROUND MOTION

D. M. Boore / The Prediction of Strong Ground Motion 109

P. Suhadolc and C. Chiaruttini / A Theoretical Study of the Dependence of the Peak Ground Acceleration on Source and Structure Parameters 143

M. Bouchon / Numerical Simulation of Earthquake Ground Motion 185

G. C. Beroza and V. F. Cormier / High Frequency Earthquake Strong Ground Motion in Laterally Varying Media: The Effect of a Fault Zone 209

M. N. Toksöz, R. S. Wu and D. P. Schmitt / Physical Mechanisms Contributing to Seismic Attenuation in the Crust 225

SECTION 3: ACQUISITION AND INTERPRETATION OF STRONG MOTION DATA (INCLUDING CASE HISTORIES)

M. Basili / Data Acquisition and Processing in Strong Motion Seismology 251

A. Rovelli / Strong Ground Motions in Italy: Accelerogram Spectral Properties and Prediction of Peak Values 333

F. K. Chang / Analysis of Strong-Motion Data From the New Hampshire Earthquake of 18 January 1982 355

Y. Ohta, H. Kagami, S. Okada and H. Ōhashi / Seismic Intensity and its Applications to Engineering: A Study in Japan 369

Y. Ohta, H. Ohashi, Ō. Ergünay and A. Tabban / Seismic Intensity and its Applications to Engineering: A Study in Turkey 385

SECTION 4: HAZARD ASSESSMENT

C. S. Oliveira / Probabilistic Models for Assessment of Strong Ground Motion 405

V. Doyuran / Seismic Source Regionalization 461

SECTION 5: SITE RESPONSE AND ENGINEERING APPLICATION

M. Erdik / Site Response Analysis 479

A. M. Ansal / Constitutive Relationships for Soil Dynamics 535

R. Scherer / Source and Local Site Effects-Preliminary Results Based on the Friuli Earthquake Sequence 1976 545

M. Erdik / Soil Structure Interaction Effects on Strong Ground Motion 559

P. Gülkan / Engineering Uses of Strong Motion Data 581

Index 605

PREFACE

This book contains selected papers presented at the NATO Advanced Study Institute on "Strong Ground Motion Seismology", held in Ankara, Turkey between June 10 and 21, 1985.

The strong ground motion resulting from a major earthquake determines the level of the seismic hazard to enable earthquake engineers to assess the structural performance and the consecutive risks to the property and life, as well as providing detailed information to seismologists about its source mechanism. From the earthquake engineering point the main problem is the specification of a design level ground motion for a given source-site-structure-economic life and risk combination through deterministic and probabilistic approaches. In seismology the strong motion data provide the high frequency information to determine the rupture process and the complexity of the source mechanism. The effects of the propagation path on the strong ground motion is a research area receiving substantial attenuation both from earthquake engineers and seismologists.

The Institute provided a venue for the treatment of the subject matter by a series of lectures on earthquake source models and near-field theories; effects of propagation paths and site conditions, numerical and empirical methods for prediction; data acquisition and analysis; hazard assessment and engineering application.

The book is organized in five sections. The first section on the Earthquake Source begins with a general paper on strong motion seismology, followed by treatments on earthquake source mechanisms with several case studies. The assessment of strong ground motion for engineering design relies both on empirical and theoretical methods. These methods are covered in the second section on the Prediction of Strong Ground Motion in a series of papers dealing with source and propagating path parameters, attenuation and scattering effects and numerical simulation procedures. The third section titled Acquisition and Interpretation of Strong Motion Data encompasses the steps for the acquisition and processing of the strong motion data with particular emphasis on network management and analog-to-digital conversion. Papers on case studies dealing with strong ground motion data analysis and seismic intensity assessments in several parts of the world complement the theoretical treatment. Probabilistic models for the assessment of Strong Ground Motion based on point process to describe its occurrence in space, time and size, and based on a continuous time-dependent process to describe its variation for a given occurence are covered under the fourth section on Hazard Assessment. The importance of the geologic and tectonic environment in occurence models are amplified in another

paper in the same section. Fifth section is devoted to the site response and engineering analysis. Determination of the site response for a given seismic environment is an important engineering problem not only for the design of structures but also for the proper interpretation of strong motion records obtained at the building foundation. Both issues are treated in depth with complementing material on the constitutive relationship for soils and on the observational data on local site effects on strong ground motion. The last paper in this section of the book deals with the engineering uses of strong motion data providing a venue for the earthquake resistant design of structures.

Strong ground motion, a problem of mutual interest to earthquake engineers and seismologists, can be ideally studied through interaction between both disciplines. The editors would be happy if this publication imparts small momentum to this communication.

We are grateful to NATO Scientific Affairs Division which provided the opportunity to carry out the institute and the grant towards its finance. The contributions by Kinemetrics Inc., U.S.Army Research and Development Office, Turkish Electricity Authority, Turkish Scientific and Technical Research Council, Middle East Technical University and Sprengnether Inc. should also be acknowledged with gratitude.

We wish to express our appreciation Sadık Bakır who assisted in arranging the format of the book and supervised the drawings and to Dilek Karakaya who typed the manuscripts in the uniform format.

Finally, we are grateful to the participants in the Advance Study Institute for their involvement and, specifically, for their contribution to this book.

M.Ö.Erdik, M.N.Toksöz

LIST OF PARTICIPANTS

Dr. Flavian Abramovici, Professor
Tel Aviv University
School of Mathematical Sciences
Ramat Aviv, 69978
Tel Aviv, Israel

Dr. William Mansfield Adams
Professor of Geophysics
University of Hawaii at Manoa
Hawaii Institute of Geophysics
2525 Correa Road
Honolulu, Hawaii 96822

Gürbüz Akçora
Turkish Electricity Authority
Nuclear Power Plants Division
Hanımeli Sok. 9
Ankara, Turkey

Suzan Akçora
TUBITAK-Building Research Inst.
Bilir Sokak, No.17
Kavaklıdere, Ankara
Turkey

Dr. Keiiti Aki, Professor
University of Southern California
Department of Geological Sciences
University Park, Los Angeles
California, 90089-0741
U.S.A.

Dr. Nuri Akkaş, Professor
Middle East Technical University
Earthquake Engineering Research Center
Ankara, Turkey

Dr. Mazin A.H.Al-Salim
Research Seismologist
Scientific Research Council
Building Research Center-
Seismology Unit
P.O.Box 2136-Baghdad
Iraq

Dr. Ömer Alptekin, Professor
Black Sea University
Dept. of Geophysics
Trabzon, Turkey

Dr.Atilla Ansal, Professor
Istanbul Technical University
Dept of Civil Engrg.
Ayazağa
Istanbul, Turkey

Ms.Ionela Apopei
Scientific Researcher
Geophysikalisches Institut
der Universitaet Karlsruhe
Hertzstrasse 16
7500 Karlstruhe-West
West Germany

Ms.Ref'an Ateş
Earthquake Research Division
Ministry of Public Works and Housing
Lodumlu, Ankara
Turkey

Mr.Alkut Aytun
TUBITAK-Building Research Inst.
Bilir Sokak, 17
Kavaklıdere, Ankara
Turkey

Mr.Günruh Bağcı
Hacettepe University
Dept of Geological Engrg.
Beytepe, Ankara
Turkey

Dr. Mauro Basili, Director
Laboratorio Ingegneria dei Siti
ENEA
S.P.Anguillarese, 301
00100 Roma A.D.
Italy

Mr.Nejat Bayülke
Earthquake Research Division
Ministry of Public Works and Housing
Lodumlu, Ankara
Turkey

Mr.Pascal Bernard
Université Pierre et Marie Curie
Institut de Physique due Globe
4, Place, Jussien
75230 Paris Cedex 05
France

Mr.Gregory C.Beroza
Massachusetts Institute of Technology
42 Carleton St., Earth Res. Lab.
Cambridge, Massachusetts, 02142
U.S.A.

Ms.Ornela Bonamassa
Istituto Nazionale di Geofisica
Via Ruggero Bonghi, 11/B
00184, Roma
Italy

Dr. David Boore
U.S.G.S.
Office of Earthquakes,
Volcanoes and Engineering
345 Middlefield Road, MS 977
Menlo Park, CA 94025
U.S.A.

Dr.Michel Bouchon, Professor
Université Scientifique et
Medicale de Grenoble
I.R.I.G.M., Domain Universitaire
Boite Postal 68
38402 St Martin d'Héres Cedex
France

Dr. Michel Campillo
Attaché de Recherce
CNRS Universite de Grenoble
IRIGM BP 68
38402 St Martin d'Héres Cedex
France

Dr.Frank K.Chang
U.S.Army, Waterways Experiment
Station
P.O.Box 631, Wicksburg
Mississippi 39180-0631
U.S.A.

Dr.Claudio Chiaruttini, Professor
Istituto di Geodesia e Gefisica
34100-Via Dell'Università N.7
Trieste, Italy

Mr.Massimo Cocco
Istituto Nazionale di Geofica
Via Ruggero Bonghi, 11/B
00184, Roma
Italy

Mr.Jim Crowder
Civil Engineering Department
Imperial College
London, SW7 2BU
United Kingdom

Mr.Rene M.Crusem
CEA/DAM CEB III
Service RCP/ER
B.P. 12 91680
Bruyeres-Le-Châtel
France

Dr.Mehmet Çelebi
U.S.G.S., Office of Earthquakes
Volcanoes and Engineering
345 Middlefield Rd., MS 977
Menlo Park, CA 94025
U.S.A.

Mr.John G.Diehl
Kinemetrics Inc.,
222 Vista Ave.
Pasadena, California 91107
U.S.A.

Dr.Vedat Doyuran, Professor
Middle East Technical University
Earthquake Engineering Research
Center, Ankara, Turkey

Dr.Mustafa Erdik
Professor and Director
Middle East Technical University
Earthquake Engineering Research Center
Ankara, Turkey

Mr.Oktay Ergünay, Division Head
Earthquake Research Division
Ministry of Public Works and Housing
Lodumlu, Ankara
Turkey

Ms.Ayfer Erken
Istanbul Technical University
Dept. of Civil Engineering
Ayazağa, İstanbul
Turkey

Dr.Stefan Freystaetter
K.W.U., Berliner Strasse, 295-303
D-6050 Offenbach Am Main
Germany

Mr.John Foley
Weston Observatory
Boston College
Weston, MA 02193
U.S.A.

Mr.Louis Bertrand Geli
Laboratorie de Mecanique des Solides
Ecole Polytechnique
91128 Palaiseau Cedex
France

Mr.Kenan Gelişli
Black Sea University
Dept. of Geophysics
Trabzon, Turkey

Mr.Muzaffer Genç
Turkish Electricity Authority
Nuclear Power Plants Division
Hanımeli Sok. No.17
Ankara, Turkey

Dr.Ruhi Gürcan, Professor
Istanbul University
Dept. of Geophysical Engrg.
İstanbul, Turkey

Mr.Fatih Güler
Middle East Technical University
Earthquake Engineering Research
Center, Ankara, Turkey

Dr.Polat Gülkan, Professor and Dean
Hacettepe University
Faculty of Engineering
Beytepe
Ankara, Turkey

Ms.Heidi Houston
California Institute of Technology,
252-21
Pasadena, CA 91125
U.S.A.

Dr.Katharine Kadinsky-Cade
Earth Resources Lab.
M.I.T.
42 Carleton St.
Cambridge, MA.02142
U.S.A.

Mr.Uğur Kuran
Earthquake Research Division
Ministry of Public Works and Housing
Lodumlu, Ankara
Turkey

Dr.Süleyman Kocaefe, Professor
Hacettepe University
Faculty of Engineering
Beytepe, Ankara
Turkey

Dr.Özer Kenar, Professor
Black Sea University
Dept. of Geophysical Engrg.
Trabzon, Turkey

Mr.Domenico Liberatore
Departimento di Ingegneria
Strutturale e Geotechnica
Via Eudossiana 18, 00184
Roma, Italia

Mr.Vasilis N.Margaris
Institute of Engineering Seismology
and Earthquake Engineering
Hapsa 1, Thessaloniki
Greece

Dr.Yutaka Ohta, Professor
Hokkaido University
Faculty of Engineering
Sapporo, Japan

Dr.Carlos S.Oliveira, Professor
Laboratòrio Nacional
de Engenheria Civil
Avenida do Brasil, 101
1799 Lisboa
Portugal

Mr.Oğuz Özel
Earthquake Research Division
Ministry of Public Works
and Resettlement
Lodumlu
Ankara, Turkey

Mr.Turgut Öztürk
İstanbul Technical University
Dept. of Civil Engrg.
Ayazağa, İstanbul, Turkey

Mr.Mithat Fırat Özer
Black Sea University
Dept. of Geophysical Engrg.
Trabzon Turkey

Dr.Kemal Özüdoğru, Professor
İstanbul Technical University
Dept. of Civil Engrg.
Ayazağa
İstanbul, Turkey

Mr.Uri Peled, Project Manager
Institute for Petroleum Research
and Geophysics
I.P.R.G., Hamashbir 1
Holon, Israel

Dr.A.Pugliese
ENEA, Via V.Brancati 48
00144 Roma
Italy

Dr.Jay Pulli
Earth Resources Lab.
M.I.T.
42 Charleton St.
Cambridge, MA 02142
U.S.A.

Dr.Antonio Rovelli, Seismologist
Instituto Nazionale di Geofica
Via Ruggero Bonghi, 11/B
00184, Roma
Italy

Mr.Fabio Sabetta
ENEA, S.P.Anguilarse, 301
00060 Roma
Italy

Mr.Halit Sav
Mineral Exploration and Researh
Ankara, Turkey

Dr.Roberto Scarpa
Osservatorio Vesuviano
80056 Ercolano (NA)
Italy

Dr.Frank Scherbaum,
Research Associate
Institut für Geophysik,
Universität Stuttgart
Richard-Wagner-Str.44
7000 Stuttgart 1
West Germany

Dr.Raimar Scherer
Dyckerhoff and Widmann AG
Erdinger Landstrasse 1
8000 München 81
West Germany

Mr.A.Mark Sereci, Manager
Kinemetrics, Inc.,
222 Vista Ave.
Pasadena, California, 91107
U.S.A.

Mr.Muhammed Slimani
Strong Motion Department
Control Technique de la Construction
Rue Kaddour Rahim Prolonge
Hussein-Dey
Algiers, Algeria

Mr.Peter Suhadolc, Research Associate
Universita'di Trieste
Istituto di Geodesia e Geofizica, v.
Università 7
34100, Trieste Italy

Mr.Eugene J.Taffra
Sprengnether Instruments Division
4150 Laclade Ave.
St. Louis, MO 63108
U.S.A.

Ms.Zuhal Taşkanal
İstanbul Technical University
Dept. of Geophysics
Maçka
İstanbul, Turkey

Mr.Nikolaos Theodolidis, Seismologist
Institute of Engineering Seismology
and Earthquake Engineering
Hapsa 1, Thessaloniki
Greece

Dr.M.N.Toksöz, Professor and Director
M.I.T., Earth Resources Laboratory
42 Carleton Strect
Cambridge, MA 02142
U.S.A.

Dr.Brian Tucker
California Division of Mines
and Geology, 2815 O St.
Sacramento, CA 95
U.S.A.

Mr.Turker Turgay
Topçular, Kazıklıbağ Sok.40
Rami, İstanbul, Turkey

Dr.Niyazi Türkelli
Middle East Technical University
Dept. of Geological Engineering
Ankara, Turkey

Dr.Önder Tüzünalp, Professor
Middle East Technical University
Dept. of Physics
Ankara, Turkey

Dr.Atilla Uluğ
Ninth of September University
Marine Sciences and Tech. Inst.
İzmir, Turkey

Dr.Diether Weichert,
Research Scientist
Pasific Geoscience Center,
Fed. Gov. Canada, Box.6000, PGC
Sidney, B.C., W8L 4B2
Canada

Prof.Dr.Rıfat Yarar, President
Turkish National Committee for
Earthquake Engineering
İstanbul, Turkey

Ms.Aysel Yatman
Earthquake Research Division
Ministry of Public Works and Housing
Lodumlu
Ankara, Turkey

Mr.Rüçhan Yılmaz
Earthquake Research Division
Ministry of Public Works and Housing
Lodumlu
Ankara, Turkey

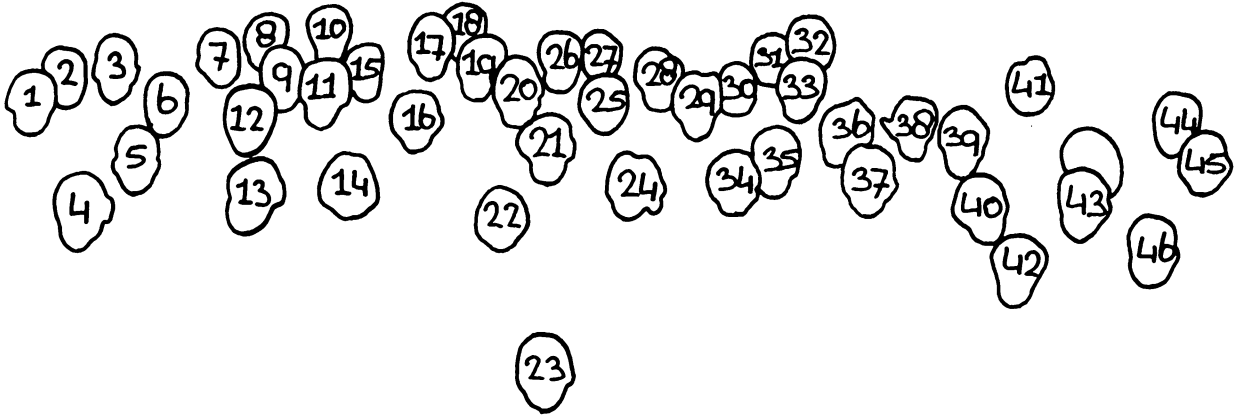

1. Fatih Güler
2. Uri Peled
3. Jim Crowder
4. Keiiti Aki
5. Atila Uluğ
6. Antonio Rovelli
7. Roberto Scarpa
8. M.N.Toksöz
9. Rene Crusem
10. Vedat Doyuran
11. Jack Foley
12. Jay Pulli
13. Domenico Liberatore
14. Heidi Houston
15. Ionela Apopei
16. Muhammad Slimani
17. Basilis Margaris
18. Brian Tucker
19. Claudio Chiaruttini
20. Mauro Basili
21. Peter Suhadolch
22. Ornella Bonamassa
23. Mustafa Erdik
24. Ayfer Erken
25. Flavian Abramovici
26. ?
27. Michel Bouchon
28. ?
29. Fabio Sabetta
30. ?
31. L.B.Geli
32. Massimo Cocco
33. Antonio Pugliese
34. Turgut Öztürk
35. Muzaffer Genç
36. Reiner Scherer
37. ?
38. M.Campillo
39. Pascal Bernard
40. ?
41. Greg Beroza
42. C.S.Oliveira
43. K.Kadinsky-Cade
44. W.M.Adams
45. Frank Scherbaum
46. D.Wiechert

Section 1

Earthquake Source

STRONG MOTION SEISMOLOGY

Keiiti Aki
Massachusetts Institute of Technology
Cambridge, Massachusetts 02139 U.S.A.

ABSTRACT. Strong motion seismology has a long history of development, owing mainly to the effort of earthquake engineers with emphasis on data collection and interpretation based primarily on empirical approaches. In the past decade or so, seismologists began to get involved in data collection and analysis, and several attempts have been made to develop quantitative models of the earthquake rupture process with the ultimate goal of predicting strong ground motion for a given potential earthquake fault on the basis of an understanding of basic physical laws governing fault mechanics. The problem is difficult because of the sensitivity of high-frequency waves to the details of fault plane irregularities and heterogeneous earth structure. To overcome this difficulty, several attempts have been made to introduce a hybrid of deterministic and stochastic models, in which the gross features of rupture propagation are specified deterministically but the details of the process are described by a stochastic model specified by a small number of statistical parameters.

In the present paper, we shall review the model parameters relevant to high-frequency generation, namely the amount of slip, rise time, barrier interval, local stress drop and f_{max} determined for actual earthquakes. It was found that the local stress drop and f_{max} (the two most important parameters for the evaluation of acceleration) are very stable among the earthquakes studied so far.

For a few earthquakes for which both the local stress drop and the slip velocity have been estimated, it was shown that the slip velocity is too low to be compatible with the local stress drop. The slip velocities estimated for many earthquakes in the past decade using various long-period seismographs may have to be revised upward for use in predicting high-frequency strong motion.

We shall also review recent works on the scaling law of source spectra and discuss the significance of the spectral bump between about 0.2 and about 10 Hz in relation to f_{max}. We point out that the bump is roughly coincident with the peak of Q^{-1} for S waves in the lithosphere, and suggest that both may be due to the unique scale-distribution of heterogeneity of the lithosphere.

M. O. Erdik and M. N. Toksöz (eds.), Strong Ground Motion Seismology, 3–39.
© 1987 by D. Reidel Publishing Company.

1. INTRODUCTION

Strong motion seismology is concerned with high-frequency seismic waves from large earthquakes, representing the least understood area in Earthquake Seismology. High-frequency waves from small earthquakes are also complicated but at least to record and study, as compared to the strong motion in the vicinity of a large earthquake which does not occur very often.

Nevertheless, significant progress has been made in the past decade in understanding how high-frequency waves are genereated during the rupture of an earthquake fault. For example, ten years ago a crucial parameter controlling high-frequency wave generation-namely, the rise time during which the opposite faces of a fault plane complete a slip motion-had been estimated for only two or three earthquakes. A recent table of source parameters published by Purcaru and Berckhemer (1982) listed the rise time for about 60 earthquakes.

Strong motion seismology is, of course, directly relevant to Earthquake Engineering. As a matter of fact, strong motion seismology was initiated by earthquake engineers who developed and operated seismographs to record strong motions. Recently an increasing number of seismologists have been involved in both collecting and interpreting strong motion data. Various deterministic and stochastic earthquake source models have been applied in their interpretation. Theoretical results on fracture mechanics as well as laboratory results on rock failure have been helpful in clarifying the physics of fault ruptures. Various attempts have also been made to relate the earthquake rupture process with the observable behavior of earthquake faults. Such a relation is vitally important in evaluating the ground motion expected for an earthquake fault mapped by geologists.

The present paper is an attempt to synthesize results from these recent seismological, rock-mechanical, and geological studies relevant to strong motion evaluation. Our ultimate goal is to predict strong ground motion from the basic understanding of fault mechanics and seismic wave propagation in the earth.

The mathematical foundation of our approach was firmly established in the early 1960's by Maruyama (1963) and Burridge and Knopoff (1964) who showed that the point-force equivalent of a fault slip is a double couple and the seismogram can be computed by a space-time convolution of slip function and Green's function. The slip-function and Green's function express quantitatively the source and the propagation effect, respectively, on seismic motion. In order to find the slip function form observed seismogram, it is necessary to know Green's function.

In the early 1960's, the propagation effect of long-period surface waves was already well understood and that part of Green's function was well known. Thus, the study of slip function was begun from the low-frequency end of the seismic spectrum-the period range longer than about 20 sec. Through a low-frequency window, we could not see the details of the earthquake rupture process, but we were able to determine a new earthquake source parameter called "seismic moment" with an unprecedented high accuracy for an earthquake source parameter. The seismic moment is the moment of equivalent point double couple and is equal to the final slip integrated over the whole area of the fault plane multiplied by the

medium rigidity. As such, it has become a key parameter in a comparative study of far-field seismic observations with near-field observations on earthquake faults by geologic and geodetic measurements. It has also been used for estimating present-day plate motion and for long-term earthquake prediction. It is a direct measure of the extent of faulting and therefore of the damage caused by static deformation, including Tsunami damage in the case of a submarine earthquake.

The seismic moment is, however, not directly useful for earthquake engineering because the strong motion depends crucially on the details of the rupture process, which cannot be seen clearly through the long-period window. We needed to extend the window to higher frequencies, which appeared enormously difficult because of the complex propagation effects on high-frequency seismic waves involving strong scattering and attenuation.

2. OUTLINE OF THE DEVELOPMENT OF KINEMATIC MODELS

Then, the Parkfield, California, earthquake took place on June 27, 1966 and produced the first recording of ground motion in the immediate vicinity of an earthquake fault. The now-famous Station No.2 was located at a distance of only 80 meters from the fault break, and it was thought that the propagation effect might be minimal at such a short distance. Fig.1 shows the horizontal component accelerogram in the direction perpendicular to the fault strike, reproduced from Housner and Trifunac (1967). The accelerogram was integrated to obtain particle velocity and displacement seismograms, as shown in the same figure. The displacement seismogram shows a simple impulsive form. The ground near the San Andreas fault moved to the north-east by about 30 cm and then returned to its original position within about a second. The simplicity of the record aroused great interest among seismologists, and it was shown by Aki (1968) and Haskell (1969) that the observed motion is precisely what is expected for a right-lateral strike slip propagating from north-west to south-east. In order to calculate a theoretical seismogram, the details of the rupture process or slip history must be completely specified. They used a simple five-parameter model, now called Haskell's model, in which a uniform slip Δu takes place over a rectangular fault with width W and length L. The rupture propagates along the length with a constant velocity v. The slip at any point on the fault starts to increase linearly with time at the arrival of the rupture front, and stops when the amount of slip reaches Δu. The time required to complete the slip is called rise time T, and is assumed to be the same at every point. Thus, Haskell's model is described completely by five parameters (length, width, final slip, rupture velocity and rise time).

The latest simulation of the Station No.2 record by Haskell's model was done by Bouchon (1979b), who included the effect of low-velocity sediment overlying the basement. Fig.2 shows the source-medium-station configuration and the theoretical displacement seismogram calculated by the discrete-wavenumber method which involves five-fold integrations: one over frequency, two over horizontal wavenumbers and an additional two over the fault plane. The displacement pulse is marked by discontinuities

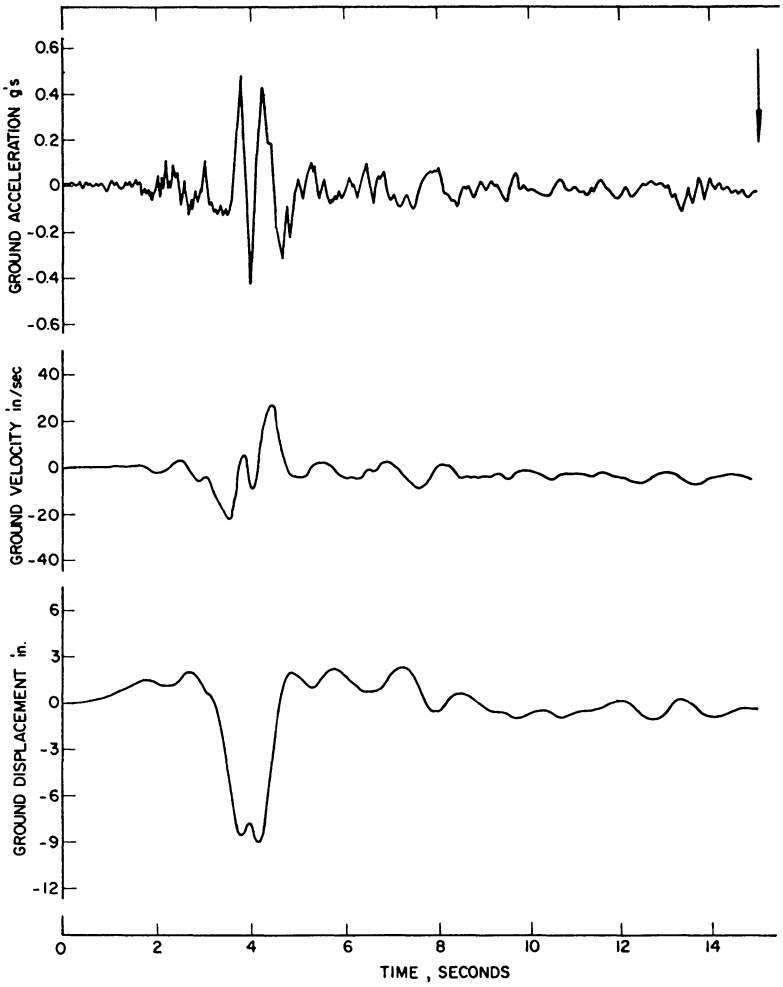

Figure 1. Horizontal transverse component (N65°E, perpendicular to the strike of the San Andreas fault) acceleration, velocity and displacment at Station 2 of the Cholame-Shandan array. Reproduced from Housner and Trifunac (1967).

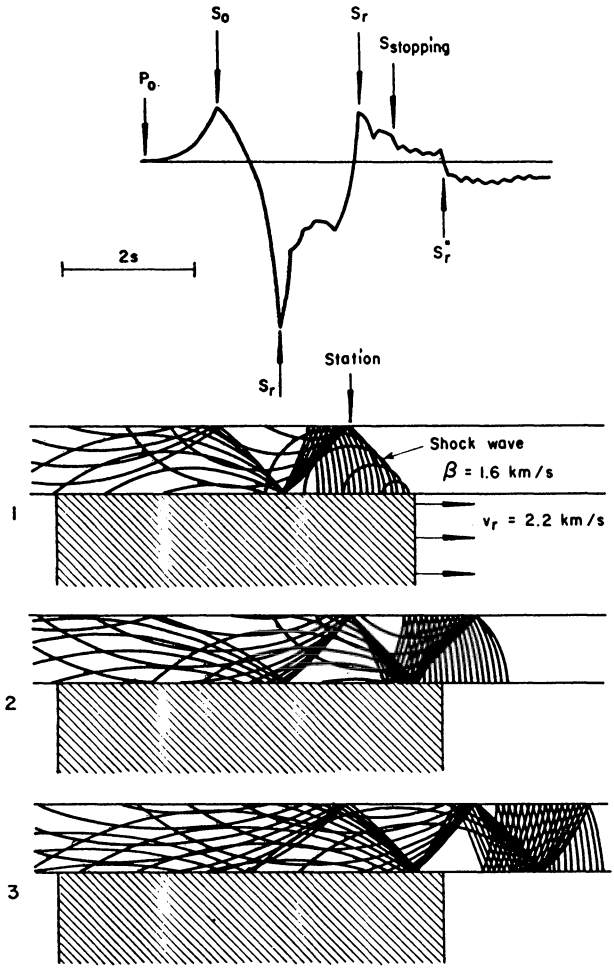

Figure 2. Synthetic horizontal transverse component displacement for a Haskell's model fault in the basement. A sediment layer with thickness 1.5 km, P velocity 2.8 km/s, S velocity 1.6 km/s and density 2.3 g/cm^3 overlies the basement with P velocity 6 km/s, S velocity 3.5 km/s and density 2.8 g/cm^3. Reproduced from Bouchon (1979b).

at arrival times of prominent phases such as the starting S phase (S_o), a shock wave in the sediment (S_r) and its first multiple reflections (S_r'). The parameters giving the best fit to the observed record were a final slip of about 40 cm and a rise time of about 0.3 sec.

Bouchon found an interesting result on the interaction of the sediment layer and the fault rupture. As shown in Fig.3, the motion decreases very quickly once the top of the fault plane (located at depth Z_o) is below the bottom of the sediment located at 1.5 km depth. On the other hand, once the top of the fault plane is in the sediment, the motion doesn't depend much on the depth however close to the surface. A similar effect of the sediment cover was found for static displacement due to a buried fault by Kasahara (1964). In the presence of a low-rigidity sediment, as soon as the fault reaches the sediment bottom, the motion is greatly amplified even if it is buried as deep as a few km.

The assumption of uniform slip in Haskell's model was probably adequate for the interpretation of close-in records such as Station No.2 of the Parkfield earthquake or Station No.6 of the Coyote Lake earthquake of 1979 (Bouchon, 1981) which are probably mainly affected by the slip across the segment of the fault close to the station.

In general, however, the assumption of uniform slip had to be modified to explain the observed strong motion. Even for the Parkfield earthquake, as soon as the other stations of the Cholame strong motion seismograph array are included in the data, Trifunac and Udwadia (1974) had to divide the fault plane into many parts and assign a different slip to each part. Non-uniform slip distribution has been found also for the Borrego Mountain earthquake of 1968 by Heaton and Helmberger (1977), for the San Fernando earthquake of 1971 by Trifunac (1974), Bouchon (1978), Heaton and Helmberger (1979), Shakal (1979), and others, and for the Imperial Valley earthquake of 1979 by Hartzel and Helmberger (1982), and Olson (1982).

The non-uniformness of fault slip over fault plane has been found also from the analysis of teleseismic body wave data for the Borrego Mountain earthquake of 1968 by Burdick and Mellman (1976) and Ebel and Helmberger (1982), for the San Fernando earthquake of 1971 by Bouchon (1978) and Langston (1978), for the Guatemala earthquake of 1976 by Kanamori and Stewart (1978), for the Santa Barbara earthquake of 1978 by Wallace et al.(1981), for the Caracas earthquake of 1967 by Rial (1978), and for the El Asnam earthquake of 1980 by Deschamps et al.

Non-uniformness of the fault slip appears to be the rule rather than the exception whenever the details of the rupture process are investigated. Non-uniform slip over a fault has two important effects on seismic motion. It tends to increase the high-frequency contents, and also to weaken the azimuthal amplitude variation such as the directivity effect of Ben-Menahem (1961).

Through these studies, the simulation technique has been advanced to include a more realistic medium. In the beginning, most simulation methods used Green's function for an unbounded homogeneous medium (Aki, 1968 ; Haskell, 1969 ; Kanamori , 1972 ; Tsai and Patton , 1973 ; Niazy, 1973 ; Boore and Zoback , 1974 ; Trifunac and Udwadia , 1974 ; Anderson, 1974 ; Anderson and Richards , 1975 ; Richards , 1976 ; Levy and Mal, 1976 ; Madariaga ,1978). Then, the free surface effect (Niazy ,1975 ;

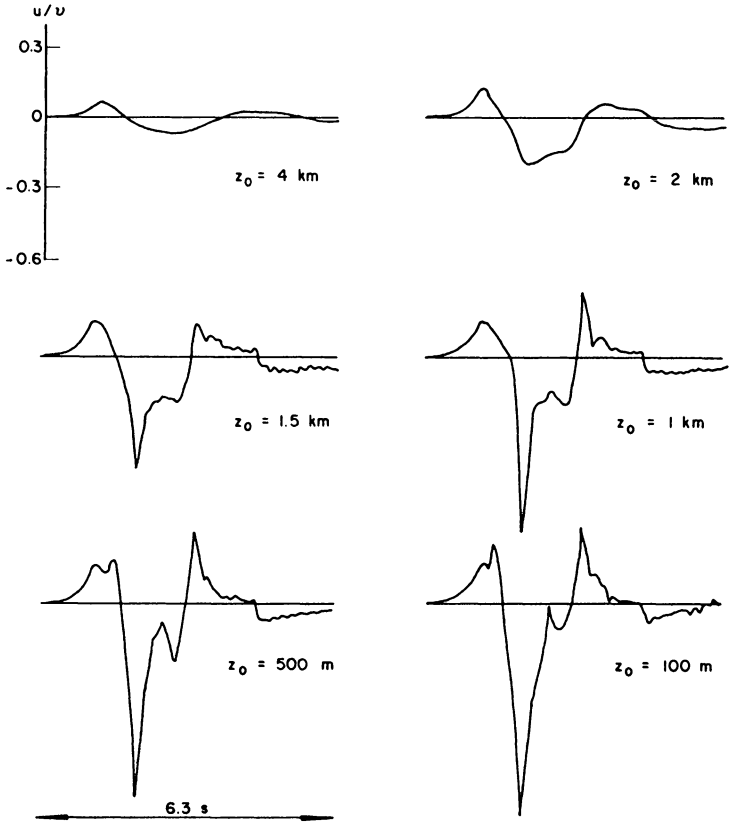

Figure 3. Synthetic seismograms for simulating the horizontal transverse displacement observed at Station No.2 during the Parkfield earthquake. The amplitude decays quickly with depth of the top of the fault plane (Z_o) as soon as Z_o exceeds the depth of the bottom of sediment located at 1.5 km depth. The amplitude is roughly constant as long as Z_o is within the sediment layer. Reproduced from Bouchon (1979b).

Kawasaki, 1975 ; Kawasaki et al.,1975 ; Anderson, 1976 ; Bouchon and Aki, 1977 ; Israel and Kovach, 1977 ; Hartzell et al.,1978 ; Archuleta and Frazier, 1978) and the effect of sedimentary layers (Heaton and Helmberger, 1977, 1978 ; Archuleta and Day ,1977,1980 ; Wiggins et al., 1977 ; Bouchon, 1979a,b, 1980 ; Bouchon and Aki, 1980) have been included in the simulation.

In order to save computer time, various approximate methods using mode and ray decompositions have been used to calculate Green's function for layered media. Fig.4 shows an example of Green's function calculated by the generalized-ray method (marked by a dotted line, computed by Heaton and Helmberger, 1977) and by the normal-mode method (Swanger and Boore, 1978 ; for the Borrego Mountain earthquake of 1968. Both methods give satisfactory agreement with the observed record shown on the top by a solid line. Analytical approaches taken by Madariaga (1976, 1981) and Achenbach (1981) would enable extending analysis to higher frequencies economically.

More general models, involving a laterally heterogeneous earth, have also been studied by various methods including finite difference (Boore ,1972), finite element (Lysmer and Drake ,1972), ray methods (Hong and Helmberger, 1978), an integral equation method (Sanchez-Sesma and Esquivel, 1979), and the Rayleigh-ansatz method (Aki and Larner, 1970 , Bard and Bouchon, 1980a,b). Some progress has also been made along the lines of a semi-emprical approach in which actual seismograms observed for small earthquakes are used as Green's function for calculating strong motion for a major earthquake (Kanamori, 1979 ; Hartzel, 1978).

3. STOCHASTIC MODELS FOR HIGH-FREQUENCY GENERATION

The simulation studies mentioned above are concerned primarily with displacement records or, at best, velocity records. High-frequency waves dominating the accelerogram are too complicated to simulate by a deterministic model because they are affected by abundant small-scale heterogeneities of the fault plane which require too many parameters to specify their detail. To avoid this difficulty, several attempts have been made to introduce a hybrid of deterministic and stochastic models, in which gross features of rupture propagation are specified deterministically but the details of the process are described by a stochastic model specified by a small number of statistical parameters (Blanford, 1975 ; Boore and Joyner, 1978 ; Hanks ,1979 ; Andrews, 1980, 1981 ; Papageorgiou and Aki, 1981 ; and Boatwright, 1981).

Let us consider a model of such a heterogeneous fault plane with an idealized geometry-a rectangular fault plane containing small circles as shown in Fig.5. There are two opposing views of how a slip can take place over this fault plane. In one of them, the circle represents a patch with strong cohesion resisting the break. The regions between circles have already slipped aseismically. Once the rupture starts, a slip will take place over each circular patch in a more or less independent manner and will generate the high-frequency waves needed to explain the observed accelerogram. After the rupture the whole fault plane is

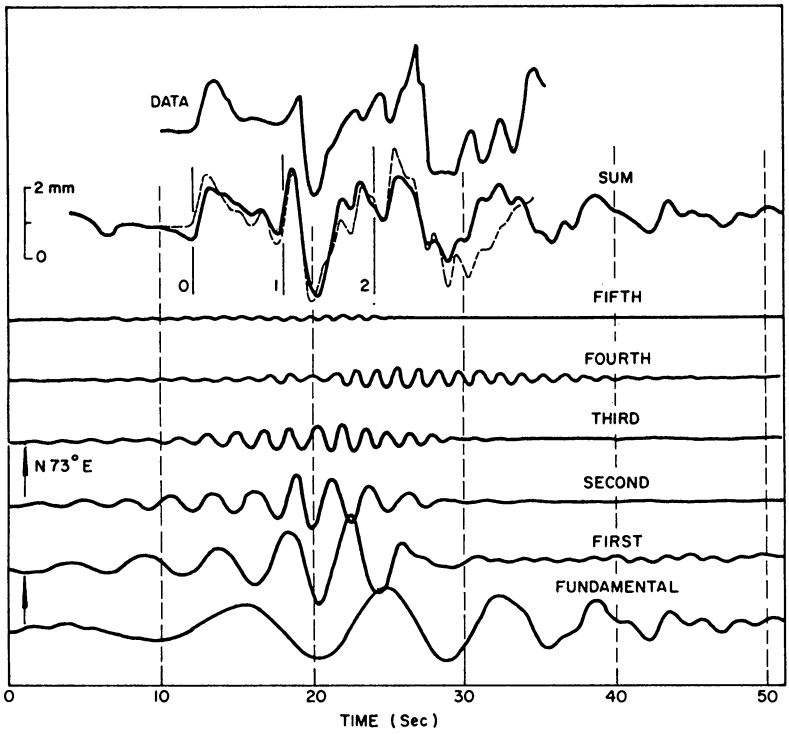

Figure 4. Comparison of an actual seismogram, a synthetic one by the generalized ray method (dashed line) and the normal-mode method. Reproduced from Swanger and Boore (1978).

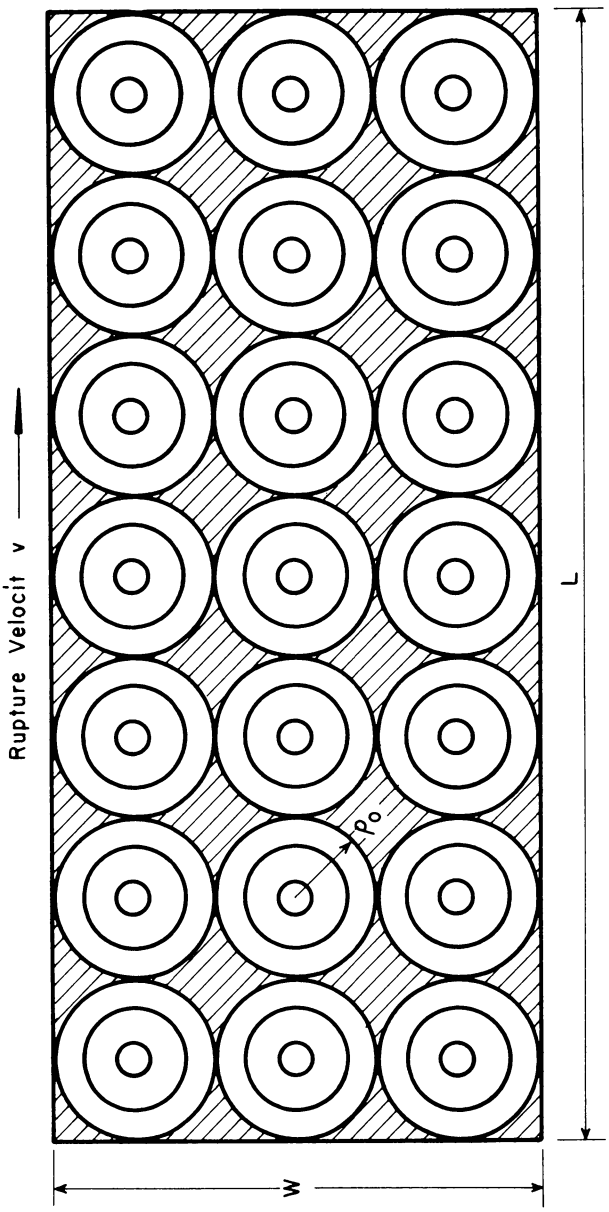

Figure 5. Heterogenous fault plane with idealized geometry used by Papageorgiou and Aki (1981) as specific barrier model.

broken, and the residual stress, if any, will be uniform over the fault plane. This view was maintained by Kanamori and Stewart (1978) to explain the teleseismic P wave-forms of the Guatemala earthquake of 1976. Such a patch model has been discussed earlier by Wesson et al. (1973) and more recently by Li and Dmowska (1981) in relation to the foreshock process.

In the other view, the circle represents a crack where a slip occurs during the fault rupture, but the region between cracks remains unbroken after the rupture. The possibility of such segmented ruptures was demonstrated by Das and Aki (1977), Mikumo and Miyatake (1978), and Burridge and Moon (1981) using numerical experiments. A rupture front may be stopped by a barrier, but elastic waves generated by the slip can break the fault plane ahead of the barrier in the case of shear crack. Then, the rupture can propagate over the whole fault plane leaving unbroken barriers behind. Resultant irregular slip can explain observed accelerograms. This model is called the "barrier model" by Aki et al. (1977) and is supported by several examples of fault segmentation mapped by geologists. In contrast to the patch model, the residual stress over the fault plane is not uniform after the rupture. The concentration of stress will occur at the unbroken barriers, and may become the cause of aftershocks.

A real fault plane may contain a mixture of patches and barriers. Papageorgiou and Aki (1981) took the viewpoint of the barrier model, and determined the model parameters using the observed acceleration power spectra for several California earthquakes, as shown in Table 1. The results have turned out to be rather encouraging for strong motion prediction. The diameter of the circular crack 2ρ (or barrier interval) was found to be nearly proportional to the maximum slip Δu_{max} of an earthquake. This means that the local stress drop $\Delta\sigma$ inside the circular crack (or within a barrier interval) is a stable parameter, ranging from 200 to 400 bars for all the earthquakes studied.

The relative constancy of local stress drop found by Papageorgiu and Aki is consistent with the result obtained by Hanks and McGuire (1981) using the data on root mean square acceleration (α_{rms}) by the method based on Brune's (1970) model and developed by Hanks (1979b) and McGuire and Hanks (1980). Their estimate of stress drop is, however, about 100 bar, significantly lower than that of Papageorgiou and Aki. The difference may be due partly to an underestimation of the acceleration power spectrum from α_{rms} by Hanks and McGuire, who used a bandwidth value much higher than that actually observed by Papageorgiou and Aki. The latter authors directly estimated the acceleration power spectrum.

The above difference may be partly due to the relatively low rupture velocity ($v = 0.75\beta$) assumed in the Papageorgiou-Aki model. The Papageorgiou-Aki formula for acceleration power spectra agrees with the Hanks' formula if we set the rupture velocity (both spreading and sweeping velocity) in the former to be equal to 0.86 of the S-wave velocity and the fault width W equal to the radius R of a circular crack that represents the entire source in Hanks' model. In the actual application, Papageorgiou and Aki set the rupture spreading velocity v to be 0.75 of the s-wave velocity. Since the acceleration spectrum is proportional to v^2 in their model, their stress drop estimate is 1.3 times higher than that of Hanks if $W = R$.

TABLE 1

SOURCE PARAMETERS OF BARRIER MODEL
(Reproduced from Papageorgiou and Aki, 1982)

EVENT	M_S	M_L	m_b	M_o x 10^{27} (dyn -cm)	L (km)	V (km)	$\Delta\sigma$ (pars)	ΔU_{max} (m)	2ρ (km)	d (km)	f_{max} (Hz)	$GX10^{10}$ (erg/ cm^2)	σ_c (bars)	D (m)
San Francisco, 1906	8.25			~3.5-4.3	~300.	~15-20.		~4.-6.	15.			2.		
Fort Tejon, 1857				~5.3-9.0	~300.	~15-20.	~370.	10.	15.	~1.-2.		10	~500-700.	~3-4.
Kern County, 1952	7.7	7.2		2.0	70.	20.	~350.	7.-9.	~13.	1.0	2.5	10	~680	~3
San Fernando, 1971	6.6	6.35	6.2	0.12	20.	14.	~300.	2.-3.	~5.	0.5	5.0	2.4	~480	~1.
Borrego Mountain, 1968	6.7	6.8	6.1	0.063	33.	11.	~200-300.	~0.90	~2.-3.	0.6	4.0	~1.2	~300-400.	~0.4
Long Beach, 1933	6.25	6.43		0.028	30.	15.	~220.	0.30	~1.	0.6	4.0	~0.3	~200	~0.4
Parkfield, 1966	6.5	5.5	5.9	0.014	35.	15.	~200-300.	0.51	~1.-2.	0.5	5.0	~0.3-0.5	~200	~0.4

Another important parameter in Table 1 is the cut-off frequency of acceleration spectra, called "f_{max}" by Hanks (1981). This parameter was also found to be very stable among the earthquakes studied.

In the following, let us concentrate on the two most crucial parameters controlling acceleration, namely the local stress drop $\Delta\sigma$ and the cut-off frequency f_{max}, and review the current state of our understanding of them.

4. REVIEW OF SOURCE PARAMETERS RELEVANT TO STRONG MOTION SEISMOLOGY

Within the scheme of kinematic models in which the slip-function is specified by a small number of parameters, the most important parameters controlling high-frequency generation are the magnitude of slip and the rise time. For most of the 243 earthquakes compiled by Purcaru and Berckhemer (1982), the average amount of slip ($\overline{\Delta u}$) is given from the estimates of seismic moment M_o and fault area S by the formula

$$M_o = \mu . \overline{\Delta u} . S \qquad (1)$$

On the other hand, the rise time is listed only for 25% of them. Of these with listed rise times, only shallow earthquakes are selected here, and the sources referenced in the Purcaru-Berckhemer table (hereafter referred to as the P-B table) are examined. Table 2 shows the average slip and rise time for 32 earthquakes, for which the reference source has been examined. To be consistent with the sources cited in Table 2, some of the parameters are modified slightly from the P-B table (No's. 57, 72, 88, 91, 96, 103, 108, 129, 133 and 32a according to the numbers given in the P-B table). Table 2 includes two additional earthquakes (No's.164 and 179) for which the P-B table does not list the rise time.

The rise time given in Table 2 were determined using several different types of data. The records of classic low-magnification long-period seismographs have been used by Kanamori (1972, 1975) Abe (1974) and others for older earthquakes. More recent ones were studied by the use of displacement records obtained from strong motion accelerograms by numerical integration. Teleseismic body-wave records also supplied valuable information about the rise time since the work of Hirasawa (1965) on the Niigata earthquake of 1964. Fukao and Furumoto (1979) combined the total process time measured from long-period surface wave phase spectra with the information on fault length, width and rupture velocity to infer the rise time.

The average slip $\overline{\Delta u}$ and rise time τ are plotted in Fig.6 for earthquakes listed in Table 2. Different data types used for determining the rise time are shown by different symbols. There is a tendency for the data containing more high-frequency waves to show shorter rise time, suggesting a possible bias due to the inability to resolve short rise times by long-period data.

Defining the slip velocity as $\overline{\Delta u}/\tau$, the lines corresponding to slip velocities 0.1, 1, and 10 m/s are also shown in Fig.6. The slip velocity varies from low values near 0.1 m/s for some tsunami earthquakes and

TABLE 2. LIST OF AVERAGE SLIP AND RISE TIME

No.*	Earthquake	$\overline{\Delta u}$(in m)	τ(in s)	Reference
2	Nobi, 1891	5	3.5	Mikumo and Ando (1976)
16	Saitama, 1931	1	2	Abe (1974)
20	Izu, 1934	0.1	0.9	Abe (1978)
32	Tottori, 1943	2.5	3	Kanamori (1972)
40	Fukui, 1948	2	2	Kanamori (1973)
45	Kern County, 1952	3	1	Kanamori and Anderson (1975)
53	Etorofu, 1958	5.2	12±2	Fuako and Furumoto (1979)
57	Kitamino, 1961	2.5	2	Kawasaki (1975)
58	Wakasa-bay,1963	0.6	2	Abe (1974)
62	Kuril, 1963	3.2	20	Furumoto (1979)
63	Kuril, 1963	2.6	20	Furumoto (1979)
72	Niigata, 1964	4~5	2~4	Hirasava (1965)
79	Chiba, 1965	0.3	0.6	Somerville (1980)
88	Parkfield, 1966	0.35	0.3	Bouchon (1979a)
91	Truckee, 1966	0.3	1	Burdick (1977)
95	Gibbs Fracture Zone 1967	1.6	7	Kanamori and Stewart (1976)
96	Caracas	1~2	2.5	Rial (1978)
99	Koyna, 1967	0.4~0.75	2.5	Langston (1976)
103	Borrego Mt.,1968	4.5	0.3~0.4	Burdick (1977), Ebel and Helmberger (1982)
105	Tokachi-oki,1968	4.1	10	Furumoto (1979)
107	Saitama, 1968	0.92	1	Abe (1975)
108	W.Shikoku,1968	0.8~1.0	0.5 ~ 1.5	Shiono and Mikumo (1975)
116	Gifu, 1969	0.6	1	Mikumo (1973)
129	S.E.Akita,1970	0.23~0.65	1.0 ~ 1.4	Mikumo (1974)
133	San Fernando,1971			Heaton and Helmberger (1979)
	lower segment:	2.5	0.8	
	upper segment:	4	0.8	
135	Solomon Is., 1971	1.3	5	Lay and Kanamori (1980)
136	Solomon Is., 1971	1.3	5	Lay and Kanamori (1980)
163	Gibbs Fracture Zone, 1974	1.8	10	Kanamori and Steward (1976)
164	Haicheng, 1975	2.8	1~2	Cipar (1979)
168	Nemuro-oki, 1975	2.4	33	Fukao (1979)
179	Guatemala, 1976	1~1.3	4	Kanamori and Stewart (1978)
32a	Thessaloniki,1978	0.28	2	Barker and Langston (1981, Soufleris and Stewart (1981))

*Earthquake numbers are those assigned by Purcaru and Berckhemer (1982).

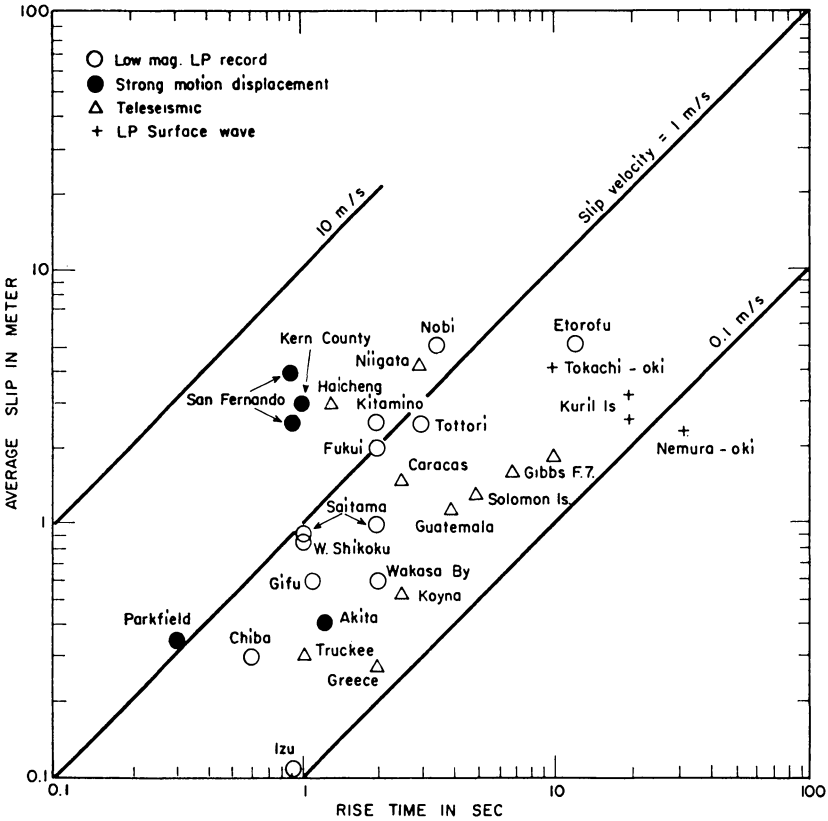

Figure 6. Relation between the average slip and the rise time. Different symbols correspond to different data from which the rise times are estimated.

fracture-zone earthquakes to high values beyond 1 m/s for some thrust earthquakes.

The slip-velocity obtained for the Borrego Mountain earthquake of 1968 by the use of short-period teleseismic body waves (Ebel and Helmberger, 1982) shows an unusually high value (13 m/s). This may indicate the high resolution of short-period data, but it could also be due in part to the large value of t* assumed in correcting for the attenuation effect, as pointed out by Der and McElfresh (1980) and Der (1981).

Let us now look at the source parameters determined directly from the acceleration data in the frequency range higher than 1 Hz. Here we show primarily the results obtained by Papageorgiou and Aki (1981) mentioned earlier. Table 3 shows the maximum slip Δu_{max} and the barrier interval 2ρ (ρ is the radius of circular cracks distributed over a fault plane as shown in Fig.5) for several California earthquakes. Table 2 also shows the maximum slip along a fault and the average length of fault segments observed by geologists on the surface after several earthquakes. The results in Table 3 are plotted in Fig.7. Fig.7 also shows the local stress drop (stress drop in each circular crack) $\Delta\sigma$, calculated by the formula

$$\Delta\sigma = \frac{7\pi}{24}\,\mu\,\frac{\Delta u_{max}}{\rho} \tag{2}$$

As shown in Fig.7, the local stress drop determined from acceleration spectra as well as from geologists' observations on fault breaks, is well defined to be a few hundred bars. This is in contrast to the global stress drop determined from the seismic moment and the total fault dimensions (Aki, 1972; Kanamori and Anderson, 1975), which usually lies between 10 and 100 bars.

From theoretical results on dynamic fracture, we find that the local stress drop and the slip velocity obtained above must be closely related.

Brune (1970) was the first to obtain a relation between slip velocity and stress drop. He considered an instantaneous stress drop over an infinite fault plane, and obtained the following formula:

$$\sigma_e = \frac{\mu}{2\beta}\,\frac{\overline{\Delta u}}{\tau} \tag{3}$$

where he introduced σ_e, called "effective stress". The effective stress is defined as the initial stress σ_0 minus the frictional stress σ_f and is considered as an available stress to drive the slip motion between the two faces of a fault plane. Brune also introduced the so-called "ε-model," in which the stress on the fault plane initially drops to the frictional stress, but recovers to the level of $\sigma_f + (1-\varepsilon)\sigma_e$, with $0 < \varepsilon < 1$. This ε-model is difficult to accept for a fault plane with more or less homogeneous stress distribution. Under the usual conditions for slip freezing (or crack healing), the final residual stress is very close to the dynamic frictional stress and ε is usually much less than 1. In a heterogeneous fault plane, we can assign any arbitrary value of stress drop at different parts of a fault as in the barrier model of Das and Aki (1977) or Papageorgiou and Aki (1981). Within the framework of a homogeneous fault plane, however, the arbitrary choice of ε is not

TABLE 3. LIST OF MAXIMUM SLIP AND BARRIER INTERVAL

No.*	Earthquake	Δu_{max}(in m)	2ρ(in km)	Reference
1	Fort Tejon,1857	11	15	Wallace(1968,1973)
2	Nobi, 1891	8	10 ~ 15	Matsuda (1974)
	Rikuu, 1896	2~3	5 ~ 8	Matsuda et al. (1980)
9	Tango, 1927	3	3	Matsuda (1976)
14	North Izu, 1930	4	7	Matsuda (1972)
18	Long Beach, 1933	0.3	1	Papageorgiou and Aki (1981)
32	Tottori, 1943	1.5	4	Tsuya (1944)
45	Kern County,1952	7~9	13	Papageorgiou and Aki (1981)
51	Gobi-Altai, 1957	8	30	Florensov and Solonenko (1963)
88	Parkfield, 1966	0.5	1~2	Papageorgiou and Aki (1981)
103	Borrego Mt.,1968	0.9	2~3	Papageorgiou and Aki (1981)
	Dasht-e Bayāz,1968	3	7	Tchalenko and Berberian (1975)
133	San Fernando,1971 initial part	2.5	3~4	Bouchon (1978)
152	Izu-oki,1974	0.5	3	Matsuda and Yamashina (1974)

TABLE 4. LIST OF LOCAL STRESS DROP $\Delta\sigma$ AND SLIP VELOCITY $\overline{\Delta u}/\tau$.

No.	Earthquake	$\overline{\Delta u}/\tau$(in m/s)	$\Delta\sigma$(in bar)
2	Nobi, 1891	1.4	350
32	Tottori, 1943	0.8	200
45	Kern County, 1952	3.0	340
88	Parkfield, 1966	1.1	180
103	Borrego Mt.,1968	12.9	200
133	San Fernando, 1971	3.1~5	390

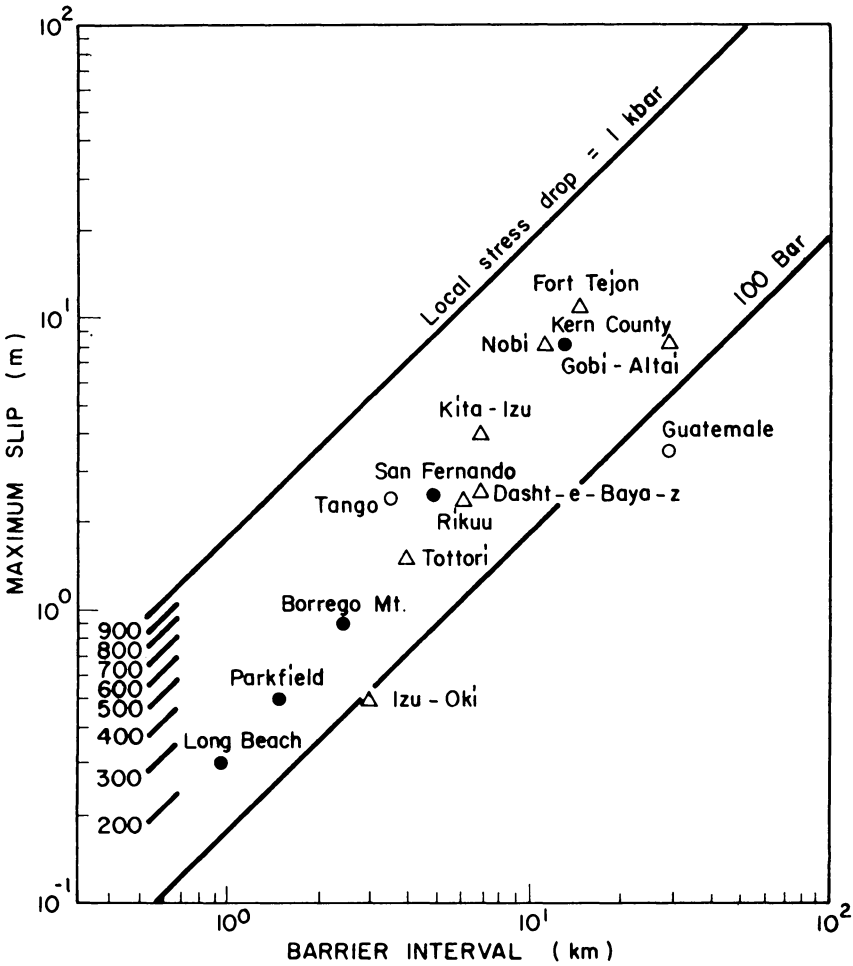

Figure 7. Relation between the maximum slip and the barrier interval. Different symbols correspond to different data from which the barrier intervals are estimated.

possible. The effective stress σ_e in formula (1) should be called stress-drop $\Delta\sigma$, defined as

$$\Delta\sigma = \sigma_0 - \sigma_f \tag{4}$$

where σ_f is the dynamic frictional stress. In fact, Ohnaka (1976, 1978) correctly interpreted Brune's effective stress as stress drop, and derives the formula

$$\Delta\sigma = \frac{\mu}{2\beta} \frac{\overline{\Delta u}}{\tau} \tag{5}$$

For a more realistic finite crack, let us consider the case of a circular crack spreading from its center as studied by Madariaga (1976) and the case of a long rectangular crack propagating lengthwise as studied by Day (1979). In the case of Madariaga's crack, the rise time increases toward the center. For the rupture velocity $v = 0.9\,\beta$, the rise time ranges from 0 at the edge to about $\sqrt{3}\rho/\beta$ at the center. From the average of the slip velocities calculated at various distances from the center by Madariaga, we find that on the average, the stress drop and slip velocity are related by

$$\Delta\sigma \simeq 0.9 \frac{\mu}{\beta} \frac{\overline{\Delta u}}{\tau} \tag{6}$$

In the case of a long rectangular crack, the rise time approaches a steady value (with increasing distance of propagation) determined by the width W of the fault plane. The corresponding relation between the stress drop and slip velocity is (since $\tau = W/2\beta$, $\Delta\sigma = \mu \ \Delta u_{max}/W$, and $\overline{\Delta u} = (\pi/4)\Delta u_{max}$) given by

$$\Delta\sigma = \frac{2}{\pi} \frac{\mu}{\beta} \frac{\overline{\Delta u}}{\tau} \tag{7}$$

Thus, for the range of crack models so far considered, we expect the following relation:

$$\Delta\sigma = (1 \sim 1/2) \frac{\mu}{\beta} \frac{\overline{\Delta u}}{\tau} \tag{8}$$

There are only a small number of earthquakes for which we can make a direct comparison of local stress drop and slip velocity. They are shown in Table 4 and Fig.8. We also show the theoretical relation (Eq.8) in Fig.8. It is clear that the observation does not satisfy the theoretical relation for a dynamic crack. There are three possibilities: (1) the local stress drop was overestimated; (2) the slip velocity was underestimated; or (3) the crack models so far considered do not apply to real earthquakes.

Since most of the slip-velocity values were obtained from measurements of seismic waves with periods longer than 1 sec, and the local stress drops were estimated using waves with periods shorter than 1 sec, the slip velocity may be estimated too low. From the theoretical relation and observed local stress drop shown in Fig.8, is is more likely that the real slip velocity associated with the observed local stress drop be in

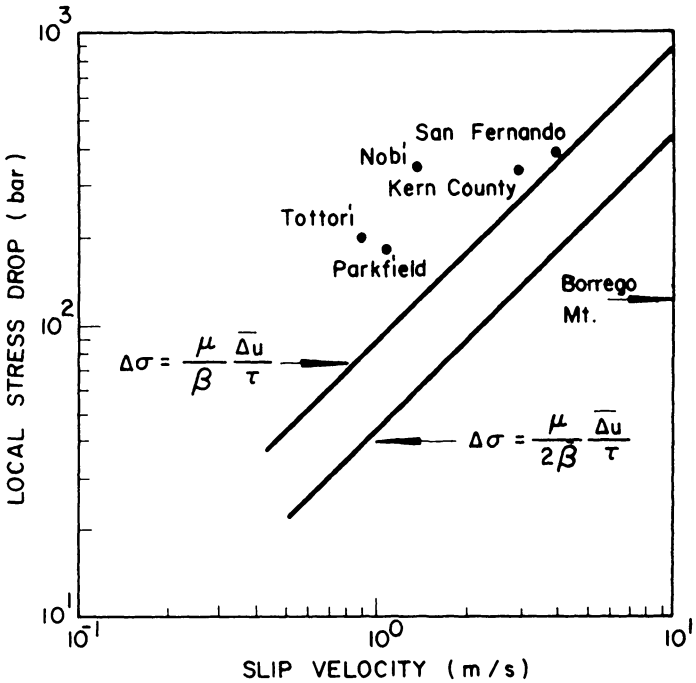

Figure 8. Relation between the local stress drop calculated by equation (2) and the slip velocity $\overline{\Delta u}/\tau$. The lines define the theoretical range given by Equation (8).

the range of 1 to 10 m/s.

It is interesting to note that the observed slip velocities are roughly consistent with the observed "global stress drop", stress drop determined from average slip and fault area assuming a smooth fault plane, via Eq.(8). Fig.9 shows the slip velocities of the earthquakes listed in Table 2 plotted against the global stress drop listed in the P-B table. The points are more scattered than in Fig.8, but fall rougly around the relations specified by Eq.(8). This compatibility between the global stress drop and slip velocity has been pointed out previously by Abe (1975), Geller (1976) and Ohnaka (1978).

In view of the fact that the global stress drop fails to explain the observed rms acceleration as demonstrated by Hanks and McGuire (1981), it is natural to conclude that the slip velocity compatible with the global, stress drop cannot explain the observed strong motion.

The local stress drop (or its associated slip velocity) determines the level of the Fourier acceleration spectrum and the corresponding power spectrum. The evaluation of peak acceleration or rms acceleration, however, requires another parameter that defines the bandwidth of the acceleration spectrum. For example, if we use the model of Papageorgiou and Aki, which is based on the solution of Sato and Hirasawa (1973) for a circular crack, the level of the acceleration power spectrum P_0 observed at a distance r_0 from an earthquake source can be written as

$$P_0 \sim \text{const} \,.\, W \,.\, V \,.\, v^4 \,.\, \left(\frac{\Delta\sigma}{\mu}\right)^2 \left(\frac{1}{\beta r_0}\right)^2, \tag{9}$$

where W is the fault width, V is the velocity of the rupture front along the fault length (sweeping velocity), v is the velocity of rupture spreading within a circular crack, $\Delta\sigma$ is the local stress drop, μ is the rigidity and β is the shear wave velocity.

If the acceleration spectrum is band-limited between f_0 and f_{max}, the rms acceleration α_{rms} can be written (Aki and Richards, 1980, p.493) as

$$\alpha_{rms} = \{P_0 \; 2(f_{max} - f_0)\}^{1/2} \tag{10}$$

If $f_{max} \gg f_0$, we get approximately

$$\alpha_{rms} = \{P_0 \; 2f_{max}\}^{1/2} \tag{11}$$

From (9) and (11), we find that two major factors controlling the acceleration amplitudes are the local stress drop $\Delta\sigma$ and the cut-off frequency f_{max}. In the next section, we shall investigate f_{max}.

5. f_{max} AND THE SCALING LAW OF EARTHQUAKE SOURCE SPECTRA AT HIGH FREQUENCIES

A direct study of the cut-off frequency f_{max} of acceleration spectra has been done only for a small number of earthquakes. As shown in Table 1, the values of f_{max} for several California earthquakes (M_L ranges from 5.5 to 7.2) determined by Papageorgious and Aki are nearly constant at

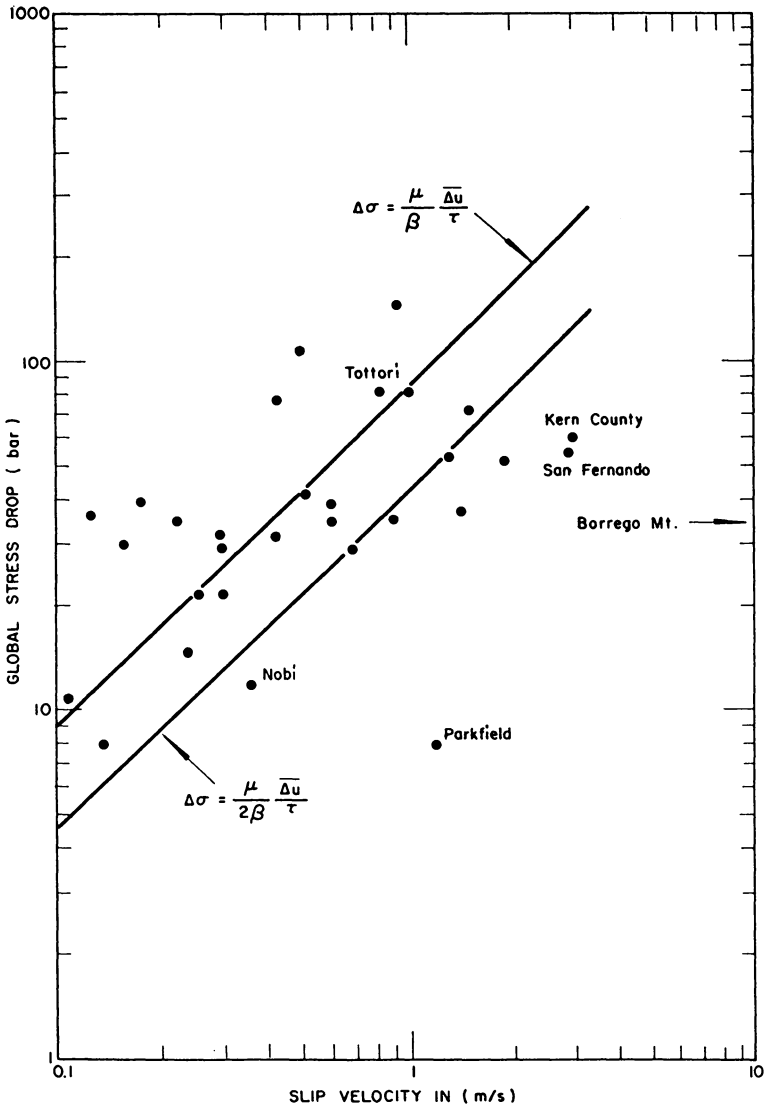

Figure 9. Relation between the global stress drop and the slip velocity. The lines define the theoretical range give by equation (8) for the local (not global) stress dr and slip velocity. The earthquakes with names corres to those also shown in Fig.8.

about 4 ~ 5 Hz, except for the largest one (Kern Country) which showed f_{max} of 2.5 Hz. We would like to know if this apparent stability of f_{max} is a universal phenomenon.

One source of information relevant to this problem is the so-called "source spectra" and their scaling law-that is, how they change with earthquake size. The source spectra may be defined as the Fourier transform $M_0(\omega)$ of the time-derivative of the seismic moment function $\dot{M}_0(t)$ of an equivalent point source of an earthquake. If the medium between the earthquake and the observer is homogeneous, the far-field body wave displacement will have the form of $\dot{M}_0(t)$. Thus the source spectrum can be considered as proportional to the Fourier transform of the far-field body wave displacement to be observed from the earthquake, if the earthquake source were placed in a homogeneous medium with properties similar to the source volume. There have been numerous studies on $\dot{M}_0(\omega)$ for earthquakes of various sizes and regions and wide range of frequency.

Results of three recent studies on $\dot{M}_0(\omega)$ by Nuttli (1981a), Koyama et al. (1982) and Gusev (1982) are compared in Fig.10 with an earlier result of Aki (1972), which is based on revising the ω^2-model (Aki, 1967) on the basis of the observed $m_b - M_s$ relation.

Nuttli's result is based on the observed relation among m_b, M_s and M_0 and shows a significant different in the scaling law between earthquakes in mid-plate and those at plate margins. For mid-plate earthquakes the seismic moment M varies as the inverse fourth power of the corner frequency, The results of Koyama et al. (1982) are for Japanese earthquakes and are based on the relation among m_b, M_s, M_{JMA} (magnitude determined at the Japan Meteorological Agency using the instrument with peak response at a period of about 4 seconds).

Gusev's (1982) results cover a greater frequency range than the others, and are based not only on the relation among various magnitude scales (including 1 Hz band ChISS magnitude, m_{pv}^{sk}, m_{pv}^{skM}, M_{LH}, M_s, and M_{JMA} through the work of Koyama et al., 1982), but also accelerogram spectra for the western United States compiled by Trifunac (1976). Gusev's results are compared with the others in Fig.10, but are also displayed in more detail in Fig.11.

Figs.10 and 11 demonstrate the existence of a pronounced "knee" in the source spectra for large (M~8) earthquakes at a frequency around 0.2Hz. At frequencies above 10 Hz, the observed accelerogram spectra fall down sharply. Thus, we see a bump in the source spectrum between about 0.2 and about 10 Hz. This bump may be interpreted as the presence of strong heterogeneity on the fault plane with a range of scale length from about 20 km to a few hundred meters.

There are two independent observations supporting the above interpretation. One is the observed frequency dependence of the apparent attenuation Q^{-1} of S waves in the lithosphere (Aki, 1980,1981). The Q^{-1} curve peaks at a frequency between 0.1 and 1 Hz, depending on the region. A tectonically active region appears to show a greater Q^{-1} peak at a relatively higher frequency. The observed frequency dependence of Q^{-1} has been explained by Sato (1982) as a loss due to scattering in a random medium. The heterogeneities causing the attenuation of S waves by scattering may be responsible for generating high acceleration when a fault plane slips in such a heterogeneous medium.

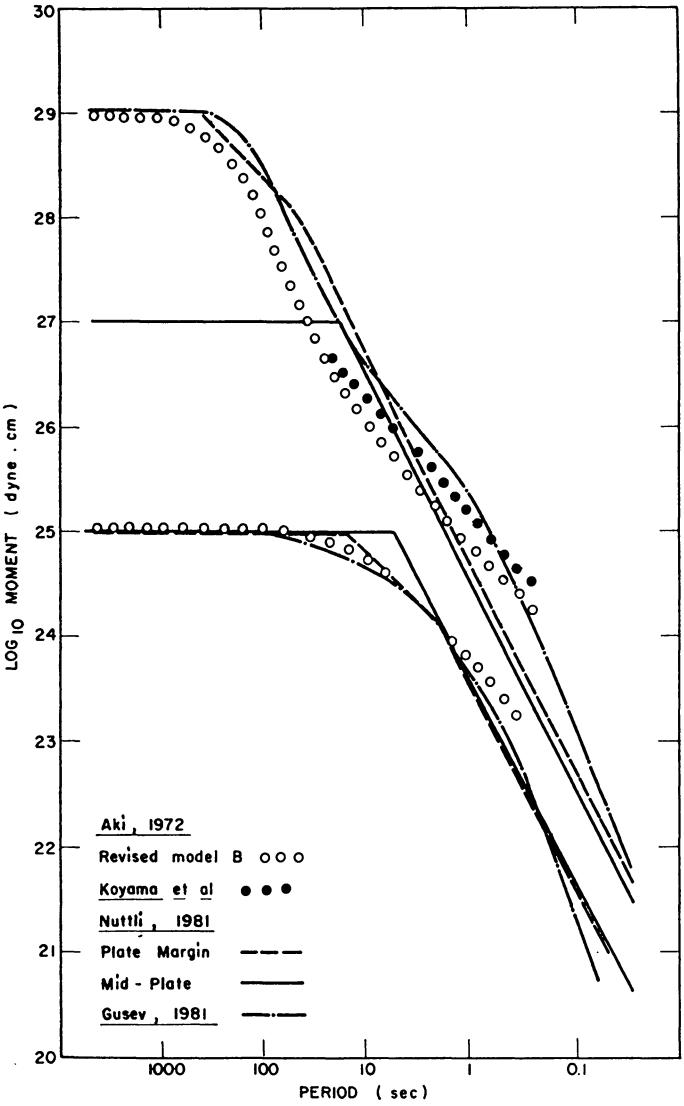

Figure 10. The source spectra $\dot{M}_o(\omega)$ estimated by various authors plotted against period in sec for earthquakes with seismic moment 10^{29} and 10^{25} dyne cm. The spectra for midplate earthquakes are shown for earthquakes with moment 10^{27} and 10^{25} dyne cm.

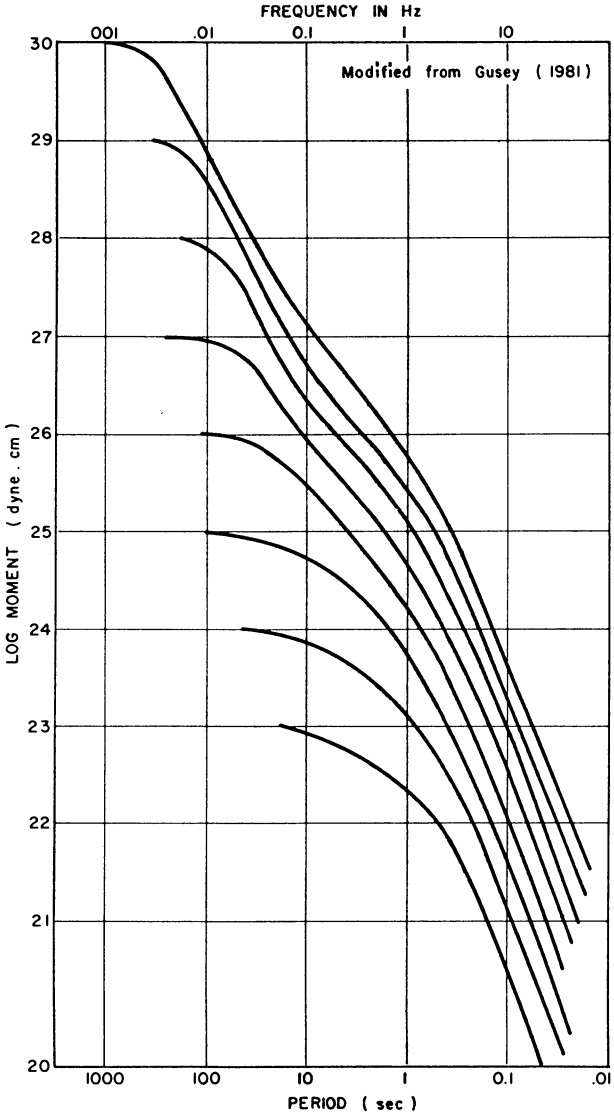

Figure 11. The source spectra $\dot{M}_o(\omega)$ obtained by Gusev (1981) for earthquakes with the range of seismic moment from 10^{23} to 10^{30} dyne cm.

The other relevant observation is the tendency for the corner frequency of very small earthquakes ($M < 2 \sim 3$ or $M_0 < 10^{19-20}$) in several areas become constant at around 10 Hz over a considerable range of seismic moment. This has been observed by Chouet et al. (1978) for various regions of the earth, and in fact was one of the motivations for developing the barrier model of Aki et al. (1977). Similar results have been observed also by Rautian and Khalturin (1978) for earthquakes in the Garm region, U.S.S.R., By Tucker and Brune(1976) for San Fernando aftershocks, by Bakun et al.(1976) for central California earthquakes, by Fletcher (1980) for Oroville, California aftershocks, by Spottiswoode and McGarr (1975) for South Africa mine tremors, and by Archuleta et al. (1981) for the Mammoth Lakes, California, earthquake sequence.

The corner frequency cannot remain constant for indefinitely smaller earthquakes as we know from the pioneering work of Asada (1957) that ultra-microearthquakes contain waves with frequencies around 100 Hz. So, the corner frequency must eventually increase beyond 10 Hz as the earthquake size decreases in any of the above regions. But the fact that it remains constant over a considerable range of seismic moment is consistent with our interpretation that the fault heterogeneity responsible for seismic generation decreases sharply for scale-lengths less than a few hundred meters (corresponding to about 10 Hz). This limiting scale length appears to play the role of the cut-off frequency for acceleration spectra of large earthquakes. It may be that the cohesive force hypothesized by Aki (1979) in the end zone of a fault rupture front acts over relative motions among blocks a few hundred meters in size.

I feel that we are now beginning to have a useful physical model for predicting high-frequency strong motion due to large earthquakes. Heterogeneity seems to be the key word. The heterogeneity of a fault plane responsible for strong motion seems also to be causing strong scattering of seismic waves. The heterogeneity responsible for the cut-off frequency of acceleration spectra of large earthquakes. For these reasons, I believe that the study of the heterogeneous structure of the lithosphere and the study of the source spectra of very small earthquakes may be useful for the prediction of strong motion by large earthquakes.

6. FUTURE PROBLEMS

As mentioned in the introduction, our goal is to predict strong ground motion from a basic understanding of fault mechanics and seismic wave propagation in the earth. Although we have made some progress, it will take a great effort and a long time to accomplish this goal. The demand from earthquake engineers, however, cannot wait so long.

One of the urgent problems in strong motion seismology is to predict the upper bounds on ground motion for a given site. This difficult task must be shared with geologists. The strategy would be to find the maximum possible fault length and width (depth in the case of a vertical fault) that can break a given section of a mapped active fault. Trenching and other archeo-seismological methods would be applied to find the maximum possible amount of fault slip along the section.

Once the expected maximum slip is found, the observed stability of local stress drop may be used to find the barrier interval or crack size. The stability of cut-off frequency, or f_{max}, would allow the extrapolation of this parameter to a larger slip. The dependence of the barrier interval and f_{max} on local geology and mechanical properties of rocks in the fault zone should be studied for a reliable estimation of these parameters.

Once these parameters (length, width, slip, barrier interval and f_{max}) are known, the time history can be calculated for the low-frequency part of strong motion at any site to which deterministic modelling applies and the power spectrum can be calculated for the high-frequency part to which stochastic modelling applies. As an example, Bouchon and Aki (1980) reconstructed the seismic motion generated by the 1857 great California earthquake for frequencies lower than 0.2 Hz deterministically, using the fault silip determined by Sieh (1978). With the increase of information about detailed fault behavior, the transition frequency between the two modelling regions can be pushed upward.

Another important problem in strong motion seismology is to extend the results obtained from California earthquakes to other parts of the world, such as the eastern U.S., for the purpose of strong motion prediction.

As shown in Fig.10, according to Nuttli (1981a) the scaling law of seismic spectra may be different between plate-margin earthquakes and mid-plate earthquakes, suggesting a higher stress drop for the latter. A higher stress drop corresponds to shorter duration of rupture process at the earthquake source. For example, from a teleseismic waveform study, Stewart and Helmberger (1981) found that the Bermuda earthquake of 1978 (similar to the Boston earthquake of 1755 in tectonic setting) had a duration of only 3 seconds at the source, which is relatively short for an earthquake with a seismic moment of about 3×10^{25} dyne cm.

Another subtle difference is that earthquakes in the eastern and central U.S. do not usually rupture to the surface whereas many western U.S. earthquakes do.

A more distinct difference between the eastern and western United States is in the attenuation of seismic amplitude with distance. In general, the attenuation is much less for the eastern U.S. than for the western U.S. The difference is strong for frequencies around 1 Hz and diminishes with increasing frequency. This means that the frequency dependence of attenuation is different between the two regions. In the western U.S., attenuation is roughly independent of frequency. This justifies the conventional practice of using the same shape of response spectra independent of distance for California earthquakes. In the eastern U.S., on the other hand, higher frequencies attenuate faster with propagation distance than do lower frequencies. Thus, as pointed out by Nuttli (1981b), the same shape of response spectra cannot be used for all distances. This effect must be taken into account when the California response spectra are applied to the eastern U.S.

Because of the extremely low attenuation in the eastern U.S. as compared to California, seismic waves travelling along multitudes of paths through the heterogeneous lithosphere of the Earth arrive at an observation site with significant amplitude. This effect tends to make the duration of shaking longer, although the source duration may be

shorter in the eastern U.S., as mentioned above. The unusually long duration (4 1/2 minutes) observed by Winthrop (1757) for the Boston earhquake of 1755 may be due to this multipath scattering effect. Such an effect is not strong in California, where the duration of strong shaking primarily represents the duration of the rupture process.

Thus, a correct undestanding of seismic wave generation and propagation in each region is absolutely essential before applying the empirical results obtained in one region to other regions. I believe that the strong motion records obtained in California can be translated to sites in the eastern and central U.S., by identifying these differences and correcting for them.

ACKNOWLEDGEMENT

This work was supported in part by the National Science Foundation under Grant No.RFP 8005720.

REFERENCES

Abe, K. (1974). Seismic displacement and ground motion near a fault: The Saitama earthquake of September 21, 193, J. Geophys. Res., 79, 4393-4399.

Abe, K. (1975). Static and dynamic fault parameters of the Saitama earthquake of July 1, 1968, Tectonophysics, 27, 223-238.

Abe, K. (1978). Dislocations, source dimensions and stresses associated with earthquakes in the Izu Peninsula, Japan, J.Phys.Earth. 26, 253-274.

Achenbach, J.D. and J.H.Harris (1980). Focusing of ground motion due to curved rupture fronts, presented at the USGS-NRC workshop on strong motion, Lake Tahoe, October 1981.

Aki, K. (1967). Scaling law of seismic spectrum, J. Geophys. Res., 72, 1217-1231.

Aki, K. (1968). Seismic displacement near a fault, J.Geophys. Res., 73, 5359-5376.

Aki, K. (1972). Scaling law of earthquake source time function, Geophys. J.Roy. Astron. Soc., 31, 3-25.

Aki, K. (1979). Characterization of barriers on an earthquake fault, J. Geophys. Res., 84, 6140-6148.

Aki, K. (1980). Scattering and attenuation of shear waves in the lithosphere, J. Geophys. Res., 85, 6496-6504, 1980.

Aki, K. (1981). Attenuation and scattering of short-period seismic waves

in the lithosphere, in Identification of Seismic Sources-Earthquake or Underground Explosion (eds. E.S. Husebye and S. Mykkeltveit), 515-541, D. Reidel Publishing Co.

Aki, K., M.Bouchon, B.Chouet, and S.Das (1977). Quantiative prediction of strong motion for a potential earthquake fault, Annali di Geofisica, 30, 341-368.

Aki, K. and K.L.Larner (1970). Surface motion of a layered medium having an irregular interface due to incident plane SH waves, J.Geophys.Res., 75, 933-954.

Aki, K. and P.G.Richards (1980). Quantitative Seismology, Theory and Methods, W.H.Freeman and Co., San Francisco.

Anderson, J.G. (1974). A dislocation model for the Parkfield earthquake, Bull. Seism. Soc. Am., 64, 671-686.

Anderson, J.G. (1976). Motions near a shallow rupturing fault: evaluation of effects due to the free surface, Geophys. J. Roy. Astron. Soc. 46, 575-593.

Anderson, J.G. and P.G.Richards (1975). Comparison of strong ground motion from several dislocation models, Geophys. J. Roy. Astron. Soc., 43, 347-373.

Andrews, D.J. (1981). A stochastic fault model, 2. Time-dependent case, J.Geophys. Res., 86, 10821-10834.

Archuleta, R.J. and S.M. Day (1977). Near-field particle motion resulting from a propagating stress-relaxation over a fault embedded within a layered medium. Trans. Amer. Geophys. Union, 58, 445.

Archuleta, R.J. and S.M.Day (1980). Dynamic rupture in a layered medium: The 1966 Parkfield earthquake, Bull. Seis. Soc. Am., 70, 671-690.

Archuleta, R.J. and G.A. Frazier (1978). Three-dimensional numerical simulations of dynamic faulting in a half-space, Bull. Seism. Soc. Am., 68, 541-572.

Archuleta, R.J., P.Spudich, E.Cranswick and C.Mueller (1981). Source parameters of the 1980 Mammoth Lakes, California, earthquake sequence, preprint.

Bakun, W.H., C.G.Bufe and R.M.Stewart (1976). Body wave spectra of central California earthquakes, Bull. Seis. Soc. Am., 66, 439-459.

Bard, P.Y. and M.Bouchon (1980a). The seismic response of sediment-filled valleys, Part 1: The case of incident SH waves, Bull. Seis. Soc. Am., 70, 1263-1286.

Bard, P.Y. and M.Bouchon (1980b). The seismic response of sediment-

filled valleys, Part 2: The case of incident P and SV waves, Bull. Seis. Soc. Am., 70, 1921-1941.

Barker, J.S. and C.A. Langston (1981). Inversion of teleseismic body waves for the moment tensor of the 1978 Thessaloniki, Greece, earthquake, Bull. Seis. Soc. Am., 71, 1423-1444.

Ben-Menahem, A., (1961). Radiation of seismic surface waves from finite moving sources, Bull. Seis. Soc. Am., 51, 401-435.

Blandford, R.R. (1975). A source theory for complex earthquakes, Bull. Seis. Soc. Am., 65, 1385-1405.

Boore, D.M. (1972). Finite difference methods for seismic wave propagation in heterogeneous materials, in Seismology: Surface Waves and Earth-Oscillations (Methods in Computational Physics, Vol.II), B.A. Bolt, Editor, Academic Press, New York.

Boore, D.M. and W.B. Joyner (1978). The influence of rupture incoherence on seismic directivity, Bull. Seis. Soc. Am., 68, 283-300.

Boore, D.M. and M.D.Zoback (1974). Near-field motions from kinematic models of propagating faults, Bull. Seism. Soc. Am., 64, 321-342.

Bouchon, M. (1978). A dynamic source model for the San Fernando earthquake, Bull. Seism. Soc. Am., 68, 1555-1576.

Bouchon, M. (1979a). Discrete wavenumber representation of elastic wave fields in three space dimensions, J. Geophys. Res., 84, 3609-3614.

Bouchon, M. (1979b). Predictability of ground displacement and velocity near an earthquake fault. An example: The Parkfield earthquake of 1966, J. Geophys. Res., 84, 6149-6156.

Bouchon, M. (1980). The motion of the ground during an earthquake, 2. The case of a dip-slip fault, J.Geophys. Res., 85, 367-375.

Bouchon, M. (1981). The rupture mechanism of the Coyote Lake earthquake of August 6, 1979, inferred from near-field data, presented at the USGS-NRC workshop on strong motion, Lake Tahoe, Oct. 1981.

Bouchon, M. and K.Aki (1977). Discrete wave-number representation of seismic-source wave fields, Bull. Seism. Soc. Am., 67, 259-277.

Bouchon, M. and K.Aki (1980). Simulation of long-period, near-field motion for the great California earthquake of 1857, Bull. Seism. Soc. Am., 70, 1669-1682.

Brune, J.N. (1970). Tectonic stress and spectra of seismic shear waves from earthquakes, J. Geophys. Res., 75, 4997-5009.

Burdick, L.J. (1977). Broad-band seismic studies of body waves, Ph.D. thesis, California Institute of Technology.

Burdick, L.J. and G.R. Mellman (1976). Inversion of the body waves from the Borrego mountain earthquake to the source mechanism, Bull. Seis. Soc. Am., 66, 1485-1499.

Burridge, R. and L. Knopoff (1964). Body force equivalents for seismic dislocations, Bull. Seis. Soc. Am., 54, 1875-1888.

Burridge, R. and R.Moon (1981). Slipping on a frictional fault plane in three dimensions: a numerical simulation of a scaler analogue, Geophys. J.Roy. Astron. Soc., 67, 325-342.

Chouet, B., K.Aki and M. Tsujiura (1978). Regional variation of the scaling law of earthquake source spectra, Bull. Seis. Soc. Am., 68, 49-79.

Cipar, J. (1979). Source processes of the Haicheng, China earthquake from observations of P and S waves, Bull. Seis. Soc. Am., 69, 1903-1916.

Das, S. and K.Aki (1977). Fault planes with barriers: a versatile earthquake model, J. Geophys. Res., 82, 5648-5670.

Day, S.M. (1979). Three-dimensional finite difference simulation of fault dynamics, Final Report SSS-R-80-4295, Systems, Science and Software, La Jolla, California.

Der, Z.A. (1981). Q of the earth in the 0.5-10 Hz band, EOS, 62, 333.

Der, Z.A. and T.W.McElfresh (1980). On the value of t_p^* and t_s^* in the short-period band and regional variations of the same across the United States, Bull. Seis. Soc. Am., 70, 921-924.

Deschamps, A., Y.Gaudemer, and A.Cisternas (in press). El Asnam earthquake of Oct. 10, 1980 (preprint).

Ebel, J. and D.V.Helmberger (1982). P-wave complexity and fault asperities: The Borrego mountain, California, earthquake of 1968, Bull. Seis. Soc. Am., 72, 413-438.

Fletcher, J. B. (1980). Spectra from high-dynamic range digital recordings of Oroville, California, aftershocks and their source parameters, Bull. Seis. Soc. Am., 70, 735-755.

Florensov, N. A., and V.P. Solonenko (1963). The Gobi-Altai Earthquake, Akad. Nauk SSSR, Moscow.

Fukao,Y. (1979). Tsunami earthquakes and subduction processes near deep-sea trenches, J.Phys. Earth.,84, 2303-2314.

Fukao, Y., and M.Furumoto (1979). Stress drops, wave spectra and recurrence intervals of great earthquakes - implications of the Etorofu earthquake of 1958, November 6, Geophys. J.Roy. Astron. Soc., 57, 23-40.

Furumoto, M. (1979). Initial phase analysis of R waves from great earthquakes, J. Geophys. Res., 84, 6867-6874.

Gusev, A.A. (1982). Descriptive statistical model of the earthquake source radiation and its application to estimation of the short-period strong motion, Geophys. J.Roy. Astron. Soc., in press.

Hanks, T.C. (1979a). b value and ω-γ seismic source models: implications for tectonic stress variations along active crustal fault zones and the estimation of high-frequency strong ground motion, J.Geophys. Res., 86, 2235-2242.

Hanks, T.C. (1979b). Seismological aspects of strong motion seismology Proc. 2nd U.S. National Conference on Earthquake Engineering, Earthquake Engineering Institute, 898-912.

Hanks, T.C. and R.K. McGuire (1981). The character of high frequency strong ground motion, Bull. Seis. Soc. Am., 71, 2071-2096.

Hartzell, S. (1978). Earthquake aftershocks as Green's functions, Geophys. Res. Letters, 5, 1-4.

Hartzell, S. H., G.Frazier, and J.N.Brune (1978). Earthquake modelling in a homogeneous half-space, Bull. Seism. Soc. Am., 68, 301-316.

Hartzell, S.H., and D.V.Helmberger (1982). Strong-motion modeling of the Imperial Valley earthquake of 1979, Bull. Seis. Soc. Am., 72, 571-596.

Haskell, N.A. (1969). Elastic displacements in the near-field of a propagating fault, Bull. Seism. Soc. Am., 59, 865-908.

Heaton, T.H. and D.V. Helmberger (1977). A study of the strong motion of the Borrego Mountain, California earthquake, Bull. Seism. Soc. Am. 67, 315-330.

Heaton, T.H., and D.V. Helmberger (1978). Predictability of strong ground motion in the Imperial Valley: modeling the M 4.9 November 4, 1976 Brawley earthquake, Bull. Seism. Soc. Am., 68, 31-48.

Heaton, T.H., and D.V.Helmberger (1979). Generalized ray models of the San Fernando earthquake, Bull.Seis. Soc. Am., 69, 1331-1341.

Hirasawa, T. (1965). Source mechanism of the Niigata earthquake of June 16, 1964 as derived from body waves, J.Phys. Earth, 13, 35-66, 1965.

Hong, T.L. and D.V.Helmberger (1978). Glorified optics and wave propagation in nonplanar structure, Bull.Seis.Soc.Am., 68, 1313-1358.

Housner, G.W. and M.D. Trifunac (1967). Analysis of accelerograms-Parkfield earthquake, Bull. Seis. Soc. Am., 57, 1193-1220.

Israel, M. and R.L.Kovach (1977). Near-field motions from a propagating strike-slip fault in an elastic half-space, Bull. Seism. Soc. Am., 67, 977-994.

Kanamori, H. (1972). Determination of effective tectonic stress associated with earthquake faulting. The Tottori earthquake of 1943, Phys. Earth Planet. Interiors, 5, 426-434.

Kanamori, H. (1973). Mode of strain release assoiated with major earthquakes in Japan, Annu. Rev. Earth Planet. Sci., 1, 213-239.

Kanamori- H. (1979). A semi-empirical approach to prediction of long-period ground motions from great earthquakes, Bull. Seis. Soc. Am., 69, 1645-1670.

Kanamori, H., and D.L. Anderson (1975). Theoretical basis of some empirical relations in seismology, Bull. Seis. Soc. Am., 65, 1073-1095.

Kanamori, H. and G.S.Stewart (1976). Mode of the strain release along the Gibbs fracture zone, Mid-Atlantic ridge, Phys. Earth. Planet. Inter., 11, 312-332.

Kanamori, H., and G.S.Stewart (1978). Seismological aspects of the Guatemala earthquake of Feb.4, 1976, J.Geophys. Res., 83, 3427-3434.

Kasahara, K. (1964). A strike-slip fault buried in a layered medium, Bull. Earthq. Res. Inst., Tokyo Univ., 42, 609-620.

Kawasaki, I. (1975). The focal process of the Kitamino earthquake of August 19, 1961, and its relationship to a Quaternary fault, the Hatogyu-Koike fault, J.Phys. Earth, 23, 227-250.

Kawasaki, I. (1975). On the dynamical process of the Parkfield earthquake of June 28, 1966, J.Phys. Earth, 23, 127-144.

Kawasaki, I., Y.Suzuki, and R.Sato (1975). Seismic waves due to a shear fault in a semi-infinite medium. Part II: moving source, J.Phys. Earth, 23, 43-61.

Koyama, J., M.Takemura, and Z.Suzuki (1982). A scaling model for quantification of earthquakes in and near Japan, Tectonophysics, 84, 3-16.

Langston, C.A., A body wave inversion of the Koyna, India, earthquake of December 10, 1967, and some implications for body wave focal mechanisms, J.Geophys. Res., 81, 2517-2529.

Langston, C.A. (1978). The February 9, 1971 San Fernando earthquake: a study of source finiteness in teleseismic body waves, Bull.Seis.Soc.Am., 68, 1-29

Lay, T. and H.Kanamori (1980). Earthquake doublets in the Solomon Islands, Phys. Earth Planet. Inter., 21, 283-304.

Levy, N.A. and A.K.Mal (1976). Calculation of ground motion in a three-dimensional model of the 1966 Parkfield earthquake, Bull.Seism.Soc.Am., 66, 403-423.

Li, V.C. and R.Dmowska (1981). Asperity model for precursory seismicity patterns for some large earthquakes, EOS, 62, No.17, p.328.

Lysmer, J. and L.A.Drake (1972). A finite element method for seismology, in Seismology: Surface Waves and Earth Oscillations (Methods in Computational Physics, Vol.II), B.A.Bolt, Editor, Academic Press, New York

Madariaga, R.(1976). Dynamics of an expanding circular fault, Bull.Seis. Soc. Am., 66, 639-666.

Madariaga, R.(1978). The dynamic field of Haskell's rectangular dislocation fault model, Bull. Seism. Soc. Am., 68, 869-887.

Madariaga, R. (1981). A string model for the high frequency radiation from earthquake faulting, presented at the USGS-NRC workshop on strong motion, Lake Tahoe, Oct. 1981.

Maruyama, T.(1963). On the force equivalents of dynamic elastic dislocations with reference to the earthquake mechanism, Bull. Earthq. Res. Inst., Tokyo Univ., 41, 467-486.

Matsuda, T.(19--). Surface faults associated with Kita-Izu earthquake of 1930 in Izu Peninsula, Japan, in The Izu Peninsula (ed.M. Hoshino and H.Aoki), Tokai Univ. Press, Tokyo.

Matsuda, T.(1974). Surface faults associated with Nobi (Mino-Owari) earthquake of 1891, Japan, Sokuho (in Japanese), Earthq.Res.Inst.Univ. Tokyo, 13, 85-126.

Matsuda, T.(1976). Active faults and earthquakes, the geological aspects, Chishitsugaku-ronshi (in Japanese), 12, 15-32.

Matsuda, T. and K.Yamashina (1974). Surface faults associated with the Izu-Hanto-Oki earthquake of 1974, Japan, Sokuho (in Japanese), Earthq. Res.Inst. Univ. Tokyo, 14, 135-158.

Matsuda, T., K.Yamazaki, T.Nakata and T.Imaizumi (1980). The surface faults associated with the Rikuu earthquake of 1896, Bull. Earthq. Res. Inst., Univ. Tokyo, 55, 795-856.

McGuire, R.K. and T.C.Hanks (1980). RMS accelerations and spectral amplitudes of strong ground motion during the San Fernando, California earthquake, Bull. Seis. Soc. Am., 70, 1907-1919.

Mikumo, T. (1973). Faulting mechanism of the Gifu earthquake of September 9, 1969, and some related problems, J.Phys. Earth, 21, 191-212.

Mikumo, T. (1974). Some considerations on the faulting mechanism of the southeastern Akita earthquake of Oct.16, 1970, J.Phys.Earth. 22, 87-108.

Mikumo, T., and M.Ando (1976). A search into the faulting mechanism of the 1891 Great Nobi earthquake, J.Phys. Earth, 24, 63-87.

Mikumo, T., and T.Miyatake (1978). Dynamic rupture process on a three-dimensional fault with non-uniform frictions and near-field seismic waves, Geophys. J.Roy. Astron, Soc., 54, 417-438.

Niazy, A. (1973). Elastic displacements caused by a propagating crack in an infinite medium: an exact solution, Bull. Seism. Soc. Am., 63, 357-379.

Niazy, A.(1975). An exact solution for a finite, two-dimensional moving dislocation in an elastic half-space, with application to the San Fernando earthquake of 1971, Bull. Seism. Soc.Am., 65, 1797-1826.

Nuttli, O.W. (1981a). Empirical spectral scaling relations for mid-plate and inter-plate earthquakes, abstract of paper presented at meeting of International Association of Seismology and Physics of Earth's Interior, London, Ontario, Canada, July 1981.

Nuttli, O.W. (1981b). Similarities and Differences between Western and Eastern United States Earthquakes, and their consequences for Earthquake engineering, Proc. of Earthquake and Earthquake Engineering: The Eastern U.S., Sept. 1981, Knoxville, Tennessee, 25-52.

Ohnaka, M.(1976). Rise time of source time function and average slip velocity, Zisin (in Japanese), 29, 318-320.

Ohnaka, M.(19--). Application of some dynamic properties of stick-slip to earthquakes, Geophys.J.Roy.Astron. Soc., 53, 311-318.

Olson, A.H. (1982). Forward simulation and linear inversion of earthquake ground motion, Ph.D. thesis, Univ. of California (San Diego, CA).

Papageorgiou, A. and K.Aki (1981). A specific barrier model for the quantitative description of inhomogeneous faulting and the prediction of strong ground motion, presented at the USGS-NRC workshop on strong motion, Lake Tahoe, Oct.1981.

Purcaru, G. and H.Berckhemen (1982). Quantitative relations of seismic source parameters and an attempt for the classification of earthquakes, Tectonophysics, 84, 57-128.

Rautian, T.G. and V. I. Khalturin (1978). The use of coda for determination of the earthquake spectrum, Bull.Seis.Soc.Am., 68, 923-948.

Rial, J.A. (1978). The Caracas, Venezuela, earthquake of July 29, 1967: A multiple source event, J.Geophys. Res., 83,5405-5414.

Richards, P.G. (1976). Dynamic motions near an earthquake fault: a three-dimensional solution, Bull.Seism.Soc.Am., 66, 1-32.

Sanchez-Sesma, F.J. and J.A.Esquivel (1979). Ground motion on alluvial valley under incident plane SH waves, Bull.Seis.Soc.Am., 69, 1107-1120.

Sato, H.(1982). Attenuation of S waves in the lithosphere due to scattering by its random velocity structure, J.Geophys. Res., in press.

Sato, T. and T.Hirasawa (1973). Body wave spectra from propagating shear cracks, J.Phys.Earth, 21, 415-431.

Shakal, A.F. (1979). Analysis and modelling of the effects of the source and medium on strong motion, Ph.D. thesis, Massachusetts Institute of Technology, Cambridge, Mass.

Sieh, K.E. (1978). Slip along the San Andreas fault associated with the great 1857 earthquake, Bull. Seis.Soc.Am., 68, 1421-1448.

Shiono, K. and T.Mikumo (1975). Tectonic implications of subcrustal, normal faulting earthquakes in the western Shikoku region, Japan, J.Phys. Earth, 23, 257-278.

Somerville, P.(1980). Earthquake mechanisms at the head of the Phillippine Sea plate beneath the southern Kanto District, Japan, J. Phys.Earth, 28, 393-408.

Soufleris, C., and G.S.Stewart (1981). A source study of the Thessaloniki (northern Greece) 1978 earthquake sequence, Geophys. J.Roy. Astron. Soc., 67, 343-358.

Spottiswoode, S.M., and A.McGarr (1975). Source parameters of tremors in a deep-level gold mine, Bull. Seis.Soc.Am., 65, 93-112.

Stewart, G.S. and D.V.Helmberger (1981). The Bermuda earthquake of March 24, 1978: A significant oceanic intraplate event, J.Geophys.Res., 86, 7027-7036.

Swanger, H.J. and D.M.Boore (1978). Simulation of strong-motion displacements using surface-wave modal superposition, Bull.Seis. Soc. Am., 68, 907-922.

Tchalenko, J.S., and M.Berberian (1975). Dasht-e Beyaz fault, Iran: earthquake and earlier related structure in bedrock, Geol. Soc. Am.Bull., 86, 703-709.

Trifunac, M.D.(1974). A three-dimensional dislocation model for the San Fernando, California, earthquake of 1971, Bull.Seis.Soc.Am., 64, 149-172.

Trifunac, M.D. (1976). Preliminary analysis of the peaks of strong earthquake ground motion, dependence of peaks on earthquake magnitude, epicentral distance and recording site conditions, Bull.Seis.Soc.Am., 66, 189-219.

Trifunac, M.D. and F.E.Udwadia (1974). Parkfield, California, earthquake of June 27,1966: a three-dimensional moving dislocation model, Bull. Seism. Soc. Am., 64, 511-533.

Tsai, Y.B. and H.J.Patton (1973). Interpretation of the strong-motion earthquake accelerograms using a moving dislocation model: The Parkfield, California, earthquake of June 28, 1966, abstract, 68 th annual national meeting of the Seismological Society of America, 1973.

Wallace, R.E. (1968). Notes on stream channels offset by the San Andreas fault, Southern Coast Ranges, California, in Proceedings of Conf. of Geologic Problems of San Andreas fault system, XI, 6-21, Stanford Univ. Press, Palo Alto, California.

Wallace, R.E. (1973). Source fracture patterns along the San Andreas fault, in Proc. Conf. on Tectonic Processes of the San Andreas fault system (ed. R.L. Kovach and A.Nur), Stanford Univ. Press, Palo Alto, California.

Wallace, T.C., D.V.Helmberger, and J.E.Ebel (1981). A broadband study of the 13 August 1978 Santa Barbara earthquake, Bull. Seis. Soc. Am., 71, 1701-1718.

Wesson, R.L., R.O.Burford, and W.L. Ellsworth (1973). Relationship between seismicity, fault creep and crustal loading along the Central San Andreas Fault, Proc.Conf. Tectonic Problems of the San Andreas Fault System, Stanford Univ. Publ. Geolog. Sc., 13, 303-320.

Wiggins, R.A., J.Sweet, and G.A.Frazier (1977). The Parkfield earthquake of 1966 - A study of the dislocation parameters based on a complete modeling of elastic wave propagation, Trans. Amer. Geophys. Union. 58, 1193.

Winthrop, J. (1757). An account of the earthquake felt in New England, and the neighbouring parts of America on the 18th of November 1755, Phil. Trns. London, 50, 1-18.

EARTHQUAKE SOURCE MECHANISMS: CASE STUDIES

M.Nafi Toksöz and Anton M. Dainty
Earth Resources Laboratory, Dept.Earth,
Atmospheric and Planetary Sciences
Massachusetts Institute of Technology,
Cambridge MA 02139, USA

John Nabelek
Lamont Doherty Observatory
Palisades NY 10964, USA

ABSTRACT. Recent studies of earthquake sources using strong motion and teleseismic waveform inversion have demonstrated the importance of asperities and non-uniform slip on the fault plane. The method consists of finding the parameters of a fault model that will reproduce the seismograms to some desired accuracy. The type of information that may be derived is either the moment release as a function of time from teleseismic records or the distribution of slip over the fault plane from strong motion data. We review studies of eleven earthquakes performed by this technique. These studies indicate that asperities and/or regions of high slip dominate the high frequency strong motion, and that this situation is ubiquitous. Events in similar tectonic settings with similar mechanisms display some common patterns. Plate boundary strike-slip earthquakes studied show the strongest asperity at some distance from the hypocenter, whereas thrust earthquakes usually have the largest asperity at or near the hypocenter, which is near the deepest point on the rupture surface. For normal faulting events initial rupture is weak.

1. INTRODUCTION

The ground motion due to an earthquake is determined by three primary factors: earthquake source properties, propagation medium, and the local site conditions. In this paper we review the source properties of some recent earthquakes which have been studied in detail. An important development in this area has been the modelling of the earthquake source as a heterogeneous rupture process, where slip, stress drop and/or the rupture propagation velocity change on the fault surface. These heterogeneities strongly affect the near-field motions and the high frequency radiation.

Models of heterogeneous earthquake sources where slip is irregular over the fault plane have been grouped into two general categories: "Asperity" and "Barrier" type source models (Aki, 1984). Figure 1

M. O. Erdik and M. N. Toksöz (eds.), Strong Ground Motion Seismology, 41–84.
© 1987 oy D. Reidel Publishing Company.

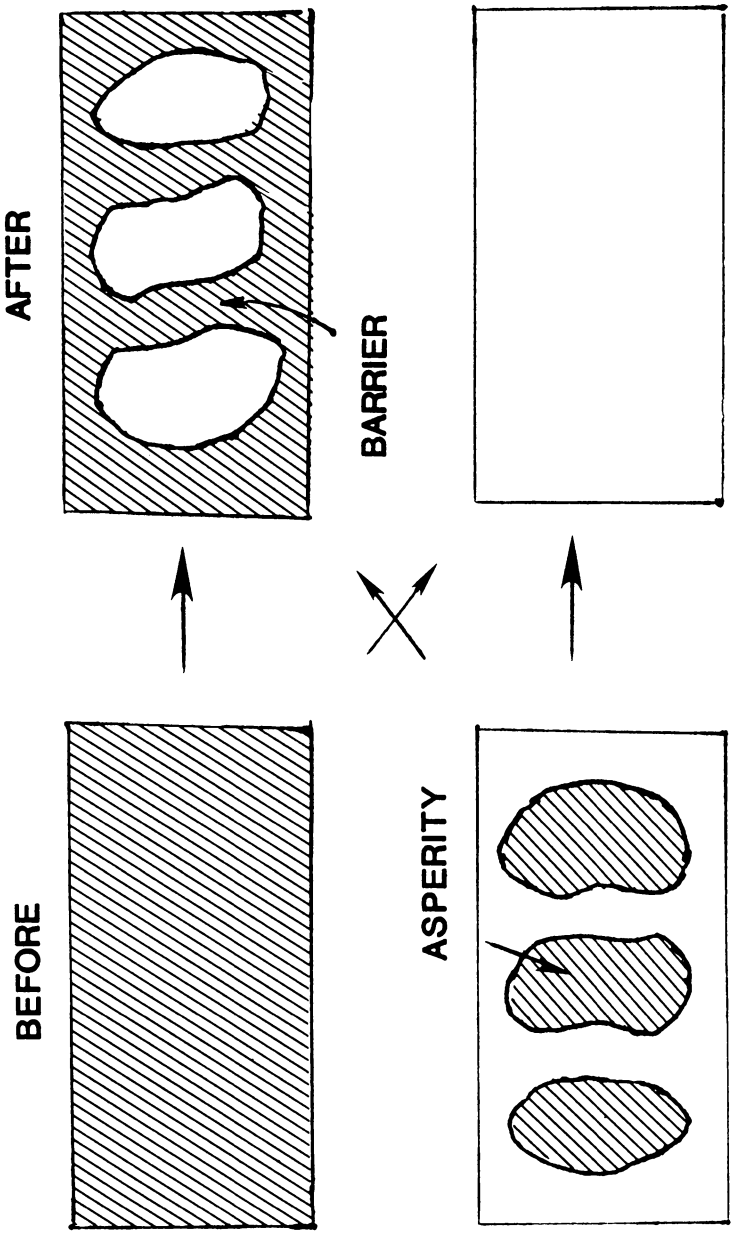

Figure 1. The barrier (top) and asperity (bottom) models. Cross hatching indicates stressed areas. From Aki (1984).

schematically illustrates these models. In the barrier model, weaker patches on the fault plane break during the earthquake but strong regions (i.e., "barriers") remain unbroken. These may eventually break in aftershocks or later earthquakes. In the asperity model, the highly-stressed regions (i.e., "asperities") break and account for most of the high frequency seismic energy radiation. The weaker portions of the fault that may be stressed less may not break at all, or when broken contribute primarily to lower frequency radiation. The rupture may initiate at an asperity or a weak zone (Toksöz and Nabelek, 1984).

Since asperities and barriers are determined by the strength or the friction coefficient distribution over a fault zone repeated earthquakes on a fault segment may be controlled by such fault surface heterogeneities. These may result in self similarity of earthquakes on a given fault, and lead to the "characteristic" earthquakes deduced primarily on the basis of seismological, paleoseismological and geological studies of fault ruptures (Coppersmith and Schwartz, 1983; Matsuda et al., 1980; Schwartz et al., 1981; Schwartz and Coppersmith, 1984; Sieh, 1981; Wallace, 1981).

The dynamic characteristics of heterogenous earthquake source models for prediction of spectral characteristics of ground motion have been studied by a number of investigators (Aki et al., 1977; Andrews, 1980, 1981; Chouet et al., 1978; Das and Aki, 1977; Hanks and McGuire, 1981; Madariaga, 1983; Mikumo and Miyataki, 1978; Papageorgiou and Aki, 1983a,b; Rudnicki and Kanamori, 1981). An important conclusion from these studies is that asperity and barrier models cannot be distinguished on the basis of high-frequency seismic radiation because they give rise to similar spectra (Madariaga, 1983). In the preceeding paper of this volume Aki describes these models in detail. In parallel with and following the spectral models, a new approach is based on matching of the observed near-field and teleseismic waveforms with theoretical synthetics in order to obtain the slip distribution and rupture characteristics of individual earthquakes. In the next section we describe this approach. In the third section we give examples of source characteristics, especially heterogeneous slip distribution over the fault surface, for eleven intermediate and large earthquakes studied by waveform inversion.

2. STUDY OF EARTHQUAKE MECHANISMS FROM STRONG MOTION AND TELESEISMIC WAWEFORM INVERSION

The fundamental method used for both teleseismic and strong motion investigations is to use inverse theory to determine the parameters of a fault model that will reproduce in some optimal sense the seismograms, or at least selected parts of them. To do this, four steps must be accomplished: selection of the data, parameterisation of the fault model, calculation of the seismograms and inversion. Data selection includes not only selecting the stations, but deciding which parts of the seismograms are to be fitted, which components of ground motion, and the frequency range to be used. For teleseismic work, P is always fitted, sometimes S or Raleigh waves. For strong motion seismograms S is used.

Both vertical (P, SV) and horizontal (SV, SH) ground motion components are used for teleseismic investigations. For strong motion records, the vertical component has proven difficult to model because of the influence of high frequency P radiation, and thus most investigators have concentrated on the horizontal components. Long period (0.01 to 0.1 Hz) teleseismic seismograms are widely used and short period (0.1 to 1 Hz) seismograms are increasingly being studied. Strong motion recordings contain frequencies up to 25 Hz, but it is usually necessary to restrict the frequency range to not much more than 1 Hz for reliable results. Another decision that must be made with strong motion records is whether to use acceleration, velocity or displacement records; velocity is the usual choice.

The most important and crucial part of the method is the parameterisation of the fault model. All investigations seek to determine, in some way, the time, location (including depth), moment, fault and slip orientation (Burdick and Mellman, 1976). Equivalently, the moment tensor may be used (Dziewonski et.al.,1981). However, for large events, or especially the higher frequency data from short period teleseismic or strong motion seismograms, the finiteness of the fault and the nature of the rupture process must be parameterised in some way. The simplest method is to model the source as a point source with a time history to be determined from the data (Nabelek, 1984). The total duration in time of the source is mainly controlled by the propagation of the rupture from one end of the fault to the other. The spectrum of the time function which may be controlled by specifying that it be constructed as the sum of some standard function shifted in time (Langston, 1981; Nabelek 1984), represents the effect of source finiteness on the spectrum (Aki and Richards, 1980). Variations of amplitude of the source time function model differing strength of radiation from different regions of the fault. Typically, the moment release as a function of time is determined. A variation of this method is to use more than one point source.

A difficulty with the time function method is that it is not a theoretically correct way to represent rupture propagation - it does not predict the azimuthal variation expected from a propagating rupture, for example. A more complex parameterisation is a line source with a rupture propagating along the line (Langston, 1978; Nabelek, 1984). Not only does this model incorporate rupture propagation, it may easily be extended to handle fault planes that change orientation at some location or movement on more than one fault plane during an earthquake. This method and the preceding method have been successfully applied to teleseismic data.

The most general model of a fault used in waveform inversion is the subfault method. In this parameterisation, the fault plane is split into many small elements (subfaults) each of which is small enough to be considered a point source within the frequency range of the seismograms (Bouchon, 1978; Heaton and Helmberger, 1979; Shakal, 1979; Papageorgiou and Aki, 1983a). The seismogram is calculated as the sum of the contributions from all of the subfaults. In principle, the inversion will determine the slip magnitude, orientation and time history for each subfault, allowing a very detailed picture of the faulting process. Detailed models of this type appear to be necessary to explain strong

motion records. One major requirement of this method is an a priori knowledge of the fault plane and the approximate extent of the faulted area. This information may be acquired from previous teleseismic investigations, geological observations, or aftershock data.

After the fault parameterisation has been decided, the forward problem, i.e., calculation of the seismograms, must be solved. We will not discuss the mathematical theory as it is beyond the scope of this paper - suffice it to say that there are several standard formulations that will calculate the displacement due to arbitrary slip on a fault; appropriate explanations and references are given in the original works. Of more importance here is an understanding of what must be calculated. In addition to the radiation from the fault plane, for teleseismic records the reflections from the earth's surface, crustal layering at the source and receiver, and geometrical spreading and attenuation in the mantle must be considered. For strong motion seismograms, a good model of the local crustal layering is very helpful, and often a neccessity.

The final step is the inversion. The error to be minimised is the difference between the calculated seismograms and the observed seismograms, usually allowing a time shift for station travel time residuals in the case of teleseismic data. Again, we will not discuss the mathematical formulations, which are voluminously discussed in the literature. It should be noted, however, that the data invariably does not allow a complete solution to the problem. One difficulty is caused by finite resolution-the lower frequencies (hence, longer wavelengths) of teleseismic data do not allow determination of the details of slip on the fault. This is usually treated by a judicious choice of the parameterisation - studies using only teleseismic data customarily use either the source time function model or the line source model. A more subtle problem is the inability of the method to distinguish between different rupture effects that produce similar seismograms, i.e., non-uniqueness. An example is the similarity of the effects of an increase in rupture velocity and an increase in slip at some point on a fault. This usually requires that some parameters be specified rather than determined-for example, in the subfault model, the time history of the slip is often partially specified by specifying that the rupture velocity is a fixed percentage of the shear wave velocity. Another common constraint is the requirement that the source time function is always positive, i.e., no back slip is allowed (Nabelek, 1984).

Examples of the quality of fit to the waveforms and the resolvable fault slip distributions are presented in the next section on earthquake examples.

3. EARTHQUAKE EXAMPLES

In this section we discuss a number of examples based on earthquakes where an irregular slip distribution on the fault plane has been determined from the inversion of strong motion and/or teleseismic seismograms. These earthquakes include the 1971 San Fernando earthquake, one of the most extensively studied events. In addition we include the 1979 Imperial Valley and 1984 Morgan Hill earthquakes - two strike-slip earthquakes

whose source heterogeneities have been well-determined from strong motion data. Other examples discussed are the 1976 Guatemala earthquake the 1976 Caldiran earthquake in eastern Turkey, and the 1983 Erzurum(Narman-Horasan) earthquake in northeastern Turkey, all primarily strike-slip events. For thrust mechanism earthquakes we show the source properties of the 1976 and 1984 Gazli earthquakes in Central Asia. For earthquakes on normal faults the 1970 Gediz earthquake in Western Turkey, the 1979 Colombia earthquake, the 1981 Corinth earthquake in Greece, and the 1983 Idaho earthquake in the United States are presented. The list of earthquakes and relevant source information such as epicenter data and magnitudes are listed in Table 1, and the epicenters are shown in Figure 2. All these earthquakes have heterogeneous slip distributions and regions of intense seismic energy radiation or asperities.

1971 San Fernando

The 1971 San Fernando earthquake was the first earthquake for which large numbers of strong motion records were available. As such, it played a key role in the development of techniques for analysing such records to obtain information about earthquakes, and in forming ideas concerning the rupture proess. Accordingly, while many papers have been published on the source mechanism (Dillinger and Espinosa, 1971; Whitcomb, 1971; Allen et al., 1971; Dillinger, 1973; Whitcomb et al., 1973; Alewine, 1974; Boore and Zoback, 1974; Hanks, 1974; Trifunac, 1974; Niazy, 1975; Bouchon, 1978), we shall concentrate on five investigations (Canitez and Toksöz, 1972; Langston, 1978; Heaton and Helmberger, 1979; Shakal, 1979; and Heaton, 1982) with the object of tracing the evolution of techniques and ideas about faulting. Figure 3 (Shakal, 1979) shows the velocity records as well as the ruptured area and the surface rupture for this thrust event.

Canitez and Toksöz (1972) examined P wave first motion, surface wave spectra, and static offsets but did not perform waveform inversions. Their work represents the state of the art before waveform inversion. They presented a model of reverse (thrust) faulting on a plane with a strike of N70°W and a dip of 52°NE with dimensions of 14 by 14 km. Rupture commenced near the bottom of the plane at a depth of 14 km and propagated towards the surface. The slip rake was 45° and the average slip was 2.8 m.

Langston (1978) performed waveform inversion using short and long period P and long SV and SH, all at teleseismic distances. He principally used the line source model with a propagating rupture. Following the suggestion of several authors (Boore and Zoback, 1974; Trifunac, 1974; Niazy, 1975; among others) a fault plane that changed dip with depth was considered. The model derived from the data showed rupture initiating at 13 km depth and propagating bilaterally along a plane dipping at 53°. Strike was N70°W and rake was 76°. Downward propagation stopped at 15 km depth, while the rupture propagated upward until it reached a depth of 5 km. At this point the rupture broke over onto a plane with a dip of 29° and propagated to the surface. Average rupture velocity was 1.8 km/s

Investigations using strong motion records were undertaken by Heaton and Helmberger (1979) and Shakal (1979); we will consider them together. In both cases only a small group of stations was considered

Table 1
Earthquakes Examined

Earthquake Name and Location	Date	Epicenter	Magnitude (Ms)	Moment (dyne cm)	Surface Faulting(km)
San Fernando, U.S.A.	9-2-71	35.5N 118.4W	6.5	1.6×10^{26}	15
Imperial Valley U.S.A.	15-10-79	32.7N 115.3W	6.6	6.7×10^{25}	32
Morgan Hill, U.S.A.	24-4-84	37.3N 121.7W	6.1	2.1×10^{25}	
Gediz Turkey	28-3-70	39.2N 29.5E	7.1	8.1×10^{26}	45
Corinth, Greece	26-2-81	40.3N 63.3E	6.6	1.1×10^{26}	
Idaho U.S.A	28-10-83	44.1N 113.9W	7.3	3.5×10^{26}	25
Gazli U.S.S.R.	8-4-76	40.3N 63.7E	7.0	2.1×10^{26}	
Gazli U.S.S.R.	17-5-76	40.4N 63.5E	7.0	2.4×10^{26}	
Gazli U.S.S.R.	4-6-78	40.4N 63.7E	5.7		
Gazli U.S.S.R.	19-3-84	40.3N 63.3E	7.0	2.5×10^{26}	
Caldiran Turkey	24-11-76	39.1N 44.0E	7.3	2.5×10^{26}	55
Narman-Horasan, Turkey	30-10-83	40.3N 43.2E	7.1	7.0×10^{25}	18
Guatemala	4-2-76	15.2N 89.2W	7.5	2.9×10^{27}	280
Colombia	12-12-79	1.6N 79.3W	7.7	2.0×10^{28}	

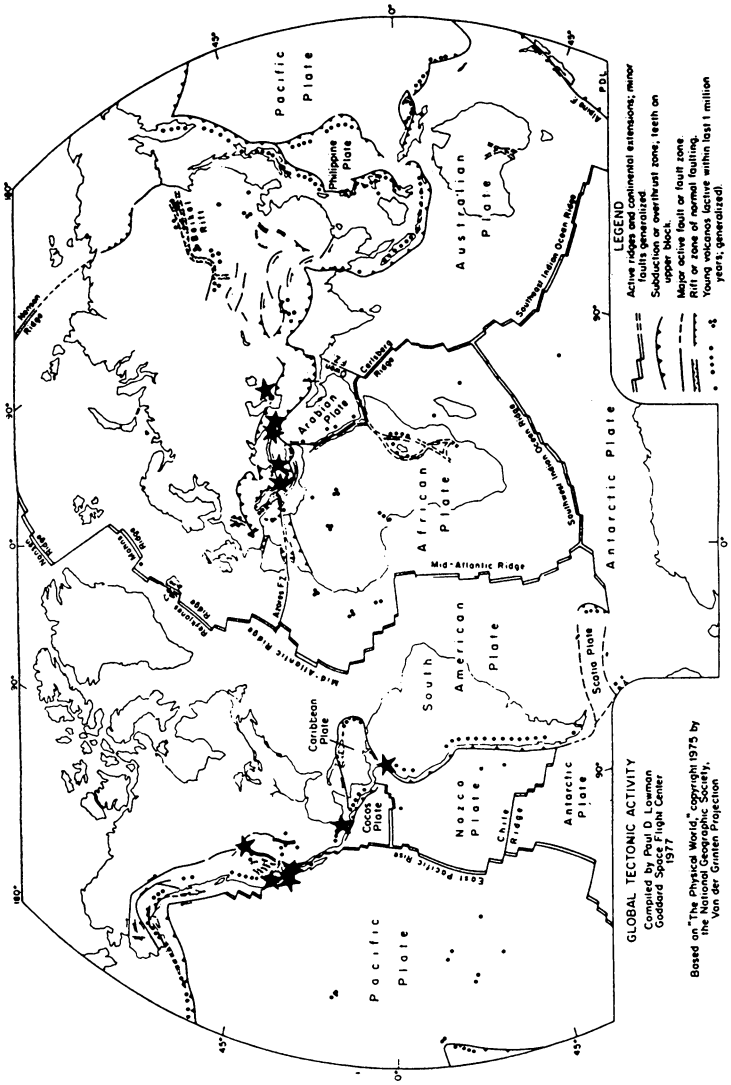

Figure 2. Epicenters of events studied (large stars)

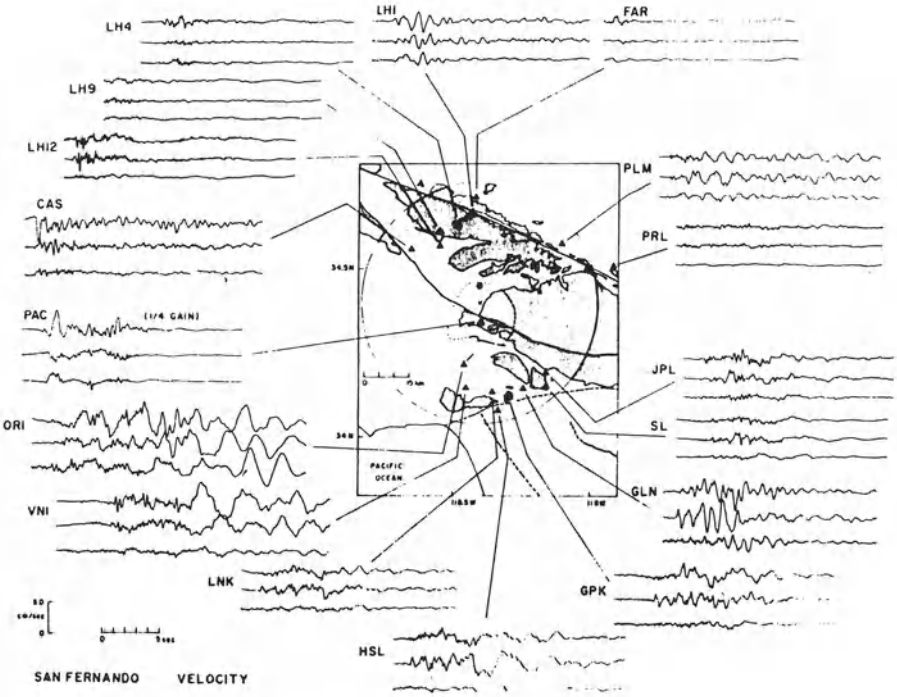

Figure 3. Area of the 1971 San Fernando earthquake and velocity records. Projection of rupture surface deduced from aftershock studies shown by dotted line, with surface rupture indicated. Triangles show location of strong motion stations, presented as radial, transverse, up components. From Shakal (1979).

and inversion was accomplished by repeated forward modelling with the strong motion seismograms matched by eye-teleseismic data was not used. Both works made extensive use of the results of Langston (1978) to determine the fault plane parameters, but used the subfault method to find the distribution of slip over the fault plane. Heaton and Helmberger fitted displacement records while Shakal used velocity records, which should be able to resolve finer details spatially because of the generally shorter wavelengths. Figure 4 summarises the distribution of slip over the fault plane determined by Heaton and Helmberger, and Figure 5 shows the distribution of slip in Shakal's model. Other fault parameters are substantially the same as those of Langston (1978), except that the rupture velocity is appreciably faster: Heaton and Helmberger use a rupture velocity of 2.8 km/s on the lower segment of the fault and 1.8 km/s on the upper segment, while Shakal used 2.7 km/s over the whole fault.

A comparison of Figures 4 and 5 with earlier studies shows that as more data at higher frequencies closer to the fault is used, the slip distribution becomes more heterogeneous and the fault plane more complicated. Both studies show highest slip on the lower fault plane at the hypocenter. Shakal's (1979) model indicates that the radiation at least at frequencies around 1 Hz is dominated by a few regions of high slip, or asperities. The last model we shall consider is that of Heaton (1982), who examined long period body waves, near field displacements and static vertical offsets. He proposed that motion occurred on two separate fault segments as shown in Figure 6. Other fault plane parameters are similar to those of Langston (1978). The rupture velocity on both planes is 2.8 km/s. Again, the highest slip on the lower (Sierra Madre) plane is near the hypocenter. Heaton points out that many features of the observed motions of this complex event remain unexplained; this summary is intended to give some sense of this complexity and what may be derived from the data using modern analysis techniques.

1979 Imperial Valley

The Imperial Valley earthquake involved slip on both the Imperial and Brawley faults; only the Imperial fault will be discussed here. Figure 7 shows the extensive set of strong motion records available, from Archuleta (1982). Because the fault plane of this strike slip earthquake broke the surface, the stations are closer to the rupture than was the case for the 1971 San Fernando earthquake-this greatly aided the interpretation. We will discuss two inversions performed by the subfault method, those of Archuleta (1984) and Hartzell and Heaton (1983). Other inversions have been performed by Olson and Apsel (1982). Hartzell and Heaton used long and short period teleseismic data as well as the strong motion records, while Archuleta used the strong motion data.

The final slip distribution on the fault plane derived by Hartzell and Heaton is shown in Figure 8. The rupture velocity is taken as 0.8 times the shear velocity and thus varies with depth. A notable feature is the region of high slip in the middle of the ruptured area, larger than the slip at the hypocenter. Figure 9 shows the model of Archuleta. In this model, not only the slip (both strike and dip components) but

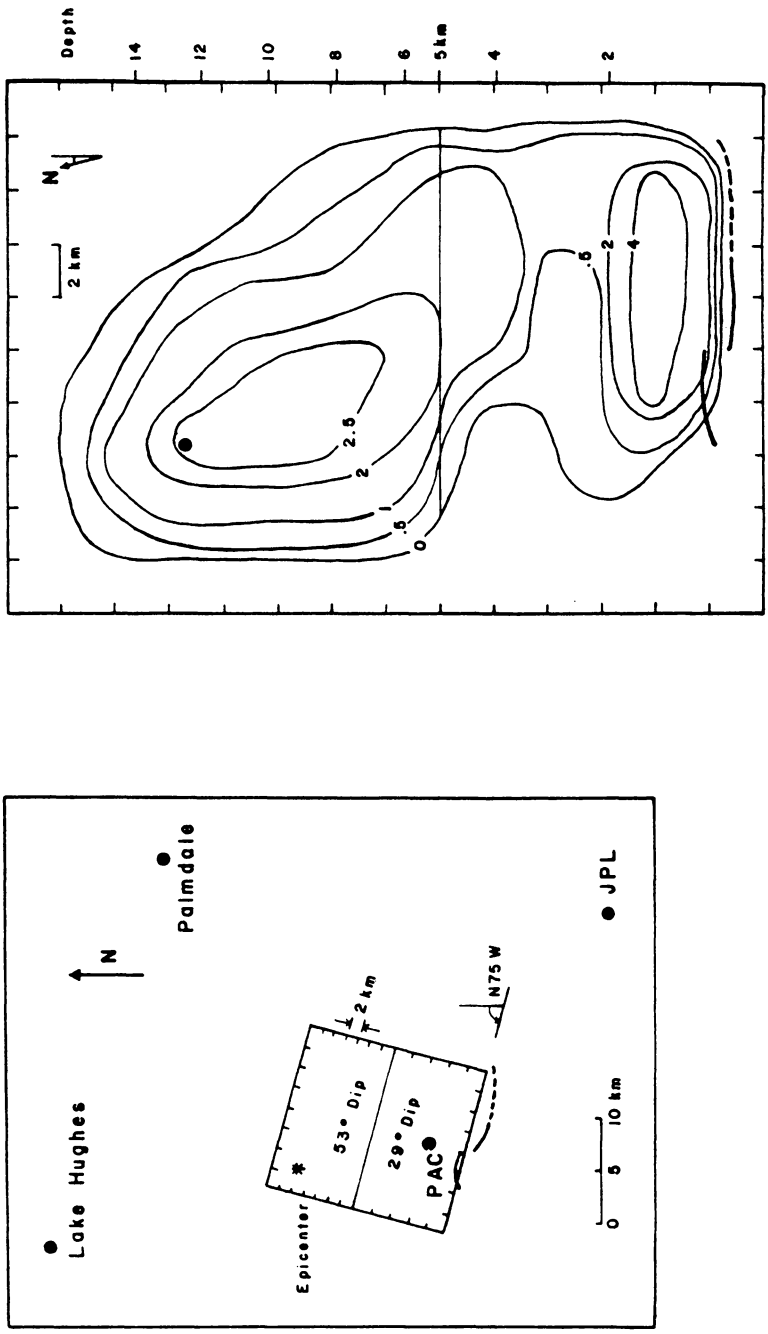

(a) (b)

Figure 4. Plan of fault model (A) and distribution of slip (m) for 1971 San Fernando earthquake. Hypocenter is shown by closed circle in (B). After Heaton and Helmberger (1979).

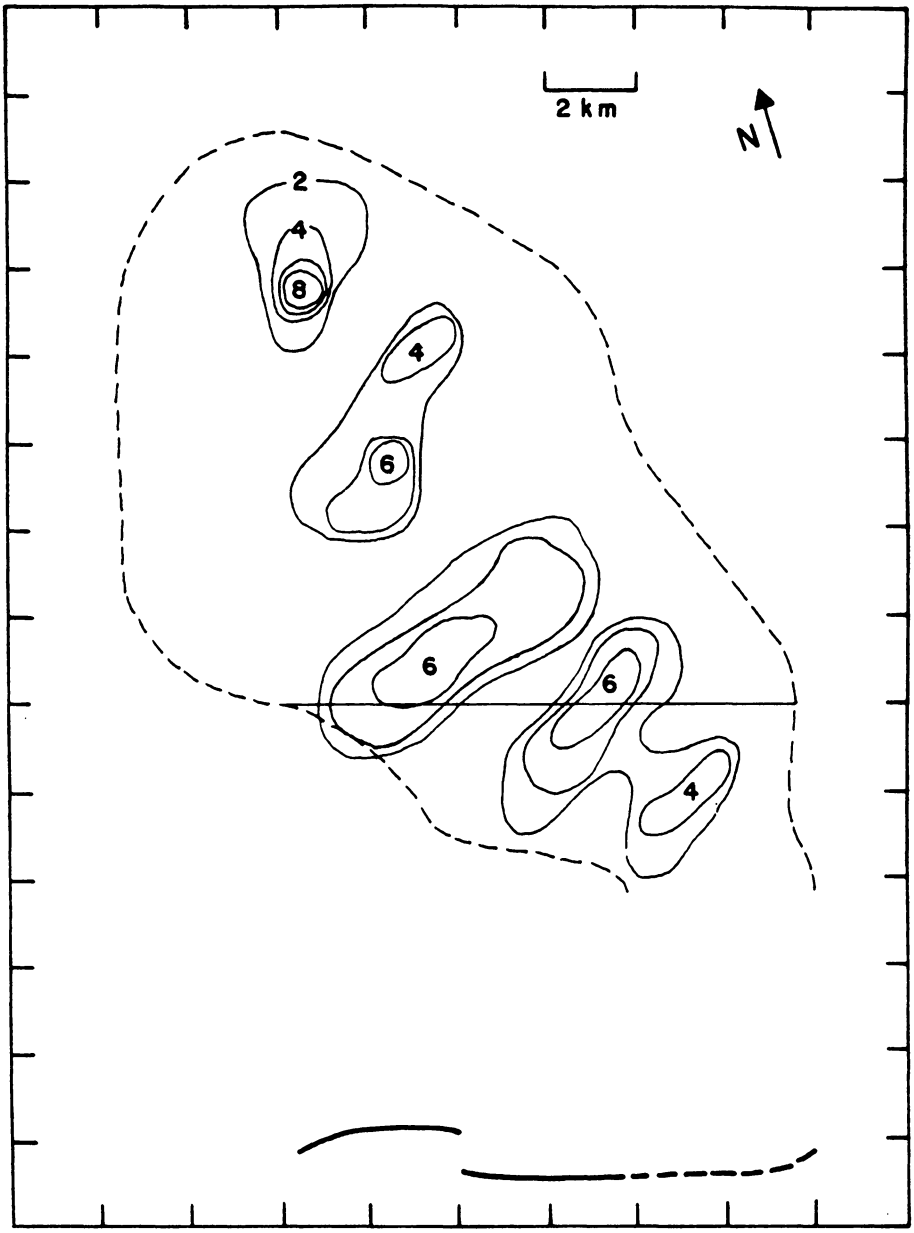

Figure 5. Slip distribution (m) for 1971 San Fernando earthquake. Dashed line shows 0-5 m contour from Figure 4. From Shakal (1979).

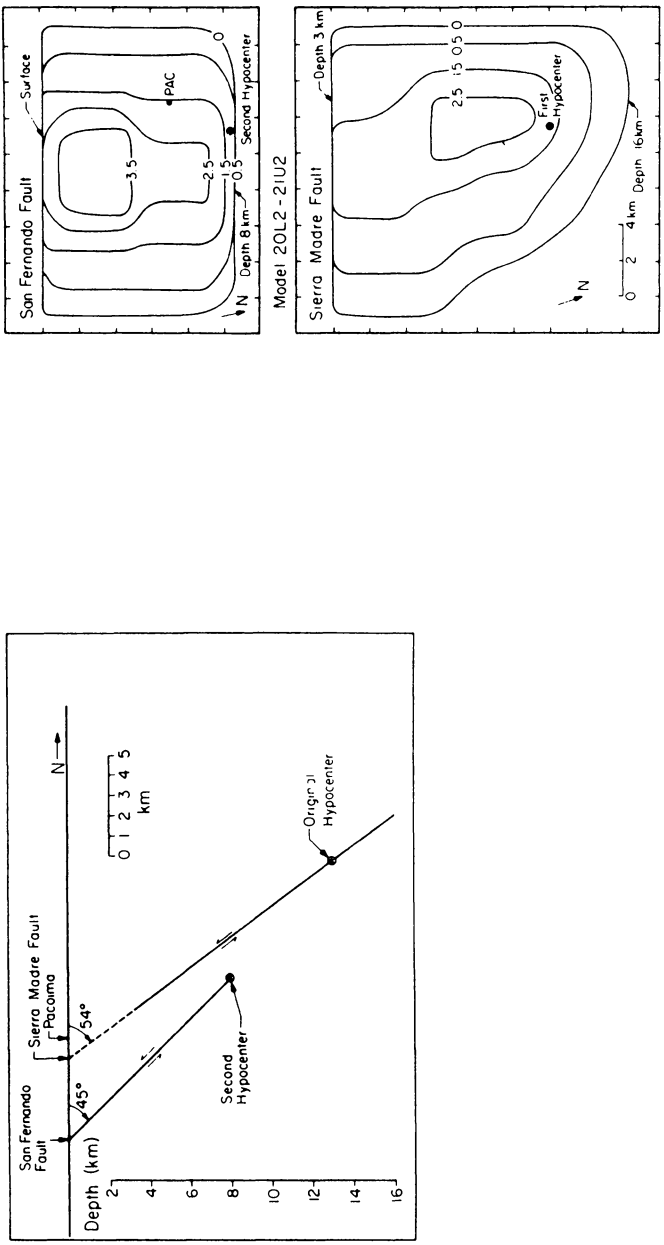

Figure 6. Section showing two fault model (left) and slip distribution (m) on the two fault planes (right) for 1971 San Fernando earthquake. From Heaton (1982).

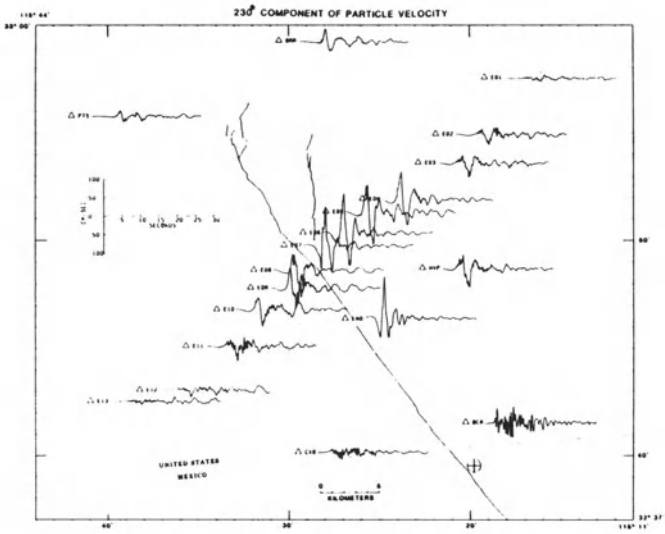

Figure 7a.

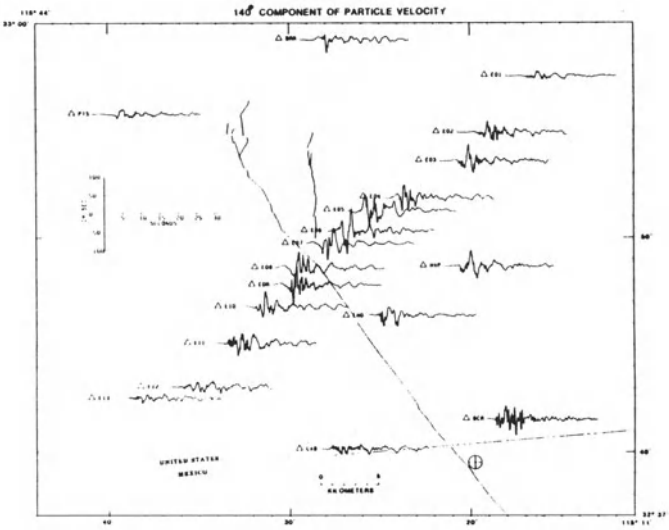

Figure 7b.

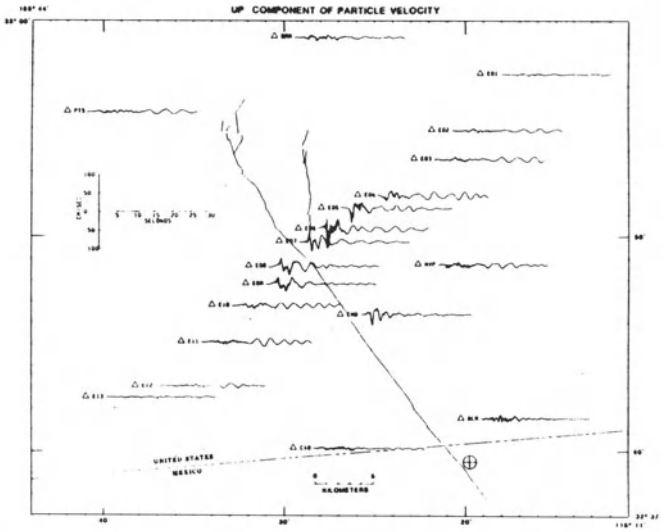

Figure 7c.

Figure 7. Velocity records for the 1979 Imperial Valley earthquake. Surface rupture on the Imperial and Brawley faults indicated. From Archuleta (1982).

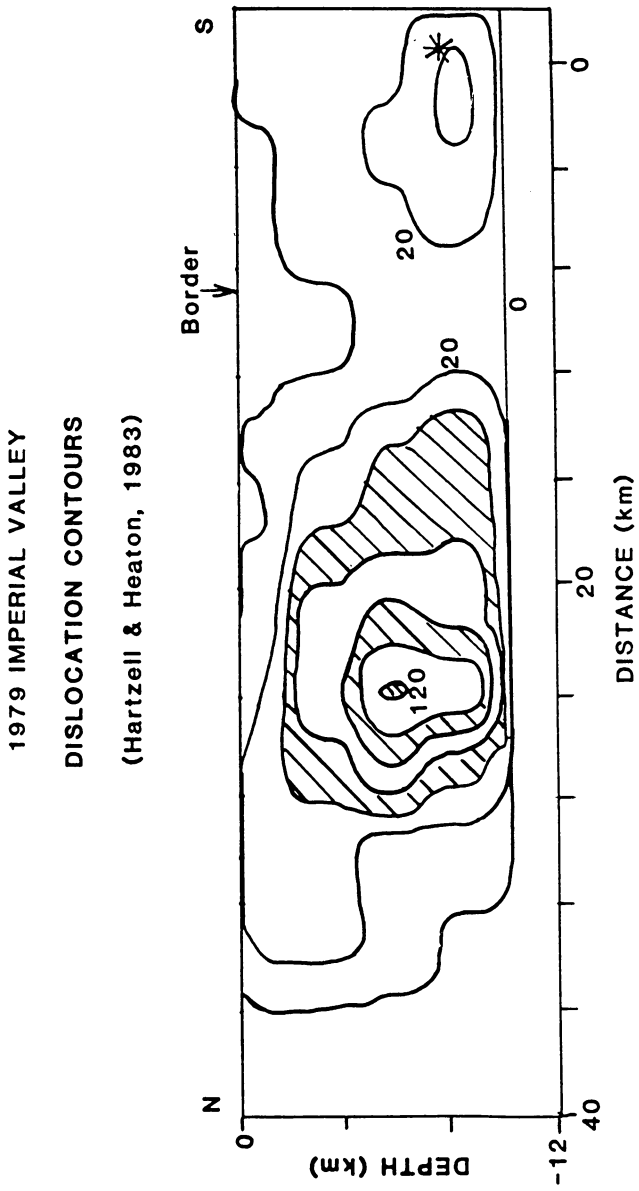

Figure 8. Slip distribution (cm) for 1979 Imperial Valley earthquake. Hypocenter shown by star. After Hartzell and Heaton, 1983.

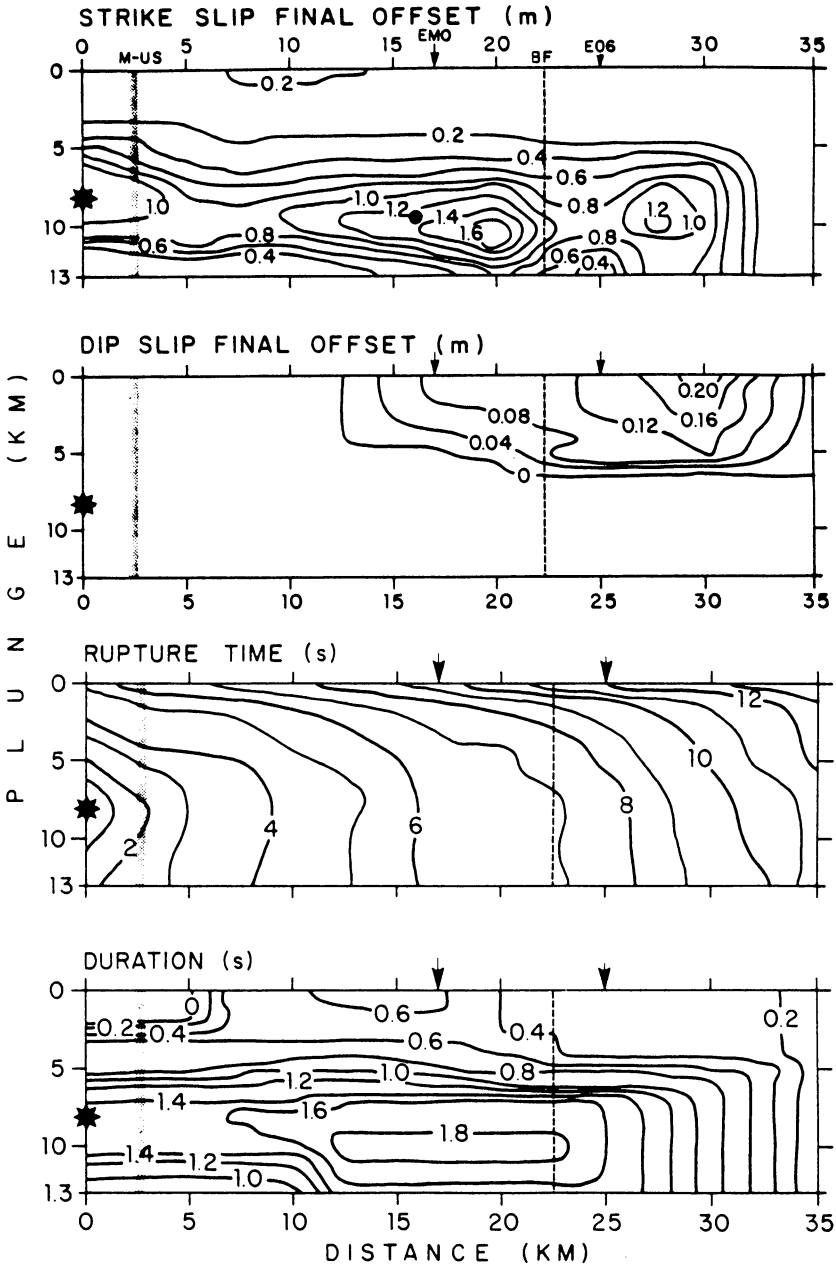

Figure 9. Fault parameters slip distribution, rupture time and duration for 1979 Imperial Valley earthquake. See text for discussion. After Archuleta (1984).

also the rupture time (time after origin that the rupture front reaches a subfault) and duration (how long the subfault slips) are determined from the data. This is as complete a model of faulting as has been presented to date. Again, the region of highest slip is in the middle of the fault, not at the hypocenter, testimony to the importance of asperities in the radiation from faults.

1984 Morgan Hill

Slip distributions for the 1984 Morgan Hill earthquake on the Calaveras fault have been presented by Hartzell and Heaton (1986). Figure 10 shows the strong motion records for this strike-slip event. The trace of the Calaveras fault is also shown in Figure 10; there was no surface rupture in this event. Teleseismic short period P waves were also used in a subfault method. In a similar manner to their Imperial Valley study a rupture velocity of 0.9 times the shear velocity was assumed. Figure 11 shows the slip distribution. To partly model the effects of varying rupture velocity and duration, Hartzell and Heaton allowed slip in three successive time windows 0.2 sec long. The cumulative slip in each time window is shown in Figure 11, and the bottommost contour plot is thus the total slip, which was constrained to have a strike slip mechanism. The fit to the strong motion records is shown in Figure 12. Once more, the slip distribution is very heterogeneous, with the highest slips occurring at asperities about 12 km from the nucleation point.

1970 Gediz; 1981 Corinth; 1983 Idaho

Source information about these events is given in Table 1. All three are intraplate earthquakes.

The Gediz earthquake in western Turkey occurred near the town of Gediz in a region of complex normal faults. Surface breaks trending NNW-SSE and E-W were observed over a 45 km length (Figure 13). North and East blocks were downthrown (Ambraseys and Tchalenko, 1972). A detailed study of the source rupture process of these earthquakes has been carried out by Eyidogan and Jackson (1985). They matched the observed long period P waveform by a series of five point sources, located as shown in Figure 13; the time function at each source was a trapezoid. The match between the observed waveforms and the synthetics is shown in Figure 14. The moment release as a function of time is given in Figure 15a. The duration of the rupture is about 40 seconds and the seismic energy release comes from five separate asperities corresponding to the five point sources of Figure 13. The rupture initiated at the NNW striking fault, and then the E-W trending segment ruptured. This was responsible for the maximum moment release; sub-events 3 and 4 might have been on the same fault or parallel faults. The final rupture (event 5) corresponds to the downward continuation of the rupture and the breaking of a segment or asperity along the deepest portion of the fault. Without near-field waveforms it is not possible to resolve the actual dimensions of the asperities and their fine spatial details. Unquestionably, however, the slip distribution for the Gediz earthquake was complex with seismic energy release from a number of asperities located on one or more fault planes.

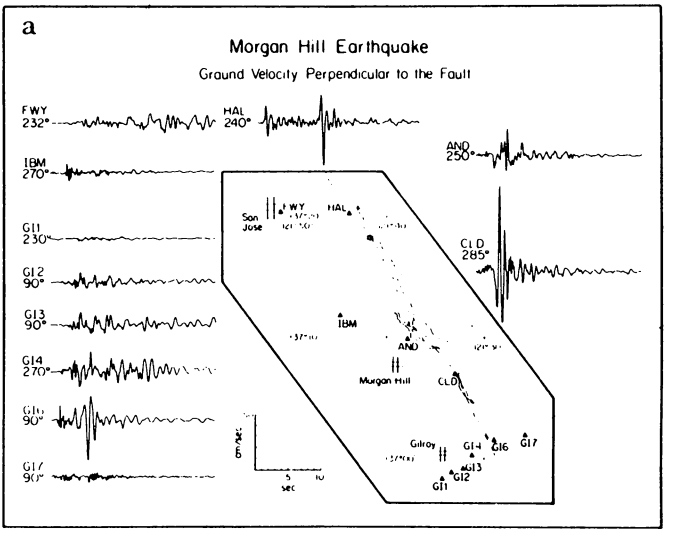

Figure 10a.

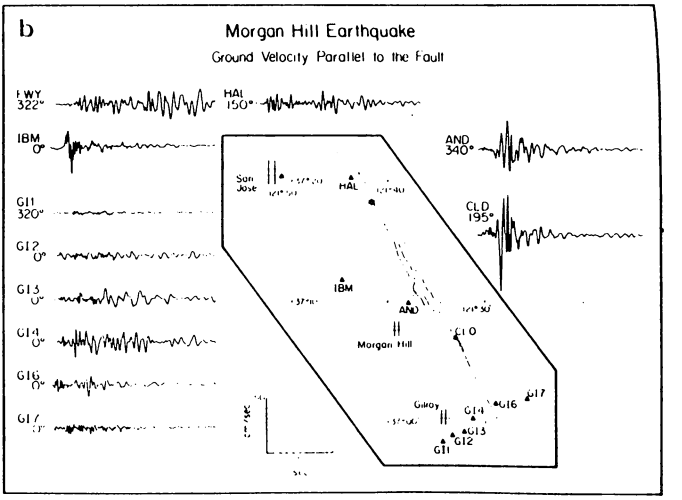

Figure 10b.

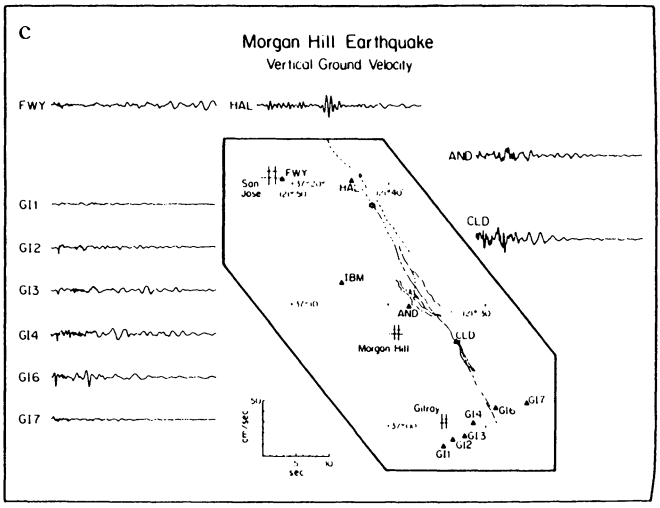

Figure 10c.

Figure 10. Velocity records for 1976 Morgan Hill earthquake. Trace of Calaveras fault and branches shown as solid and dashed lines (inferred). From Hartzell and Heaton (1986).

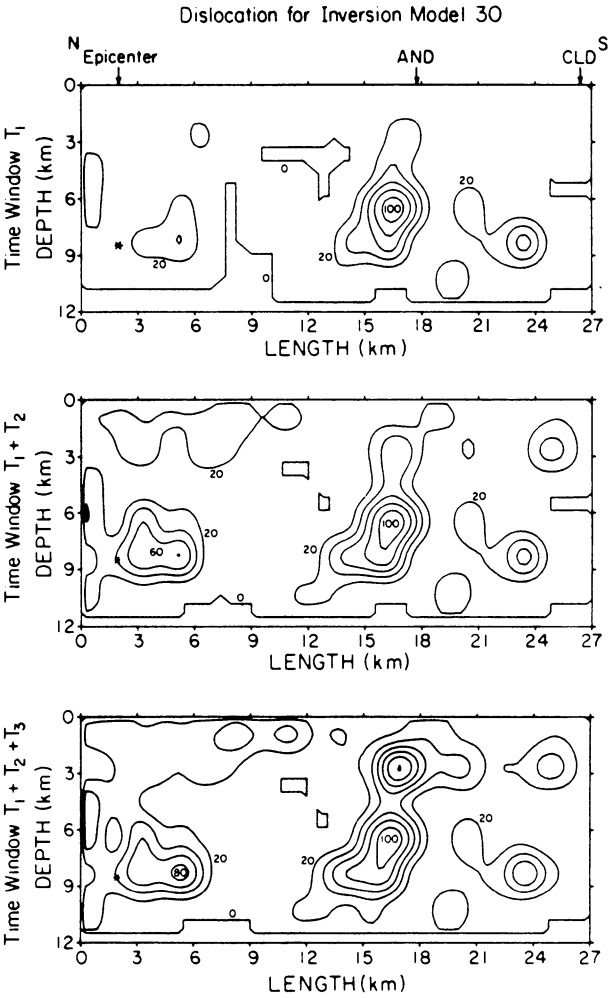

Figure 11. Cumulative slip on fault plane (cm) for three successive time windows. From 1986 Morgan Hill event. See text for discussion. From Hartzell and Heaton (1986).

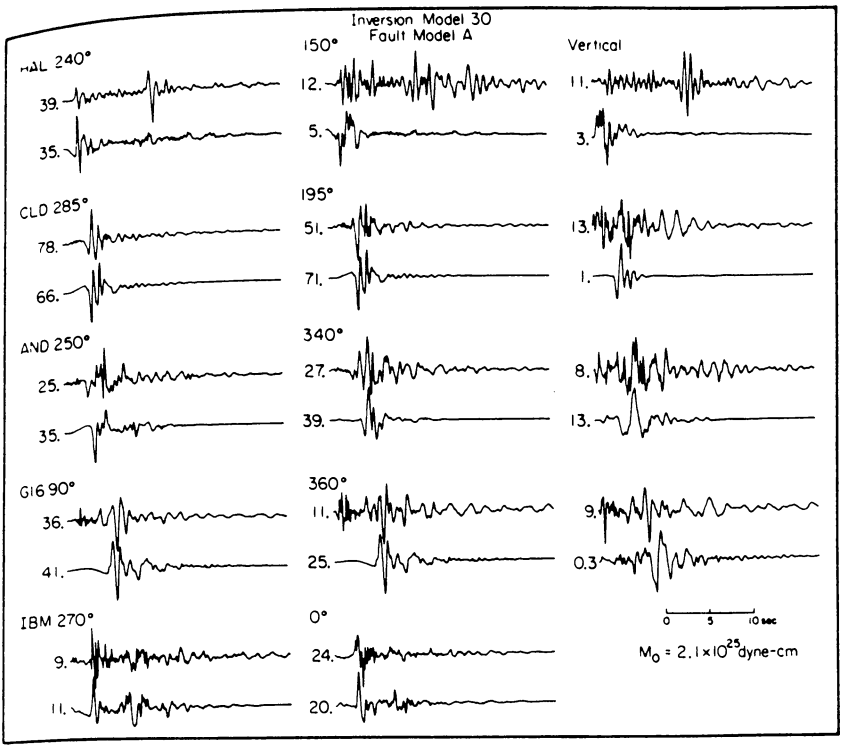

Figure 12. Fit of observed (top) and synthetic (bottom) seismograms for 1986 Morgan Hill earthquake. From Hartzell and Heaton (1986).

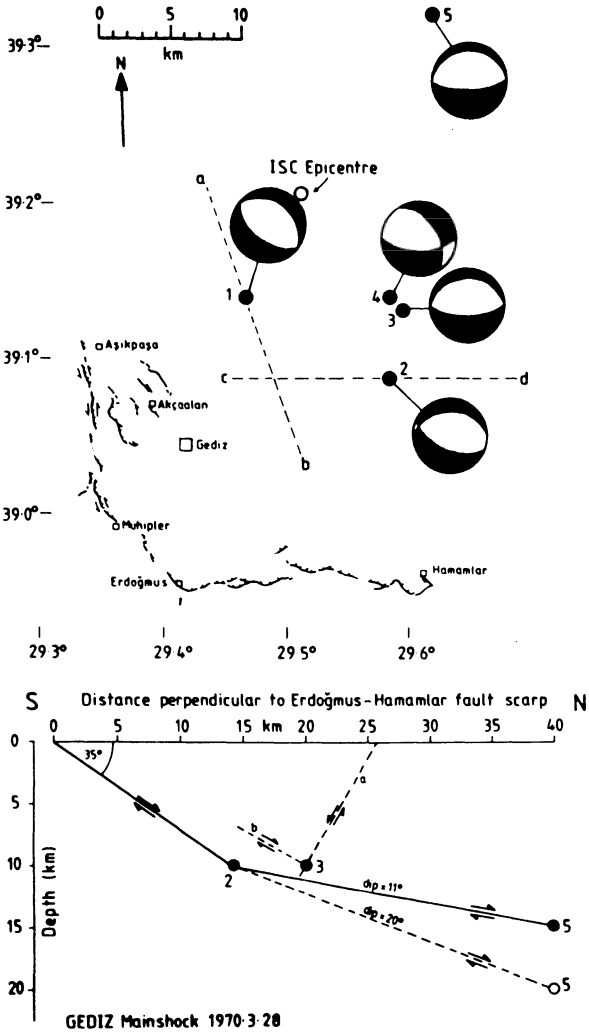

Figure 13. 1970 Gediz epicentral area (top) showing location of fault scarps and point sources and focal mechanisms used for modelling. (Bottom) N-S cross-section showing the relationship in depth of point sources 2, 3, and 5. From Eyidogan and Jackson (1985).

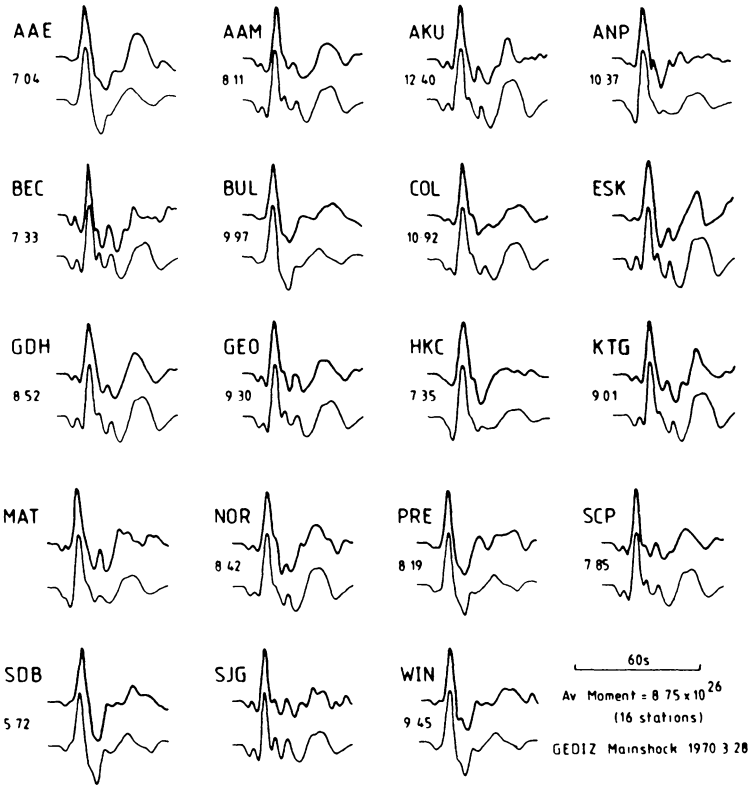

Figure 14. Fit of observed (top) and synthetic (bottom) long period P seismograms for 1970 Gediz earthquake. From Eyidogan and Jackson (1985).

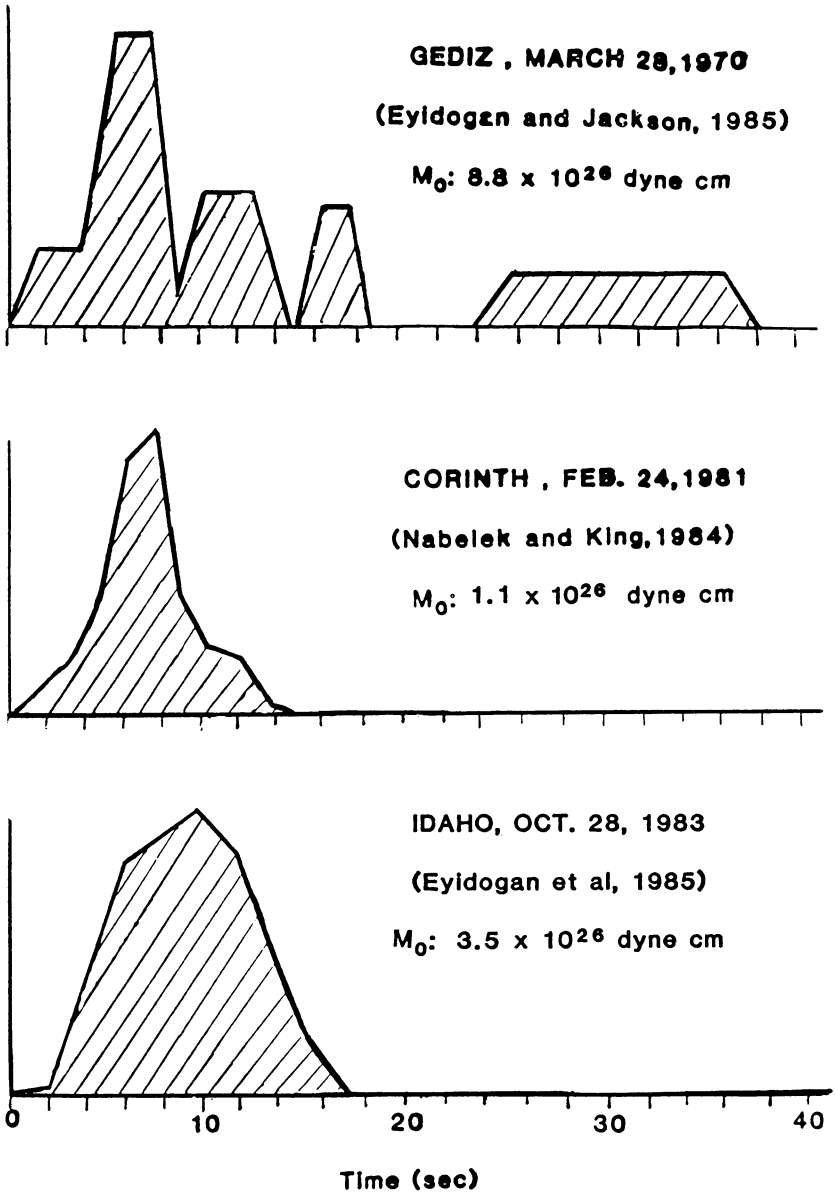

Figure15. Moment release as a function of time. From top:
a) 1970 Gediz, from Eyidoğan and Jackson (1985).
b) 1981 Corinth, from Nabelek and King (1984).
c) 1983 Idaho, from Eyidoğan et al. (1985).

The source time-functions for the Corinth (Nabelek and King,1985) and Idaho (Eyidogan et al., 1985) earthquakes are also shown in Figure 15. These smaller events had shorter rupture durations ($\leq$20 seconds) than that of the Gediz earthquake (36 seconds). The source function indicates multiple sub-events. In each case the initial rupture from a small asperity was followed by much larger one or more sub-events. Most seismic moment releases occur between 4 and 10 seconds after the initiation of the rupture. On the basis of long period teleseismic waveform inversion it is not possible to resolve in detail the space-time distribution of slip function on the fault surface.

Gazli

Between 1976 and 1984 four earthquakes occurred on neighbouring fault segments in the Gazli area of Western Uzbekistan, USSR. The locations and fault plane solutions of the events are given in Figure 16. Events that occurred on April 8, 1976 (M_s=7.0) and May 17, 1976 (M_s=7.0) were studied by Hartzell (1980), Kristy et al. (1980), Shteynberg et al.(1980), and Kopnichev et al. (1981). The source characteristics of the March 19, 1984 (M_s=7.0) earthquake and a smaller event on June 4, 1978 (M_s=5.7) were studied by Eyidogan et al. (1985). These earthquakes showed an interesting sequence of earthquake migration and the filling of a seismic gap.

In this section we show the teleseismic waveform inversion of Eyidogan et al. (1985) to obtain the moment release with time for the March 19,1984 event. Figure 17 shows long period P and SH waveforms and the corresponding synthetic seismograms. Figure 18 shows broad-band P-waveforms and synthetics for successively shorter periods-first down to 10 seconds and then down to 5 seconds. Figure 19 shows the corresponding source time functions. In all cases we note a source duration of about 15 seconds and radiation from two major asperities. The asperities were at depths of about 10 km and rupture propagation was to the NW. As we go to higher frequencies the source complexity increases, and smaller source heterogeneities become apparent. This evolution toward more complex asperity distribution is similar to the 1971 San Fernando earthquake discussed earlier. Note also that the first asperity to break was the largest in terms of source radiation.

The smallest Gazli event of 1978 (M_s=5.7) had a source function of duration less than 1 second,essentially an impulse as far as the limited resolution can determine. This earthquake might have broken a "barrier" between the two 1976 events.

Hartzell (1980) used both teleseismic and near-field data for the source-slip distribution for the May 17, 1976 event. His map of slip over the fault plane (Figure 20) shows a rupture initiation at about 15 km and a significant single asperity near the nucleation point. In some respects this is similar to the San Fernando rupture, but finer details of the Gazli source are not as well resolved because of the limited amount of near-field data. All Gazli earthquake source slip heterogeneities are distinctly different from those of the Imperial Valley and Morgan Hill strike-slip earthquakes.

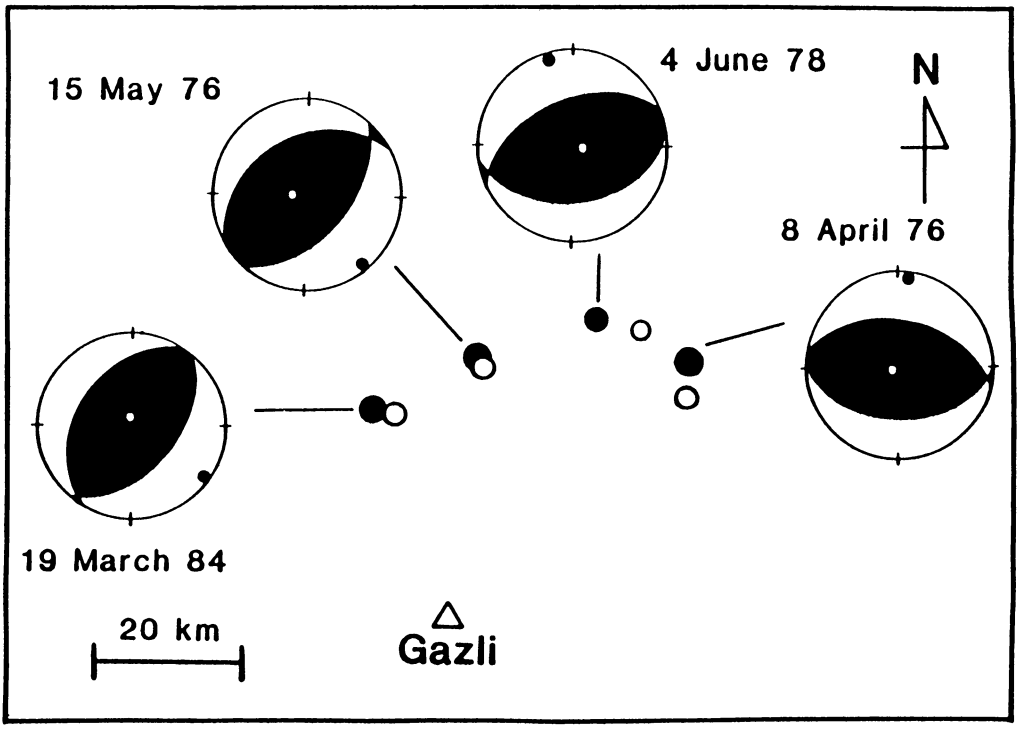

Figure 16. Epicenters and focal mechanisms, Gazli earthquakes. From Eyidogan et.al. (1985).

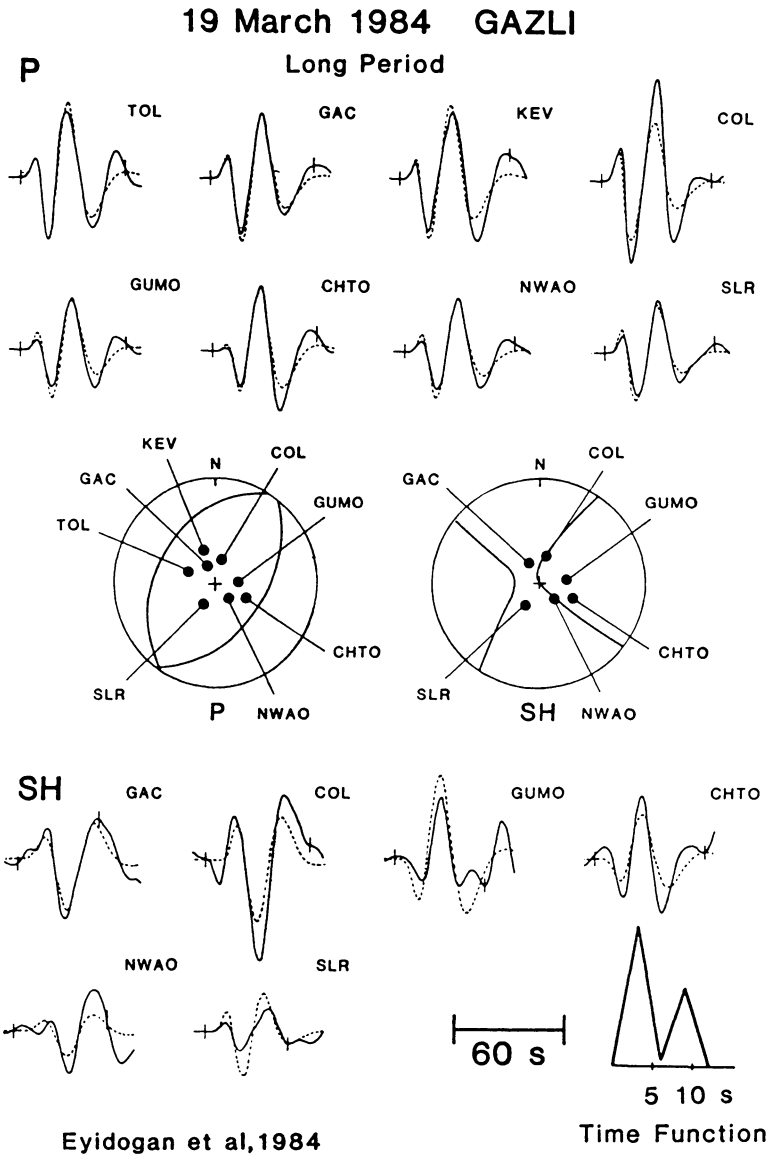

Figure 17. Fit of observed (solid line) to synthetic (dashed) long period P and SH seismograms, 1984 Gazli earthquake. Focal mechanism shown. From Eyidogan et al.(1985).

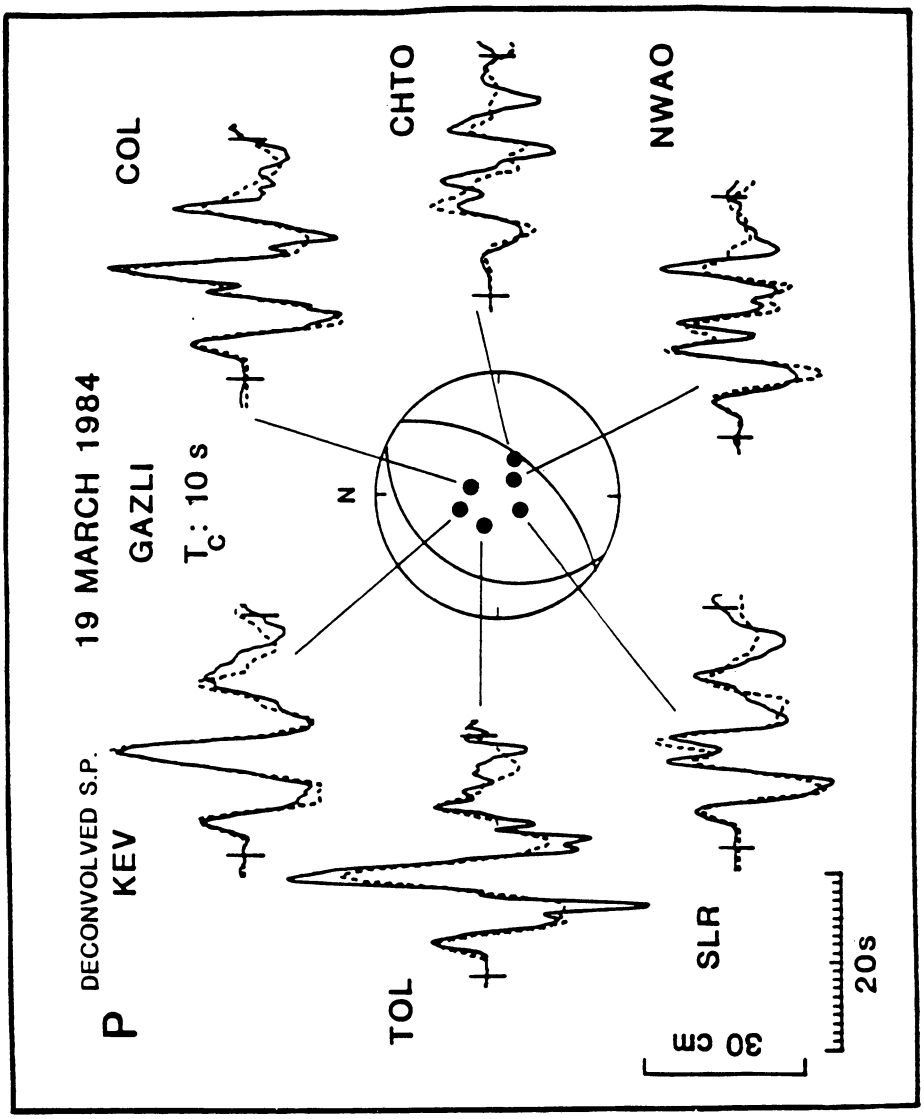
P
DECONVOLVED S.P.
KEV
19 MARCH 1984
GAZLI
T_c: 10 s
COL
N
TOL
CHTO
SLR
NWAO
30 cm
20s

Figure 18a.

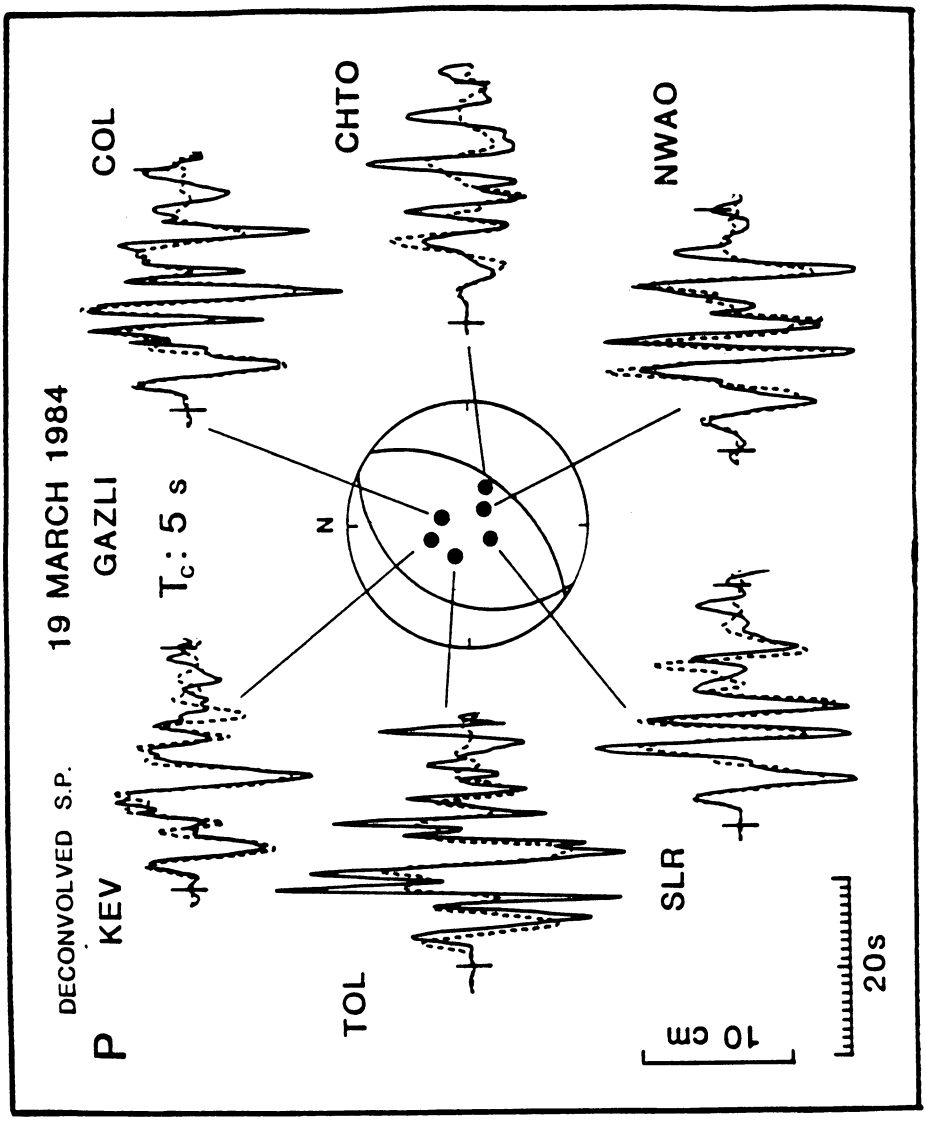

Figure 18. (a) Fit of observed (solid) and synthetic (dashed) broad band P seismograms, deconveld to 10 sec period, 1984 Gazli. Focal mechanism shown.From Eyidogan et al. (1985). b) Deconvoluca to 5 sec period.

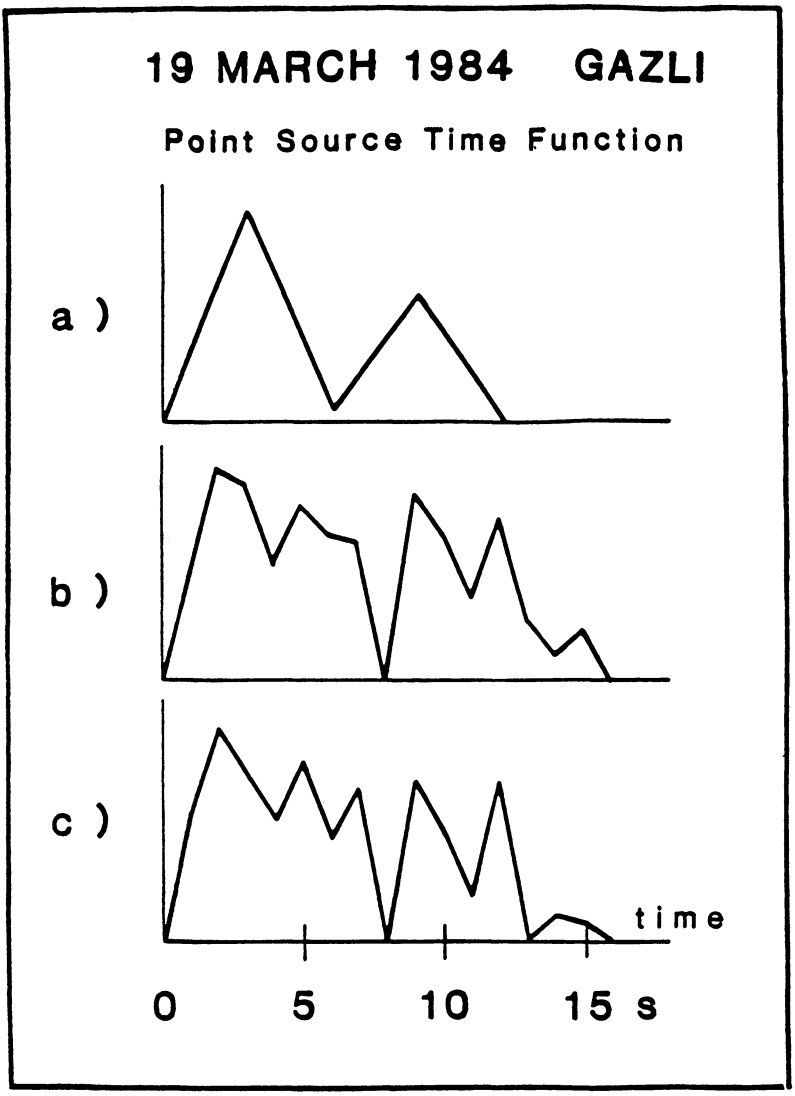

Figure 19. Moment release as a function of time for 1984 Gazli. (a) Long period fit. (b) Broad band deconvolved to 10 sec period. (c) Broad band deconvolved to 5 sec period. From Eyidogan et al.(1985).

1976 Caldiran; 1983 Narman-Horasan

We present two strike-slip earthquakes in eastern Turkey which were studied in the field and whose teleseismic seismograms were inverted to determine the source time functions. The earthquakes are the 1976 Caldiran earthquake (M_s=7.3) in eastern Turkey and the 1983 Narman-Horasan event (M_s=6.9) in northeastern Turkey.

The Caldiran earthquake had a surface rupture of 55 km with right-handed strike-slip displacements ranging from 3.30 m to 1.60 cm (Toksöz et al., 1977; Toksöz and Nabelek, 1984; Arpat et al., 1977). The source time function derived from long period inversion (Figure 21) shows a total duration of about 25 seconds and radiation from two asperities (Figure 22). The first asperity is larger. We believe fault rupture initiated at a highly stressed region close to the central part of the fault. The large moment release comes from the nearly E-W segment of the fault where surface slip was the largest. The smaller asperity probably corresponds to the SE trending branch of the fault where observed surface displacements are smaller.

The source rupture characteristics of the Narman-Horasan (Erzurum) earthquake were studied by Toksöz et al. (1984) from the inversion of short and long period teleseismic waves and one strong motion record 30 km from the source. Long period seismograms and synthetics are shown in Figure 23. The complex source function is shown in Figure 22. There is an initial large moment release followed by about 10 seconds of relatively little or no slip and then again a release of moment lasting about 2 seconds. The tectonics of the region is complex with sets of conjugate faults; the damage distribution and isoseismals suggest motion on two such conjugate faults.

Eastern Turkey is an area of compression between the northward moving Arabian plate and the stable Eurasian plate and fault patterns are complex. A characteristic of earthquakes in this area, and similar regions such as northeast China, seems to indicate shorter fault lengths, greater slip and/or stress drop, and, possibly, dislocations on more than one fault during a major earthquake. The differences between the two earthquakes in eastern Turkey and the plate boundary strike-slip earthquakes, such as Imperial Valley, Morgan Hill, and Guatemala, are obvious in terms of fault lengths, heterogeneities of slip distribution and amount of slip for a given fault length. This will affect the magnitude of strong ground motion and the shape and the areal extent of damage zones.

1976 Guatemala; 1979 Colombia

Two examples of the major plate-boundary earthquakes are the Guatemala earthquake of February 4,1976 (M_s=7.6) and the Colombia earthquake of December 12, 1979 (M_s=7.9).

The Guatemala earthquake was a major strike-slip event on the southern boundary of the Caribbean plate. It had a well studied fault break mapped continously for 280 km (Plafker et al., 1976). The left-handed surface displacements were very small near the epicenter (<50 cm) and increased westward along the fault. The largest

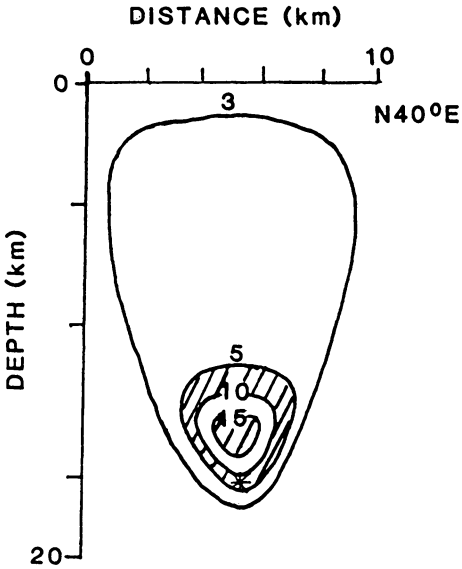

Figure 20. Slip distribution on the fault plane, 1984 Gazli. Hypocenter indicated by star. After Hartzell (1980).

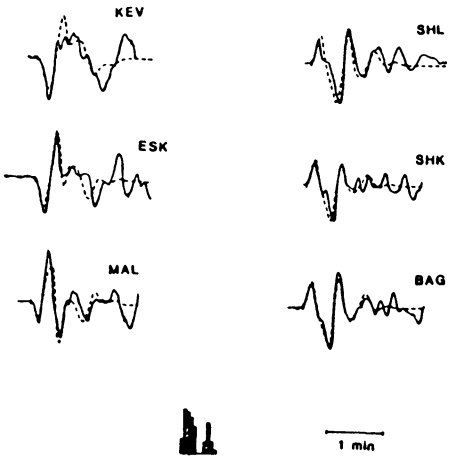

Figure 21. Fit of long period waveforms, 1976 Caldiran.

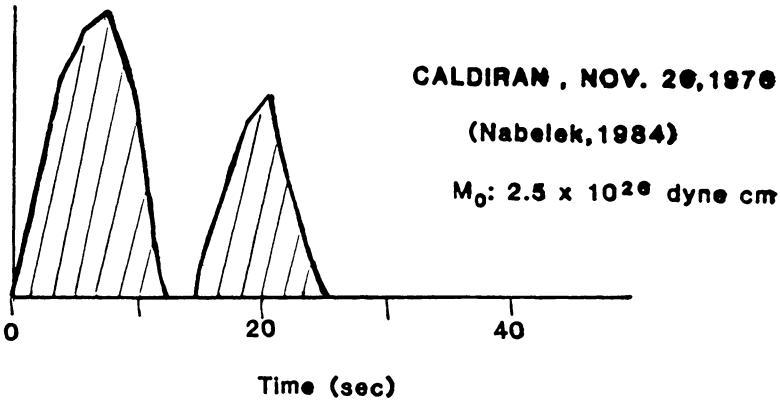

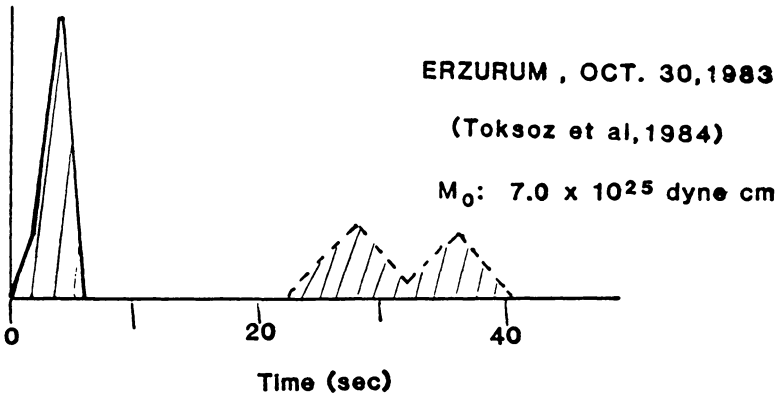

Figure 22. Moment release as a function of time, 1976 Caldiran and 1983 Narman-Horasan (Erzurum).

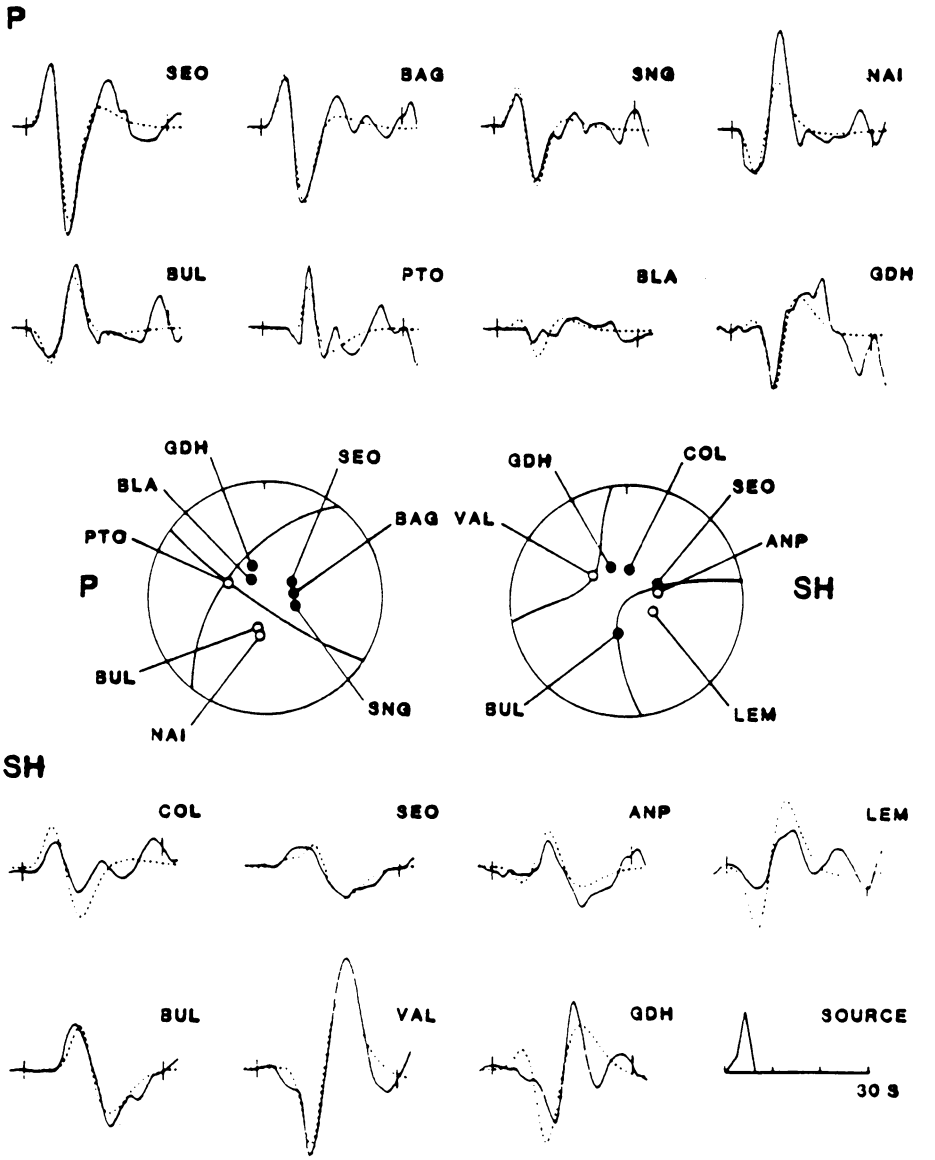

Figure 23. Fit of long period waveforms, 1983 Narman-Horasan (Erzurum).

displacements (about 3.5 m) were observed about 180 km from the epicenter.

The source heterogeneities and moment release from this earthquake were studied using long period body and surface waves by Kanamori and Stewart (1978) and by Kikuchi and Kanamori (1982). Figure 24 shows the observed and synthetic seismograms for this event, and Figure 25 the moment release as a function of time. It is clear from the long duration and the complexity of the P-waves that the slip distribution on the fault plane was very heterogeneous. Slip increased westward. There are numerous asperities and zones of relatively small slip or low stress drop between them. The isoseismals and the extended damage zone support the teleseismic source characterization.

The Colombia earthquake occurred along the subduction zone of the Nazca plate under South America (Figure 26). The mechanism is low angle thrust, with one fault striking in a northeasterly direction, parallel to the trench. The source heterogeneities and the moment release pattern have been studied by Beck and Ruff (1984) by inverting the long period body waves and aftershock distributions. The fault length is about 250 km. The epicenter is at or near the southern tip and rupture propagates to the northwest. The seismograms are of long duration (~120 sec) and complex. The match of the observed and synthetic seismograms are shown in Figure 27. The moment release diagram shown in Figure 25 indicates the heterogeneity of the slip on the fault rupture surface. The maximum slip occurs between 50 and 120 km from the epicenter. In this major asperity slip is estimated to be 6 m while at other parts of the fault slip ranged between 1 to 2 m. Long fault lengths and complex slip distribution on major subduction zone earthquakes have been observed for other earthquakes along the South American subduction zone such as the 1960 Chile (Kanamori and Cipar, 1974) and the 1984 Chile (Kadinsky-Cade and Toksöz, 1986) earthquakes. The 1979 Colombia earthquake serves as a representative example of the characteristics of such earthquakes.

4. DISCUSSION AND CONCLUSIONS

Heterogeneities of slip distribution on the earthquake rupture surface (fault asperities) are the most significant factors that affect the high frequency seismic radiation and near-field motions. In this paper we reviewed rupture charcteristics and source heterogeneities of eleven earthquakes of different magnitudes, tectonic settings and mechanisms. In all cases we found the source of these earthquakes to be heterogeneous. It is reasonable to generalize that all intermediate and large earthquakes have heterogeneous fault ruptures and that uniform models and simple scaling laws cannot be applied to predict strong ground at specified points near the fault.

As we look at the earthquakes discussed in this paper several features stand out. First, as one examines higher frequencies and near field seismograms we find the scale lengths of the heterogeneities decrease. The San Fernando, Morgan Hill, Imperial Valley and Gazli earthquakes illustrate this point. These indicate asperity dimensions may be in the order of kilometers or less. It is not known if the giant

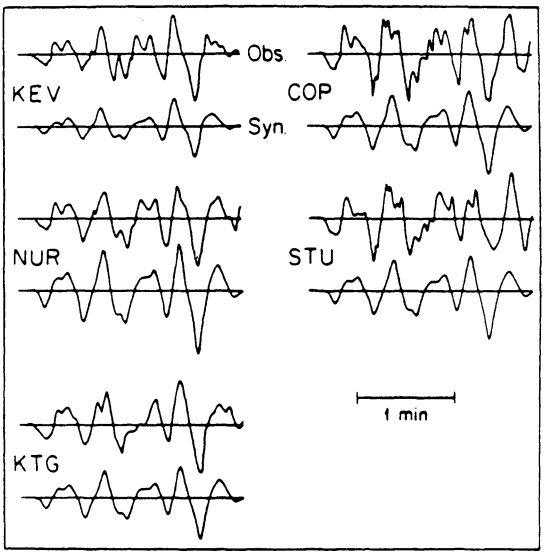

Figure 24. Fit of observed and synthetic seismograms, 1976 Guatemala. From Kikuchi and Kanamori (1982).

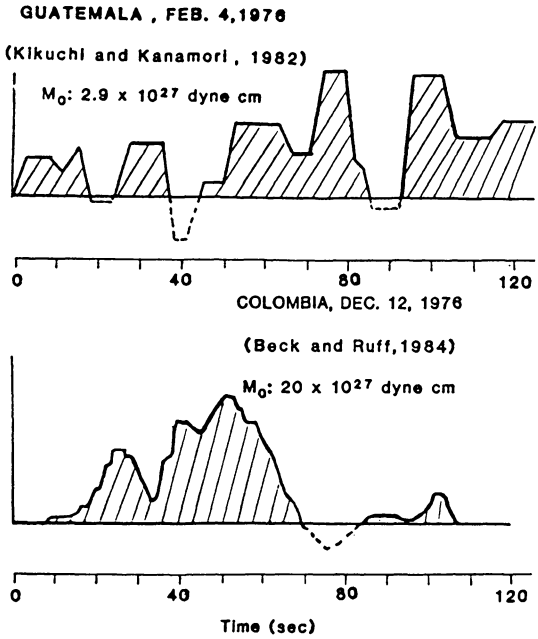

Figure 25. Moment release as a function of time, 1976 Guatemala and 1979 Colombia. After Kikuchi and Kanamori (1982) and Beck and Ruff (1984).

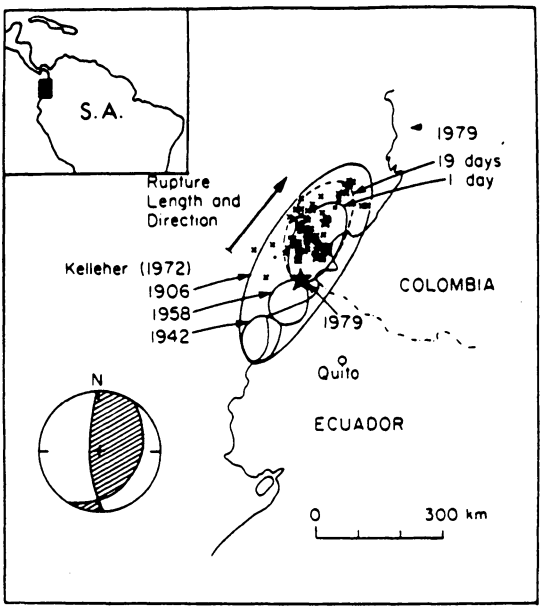

Figure 26. Epicenter (star) and aftershock distribution for 1979 Colombia. Rupture zones of 1906, 1942 and 1958 events also shown (Kelleher, 1972). From Beck and Ruff (1984).

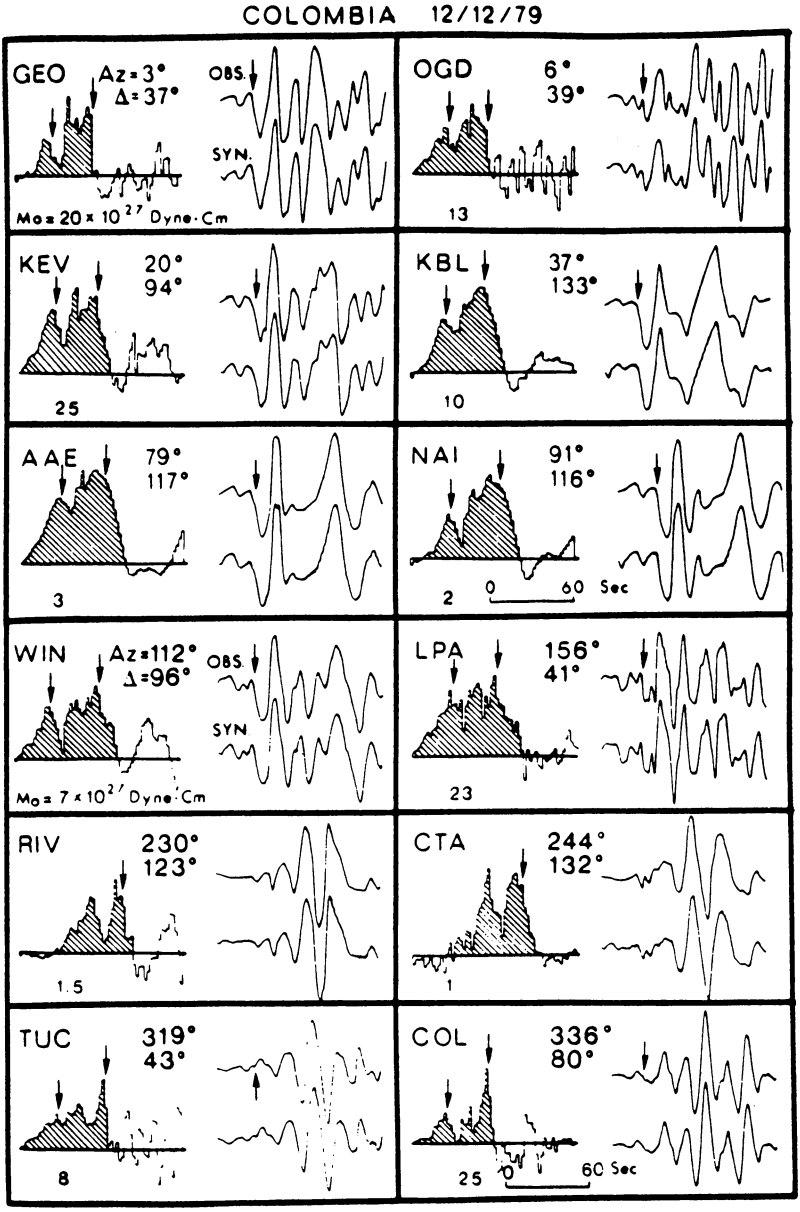

Figure 27. Fit of observed and synthetic long period P waveforms, 1979 Colombia. Moment release as a function of time is shown for each fit. From Beck and Ruff (1984).

asperities of the larger assemblage of heterogeneities.

An encouraging result for application to strong ground motion is the self similarity of earthquakes in certain tectonic settings. Plate boundary earthquakes such as Guatemala, Imperial Valley and Morgan Hill initiate at smaller asperities and cut the larger ones as rupture progresses. In the case of the intraplate earthquakes in eastern Turkey, rupture may nucleate close to a major asperity and then activate other portions of the fault or even conjugate faults. For thrust earthquakes (San Fernando, Gazli events) rupture seems to nucleate at depth at or near a strong asperity and expand upward. On the other hand, for normal faulting (dip-slip) events initial rupture seems to be weak. Although these findings do not provide a deterministic method of strong ground motions prediction at a specific site, they can provide general patterns for geographic areas in the light of the overall tectonic setting.

5. ACKNOWLEDGEMENTS

We thank Aykut Barka for his help in preparing this paper. The work on which this paper was based was supported in party by the U.S.Department of the Interior, Geological Survey, under contracts USGS 14-08-0001-G-818 and USGS 14-08-0001-G-959. The views expressed, however, are those at the authors and do not necessarily represent the views of the United States Geological Survey or the United States Government.

6.REFERENCES

Aki, K.(1984), Asperities, barriers, characteristic earthquakes and strong motion prediction. J.Geophys. Res., 89, 5867-5872.

Aki, K., M.Bouchon, B.Chouet, and S.Das (1977),Quantitative prediction of strong motion for a potential earthquake fault, Ann.Geofis., 30, 341-368.

Aki, K., and P.G.Richard (1980),Quantitative Seismology: Theory and Methods, W.H.Freeman, San Francisco.

Alewine, R.W. (1974).Applications of linear inversion theory toward the estimation of seismic source parameters, Ph.D. Thesis, C.I.T., Pasadena.

Allen, C.R., G.R. Engene, T.C.Hanks, J.M.Nordquist and W.R. Thatcher (1971),Main shock and larger aftershocks of the San Fernando earthquake, February 9 through March 1, 1971, USGS Prof.Paper 733, 17-20.

Ambraseys, N.N., and J.Tchalenko (1972),Seismotectonic aspects of the Gediz, Turkey, earthquake of March 1970, Geophys. J.R.Astr.Soc., 30, 229-252 .

Andrews, D.J. (1980),A stochastic fault model, 1, Static case, J. Geophys. Res., 85, 3867-3877.

Andrews, D.J. (1981), A stochastic fault model, 2, Time-dependent case, J.Geophys. Res., 86, 10831-10834.

Archuleta, R.J. (1984), A faulting model for the 1979 Imperial Valley earthquake, J.Geophys.Res., 89, 4559-4585.

Arpat, E., F.Saroglu, and H.B. Iz (1977), 1976 Caldiran earthquake, Yeryuvarı ve Insan, 2, 29-41.

Beck, S.L. and L.J.Ruff (1984), The rupture process of the great 1979 Colombia earthquake: Evidence for asperity model, J.Geophys. Res. 89, 9281-9291.

Boore, D.M. and M.D.Zoback (1971), Two-dimensional kinematic fault modelling of the Pacoima Dam strong-motion recordings of the February 9, 1971, San Fernando earthquake, Bull. Seism. Soc. Am., 64, 555-570.

Bouchon, M. (1978), A dynamic source model for the San Fernando earthquake, Bull. Seism. Soc. Am., 68, 1555-1576.

Burdick, L.J. and G.R.Mellman (1976), Inversion of the body waves from the Borrego Mountain earthquake to the source mechanism, Bull. Seism. Soc. Am., 66, 1485-1499.

Canitez, N. and M.N.Toksöz (1972), Static and dynamic study of earthquake source mechanism: San Fernando earthquake, J.Geophys. Res., 77, 1583-2594.

Chouet, B., K.Aki, and M.Tsujiura (1978), Regional variation of the scaling law of earthquake source spectra, Bull. Seismol. Soc. Am., 68, 49-79.

Coppersmith, K.J., and D.P.Schwartz (1983), The characteristic earthquake model: Implications to recurrence on the San Andreas fault (abstract), Earthquake Notes, 54, 61.

Das, S., and K.Aki (1977), Fault planes with barriers: A versatile earthquake model, J.Geophys. Res., 82, 5648-5670.

Dillinger, W.H. (1973), Focal mechanism of San Fernando earthquake, in San Fernando, California, Earthquake of February 9, 1971, Vol.III, Geological and Geophysical Studies, USGPO, 49-67.

Dillinger, W. and A.F. Espinosa (1971), Preliminary fault-plane solution for the San Fernando earthquake, USGS Prof. Paper, 733, 142-149.

Dziewonski, A.M., and J.H.Woodhouse (1983), An experiment in systematic study of global seismicity: Centroid-moment tensor solutions for 201 moderate and large earthquakes of 1981, J.Geophys. Res., 88, 3247-3271.

Eyidoğan, H. and J.Jackson (1985), A seismological study of normal faulting in the Demirci, Alasehir and Gediz earthquakes of 1969-70 in western Turkey: implications for the nature and geometry of deformation in the continental crust, Geophys. J.R. Astr. Soc., 81, 569-607.

Eyidoğan, H., J. Nabelek and M.N.Toksöz (1985), The Gazli USSR 19 March 1984 earthquake: The mechanism and tectonic implications, Bull. Seism. Soc. Am., 75, 6611-6675.

Hanks, T.C. (1974), The faulting mechanism of the San Fernando earthquake, J.Geophys. Res., 79, 1215-1229.

Hanks, T.C., and R.K. McGuire 1981 The character of high frequency strong ground motion, Bull. Seism . Soc. Am., 71, 2071-2096.

Hartzell, S. (1980), Faulting process of the May 17, 1976 Gazli, USSR earthquake, Bull. Seism. Soc. Am., 70, 1715-1736

Hartzel, S.H. and T.H. Heaton (1986), Rupture history of the 1984 Morgan Hill, California, earthquake from the inversion of strong motion records, Bull. Seism. Soc. Am., 76, 649-674.

Heaton, T.H. and D. Helmberger (1979), Generalized ray models of the San Fernando earthquake, Bull. Seism. Soc. Am., 69, 1311-1341.

Heaton, T.H. (1982), The 1971 San Fernando earthquake: A double event? Bull. Seism. Soc. Am., 72, 2037-2062.

Kadinsky-Cade, K. and M.N.Toksöz (1986), Rupture characteristics and strain release for the Central Chile M_s=7.8 earthquake of March 3,1985 Science, in press.

Kanamori, H. and J.J. Cipar (1974), Focal process of the great Chilan earthquake May 22, 1960, Phys. Earth Planet. Interiors, 9, 128-136.

Kanamori, H. and G.S.Stewart (1978), Seismological aspects of the Guatemala earthquake of February 4, 1976, J.Geophys. Res., 83, 3427-3434.

Kelleher, J. (1972), Rupture zones of large South American earthquakes and some predictions, J.Geophys. Res., 77, 2087-2103.

Kikuchi, K. and H.Kanamori (1982), Inversion of complex body waves, Bull. Seism. Soc. Am., 72, 491-506.

Kopnichev, Yu. F., I.L. Nesesov, and G.L.Shpil'ker (1981), The result of a strong-motion calculation: modeling the accelerograms of the Gazli and Alay earthquakes, Bull. (Izv.). Acad. Sci. USSRS, Earth Physics, 17, 650-661.

Kristy, M.J., L.C.Burdick, and D.W.Simpson (1980), The focal mechanisms of the Gazli, USSR, earthquakes, Bull. Seism. Soc. Am., 70, 1737-1750.

Langston, C.A. (1978). The February 9, 1971 San Fernando earthquake: A study of source finiteness in teleseismic body waves, Bull. Seism. Soc. Am., 68, 1-29.

Madariaga, R. (1983),High frequency radiation from dynamic earthquake fault models, Ann. Geofis., 1, 17-24.

Matsuda, T., K.Yamazaki, T.Nakara, and I.Imaisumi (1980), The surface faults associated with the Rikuyu earthquake of 1896, Bull. Earthquake Res. Inst. Univ. Tokyo, 55, 795-856.

Mikumo, R., and T.Miyatake (1978), Dynamic rupture process on a three-dimensional fault with non-uniform frictions and near-field seismic waves, Geophys. J.R.Astr. Soc., 54, 417-438.

Nabelek, J.L. (1984), Determination of earthquake source parameters from inversion of body waves, Ph.D. Thesis, Massachusetts Institute of Technology, Cambridge, MA.

Niazy, M. (1975), An exact solution for a finite, two-dimensional moving dislocation in an elastic half-space with application to the San Fernando earthquake of 1971, Bull. Seism. Soc. Am., 65, 1797-1826.

Olson, A.H. and R.J. Apsel (1982), Finite faults and inverse theory with applications to the 1979 Imperial Valley earthquake, Bull. Seism. Soc. Am., 72, 1969-2001.

Papageorgiou, A., and K.Aki (1983a), A specific barrier model for the quantitative description of inhomogeneous faulting and the prediction of strong ground motion. I. Description of the model, Bull.Seism. Soc. Am., 73, 693-722.

Papageorgiou, A., and K.Aki (1983b). A specific barrier model for the quantitative description of inhomogeneous faulting and the prediction of strong ground motion, II, Applications of the model, Bull. Seism. Soc. Am., 73, 953-978.

Plafker, G., M.G. Bonilla and S.B.Bonis (1976), Geologic effects, the Guatemalan earthquake of February 4, 1976, a preliminary report, U.S. Geol. Surv. Prof. Paper 1002, 38-51.

Rudnicki, J., and H.Kanamori (1981), Effects of fault interaction on moment, stress drop, and strain energy release, J.Geophys. Res.,86, 1785-1793.

Schwartz, D.P., and K.J.Coppersmith (1984), Fault behavior and characteristic earthquakes. Examples from the Wasatch and San Andreas fault zone, J.Geophys. Res., 89, 5681-5698.

Schwartz, D.P., K.J.Coppersmith, F.H.Swan III, P.Somerville, and W.U. Savage (1981), Characteristic earthquakes on intraplate normal faults (abstract), Earthquake Notes, 51, 71.

Shakal, A.F. (1979), Analysis and modelling of the effects of the source and medium on strong motion, Ph.D.Thesis, Massachusetts Institute of Technology, Cambridge, Ma.

Sieh, K.E. (1981), A review of geological evidence for recurrence times of large earthquakes, in Earthquake Prediction: An International Review, Maurice Ewing Ser., 4, edited by D.W.Simpson and P.G.Richards, pp.181-207.

Toksöz, M.N., E.Arpart and F. Saroglu (1977), East Anatolian earthquake of 24 November 1976, Nature, 270, 423-425.

Toksöz, M.N., M.Guenette, L.Gulen, G.Keough and J.J.Pulli (1984), Source mechanism of the Narman-Horasan earthquake of 30 October 1983 in north eastern Turkey, (in Turkish), Yeryuvarı ve Insan, 8, 47-52.

Toksöz, M.N. and J.Nabelek (1984), Can the time of earthquakes be predicted? (abs.), EOS, 65, 987.

Trifunac, M.D. (1974), A three-dimensional dislocation model for the San Fernando, California, earthquake of February 9,1971, Bull. Seism. Soc. Am., 64, 149-172.

Wallace, R.E. (1981), Active faults, paleoseismology, and earthquake hazards in the western United States, in Earthquake Prediction: An International Review, Maurice Ewing Ser., 4, edited by D.W.Simpson, and P.G.Richards, pp. 279-289, AGU, Washington, D.C.

Whitcomb, J.H. (1971), Fault-Plane solutions of the February 9, 1971, San Fernando earthquake and some aftershocks, USGS Prof.Paper 733, 30-32.

Whitcomb, J.H., C.R.Allen, J.D.Garmany and J.A.Hileman (1973), San Fernando earthquake series, 1971: Focal mechanism and tectonics, Rev. Geophys. Space Phys., 11, 693-730.

SOURCE PARAMETERS OF SOME FRIULI EARTHQUAKES (1976-1977) FROM STRONG MOTION DATA

De Natale G.[1], Madariaga R.[2], Scarpa R.[1] and Zollo A.[1]

[1]Osservatorio Vesuviano, 80056 Ercolano (NA), Italy

[2]Laboratoire de Sismologie, Institut de Physique du Globe, 4 Place Jussieu, 75230 Paris Cedex 05, France

ABSTRACT. An interactive method for processing strong motion data and inverting seismic source parameters has been developed. An application is made to 138 three component accelerograms obtained by the CNEN-ENEL agencies during the 1976-1977 earthquake sequence occurred in Friuli, Northern Italy. A simultaneous procedure for inverting source parameters and Q from earthquake spectra has been applied to derive seismic moment, source dimension and static stress drop. Hypocenters and fault plane solutions have been obtained from the analysis of all existing data of temporary and permanent seismic networks operating in northern Italy. The source parameters are compared with scaling relationships between source parameters estimated with different methods and data sets, in time and frequency domain.

1. INTRODUCTION

The Friuli region lies in an area of complex tectonics, characterized by underthrusting motion due to interaction between Alpine structures in the Northwest and Dinaric structures oriented SE-NW in the Southeast. In the central part many faults oriented NNE-SSW and N-S, characterized by transcurrent motion, separate these structures (Carulli et al., 1981; Zanferrari et al., 1982; see also Fig.1). Available fault-plane solutions are in agreement with the stress pattern inferred from the neotectonic studies, showing that thrust faults along low dip planes are located east of the Tagliamento river; strike slip earthquake motion has been found north of the periadriatic faults and west of the Tagliamento river; thrust faulting motion has been identified between these two regions (Slejko and Renner, 1984; Barbano et al., 1985).

After a quiescence of several centuries, on May 6,1976 at 20H00M an earthquake having $M_S = 6.5$ (NEIS) occurred, preceded by a $M_L = 4.5$ foreshock at 19H55M and followed by a sequence of aftershocks, some of them having magnitude values close to the main event. On September 11, 1976 at 16H31M and 16H35M, two earthquakes having $M_S = 5.5$ and 5.4 (NEIS) occured. Then on September 15, 1976 at 03H15M and 09H21M other two events having $M_S = 6.0$ and 5.9 were recorded. The seismic activity then decayed

M. O. Erdik and M. N. Toksöz (eds.), Strong Ground Motion Seismology, 85–97.
© 1987 by D. Reidel Publishing Company.

in frequency and magnitudes until September 16, 1977 when a $M_S = 5.1$ event occurred. In the same area previous sequences having comparable size and pattern of occurrence of large shocks are reported in the years 1348 and 1511 A.D.

The 1976-1977 Friuli seismic sequence provides up to present an unique opportunity for understanding the mechanisms of earthquakes and rupture complexity in an area of continental collision, located between Africa and Eurasia.

Many features of this sequence have been described in the literature written on this subject since 1976: earthquake mechanisms (e.g.Lyon-Caen, 1980; Cipar, 1980; 1981), intensity distribution and engineering damage (Giorgetti, 1976; Proc.CNEN-ENEL, 1977); space-time distribution of aftershocks (Finetti et al., 1979; Wittlinger, 1980; Siro and Slejko, 1982; Briole et al., 1985); ground deformation (Livieratos, 1980; Bencini et al., 1982; Ebblin et al., 1982; Briole et al., 1985); scaling law of source parameters and seismic attenuation (Console and Rovelli, 1981; Seidl and Berckhemer, 1982; Rovelli, 1982; 1984; Bonamassa et al.,1984); strong ground motion (CNEN-ENEL, 1976, 1977, 1978, 1979; Faccioli et al., 1984).

In spite of the large amount of seismological information collected on this earthquake sequence, detailed studies of strong motion and the rupture mechanisms associated with the large events have not yet been performed. This is mostly due to the low reliability of some hypocenter parameters and the fault-plane solutions of most of the events, which were in some disagreements between various authors. The studies made by Cipar (1980,1981) and simultaneously by Lyon-Caen (1980) provide however a good reference for the source parameters of the three largest events of this sequence. Recently Barbano et al.(1985) obtained reliable estimates of the depths of many large events, by matching synthetic seismograms with the observed broad-band records at Grafenberg array, located at a distance of about 400 km from the Friuli region. These authors critically discussed the available fault-plane solutions for the major events, most of them calculated by Slejko and Renner (1984).

In this paper we report some source parameters estimated from the CNEN-ENEL accelerometer data associated to these events, derived from a set of 138 three component uncorrected accelerograms (CNEN-ENEL, 1976, 1977, 1978, 1979).

2. SOURCE PARAMETERS OF THE MAIN EVENTS

Short period seismograms at WWSSN stations of the three largest shocks of this sequence (May 6, 1976, 20H00M; September 15,1976, 03H15M and 09H21M) are quite complex: 3-4 point sources are required to match the observed waveforms. For the main-shock there is a poor agreement between long-and short-period seismic moments, the former is lower by a factor 4 when compared to the latter (2.9 and $.65 \times 10^{25}$ dyne cm respectively, see Tab.8 in Cipar, 1981). Short period P waves for each earthquake were modeled by Cipar (1981) and Lyon-Caen (1980) using several point sources of radiation, each having time duration on the order of 1 to 3 sec. Stress drop estimated by using a circular fault model gave values ranging

from 35 to 256 bars, higher than the values inferred from the long-period seismograms (12 bars for the main event, 24 bars for the 09H21M aftershock). The results by Lyon-Caen are in a very good agreement with Cipar (1981) in spite of the different assumptions made in the modeling. The envelopes (Farnbach, 1975) of velocity and displacement waveforms at the accelerometer stations close to the epicenters of these events show a duration of the maximum amplitude episodes consistent with the rise times inferred from modeling at teleseismic distances (Fig.2). Effects due to the close distance and the finitness of the source with respect to the low number of accelerograms, where no absolute timing is present, do not allow however a reliable study of the space-time history of the rupture process associated to these earthquakes.

3. METHOD OF ANALYSIS

Each component of the 138 free-field ground accelerograms has been corrected for the instrument response and then the two horizontal components have been rotated to obtain transverse SH ground motion. An interactive procedure for displaying these data and to perform selection and processing for retrieval of some basic source parameters has been developed on a computer HP 1000F. Fig.1 shows a map of the Friuli region with the epicenters of these events (the circle size is proportional to earthquake magnitude) and the station locations. In the following sections time and frequency domain analyses performed to estimate source parameters are described.

3.1. Time Domain Analysis

Transverse components of the first 10 sec.of recorded accelerograms have been integrated by convolving the time series with a causal band-pass function derived from the step-response of a critically damped harmonic oscillator, characterized by a fundamental period of 2 sec. The dynamic stress drops have been calculated by using the following formula of Boatwright (1980):

$$\tau_e = \frac{(\rho(\xi)\,\rho(\underline{x})\,V_s(\underline{x})^{1/2}\,V_s(\xi)^{5/2}}{2\gamma^3}\;\frac{R(1-\tau^2)^2}{F_{\theta\psi}}\;\left(\frac{\dot{u}}{t}\right)$$

where $\rho(\xi)$ and $\rho(\underline{x})$ are the densities at the source and the receiver respectively (2.8 and 2.6 gr/cm^3), $V_s(\xi)$ and $V_s(\underline{x})$ are the shear wave velocities at the source and the receiver (3.3 and 2.5 km/sec); γ is the rupture velocity, assumed for this study equal to 0.8 $V_s(\xi)$; R is the geometrical spreading, $F_{\theta\psi}$ is the radiation pattern coefficient, evaluated on the basis of the available fault-plane solutions. $\tau=\gamma/V_s(\xi)\sin\theta$ where θ is the take off angle from the fault normal, also derived from the local velocity model (Briole et al.,1985) and the available fault-plane solutions; $\dot{u}/t$ is the slope of the velocity pulse. Envelopes of the velocity waveforms have been used as a tool for the identification of SH arrivals. In this type of analysis errors arise mostly due to the

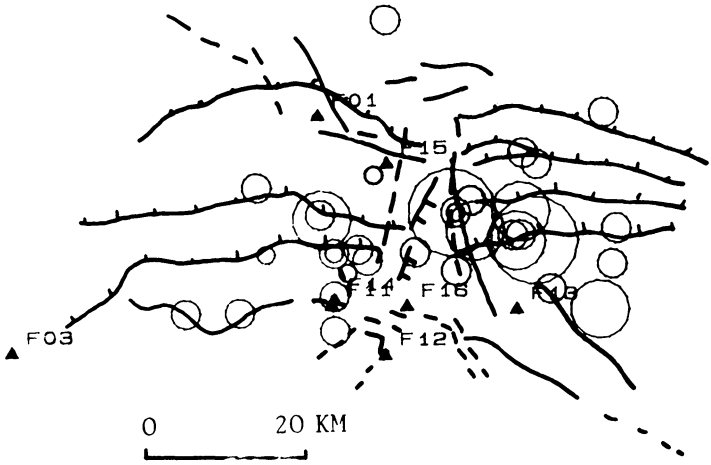

Figure 1. Epicenters of the 1976-1977 largest events. Triangles are accelerometric stations. Pleistocene-Olocene faul are also shown (Zanferrari et al., 1982)

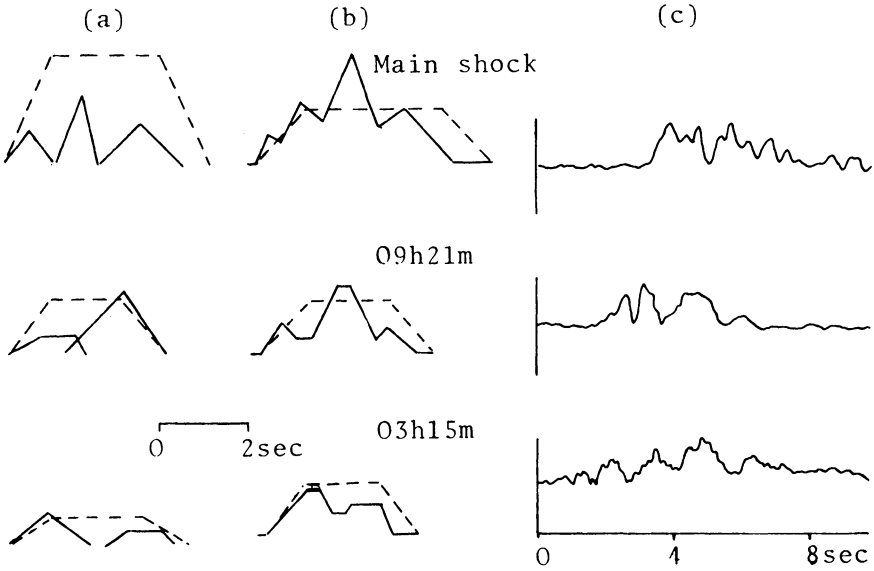

Figure 2. Comparison of far field time functions for the 3 largest events (a) Cipar(1981), (b) Lyon-Caen (1980) and (c) envelopes of nearfield displacements

uncertainty in the radiation pattern and phase identification. The slopes of the velocity waveforms were simply corrected for the attenuation by subtracting $t^*/2$ for each record and using the average value of 250 for coda Q (assumed here to be coincident with S quality factor) obtained by Console and Rovelli (1981) and Rovelli (1982;1983).

Fig.3 shows some examples of integrated accelerograms used to estimate the dynamic stress drops and pulse rise times. The lengths of the velocity pulses have been used to estimate the seismic radius. The results are reported in Table 1 and 2.

3.2. Frequency Domain Analysis

S portions of the recorded accelerograms (transverse motion) were selected for each track. Depending on the time duration of the SH signals and characteristics of the records, samples of 2.56 and 5.12 sec were selected for the spectral analysis (input data were previously equally interpolated at 100 Hz sampling rate). The resulting time series were tapered with 10% cosine windows before applying a FFT procedure to calculate the displacement amplitude spectra, obtained by dividing the acceleration amplitude spectra, obtained by dividing the acceleration amplitude spectra for ω^2. A spectral model as suggested by Boatwright (1978) having the form:

$$\log V(\rho) = \log \Omega_o - \pi\rho t/Q_s - \frac{1}{2} \log(1+\rho/\rho_e)^{2\gamma}$$

was used to estimate the low frequency spectral level Ω_o, the corner frequency ρ_e, high frequency decay γ and the S-wave quality factor Q_S. The simultaneous inversion of these parameters has been made through the generalized inverse method, using the singular value decomposotion for matrix inversion, For each point in the spectra a standard deviation was obtained by comparing the derived estimates of the digitization error (see Appendix II in Boatwright, 1978) and the statistical errors associated with the spectral estimates (Bendat and Piersol, 1971). Some preliminary tests indicated the instability of a simultaneous inversion of the above mentioned parameters, due mainly to the tradeoff between Q and the low number of spectral points. Stable estimates of the spectral parameters were obtained by fixing the Q_S value for each inversion run, leading to a generally small number of iterations (4-5) to reach convergence. In this last case the observed residual fall within the errors, confirming the goodness of fit. To overcome the problem of Q_S indetermination, inversions with different fixed Q_S values (ranging from 50 to 1000) have been performed and the set of spectral parameters furnishing the best fit was chosen. A Q frequency dependent ($Q=80\ f^{1.1}$) was also used on the basis of the study made by Console and Rovelli (1981) and Rovelli(1982, 1983). Q ranging from 150 to 500 furnished the minimum residuals and a general agreement with data. For this range of Q however, low frequency spectral levels were coherent, while corner frequencies showed more scattered values due in general to observed spectra with double corner frequency, not taken into account in our parameter estimation procedure (Fig.4). In dubius cases plots of synthetic and real spectra for different corner frequencies and Q values were compared and the minimum corner frequency was chosen. Seven of the 18 events were selected on the

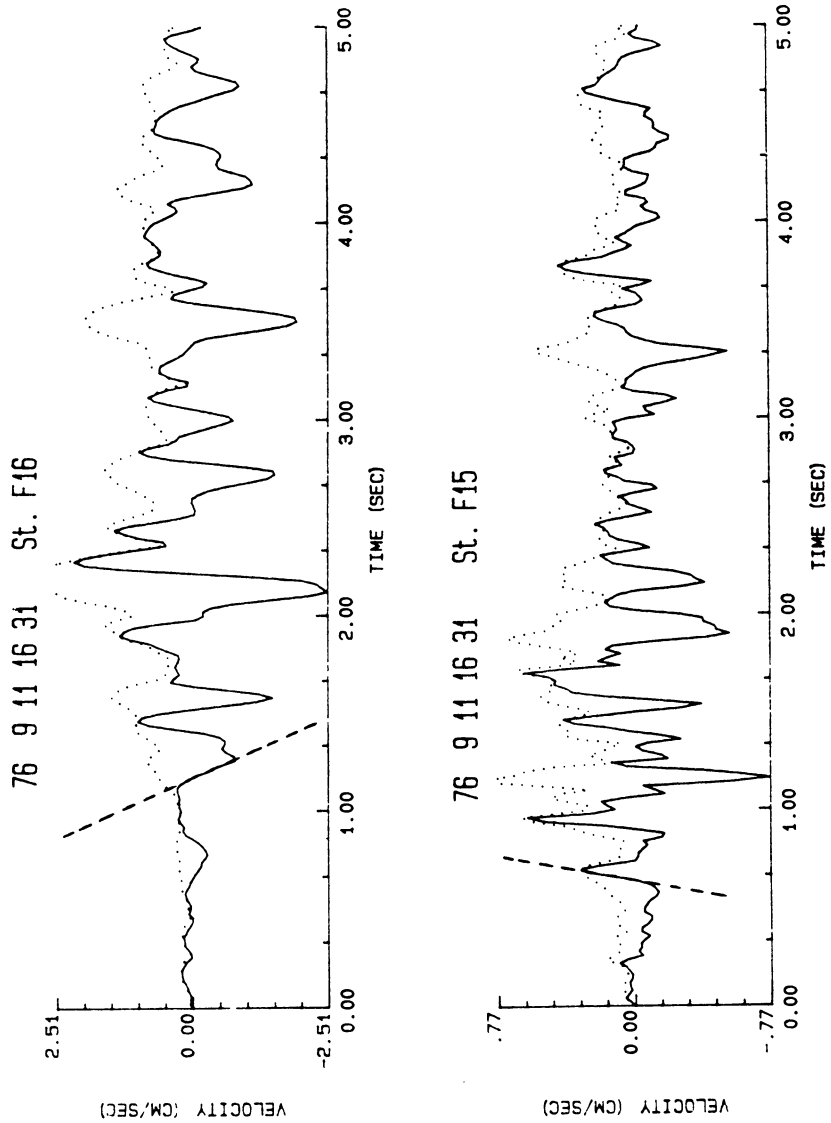

Figure 3. Examples of integrated accelerograms used to estimate the dynamic stress drop.

TABLE 1. SUMMARY OF SOURCE PARAMETERS

N.	DATE	LATITUDE (N)	LONGITUDE (E)	DEPTH (km)	ML	STATIONS
1	76/05/11 22:44 02.0	46 15.62	13 02.46	6.00	4.8	F01-F11
2	76/05/18 01:30 08.0	46 16.20	13 01.80	7.00	4.3	F11-F14
3	76/06/11 17:16 37.0	46 13.80	13 00.00	9.00	4.4	F01-F11-F12
4	76/09/11 16:31 12.0	46 18.00	13 13.80	6.00	5.5	F15-F16
5	76/09/11 16:35 00.0	46 16.50	13 13.47	6.50	5.1	F11-F14-F16
6	76/09/15 03:15 19.0	46 17.05	13 10.43	5.00	5.8	F16-F14
7	77/09/16 23:48 06.0	46 17.75	12 59.12	10.00	5.2	F01-F14-F15

	⟨ M0 ⟩ (dynexcm)	⟨ fc ⟩ (hz)	⟨ Fmax ⟩ (hz)	⟨ $\tau_{1/2}$ ⟩ (sec)	⟨ radius(B) ⟩ (meters)	⟨ Ω_0 ⟩ ++ (cmxsec)
1	(.30+-.10)E24	1.5+-.2	6.1+- .2	.13	804+-106	.46+-.15
2	(.6+-.2)E23	2.3+-.2	7.2+-1.6	.12+-.01	544+- 56	.10+-.04
3	(1.2+-.6)E23	2.5+-.1	6.0+-0.9	.11+-.02	488+- 55	.12+-.01
4	(1.6+-.9)E23	1.1+-.1	5.9	.15+-.08	1144+- 90	.39+-.28
5	(.4+-.3)E24	1.5+-.3	6.9+-2.6	.33+-.10	808+-148	1.10+-.86
6	(8.0+-.6)E24	.7+-.1	6.3+-0.9	.31+-.10	1640+- 32	6.03+-.43
7	(.5+-.1)E24	1.6+-.7	7.2+-1.5	xxx	747+-156	.66+-.33

	⟨ $\Delta\sigma_B$ ⟩ (bars)	⟨$\Delta\sigma_{rms}$ ⟩ (bars)	⟨ τ_e ⟩ (bars)
1	250+- 99	118+- 43	163
2	177+- 83	82+- 44	49+- 30
3	442+-227	134+- 45	111+- 25
4	46+- 30	38+- 4	77+- 57
5	352+-332	160+- 57	21+- 7
6	834+- 77	253+- 11	198+- 53
7	500+-337	206+-112	220+-131

(++)
The values are normalized to 5 km

TABLE 2. SUMMARY OF SOURCE PARAMETERS

N.	Date	STA	R (km)	$R_{\theta\phi}$	ML	Ω0 (cm×s)	M0 (dyne×cm)	fc (hz)	fmax (hz)	Arms (cm/sec××2)	Amax (cm/sec××2)	$\Delta\sigma_{rms}$ (bars)	$\Delta\sigma_B$ (bars)	τ_e
1	76/05/06 20:00	F01	24.6	.70	6.4	–	–	–	6.7	98	290	–	–	187
2	76/05/07 00:23	F01	32.4	.71	4.5	.03	8.5E22	2.0	14.2	31	135	186	154	–
3	76/05/10 04:43	F12	17.3	.47	4.7	.09	2.1E23	1.3	11.1	14	58	62	116	–
4	76/05/11 22:44	F11	8.1	.62	4.8	.39	3.1E23	1.7	6.3	67	245	162	371	163
5	76/05/11 22:44	F01	15.7	.34	4.8	.11	2.9E23	1.4	5.9	10	34	75	170	–
6	76/05/13 13:04	F11	10.3	.47	4.3	.06	8.4E22	2.2	11.0	24	83	83	217	–
7	76/05/18 01:30	F11	9.2	.47	4.3	.08	9.2E22	2.5	5.8	28	125	126	240	79
8	76/05/18 01:30	F14	8.8	.47	4.3	.04	4.4E22	2.1	9.1	12	44	37	130	20
9	76/05/18 02:39	F11	5.9	.47	3.7	–	–	–	6.8	9	45	–	–	–
10	76/06/09 18:48	F11	13.9	.51	4.2	.05	8.2E22	2.2	13.2	25	121	99	210	267
11	76/06/09 18:48	F12	17.0	.62	4.2	–	–	3.5	–	43	–	–	–	–
12	76/06/11 17:16	F11	9.0	.58	4.4	.06	5.7E22	2.5	7.5	26	149	82	433	134
13	76/06/11 17:16	F01	19.4	.22	4.4	.03	1.9E23	2.6	5.6	6	43	128	470	72
14	76/06/11 17:16	F12	11.7	.22	4.4	.04	1.5E23	2.5	5.2	15	52	193	454	–
15	76/06/11 17:16	F14	9.0	.42	4.4	–	–	–	10.4	15	44	–	–	122
16	76/06/17 14:28	F11	13.9	.18	4.4	.04	2.2E23	1.7	8.7	15	57	179	267	261
17	76/09/06 19:28	F16	13.0	.43	4.0	.09	1.6E22	2.5	12.6	5	28	36	58	16
18	76/09/11 16:31	F11	20.9	.39	5.5	.08	2.5E23	2.0	6.2	29	98	311	465	199
19	76/09/11 16:31	F15	14.7	.65	5.5	.06	8.6E22	1.0	–	11	50	–	37	13
20	76/09/11 16:31	F16	15.2	.85	5.5	.26	2.9E23	1.2	6.0	15	58	42	60	13
21	76/09/11 16:35	F11	19.7	.84	5.1	.39	5.5E23	2.0	7.9	46	182	190	717	15
22	76/09/11 16:35	F14	19.3	.73	5.1	.09	1.5E23	1.3	10.0	24	80	80	202	12
23	76/09/11 16:35	F15	15.7	.65	5.1	–	–	–	–	19	58	–	–	25
24	76/09/11 16:35	F16	13.7	.72	5.1	.82	9.2E23	1.4	–	53	192	–	253	31
25	76/09/13 18:54	F16	18.2	.11	4.4	.05	4.9E23	1.6	11.9	16	63	328	442	373
26	76/09/15 03:15	F11	16.1	.21	5.8	2.06	9.3E24	.6	7.2	77	329	587	439	251
27	76/09/15 03:15	F14	15.7	.21	5.8	1.77	7.8E24	.7	7.4	29	107	242	748	484
28	76/09/15 03:15	F16	10.9	.21	5.8	2.94	8.9E24	.8	5.5	39	123	263	843	145
29	76/09/15 04:38	F16	14.2	.73	4.7	.02	2.8E22	1.6	7.9	12	39	37	26	20
30	76/09/15 09:21	F11	16.1	.46	6.1	.81	1.7E24	.8	6.8	151	397	633	193	61
31	76/09/15 09:21	F14	15.6	.46	6.1	2.10	4.2E24	.4	6.2	52	191	160	71	51
32	76/09/15 09:21	F16	12.1	.28	6.1	–	–	–	7.4	31	102	–	–	5
33	76/09/16 23:48	F11	13.0	.21	5.2	1.07	8.9E24	.6	6.8	81	297	518	194	374
34	76/09/16 23:48	F14	12.7	.20	5.2	.14	5.4E23	2.2	7.2	229	128	362	1280	327
35	76/09/16 23:48	F01	14.0	.62	5.2	.55	7.4E23	1.4	5.6	37	106	148	337	98
36	76/09/16 23:48	F15	12.9	.54	5.2	.23	3.3E23	1.4	9.3	33	122	108	337	80

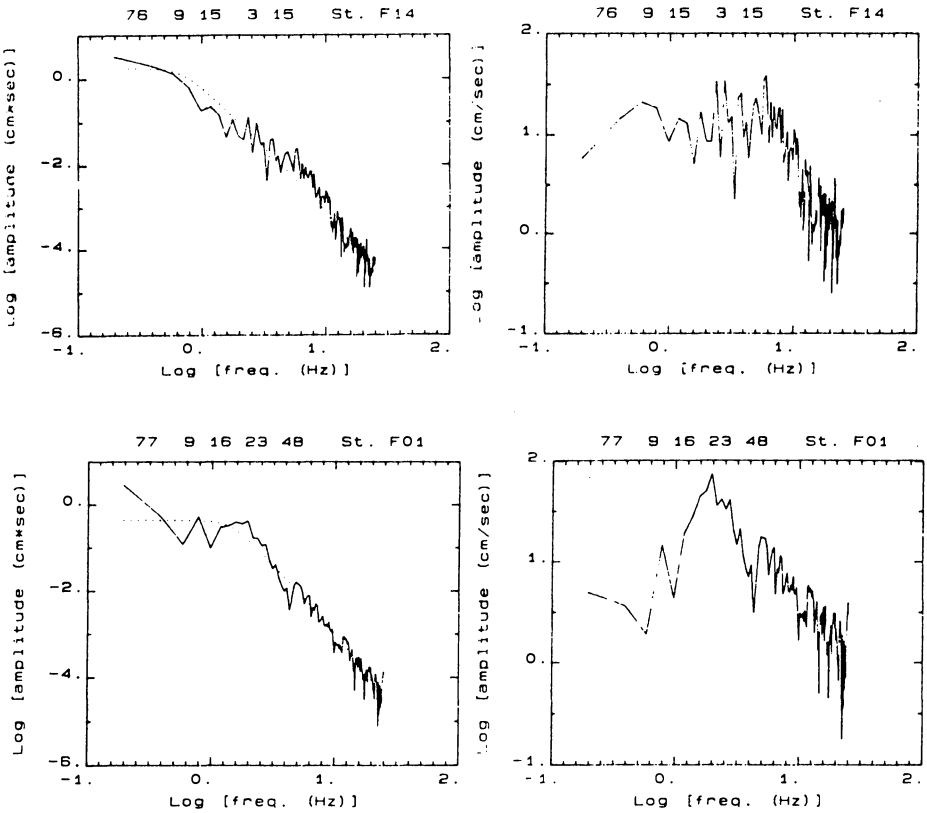

Figure 4. Examples of observed displacement (left side and acceleration (right side) spectra.
Dots indicate the least square fits.

basis of data quality and a minimum number of 2 recording stations. Low frequency spectral level normalized to a distance of 5 km, corner frequency, Brune radius, seismic moments and static stress drops were obtained using the averaging procedure described in Archuleta et al.(1981) and Boatwright et al.(1984). Results are shown in Table 1. A mixed time-frequency domain analysis has been performed to get another estimate of stress release proposed by Hanks and McGuire (1981):

$$\Delta\sigma_{rms} = 1.35 \frac{\rho R}{F_{\theta\psi}} (\rho_o/\rho_{max})^{1/2} a_{rms}$$

where ρ_o is the corner frequency and f_{max} is the high frequency limit of the acceleration spectrum, $F_{\theta\psi}$ the radiation pattern coefficient, ρ the density, R the hypocentral distance and a_{rms} is the rms value of the instrument corrected acceleration in the time window of shear wave arrival.

In Table 1, the three stress release estimates for the selected events are summarized. The dynamic stress release estimates ($\Delta\sigma_{rms}$ and τ_e) appear almost stable, except for the event N.5. Since τ_e is an estimate of the stress released from the rupture episode which radiated the measured velocity pulse (Boatwright,1980), the complexity of the fracture process could produce the discrepancy between these two values.

Static Brune stress drops appear overestimated and scaled with the other two, showing minimum and maximum values to the same events. The uncertainty of radius estimates and in some cases the inappropriate Brune model can explain the differences. Bias can be also introduced by local ground response effects, like the systematic presence of peaks in the spectra of the station F11 (Forgaria Cornino).

All the 36 selected records have been processed and analyzed in order to get Table 2, where single station estimates of source parameters are also shown. In some cases discrepancy exists (see for example records 20/21 and 33/34) for the same event, between the spectral levels and radiation pattern coefficients for stations located at almost the same distance to the hypocenters. Averaging over the values at each stations, stable estimates of f_{max} around 7 hz have been found, for hypocentral distances ranging between 6 and 20 km, showing no substancial scatter among the stations. These values are smaller than those estimated for Californian earthquakes by Hanks (1982). The single station stress drop release estimates show the general trend described before, with dynamic stress drops almost coherent and higher Brune stress drop values.

4. CONCLUSIONS

The basic results of this study are a quantification of source parameters for some Friuli atershocks derived from time and frequency analysis of accelerometer data. The uncertainties on the measured parameters are still quite high, not comparable for instance to the errors around 15% estimated by Boatwright (1984) for the Oroville, California, events, but the importance of this work consist in a first systematic analysis of the source parameters of the Friuli strong motion data, by comparing different methodologies.

The obtained results can be summarized as follows:

- The stress drop values are quite high, in the range 100-300 bars;
- The source parameters derived from Brune's model (1970;1971) give higher stress drops and in some cases unreliable seismic moment and high frequency decays. The use of the traditional asymptotic-intercept method to estimate corner frequency and then the source size is limited by the low number of spectral points near the knee and the possible presence of two corner frequencies;
- Local site behaviour influences the spectral shape, causing the occurrence of peaks: this is the case of the station F11 (Forgaria Cornino);
- f_{max} have average values of 7 Hz.

REFERENCES

Barbano M.S., Kind R., Zonno G. (1985), Interpretazione dei parametri focali di alcuni terremoti del Friuli (1976-1977) con l'uso dei sismogrammi sintetici. Preprint.

Bencini P., Der, anis A., Livieratos E., Rossikopoulos D. (1982), Crustal deformation at the Friuli area from discrete and continuous geodetic prediction techniques. Boll.Geod.Sci.Aff., 41, 137-148.

Bendat J.S., Piersol A.G. (1971), Random data: analysis and measurement procedures. Wiley-Interscience, 407 pp.

Boatwright J. (1978), Detailed spectral analysis of two small New York state earthquakes. Bull. Seism. Soc. Am., 68, 1117-1131.

Boatwright J. (1980), A spectral theory for circular seismic sources: simple estimates of source dimension, dynamic stress drop and radiated seismic energy. Bull. Sesim. Soc. Am., 70, 1-27.

Bonamassa O., De Santis A., Console R., Rovelli A. (1983), Seismic moment, local magnitude and recording length of small earthquakes for a Friuli sequence (May 1976). Ann.Geophys., 2, 77-88.

Briole P., De Natale G., Gaulon R., Pungue F., Scarpa R. (1985), Inversion of geodetic data and seismicity associated with the Friuli earthquake sequence (1976-1977). Submitted to Annales Geophys.

Brune J.N. (1970), Tectonic stress and the spectra of seismic shear waves. J.Geophys.Res., 75, 4997-5009 (Correction, J.Geophys. Res., 76, 5002, 1971).

Carulli G.B., Giorgetti.F., Nicolich R., Slejko D. (1981), Considerazioni per un modello seismotettonico del Friuli. Rend.Soc.Geol.It., 4, 605-611.

Cipar J. (1980), Teleseismic observations of the 1976 Friuli, Italy earthquake sequence. Bull.Seism.Soc.Am., 70. 963-983.

Cipar J. (1981), Broadband time domain modeling of earthquakes from Friuli, Italy. Bull.Seism.Soc.Am., 71, 1215-1231.

CNEN-ENEL,(1976,'77,'78,'79),Strong motion earthquake accelerograms digitized and plotted data. Vol.I, Part 1,2,3,4,5, Rome, Italy.

Console R. Rovelli A. (1981), Attenuation parameters for Friuli region from strong-motion accelerogram spectra. Bull.Seism.Soc.Am., 71, 1981-1991.

Ebblin C., Salahoris M., Zadro M. (1982), Variations of mechanical properties of rocks as a source of vertical ground displacements. Tectonophysics, 88, T17-T23.

Faccioli E., Rovelli A., Fregonese R. (1984), A study of the spectral characteristics of accelerograms from recent earthquakes of Italy and nearby regions. Proc.8th World.Earth.Eng., S.Francisco, p.361-368, Vol.4.

Farnbach J.S. (1975), The complex envelope in seismic signal analysis. Bull.Seism.Soc.Am., 65, 951-962.

Finetti I., Russi M., Slejko D. (1979), The Friuli earthquake (1976-1977) Tectonophysics, 53, 261-272.

Giorgetti F. (1976), Isoseismal map of the May 6,1976 Friuli earthquake. Boll.Geofis.Teor.Appl., 19, 707-714.

Hanks T.C., McGuire R.K. (1981), The character of high-frequency strong ground motion. Bull.Seism.Soc.Am., 71, 1897-1919.

Livieratos E. (1980), Crustal deformations from geodetic measurements. Boll.Geofis.Teor.Appl., 22, 255-260.

Lyon-Caen H. (1980), Séismes du Frioul (1976): modelés de source à l'aide de seismogrammes synthétiques d'ondes de volume. Thése de 3éme cycle. Univ.Paris VII.

Proc.CNEN-ENEL (1977), Specialist Meeting on the 1976 Friuli earthquake and the antiseismic design of nuclear installations, CNEN, Rome, Italy.

Rovelli A. (1982), On the frequency dependence of Q in Friuli from short-period digital records. Bull.Seism.Soc.Am., 72, 2369-2372.

Rovelli A. (1983), Time-frequency analysis of seismic excitation and estimates of attenuation parameters for the Friuli (Italy) local earthquakes. Phys.Earth.Plan.Int., 33, 457-469.

Seidl D., Berckhemer H. (1982), Determination of source moment and radiated seismic energy from broadband recordings. Phys.Earth.Plan.Int. 30, 209 - 21

Siro L., Slejko D. (1982), Space-time evolution of the 1977-1980 seismicity in the Friuli area and its seismotetonic implications.Boll.Geofis.Teor. Appl., 24, 77-88.

Slejko D., Renner G. (1984), La sequenza sismica iniziata con il terremoto del 6 maggio 1976 in Friuli. Preprint.

Wittlinger G. (1980). Etude de la sismicité en champ proche par un réseau sismologique à faible ouverture: application au Frioul (Italie) et au gisement de Lacq (France). These de 3éme cycle, Univ. Louis Pasteur, Strasbourg, France.

Zanferrari A., Bollettinari G., Carobene L., Carton A., Carulli G.B., Cartaldini D., Cavallin A., Panizza M., Pellegrini G.B., Pianetti F., Sanza U. (1982). Evoluzione neotettonica nell'Italia nord-orientale. Mem. Soc.Geol.It., 35, 355-376. Padova.

THE SEISMIC INVERSE PROBLEM FOR A FLAT STRUCTURE

F.Abramovici and J.Baumgarten
School of Mathematical Sciences
Tel-Aviv University

ABSTRACT. The Backus-Gilbert theory is applied to the case of an inhomogeneous layer over a homogeneous half-space. The layer consists of a number of sublayers with continuous elastic properties. At interfaces there may be discontinuities of any type. The locations of the interfaces and the variation of elastic properties within each layer may be totally unknown or may have a known form, so that only a number of discrete parameters are to be determined. The data consists in seismograms recorded at the surface. The Frechet kernels and the resolution analysis are presented in a framework that extends the Backus-Gilbert theory to this type of structures.

1. INTRODUCTION

In a recent paper (Abramovici and Boumgarten, 1985), we presented an extension of the Backus-Gilbert theory to the case of a flat structure consisting of one non-homogeneous layer over a homogeneous half-space, the layer being divided into sublayers within which the elastic parameters and density varies continuously. We considered two types of such sublayers: "discrete" sublayers, having their structure described by linear combinations of known functions and "continuous" ones, where the variation is completely arbitrary. The levels of the separation planes between the sublayers were assumed unknown. The advantage of such a combination is that when the form of the variation is known, e.g. linear, the numerical process leading to the solution of the inverse problem is very rapid, since it consists in solving a discrete problem with a few parameters.

In Abramovici and Baumgarten (1985) we applied the theory to the magnetotelluric problem. Here, we show how to use the same formalism for the seismic inverse problem of determining the elastic parameters λ, μ and the density ρ as functions of depth, when we have a seismograph recorded at the surface.

2. THE PROBLEM'S FORMULATION

We assume for simplicity an explosive point source acting somewhere in

M. O. Erdik and M. N. Toksöz (eds.), Strong Ground Motion Seismology, 99–106.
© 1987 by D. Reidel Publishing Company.

the layer and we use as data the Fourier transforms of the displacement components for several frequencies.

Using the customary definition of the transform preferred by seismologists (Aki and Richards, 1980)

$$F(\omega) = \int_{-\infty}^{+\infty} f(t)e^{i\omega t}dt \tag{1}$$

we can write the transformed displacement components in the form :

$$S_z(\omega) = \frac{V_0 c_0}{H^3} h(\omega) \int_0^\infty k \left[\frac{u_3 v_3 - u_4 v_2}{v_6} - u_1 \right]_{\zeta=1} J_0(kr)dk$$

$$S_r(\omega) = \frac{V_0 C_0}{H^3} h(\omega) \int_0^\infty \left[\frac{u_3 v_5 - u_4 v_4}{v_6} - u_2 \right]_{\zeta=1} \frac{dJ_0(kr)}{dr} dk \tag{2}$$

where V_0 is the volume injected at the source per unit time, c_0 is a scale factor for elastic velocities, $h(\omega)$ is the transform of the time-variation of the source, ζ is the normalized vertical coordinate and J_0 is the zero-order Bessel function.

The vector functions u and v satisfy the following differential systems:

$$\frac{du}{d\zeta} = Au \ , \ \frac{dv}{d\zeta} = Bv \tag{3}$$

with

$$A = \begin{pmatrix} 0 & \lambda k/(\lambda + 2\mu) & 1/(\lambda + 2\mu) & 0 \\ -k & 0 & 0 & 1/\mu \\ -\rho\omega^2 & 0 & 0 & k \\ 0 & \chi & -\lambda k/(\lambda + 2\mu) & 0 \end{pmatrix}$$

$$B = \begin{pmatrix} 0 & 0 & 1/\mu & -1/(\lambda + 2\mu) & 0 & 0 \\ 0 & 0 & k & \lambda k/(\lambda + 2\mu) & 0 & 0 \\ \chi & -\lambda k/(\lambda + 2\mu) & 0 & 0 & \lambda k/(\lambda + 2\mu) & 1/(\lambda + 2\mu) \\ \rho\omega^2 & -k & 0 & 0 & k & -1/\mu \\ 0 & 0 & -k & -\lambda k/(\lambda + 2\mu) & 0 & 0 \\ 0 & 0 & -\rho\omega^2 & -\chi & 0 & 0 \end{pmatrix} \tag{4}$$

$$\chi = -\rho\omega^2 + 4k^2\mu(\lambda + \mu)/(\lambda + 2\mu)$$

The components of u represent scaled displacements and stresses

due to the source located at $\zeta = \zeta_s$. Accordingly, u is obtained integrating the first system (Eq.3) from $\zeta = \zeta_s$ to $\zeta = 1$ with the following initial conditions:

$$u_{|\zeta = s} = (-1,\ 0,\ 0,\ -2k\mu)^T \tag{5}$$

T meaning "transpose".

The components of v are second-order determinants formed by the components of two linearly independent solutions u_1 and u_2 and are obtained integrating the second system from $\zeta = 0$ within the following initial conditions (Abramovici and Baumgarten, 1985):

$$u_{|\zeta = 0} = \left[1/(\mu_0 \nu_s)\right](\nu_p \nu_s - k^2, \psi, -\nu_p \rho_0 \omega^2, -\nu_s \rho_0 \omega^2, -\psi, \phi^2 - 4k^2 \mu_0 \nu_p \nu_s)^T \tag{6}$$

where

$$\nu_p = (k^2 - \omega^2/\alpha_0^2)^{1/2}, \nu_s = (k^2 - \omega^2/\beta_0^2)^{1/2},$$

$$\phi = 2\mu_0 k^2 - \rho_0 \omega^2, \psi = 2\mu_0 \nu_p \nu_s - \phi \tag{7}$$

$\rho_0, \nu_0, \alpha_0, \beta_0$ being the density, shear modulus, P-velocity and S-velocity in the half-space respectively.

Leaving aside the constant factor in front, the integrals (Eq.2) are the data for our inverse problem. The unknowns to be determined from these data are the values of λ, μ and ρ as functions of the depth variable ζ.

3. THE EXTENDED BACKUS-GILBERT PROCEDURE

In a general framework, our problem is to find solutions to the equations

$$\gamma_l = g_l(q) \qquad (l = 1, \ldots, L) \tag{8}$$

where g_l are Frechet differentiable functionals of an unknown model q. In order to take into account that the discontinuity levels ζ_j are also unknown, we map the components of q, consisting in the functions $\lambda(\zeta)$, $\mu(\zeta), \rho(\zeta)$ in all the subintervals, through linear applications of the intervals $[\zeta_{j-1}, \zeta_j]$ onto a standard interval $0 \le \tau \le 1$, into functions of the standard variable τ. Our model space $\hat{M}$ will consist therefore of the pairs $q = (p(\tau), \zeta)$ where $p(\tau)$ is a vector function representing the variation of λ, μ, ρ with depth in all the subintervals and $\hat{p}$ a constant vector of components $\zeta_1, \ldots \zeta_{k-1}$, k being the number of sublayers. We use the inner product

$$(q^{(1)}, q^{(2)}) = \langle p^{(1)}, p^{(2)} \rangle + \hat{p}^{(1)} \hat{p}^{(2)} \tag{9}$$

where the first term is the usual L_2 inner product and the second is the ordinary scaler product of two vectors in a finite-dimensional space. By completing the inner product, space $\hat{M}$ in the standard manner, we obtain a Hilbert space, called again $\hat{M}$. The models we are looking for form a subspace $\hat{M}_d$ of $\hat{M}$, for which some of the components of $p(\tau)$ are "discrete", i.e. are linear combinations of known functions $\phi_m(\tau)(m = 1,\ldots,M)$. Thus, it would be convenient to write the elements of $\hat{M}$ as triples $p=(p_c,p_d,\hat{p})$ where p_c is a vector function representing the "continuous" layers, i.e. in which the variation of the components is arbitrary and p_d represents the discrete layers, i.e. those defining the subspace $\hat{M}_d$. For the elements in $\hat{M}_d$, p_d has a particular form:

$$p_d = \sum_m c_m \phi_m(\tau) \tag{10}$$

with c_m constant vectors. The inner product between an element $p^{(1)} \in M_d$ and any element $p^{(2)}$ of $\hat{M}$ takes the special form:

$$(p^{(1)},p^{(2)}) = \langle p_c^{(1)}, p_c \rangle + \sum_m C_m^{(1)} . \overset{*}{p}_m^{(2)} + \hat{p}^{(1)} . \hat{p}^{(2)} \tag{11}$$

where the vector $\overset{*}{p}_m^{(2)}$ is defined as follows:

$$\overset{*}{p}_m^{(2)} = \langle \phi_m, p_d^{(2)} \rangle \tag{12}$$

Moreover, the inner product of two elements $p^{(1)},q^{(2)}$ of $\hat{M}_d$ takes the special form

$$(p^{(1)}, p^{(2)}) = \langle p_c^{(1)}, p_c^{(2)} \rangle + \sum_{m,\bar{m}} \Phi_{m,\bar{m}} c_m^{(1)} . c_{\bar{m}}^{(2)} + \hat{p}^{(1)} . \hat{p}^{(2)} \tag{13}$$

where

$$\Phi_{m,\bar{m}} = \langle \phi_m, \phi_{\bar{m}} \rangle \tag{14}$$

Using Lagrange multipliers α_l $(l = 1,\ldots,L)$ and an ordinary variational procedure, we get the following iterative process (Backus and Gilbert, 1967) :

$$p_c^{(n+1)} = p_c^{(n)} + \sum_l \alpha_l (K_l^{(n)})_c$$

$$c_m^{(n+1)} = c_m^{(n)} + \sum_l \alpha_l \sum_{\bar{m}} \Phi^{-1}_{m\bar{m}} \overset{*}{K}_{\bar{m}l}^{(n)} \tag{15}$$

$$\hat{p}^{(n+1)} = \hat{p}^{(n)} + \sum_l \alpha_l \hat{K}_l^{(n)}$$

where $\Phi^{-1}_{m\bar{m}}$ are the elements of the inverse matrix Φ^{-1} of $\Phi = (\Phi_{m\bar{m}})$ and

$$\overset{*}{K}{}^{(n)}_{\overline{m}l} = \langle \phi_{\overline{m}}, (K_l)_d \rangle \tag{16}$$

The coefficients α_l are obtained by solving the following linear system:

$$\sum_{\tau} \left[\sum_{m,\overline{m}} \Phi^{-1}_{m\overline{m}} \overset{*}{K}{}^{(n)}_{ml} \overset{*}{K}{}^{(n)}_{ml} + \langle (K_l{}^{(n)})_c, (K_\tau^{(n)})_c \rangle + (\hat{K}_l{}^{(n)}) \cdot (\hat{K}_\tau{}^{(n)}) \right] \alpha_l = \gamma_l - g_l(p^{(n)}) \tag{17}$$

Resolution is analysed along the lines of the Backus-Gilbert theory, obtaining resolution kernels for the "continuous" part of the model to which the procedure converges and resolution matrices for its "discrete" part, i.e. for the coefficient c_m and for the discontinuity levels ζ_j (Backus and Gilbert, 1970, 1966).

4. THE FRECHET KERNELS

By changing the model slightly from, p to $p + \delta p$, where $\delta p = (\delta p, \sum_m (\delta c_m)\, \phi m, \delta \hat{p})$ the displacement components $S_z(\omega), S_r(\omega)$ given by (Eq.2) are also changed by a small quantities $\delta S_z(\omega)$ and $\delta S_r(\omega)$. The Fréchet kernels of the functionals $S_z(\omega)$ and $S_r(\omega)$ are obtained by taking the first variation of the integrals in (Eq.2). Differentiating under the integral sign, we obtain

$$\delta S_z(\omega) = \frac{V_0 c_0}{H^3} h(\omega) \int_0^\infty k \delta S_z(\omega,k) J_0(kr)\, dk$$

$$\delta S_r(\omega) = \frac{V_0 c_0}{H^3} h(\omega) \int_0^\infty \delta S_z(\omega,k) \frac{dJ_0(kr)}{dr}\, dk \tag{18}$$

where

$$\delta S_z(\omega,k) = \left[(u_3 \delta\nu_3 + \nu_3 \delta u_3 - u_4 \delta\nu_2 - \nu_2 \delta u_4)\nu_6 - (u_3\nu_3 - u_4\nu_2)\delta\nu_6 - \nu_6 \delta u_1 \right] / \nu_6^2$$

(19)

$$\delta S_r(\omega,k) = \left[(u_3 \delta\nu_5 + \nu_5 \delta u_3 - u_4 \delta\nu_4 - \nu_4 \delta u_4)\nu_6 - (u_3\nu_5 - u_4\nu_4)\delta\nu_6 - \nu_6 \delta u_2 \right] / \nu_6^2$$

δu and δv being obtained by integrating the systems obtained from (Eq.3) by a small perturbation. The result expressed in terms of the original normalized vertical variable ζ and the variation of the elastic parameters and density of the model, is

$$\delta v = \int_0^1 F(1) F^{-1}(\zeta) \left[\nu_\rho(\zeta) \delta\rho(\zeta) + \nu_\mu(\zeta) \delta\mu(\zeta) + \nu_\lambda(\zeta) \delta\lambda(\zeta) \right] d\zeta$$

$$+ \sum_j \left\{ \frac{1}{d_j}\left[\nu(\zeta_j) - \nu(\zeta_{j-1})\right] - \frac{1}{d_{j+1}}\left[\nu\ \zeta_{j+1}) - \nu\ \zeta_j\ \right] \right\} \delta\zeta_j \quad (20)$$

$$\delta u = \int_{\zeta_s}^{1} E(1)E^{-1}(\zeta)\left[\nu_p(\zeta)\delta\rho(\zeta) + u_\mu(\zeta)\delta\mu(\zeta) + u_\lambda(\zeta)\delta\lambda(\zeta)\right] d\zeta$$

$$+ \sum_{j=j_s} \left\{ \frac{1}{d_j}\left[u(\zeta_j) - u(\zeta_{j-1})\right] - \frac{1}{d_{j+1}}\left[u\ (\zeta_{j+1}) - u(\zeta_j)\right] \right\} \delta\zeta_j \quad (21)$$

where $E(\zeta)$, $F(\zeta)$ are the solution matrices of the systems (3), respectively, and

$$u_p(\zeta) = \omega^2 M_1 u(\zeta), \qquad \nu_p(\zeta) = \omega^2 N_1 v(\zeta)$$

$$u_\mu(\zeta) = M_2(\zeta)u(\zeta), \qquad \nu_p(\zeta) = N_2(\zeta)v(\zeta) \quad (22)$$

$$u_\lambda(\zeta) = \gamma_1 M_3(\zeta)u(\zeta), \qquad \nu_\lambda(\zeta) = \lambda_1 N_3(\zeta)v(\zeta)$$

with

$$M_1 = \begin{pmatrix} 0 & 0 & 0 & 0 \\ 0 & 0 & 0 & 0 \\ -1 & 0 & 0 & 0 \\ 0 & -1 & 0 & 0 \end{pmatrix}$$

$$M_2(\zeta) = \begin{pmatrix} 0 & -2k\lambda\lambda_1 & -2\lambda_1 & 0 \\ 0 & 0 & 0 & -\mu_1 \\ 0 & 0 & 0 & 0 \\ 0 & \lambda_1\mu_1 & 2k\lambda\lambda_1 & 0 \end{pmatrix} \quad (23)$$

$$M_3(\zeta) = \begin{pmatrix} 0 & -2k\mu & -1 & 0 \\ 0 & 0 & 0 & 0 \\ 0 & 0 & 0 & 0 \\ 0 & 4k^2\mu^2 & -2k\mu & 0 \end{pmatrix}$$

$$N_1 = \begin{pmatrix} 0 & 0 & 0 & 0 & 0 & 0 \\ 0 & 0 & 0 & 0 & 0 & 0 \\ -1 & 0 & 0 & 0 & 0 & 0 \\ 1 & 0 & 0 & 0 & 0 & 0 \\ 0 & 0 & 0 & 0 & 0 & 0 \\ 0 & 0 & -1 & -1 & 0 & 0 \end{pmatrix}$$

$$N_2(\zeta) = \begin{pmatrix} 0 & 0 & -\mu_1 & 2\lambda_1 & 0 & 0 \\ 0 & 0 & 0 & 2k\lambda\lambda_1 & 0 & 0 \\ \lambda_1\nu_1 & 2k\lambda\lambda_1 & 0 & 0 & -2k\lambda\lambda_1 & -2\lambda_1 \\ 0 & 0 & 0 & 0 & 0 & \mu_1 \\ 0 & 0 & 0 & 2k\lambda_1 & 0 & 0 \\ 0 & 0 & 0 & -\lambda_1\nu_1 & 0 & 0 \end{pmatrix} \tag{24}$$

$$N_3(\zeta) = \begin{pmatrix} 0 & 0 & 0 & 1 & 0 & 0 \\ 0 & 0 & 0 & 2k\mu & 0 & 0 \\ 4k^2\mu^2 & -2k\mu & 0 & 0 & 2\mu k & -1 \\ 0 & 0 & 0 & 0 & 0 & 0 \\ 0 & 0 & 0 & -2k\mu & 0 & 0 \\ 0 & 0 & 0 & -4k^2\mu^2 & 0 & 0 \end{pmatrix}$$

and

$$\lambda_1 = 1/(\lambda + 2\mu)^2, \mu_1 = 1/\mu^2, \nu_1 = 4k^2(\lambda^2 + 2\lambda\mu + 2\mu^2) \tag{25}$$

REFERENCES

F. Abramovici,(1968), Mode theory versus theoretical seismograms for a layered solid. Geophys. J.R.Astr.Soc.vol.16, 9 - 20.

F. Abramovici,(1968), Diagnostic diagrams and transfer functions for oceanic wave-guides. Bull.Seism.Soc.Am. vol.58, 427 - 456.

F. Abramovici and J. Baumgarten,(1985), The Backus-Gilbert theory for piecewise continuous structures with variable discontinuity levels and its application to the magnetotelluric problem. Geophy. J.Roy. Astr. Soc., vol. 81.

K.Aki and P.Richards,(1980), Quantitative seismology, Freeman and Co.

G. Backus and F.Gilbert,(1967), Numerical application of a formalism for geophysical inverse problem. Geophy. J.Roy.Astr. Soc. vol. 13,247-276.

G. Backus and F.Gilbert,(1968), The resolving power of gross earth data. Geophy. J.Roy.Astr.Soc. vol. 16, 169-205.

G. Backus and F.Gilbert,(1970), Uniqueness in the inversion of inaccurate gross earth data. Phil Trans. Roy.Soc.London, Sec A. vol.266, 123 - 192.

G.Backus and F.Gilbert,(1966), Propagator matrices in elastic wave and vibration problems. Geophysics, vol.31, 326-332.

SECTION 2

PREDICTION OF STRONG GROUND MOTION

THE PREDICTION OF STRONG GROUND MOTION

David M. Boore
U.S. Geological Survey
Mail Stop 977
345 Middlefield Road
Menlo Park, California 94025

ABSTRACT. The prediction of motion for use in engineering design must rely both on empirical and theoretical methods. The methods complement on another, for the empirical analyses provide checks on the theory and help to determine the parameters necessary in the theoretical predictions. In this paper, I will give short discussions of both the empirical and theoretical methods for predicting strong motion that I and my colleagues have been doing over the last several years.

1. INTRODUCTION

Predictions of strong ground motions have many uses, ranging from the specification of a time series for nonlinear response calculations of a particular engineered structure, to predictions of peak motions needed in the construction of earthquake hazard maps covering broad geographic area. In some cases the predictions can be based on empirical analyses of existing data; when this is not possible, theoretical models must be used as the basis for the predictions. In this paper, I will give short discussions of both the empirical and theoretical methods for predicting strong motion that I and my colleagues have been doing over the last several years. Although the paper covers most of the important topics, it is not intended to be a comprehensive review of the literature on the subject.

2. EMPIRICAL PREDICTION

The existing recordings of ground motions within several hundred kilometers of the earthquake source can be used in several ways to predict ground motions for engineering design and seismic hazard planning. The most straightforward use occurs when recording are available in magnitude and distance ranges for which the design motions must be specified. This is sometimes referred to as site specific prediction. As seen in Figure 1, however, recordings are generally lacking close to large earthquakes, and thus design motions for such cases must be based on

M. O. Erdik and M. N. Toksöz (eds.), Strong Ground Motion Seismology, 109–141.
© 1987 by D. Reidel Publishing Company.

extrapolations of the data. This is commonly done by using regression analysis to fit a mathematical function involving distance and magnitude to the existing data, and then using this function to make predictions. The determination of the empirical prediction equations is the subject of this section (see Boore and Joyner, 1982, for a more complete discussion). Representing, as they do, the average value of ground motions for a specified magnitude and distance, the empirically-derived prediction equations are also useful in checking theoretical predictions if care is made to make comparisons in the range of magnitudes and distances for which the empirical functions are constrained by the data.

2.1. Choice of Variables

Empirical predictions are generally based on a mathematical function connecting response variables, such as peak acceleration, velocity, or oscillator response, with explanatory variables, the most common of which are distance and magnitude. Unfortunately, definitions of distance and magnitude are not standard, and thus care must be used in comparing predictions made by various authors. Because the fault rupture occurs over an extended surface, a variety of possible distance definitions are possible (Figure 2). My colleague William Joyner and I have adopted as our measure the closest distance from the site to the surface projection of the fault rupture. We have used this, rather than another definition, with the goal of prediction in mind: in future earthquakes it is unlikely that the hypocenter or high-stress zones will be known beforehand, and thus distance measures such as M1, M2, and M3 will be of little use, even they may lead to reduced scatter in analyzing existing data.

Many measures of magnitude are available (Figure 3), according to the type of wave and its period. A number of people seem to prefer magnitude measures based on motions with periods close to those of interest in engineering. The problem with this, however, is that the explanatory variable (magnitude) and the response variable (the ground motion parameter) are virtually the same quantity. A more sensible magnitude is the moment magnitude (Hanks and Kanamori, 1979), which is defined by the seismic moment by the relation:

$$M = 2/3 \log M_o - 10.7 \qquad (1)$$

where M_o is the seismic moment in dyne-cm. Because of the definition of moment in terms of overall fault area (Σ) and fault slip (D) according to

$$M_o = \mu D \Sigma \qquad (2)$$

where μ is the rigidity of the earth in the vicinity of the source,moment magnitude has a clear physical meaning as a measure of the size of an earthquake. Furthermore, geologic investigations can be of some use in predicting the possible moment magnitudes of future earthquakes.

Other explanatory variables are sometimes used in regression analysis; these can include variables to represent the geologic conditions at the recording sites, the tectonic environment (for example, thrust vrs. strike-slip faulting), the type of structure in which the recording was

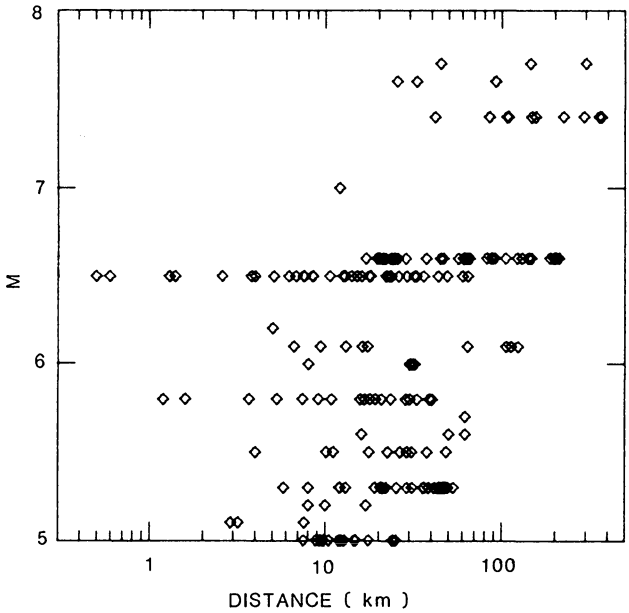

Figure 1. Distribution in magnitude and distance of the peak horizontal data used by Joyner and Boore (1981). Each point represents one recording.

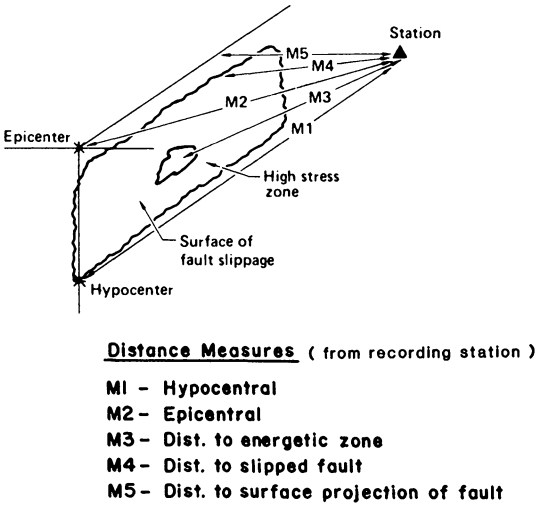

Figure 2. Distance measures used in the prediction equations (from Shakal and Bernreuter, 1981).

made, and the fault geometry (used to account for directivity). All of these can be shown to influence the response, but the most commonly used variable is the one used to quantify the influence of geologic conditions.

2.2. The Regression Model

The following equation is the one most commonly used in regression analysis:

$$\log Y = c_0 + c_M M - c_D D(M) - c_{LD} \log D(M) + c_s S + c_p P \qquad (3)$$

where Y is the response variable, D is the distance measure, S is a geologic variable (taken by Joyner and Boore, 1981, to be 0 for rock and 1 for soil), P is the uncertainty in the prediction (0 and 1 for 50 and 84 percentile values, respectively, assuming a lognormal distribution for Y), and the c's are coefficients to be determined. The distance may be a function of magnitude; a physically motivated equation that allows this is

$$D(M) = \left[d^2 + (h_1 e^{h_2 (M-6)})^2\right]^{1/2} \qquad (4)$$

where d is the distance to the surface projection of the fault (M5 in Fig.2), h_1 and h_2 are parameters determined by the regression analysis.

The determination of the regression coefficients is easily done using standard least-square techniques. Some care should be given in the weighting and selection of the data, however, to avoid biases in the result. For example, beyond some distance for any earthquake some accelerographs will not be triggered; readings from those that do will bias the results to large values and should not be included in the regression analysis. It is often the case that a few earthquakes are particularly well-recorded over a range of distances; these events should exert a strong influence on the distance-attenuation coefficients c_D and c_{LD}, but they say little about the scaling with source size (as given by c_M). It is therefore natural to separate the regression into two parts (as shown schematically in Figure 4). In the first, the attenuation coefficients are determined. If h_2 in Equation 4 , is constrained to be zero (unless forced by the data to do otherwise), the magnitudes of the events will not enter into the first regression, and therefore errors in magnitude will not be mapped into the distance coefficients. The result of this regression is a set of offset factors A_i , one for each earthquake. The second regression fits these offset factors by a polynomial in magnitude

$$A_i = p_0 + p_1(M_i - 6) + p_2(M_i - 6)^2 + \ldots \qquad (5)$$

Often only a linear term is needed, in which case c_M in Equation 3 equals p_1. There are instances, however, when magnitude saturation requires higher order terms. The term 'M - 6' was used rather than 'M' for convenience, for then p_1 is the slope at magnitude 0. In the published regression work of Joyner and Boore (1981, 1982), no weighting

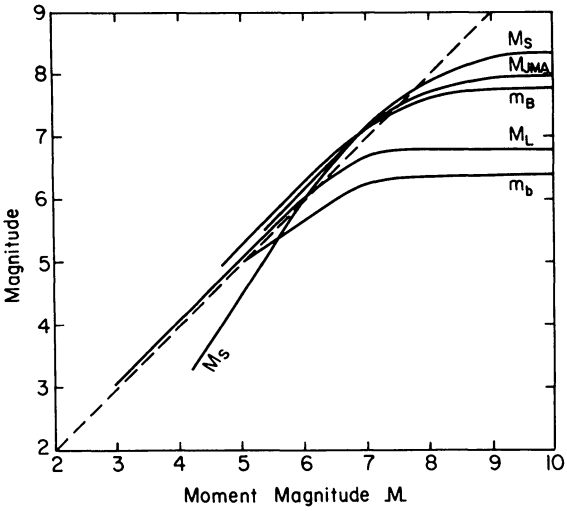

Figure 3. Relation between moment magnitude and various magnitude scales : M_s(surface wave); m_b(short-period body wave); M_B(long-period body wave); M_L(local); and M_{JMA}(Japan Meteorological Agency). Dashed line shows a 1:1 relation for reference. Figure adapted from T.Heaton (unpublished data, 1982).

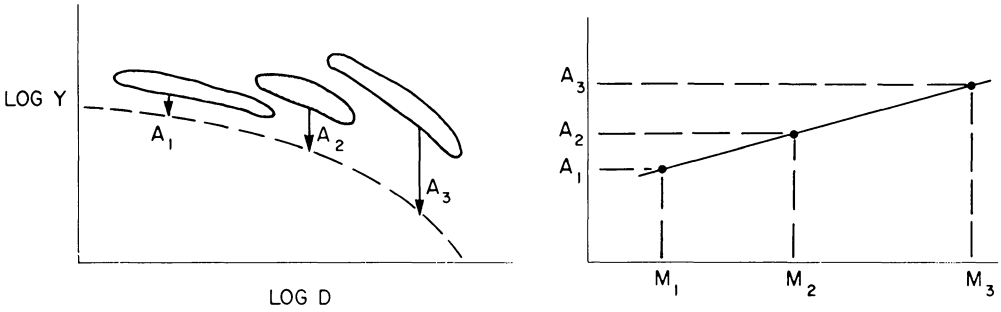

Figure 4. Schematic diagram showing the two-step regression procedure of Joyner and Boore (1981). The top figure shows the first regression, in which the shape of the dashed curve is varied, and all the data points from the *i*th earthquake (contained within each enclosed area) are shifted by a distance A_i so that the sum of the squares of the residuals is minimized. The bottom figure shows the second regression of the offset factors versus magnitude. An advantage of the two-step procedure is that the variance due to site and travel path complexities is treated separately from the inter-earthquake variance due to source complexities. These two contributions to the overall variance are physically distinct and should be treated as such.

was used in the second regression, even though the A_i for some earthquakes might have much less uncertainty than for others (in particular, those recorded at only one station). As a result of the work of Brillinger and Preisler (1985), we have modified our procedure to include weighting. The scheme is as follows: we let the variance of A_i be the sum of σ_1^2/n_i and σ_2^2, where σ_1 is the standard deviation of the residuals in the first regression, n_i is the number of data from the i th earthquake, and σ_2^2 is the variance of the response variable in the second regression. σ_2^2 is unknown at first, and must be determined iteratively by doing the second regression with a sequence of σ_2^2 values. In each analysis, the squared residuals are weighted by the inverse of the combined variance.

2.3. Analysis of Regression Results

It is essential that the residuals (predicted response minus observed response) be plotted against the various explanatory variables in order to check for systematic trends indicative of an improper regression model and, consequently, biased predictions. An example is shown in Figure 5. From that figure we can conclude that no bias exists; perhaps most striking, however, is the large scatter. Introducing more explanatory variables may help in reducing the scatter somewhat, but a large amount will probably still persist. There are many sources of scatter, ranging from earthquake-to-earthquake stress variations to changes in local site properties within a small horizontal distance. It should be recognized that some level of uncertainty (and perhaps a large one)will exist in spite of intensive efforts to reduce it.

The treatment of uncertainty is important, for often design motions are based on predictions other than the mean. The uncertainty in the predictions is a combination of the scatter in the residuals and the uncertainty in the regression coefficients. In a nonlinear regression (as is the one discussed above, because of the h_1 and h_2 terms in Equation 4), a Monte Carlo procedure is a useful way of estimating the uncertainty. The basic idea is to generate a suite of synthetic data at magnitude, distance points corresponding to the real set of data. The regression equation with fixed parameters is used to generate the data, and random error with variance determined by the residuals of the real data is added. The two-stage regression analysis is then performed. This is repeated for many sets of data, and variations in the assumed model can also be made. Statistical statements can then be made about the uncertainty in the regression coefficients. An example is shown in Figure 6. Here the question was whether or not a nonzero h_2 (and therefore attenuation curves whose shape depended on magnitude) was required by the data. Analysis of the real data gave a nonzero h_2 (the open square). The h_2 coefficient determined from the regression analysis of thirty sets of simulated data, all of which used a zero value for h_2 (open circle) in generating the data, were scattered about the zero line, with a bias to positive values. Six values were greater than or equal to the derived value, indicating that the particular value for h_2 found from the real data could be nonzero by chance alone. This doesn't say

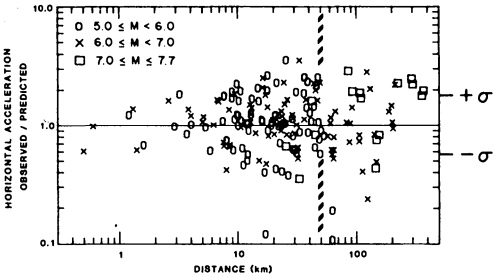

Figure 5. Residuals of peak horizontal acceleration with respect to empirically-determined prediction equation of Joyner and Boore (1981), plotted against distance (ignore vertical dashed line).

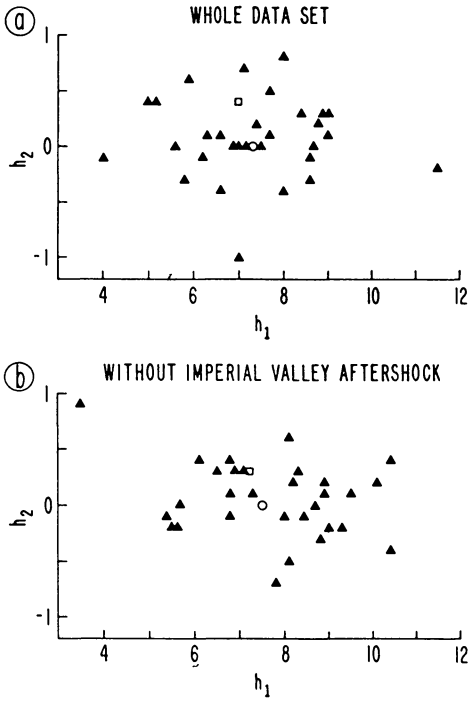

Figure 6. (h_1,h_2) pairs obtained from the Monte Carlo study described in the text. Solid triangles are derived from simulated data, which used the (h_1,h_2) value shown by the open circle, and the open square shows the (h_1,h_2) pair from analysis of the observed data.

that a nonzero value is wrong, only that the hypothesis of a zero value cannot be rejected at a reasonable level of confidence. The next step would be to do a similar analysis with a range of h_2 values and thereby determine confidence intervals for h_2.

2.4. Selected Results

Predictions of peak acceleration and velocity from analysis of many strong-motion data from western North America (primarily California)are shown in Figure 7. Note that the curves for both acceleration and velocity have similar shapes beyond about 20 km, although the frequency content of the two measures of ground shaking is quite different. This implies that the effective attenuation parameter Q is frequency dependent (e.g., Boore,1984, Fig. 2). Also note the difference in spacing between the curves: the peak velocity is a more sensitive function of moment magnitude than is peak acceleration. As I will show later, this is in agreement with a commonly used seismological model of spectral radiation.

Although peak acceleration is widely used to specify design motions (often to scale a fixed spectral shape), many engineers and seismologists bemoan this and urge that response spectra be specified directly. With the increasing amount of digitized data it is now possible to accomplish this, using the same procedures used for the derivation of predictive equations for peak acceleration. Figure 8 shows an example, in which response spectra for a range of magnitude and site geology are shown for a fixed distance. The dashed curves are not constrained by data (and thus emphasize the crucial need for more data close to large earthquakes). Note that the shape of the curves is strongly magnitude dependent, in contradiction to the assumption underlying the commonly used method of deriving design motions by scaling a fixed spectral shape.

3. THEORETICAL PREDICTION

As with the empirical prediction of ground motion, there are many uses for theoretical predictions, both in seismology and in engineering. Theoretical predictions can be used to specify a suite of time series for use in dynamic structural analysis, they can provide estimates of ground-motion parameters in geographic regions or portions of magnitude-distance space lacking observations, and they can be used as an essential part of understanding the physics of earthquake sources and wave propagation. Much effort in seismology has been devoted to deterministic simulations of ground motion from specified faults in laterally-uniform geologic materials whose properties are a function of depth. Although these simulations can be useful in predicting low-frequency motions (e.g.,Figure 9), they are generally not relevant for simulations of high-frequency motions: not only does the cost of doing the simulations increase dramatically with frequency, but the basic model assumptions are invalid. Engineers, on the other hand, usually use a purely stochastic approach in deriving time series for design purposes. The parameters that control the duration, frequency content, and amplitude of these

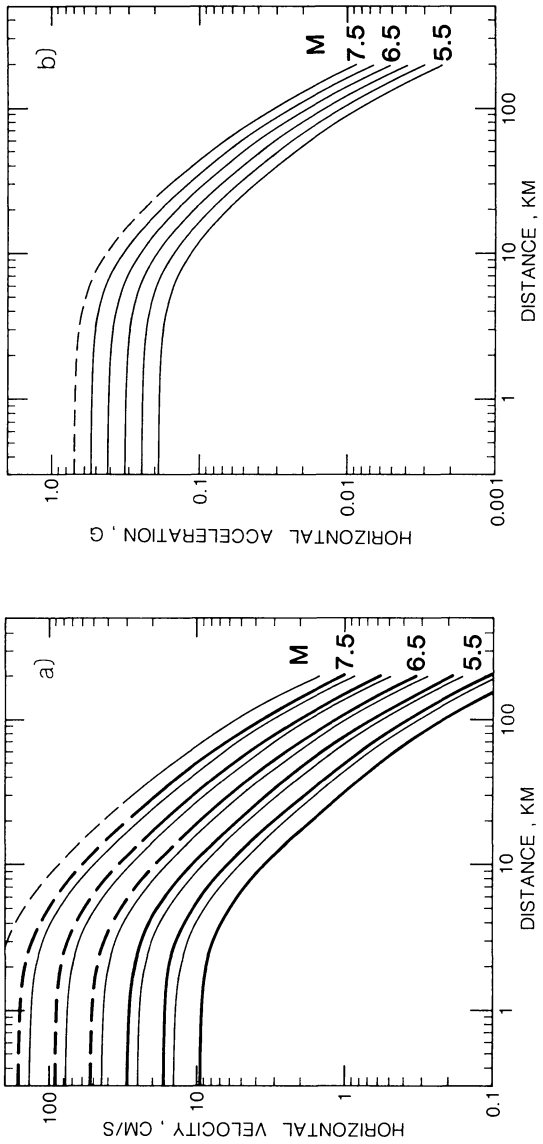

Figure 7. Peak horizontal acceleration and velocity from empirical analysis of randomly chosen horizontal components. Light lines: soil sites; heavy lines; rock sites. Curves dashed where not constrained by data (from Joyner and Fumal, 1985).

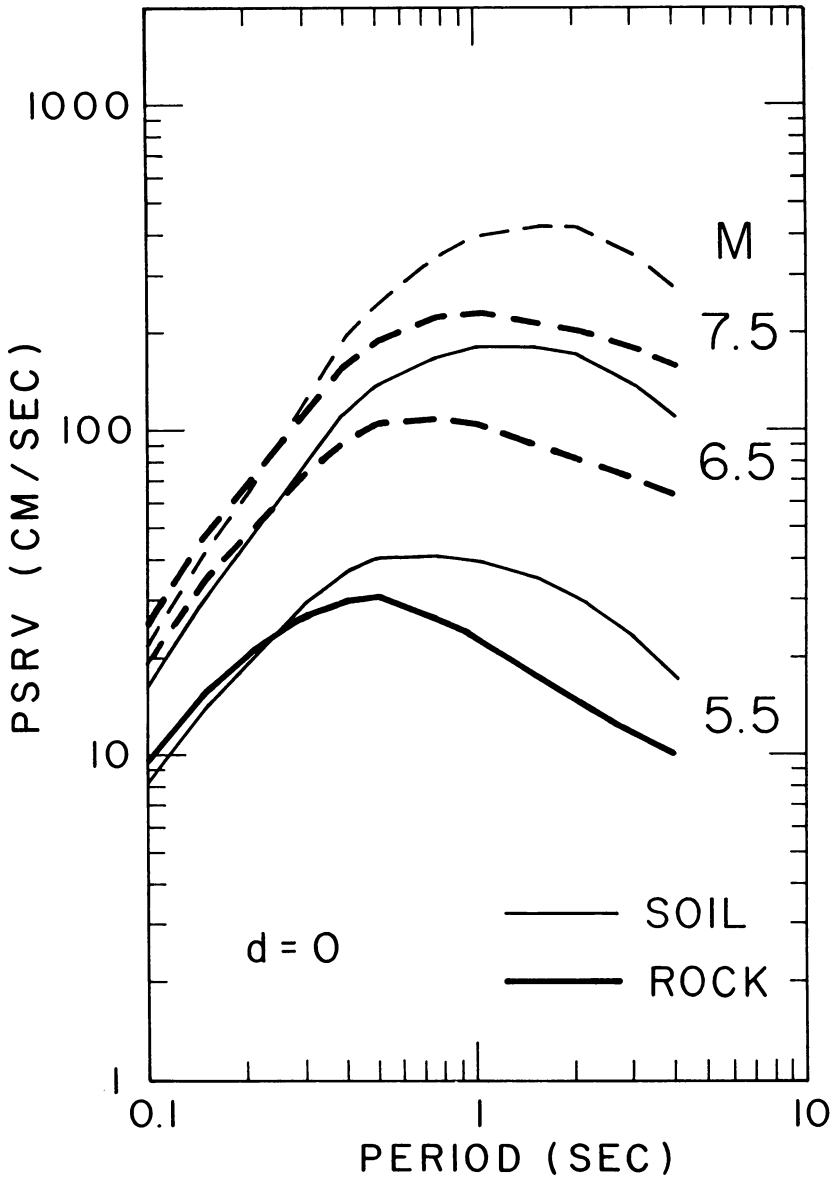

Figure 8. Predicted pseudo-velocity response spectra for 5 percent damping at rock sites (heavy line) and soil sites (light line) for zero distance, for larger of peaks on the two horizontal components. Curves are dashed where not constrained by data.

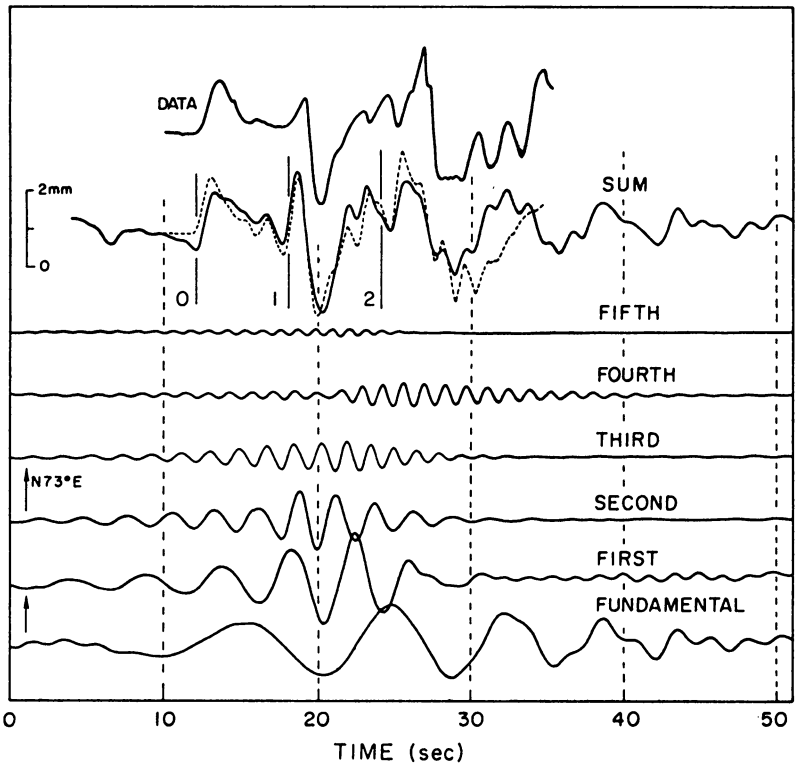

Figure 9. Comparison of Love-wave synthetic ground displacements (solid lines) with Heaton and Helmberger's (1978) model of the 1976 Brawley earthquake as recorded at station IVC, 33 km from the epicenter (dashed lines). The actual ground displacements are given by the top curve. Details are given in Swanger and Boore (1978).

motions are taken from empirical analysis of the existing data. Because of this, however, the usual stochastic techniques share the same problems as do the empirical techniques in predicting motions for situations in which no data exist.

Recently a hybrid approach has been developed that assumes random ground motion with properties determined from seismological models of the source and the wave propagation (McGuire and Hanks, 1980; Hanks and McGuire, 1981; Boore,1983; McGuire et al,1984; Boore,1986a). This new method does not have the limitations of the methods just discussed. The basic idea of the method is a simple one: the ground motion is represented by windowed and filtered white noise,with the average spectral content and the duration over which the motion lasts being determined by a seismological description of seismic radiation that depends on source size.

3.1. Spectral Content

The spectrum at a distance r from an earthquake can be written as a cascade of a number of filters. A common description of the spectrum at a site is:

$$R(f) = C\, S(f)A(f)D(f)I(f) \tag{6}$$

where the factors C,S,A,D, and I stand for a scaling factor, the source spectrum, an amplification factor, a diminution factor, and a factor used to specify the type of motion being computed, respectively. Only S(f) depends on seismic moment. C is given by

$$C = \frac{R_{\Theta\Phi}\, FH}{4\pi\rho\beta^3} \left(\frac{1}{r}\right), \tag{7}$$

where $R_{\Theta\Phi}$ is the radiation pattern averaged over an appropriate range of azimuth and takeoff angle (e.g., Boore and Boatwright, 1984), F accounts for free surface effects, H represents the partition of energy from a vector into horizontal components (if needed, depending on the value of $R_{\Theta\Phi}$ used),ρ and β are the density and shear velocity in the source region, and r is the hypocentral distance (the 1/r geometrical spreading may have to be changed to $1/\sqrt{r}$ for predictions at distances great enough that surface waves dominate the motions). F and H are usually given values of 2 and $1/\sqrt{2}$, respectively. The most commonly used form of the source factor S(f) is

$$S(f) = M_o / \left[1 + (f/f_o)^2\right], \tag{8}$$

where M_0 is the seismic moment and f_0 is the corner frequency. Joyner (1984) has proposed an enhanced version of this model.

The amplification factor A(f) can be given in a variety of ways. Probably most familiar is the frequency-dependent transfer function that results from wave propagation in a stack of layers with a strong impedan-

contrast at the base of the stack (e.g., Boore and Joyner, 1984a). There is another source of amplification, however, that may be more generally important, since it will operate even in the absence of strong impedance contrasts. Equation (7) was derived for homogeneous materials, but in general both ρ and β will decrease toward the earth's surface. Conservation of energy for waves traveling through materials with decreasing velocity requires an insrease in wave amplitude as the wave speed slows down. Thus as seismic waves approach the earth's surface, they are amplified by gradual decreases in seismic impedance. This amplification can be greater than a factor of two for typical California rock recordings, and increases with frequency (Boore, 1986a). The correction needed to account for propagation from average crustal depths up to the surface can be approximated by multiplying the estimate of spectral amplitude by $\sqrt{\rho_0\beta_0/\rho_r\beta_r}$, where the subscripts 0 and r refer to material properties in average crustal material near the source and near the receiver, respectively. The frequency dependence of the correction arises through the assumption that ρ_r and β_r are effective properties averaged over a depth equal to a quarter-wavelength (Joyner and Fumal, 1984). A sample calculation for S waves in fractured and weathered rock is given in the Appendix.

The following form has been chosen for the diminution factor D(f)

$$D(f) = \exp(-\pi f r/Q(f)\beta)P(f,fm) \tag{9}$$

where Q is a frequency-dependent attenuation function and P is a high-cut filter of arbitrary shape. For high frequencies, a number of studies have found that Q is a strongly increasing function of frequency. A form that fits a number of observations collected by Aki(Figure 10) is

$$Q = 29.4\,\frac{1 + (f/0.3)^{2.9}}{(f/0.3)^2} \tag{10}$$

The high-cut filter P is needed to account for the general observation that acceleration spectra often show an abrupt depletion of high-frequency energy above some frequency (Hanks, 1982). This filter can be represented in several ways. In one, it is given by a Butterworth filter (Boore,1983, Equation 4) with a steep rolloff (on the order of 24 db/octave) above the corner frequency f_m. Another form of the P filter is

$$P(f) = \exp(-\pi\kappa f) \tag{11}$$

Anderson and Hough (1984) represent the entire diminution term by Equation (11), allowing κ to be a function of distance. For the sake of convenience and at the risk of some confusion in terminology, I have taken κ to be independent of distance and have represented the distance dependence by the first factor in Equation (9). When partitioned as I have done, the second factor in the diminution equation might represent near-site attenuation in the upper kilometer or so of the ray path. For small distances or large Q,the second term contributes most of the

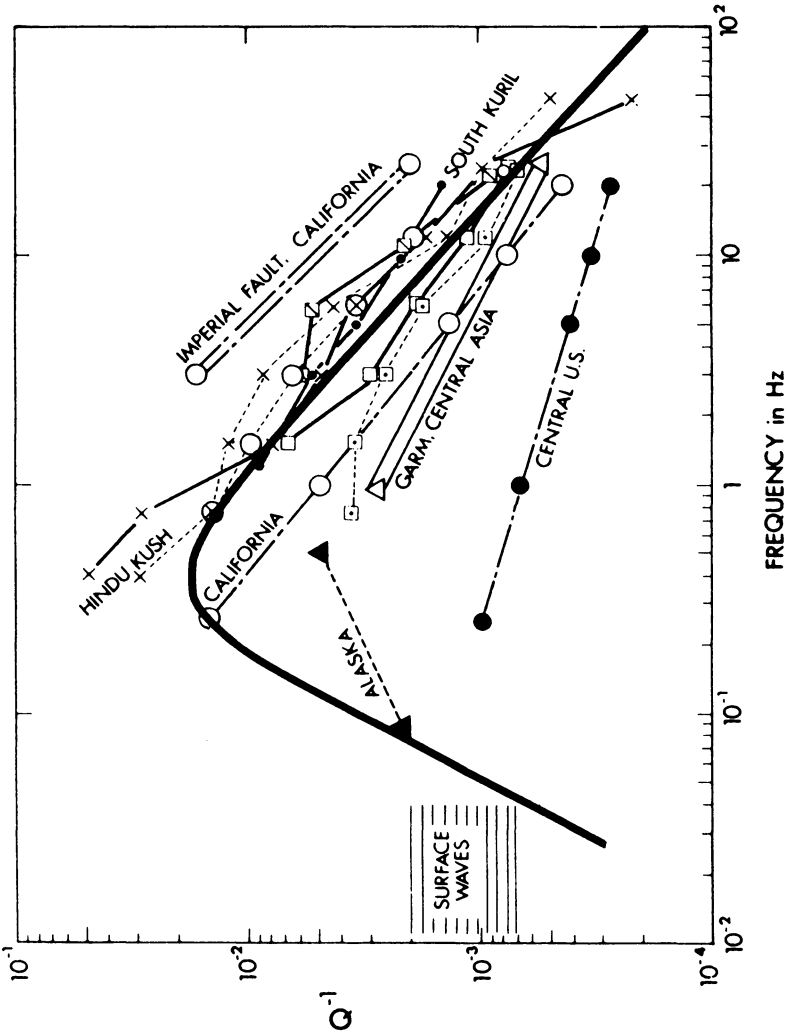

Figure 10. Observed inverse shear-wave Q versus frequency, from Aki (published by Cormier, 1982) and the attenuation function given by Equation (10) in the text (heavy line).

attenuation and the filter D(f) on peak velocity and acceleration is then roughly equivalent to a step high-cut filter with cut-off frequency (f_m) equal to $1/\pi\kappa$ (a relation pointed out to me by J. Boatwright and subsequently confirmed by simulations).

Finally, the filter I(f) is used to shape the spectrum so that the predicted motions correspond to the particular ground motion measure of interest. For example, if response spectra, Richter magnitude, or accelerograph output are to be computed, I is the response to ground displacement of an oscillator of frequency f_r, fractional damping η, and magnification V:

$$I(f) = \frac{V f^2}{(f^2 - f_r^2) - i(2\eta f f_r)} \tag{12}$$

Some typical values for f_r, η, and V are given in Table 1. If peak velocity or peak acceleration are the quantities of interest, then

$$I(f) = (2\pi f)^{\gamma} \tag{13}$$

where $\gamma = 1$ or 2 for velocity or acceleration, respectively. The response equations for other instruments, such as World Wide Standardized Seismograph Network short-period instrument, can be included if desired.

In all applications published to date comparing peak acceleration data to the theoretical predictions, I have assumed that the data have been corrected for the accelerometer response, and therefore Equation (13) has been used in computing acceleration. In a number of instances, however, either the instrument correction has not been performed (for example, on peak motions read directly from analog records) or the demands of the processing techniques have imposed an effective high-cut filter that alters the true ground acceleration. In either case, the distortion of the true ground acceleration should be accounted for (by a suitably defined filter I(f))in the theoretical predictions.

The long-period level of the spectrum is (by definition) determined by the seismic moment of the event. The consequent features of the amplitude spectrum for acceleration are that it increases as f^2 (where f is frequency) for frequencies below the source corner frequency f_0, then is constant for frequencies above f_0 until a cut-off frequency f_m is approached. Amplitudes decay rapidly for frequencies above f_m. Anelastic attenuation acts as a filter on this source spectrum shape, reducing high frequencies more rapidly with distance than lower frequencies (unless Q is proportional to frequency to the first power, in which case the spectrum does not change shape with distance). At large distances this causes the 'flat' portion of the spectrum to slope significantly, and obscures the corner frequency. The spectral shape described by the series of equations above captures most of the salient features concerning the shape of earthquake spectra, but the themselves the equations are not useful for prediction since I have not yet specified how the various parameters depend on earthquake size. This is the subject of source scaling, which is the subject of the next section.

TABLE 1. TYPICAL FILTER PARAMETERS FOR INSTRUMENT RESPONSE

Response	f_r (Hz)	η	V
Accelerograph	25	0.6	25†
Wood-Anderson Seismograph	1.25	0.8	2800*
5%-damped, 1 Hz displacement response spectrum	1	0.05	1‡

† Magnification is usually specified as cm/g; this quantity is equal to $10^{-3}\ V/(2\pi f_r)^2$, after taking the conversion from g to cm/s^2 into account.

* This is a design value; the actual magnification of operating systems could be lower (on the order of 2000). This is a subject currently under investigation.

‡ For pseudo relative-velocity response, $V = 2\pi f_r$.

3.2. Source-spectral Scaling

At close distances, where the whole-path attenuation is of little importance, the shape of the spectrum is governed by two corners $-f_o$ and f_m. The spectral amplitudes for $f < f_0$ scale as seismic moment M_o, and the level of the portion of the spectra between the corners is proportional to $M_0 f_0^2$. In order to predict ground motions for any particular size earthquake, it is necessary to express the corner frequencies as functions of seismic moment. This is a crucial step in the method, especially for high-frequency motions, which are controlled by the part of the spectrum whose amplitude depends on corner frequency squared. A number of studies have found that very simple relations between the corner frequencies and moment lead to predictions that are in excellent agreement with many measures of strong ground motion (McGuire and Hanks, 1980; Hanks and McGuire, 1981; Boore, 1983; Atkinson, 1984; Hanks and Boore, 1984; McGuire et al, 1984; Boore, 1986a, 1986b; Boore and Atkinson, 1986). In these studies,

$$f_m = \text{constant} \tag{14}$$

and

$$f_0 = 4.9 \times 10^6 \beta (\Delta\sigma / M_0)^{1/3} \tag{15}$$

where β and M_0 have units of km/s and dyne-cm, respectively, and $\Delta\sigma$ is a scaling parameter with the dimensions of stress (in bars). The studies referred to above found that choosing a constant value for $\Delta\sigma$ leads to predictions in good agreement with the data; the specific value required to fit the data may depend on tectonic region, as well as details in the modeling, including the values used for the radiation pattern, the vector partition of motion, the value of f_m, and the presence or absence of site amplification. The use of a constant $\Delta\sigma$ leads to a prediction model in which the scaling of motions with earthquake size depends on only one parameter: seismic moment.

Other scaling laws have been proposed. For example, Nuttli's(1983) scaling for midplate earthquakes has the corner frequency proportional to moment to the inverse quarter power, rather than the inverse cube root as in Equation (15). The implication is that the stress parameter increases with source size, and therefore the ground motions are more sensitive to moment than for the constant stress model. Boore and Atkinson (1986) show that predictions made with this scaling relation do not match the relatively sparse data recorded close to mid-plate earthquakes. Another model by E. Faccioli and A.Rovelli (personal commun., 1985) uses a moment dependence for f_0 similar to that of Nuttli, and a weak dependence of f_m on moment. A third source scaling model is that of Gusev (1983), who based his model on a variety of empirical correlations between various magnitudes at teleseismic distances and peak acceleration versus magnitude at close distances. His results are presented graphically. A detailed comparison of predictions using

Gusev source spectra and those for the constant stress parameter modeled discussed above is given in Boore (1986). The basic conclusion is that the constant stress model works as well or even better than the Gusev model in predicting motions with frequencies higher than about 0.5 Hz; the model breaks down, however, in predicting 20 s motions from great earthquakes. From these various studies, it seems that the simplest model (that with constant stress parameter) should be adequate for many applications.

3.3. Predicting Peak Motions

All of the discussion above is directed to specifying the spectrum at a given distance and moment magnitude; how is this converted to estimates of peak motion, a quantity of particular importance to engineers? There are several paths available to do this. One uses time-domain, Monte Carlo simulation, and the other uses random-process theory (RPT). The former method is useful in applications demanding time series and is subject to fewer assumptions than is the RPT. On the other hand, it is much more costly than RPT to predict the peak motion.

The time-domain method, discussed in detail in Boore (1983), is very simple: Gaussian white noise is generated with a random-number generator. This noise is windowed with either a shaping function or a box car whose duration is related to the source corner frequency (at distances of several kilometers from moderate to large earthquakes the duration is given by the inverse of f_0, and farther away an additional term involving distance might be added to account for the spreading out of the source energy due to scattering and wave propagation effects; see Herrmann, 1985). The amplitude of the window is chosen such that the mean level of the white spectrum is unity. Filtering is then performed in the frequency domain by multiplying the spectrum of the windowed white noise by the spectral shape given by the equations in the previous two sections. Fourier transformation back to the time domain then yields the desired time series. Peak motions are then obtained, and the whole process is repeated with a different seed for the random-number generator. Between 20 and 100 simulations is usually sufficient to derive a good estimate of the peak motion. The spectrum of any one realization of the process will not match the target spectrum, but the spectrum averaged over the whole suite of simulations will (Figure 11). The time series for one realization for two magnitudes are shown in Figure 12; in the computer program used to generate these motions, only one input parameter (magnitude) needed to be changed to produce the motions from the different earthquakes.

The random-process theory provides a very convenient and powerful means to estimate peak motions from a description of the spectra. A detailed discussion of the applicable theory, largely taken from Cartwright and Longuet-Higgins (1956), is contained in Boore (1983) and Boore and Joyner (1984b). I will summarize the procedure here. Random-process theory can be used to derive a relation between the root-mean-square and the peak motion of a stochastic series. In its simplest form, good for a large number of extrema N, this relation is

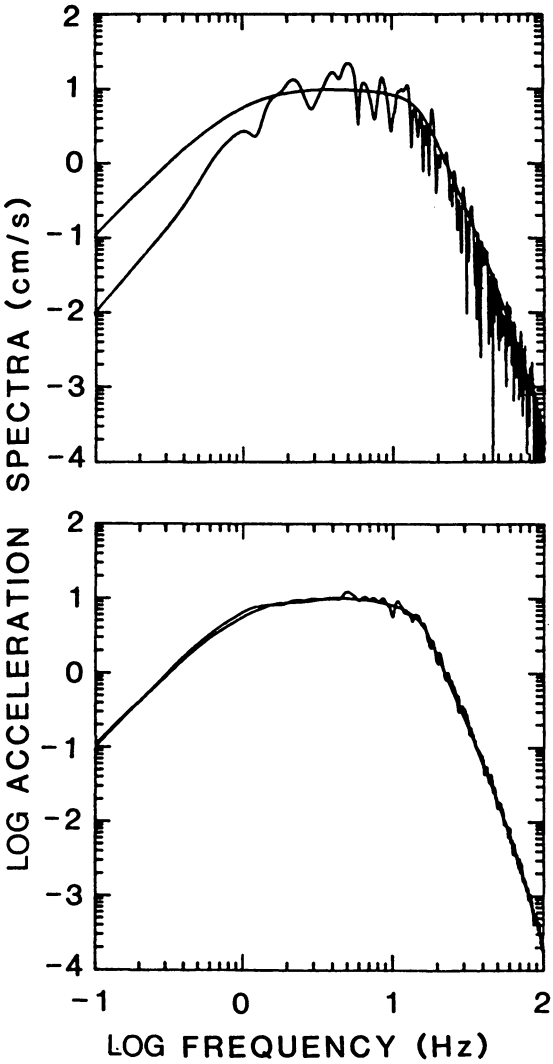

Figure 11. Fourier amplitude spectrum of ground acceleration at 10 km from a magnitude 5 earthquake. (Top) smooth curve: given spectra; jagged curve: spectra for one realization of the simulation process. (Bottom) as above, but averaged over 20 simulations (the averaged spectrum is the square root of the arithmetic mean of the energy density spectrum).

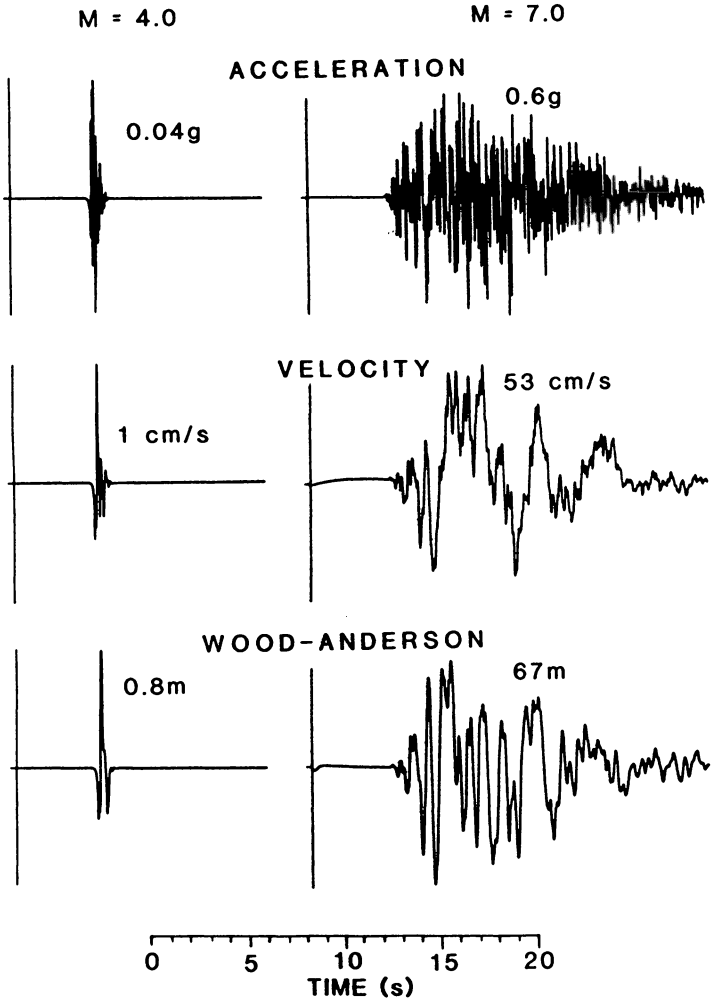

Figure 12. Time series for magnitude 4 and 7 earthquakes. Peak motions are the average of peaks from 20 such time series. A low-cut filter with a cut off frequency of 0.10 Hz has been applied to the velocity trace.

$$\frac{a_{max}}{a_{rms}} = [2\ln(N)]^{1/2} \tag{16}$$

The number of extrema in the specified duration T is given in terms of a characteristic frequency f by

$$N = 2fT \tag{17}$$

Since T is related to the spectral model, it remains to estimate $\tilde{f}$ and a_{rms}. Fortunately, these are given by simple formulas involving integrals of the spectra:

$$f = \frac{1}{2\pi}(m_2/m_0)^{1/2} \tag{18}$$

and

$$a_{rms} = (m_0/T)^{1/2} \tag{19}$$

where Parseval's theorem has been used and the spectral moments m_0 and m_2 are given by

$$m_k = 2(2\pi)^k \int_0^\infty f^k |R(f)|^2 df \tag{20}$$

The equations above constitute the simplest form of the random-process theory. For many applications it is entirely adequate; see Boore (1983) for more details and comparisons with the time-domain simulations.

A further refinement to the basic random-process theory is required when making estimates of response spectra. The RPT approach assumes a stationary time series. For small to moderate magnitude earthquakes, or low ascillator frequencies, or light damping, the duration of motion will not be sufficiently long to generate a pseudo-stationary response. Boore and Joyner (1984) developed an empirical correction to the duration of motion to be applied in estimating the rms response, to account for the distribution of energy content of oscillators beyond the source duration.

3.4. Examples of Predictions

A suite of spectra derived from Equation (6) are shown in Figure 13. Some general conclusions can be drawn without complex calculations, simply from the spectral shapes and the spacing between the spectra: for large earthquakes, the peak velocity will be a stronger function of seismic moment (or, equivalently, moment magnitude) than will peak acceleration. In contrast,the moment dependence of both peak acceleration and peak velocity will be identical for small earthquakes and will have

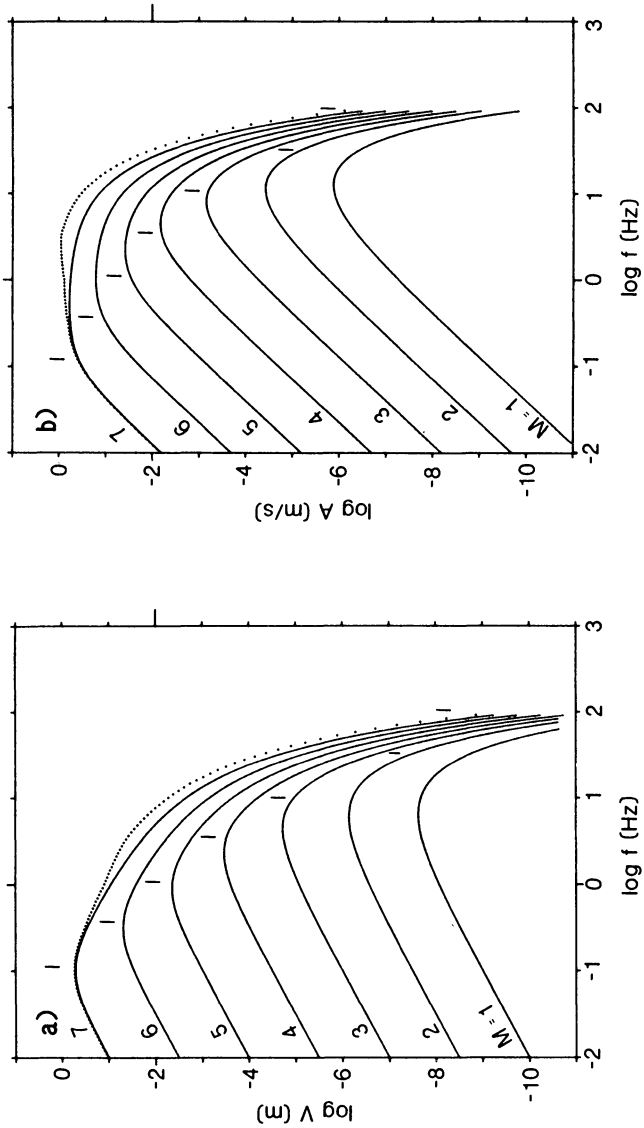

Figure 13. Velocity and acceleration spectra for a range of moment magnitudes, computed for $r = 10$ km, $\rho_s = 2.7$ gm/cc, $\beta = 3.2$ km/s, $R_{\theta\Phi} = 0.5$, $F = 1.0$, $V = 1.0$, $\kappa = 0.05$, and a stress parameter of 10 MPa (100 bars). The vertical bars indicate corner frequencies, computed from Equation (15). Dots show modification of $M = 7$ spectra for amplification factors given in Table 3 in Boore (1986a).

a stronger dependence on moment than do either a_p and v_p for large earthquakes.

Quantitative analysis of the expected scaling gives

$$\log v_p \propto 0.37 \log M_0 + 0.64 \log \Delta\sigma \tag{21a}$$

and

$$\log a_p \propto 0.21 \log M_0 + 0.80 \log \Delta\sigma \tag{21b}$$

for large M_0 (Boore, 1983) For small events, the scaling is

$$\log v_p \propto 1.0 \log M_0 \tag{22a}$$

and

$$\log a_p \propto 1.0 \log M_0 \tag{22b}$$

The scaling for small M_0 is a direct consequence of the upper limit on the bandwidth. If frequencies are not present above a cutoff which is small compared to the reciprocal source duration, then the seismic record will be a simple impulse response with amplitude proportional to M_0. The time series for any particular type of ground motion or instrument type will have the same shape independent of M_0 and the amplitude will be proportional to M_0. In particular, the logarithms of the peak response of a Wood-Anderson instrument (and thus M_L, as shown by Hanks and Boore, 1984) the peak ground displacement and the peak response spectra will scale the same way as do v_p and a_p in Equation (22); radiated energy will scale as $M_0^{2.0}$.

The asymptotic behavior just discussed is useful for a general understanding of what to expect in the way of ground-motion scaling with source size and requires little effort. It only applies to large and small earthquakes, however. Detailed predictions of motions for arbitrary size events can be made by evaluating the integral in Equation (20). With some assumptions, these integrals can be evaluated analytically, but numerical evaluation is not costly and allows for much more flexibility in the spectral model. In the following examples,some selected results based on the complete analysis will be presented. These results were derived from both time-domain simulation and random-process theory.

A comparison of predicted and observed peak acceleration and peak velocity is shown in Figure 14, with f_m as a parameter. The observed values are based on the comprehensive regression work of Joyner and Boore (1981, 1982), which used earthquakes greater than moment magnitude 5. As seen in the figure, the simple constant-stress-parameter model gives predictions that are in good agreement with the observations. As expected, the effect of f_m is seen to be most important for motions that contain high frequencies (peak accelerations from small earthquakes). This is emphasized in Figure 15, in which the κ parameter in Equation (11) rather than f_m is used to control the high-frequency filtering.

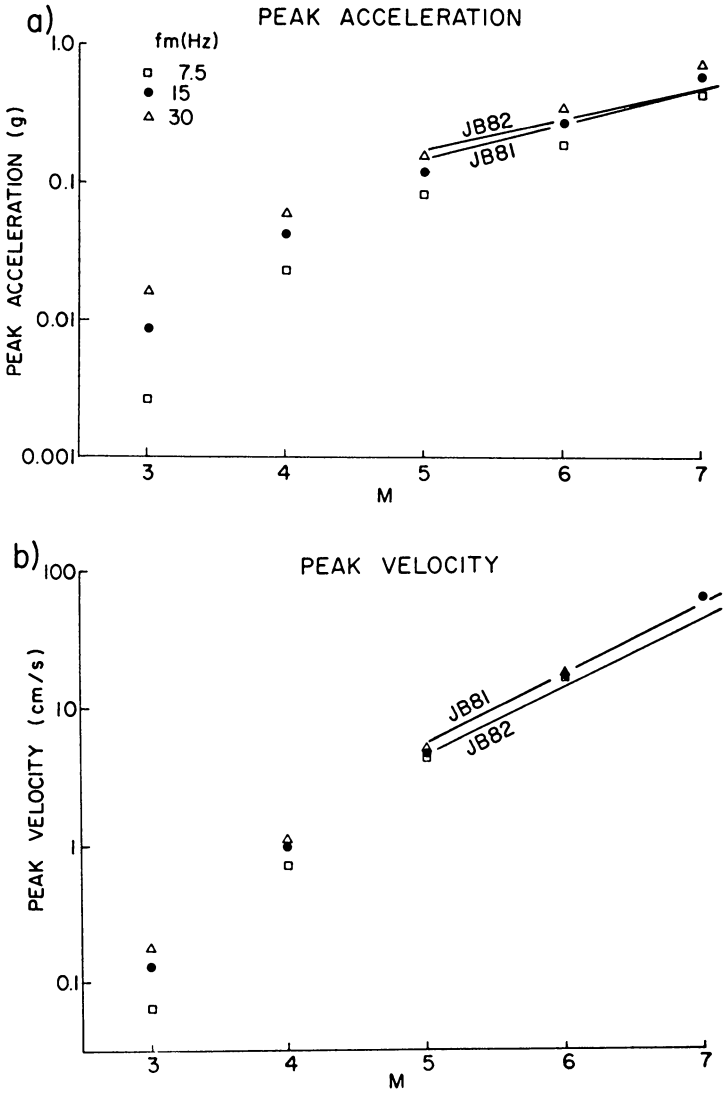

Figure 14. Magnitude scaling of simulated peak ground accelerations and velocities for three values of f_m. The regression curves of Joyner and Boore (1981-1982) are shown for reference.

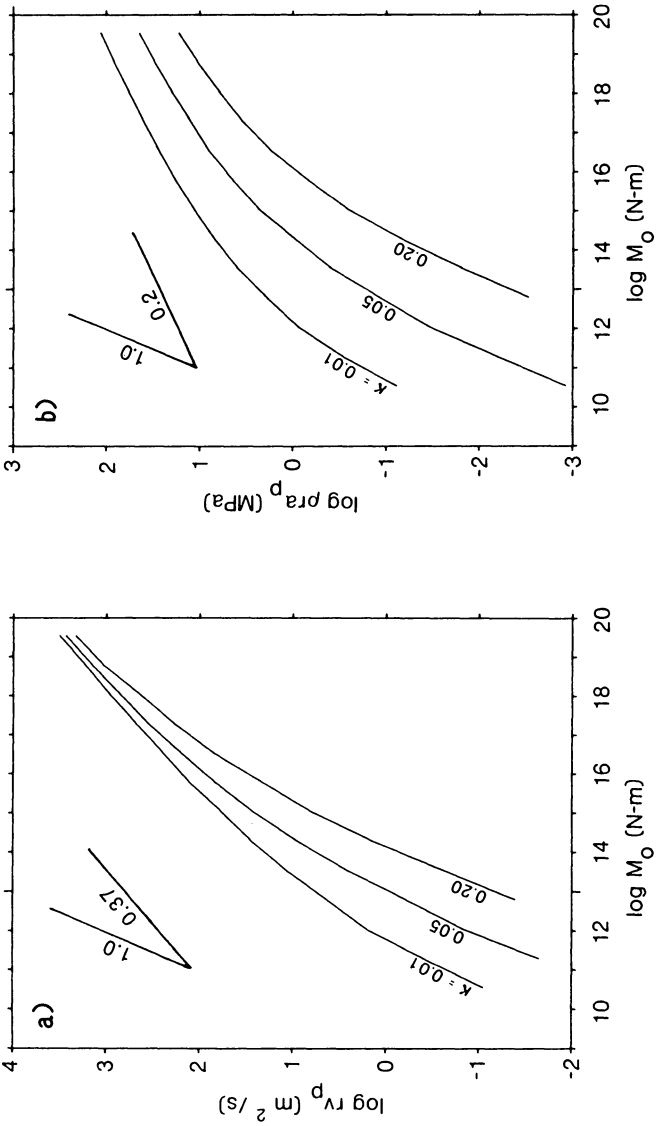

Figure 15. Peak velocity and acceleration, corrected for geometrical spreading, as a function of moment for a range of κ values. Other parameters given in caption to Figure 13. Short lines show expected scaling for earthquakes with large and small seismic moments (Equations (21) and (22)).

Of particular interest here is the steep slope for small earthquakes (in agreement with Equation 22) and relative level of the curves for the various κ values. These results may explain many studies of small earthquakes that seem to show a breakdown of similarity (i.e., non-constant $\Delta\sigma$), and they also predict that the magnitude at which the apparent breakdown occurs will be a function of the local site conditions (to the extent that κ is determined by these local conditions). Thus, for the same stress parameter, peak motions from hard rock sites (low κ) should be larger than those from soil sites (high κ).

The predicted values of the peak response of various oscillators are in good agreement with the data. Boore (1983) discusses such a comparison for pseudo-relative velocity spectra, and Figures 16 and 17 show comparisons for the output of a Wood-Anderson seismograph (used in determining M_L) and a World-Wide Standardized Seismograph Network short-period instrument, respectively. Note that the motions are being predicted for a range of over 12 orders of magnitude in seismic moment, with good agreement with the data over this enormous range of earthquake size.

The final example combines estimates of peak velocity and seismoscope response, in an investigation of how seismoscope response can be used to estimate peak velacity (Figure 18). For any distance, the relation is complicated, but when many distances are considered, a linear relation emerges that is a lower limit of peak velocity for a given seismoscope amplitude.

4. DISCUSSION

The prediction of motions for use in engineering design must rely both on empirical and theoretical methods. The methods complement on another, for the empirical analyses provide checks on the theory and help determine the parameters necessary in the theoretical predictions. An example of this is in the predictions of ground motions in regions devoid of large earthquakes during this century, for which no instrumental records are available. A good example is eastern North America. Recording of a few moderate earthquakes suggest that the source scaling follows the constant-stress-parameter relation in Equation (15), and fitting the amplitudes of the data determines the value of $\Delta\sigma$. The theoretical model can then be used to predict values of ground motion for the large earthquakes of most interest to engineering design and seismic hazard evaluation (Atkinson, 1984; Boore and Atkinson, 1986). Of course, the predictions remain just that... predictions. There is no substitute for data, and continuing world-wide efforts should be maintained to record strong motions, particularly close to large earthquakes.

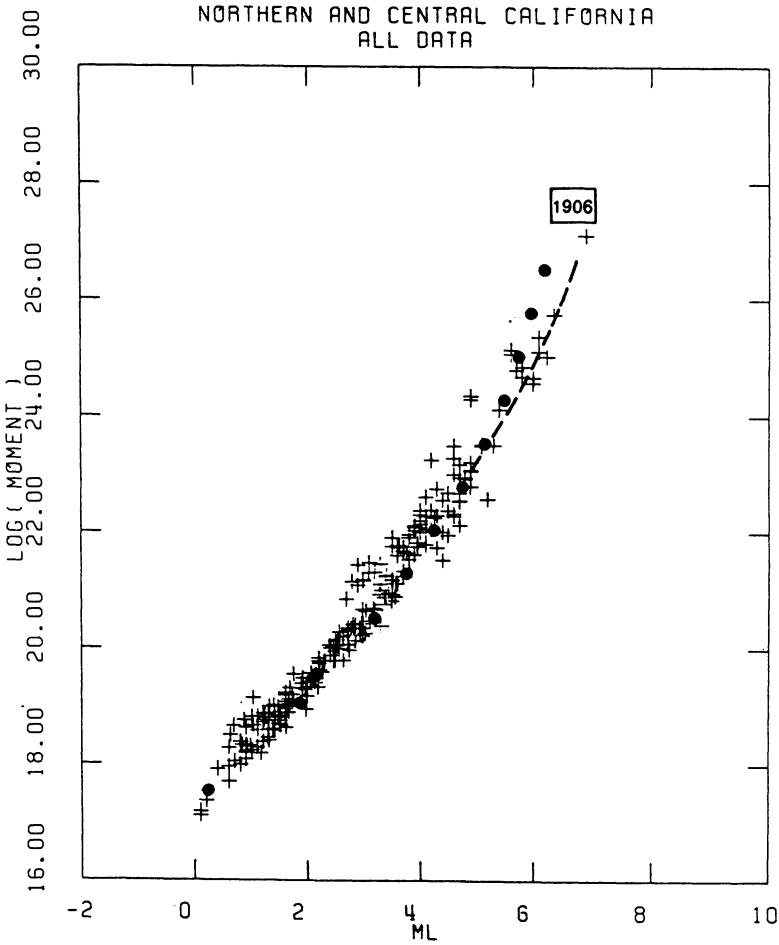

Figure 16. Moment-magnitude data for central California earthquakes (crosses, box for 1906 earthquake) and model calculations after Boore (1983) (solid circles; dashed line for Luco, 1982, correction for difference in near-source and far-source estimates of M_L); see Hanks and Boore (1984) for details.

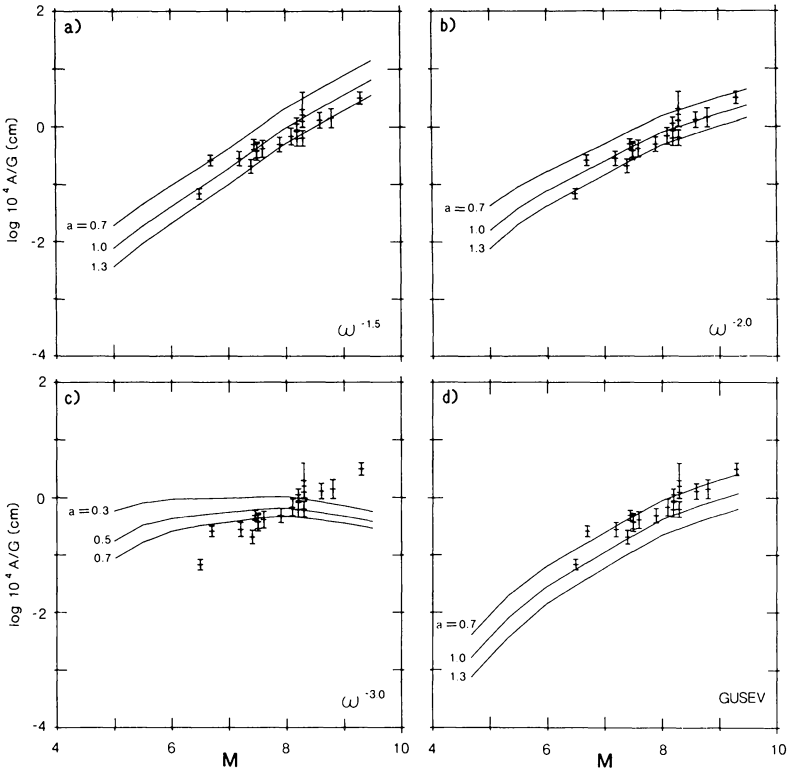

Figure 17. Observed (symbols) and predicted (lines) amplitudes on WWSSN short-period instruments as a function of moment magnitude. Observations reduced to a distance of 70 degrees. Predictions for various attenuations and source spectral models. Stress parameters for a),b), c) were 5,50, and 300 bars, respectively. See Boore (1986a) for details.

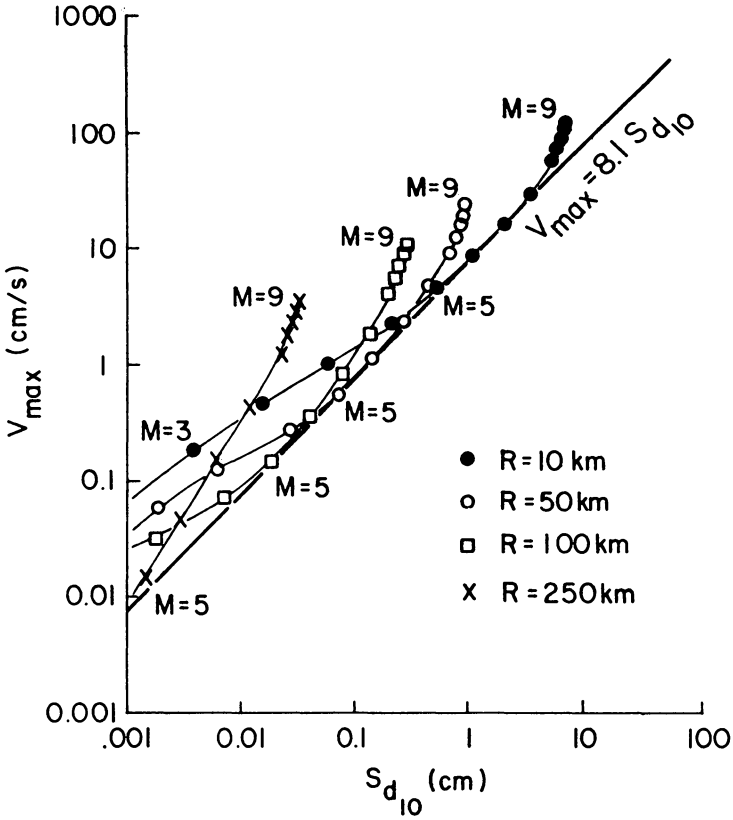

Figure 18. Correlation between peak horizontal velocity (v_{max}) and the displacement response of a unit gain, 10% damped oscillator with 1-3 Hz resonant frequency (S_{d10}). At each of four distances, simulations were made for moment magnitudes ranging in half-unit decrements from M=9. For convenience, the M = 9, M = 5, and in one case, M = 3 points have been labeled. The light lines connect points at the same distance.

TABLE 2. CALCULATION OF EFFECTIVE FREQUENCIES AND VELOCITIES

Thickness (km)	Depth to Bottom (km)	β(km/s)	Cumulative Time (s)	Frequency (Hz)	β_r(km/s)
0.04	0.04	0.59	0.07	3.6	0.59
0.04	0.08	1.56	0.09	2.8	0.89
0.04	0.12	1.78	0.12	2.1	1.00
0.14	0.26	2.17	0.18	1.4	1.44
0.17	0.43	2.60	0.25	1.0	1.72
0.26	0.69	2.95	0.33	0.8	2.09
0.30	0.99	3.10	0.43	0.6	2.30
-	-	3.20	-	-	-

TABLE 3. AMPLIFICATION FACTORS FOR S WAVES

Frequency (Hz)	0.1	0.32	1.0	3.2	10
Log Amplification:	0.01	0.04	0.13	0.34	0.37

ACKNOWLEDGEMENTS

I thank William Joyner and Erdal Şafak for thoughtful reviews, and Mustafa Erdik and Nafi Toksöz for organizing a stimulating and productive NATO Advanced Studies Institute. Partial funding for this work was provided by a grant from the U.S. Nuclear Regulatory Commission.

APPENDIX

In the absence of large impedance contrasts, the amplification of S waves propagating through materials whose velocities decrease near the earth's surface can be represented by the factor $\sqrt{\beta_0/\beta_r}$, where changes in density have been ignored. For typical earthquakes in California, $\beta_0 = 3.2$ km/s and β_r can be estimated as follows. For weathered and fractured rock, the shear velocity at the surface can be about 0.6 km/s, and it must increase to 3.2 km/s at depth. Based partly on the relative amplifications found by Joyner and Fumal (1984), as well as P_g intercept times from seismic refraction experiments, I have estimated that the value of 3.2 km/s is reached by 1.0 km depth. Drawing a smooth increase with depth then gives the velocity profile in Table 2. The cumulative travel time from the surface to the bottom of each layer and an effective velocity for waves travelling from the bottom of the layer to the surface are then calculated. The wave frequency corresponding to each effective velocity is then taken to be the inverse of four times the associated cumulative travel time. The results for the specific velocity model being considered here are given in Table 2. A similar procedure can be used to calculate an effective velocity given a wave frequency. For the velocity model given in Table 2, the logarithm of the resulting amplification factors are given in Table 3.

REFERENCES

Anderson, J.G. and S.E. Hough (1984). A model for the shape of the Fourier amplitude spectrum of acceleration at high frequencies, Bull. Seismol.Soc. Am. 74, 1969-1994.

Atkinson, G.M. (1984). Attenuation of strong ground motion in Canada from a random vibrations approach, Bull.Seismol.Soc. Am.74, 2629-2653.

Boore, D.M. (1983). Stochastic simulation of high-frequency ground motions based on seismological models of the radiated spectra, Bull. Seismol. Soc. Am. 73, 1865 - 1894.

Boore, D.M. (1986a). Short-period P- and S-wave radiation from large earthquakes: implications for spectral scaling relations, Bull. Seismol. Soc. Am. 76, in press.

Boore, D.M. (1986b). The effect of finite bandwidth on seismic scaling relationships, Proceedings of Fifth Maurice Ewing Symposium on Earthquake Source Mechanics American Geophysical Union monograph, in press.

Boore, D.M. and G.M. Atkinson (1986). Prediction of ground motion and spectral response parameters in eastern North America, Bull.Seismol.Soc. Am., submitted.

Boore, D.M. and J. Boatwright (1984). Average body-wave radiation coefficients, Bull. Seismol. Soc. Am.74, 1615-1621.

Boore, D.M. and W.B. Joyner (1982). The empirical prediction of ground motion, Bull. Seismol. Soc. Am. 72, 5269-5286.

Boore, D.M. and W.B. Joyner (1984a). Ground motions and response spectra at soil sites from seismological models of the radiated spectra, Proceedings of Eighth World Conference on Earthquake Engineering II, 457-464.

Boore, D.M. and W.B. Joyner (1984b). A note on the use of random vibration theory to predict peak amplitudes of transient signals, Bull. Seismol. Soc. Am.74, 2035-2039.

Brillinger, D.R. and H.K. Preisler (1985). Further analysis of the Joyner-Boore attenuation data, Bull.Seismol.Soc. Am.75, 611-614.

Cartwright, D.E. and M.S. Longuet-Higgins (1956). The statistical distribution of the maxima of a random function, Proc. Roy. Soc. London, Ser. A237, 212-232.

Cormier, V.F. (1982). The effect of attenuation on seismic body waves, Bull.Seismol. Soc. Am.72, No.6B, S169-S200.

Gusev, A.A. (1983). Descriptive statistical model of earthquake source radiation and its application to an estimation of short-period strong motion, Geophys. J.R. Astron. Soc. 74, 787-808.

Hanks, T.C. (1982). f_{max}, Bull. Seismol. Soc. Am.72, 1867-1879.

Hanks, T.C. and D.M.Boore (1984). Moment-magnitude relations in theory and practice, J. Geophys. Res. 89, 6229-6235.

Hanks, T.C. and H.Kanamori (1979). A moment-magnitude scale, J.Geophys. Res. 84, 2348-2350.

Hanks, T.C. and R.K. McGuire (1981). The character of high frequency strong ground motion, Bull.Seismol. Soc. Am. 71, 2071-2095.

Heaton, T.H. and D.V. Helmberger (1977). A study of the strong ground motion of the Borrego Mt., California earthquake, Bull. Seismol. Soc.Am. 67, 315-319.

Herrmann, R.B. (1985). An extension of random vibration theory estimates of strong ground motion to large distances, Bull. Seismol. Soc. Am. 75, in press.

Joyner, W.B. (1984). A scaling law for the spectra of large earthquakes, Bull. Seismol. Soc. Am. 74, 1167-1188.

Joyner, W.B. and D.M. Boore (1981). Peak horizontal acceleration and velocity from strong-motion records including records from the 1979 Imperial Valley, California, earthquake, Bull. Seismol. Soc. Am. 71, 2011-2038.

Joyner, W.B. and D.M. Boore (1982). Prediction of earthquake response spectra, U.S. Geol. Surv. Open-File Rep. 82-977, 16pp.

Joyner, W.B. and T.E. Fumal (1984). Use of measured shear-wave velocity for predicting geologic site effects on strong ground motion, Proc. 8th World Conf. Earthquake Engineering II, 777-783.

Joyner, W.B. and T.E. Fumal (1985). Predictive mapping of ground motion, in Evaluating Earthquake Hazards in the Los Angeles Region, U.S. Geol. Surv. Profess. Paper 1360, 203-220.

Luco, J.R. (1982). A note on near-source estimates of local magnitude, Bull. Seismol, Soc. Am. 72, 941-958.

McGuire, R.K., A.M. Becker, and N.Ç. Donovan (1984). Spectral estimates of seismic shear waves, Bull. Seismol. Soc. Am. 74, 1427-1440.

McGuire, R.K. and T.C. Hanks (1980). RMS accelerations and spectral amplitudes of strong ground motion during the San Fernando, California earthquake, Bull. Seismol. Soc. Am. 70, 1907-1919.

Nuttli, O.W. (1983). Average seismic source-parameter relations for mid-plate eartquakes, Bull. Seismol. Soc. Am. 73, 519-535.

Shakal, A.F. and D.L. Bernreuter (1981). Empirical analysis of near-source ground motion, NUREG/CR-2095, 66 pp., U.S. Nuclear Regulatory Commission, 1981.

Swanger, H.J. and D.M. Boore (1978). Simulation of strong-motion displacements using surface-wave modal superposition, Bull. Seismol. Soc. Am. 68, 907-922.

A THEORETICAL STUDY OF THE DEPENDENCE OF THE PEAK GROUND ACCELERATION ON SOURCE AND STRUCTURE PARAMETERS

P. Suhadolc and C. Chiaruttini
Istituto di Geodesia e Geofisica
Università di Trieste, Trieste,
Italy

ABSTRACT. The attenuation laws of peak ground acceleration (PGA) and root mean square acceleration (a_{rms}) are theoretically simulated for 6 differently laterally homogeneous models of the lithosphere. The anelastic properties of the structures are parametrized by quality factors. Complete synthetic accelerograms for P-SV waves are generated by the superposition of the Rayleigh modes for frequencies as high as 10 Hz. The theoretical analysis of the scattering of PGA and a_{rms} due to: 1) the different seismic phases carrying the largest motion at different distances (like Sg and Lg waves), 2) The structural variations of the lithosphere, 3) The depth of the source, 4) the azimuth with respect to the orientation of the fault, 5) the source finite rise time and 6) the variation of the quality factor, indicates that the larger causes of scatter are the differences in the crustal structure, the source mechanism and its orientation with respect to the receiver. From the analysis we give indications on how to reduce significantly the standard deviation in the estimate of ground motion by attenuation laws.

1. INTRODUCTION

In the last 15 years, the availability of good quality strong motion records of earthquakes located mainly in Italy and in the United States has made possible intense studies of the wave field in the vicinity of the source. In seismic risk analyses the attenuation with distance of the peak ground acceleration PGA and other ground motion parameters-like root mean square acceleration a_{rms}, effective peak acceleration, peak velocity, Arias intensity- are among the basic information. In many investigations carried on so far, remarkable differences in response have been put into evidence, especially with regard to soil types and to seismic regions (e.g.: Seed et al., 1976; Chiaruttini and Siro, 1981). Similar results have been obtained analysing the frequency domain (e.g.: Trifunac, 1976; Chiaruttini, Crosilla and Siro, 1979). The standard deviation of the estimated ground motion has remained very large, even, when using the more sophisticated measures of the intensity of ground motion (Husid,1967; Arias,1969; Idriss,1978; McCann and Boore,1983). In

M. O. Erdik and M. N. Toksöz (eds.), Strong Ground Motion Seismology, 143–183.
© 1987 by D. Reidel Publishing Company.

fact, standard deviations are often as large as a factor of two (Murphy and O'Brien, 1977; Chiaruttini and Siro, 1981). The models for attenuation laws now commonly account for the dependence of PGA with seismic moment (or magnitude), distance, soil type, and the anelastic attenuation of the earth. Non-linear models, allowing for a near-source behaviour different than the far-source one, are frequently in use(Campbell, 1981; Joyner and Boore, 1981). The reason of such big scatter is to be looked for in the poor modeling of the source, in the heterogeneity of the crust and in a too simple classification of the sites. Concerning site effects, besides the commonly used soil type parameter, thickness and quality of alluvial deposits, topography and local lateral variations of the elastic and anelastic properties of the crust (like in valleys) are extremely important in determining the site response (King and Tucker, 1984). Concerning the medium, some properties of the crust, like the presence of sedimentary basins and the anelastic attenuation of rocks or sediments, are of great importance. They may be responsible for the scattering of the PGA data when the stations are located in geologically inhomogeneous regions. In this paper we shall focus our attention on the effects of the source and the earth structure.

At present, one of the main limits to most of the models used to estimate PGA is that they do no allow for azimuthal variations, although the observation of the macroseismic field of earthquakes clearly shows a non-circular distribution of damages. This asymmetry may be due to either the source radiation pattern or to variations of the crustal properties. The importance of the radiation pattern in determining the severity of damage in different azimuths has been shown by Panza and Cuscito (1982). Directivity effects, due to finite velocity rupture propagation processes have also been evidenced (Madariaga , 1977 ; Boatwright, 1982; Boatwright and Boore, 1982). However, the radiation pattern of direct S-waves does not appear correlated to the peak amplitude of strong motion records. Boatwright and Boore (1982) attributed this to the effect of both crustal heterogereity and source complexity. A competing effect is the change with azimuth of the phase carrying the strongest motion. The difficulty of retrieving a known radiation pattern and the conservative assumption of ignoring the source mechanisms of future earthquakes is probably the reason of considering only distance as the geometrical parameter and of using averages of the radiation coefficients of body waves for the corretion of strong motion measures (Boore and Boatwright, 1984). We think, however, that the radiation pattern, along with structural crustal variations, is one of the most important reasons of the scarreting of the data.

Theoretical seismology may give an important contribution in understanding the propagation in real media of waves generated by real sources. This will allow to set up procedures of data analysis less and less based on empirical reasoning. In particular, the prossibility to generate complete theoretical seismograms in a very efficient way allows to investigate attenuation laws for realistic earth models and sources. This is the aim of our paper in which the method of summation of Rayleigh modes (Harkrider, 1970; Panza, Schwab and Knopoff, 1973 ; Panza, 1985) will be used to generate radial and vertical component accelerograms. Even if the tangential (SH) component is usually the

strongest one in the accelerograms, we will not include it in our examples. In fact the scatter of ground motion parameters is so large that the inclusion of SH-waves will not significantly alter our analysis.

2. THEORY

It was shown by Harkrider (1970), assuming a double couple source model, that it is possible to represent the Fourier transform of the displacement due to a Rayleigh mode by the following expressions:

$$U_r = R(\omega)\ |\bar{n}|\ k^{1/2} \exp(-i3\Pi/4)\ \chi(\theta,h)\varepsilon_0\ G \exp(-ikr)/(2\Pi r)^{1/2}$$

$$U_z = (\ \varepsilon_0 \exp(i\Pi/2))^{-1}\ U_r \qquad (1)$$

$$U_t = 0$$

where $R(\omega)$ is the Fourier transform of the point source time function, $\bar{n}$ is the unit vector perpendicular to the fault plane with dimensions of length, k is the wavenumber, r is the epicentral distance, $\chi(\theta,h)$ represents the azimuthal dependence of the source radiation which contains the fault-plane parameters and the eigenfunctions at the source depth, ε_0 is the ellipticity and $G = (2cUI_1)^{-1}$ with c, U and I_1 the phase velocity, group velocity and energy integral, respectively (see Panza, Schwab and Knopoff, 1973 for details). The factor $(2\Pi r)^{-1/2}$ comes essentially from the first term of the asymptotic expansion of the Hankel functions. This approximation, together with neglecting terms of higher order in $r^{-1/2}$, enables results to be obtained with at least three significant figures whenever $kr > 10$ (Panza, Schwab and Knopoff, 1973).

The attenuation is included by making k complex (e.g. Panza, 1985). Causality is preserved by introducing the body-wave dispersion according to Futterman (1962).

In these computations we deliberately neglect the contribution of the branch line integrals corresponding to the half-space. This may have some effect on the P-wave arrivals from layers with compressional wave velocity close to or larger than the S-wave velocity in the half-space (Harvey, 1981). However, the capability of handling large quantities of structure enables the synthesis of most arivals from crustal layers (Panza, 1985). In any case PGA is not affected by such a limitation since tle S-wave branch line integral contribution is satisfactorily approximated by the poles of the Rayleigh higher modes.

Examples of the computation of the quantities which appear in Eq.(1) and examples of synthetic displacements obtained with this method are given by Panza (1985), Chiaruttini, Costa and Panza (1985), Suhadolc and Panza (1985), Panza, Suhadolc and Chiaruttini(1985).In this paper we will be dealing with synthetic accelerations in the time domain, which can be obtained by multiplying the quantities in Eq.(1) by $-\omega^2$ and inverse Fourier transforming.

3. STRUCTURAL MODELS

Six structures, having quite different characteristics, have been considered. Two of them. FRI1 and AMP2, have no sedimentary cover, the others, IMP1, APN1, IRP1 and FRI2, have different sedimentary covers. IMP1 (see Fig. 1) is a realistic model of the Imperial Valley, California (Fuis et al., 1982), having a 6 km thick sedimentary cover on top, represented by a gradient in velocities; the IMP2 model (see Fig. 1) is, on the other hand, fictitious: it is equal to the IMP1 model with the sediments replaced by the rock basement. The FRI1 and FRI2 models (Fig. 2) represent two models of the Friuli area, NE Italy, near the May 6, 1976 Friuli erthquake (IESG and ETH, 1981). FRI2 has a thin, 1 km, sedimentary layer on top of the rock basement; the FRI1 model has no sediments. The IRP1 (Fig. 3) model has 2 km of homogeneous sediments and a low velocity channel in the lower crust; it approximates the structure near the 1980 Irpinia, South Italy, earthquake (Mantovani, Farsi and Babbucci, 1980; Panza and Cuscito, 1982). The APN1 model (Fig.3) is adapted from a refraction profile interpretation in the northern Apennines (Scarascia, Pellis and Giese, 1985) and has a 3-layer, 8 km thick sedimentary cover.

In each layer, the seismic energy attenuation(*) due both to absorption by intrinsic anelasticity and scattering by heterogeneities is parametrized by the quality factor of S-waves Q_β and of P-waves Q_α. They are assumed to be frequency independent. The relation between the P-wave quality factor Q_α and the S-wave quality factor Q_β proposed in the literature (e.g. Anderson, Ben-Menahem and Archambeau, 1965; Kijko and Mitchell, 1983) allows to write $Q_\alpha = k\, Q_\beta$ with $1 \leq k \leq 2.5$. We have chosen $k = 2.5$, so that in our examples the effect of attenuation, for a given Q_β model, can be considered to be minimal.

4. COMPLETE SYNTHETIC ACCELEROGRAMS AND ATTENUATION LAWS

Theoretical accelerograms for the above six earth crustal models have been computed at epicentral distances of 10, 25, 50, 100 and 200 km. The source is a pure right-lateral strike-slip on a vertical fault plane with unitary (1 dyne x cm) seismic moment. The receiver is placed at 45° with respect to the strike of the fault. The depth of the source is variable around 5 km. A Heaviside step function is taken as the source time function. The amplitudes of all accelerograms are normalized, the maximum zero-to-peak amplitude (PGA) being given in the upper right corner of each accelerogram in units of 10^{-22} cm/s^2. The accelerograms have not been filtered to eliminate ringing due to frequency cutoff (10 Hz), so some ringing may be seen in the accelerograms especially before the first arrivals. Some of the accelerograms are shown in Figs. 4 to 8.

(*) Here and in the sequal, the reader should be careful not to confuse the intrinsic attenuation, which is a property of the medium, and the amplitude attenuation of seismic waves with distance, resulting from the effect of the intrinsic attenuation and the geometrical spreading.

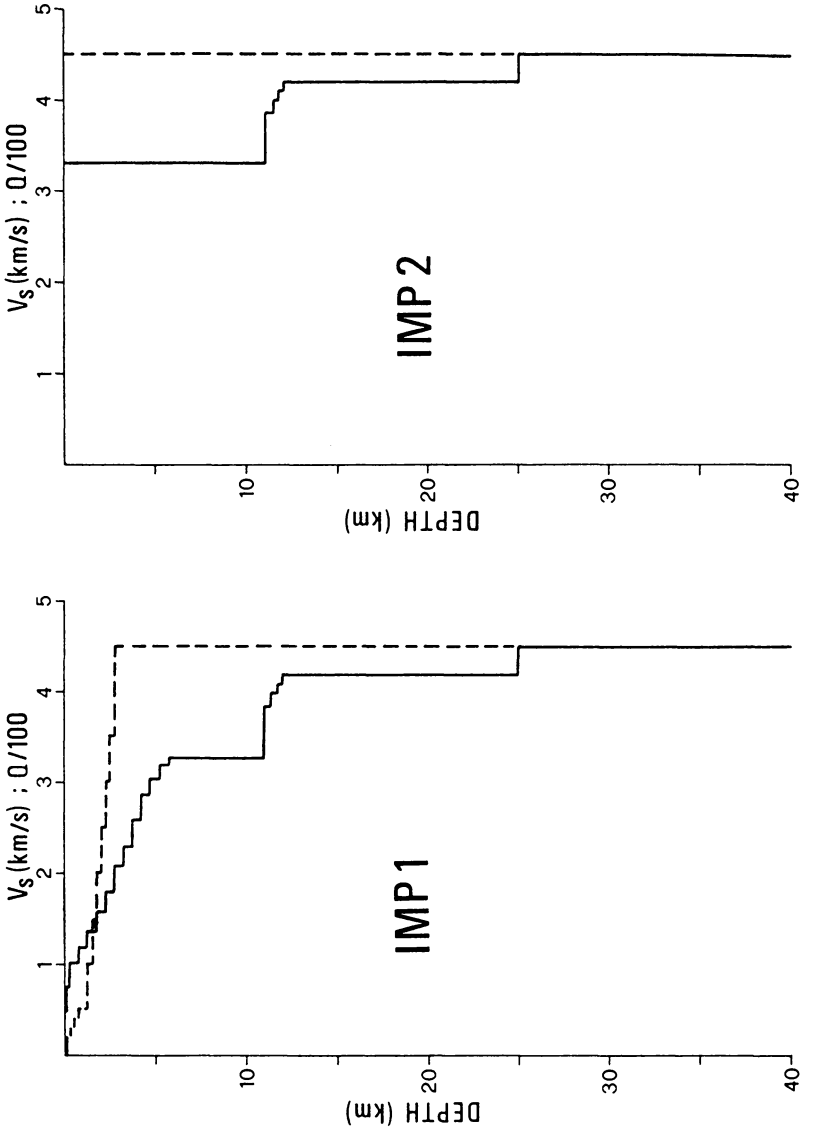

Figure 1. IMP1 and IMP2 crustal structure models. Continuous line : S-wave velocity; dashed line: quality factor/100.

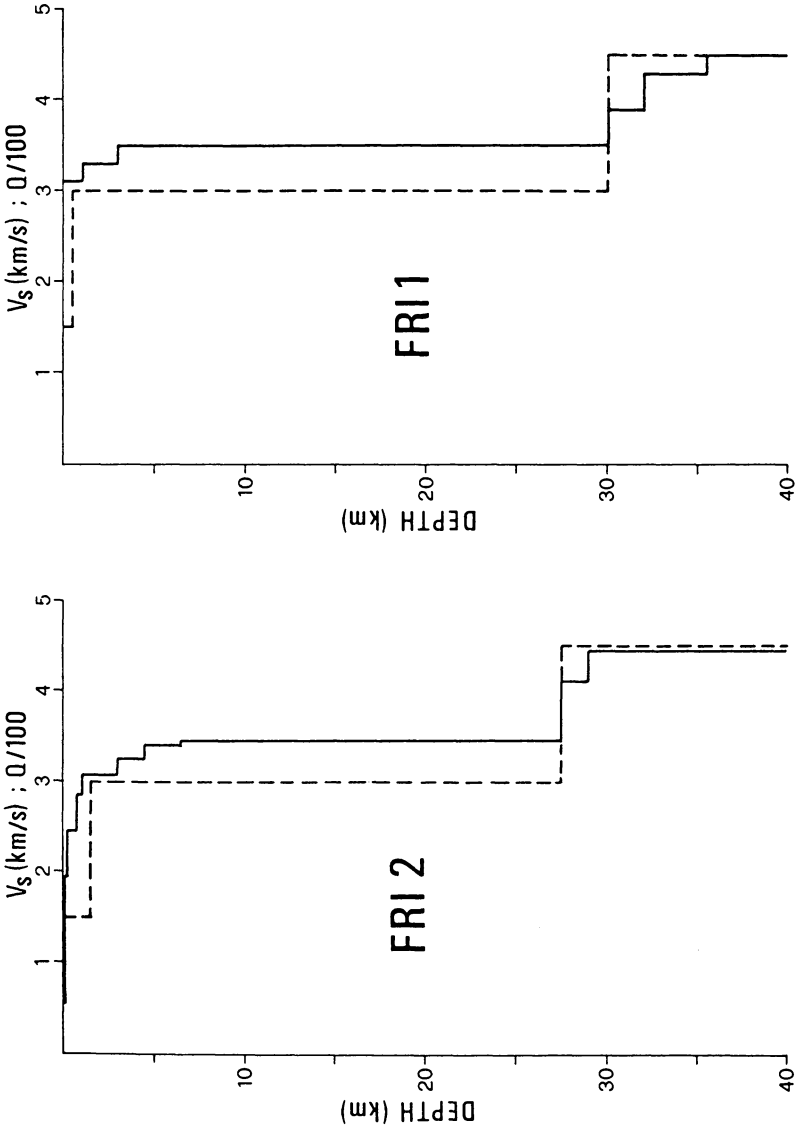

Figure 2. FRI1 and FRI2 crustal structure models. Continuous line: S-wave velocity; dashed line: quality factor/100.

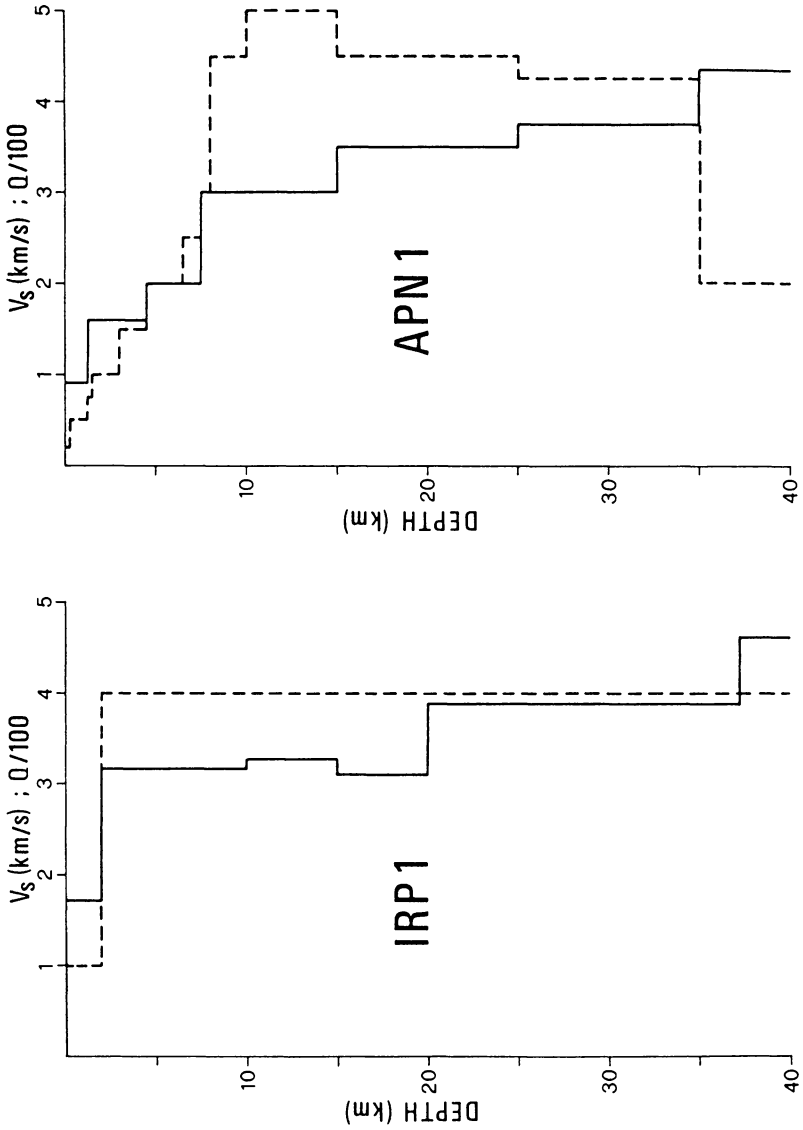

Figure 3. IRP1 and APN1 crustal structure models. Continuous line: S-wave velocity; dashed line: quality factor/100.

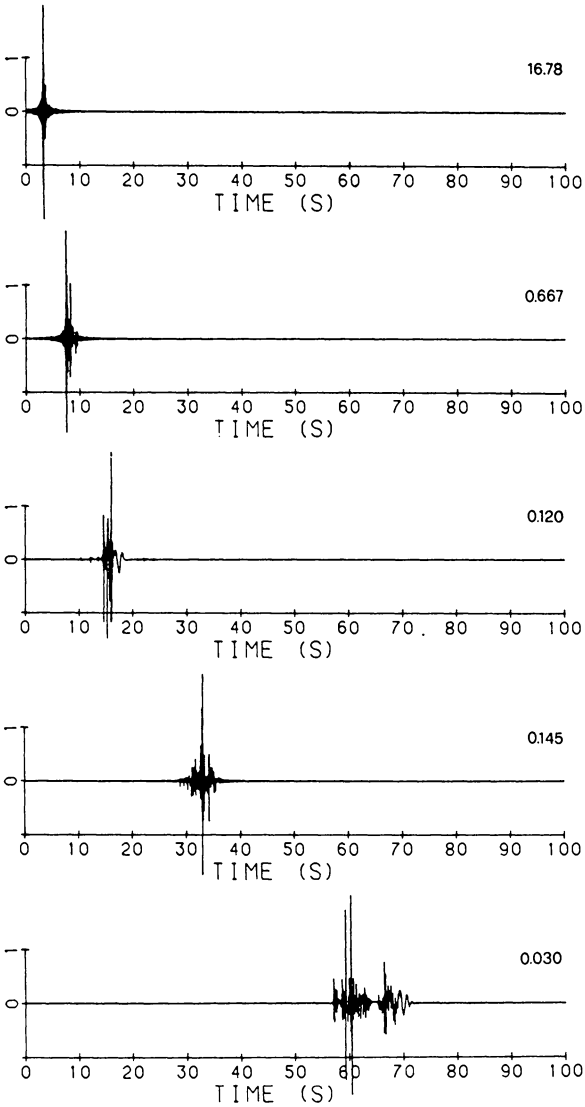

Figure 4. Synthetic accelerograms, radial component, right-lateral instantaneous strike-slip source, model FRI1. The epicentral distances are, from top to bottom, 10, 25, 50, 100 and 200 km. All the amplitudes are normalized. The figure in the upper right corner of each accelerogram is the zero-to-peak amplitude in units of 10^{-22}cm/s^2 for a unitary (1 dyne x cm) seismic moment.

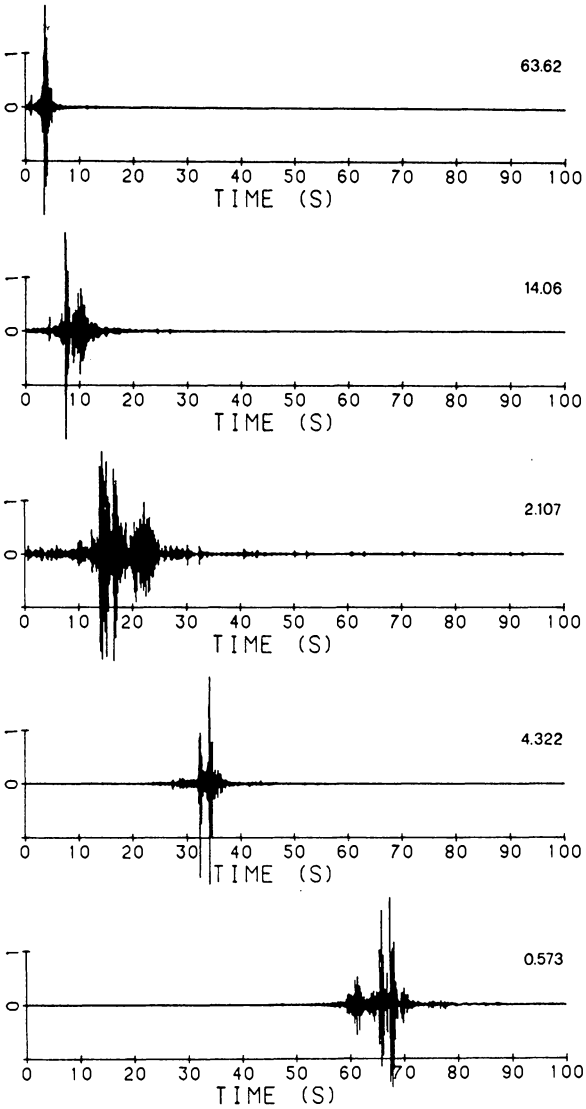

Figure 5. Synthetic accelerograms, radial component, right-lateral instantaneous strike-slip source, model FRI2. For explanations see the caption of Fig.4.

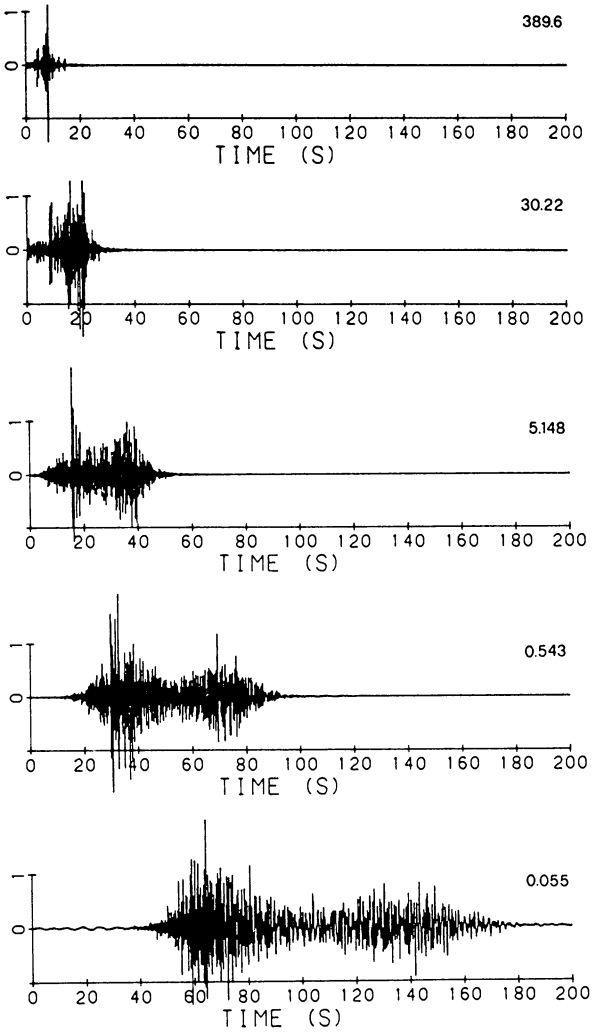

Figure 6. Synthetic accelerograms, radial component, right-latera instantaneous strike-slip source, model APN1. For explanations see the caption of Fig.4.

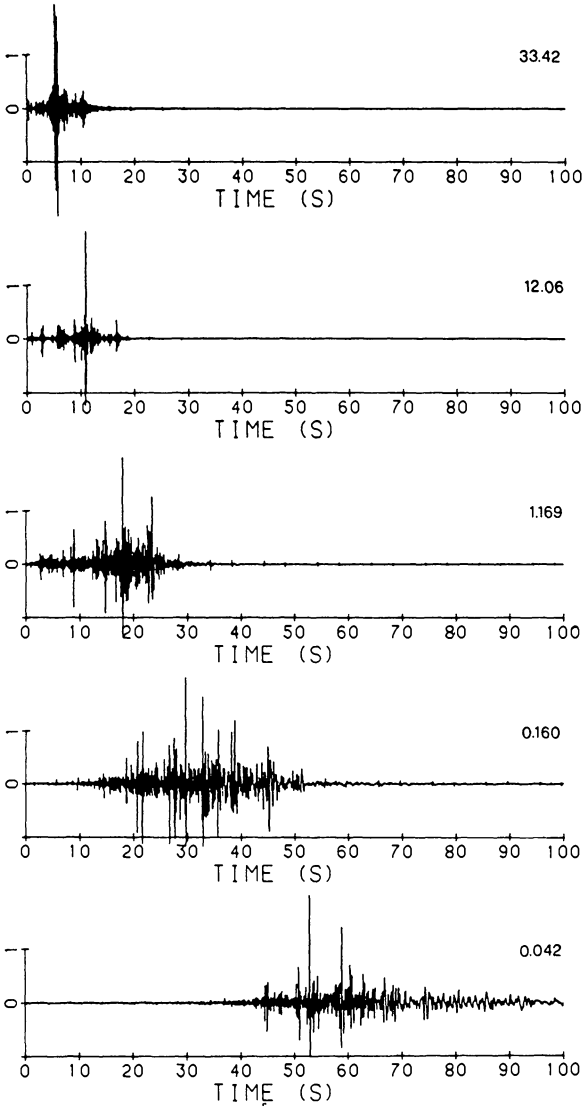

Figure 7. Synthetic accelerograms, radial component, right-lateral instantaneous strike-slip source, model IMP1. For explanations see the caption of Fig.4.

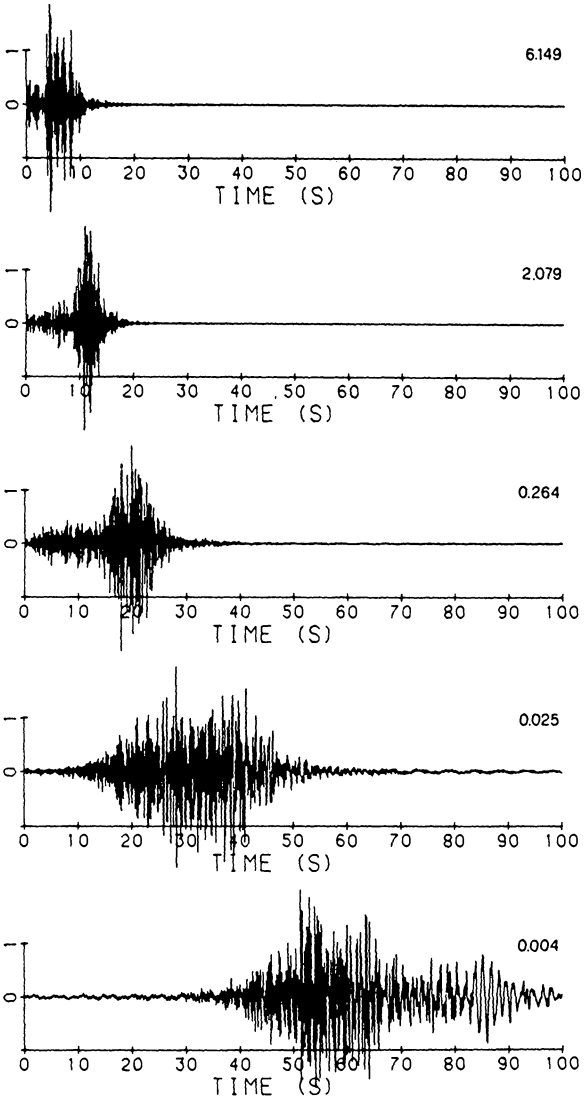

Figure 8. Synthetic accelerograms, vertical component, right-lateral instantaneous strike-slip source, model IMP1. For explanations see the caption of Fig.4.

Let us now consider the radial component only. In general the accelerograms for models with a sedimentary cover (e.g. FRI2, IMP1) show a large number of arrivals (see Figs. 5 and 7), the effect being more prominent for models with very thick sediments (as APN1, see Fig. 6). In this last case the accelerograms are the longest ones among our examples.

A synoptic representation of the effect of the different structures on PGA is shown in Fig. 9. As we see, the dispersion of the points is very large, up to about 2 orders of magnitude. Up to the distance of 25 km from the source, high values of PGA are determined by the presence of low velocity sediments trapping the energy (see open symbols). Starting from the near-source level, PGA is attenuated faster for models with low Q. Thus four extreme situations result: channelling in the sediments and strong attenuation with distance like for APN1 and IMP1 (thick sediments and low Q); channelling and moderate attenuation like for IRP1 and FRI2 (thin sediments and intermediate Q); no channelling and moderate attenuation like for FRI1 (no sediments an intermediate Q); no channelling and low intrinsic attenuation like for IMP2 (no sediments and high Q). The comparison between the PGA for IMP2 and FRI1 shows the importance of the quality factor. The feature determining the larger attenuation with distance of FRI1 is the presence of a relatively low Q even if restricted within 1 km from the surface.

As we shall show later in more detail, at distances closer to the source than 60-80 km, the PGA is due to the crustal Sg phase or to the sedimentary waves, depending on the depth of the source. At greater distances, the peak values of motion are due to the S-wave reflections at the Moho, which gradually become part of the Lg wave group (Panza and Calcagnile, 1974; Herrmann, 1979; Campillo and Bouchon, 1983).

As it could be expected from the results shown by Chiaruttini, Costa and Panza (1985), the PGA on the vertical component accelerograms for structures with sediments is consistently lower than that of the radial one (the factor varying from about 1.5 to 10), while for the structure with no sediments the vertical component turns out to be the bigger one (by a factor of about 2). An example of vertical component accelerograms (model IMP1) is shown in Fig. 8.

If we scale the acceleration computed for a unitary seismic moment to a seismic moment of 10^{22} dyne x cm - which corresponds to a moment magnitude M_W of 4.0 (Kanamori, 1983) - the resultant PGA's at a distance of 10 km are in the range from 10 to 400 cm/s^2. This range is consistent with the PGA's recorded in the field for shocks of comparable magnitude (Commissione CHEN-ENEL, 1976-1979; Chiaruttini and Siro, 1981). For stronger shocks, the PGA's computed assuming an instantaneous point source are by far too large. Obviously, in the case of large earthquakes, the finite rise time and the extension of the source drastically limit the PGA to maximum values of the order of 10^3 cm/s^2, which seem independent of magnitude. In our case, if we consider a source of 1 s duration, the PGA is reduced by a factor of about 100 (Fig. 10). Furthermore, considering a source of 5 s duration, which corresponds approximately to an earthquake of moment magnitude about 6.5, the resultant PGA for a distance of 25 km falls in the range 5 to 45 cm/s^2, in the case of the models FRI1 and FRI2. This PGA is considerably lower than

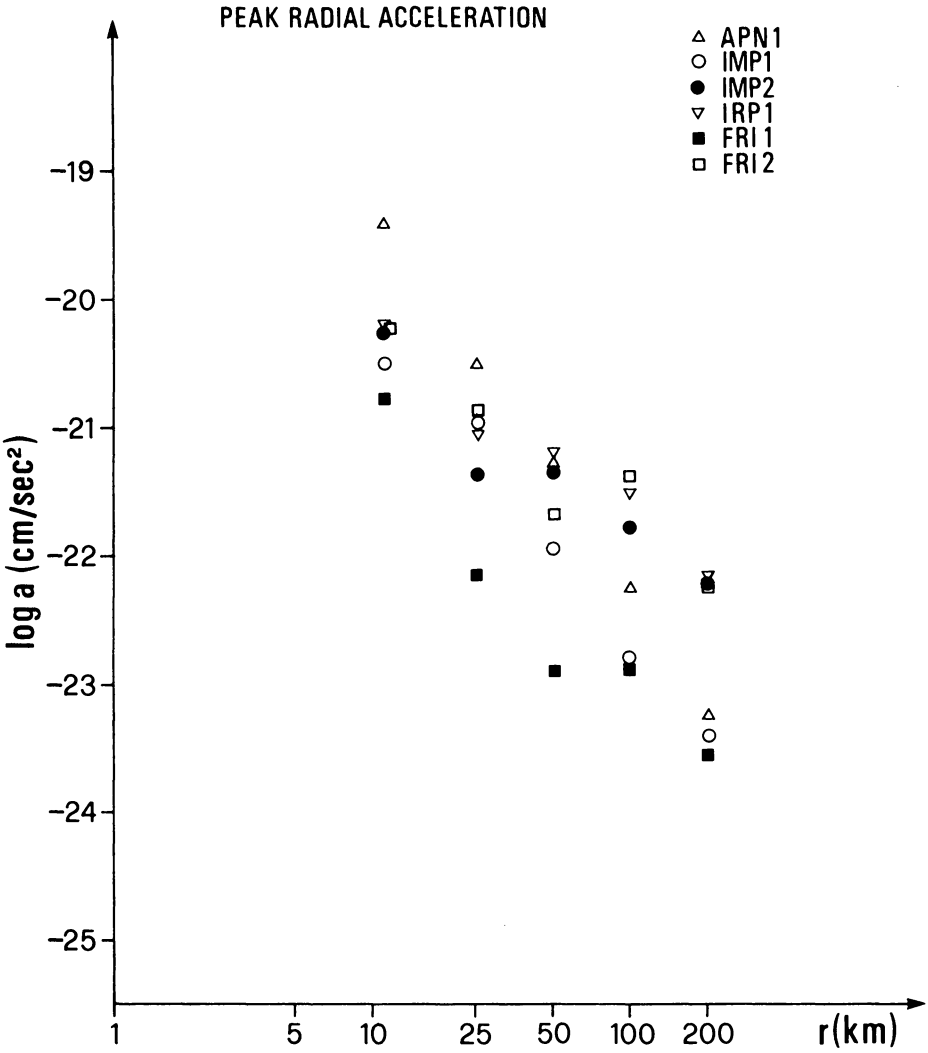

Figure 9. Attenuation of the radial component PGA with distance for all the six considered crustal models.

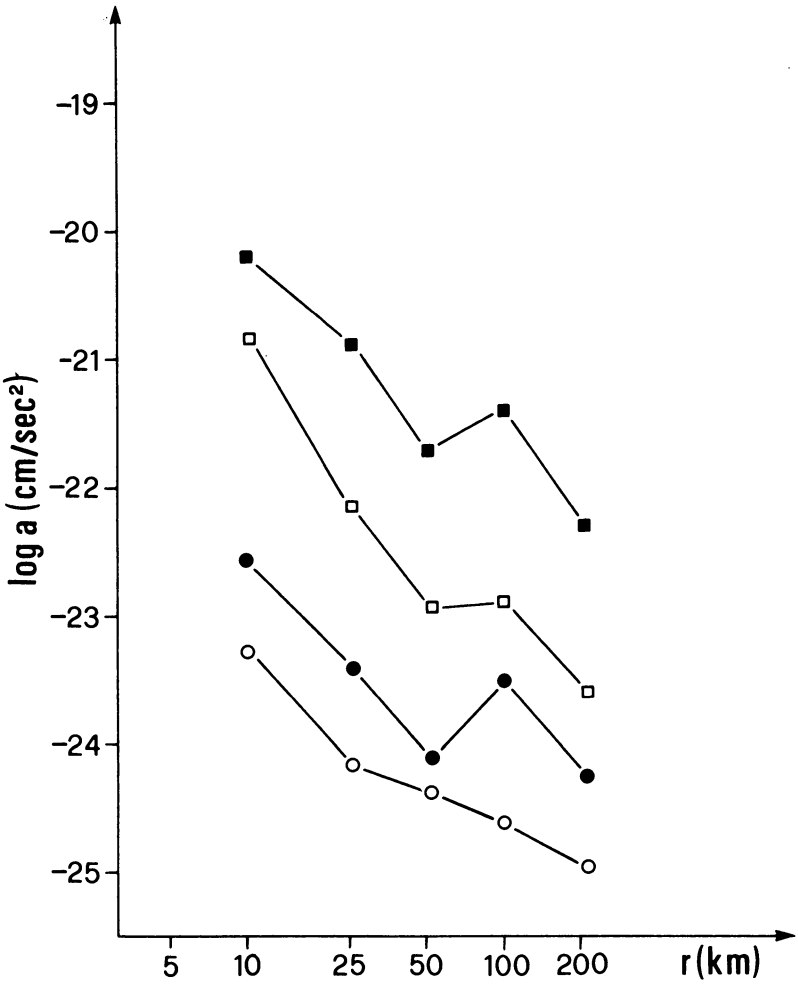

Figure 10. Comparison between the attenuation curves of the radial component PGA with distance for the FRI1 (open symbols) and FRI2(solid symbols) model with an instantaneous (squares) and a 1 s duration (circles) source.

that estimated from the Friuli field records, which is of the order of 200 cm/s^2. These low values are very likely due to the fact that we neglect the fault rupture process, which is usually quite complex for events with this magnitude.

Comparing the accelerograms for 1 s duration of the source in the case of models FRI1 and FRI2 (Figs. 11 and 12), we see that frequencies larger than 1 Hz still dominate the signal in the case of FRI2. This is due to the thin sedimentary cover which traps most of the high frequency energy.

5. DEPENDENCE OF ATTENUATION LAWS UPON THE CRUSTAL STRUCTURE

The attenuation with distance of PGA and a_{rms} for some of the considered models are shown in Figures 13 and 14. a_{rms} has been computed - according to Jennings (1983) - in the time window containing 90% of the energy of the signal. Different choices of the integration limits in the defining equation do not lead to statistically significant differences (McCann and Boore, 1983). As one can see in the figures, the attenuation curves are not always monotonic since, depending on distance, different phases, like Sg and Lg, constitute the strongest part of the signal. a_{rms} is smaller that PGA, but its trend is always very close to the latter and does not show a smaller scatter. This indicates that the observed failure of a_{rms} in reducing the scatter of experimental data resides directly in the characteristics of the wave wield and is not necessarily due to the source complexity or the scattering of waves in the crust. On the other hand, being a_{rms} a mean, it somewhat reduces the kinks present in some of the PGA profiles.

The standard errors of the estimate obtained by linearly regressing both log PGA and log a_{rms} with respect to the log hypocentral distance for the considered six structural models are summarized in Table 1. For each structure separately the standard errors of the estimate cluster at about 0.20 - 0.25, since about 50% of them fall in this range, while the standard erors of the estimate for the whole data set are about 0.6. This confirms that the grouping of data recorded on different crustal structures has a large influence in scattering the observations, as already observed from field data (e.g. Chiaruttini and Siro, 1981).

6. DEPENDENCE OF ATTENUATION LAWS ON SOURCE DEPTH

In order to investigate the variation of the wave field with the depth of the source, we have computed synthetic accelerograms for the model IRP1, for depths of 1.0 km, 5.0 km, 10.0 km and 17.5 km. The fault dips 60° and the mechanism is a combination of strike-slip and normal faulting. The signals have been computed at a close spacing in order to be able to follow the evolution of the wave field with distance. Some of the synthetics are shown as record sections in the Figures 15, 16 and 17.

Figures 15 and 16 show the two components of ground acceleration for a 1.0 km deep source. One can see the strong sedimentary waves generated at this very shallow depth. The slowest of these waves propagate

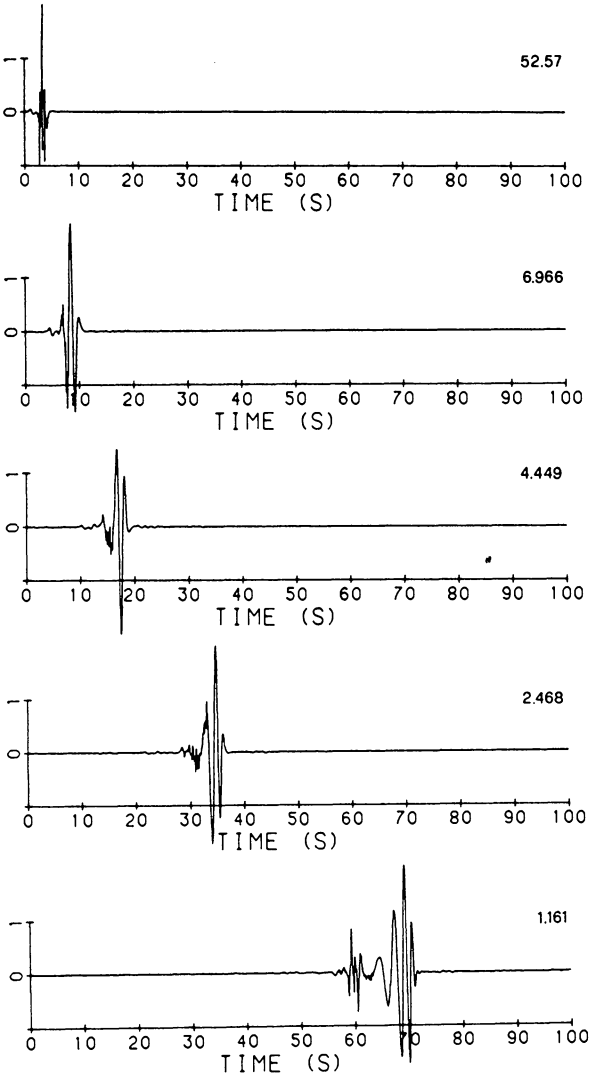

Figure 11. Synthetic accelerograms, radial component, right-lateral strike-slip source on a vertical fault, 1 s source duration, model FR11. For explanations see the caption of Fig.4.

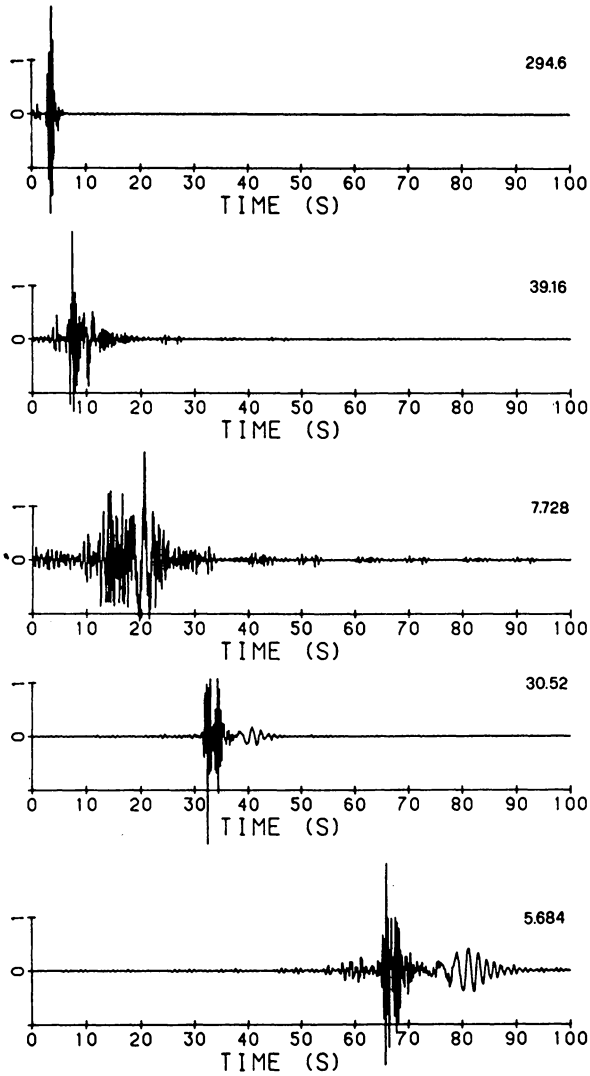

Figure 12. Synthetic accelerograms, radial component, right-lateral strike-slip source on a vertical fault, 1 s source duration, model FRI2. For explanations see the caption of Fig.4.

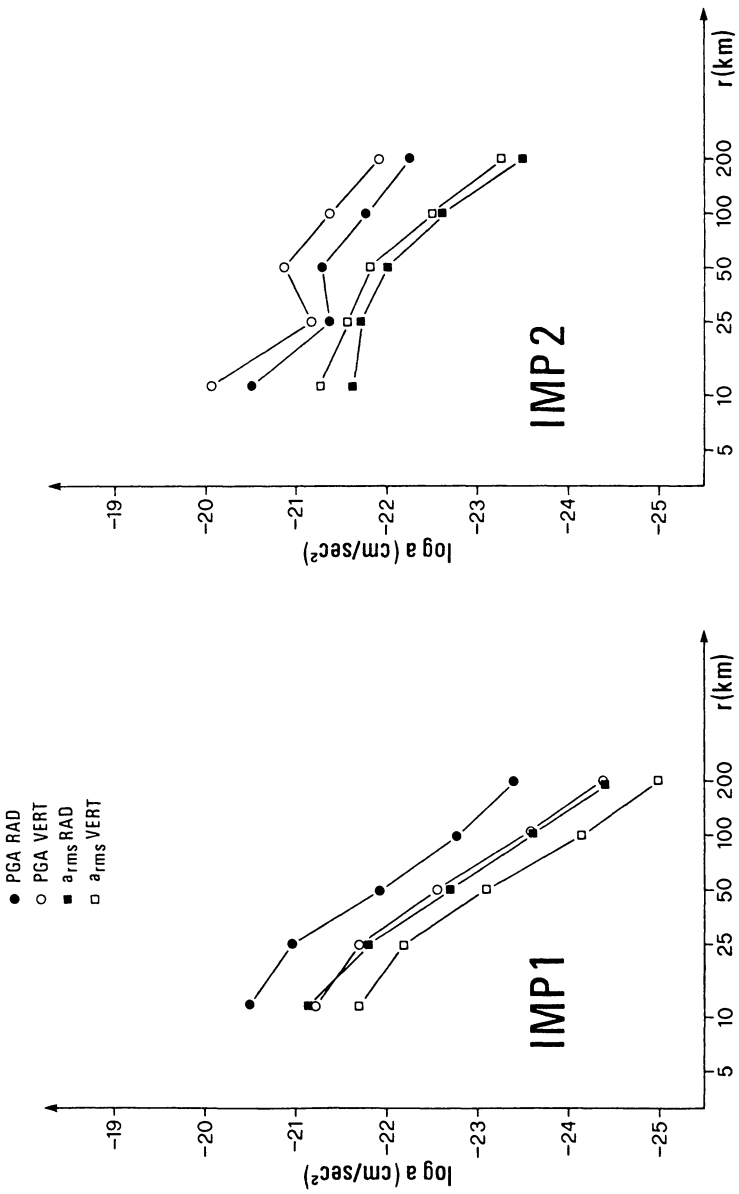

Figure 13. Attenuation curves for the radial and vertical component PGA and a_{rms} with distance for the models IMP1 and IMP2.

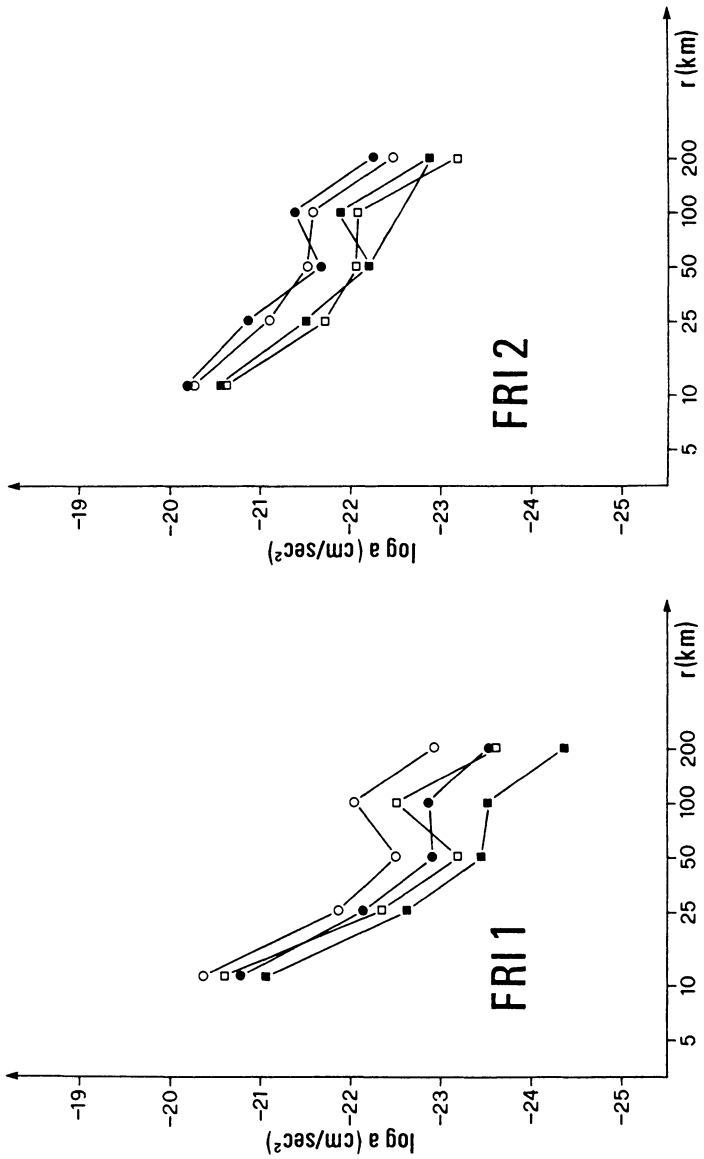

Figure 14. Attenuation curves for the radial and vertical component PGA and a_{rms} with distance for the models FRI1 and FRI2. For the explanation of the symbols see Fig.13.

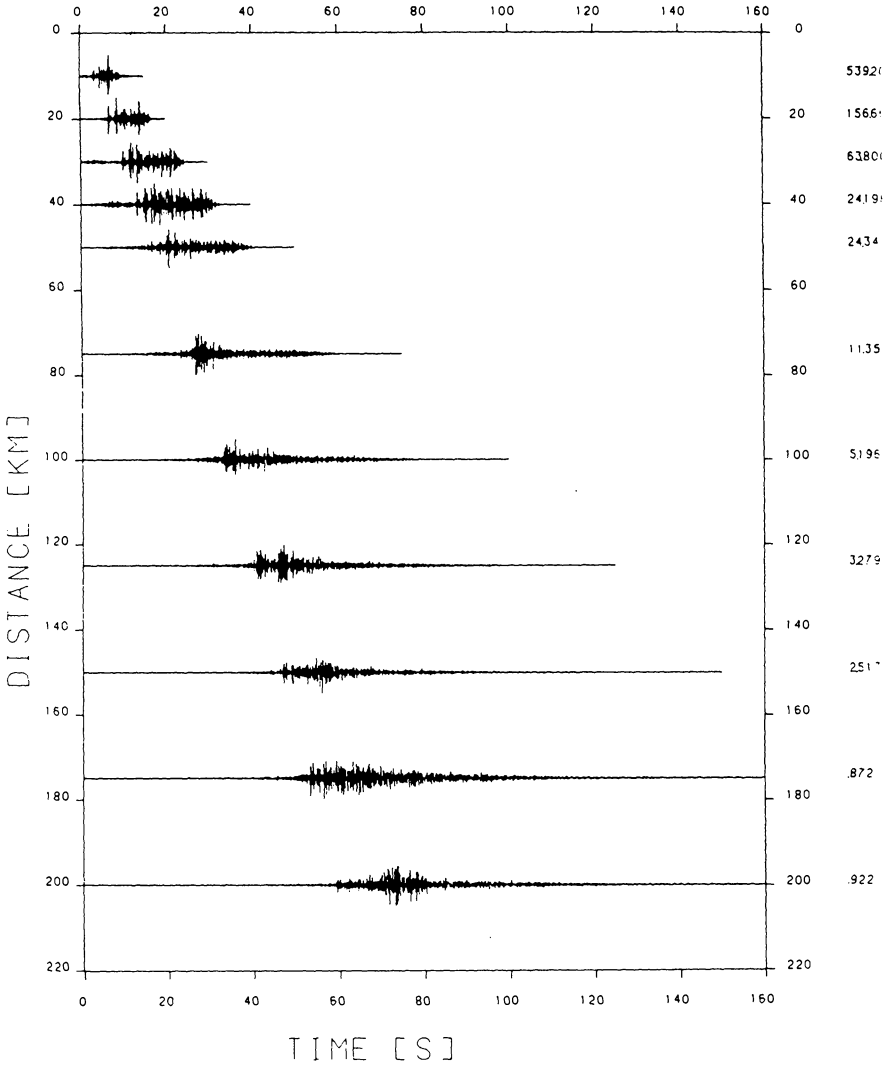

Figure 15. Synthetic accelerogram profile, radial component, for a 1 km deep seismic source (dip 60°, rake 340°) at an azimuth of 150° from the strike, model IRP1. The number at the right of each accelerogram is the PGA in units of 10^{-22}cm/s^2.

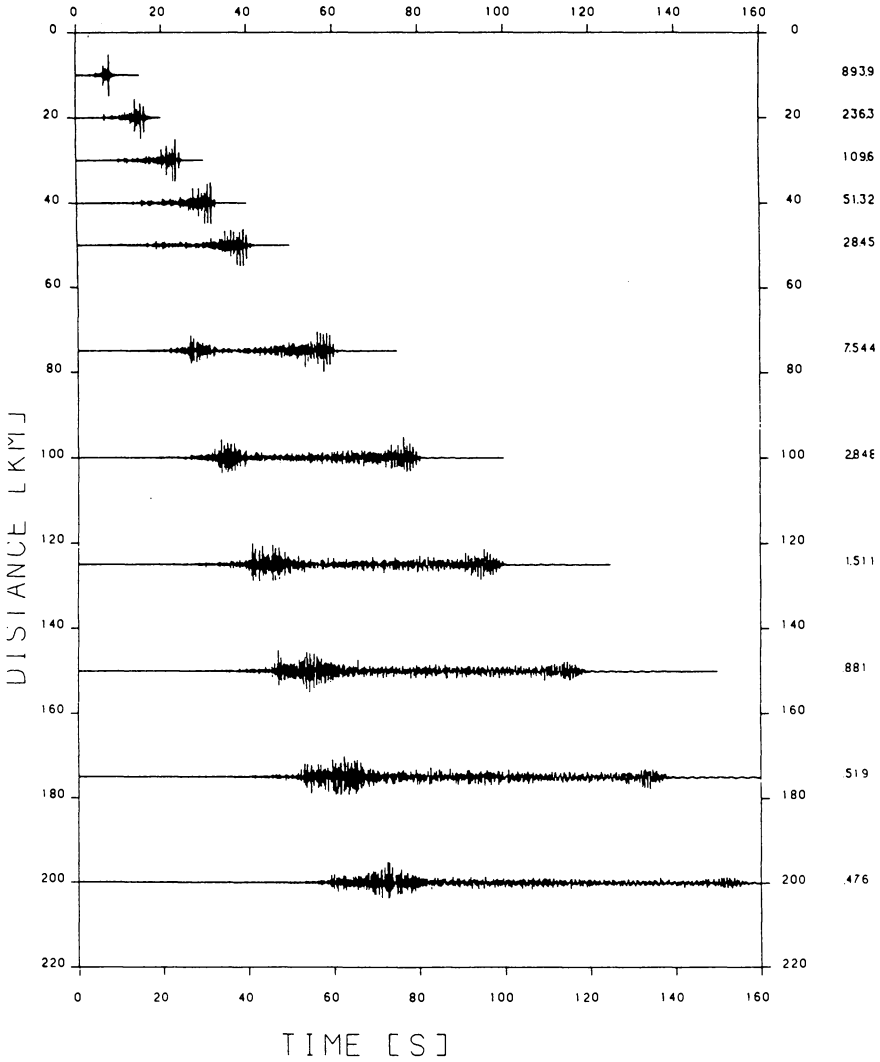

Figure 16. Synthetic accelerogram profile, vertical component, for a 1 km deep seismic source, model IRP1. Same source mechanism as in Fig.15.

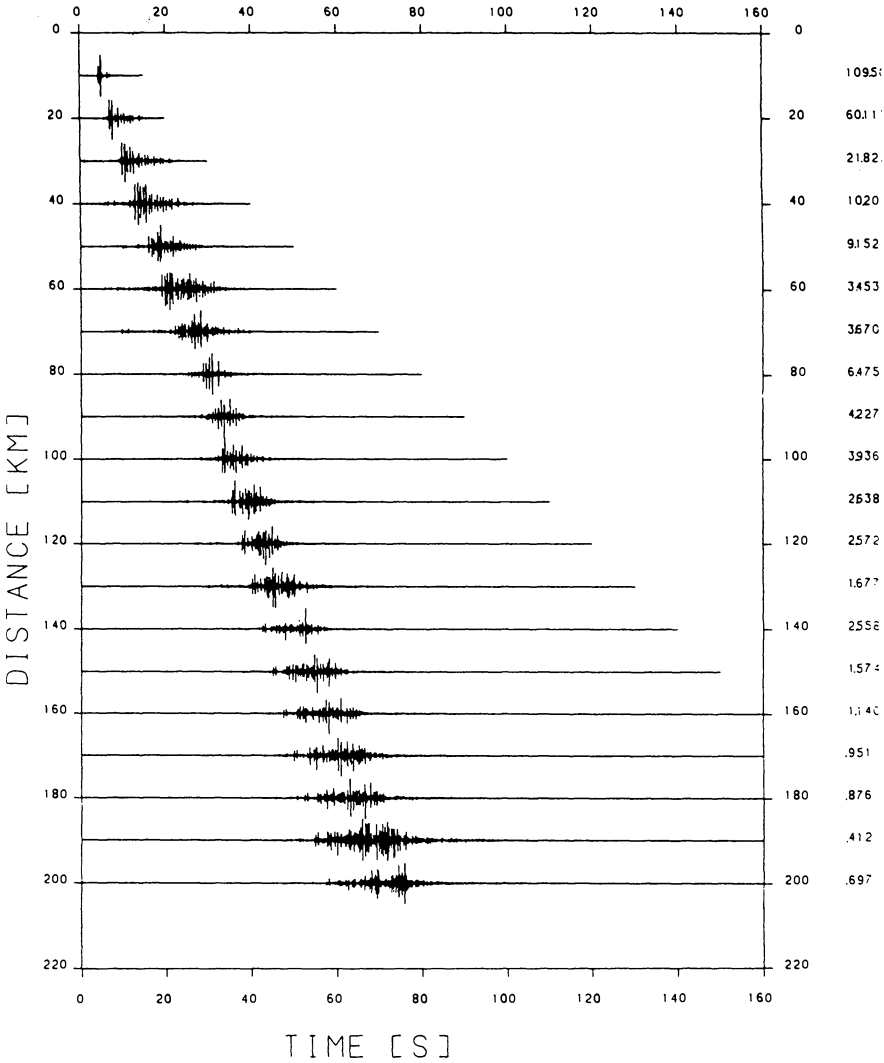

Figure 17. Synthetic accelerogram profile, radial component, for a 10 km deep seismic source, model IRP1. Same source mechanism as in Fig.15.

in the sediments at a velocity of about 1.3 km/s. Up to a distance of 50 km, sedimentary waves dominate the motion and the largest accelerations are found in the vertical component. At larger distances sedimentary waves are rapidly extinguished by the low Q of the sediments. At distances of 75 km and more, the horizontal component of motion becomes dominant. In this distance range, the strongest phases are Lg waves, travelling at velocities between 2.6 km/s and 3.5 km/s. As one can see, the largest component of motion is now the horizontal one, which is about twice as large as the vertical one. This is due to the sedimentary cover, as already pointed out discussing the effect of the crustal model.

When the source is placed below the sediments the excitation of sedimentary waves is drastically reduced but the strongest component remains the horizontal one. At short distances PGA is due to crustal Sg waves, while at larger distances it is due to Lg waves. The appearance of Lg waves produces a sudden increase of the PGA with increasing distance. As an example, Fig. 17 shows the radial component section for a source depth of 10 km. In this section another sudden increase in PGA occurs between 130 km and 140 km and a third one at 200 km as a consequence of later groups of Lg waves (see also Bouchon,1982).

In Fig. 18 we see that the part of the profiles dominated by the sedimentary and Sg waves (up to about 80 km) have a larger scatter than the part dominated by Lg waves (beyond 80 km). In general, PGA is consistently larger in the whole considered distance range for a source depth of 1 km. There is instead no clear correlation of PGA with depth when the source is located below the sediments between 5 km and 17.5 km. We also see that Lg waves attenuate with distance faster than Sg and sedimentary waves. This is likely to be due to the effect of anelasticity -which attenuates the energy at an exponential rate rather than at the power- law one implied by the regression model. The standard deviation of the residuals from the best fitting straight lines are shown in Table 2. They are around 0.15 log units when considering separately each curve corresponding to different source depths. Significant improvement of the regressions is obtained splitting in two parts the distance range. Profiles for source depths of 5 km, 10 km and 17.5 km can be regressed together without impairing the results for the whole distance range, but grouping all source depths togetler results in considerable worsening of the fit. The effect of depth is present only at short distances, in the Sg dominated part; the Lg dominated part has a scatter of about 0.10 irrespective of any depth selection. For the vertical component the results are similar, with only a slightly larger scatter of the profiles in the Sg dominated distance range.

7. DEPENDENCE OF THE PGA ON FAULT AZIMUTH

To investigate the scatter of the PGA with fault azimuth, the PGA of the radial component were computed for the structure IRP1 at a spacing of 10° in azimuth and at epicentral distances of 25, 50 and 100 km. PGA isolines have been subsequently eye-fitted to them. The shape of these isolines can be used to study the shape of isoseismals (Panza and Cuscito, 1982).

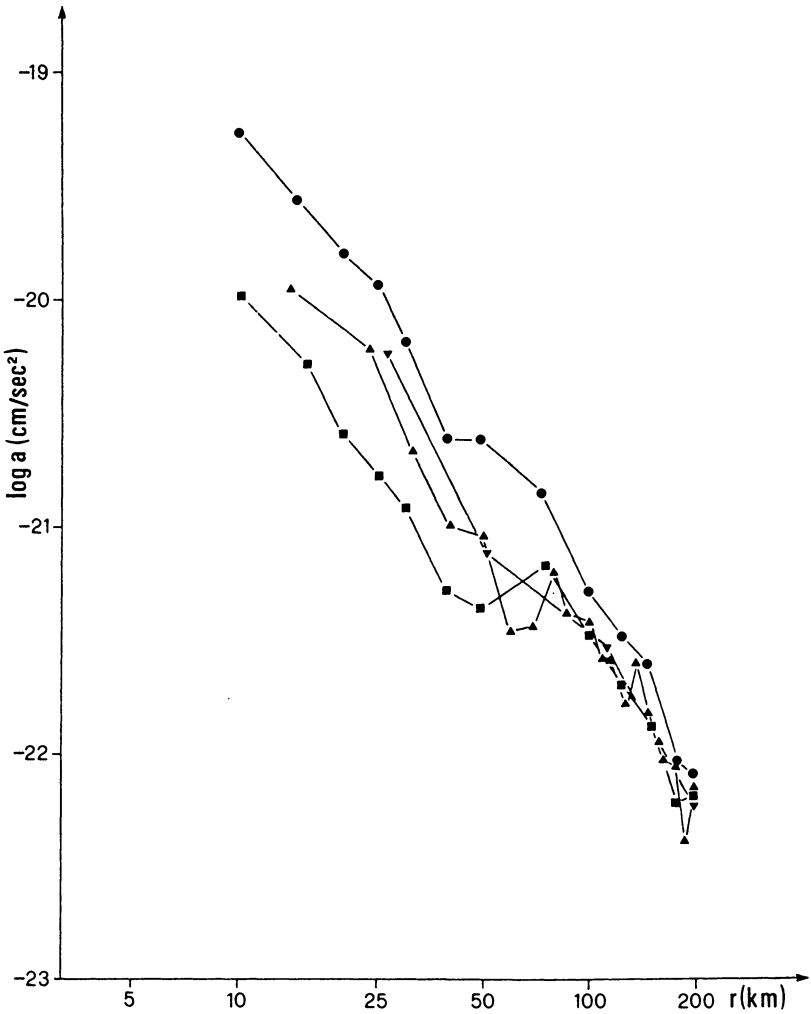

Figure 18. Attenuation of the radial component PGA with distance for various source depths, model IRP1. Same source mechanism as in Fig.15. Circles correspond to a 1 km deep, squares to a 5 km deep triangles to a 10 km deep and upside-down triangles to a 17.5 km deep source.

The result for a pure strike-slip source on a vertical fault is shown in Fig. 19, while the results for a pure dip-slip source of both thrust and normal type on a 45° dipping plane is shown in Fig. 20. The sources are at a depth of 5.0 km. The relative dispersion coefficients -standard deviation over the arithmetic mean - are 0.52 for all the three distances in the strike-slip case and 0.24 for the dip-slip case. The dispersion coefficient are the same for both the radial and the vertical component. The ratio of strike-slip and dip-slip means is 0.42. The results are very simple and seem to indicate that: 1) for these simple source mechanisms and the considered distances Sg and Lg waves have comparable radiation patterns; 2) the dispersion is much bigger in the strike-slip case, but the PGA are on the average about half as big as in the dip-slip case (see Fig. 21). The symmetry in these results is due to the considered sources and is not a general property, as shown by the calculations made for a source mechanism with a dip of 60° and a rake of 340°. In this case the dispersion coefficient is slightly dependent on distance: 0.23 to 30 km and 0.29 at 100 km.

It should be noted that the stronger surface shaking due to a dip-slip source in comparison to a strike-slip source of the same strenth is probably not apparent in practice, when magnitude is used as source size. In fact, a discrepancy similar to the discrepancy between the PGA of strike-slip and dip-slip sources is to be expected in magnitude determinations, especially if regional phases are used.

Figure 22 is an example of how meaningless can be to try to correct PGA for the radiation pattern of body waves. In different azimuths, PGA is carried either by a phase in the group of Sg waves - arriving at about 17 s - or by the critically reflected wave at the bottom of the low velocity channel - arriving at 19 s. The radiation coefficient of PGA is thus a combination of the coefficients for two different phases. The dispersion coefficient in this case is 0.37.

8. DEPENDENCE OF THE PGA ON ANELASTICITY OF THE EARTH

In most of our models the attenuation of acceleration with distance for an instantaneous point source is too strong compared to the experimental results. The slope of the attenuation law is compatible with the observable slope of about -1 (Boore and Joyner, 1982) when a source of finite rise time is taken into account (see Fig. 10) or in case of a high Q model such as IMP2 (see Fig. 9). We will try in this section to elucidate better the effect that anelasticity can have on the attenuation laws of strong ground motion.

The anelastic properties of the earth are at present not satisfactorily understood, especially because of the difficulty in making physically meaningful measurements of Q (Panza, Suhadolc and Chiaruttini, 1985). At present a constant Q model (Knopoff, 1964) should be adequate considering the state of the art, as is illustrated, for example, by Chiaruttini and Qaisar (1984).

A systematic analysis of the Q effect can be done by comparing the results described above with those obtained for perfectly elastic models.

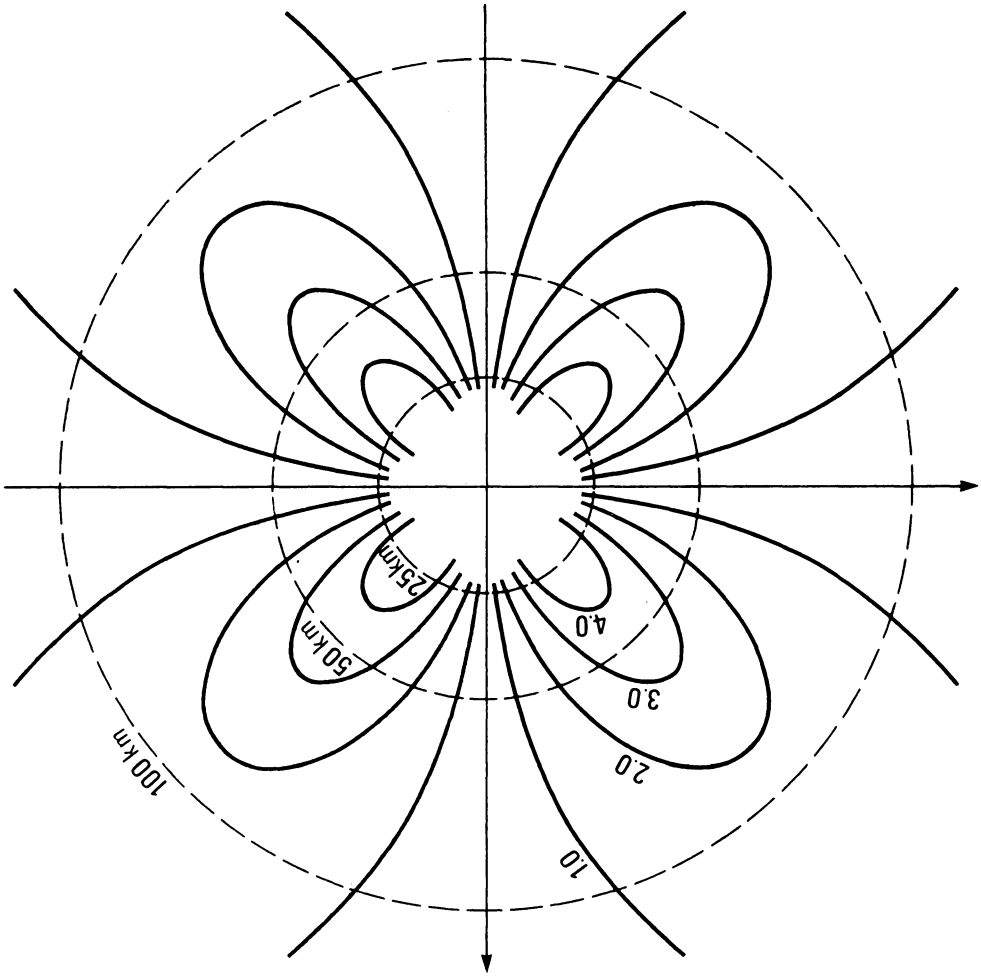

Figure 19. Radiation profile of the radial component PGA for a 5 km deep strike-slip source on a vertical fault plane, model IRP1. The values of the isolines are in units of 10^{-22}cm/s^2 for a unitary (1 dyne x cm) seismic moment.

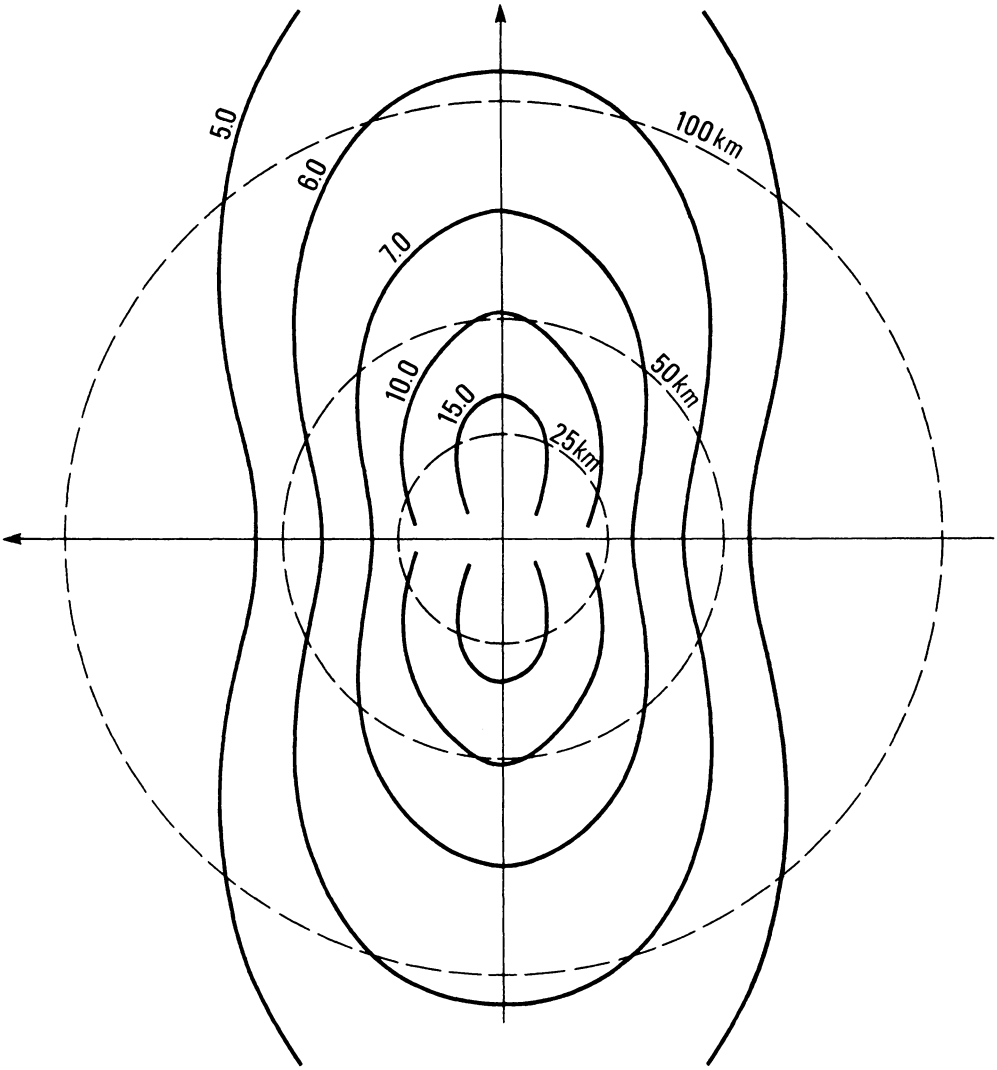

Figure 20. Radiation profile of the radial component PGA for a 5 km deep dip-slip source on a 45° dipping plane, model IRP1. The values of the isolines are in units of 10^{-22} cm/s^2 for a unitary (1 dyne x cm) seismic moment.

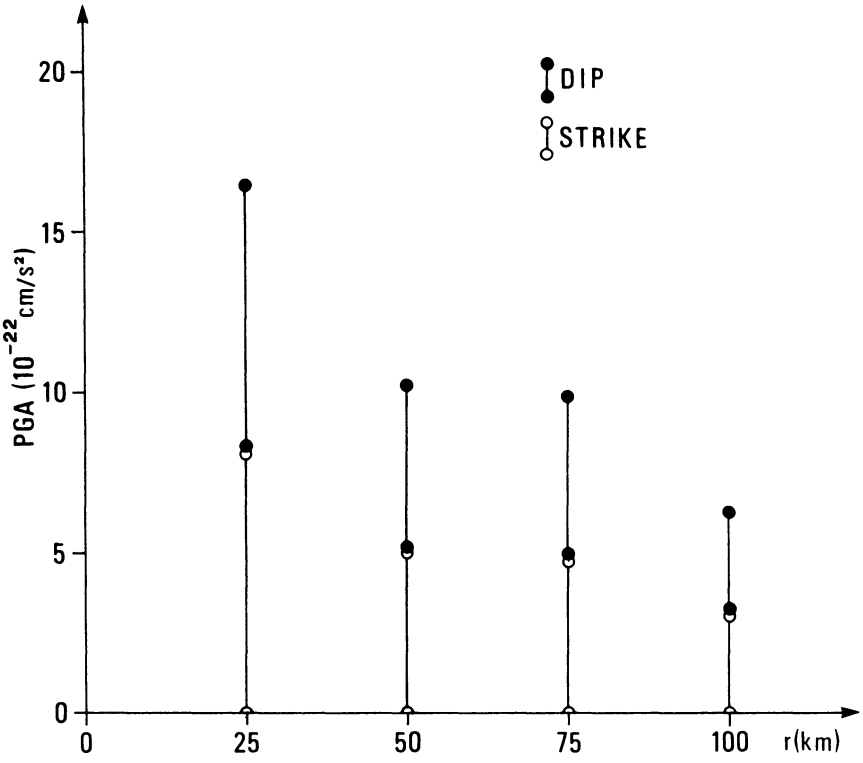

Figure 21. Range of variation of the radial component PGA in azimuth at different distances for 5 km deep strike-slip and dip-slip sources, model IRP1.

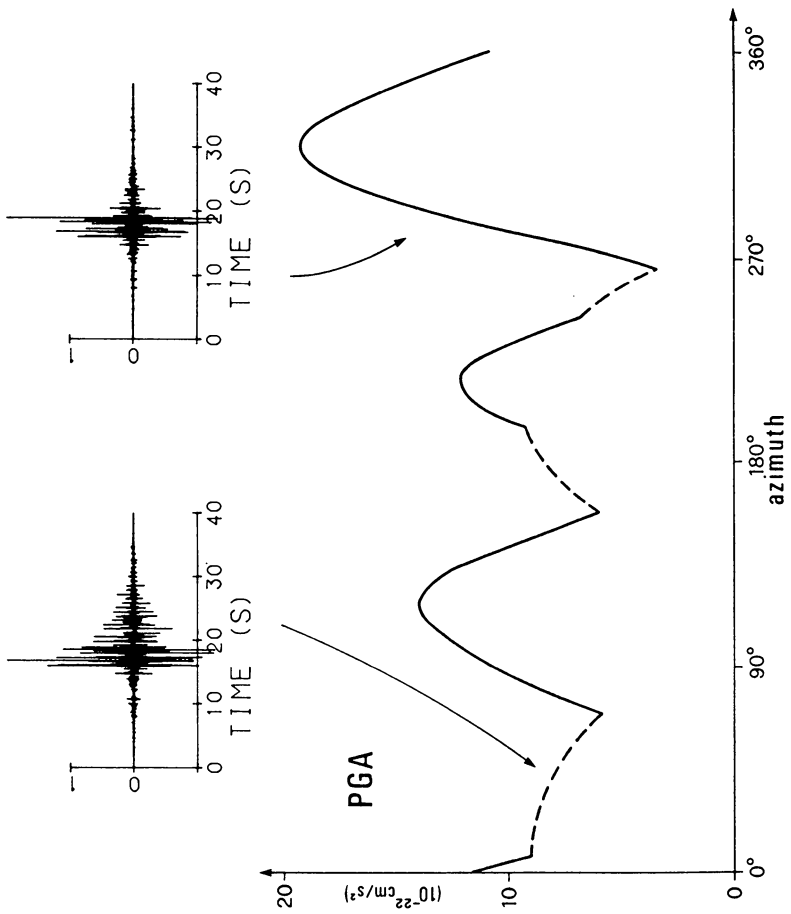

Figure 22. Radiation profile of the radial component PGA for the mechanism with dip 60° and rake 340° at 10 km depth 10, model IRP1. The source distance is 50 km.

Thus the models FRI1, FRI2 and IRP1 have been modified by taking $Q = \infty$ for all the layers. The radial component accelerograms corresponding to the perfectly elastic models FRI1 and FRI2 are shown in Fig. 23 and Fig. 24.

By comparing these accelerograms with those of Fig. 4 and Fig. 5, one can observe that, apart from the expected larger amplitudes of the late-arriving sedimentary waves at greater distances for the perfectly elastic case, the main visible difference is the change in the relative amplitudes of the different Lg wave groups. This is explained if we remember that the Lg waves are multiple S-wave reflections between the Moho and the free surface (e.g. Panza and Calcagnile, 1974). In the perfectly elastic case the different reflections are no longer so crucial for the amplitudes.

The attenuation curves with distance for the elastic and anelastic cases of the FRI1 and FRI2 models are shown in Fig. 25. The $Q = \infty$ effect is evident especially at greater distances, while around 10 km it is very small, as we could expect. The overall effect is to render the attenuation curves less steep.

$Q = \infty$ has been assumed also for the model IRP1 and PGA attenuation curves have been computed for 1, 5, 10 and 17.5 km deep sources. The curves are shown in Fig. 26. Comparing this figure with Fig. 18 we see that the curve for a 1 km deep source in the perfectly elastic case is about one order of magnitude above the curves for the other source depths. In fact, in absence of intrinsic attenuation, sedimentary waves remain the dominant phases in all the considered distance range.

The regression analysis on the data contained in Figures 25 and 26 show that the range of standard deviations is the same as that for the attenuating models (Tables 1 and 2). This means that our conclusions about the origin of scattering in the attenuation laws have a general validity and are not affected by the Q model.

Figures 25 and 10 quantify the obvious trade-off between the effects of anelasticity of the medium and time duration of the source. The steep slopes of the attenuation curves of Fig. 13 and Fig. 14 can be reconciled with the experimental slope either by considering sources of finite duration or by increasing the quality factor of the medium.

9. CONCLUSIONS

The behavior of the PGA and a_{rms} has been theoretically investigated for realistic models of the earth and seismic sources. The theoretical vertical and radial component accelerograms have been obtained using the method of summation of Rayleigh modes in the frequency range 0.05 Hz - 10 Hz.

Although the strongest earthquake shaking is generally due to SH-waves, SV-waves should be considered too, especially in a sedimentary environment, where the polarization of Rayleigh higher modes is mainly horizontal. In fact PGA on radial components are generally much larger than on vertical ones in structural models containing low velocity sediments, while they are slightly lower for structures without sediments.

Six different earth crustal models have been taken into account.

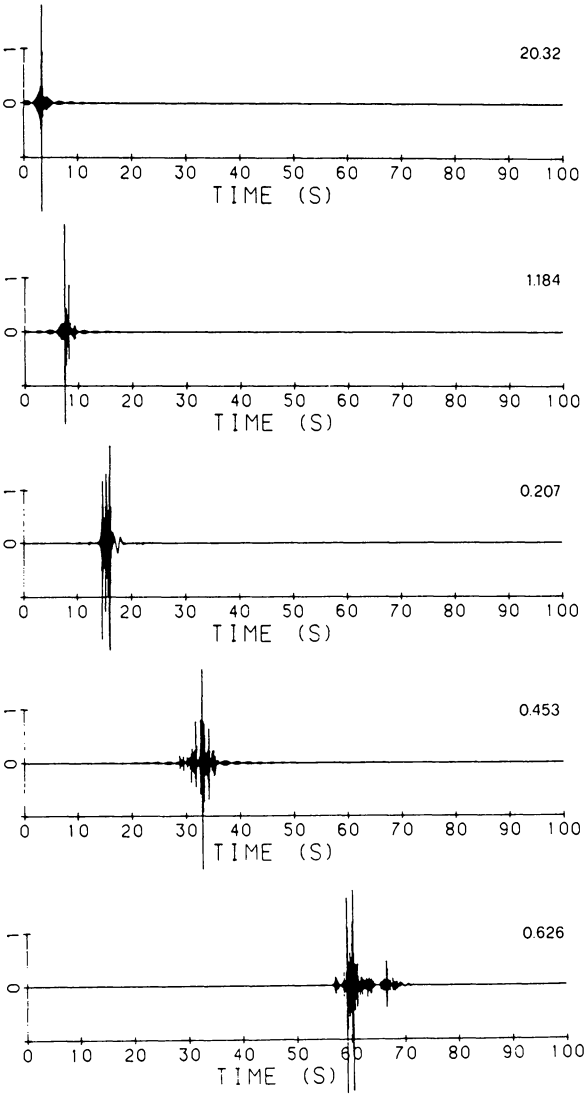

Figure 23. Synthetic accelerograms, radial component, 5 km deep right-lateral instantaneous strike-slip source, model FRI1 with $Q = \infty$. For explanations see the caption of Fig.4.

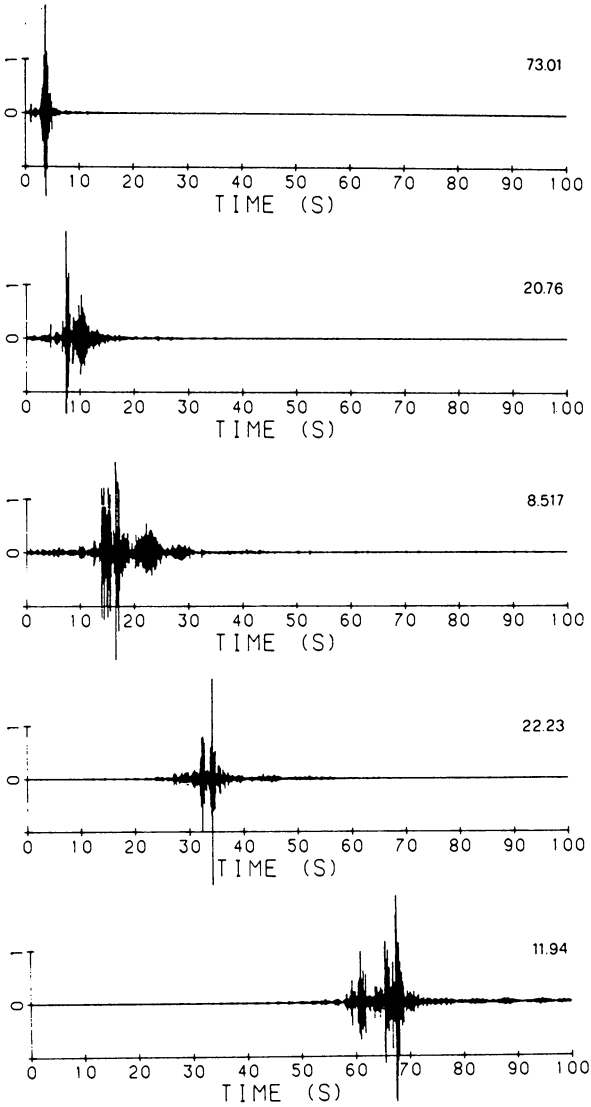

Figure 24. Synthetic accelerograms, radial component, 5 km deep right-lateral instantaneous strike-slip source, model FRI2 with $Q = \infty$. For explanations see the caption of Fig.4.

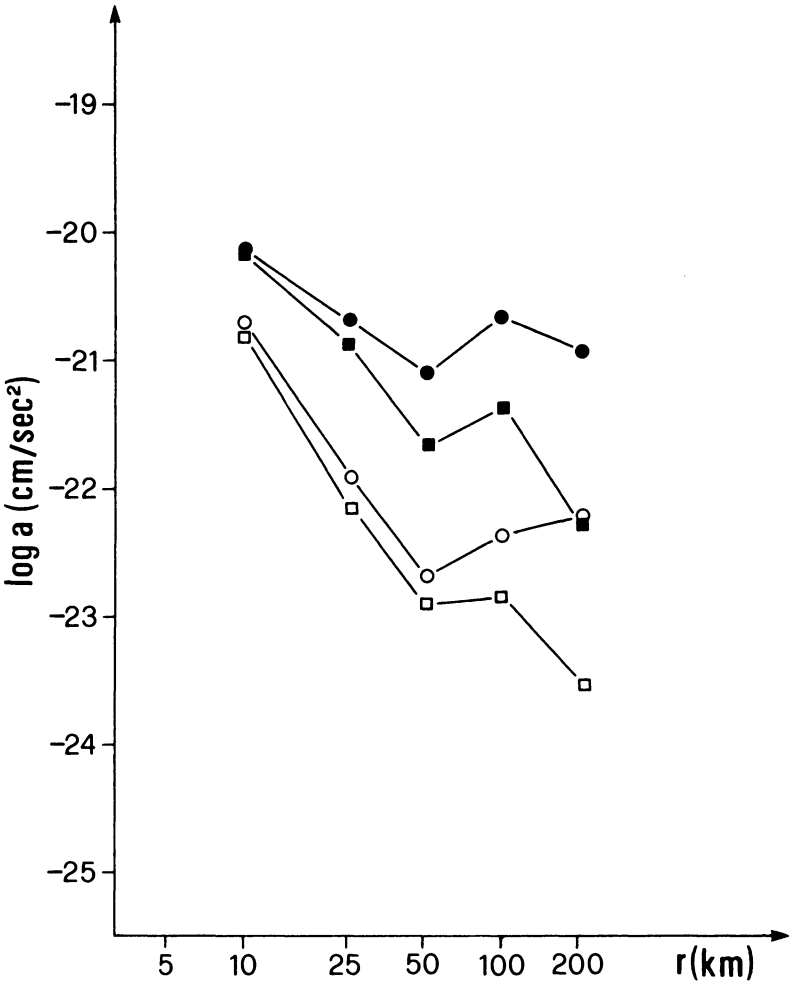

Figure 25. Comparison between the attenuation curves of the radial component PGA with distance for the FRI1 and FRI2 models of Fig.2 (squares) and the FRI1 and FRI2 models with $Q=\infty$ (circles). Open symbols for FRI1, solid symbols for FRI2.

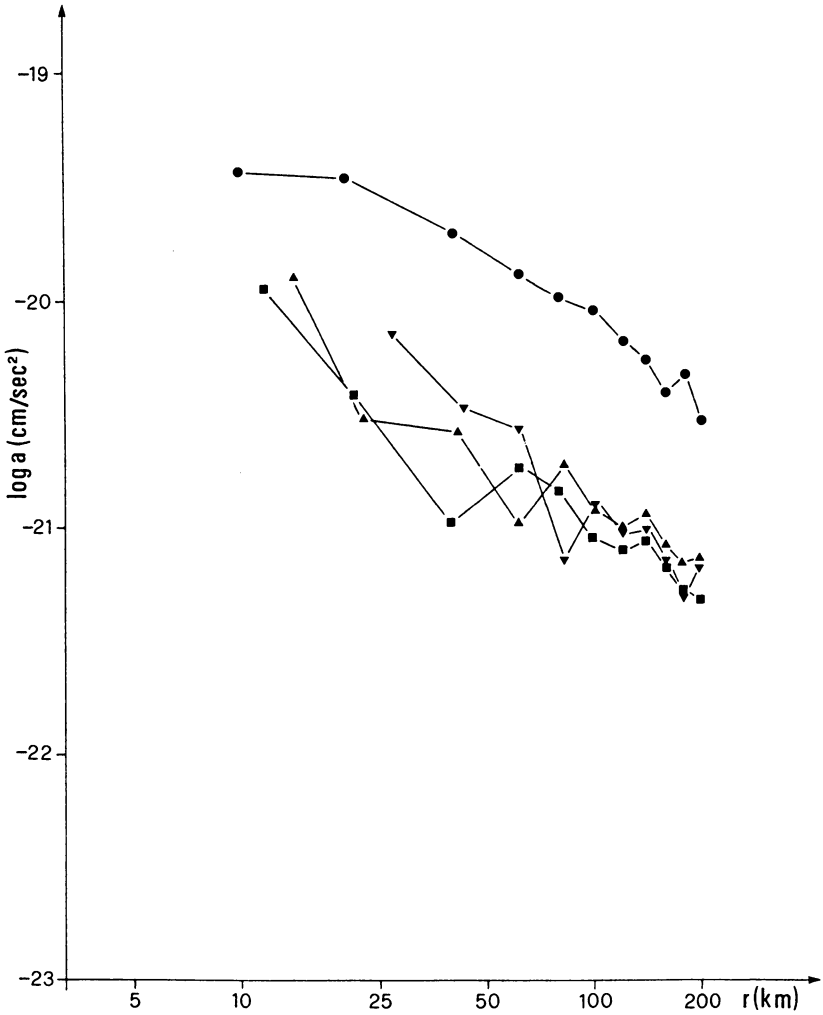

Figure 26. Attenuation of the radial component PGA with distance for various source depths, model IRP1 with Q = ∞. Same source mechanism as in Fig.15. Circles correspond to a 1 km, squares to a 5 km, triangles to a 10 km and upside-down triangles to a 17.5 deep source.

TABLE 1. STANDARD ERROR OF THE LINEAR REGRESSION ESTIMATE FOR THE SIX STRUCTURAL MODELS.

Model	Standard Error			
	PGA		a_{rms}	
	rad	ver	rad	ver
IMP 1	0.26	0.20	0.32	0.23
IMP 2	0.21	0.33	0.31	0.24
IRP 1	0.24	0.22	0.19	0.23
APN 1	0.10	0.21	0.06	0.09
FRI 1	0.41	0.55	0.41	0.78
FRI 2	0.32	0.23	0.35	0.31
Total	0.57	0.63	0.56	0.53

TABLE 2. STANDARD ERRORS OF THE LINEAR REGRESSION ESTIMATE AS A FUNCTION OF SOURCE DEPTH AND DISTANCE RANGE: MODEL IRPI, RADIAL COMPONENT.

Source Depth (km)	Distance Range (km)		
1.0	0.12	0.09	0.10
5.0	0.18	0.04	0.07
10.0	0.15	0.11	0.11
17.5	0.12	0.07	0.06
5.0 to 17.5	0.17	0.20	0.09
1.0 to 17.5	0.24	0.31	0.12

It has been found that at short ($r < 80$ km) distances the structures with thick sediments give the highest PGA. On the other hand these structures, having usually low Q values near the surface, attenuate the ground motion more rapidly with distance.

For distances up to about 80 km the phase contributing to the PGA is the Sg or the sedimentary wave - depending upon the depth of the source - while for distances greater than 80 km the PGA is to be found among the developing Lg groups.

The variation of PGA with azimuth is shown to be also quite important, especially for strike-slip earthquakes. On the other hand, for a given modulus of the seismic moment, the PGA's due to dip-slip point sources are about twice those due to strike-slip point sources.

The use of a_{rms} instead of PGA has practically no effect in reducing the scatter of attenuation laws derived from deterministic synthetic signals, as it has no effect in the case of field records.

From all the analysis presented here we can derive the following guidelines for improving the rather empirical methods used nowadays to estimate the intensity of the ground shaking employed in seismic hazard studies:

1) Group data from regions having similar crustal structures. Not taking into account this criterion may result in standard deviations of log PGA as large as 0.5 and more.

2) Use macroseismic information from the field (unsmoothed isoseismals) to take into account the radiation pattern at the surface. The effect of radiation pattern may result in a dispersion coefficient up to 0.3 log units.

3) Separate strike-slip from dip-slip shocks. The average responses differ by a factor 2.4 corresponding to about 0.4 log units for sources of identical seismic moment.

4) Allow for an Sg slope of the attenuation laws near the source and an Lg slope at greater distances. The threshold for distance depends on the crustal structure and is to be found in the range from 60 to 100km. An experimental proof of this is found in the calibration of the Swiss Seismological Network (Mayer-Rosa, 1985).

5) In presence of a few kilometres of low-velocity sediments at the top of the crust, most of the seismic energy generated by sources within these layers remains trapped close to the surface. This may be a reason of scattering when considering together small shocks within and below the sediments and, in case of large earthquakes, if asperities break within or the rupture propagates into the sedimentary cover. The effect of sediments can result in a standard deviation of the order of 0.3 log units.

If we consider any of the attenuation profiles shown in this study, the scatter of the data points is due only to wave propagation effects in laterally homogeneous media. This is the lowest possible limit after removing all te above reasons of scatter. It can be estimated to be lower than 0.2 log units for the Sg dominated distance range, and 0.1 log units for the Lg range.

Acknowledgements We are very indebted to Prof. G.F. Panza for the numerous discussions about the topics presented in this paper and for critically reading the manuscript. Moreover we would like to thank Dr. G. Costa for helping in the implementation of the computer programs which are the basis of the present work. Thanks are also due to Mr. G.Cavicchi, who has drawn some of the figures.

This research has been carried on with the contribution of MPI grants (40% and 60%) and ENEA contract n. 16094.

11. REFERENCES

Anderson, D.L., Ben-Menahem, A. and Archambeau, C.B.,(1965),Attenuation of seismic energy in the upper mantle. J. Geophys. Res., 70, 1441-1448.

Arias, A.,(1969), A measure of earthquake intensity. In: Seismic Design for Nuclear Power Plants, R.Hansen, Editor, Massachusetts Institute of Technology Press, Cambridge.

Boatwright, J.,(1982), A dynamic model for far-field acceleration. Bull. Seism. Soc. Am., 72, 1049-1064.

Boatwright, J. and Boore, D.M.,(1982), Analysis of the ground accelerations radiated by the 1980 Livermore valley earthquakes for directivity and dynamic source characteristics. Bull. Seism. Soc. Am., 72, 1843-1865.

Boore, D.M. and Joyner, W.B.,(1982), The empirical prediction of ground motion. Bull. Seism. Soc. Am., 72, S43-S60.

Boore, D.M. and Boatwright, J.,(1984), Average body-wave radiation coefficients. Bull. Seism. Soc. Am., 74, 1615-1622.

Bouchon, M.,(1982), The complete synthesis of seismic crustal phases at regional distances. J.Geophys. Res., 87, 1735-1741.

Campillo, M. and Bouchon, M.,(1983), A theoretical study of the radiation from small strike-slip earthquakes at close distances. Bull.Seism. Soc. Am., 73, 83-96.

Campbell, K. W.,(1981), Near-source attenuation of peak horizontal accelerations. Bull. Seism. Soc. Am., 71, 2039-2070.

Chiaruttini, C., Crosilla, F. and Siro, L.,(1979), Some maximized acceleration analyses of the 1976 Friuli earthquakes. Bull. Geof. Teor. Appl., 21, 38-52.

Chiaruttini, C. and Siro, L.,(1981), The correlation of peak ground horizontal acceleration with magnitude, distance and seismic intensity for Friuli and Ancona, Italy, and the Alpide Belt. Bull. Seism. Soc. Am., 71, 1993-2009.

Chiaruttini, C., Costa, G. and Panza, G. F.,(1985), Wave propagation in multilayered media: the effect of wave guides in oceanic and continental earth models. J. Geophys., in press.

Chiaruttini, C. and Qaisar, M.,(1984), Attenuation properties of the Friuli seismic area. Acta Geophys. Pol., 32, 141-151.

Commissione CNEN-ENEL per lo studio dei problemi sismici connessi con la realizzazione di impianti nucleari (1976-1979). Strong motion earthquake accelerations, digitized and plotted data, Parts 1 to 5, Rome, Italy.

Fuis, G.S., Money, W.D., Healey, J.H., McMecham, G.A. and Lutter, W.S., (1982), Crustal structure of the Imperial Valley region. U.S. Geol. Surv., Prof. Paper 1254, 25-49.

Futtermann, W.I.,(1962), Dispersive body waves. J.Geophys. Res., 67, 5279-5291.

Harkrider, D.G.,(1970), Surface waves in multilayered elastic media. Part II. Higher mode spectra and spectral ratios from point sources in plane layered earth models. Bull. Seism. Soc. Am., 60, 1937-1987.

Harvey, D. J.,(1981), Seismogram synthesis using normal mode superposition: the locked mode approximation. Geophys. J.R. astr. Soc., 66, 37-69.

Herrmann, R.B.,(1979), SH-wave generation by dislocation sources - A numerical study. Bull. Seism. Soc. Am., 69, 1-15.

Husid, R.,(1967), Gravity effects on the earthquake response of yielding structures. Report of Earthquake Engineering Research Laboratory, California Institute of Technology, Pasadena.

Idriss, I.M.,(1978), Characteristics of earthquake ground motions. ASCE Earthquake Eng. Soil Dyn. Conf. and Exhibit, Pasadena, California, June 19-21, 1151-1265.

IESG and ETH,(1981), Crust and upper mantle structures in the Southern Alps from deep seismic sounding profiles (1977, 1978) and surface wave dispersion analysis. Boll. Geofis. Teor. Appl., 23, 297-330.

Jennings, P.C.,(1983), Engineering seismology. In: Earthquakes: Observation, Theory and Interpretation. Proceedings of the International School of Physics "Enrico Fermi", Varenna, Italy.

Joyner, W.B. and Boore, D.M.,(1981), Peak horizontal acceleration and velocity from strong-motion records including records from the 1979 Imperial Valley, California, earthquake. Bull. Seism. Soc. Am., 71, 2011-2038.

Kanamori, H.,(1983), Magnitude scale and quantification of earthquakes. Tectonophysics, 93, 185-199.

Kijko, A. and Mitchell, B.J.,(1983), Multimode Rayleigh wave attenuation and Q in the crust of the Barents shelf. J. Geophys. Res., 88, 3315-3328.

King, J.L. and Tucker, B.E.,(1984), Observed variations of earthquake motion across a sediment-filled valley. Bull. Seism. Soc. Am., 74, 137-151.

Knopoff, L.,(1964),Q. Reviews of Geophys., 2, 625-660.

Madariaga, R.,(1977), High-frequency radiation from crack (stress-drop) models of faulting. Geophys. J.R. astr. Soc., 51, 625-652.

Mantovani, E., Farsi, F. and Babbucci, D.,(1980), Body wave velocities and lateral heterogeneity in the Italian region. Boll. Geofis. Teor. Appl., 22, 211-221.

Mayer-Rosa, D.,(1985), Attenuation of seismic ground motion in Switzerland. Preprint, Swiss Seismological Service, Federal Institute of Technology, 8093 Zuerich.

McCann, M.W. and Boore, D.M.,(1983), Variability in ground motions: root mean square acceleration for the 1971 San Fernando, California, earthquake. Bull. Seism. Soc. Am., 73, 615-632.

Murphy, J.R. and O'Brien, L.J.,(1977), The correlation of peak ground acceleration amplitude with seismic intensity and other physical parameters. Bull. Seism. Soc. Am., 67, 877-915.

Panza, G.F., Schwab, F. and Knopoff, L.,(1973), Multimode surface waves for selected focal mechanisms. I. Dip-slip sources on a vertical fault plane. Geophys. J.R. astr. Soc., 34, 265-278.

Panza, I.G. and Calcagnile, G.,(1974),Lg, Li and Rg from Rayleigh modes. Geophys. J.R. astr. Soc., 40, 475-487.

Panza, G.F. and Cuscito, M.,(1982), Influence of focal mechanism on shape of isoseismals: Irpinia earthquake of November 23, 1980. PAGEOPH, 120, 577-582.

Panza, G.F.,(1985), Synthetic seismograms: the Rayleigh waves modal summation. J. Geophys., in press.

Panza, G.F,, Suhadolc, P. and Chiaruttini, C.,(1985), Exploitation of broadband networks through broadband synthetic seismograms. Submitted to Ann. Geophys.

Scarascia, S., Pellis., G. and Giese, P.,(1985), Crustal structure of the northern Apennines. Proceedings of the 2. Workshop - European

Geotraverse, southern segment, Venezia,(1984),Ed. by European Science Foundation, July 1985.

Seed, H.B., Murarka, R., Lysmer, J. and Idriss, I. M.,(1976), Relationships of maximum acceleration, maximum velocity, distance from source, and local site conditions for moderately strong earthquakes. Bull. Seism. Soc. Am., 66, 1323-1342.

Suhadolc, P. and Panza, G.F.,(1985), Some applications of seismogram synthesis through the summation of modes of Rayleigh waves. J. Geophys., in press.

Trifunac, M.D.,(1976), Preliminary empirical model for scaling Fourier amplitude spectra of strong ground acceleration in terms of earthquake magnitude, source-to-station distance, and recording site conditions. Bull. Seism. Soc. Am., 66, 1343-1373.

NUMERICAL SIMULATION OF EARTHQUAKE GROUND MOTION

Michel Bouchon
Laboratoire de Geophysique Interne et Tectonophysique
Universite Scientifique et Medicale de Grenoble
BP 68, 38402 Saint Martin d'Heres, France

ABSTRACT. Using numerical simulation we present and assess the major features and characteristics of the around motion which takes place during an earthquake. We study the cases of strike-slip and dip-slip faulting. In the former case we show that large surface displacements and high-frequency motions are confined to a narrow zone around the fault and to the region which extends beyond the source along the trend of the fault. The results show the strong directivity effect of the propagating rupture and the large increase in amplitude of motion and duration of shaking when sediments are present. The good agreement between the numerical results and the observations made during earthquakes demonstrates that many of the characteristics of the ground motion can be predicted by numerical simulation. Such an attempt is made to obtain quantitative estimates of differential motions in earthquakes.

1. INTRODUCTION

Accounts describing the motion of the ground produced by earthquakes can be found in the literature throughout historic times. It is only in the middle of the nineteenth century, however, with the work of Mallet (1846, 1862), that the first scientific investigations of earthquake ground motion began. In 1846 and in the subsequent years, Mallet applied the principles of elasticity to the study of earthquakes. In his work on the Neapolitan earthquake of 1857 he made the first scientific study of the ground motion produced by an earthquake, attempting to determine, from numerous observations, the major directions of motion and the amplitudes of ground displacement and velocity throughout the Neapolitan region. Mallet's quantitative approach was subsequently applied to the study of many earthquakes. However, it is only with the installation of strong motion instruments in seismic areas that the true nature of the ground motion in the vicinity of an earthquake became known.

The first theoretical calculation of the ground displacement near an earthquake fault is due to Aki (1968). Following his work this problem has attracted considerable attention. We shall present here numerical

M. O. Erdik and M. N. Toksöz (eds.), Strong Ground Motion Seismology, 185–207.
© 1987 by D. Reidel Publishing Company.

simulations of the motion of the ground during earthquakes. We shall rely for the calculations on the discrete wavenumber method (Bouchon and Aki, 1977; Bouchon, 1979, 1981). We shall consider various source-medium configurations and, from the results obtained, we shall try to assess the major features and characteristics of the ground motion.

2. CASE OF STRIKE-SLIP FAULTS

2.1. Numerical simulations

Strike-slip earthquakes which occur at plate boundaries are fairly shallow events. Along the San Andreas fault, for instance, seismic activity seldom extends below a depth of 12 km. Consequently, large and intermediate size earthquakes tend to have a rectangular-shaped fault plane whose depth is constrained to the upper crustal region, where seismic deformation occurs, but which can extend in length from a few tens of kilometers to several hundred kilometers. We shall in this study restrict our attention to the case of intermediate size earthquakes, but some of the results that we shall obtain are applicable as well to larger-magnitude events, which can be represented as a succession of intermediate size earthquakes.

The first source-medium-receivers configuration that we consider is shown in Figure 1. The earthquake is modeled as a rectangular strike-slip dislocation propagating in one direction at constant velocity and stopping suddenly. The slip time dependence assumed is a ramp function of 0.5s duration. The fault is 30 km long and extend from 1.5 km below the surface down to 10 km. The resulting ground motion is computed at more than 1300 sites arranged in a quadrangular network in which each grid element is a square of 2x2 km. The array extends over 100 km along the fault strike, and all the receivers are located on one side of the fault, at horizontal distances ranging between 0 and 50 km from the source plane.

We first consider the case where the fault is located in a homogeneous half-space. We take for the compressional velocity, shear velocity, and density of the medium the values, typical for crystalline basement rocks, of 6 km/s, 3.5 km/s, and 2.8 g/cm^3, respectively. The rupture velocity is set equal to 2.2 km/s. The time history and spatial dependence of the surface displacement are shown in Figure 2. Each element of the figure represents one component of ground motion at a given time. The first snapshot, seen at the top of the figure, is taken 2s after the start of the rupture. The succeeding frames are taken 4s apart, the last snapshot depicting the surface motion 26s after the initiation of the rupture process. The final frames show the corresponding static displacement obtained using Chinnery's (1961) solution. The progressive buildup of the surface displacement, the propagation of disturbances and wave fronts over the surface, and the gradual change from the dynamic motion to the static residual displacement can be clearly followed. The major characteristics of the ground motion are the relatively low-frequency of the displacement parallel to the fault, which mostly represents the displacement discontinuity between the two

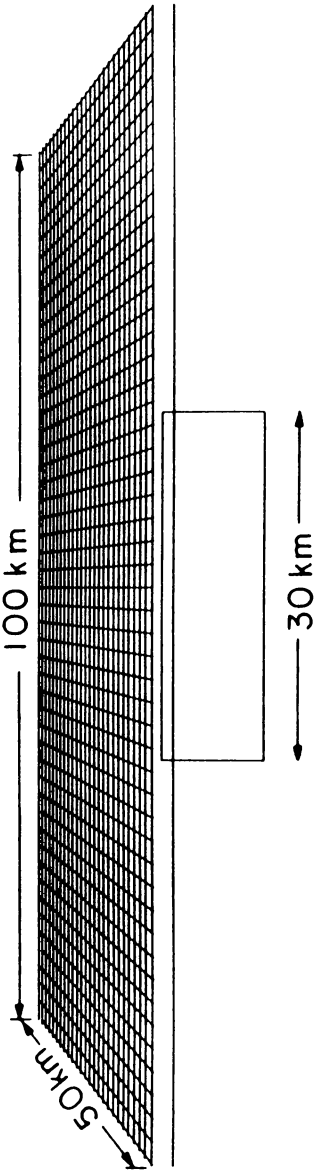

Figure 1. Source-medium-receivers configuration used in the study. The rupture nucleates along the left edge of the fault and propagates to the right.

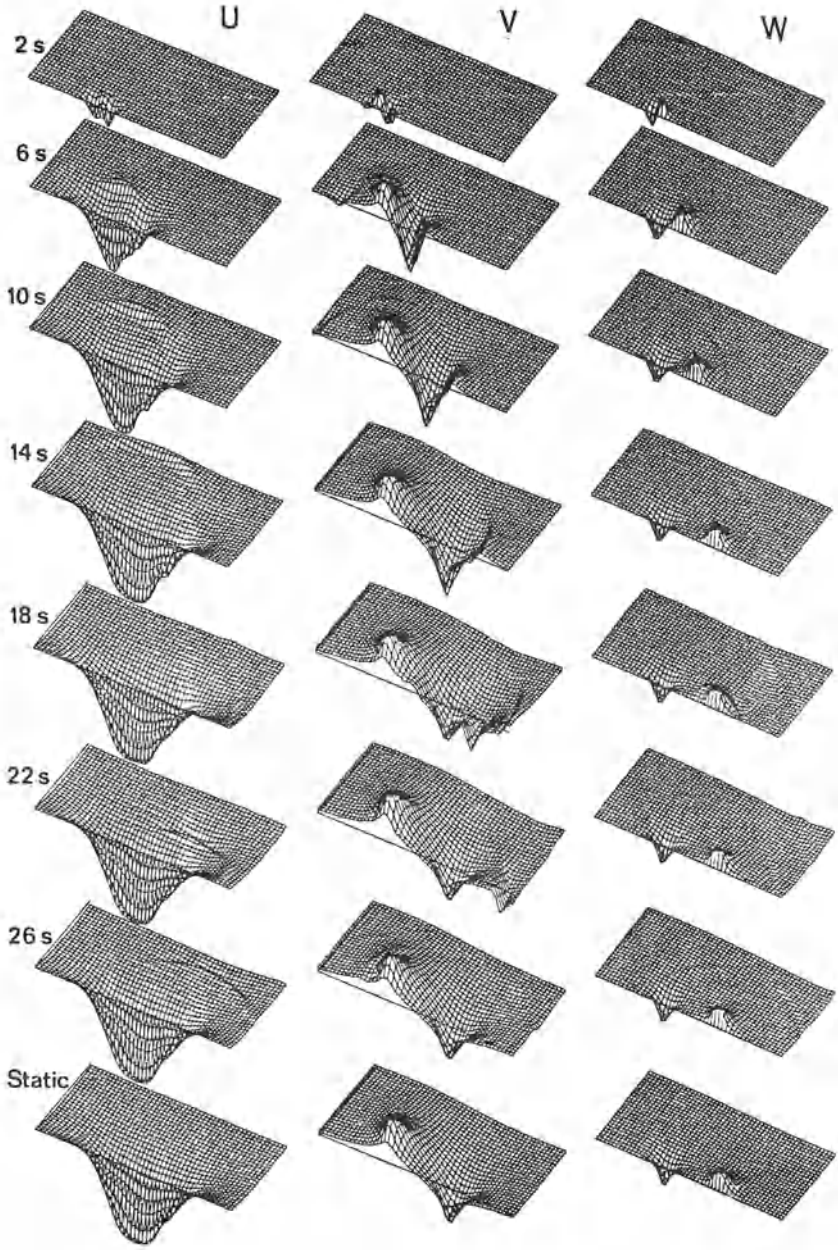

Figure 2. Snapshots, at equal time intervals, of the ground motion. U, V, and W denote the components of displacement parallel to the fault, perpendicular to the fault, and vertical.

sides of source, and the large amplitude and higher frequency content of the motion normal to the fault plane. The three components of displacement reach their maximum amplitude a few kilometers away from the trace of the fault plane. Outside the immediate source region, the dynamic motion is dominated by the starting and stopping shear phases. The spreading of the circular wave fronts associated with these disturbances can be particularly well followed on the component of motion parallel to the fault. Most of the energy is radiated in the direction of propagation of the rupture.

We shall now try to assess the effect of a sedimentary layer on the ground motion. The crustal model that we consider consists of a half-space, identical to the medium previously studied, overlain by a layer of sediments, 1.5 km thick, in which the compressional velocity, shear velocity, and density are 3 km/s, and 2.3 g/cm^3 respectively. The source is the one used in Figure 2 and extends from the base of the sediments to a depth of 10 km. The resulting surface displacement is shown in Figure 3. The time sequence is the same as the one used in Figure 2: the first snapshot is taken 2s after the initiation of the rupture, and the following ones lie 4s apart. The striking feature of the solution is the large-amplitude high-frequency motion normal to the fault plane which takes place in the vicinity of the source. This pulselike disturbance which travels with the rupture front is similar to a shock wave which would be produced in the sediments by the propagating rupture. Such a phenomenon occurs because the rupture velocity is higher than the sear wave velocity in tne sediments. As time increases, a lower-frequency component made up of multiply reflected SH waves and Love waves is added to the high-frequency pulse. The disturbances associated with the starting and stopping phases give rise to a series of concentric circular wave fronts which spread over the surface from the two edges of the fault. Another feature of the results is the strong directivity effect of the source which beams most of the radiated energy in the direction of propagation of the rupture.

2.2. Examples

A remarkable illustration of our results is provided by recordings and observations made during the Parkfield, California, earthquake of 1966. The earthquake was a strike-slip event which ruptured a 30 to 40 km long segment of the San Andreas fault (Figure 4). The ground motion recorded close to the fault (Station 2 of the Parkfield-Cholame array) is characterized by a large displacement pulse in the direction transverse to the fault strike (Figure 5). The confinement of the strong ground shaking to a narrow band along the fault zone is also well established (e.g. Yerkes and Castle, 1967), and the predominance of motions normal to the fault strike is supported by seismoscope data (Hudson and Cloud, 1967) and by various observations (Von Hake and Cloud, 1968). Some reports also indicate that the prevailing motions at sites located along the trend of the fault, but distant from the source, was perpendicular to the fault strike. The following is such a report taken from Yerkes and Castle (1967): "Heavy furniture was reported shifted about 6 inches in directions normal to the trend of the San Andreas fault

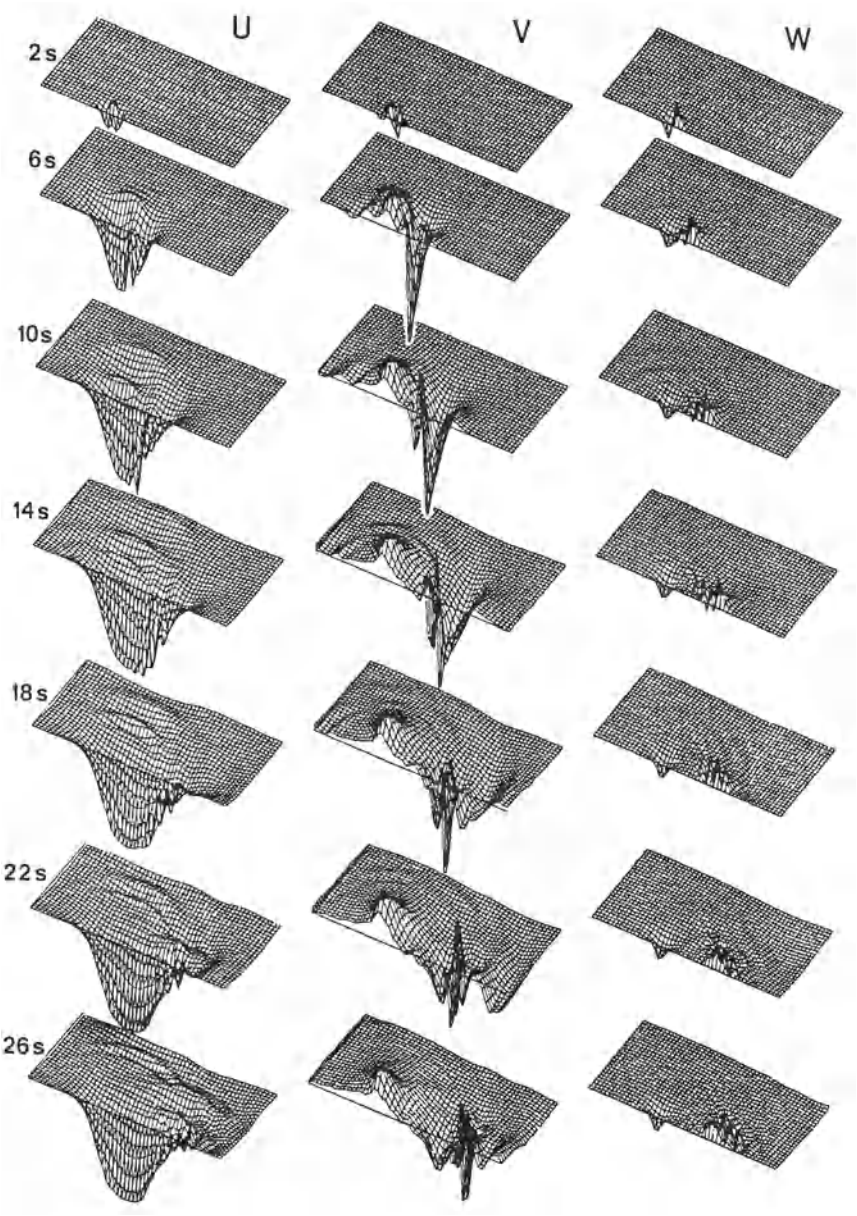

Figure 3. Snapshots of the surface displacement in presence of sediments. The ratio of displacement amplitude to horizontal distance is 4/5 of the ratio used in Figure 2.

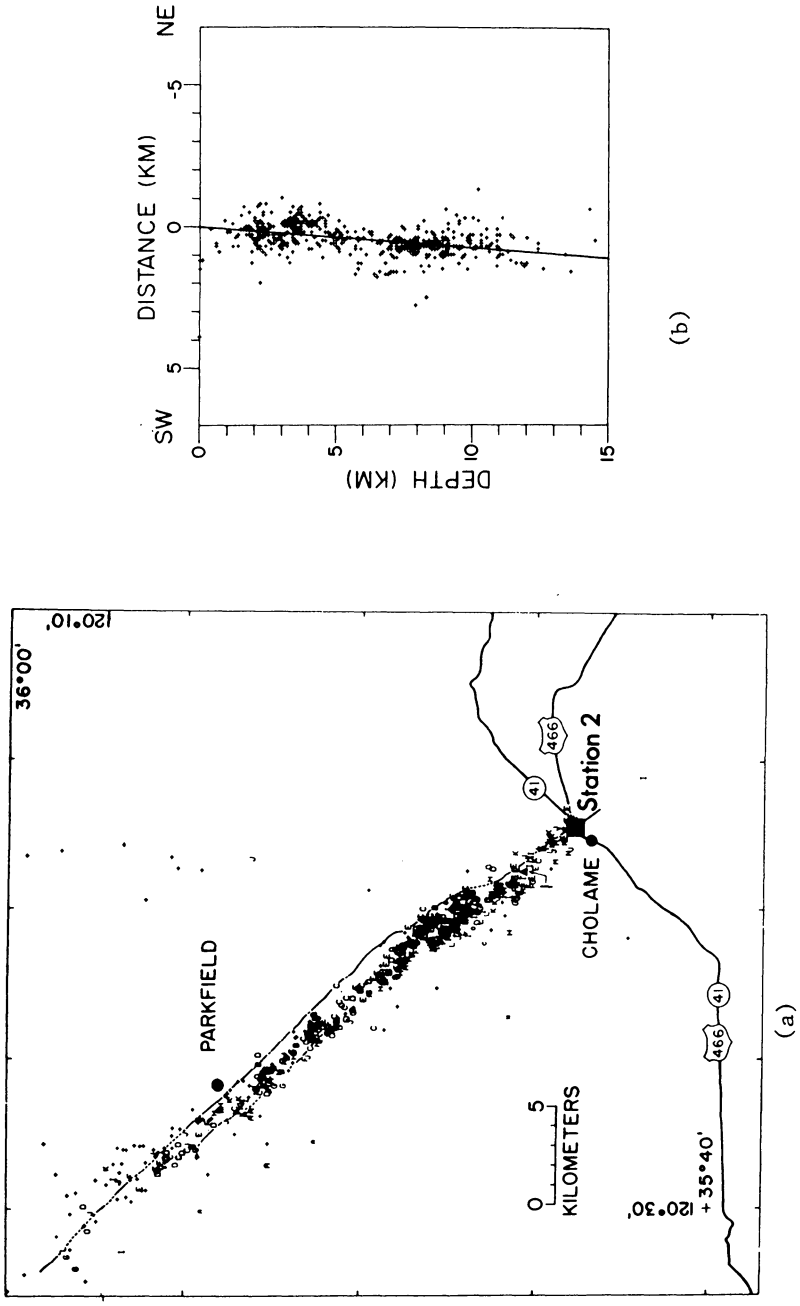

Figure 4. a.Map of the surface fractures associated with the Parkfield earthquake and aftershock epicentral locations.
b.Projection of well located hypocenters onto a vertical plane perpendicular to the strike of the fault (from Eaton et al., 1970).

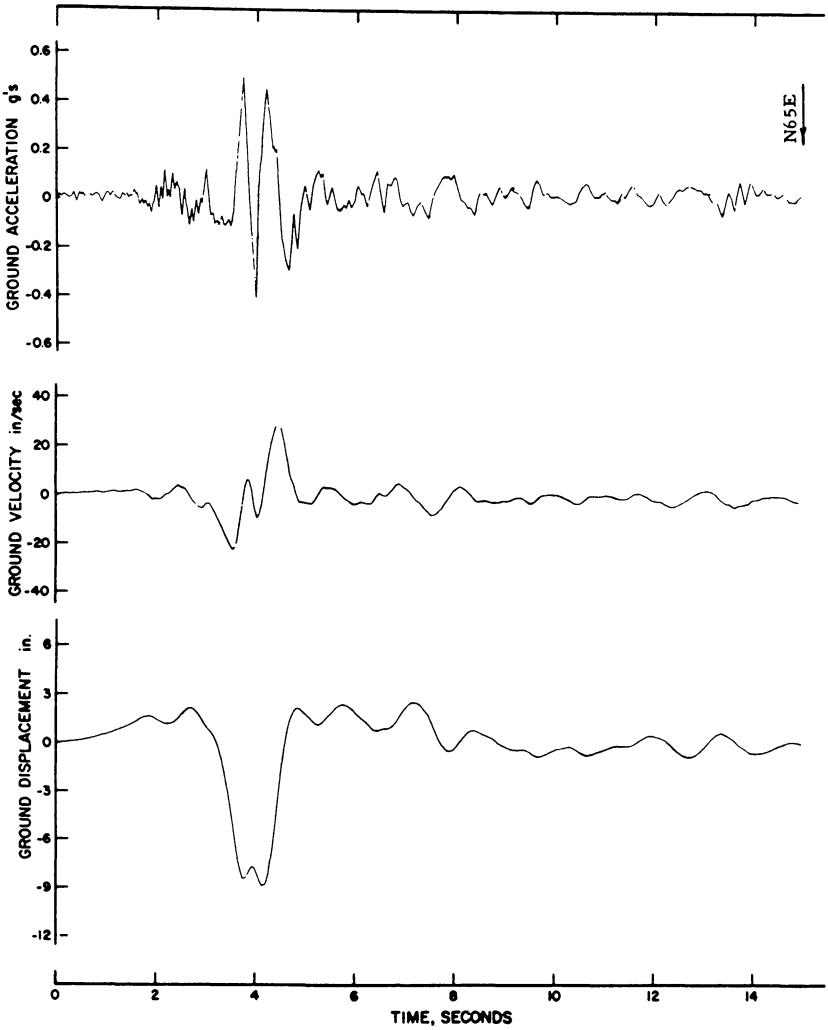

Figure 5. Transverse acceleration, velocity and displacement at station 2 of the Cholame array. (from Housner and Trifunac, 1967)

zone at two localities in the Choice Valley area, 7 miles and 13.6 miles beyond the southeast end of the main fracture."

The Guatemala earthquake of 1976 is another strike-slip event for which the distribution of strong ground shaking is well documented (Espinosa et al., 1976). Maps of the damage distribution and of the intensity of shaking are shown in Figure 6. The surface break associated with the earthquake is more than 200 km long. The rupture originated toward the eastern end of the surface fractures and propagated to the west. The isoseismal pattern and the damage distribution inferred are in remarkable agreement with the results of the numerical simulation.

Another example of strike-slip earthquake motion very close to the fault is provided by recordings of the Coyote Lake earthquake of 1979. This moderate size event ($M_L = 5.7$) occurred on the Calaveras fault in central California. Aftershocks are spread over an 18 km long segment of the fault (Figure 7). Two accelerometers located in the fault zone recorded the event. One of the stations (Coyote Creek) lies very close to the epicenter while the other one (Gilroy 6) is 10 km away from it in the direction toward which the rupture supposedly propagated. In good agreement with the numerical results, the displacement at Gilroy 6 consists mostly of a transverse pulse and is much larger (about 4 times) than the motion at Coyote Creek. We will now take into account the specific parameters of this earthquake to synthesize more accurately the displacement observed at Gilroy 6.

We model the earthquake as a propagating strike-slip fault embedded in a layered medium. The rupture starts at a point - the hypocenter - and spreads radially, as schematically shown in Figure 8. The final fractured area is assumed to be rectangular. The source time dependence is a step-function and the final slip is uniform over the fault. The coordinates of the hypocenter and the origin time of the earthquake are fairly well known since the shock occurred within the dense seismic network of central California (Lee et al., 1979). We shall take for the hypocentral depth the value of 9.5 km inferred by Lee et al.(1979), and assume that the fault plane is purely vertical. Furthermore, as the near-field data are not very sensitive to the lower depth of faulting, we shall assume that the dislocation extends to the depth of 10 km defined by the aftershock distribution.

The crustal structure in the vicinity of the source has been determined by carrying out refraction experiments (Mooney and Luetgert, 1980). The velocity structure in the fault zone, shown in Figure 8, consists of an upper layer, about 1.75 km thick, having a compressional velocity of 4.2 km/s and an underlying crust with a P-wave velocity of 6 km/s.

Synthetic displacements computed for rupture velocities of 2.2, 2.4, 2.6, and 2.8 km/s are compared to the data in Figure 9. Two fault lengths are considered: in one case the rupture stops before reaching the station, in the other one, rupture propagates beyond the station. The top of the fault is at a depth of 2 km and rupture propagates toward the southeast. The shorter fault length considered ($L = 8$ km) makes the fault stop at the jump in aftershock location. A high-pass Ormsby filter similar to the one used to process the data has been applied to the synthetics. Frequencies up to 3.2 Hz are included in the solution.

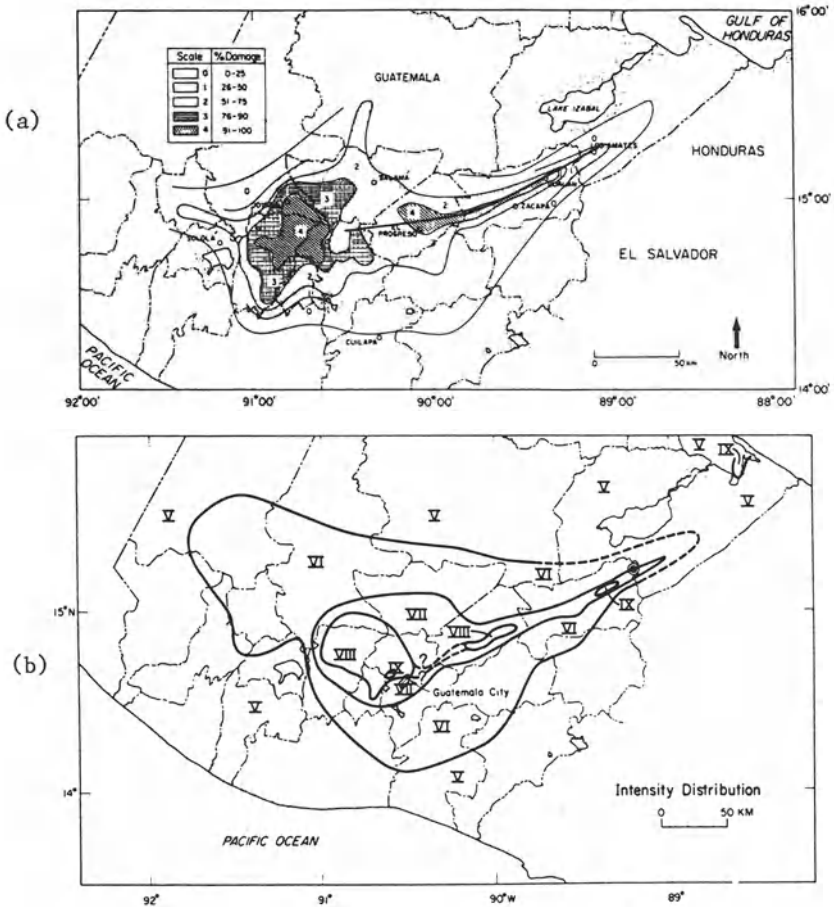

Figure 6. a. Contour map showing the damage caused to adobe-type structures by the Guatemala earthquake of 1976. The trace of the major fault zone is indicated.
b. Modified Mercalli intensity distribution. The circle indicates the epicenter location. (after Espinosa et al.,1976).

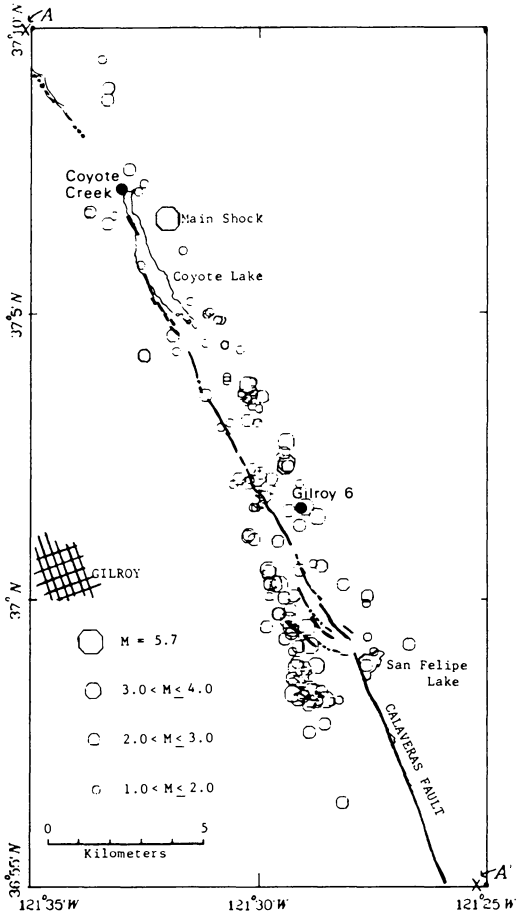

Figure 7. Epicenters of the main shock and aftershocks of the Coyote Lake earthquake sequence. The location of the two accelerograph station is indicated. (modified after Lee et al., 1979)

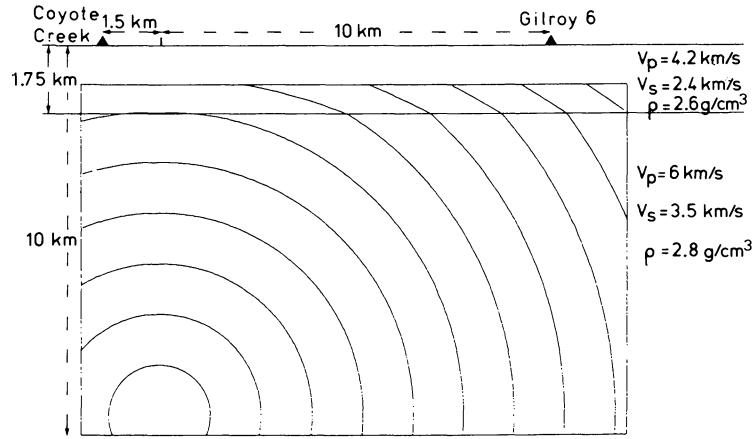

Figure 8. Source-medium-station configuration used to model the Coyote Lake earthquake. The circles indicate the position of the rupture front at successive times.

The gradual displacement buildup associated with P-wave arrivals, the rapid change of direction of motion produced by the shear wave coming from the hypocentral region, and the large northeast displacement pulse are well reproduced by the synthetics. Whether rupture stops at the jump in aftershock location or propagates beyond it, does not affect the arrival time of the pulse. This pulse can be interpreted either as the stopping phase (L = 8 km) or as the passage of the rupture front below the station (L = 12 km). In both cases, the rupture velocity required to bring the timing of the computed and recorded SH pulses into agreement is about 2.6 km/s. Changes in the position of the fault top have little effect on the arrival time of the pulse and will not affect this value.

3. CASE OF DIP-SLIP FAULTS

3.1. Numerical Simulations

The ground motion generated by a dip - slip earthquake fault is considerably different from the one resulting from a strike-slip dislocation. While in the latter case SH waves and Love waves are the major contributions to the ground motion, the radiation from thrust and normal faults consists mainly of P, SV, and Rayleigh waves.

The source-medium-receivers configuration that we shall use in the calculation is shown in Figure 10. The fault geometry is chosen to approximate the fault model of the 1971 San Fernando earthquake. The rupture starts at a depth of 13 km and propagates upward. In order to minimize the computer time involved we shall assume that the fault stays buried below the surface. The width of the fractured zone is taken equal to 12 km. The time dependence of the dislocation is a ramp function of 0.2s duration and the final slip is uniform over the fault. The surface motion is computed at 1326 sites arranged in a quadrangular network in which each grid element is a square of 2x2 km. The receiver array extends over 50 km in the direction parallel to the fault strike and for a length of 100 km in the orthogonal direction. One of its side coincides with the plane of symmetry of the source (the bisecting plane of Figure 10).

The first set of results, shown in Figure 11, corresponds to the case where no sediments are present. The medium is modeled as a homogeneous half-space with compressional velocity, shear velocity, and density equal to 5.6 km/s, 3.2 km/s, and 2.8 g/cm^3 respectively. The rupture velocity is 2 km/s. Full seismograms are computed at each grid point and are then combined together to yield the ground motion over the whole area at different times. U and V denote the horizontal displacements in the directions parallel and normal to the fault strike respectively. W is the vertical component of motion. The first snapshot, seen at the top of the figure, shows the three components of ground motion 6s after the start of the rupture. The succeeding frames are taken 2s apart, the last snapshot depicting the ground motion 18s after the initiation of the earthquake. The figure provides an overall view of the displacement buildup and of the propagation of disturbances and wave fronts over the surface. Particularly notable are the overshoot of the vertical displacement above the fault plane relatively to its static

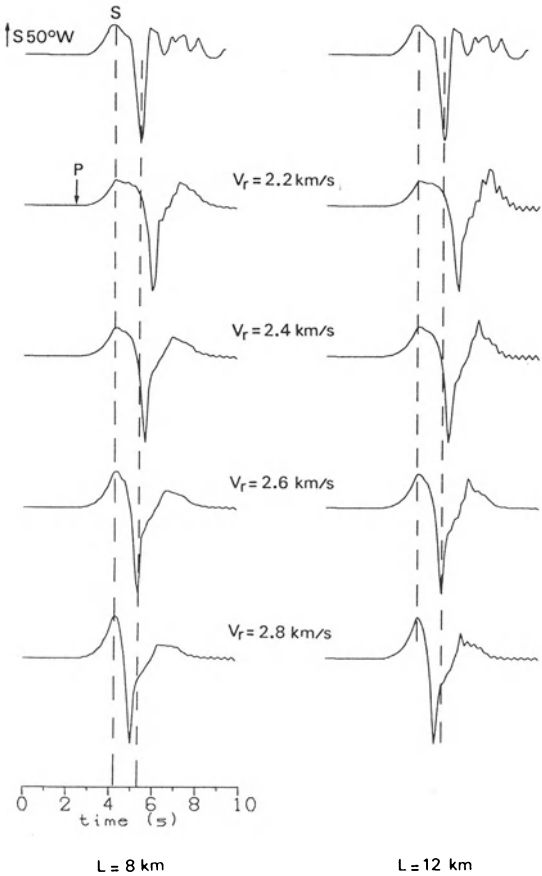

Figure 9. Comparison of recorded (top) and synthesized displacements at Gilroy 6. P and S indicate the computed arrival times of the P and S waves.

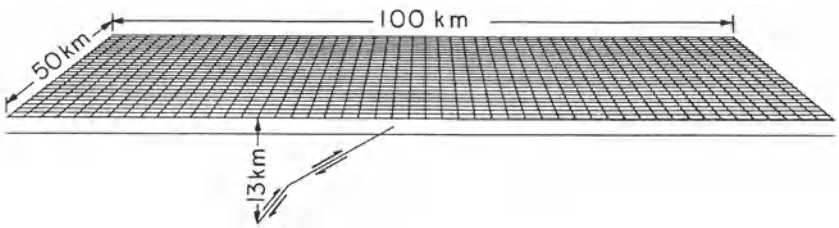

Figure 10. Source-medium-receivers configuration used in the study. This figure is a cross-sectional view bisecting the fault plane.

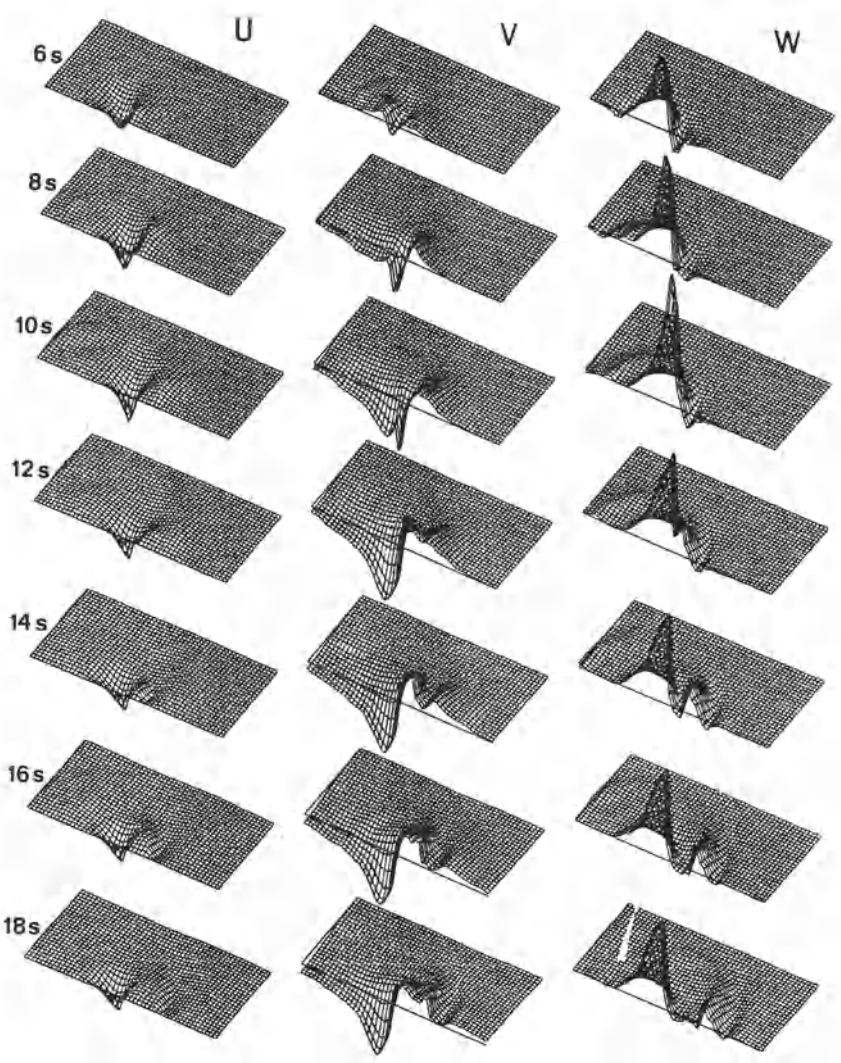

Figure 11. Time history and spatial dependence of the three components of surface displacement obtained when the medium is a homogeneous half-space.

value, the gradual development and individualization of the Rayleigh wave, and the facusing of energy in the direction in which the rupture propagates. The sharpness of the Rayleigh pulse indicates that this wave is mostly generated by the upper part of the fault. It is preceded by a disturbance associated with shear and SP wave arrivals.

We shall now study the effect on the ground motion of a layer of low-velocity material. The sediment thickness considered is 2 km and the density, compressional velocity and shear velocity are respectively 2.3 g/cm^3, 2.8 km/s, and 1.6 km/s. The elastic parameters of the half-space are unchanged. The rupture propagates in the sediments at a velocity of 1 km/s. The resulting ground motion is depicted in Figure 12. The vertical dynamic motion is strongly amplified by the sediments at the sites located above the fault plane. Compared to the previous case, the complexity of the surface motion outside the immediate source region is drastically increased. A considerably larger amount of energy is radiated along the surface than in the case where no sediments are present. Away from the source, the duration of shaking is greatly increased. The energy radiated is focused within a narrow beam by the propagating rupture and is subsequently trapped at proximity of the surface by the sediments.

3.2. Example

The velocity records obtained during the San Fernondo earthquake at stations within 40 km of the epicenter are shown in Figure 13 (Shakal, 1979). They display the major features and characteristics found in the numerical simulation. Little energy is radiated to the north of the epicenter, away from which direction the rupture propagated. On the contrary, large amplitude motions and long duration of shaking characterize the sites located to the south of the surface breaks. An analysis of particle velocity at station ORI, located about 10 km ahead of the fault breaks, (Figure 14; Shakal, 1979) shows that the highest amplitudes of ground velocity correspond to Rayleigh waves coming from the top of the fault.

4. DIFFERENTIAL MOTIONS

The potential effects of differential ground motions on structures have long been recognized. Newmark (1969), Luco (1976) and others have shown that such motions can induce pronounced torsional and rocking effects in structures. Several authors have attributed some of the structural damage and failure caused by earthquakes to differential ground motions. The true importance of these motions is however difficult to assess because to date no records of them have been obtained in the near-field of earthquakes. We shall try now to get some quantitative estimates of the amplitude of these motions through numerical simulation.

We first consider the case of a strike-slip fault. The seismic wave field radiated by such a source is dominated by SH waves and Love waves. These disturbances are characterized by horizontal motion transverse to the direction of wave propagation. The passage of these

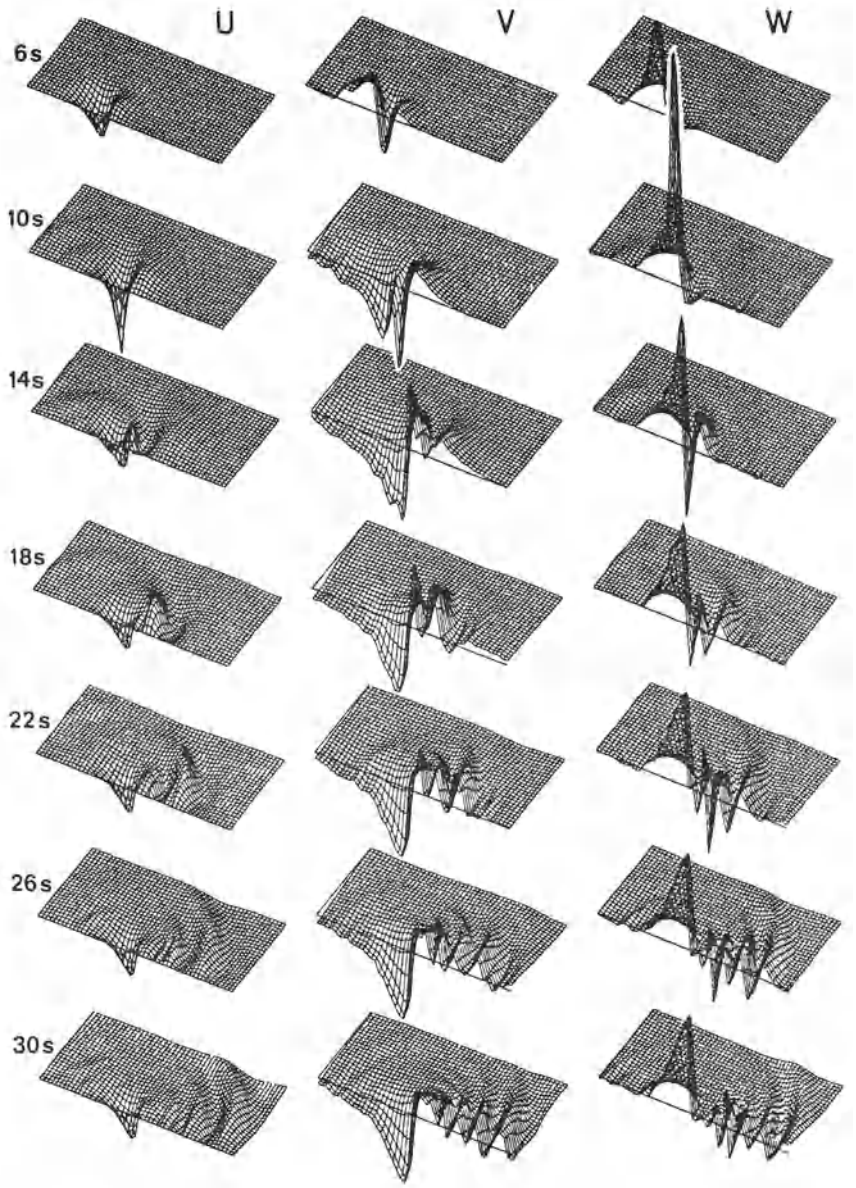

Figure 12. Snapshots of the three components of surface motion obtained when sediments are present. The ratio of displacement amplitude to horizontal distance is the same as in Figure 11.

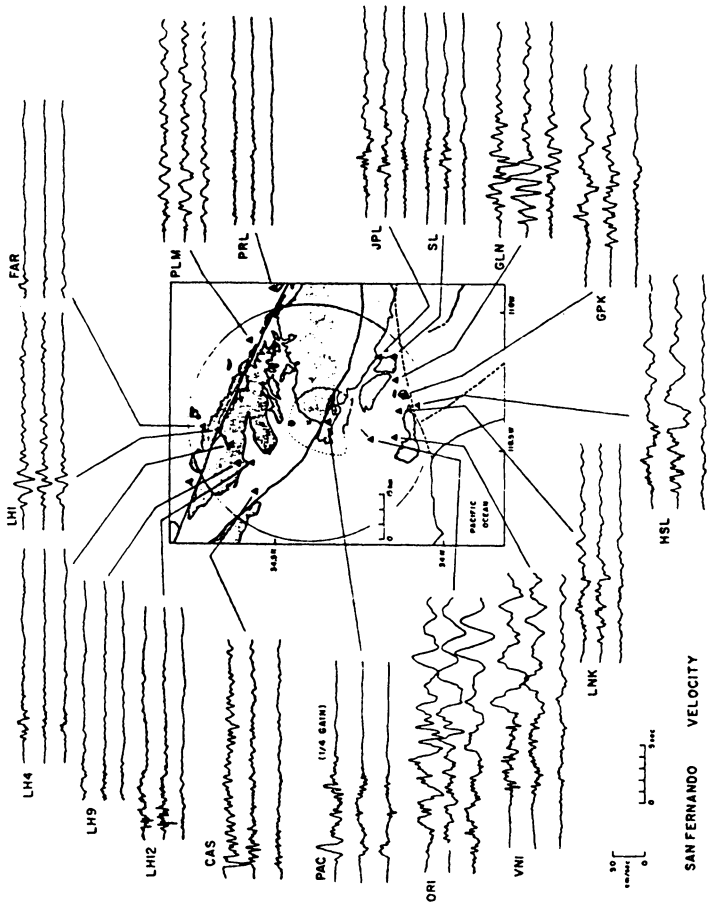

Figure 13. The three component (radial, transverse, up) velocity records from the San Fernando earthquake at the stations within 40 km of the epicenter. The epicenter as well as the approximate fault trace and aftershock zone are indicated (from Shakal, 1979)

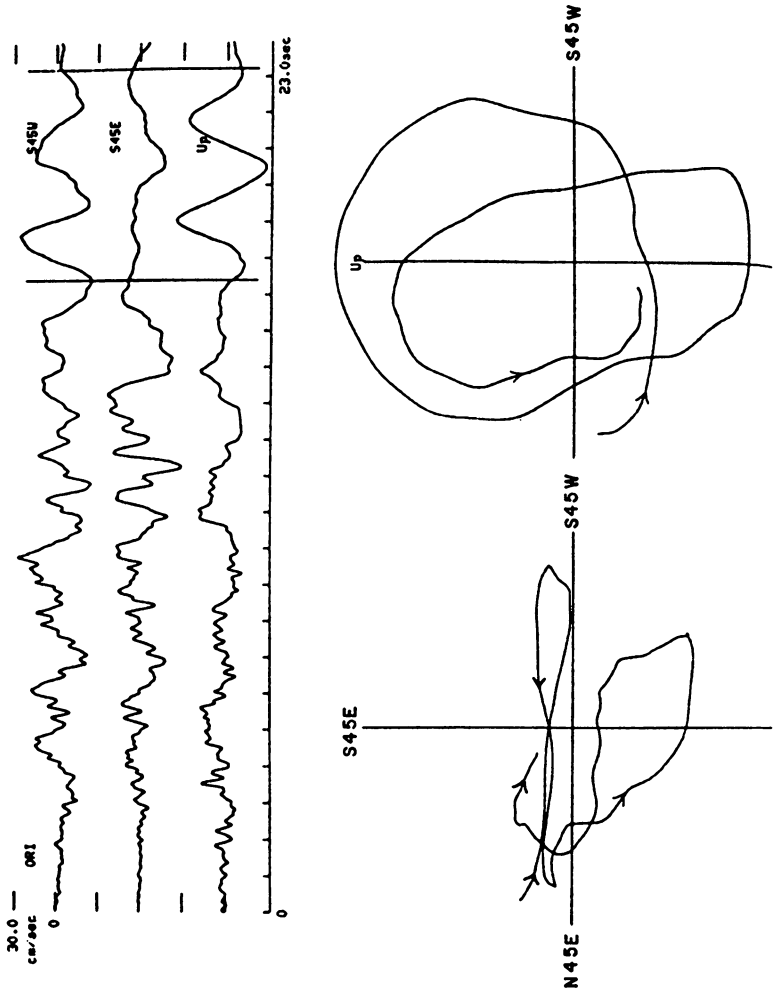

Figure 14. The three component velocity record at ORI and the particle motion for the segment within the cursors. The particle motion is plotted in the horizontal and vertical planes. (from Shakal, 1979)

disturbances at a site will therefore result in a translation and a rotation. We chose to evaluate the rotational component of ground motion for the configuration displayed in Figure 15. The earthquake source is a 30 km long vertical fault buried 1.5 km below the surface and extending down to a depth of 10 km. The rupture nucleates along one edge of the fault and propagates horizontally at 2.2 km/s. The dislocation time dependence at the rupture front is a ramp function with a rise time of 0.3s. The crustal structure consists of a 1.5 km thick sedimentary layer with compressional and shear wave velocities of 3 km/s and 1.75 km/s overlying a half-space with velocities of 6 km/s and 3.5 km/s. The densities in the surface layer and in the basement crust are 2.3 g/cm^3 and 2.8 g/cm^3. The ground rotation obtained is displayed in Figure 15. The frequency range considered extends from 0 Hz (static) to 2.5 Hz. The amplitude given corresponds to a fault slip of 1 m. The largest rotations occur in the zone around the fault strike and decay rapidly in the direction transverse to the fault. For a 1 m slip on the fault, the maximum rotation is of the order of 2×10^{-4} radian.

We now consider the case of a dip-slip fault. As before, we choose for the source geometry the one inferred for the San Fernando earthquake except that we make the fault stop at 1 km below the surface (Figure 16). The rupture starts at a depth of 13 km and propagates upward at 2 km/s. The width of the fault is 12 km. The crustal model consists of a 1 km thick low velocity sedimentary layer overlying a homogeneous half-space. The P and S wave velocities and density are respectively 2 km/s, 0.8 km/s and 2.3 g/cm^3 in the sediments and 5.6 km/s, 3.2 km/s and 2.8 g/cm^3 in the basement rock. The longitudinal strain and horizontal velocity produced by the earthquake are depicted in Figure 16. The sites considered are located along the trace of the plane of symmetry of the source. The amplitudes given correspond to a fault slip of 1 m. As this value is about the one inferred for the San Fernondo earthquake, the results obtained can be considered as a numerical simulation of the strain field radiated during the 1971 earthquake. The low velocity values taken in the sediments are chosen to emphasize the effect on differential ground motions of a low velocity surface layer. The earthquake produced extensive damage to freeway bridges located in a belt about 4 miles wide surrounding the fault breaks (Elliot and Nagai, 1973). The heaviest damage was sustained at the Route 210/5 Interchange located above the shallow segment of the fault, about 2 miles from the surface break. In this area the computed strain is about 8×10^{-4}. The main structure which completely collapsed was a 770 ft long reinforced concrete bridge with a framing consisting of seven spans. As the bridge was oriented transverse to the fault strike, our results indicate that the structure must have undergone longitudinal differential motions with a relative displacement between piers of the order of a few (3) centimeters. Although such a displacement can induce substantial stresses in the piers and the bridge decking, it is small in comparison to the amplitude of ground shaking.

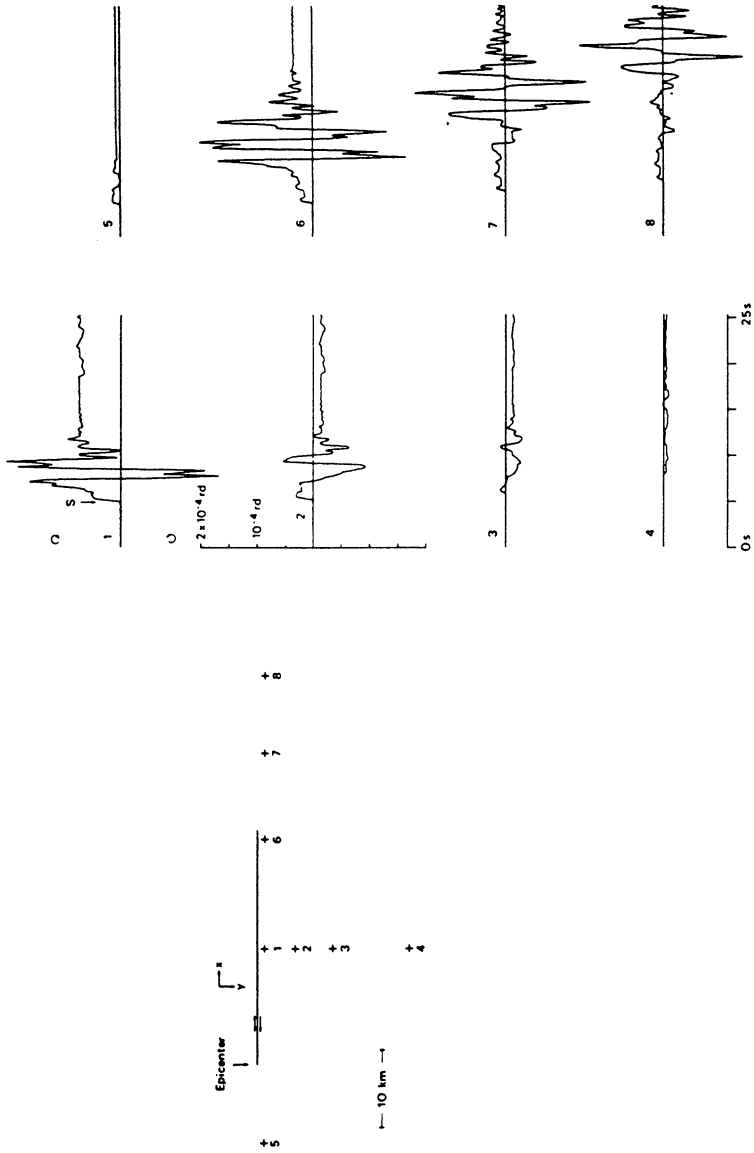

Figure 15. Source-receiver configuration and corresponding results of the simulation. S indicates the S wave arrival.

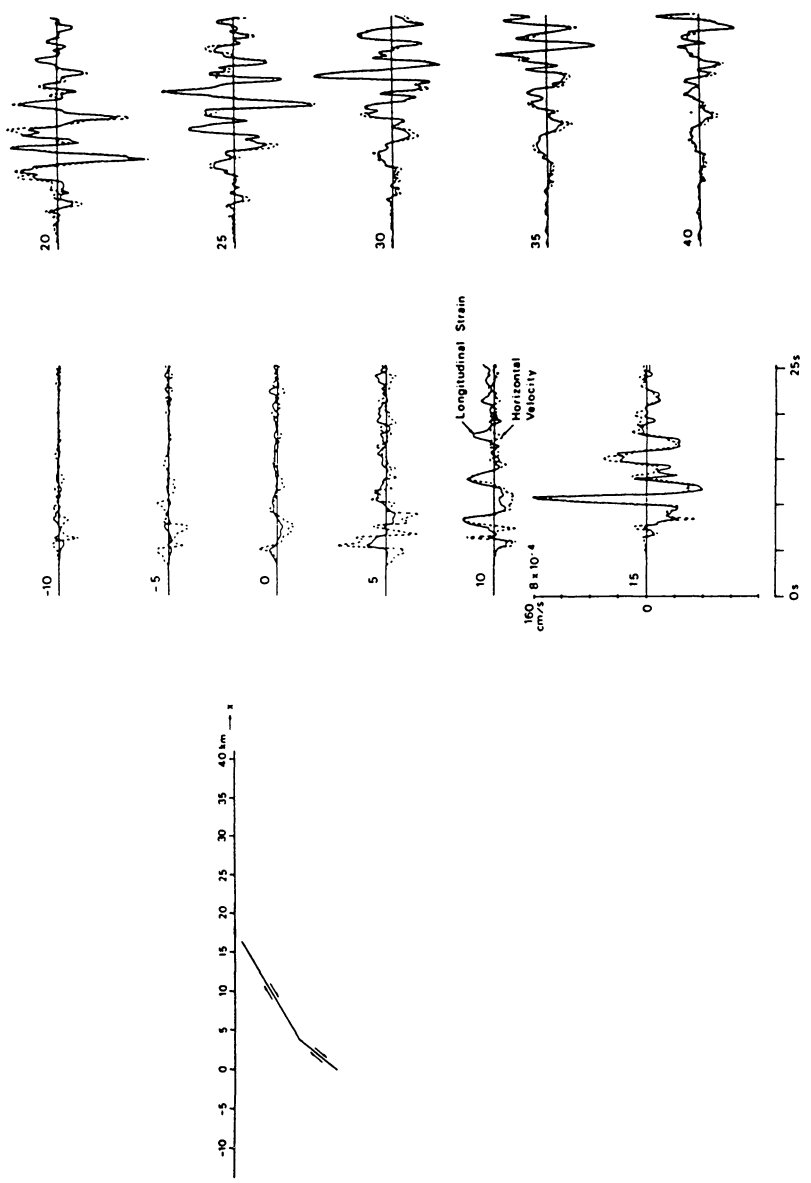

Figure 16. Source-receiver configuration for the thrust fault model and results of the calculation.

5. CONCLUSION

We have tried to present the major features and characteristics of the ground motion which takes place during an earthquake. In the case of a strike-slip fault, we have shown that large surface displacement and high frequency motions are confined to the fault zone and to the region which extends beyond the source along the trend of the fault. We have shown the striking directivity effect exerted by the propagating rupture on the surface motion for both strike-slip and dip-slip faults. We have also demonstrated the strong amplification of near-field motion in the presence of sediments. By comparing synthesized results and observations, we have shown that the major characteristics of the ground displacement can be inferred through numerical simulation. We have used such a simulation to obtain quantitative estimates of differential motions during earthquakes.

REFERENCES

Aki, K.(1968), Seismic displacement near a fault, J.Geophys.Res.,73, 5359-5376, 1968.

Bouchon, M.(1979), Discrete wavenumber representation of elastic wave field in three space dimensions, J.Geophys. Res., 84, 3609-3614, 1979.

Bouchon, M.(1981), A simple method to calculate Green's functions for elastic layered media, Bull.Seism.Soc.Am., 7., 959-971, 1981.

Bouchon, M. and K. Aki,(1977), Discrete wavenumber representation of seismic source wave fields, Bull.Seism.Soc.Am., 67, 259-277, 1977.

Chinnery, M.A.(1961), The deformation of the ground around surface faults, Bull.Seism. Soc.Am., 51, 355-372, 1961.

Eaton, J.P., M.E. O'neill, and J.N. Murdock,(1970), Aftershocks of the 1966 Parkfield-Cholame, California, earthquake: a detailed study, Bull.seism. Soc.Am., 60, 1151-1197, 1970.

Elliott, A.L. and I.Nagai,(1973), Earthquake damage to freway bridges, published in the San Fernando, California, earthquake of 1971, U.S. Dept. of Commerce, Washington D.C., Vol 2, 201-233, 1973.

Espinosa, A.F., R. Husid and A. Quesada,(1976), Intensity distribution and source parameters from field observations, published in the Guatemala earthquake of February 4, 1976, A preliminary Report, U.S. Geol. Surv. Prof. Pap., 1002, 52-66, 1976.

Housner, G.W. and M.D. Trifunac,(1967), Analysis of accelerograms-Parkfield earthquake, Bull. Seism.Soc.Am., 57, 1193-1220, 1967.

Hudson, D.E. and W.K.Cloud (1967), Analysis of seismoscope data from Parkfield earthquake of June 27, 1966, Bull.Seism.Soc.Am., 57, 1143-1159, 1967.

Lee, W.H.K., D.G. Herd, V.Cagnetti, W.H.Bakun and A.Rapport (1979), A preliminary study of the Coyote Lake earthquake of August 6, 1979 and its major aftershocks, U.S.Geol. Surv. Open-File Rept., 79-1621, 1979.

Luco, J.E. (1976), Torsional response of structures to obliquely incident seismic SH waves, Earthq. Engng. Struct. Dyn., 4, 207-219, 1976.

Mallet, R. (1846), On dynamics of earthquakes, Trans. Roy. Irish Acad., 21, 51-105, 1846.

Mallet, R. (1962), Great Neapolitan earthquake of 1857: the first principles of observational seismology, Chapman and Hall, London, 1862.

Mooney, W.D. and J.H.Luetgert (1980), Seismic-refraction study of the Santa Clara Valley, west-central California (abstract), Trans. Am. Geophys. Union, 61, 1025, 1980.

Newmark, N.K. (1960), Torsion in symmetrical buildings, Proc. Fourth. World Conf. Earthq. Engng. Santiago, Chile, 3, 19-32, 1969.

Shakal, A.F. (1979), Analysis and modelling of the effects of the source and medium on strong motion, Ph.D. thesis, Mass. Inst. of Tech., Cambridge, Mass., 1979.

Von Hake, C.C. and W.K.Cloud (1968), United States Earthquakes 1966, U.S. Dept. of Commerce, Washington D.C., 1968.

Yerkes, R.F. and R.O. Castle (1967), Engineering geology aspects, published in the Parkfield-Cholame, California, earthquakes of June-August 1966, U.S. Geol. Surv. Prof. Pap., 579, 50-53, 1967.

HIGH FREQUENCY EARTHQUAKE STRONG GROUND MOTION IN LATERALLY VARYING MEDIA: THE EFFECT OF A FAULT ZONE

Gregory C.Beroza and Vernon F.Cormier
Earth Resources Laboratory
Department of Earth, Atmospheric, and Planetary Sciences
Massachusetts Institute of Technology
Cambridge, MA 02139

ABSTRACT. Crustal heterogeneity and the effects of a complex earthquake source may account for observations of strong ground motion not easily explained by simplified source models in a laterally homogeneous medium. Both the effects of a complex source and lateral heterogeneity can be examined using a forward modeling technique that combines distributed, non-uniform slip on a fault plane with dynamic ray tracing in a three dimensional medium. Iterative paraxial ray tracing is used to solve the two point ray tracing problem. The validity of the results are limited to relatively high frequencies at which ray theory provides and accurate approximation to the Green's function; however, these frequencies are often those of greatest interest in seismic engineering.

Using this technique, velocity seismograms are calculated at ranges less than 10 km for a finite earthquake source, which occurs in a wedge-shaped zone of low velocity. This example is chosen to approximate the structure of fault zones found in reflection and refraction surveys across active faults in California. The low velocity zone surrounding the fault causes arrivals in the laterally varying structure to be delayed and rays to leave the fault more closely to the fault normal. At most locations examined, the effect of the 3-D structure on directivity is small compared to the effects on geometric spreading and radiation pattern. Because rays are bent substantially in the near source region, the seismograms calculated for the laterally varying structure vary substantially in amplitude and polarity from seismograms calculated for the laterally homogeneous structure.

1. INTRODUCTION

As the number of recorded accelerograms from earthquakes has increased, many observations of anomalous strong ground motion have been made. Possible explanations of these observations are the effects of strongly heterogeneous rupture and the effect of laterally heterogeneous structure on the propagation of radiated seismic waves. By improving our understanding of these possible causes of variability in strong

M. O. Erdik and M. N. Toksöz (eds.), Strong Ground Motion Seismology, 209–224.
© 1987 by D. Reidel Publishing Company.

motion records it should be possible to refine predictions of strong ground motion used in engineering seismology.

For high frequency records of near source motion details of rupture history may become the most important contribution to ground motion (Bernard and Madariaga, 1984). In this higher frequency band, it also becomes more important to include the effects of laterally heterogeneous structure such as: surface topography, basins, anticlines, fault zones and dipping layers which can focus seismic energy and distort the radiation pattern of an earthquake. The computational expense involved in numerically modeling these effects, however, has generally prevented its application to 3-D models.

In the domain in which the scale length of the heterogeneity is much greater than the wavelength, ray theory is a powerful and economical method for estimating the effects of these structures on strong ground motion. Relative ground motions have been predicted simply by contouring and comparing ray densities over the free surface (Rial, 1984; Ihnen and Hadley, 1986). Cohn et al.(1982) have modeled the recordings of aftershocks of the Oroville earthquake by including a gently dipping layer using a ray technique described by Hong and Helmberger (1978). Langston and Lee (1983) have computed the high frequency response of a two dimensional valley to explain strong motion recordings of the Puget Sound Earthquake.

The development of the technique of isochrone integration (Bernard and Madariaga, 1984; Spudich and Frazer, 1984) has made it possible to compute efficiently the effects on ground motion of both detailed models of the rupture history of an earthquake and 3-D structure. This technique computes ground motion by approximating the Green's functions with the far-field term for individual body waves propagating from the rupture front. Because this technique is formulated using ray theory, it is possible to perform the calculations in any crustal structure in which ray theory is applicable. The dynamic ray tracing approach (Popov and Pšenčík, 1978; Červený, 1985) is a convenient method for computing ray trajectories. S wave polarization, and geometric spreading needed to calculate the ray theoretical Green's functions.

In this study, the results are shown for several test calculations in which dynamic ray tracing has been combined with isochrone integration to examine the effects of a fault zone structure on the strong ground motion recorded on the flanks of the fault zone. Paraxial ray tracing has been used to solve the two point ray tracing problem from points on the fault plane to the receiver.

In the following sections, the computational algorithms are first outlined. Then a comparison is made of seismograms synthesized in model having a fault zone versus seismograms synthesized in a simple 1-D model without a fault zone.

2. RAY TRACING

The ray tracing is performed in ray centered coordinates described by Popov and Pšenčík (1978), Červený and Hron (1980), and Cerveny (1985). A system of first order, differential equations are integrated along

the ray. These include equations for ray trajectory:

$$\frac{dx_i}{dt} = v^2 p_i$$
$$\frac{dp_i}{dt} = -v^{-1} \frac{\partial v}{\partial x_i} \tag{1}$$

where t is time, x_i are the coordinates of the position vector, v is the local P or S vawe velocity, and p_i are the cartesian components of the slowness vector. The accumulated rotation of the vector basis of ray-centered co-ordinates is ν is calculated by the equation:

$$\frac{d\nu}{dt} = \frac{p_3(p_2 \frac{\partial v}{\partial x_1} - p_1 \frac{\partial v}{\partial x_2})}{p_1^2 + p_2^2} \tag{2}$$

Cerveny and Hron (1980). The remaining equations are used to calculate geometrical spreading and in performing the iterative ray tracing. The quantities to be calculated are:

$$Q_{ij} = \frac{\partial q_i}{\partial \gamma_j} \; ; \quad P_{ij} = \frac{\partial p_j}{\partial \gamma_j} \quad (i, j = 1,2) \tag{3}$$

where γ_i are the ray parameters chosen to be the vertical and azimuthal take-off angles, q_i are the ray centered coordinates, and p_i are the components of the slowness vector in the ray centered coordinates. The governing differential equations are:

$$\frac{dQ_{ij}}{dt} = v^2 P_{ij} \; ; \quad \frac{dP_{ij}}{dt} = -v^{-1} \left(\frac{\partial^2 v}{\partial q_i \, \partial q_1} Q_{ij} + \frac{\partial^2 v}{\partial q_j \, \partial q_2} Q_{2j}\right) \tag{4}$$

The geometric spreading S, is easily determined from the determinant of the Q matrix:

$$S = \frac{1.}{\sqrt{\det \underline{\underline{Q}}}} \tag{5}$$

In order to calculate the radiation from a finite fault, the fault plane is discretized and the ray equations are integrated from the receiver to a grid of points on the fault plane. A convenient method for solving the two point ray tracing problem is paraxial ray tracing. In the paraxial approximation, the phase in the vicinity of a central ray is expanded up to second order in the ray centered coordinate system. Iterative paraxial ray tracing consists of using the elements of the Q

matrix to estimate the correction to the initial ray parameters. The correction is calculated from the misfit between the ray endpoint and the target point projected onto the wavefront, that is, the (q_1, q_2) coordinates of the misfit vector. The new estimate of the initial ray parameters γ_j is given by

$$\begin{bmatrix} \gamma_1 \text{ new} \\ \gamma_2 \text{ new} \end{bmatrix} = \begin{bmatrix} \gamma_1 \text{ old} \\ \gamma_2 \text{ old} \end{bmatrix} + \underline{\underline{Q}}^{-1} \begin{bmatrix} m_1 \\ m_2 \end{bmatrix} \tag{6}$$

where $m = (m_1, m_2)$ is the vector between the target point and the point actually hit, perpendicular to the ray, in the local ray centered coordinate system. Knowledge of the local curvature of the wavefront at the ray end point has been used to estimate the ray parameters of a neighboring point on the wavefront.

The technique used in the present study requires many rays to calculate the radiation from a finite fault. Paraxial ray tracing has proven a convenient alternative to shooting and bending algorithms in this application especially for three dimensionally varying media. An example of an iterative sequence of paraxially traced rays in shown in Figure 1. A small number of iterations converges to a desired target point at an accuracy of 10 meters for a pathlength on the order of 10 km.

Note that in equation (6) the technique fails if $\underline{\underline{Q}}^{-1}$ does not exist. This is the case at caustics where the ray tube collapses. Since we use the iterative ray tracing technique to find geometric spreading and travel times at specified points on the fault plane, calculations are restricted to receivers removed from caustic surfaces.

3. CALCULATING SEISMOGRAMS

The theoretical seismograms are calculated by assuming that the far field term in the Green's function is dominant, and that it can be accurately calculated using ray theory. Following Spudich and Frazer (1984), the a component of far-field displacement radiated by a distribution of slip on a fault plane can be written as:

$$a \cdot u(x,t) = f(t) * \iint_A s_r \cdot G_a \, \delta(t - \tau) dA \tag{7}$$

where

- y spans the fault plane
- x is the receiver position
- $s(y)$ is the slip distribution on the fault.
- $f(t)$ is the time dependence of slip rate
- τ is the arrival time
- G_a is the far field Green's function.

For P waves:

$$G_a^P = \frac{\mu}{2\pi S^P} \quad \frac{\left[F^t(\hat{a}.\hat{t}_o)(\hat{t}.\hat{n})\hat{t}\right]}{\sqrt{\rho_o \; \rho\alpha_o \; \alpha^5}} \tag{8}$$

And for S waves:

$$G_a^S = \frac{\mu}{4\pi S^S(\sqrt{\rho_o \rho\beta_o \beta^5})} \left[(\hat{a}.\hat{e}_{o_1})F^{e_1}\left[(\hat{t}.\hat{n})e_1 + (\hat{n}.\hat{e}_1)\hat{t}\right] + (\hat{a}.\hat{e}_{o_2})F^{e_2}\left[(\hat{t}.\hat{n})\hat{e}_2 + (\hat{n}.\hat{e}_2)\hat{t}\right]\right] \tag{9}$$

where μ is the shear modulus.

$F^{e_1.e_2.t}$

is the product of transmission and reflection coefficients for the wave and component considered.

- n is the fault normal.
- ρ is the density.
- β is the shear wave velocity.
- α is the compressional wave velocity.

Quantities with the subscript o refer to quantities to be evaluated at the observer. Other quantities are evaluated at the source.

The selection of the vector basis of the ray-centered coordinate system is made such that e_{0_1} and e_{0_2} correspond to natural definitions of SH and SV at the observer. To make e_{0_1} correspond to the natural SH direction, its direction is selected to be perpendicular to the plane defined by the local tangent $\hat{t}_0$ and the vertical Cartesian axis. e_2 is then determined by the criterion that the triplet (e_1, e_2, $\hat{t}$) be orthogonal and right-handed. The transverse components, e_1 and e_2, can rotate along the ray in a three-dimensionally varying medium, but the S polarization remains fixed in this system, having the same relative components in the e_1 and e_2 directions at the fault plane as at the receiver. It should be noted that e_1 and e_2 do not generally correspond to the Frenét frame in a three-dimensional medium. In fact, Hubral (1979) notes that the transport equation does not generally decouple into separate equations for the two principal components of shear waves even in the zeroth asymptotic order in the Frenét frame.

Thus, by combining ray theory with the representation theorem, one can calculate high frequency ground motions for finite faults embedded in a laterally varying medium. Additional savings in computation time are made by the change of variables:

$$dA \; \delta(t - \tau) = c \; dl \tag{10}$$

where dA is the differential area element of fault surface, dl is the differential arclength along an isochrone, and c is the isochrone

velocity as discussed by Spudich and Frazer (1984). The primary advantages that the approximate, ray theoretical technique has over other techniques such as finite difference algorithms (e.g., Vidale et al.,1984), are its computational speed and the insight one obtains from knowing what individual rays contribute to the seismogram.

4. EXAMPLE: A FAULT ZONE

To demonstrate the technique we will examine the effects of a fault zone structure. Evidence of three dimensionally varying structure in the vicinity of fault zones has been found in many different types of studies. For example, in central California, studies have documented the existence of a low velocity zone extending below the surface trace of both the Calaveras and San Andreas Faults. This has been inferred from earthquake arrival time residuals (Mayer-Rosa, 1973; Thurber, 1983), refraction profiles (Mooney and Luetgert, 1982; Blümling et al., 1985), reflection sections (Feng and McEvilly, 1983), and waveform modeling of aftershocks (Cormier and Spudich, 1984).

Evidence for three dimensionally varying structure can also be found in strong motion data. Tucker and King (1984) have documented strong effects of sediment filled valleys on amplitude spectra for earthquakes recorded in the Garm region of the U.S.S.R. The variations in acceleration across the El Centro Array in the Imperial Valley earthquake, particularly the large accelerations at station 6, have been attributed by some authors, (Singh, 1981; Rial et al., 1986) to lateral variations in the local velocity structure. Records from the Morgan Hill earthquake indicate strong lateral variations in velocity both in arrival time of shear waves from the hypocenter and in amplitude fluctuations across the Gilroy Array (Beroza, et al., 1984; Hartzell and Heaton, 1986). Vidale and Helmberger (1985), using a two dimensional structure, have obtained a better fit to records of the San Fernando earthquake.

A simple structure is chosen to demonstrate the effect on strong motion seismograms. The structure is based on the laterally homogenous structure determined for the Calaveras fault zone in central California by Blümling et al (1985). The structure is perturbed from a laterally homogeneous structure by subtracting an exponential function, that decays with distance from the fault and with depth. The perturbation is:

$$v(y,z) = v_0(z) \left[1.0 - Ce^{(y/w)^2 - z/d}\right] \tag{11}$$

where v is the velocity, y is the distance perpendicular to the fault, and z is the depth. The parameters are chosen to approximate the wedge shaped fault zone structure of Feng and McEvilly (1983). The parameters chosen are:

$$w = 2.\text{km}; \quad d = 10.\text{km}, \quad C = 0.4 \tag{12}$$

The resulting velocity structure is shown in Figure 2. The S wave velocities are derived assuming a Poisson solid. Because an analytic perturbation to the velocity structure is used, it is a simple matter

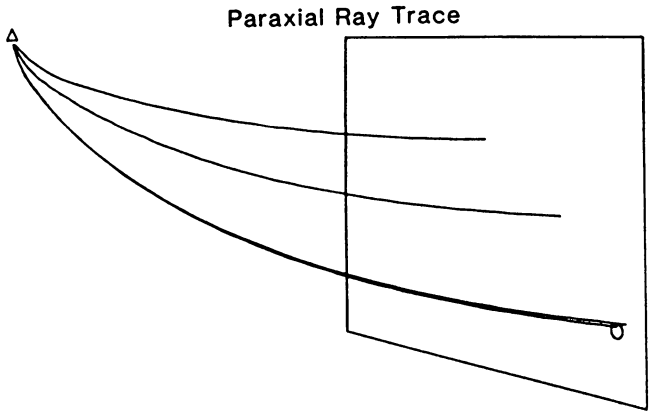

Figure 1. A sequence of paraxially traced rays is shown for a laterally varying medium from the receiver (triangle) to the fault plane. The target point is at the center of the circle. The initial guess misses by several kilometers, but subsequent estimates of the ray parameters, based on the paraxial approximation, converge rapidly to the ray connecting source and receiver.

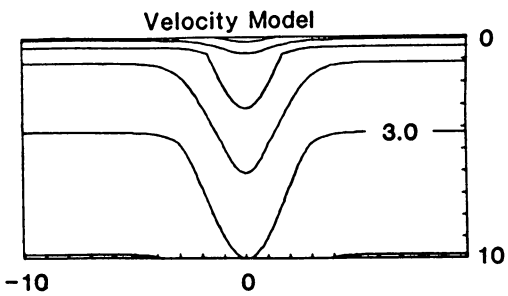

Figure 2. Lines of equal shear wave velocity are shown for the laterally varying structure used in this study. The contour interval is 0.5 km/sec. The laterally homogeneous structure is a smoothed version of the Blumling et al (1985) structure. The laterally homogeneous model is perturbed by an analytic function of the form $f(y,z) = (1.0-0.4e^{-(y/w)^2-z/d})$ where the w and d parameters describe the width and depth of the perturbed region. They are chosen to be 2 and 10 km respectively to approximate the fault zone structure found by Feng and McEvilly (1983).

to evaluate the first and second partial derivatives of the velocity. Although the velocity structure chosen is not a function of x, the distance parallel to the fault, the ray tracing is a three dimensional problem since the rays from different locations on the fault have markedly different trajectories to the receiver. A very simple model is chosen for the velocity structure. This was done for convenience only. The method described in this paper is valid for any medium provided that ray theory itself is valid. Beydoun and Ben Menahem (1985) and White et. al. (1987) give through discussions of the relevant inequalities that must be satisfied to insure validity and accuracy of asymptotic ray theory.

Figure 3 shows how fault zone structure may affect the wavefield within the fault zone. A sequence of rays have been shot from a 5 km. deep point source in an azimuthal range that spans the axis of the fault zone. Also shown are the accelerograms of the April 24,1984, Morgan Hill earthquake recorded by stations G06 and G07 of the Gilroy array. The location of the point source has been chosen to be approximately coincident with an energetic second source that occurred well after the initiation of rupture. Although G06 and G07 are less than 5 km apart, the relative amplitudes of the first and second sources are quite different at G06 compared to those observed at G07. Peak velocities recorded at G06 are about five times larger than at G07. Since both stations are located on similar hard rock sites (Abrahamson, personal communication), this difference is not likely to be due to differences in local crustal and soil structure. Also the stations are too close to one another to exhibit significant differences due to source directivity. The ray trace shown in Figure 3 suggests that the focusing effect of the fault zone structure may explain the differences observed between the secondary source at G06 and G07.

Note that many rays touch caustic surfaces that are roughly coincident with the strong lateral gradients that define the edges of the fault zone. For a fault zone with axial symmetry, the caustics can collapse to vertical lines as shown. Since the iterative ray tracing was used in this paper to determine travel times and Green's functions at specified points on the fault plane, the examples have been restricted to stations outside the caustic surfaces in order to avoid the singularities in $1/\sqrt{\det \underline{\underline{Q}}}$ and $-\frac{\pi}{2}$ phase advances associated with changes in the KMAH index. It is shown that even in this region on the flanks of the fault zone, the fault zone structure can produce large perturbations in amplitudes and particle motion predicted by a laterally homogeneous model.

5. DISCUSSION

Theoretical seismograms have been calculated for the structure described above. The locations of the receivers used as well as the fault geometry are shown in Figure 4. The receivers are placed at one kilometer intervals at the free surface from 3 to 7 kilometers from the fault. The three vertical subfaults considered are circular with a diameter of one kilometer centered at a depth of 4.5 km and a distance along strike from

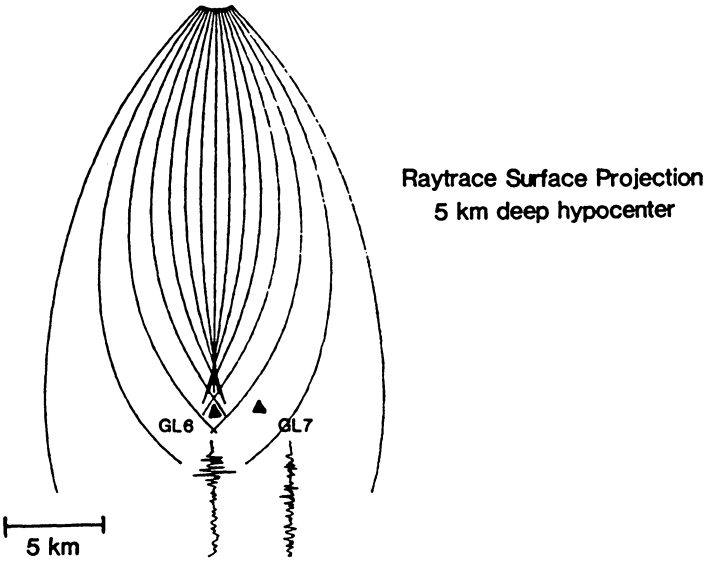

Figure 3. Rays shot in a 2-D structure of the Hayward-Calaveras fault zone from a 5 km deep source. Take off angle has been kept constant and the location has been placed approximately to agree with the location estimated for the second source responsible for the late pulse observed at several stations recording accelerations from the Morgan Hill earthquake. The variations in the amplitudes of this pulse at GL6 and GL7 may be related to their location in or out of the fault zone.

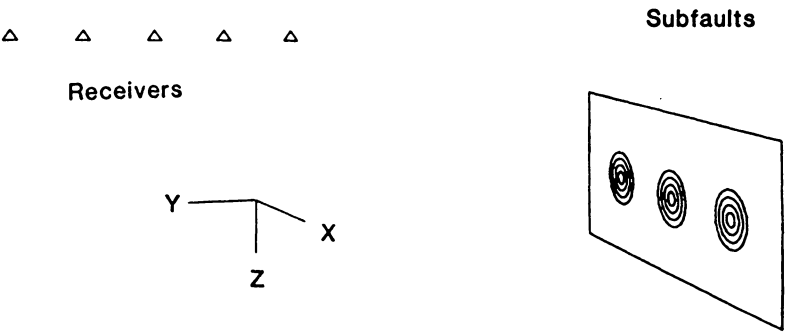

Figure 4. The set of five receivers (triangles) range from 3 to 7 km from the fault at 1 km intervals and are shown in perspective with the subfaults (circles) which are vertical, circular, and located 0.5, 2.5, and 4.5 km along strike. The coordinate system is as shown with $\hat{x}$ parallel to the strike of the fault, $\hat{z}$ positive downward, and $\hat{y}$ normal to the fault such that the coordinates are right handed.

the receiver of 0.5, 2.5, and 4.5 km. Slip on each subfault is assumed to be a uniform 10 cm of right lateral strike-slip. Rupture propagates radially at a uniform velocity of 2.0 km/sec. The rise time is assumed to be a uniform 0.2 seconds across the fault. The source description is purely kinematical. The only purpose of the present study is to examine propagation effects.

A surface projection of rays shot from the center of each subfault to the observer is shown in Figure 5 for the receiver 3 km from the fault in the laterally homogeneous and inhomogeneous cases. The surface projection of the rays in the laterally homogeneous case are straight lines. In the laterally inhomogeneous case; however, the rays are bent towards the fault normal. This occurs because the minimum time path is one in which the slow area surrounding the fault is traversed quickly. Because the rays are bent when propagating through the fault zone they arrive at the receiver with a different orientation. The consequences for a component of motion observed at the receiver are that the excitation at the fault zone will be different for the two cases, and that the resulting motion at the receiver will be different both because the excitation is different and because the orientation of the incident ray is different. Except for the delay in arrivals in the laterally heterogeneous case, these are the dominant effects on the seismograms for the geometry we have studied. The effects can be demonstrated by a comparison of the waveforms in the laterally homogeneous and heterogeneous cases for the simple sources we have studied.

Figure 6 shows the seismograms for the subfault that is 0.5 km along strike from the observer. For right lateral strike-slip on a vertical fault plane, these receivers are close to a node in P and SV radiation. The SH radiation is on a lobe and consequently dominates the seismograms. The S wave shows up primarily on the $\bar{x}$ component of motion. The polarity on the $\bar{y}$ component is different for the two cases. This is due to the trajectory of the incoming ray at the receiver (Figure 5). The S wave comes in at a greater angle with respect to the $\bar{y}$ direction for the laterally inhomogeneous case, and as a result a substantial amount of SH radiation is recorded on the $\bar{y}$ component of motion. Since for this geometry SV and SH have opposite signs the polarity of the S wave arrival at the observer is reversed. For the receiver at 5 km the SV contribution is close to a node, and for receivers greater than 5 km from the fault the SV and SH contributions to the $\bar{y}$ component of motion have the same sign. This demonstrates the effects of the trajectory of the incoming ray at the receiver for the two cases.

Another feature common to the comparisons in Figures 6-8 is that the contribution of the P wave relative to the S wave is greater for the laterally inhomogeneous case. This can be explained by the relative excitation of P and S waves in the two cases. The components of the S waves e_1 and e_2 have a larger component parallel to the fault normal in laterally homogenous case. Thus by equation 8 they are more strongly excited. For the P waves however, the ray and therefore the ray tangent vector have a larger component parallel to the fault normal in the laterally inhomogeneous case (Figure 5), and by equation 9 the P waves are excited more strongly. These two effects act to enhance the P wave contribution relative to the S wave contribution in the laterally heterogeneous case.

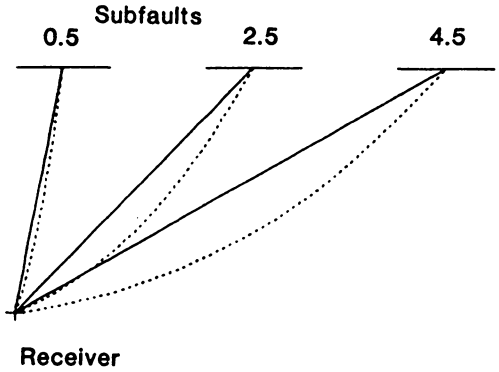

Figure 5. A map view is shown of the rays connecting the receiver (cross) at 3 km from the fault with the center of each of the subfaults (straight line segments) for the laterally homogeneous case (solid lines) and laterally inhomogeneous case (dashed lines).

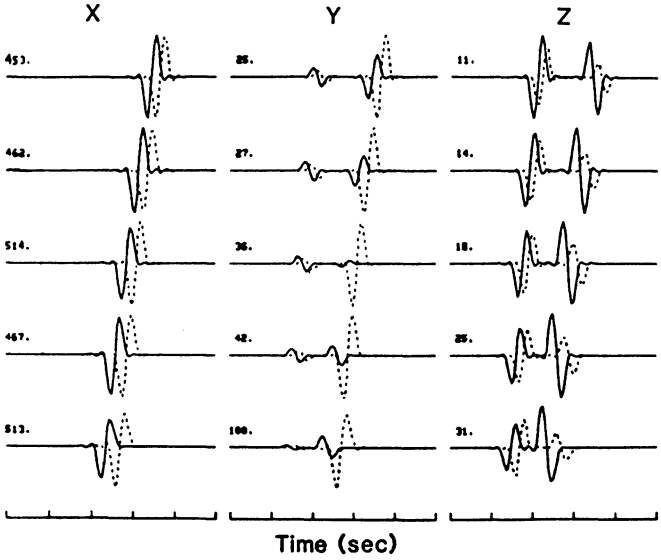

Figure 6. Theoretical velocity seismograms for the laterally homogeneous model (solid lines) and for the laterally varying model (dashed lines) are compared for the $\hat{x}$, $\hat{y}$, and $\hat{z}$ components of motion using the coordinate system shown in figure 1. The seismograms are for receivers ranging from 3 km from the fault (bottom) to 7 km from the fault (top) at 1 km intervals. The peak amplitude of the two traces is shown in units of cm/sec x 10^{-3}. In this figure the subfault is 0.5 km along strike.

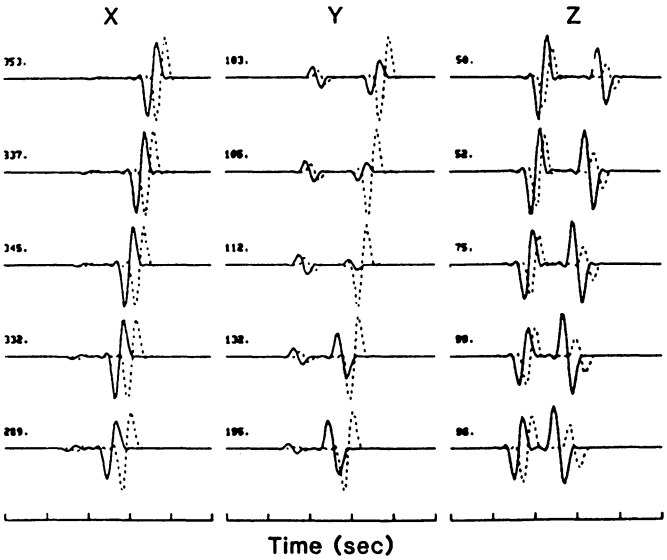

Figure 7. Same as figure 6 for the subfault 2.5 km along strike.

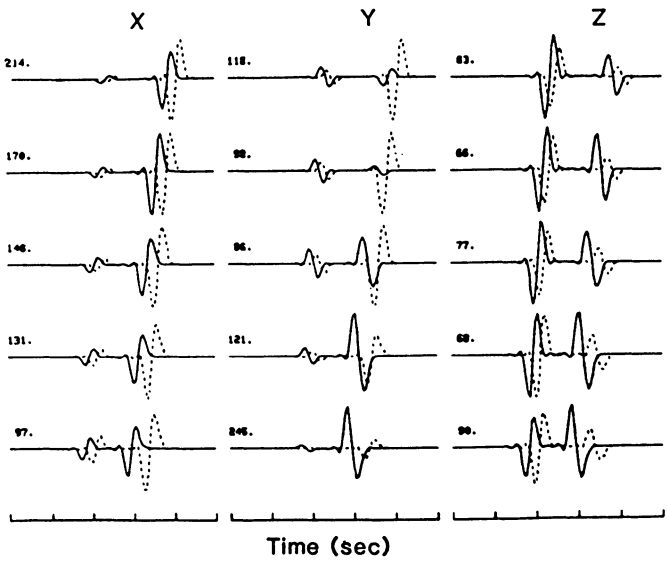

Figure 8. Same as figure 6 for the subfault 4.5 km along strike.

6. CONCLUSIONS

The use of ray theory in the near source region is an efficient method for calculating high frequency theoretical seismograms in smoothly inhomogeneous media. The technique presented in this paper allows one to explore the effect of heterogeneous media on earthquake strong ground motion. The primary advantage this technique has over other techniques is that fully three-dimensional models of crustal structure are only slightly more computationally expensive to incorporate than one-dimensional models.

Seismograms were synthesized for extended sources along a fault plane embedded in a low velocity wedge designed to simulate a structure often observed for fault zones. Combined with the results for point sources in a 2-D geometry in such a structure (Cormier and Spudich, 1984), the following can be concluded:

(1) Fault zone structure can strongly affect the arrival time, amplitude, and polarity of phases recorded at stations located within and near a 2-3 km zone centered on the fault trace.

(2) The largest effects are on geometric spreading within the fault zone and on the radiation pattern and ray trajectory elsewhere.

(3) The effects on radiation pattern can remain strong more than several kilometers away from the borders of the fault zone.

(4) The effects of fault zone structure may be incorrectly mapped into source parameters if a laterally homogeneous crustal structure is assumed.

(5) The effects on focusing and radiation pattern of fault zones are important to quantify for hazards assessment in fault zones, particularly in refining empirical relations for ground motion based on distance to the observed fault trace.

A simple two point ray tracing scheme was used to calculate ray theory Green's functions. The ray tracing was performed using the paraxial approximation iteratively to determine the take-off angles of the ray hitting a specified target point. The iterative technique fails near caustic surfaces. This restricted our theoretical calculations to stations removed from the caustic surfaces on the borders of the fault zone. The far-field representation theorem itself, however, remains regular at point and line intersections of caustics with the fault plane. Moreover, paraxial rays and beams have recently been applied in a fashion that does not require solution of the two-point ray tracing problem (Červený et al., 1987). In one such approach by Červený et al., each member of a dense fan of narrow Gaussian beams are analytically integrated over fault plane area. These and similar approaches illustrate that asymptotic ray theory combined with the far-field representation theorem can be a valuable and computationally efficient tool to investigate the combined effects of complex earthquake rupture and three-dimensional crustal structure. The limitations of these approaches are that the (i) the far field approximation must be sufficiently accurate in the range and frequency band of application,

(ii) the wavefield can be accurately represented by a sum of direct and multiply reflected and refracted body waves, and (iii) the scale lengths of crustal heterogeneities and boundary curvatures must be larger than the wavelength band of application.

7. ACKNOWLEDGEMENTS

This research was supported by the National Science Foundation under Grant EAR-85-18151. Greg Beroza was supported by an N.S.F. fellowship. We thank Paul Spudich for providing us with his programs for strong ground motion synthesis. These formed the basis from which we extended calculations to three-dimensional structure. We also thank Vyastislav Cervený and his co-workers for making available to us many of their publications that were still in press at the start of this project.

8. REFERENCES

Beroza, G.C., P.K.Spudich, and V.F.Cormier, (1984). Modeling rupture of the Morgan Hill earthquake using near field data (abstract), EOS Trans. Am. Geophys. Un., 65, 1004.

Bernard, P., and Madariaga, R.(1984). A new asymptotic method for modeling of near field accelerograms, Bull. Seism. Soc. Am., 74, 539-558.

Beydoun, W., and A Ben Menahem (1985). Range of validity of seismic ray and beam methods in general inhomogeneous media - I.general theory, Geophys. J., 82, 207-234.

Blümling, P., W.D.Mooney, and W.H.K.Lee (1985). Crustal structure of the southern Calaveras Fault zone, Central California, from seismic refraction investigations, Bull. Seismol. Soc.Am., 75, 193-309.

Červený, V., and F.Hron (1980). The ray series method and dynamic ray tracing systems for 3-D inhomogeneous media, Bull. Seism. Soc. Am., 70, 47-77.

Červený, V., Klimeš, L., and I.Pšenčík (1984). Paraxial ray approximations in the computation of seismic wavefields in inhomogeneous media, Geophys. J., 79, 89-104.

Červený, V. (1985). The application of ray tracing to the propagation of shear waves in complex media, in Seismic Exploration, (Treitel and Helbig eds.) vol. on Shear Waves (G.Dohr, ed.), Geophysical Press, London.

Červený, V., L.Klimeš, J.Pleinerová, and I.Pšenčík, (1987). High-frequency radiation from earthwuake sources in laterally varying structures, Geophys. J., 88, 43-80.

Cohn, S.N., T.Hong, and D.V.Helmberger (1982). The Oroville earthquakes: a study of source characteristics and site effects, J.Geophys. Res., 87, 4585-4594.

Cormier,V.F., and P.Spudich (1984). Amplification of ground motion and waveform complexity in fault zones: examples from the San Andreas and Calaveras Faults, Geophys. J., 79, 135-152.

Cormier,V.F., and G.Beroza (1985). Prediction of Strong Ground Motion due to Extended Earthquake Sources in a Three-Dimensionally Varying Crust: The Effect of a Fault Zone, EOS Trans. Am. Geophys. Un.,

Feng, R., and T.V.McEvilly (1983). Interpretation of seismic reflection profiling data for the structure of the San Andreas fault zone, Bull. Seism. Soc. Am., 76, 649-674.

Hartzell, S.H., and T.H.Heaton (1986). Rupture history of the 1984 Morgan Hill earthquake from the inversion of strong motion records, Bull. Seism. Soc. Am., 76, 649-674.

Hong, T.L., and D.V.Helmberger (1978). Glorified optics and wave propagation in nonplanar structure, Bull. Seism. Soc. Am., 68, 1313-1330.

Hubral, P. (1979). On the computation of shear waves by the ray method, Geophys. J., 57, 445-449.

Ihnen, S.M., and D.M.Hadley (1986). Prediction of strong ground motion in the Puget Sound region: The 1965 Seattle earthquake, Bull. Seism. Soc. Am., 76, 905-938.

Langston, C. and J.Lee (1983). Effect of structure on strong ground motions: the Duwamish River Valley, Seattle, Washington, Bull. Seism. Soc. Am., 73, 1851-1863.

Mayer-Rosa, D.(1973). Travel time anomalies and distribution of earthquakes along the Calaveras fault zone, California, Bull. Seismol. Soc. Am., 63, 713-729.

Mooney, W.D., and J.H.Luetgert (1982). A seismic refraction study of the Santa Clara Valley and Southern Santa Cruz Mountains, West-Central California, Bull. Seismol. Soc. Am., 72, 901-909.

Olson, A., and R.Apsel (1982). Finite faults and inverse theory with applications to the 1979 Imperial Valley earthquake, Bull. Seismol. Soc. Am., 72, 1969-2001.

Popov, M.M., and I.Pšenčík (1978). Computation of ray amplitudes in inhomogeneous media with curved interfaces, Studia Geoph. et Geod., 22, 248-258.

Rial, J.A.(1984). Caustics and focusing produced by sedimentary basins, applications of catastrophe theory to earthquake seismology, Geophys. J., 79, 923-938.

Rial, J.A., V.Pereyra and G.L. Wojcik (1986). An explanation of USGS station 6 record, 1979 Imperial Valley earthquake: a caustic induced by a sedimentary wedge, Geophys. J., 84, 257-278.

Singh, J.P.(1981). The influence of seismic source directivity on strong ground motions, PhD. Dissertation, Univ. of Calif. Berkeley.

Spudich, P., and Angstman, B. (1980). Lateral variations in velocity and Q structure in the region of the 1979 Coyote Lake, California, earthquake, Earthq. Notes, 50, 64.

Spudich, P. and L.N.Frazer (1984). Use of ray theory to calculate high-frequency radiation from earthquake sources having variable rupture velocity and stress drop, Bull. Seismol. Soc. Am., 74, 2061-2082.

Thurber, C. H.(1983). Earthquake locations and three dimensional crustal structure in the Coyote Lake area, Central California, J.Geophys. Res., 88, 8226-8236.

Tucker, B.E., and J.L.King (1984). Dependence of sediment-filled valley response on input amplitude and valley properties, Bull. Seism. Soc. Am. 74, 153-165.

Vidale, J., D.V.Helmberger, and R.W.Clayton (1984). Strong motion seismograms for laterally varying structures (abstract), EOS Trans. Am. Geophys. Un., 65, 1005.

Vidale, J., and D.V.Helmberger (1985). Finite difference modeling of strong motions (abstract), EOS Trans. Am. Geophys. Un., 66, 967.

White, B.S., R.Burridge, A.Noriss, and A.Bayliss (1987). Some remarks on the Gaussian beam summation method, Geophys. J., in press.

PHYSICAL MECHANISMS CONTRIBUTING TO SEISMIC ATTENUATION IN THE CRUST

M.N.Toksöz, R.S.Wu and D.P.Schmitt
Earth Resources Laboratory
Department of Earth, Atmospheric, and Planetary Sciences
Massachusetts Institute of Technology
Cambridge, MA 02139
U.S.A.

ABSTRACT. The mechanisms contributing to the attenuation of earthquake ground motion in the distance range of 10 to 200 km are studied with the aid of laboratory data, coda waves and strong motion attenuation measurements in northeast United States and Canada and theoretical models. The relative contributions to attenuation of anelasticity of crustal rocks (constant Q), fluid flow and scattering are evaluated. Scattering is found to be strong with albedo of B_0=0.9 and scattering extinction length of about 17 km. The intrinsic attenuation in the crust can be explained by a high constant Q($500 \leq Q_0 \leq 2000$) and a frequency dependent mechanism most likely due to fluid effects in rocks and cracks. A fluid-flow attenuation model gives a frequency dependence ($Q \simeq Q_0 f^{0.5}$) similar to those determined from the analysis of coda waves of regional seismograms.

1. INTRODUCTION

The amplitude of seismic waves from an earthquake source decreases with increasing distance because of geometric spreading and because of attenuation resulting from the absorption and conversion of seismic energy into heat. Just like seismic velocities, the attenuation properties vary in the crust both as a function of depth and laterally. Generally, attenuation variations are larger by about one order of magnitude than the velocity variations. In this paper, we study the physical processes contributing to seismic attenuation in the crust. The primary mechanisms we consider are the anelasticity of crustal rocks, scattering due to heterogeneities, and fluid movements within pores and cracks in the crust. These are shown schematically in Figure 1.

We consider attenuation in the distance range of 10 to 100 km. This interval is ideal for several important reasons. At distances shorter than about 10 km from the source, non-linear behavior of materials due to high strains ($\varepsilon \geq 10^{-5}$) can dominate. At distances greater than 100 km, the geometric spreading effects, due to velocity-depth functions and multiple branches of travel-time curves, become site-specific and uncertain. Another important factor for favoring this distance range is

M. O. Erdik and M. N. Toksöz (eds.), Strong Ground Motion Seismology, 225–247.
© 1987 by D. Reidel Publishing Company.

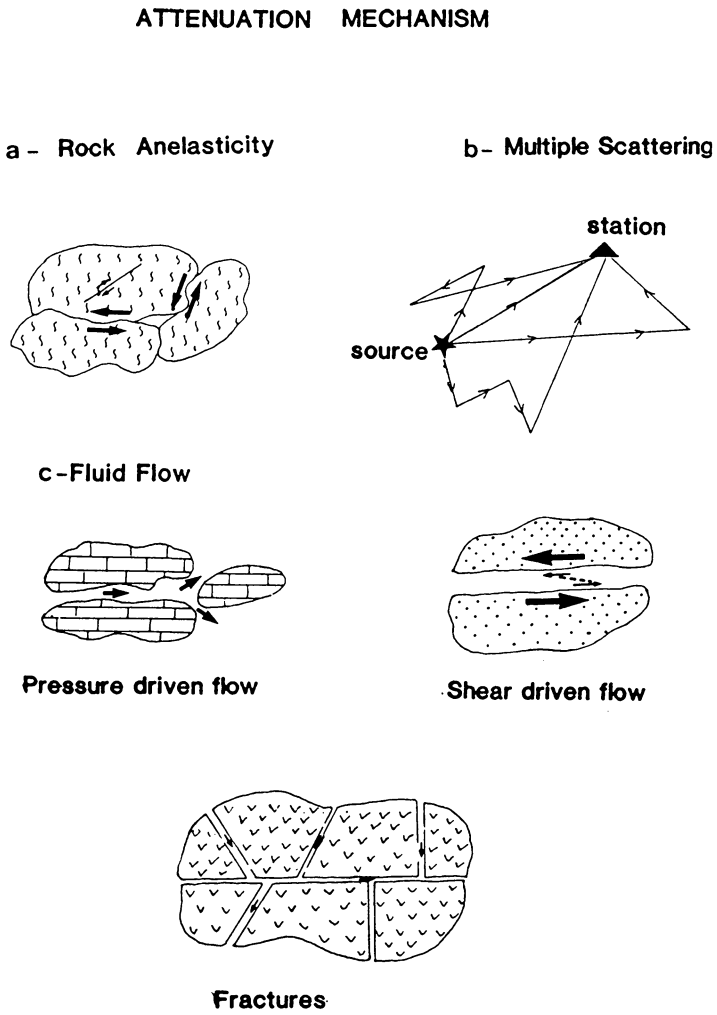

Figure 1. Schematic illustration of earthquake strong ground motion attenuation mechanism discussed in this paper. a)Rock anelasticity refers to frequency independent Q associated with relative motions and frictional losses across grains and dislocations. b)Scattering is due to structural and geologic heterogeneities in the crust. c)Fluid flow incorporates fluid motions in pores and fractures induced by P and S waves.

that a considerable amount of new attenuation data has been obtained both from strong motion records and the analysis of seismic coda waves.

Before reviewing the attenuation data, it is important to define the terminology. The attenuation for a given wave type (P or S) is defined as the inverse of the quality factor Q, and related to other measures by:

$$\frac{1}{Q} = \frac{\alpha V}{\pi f} = \frac{\delta}{\pi} \tag{1}$$

where α is the attenuation coefficient, V the wave velocity, f the frequency, and δ the logarithmic decrement.

Attenuation Q^{-1} or the quality factor Q are dimensionless quantities. Physically, Q^{-1} is equal to the ratio of energy dissipated per cycle to the total energy. For small attenuation, (i.e. $Q^{-1} \leq 0.1$), additional relationships can be established in terms of stress-strain relationships:

$$\frac{1}{Q} = \frac{M_I}{M_R} = \tan \phi \simeq \phi \tag{2}$$

where M_I and M_R are the imaginary and real parts of the appropriate elastic modulus ($M = M_R + iM_I$) and ϕ is the phase lag of the strain behind the stress (i.e., loss tangent). The dimension of the attenuation coefficient α is generally given as dB/unit length or nepers per unit length. The relationship between the two is α(dB/unit length) = 8.686 α(nepers/unit length).

Most of the data for crustal attenuation comes from coda waves (Aki and Chouet, 1975; Aki, 1980; Pulli, 1984; Singh and Herrmann, 1983; Singh, 1985; Gupta et al., 1983; Rautian and Khalturin, 1978; Roecker et al., 1982; Herrmann, 1980). These measurements generally give attenuation that decreases with frequency in the frequency range of f=0.5 to 25 Hz. Some typical coda Q values are:

$$Q_c(f) = 460f^{0.4} \tag{3}$$

for New England (Pulli, 1984);

$$Q_c(f) = 1000\ f^{0.2} \tag{4}$$

for the Central United States (Singh and Hermann, 1983); and

$$Q_c(f) = 150\ f^{0.45} \tag{5}$$

for the Western United States (Singh and Hermann, 1983).

The increase of Q with frequency and the high values ($Q \geq 1000$) at frequencies above 10 Hz in the Eastern United States cannot be reconciled with the laboratory measurements of Q in crustal rocks (see Toksöz and Johnston, 1981 for a comprehensive compilation). Most laboratory data suggest that, at least for dry rocks, Q is independent of frequency (Birch and Bancroft, 1938; Peselnick and Outerbridge, 1961; Klima et al.,

1964; Knopoff, 1964; Pandit and Savage, 1973; Toksöz et al., 1979; Nur and Winkler, 1980; Johnston and Toksöz, 1980; Tittman et al., 1981). Water saturation generally decreases Q values of both P and S waves, although the decrease is much greater for S-waves than for P-waves.

Q increases with increasing confining pressure. However, the laboratory Q values at pressures of 2 kilobars or more in crystalline rocks are generally less than 1000 (Klima et al., 1964; Bradley and Fort, 1966; Mason et al., 1970). It is only in the case of totally outgassed and volatile free rocks that Q values of 2000 or more have been obtained (Clark et al., 1980; Tittman et al., 1974). These values have been observed in the completely dry environment of the moon (Dainty et al., 1976). The Earth's crust is not free of water and volatiles and the high Q values cannot be attributed to dehydration. The high Q values still need to be explained.

Although Q is independent of frequency in dry rocks, it may be frequency dependent in saturated and partially saturated rocks (Gardner et al., 1964; Winkler and Nur, 1979; Spencer, 1981; Tittman et al., 1981). The saturation may produce relaxation peaks at certain frequencies and increase and decrease of Q on two sides of a peak. The question we wish to investigate is whether such relaxation phenomena and fluid motions can explain the frequency dependence of crustal Q values measured from coda waves.

Attenuation measurements in the Earth using coda waves or strong motion seismograms include the contribution of scattering due to heterogeneities, fluid-flow effects in fractures and intrinsic anelasticity of crustal rocks. The laboratory measurements incorporate effects of anelasticity and fluids in pores and coating the grains. In order to compare the Earth data with the laboratory results, it is necessary to separate the effects of scattering and fluid motions in fractures. In this study, we do this in two steps. First, we calculate the scattering effects. Then we interpret the remaining attenuation and its frequency dependence in terms of constant-Q type intrinsic attenuation and fluid flow attenuation. Each of these steps are model-dependent so that the results depend on the validity of the models.

2. SCATTERING ATTENUATION

Scattering of elastic waves propagating in a heterogeneous medium contributes to the attenuation of these waves. Scattering attenuation is not an energy dissipation mechanism, but only an energy redistribution in space and time, therefore, it is a geometric effect. Under the single scattering approximation, the scattering attenuation cannot be separated from the intrinsic attenuation. In order to separate these two attenuation mechanisms, we need to use the multiple scattering theory. There is no general solution for the multiple scattering theory. However, several special cases have been studied (O'Doherty and Anstey, 1971; Kopnichev, 1977; Dainty and Toksöz, 1977, 1981; Richards and Menke, 1983; and Gao et al., 1983a, b). Wu(1984, 1985) formulated the multiple scattering problem in the frequency domain using radiative transfer theory. In the case of isotropic scattering with a point source in an

infinite random medium, an exact solution can be obtained (Appendix A).

Figure 2 shows the distribution of seismic wave energy with distance calculated by the theory. In the figure, the energy density is normalized by the extinction length L_e, which is the reciprocal of the extinction coefficient η_e:

$$L_e = 1/\eta_e \qquad \eta_e = \eta_a + \eta_s \tag{6}$$

where η_a is the energy absorption coefficient due to anelasticity of the medium and η_s is the scattering coefficient which is defined as the total scattered power by a unit volume of random medium per unit incident power flux density. Note that η_a is related to the attenuation coefficient given in equation (1) by $\eta_a = 2\alpha$. In Figure 1 the curve shapes change depending on the seismic albedo B_0 of the medium, which is defined as :

$$B_0 = \frac{\eta_s}{\eta_e} = \frac{\eta_s}{\eta_s + \eta_a} \tag{7}$$

For the case of large albedo ($B_0 > 0.5$), i.e. when the medium is strongly heterogeneous, and scattering is significant, the curves are of arch shape. The maxima of the curves depend on the extinction coefficient ($\eta_e = \eta_s + \eta_a$). Therefore it is possible to obtain B_0 and η_e from the energy density-distance curves, and thus separate the scattering effect from the intrinsic attenuation.

The theory has been applied to local earthquakes in Hindu Kush region (Wu, 1984; Wu and Aki, 1985) with the conclusion that the scattering attenuation in that region is not the dominant factor ($B_0 \leq 0.5$). In this study, we look at the attenuation data in the eastern United States where anelastic attenuation may be low.

Figures 3a and 3b are the strong motion data (pseudo velocity) in Northeastern America for the case of f=5Hz and 1 Hz respectively (with 5% damping). The solid lines in the figures are the best fits to the data. If we assume that the received strong motions are composed of both the direct arrivals and the scattered waves, then we can compare curves given in Figure 2 with the data to obtain the seismic albedo B_0 and the intrinsic quality factor Q_a. In Figure 4, the PSV data are corrected for the geometric spreading (1/R for body waves) and then squared to compare with the theoretical predictions. The best theoretical curves are also drawn in the figure. We can see that in the first 100 km the fit between theory and data is generally good except for a few points which are very close to the source. For greater distances, the data gradually deviate from the theory and become flatter. This may be due to the dominance of L_g waves at great distances. The discrepancy of data and theory at very close distances is probably due to the non-linear effects. From these comparisons of data with theory, we obtain the average seismic albedo B_0=0.9 and the extinction length L_e = 15 km for both the 1 Hz and 5 Hz waves. The medium parameters based on these values are listed in Table 1.

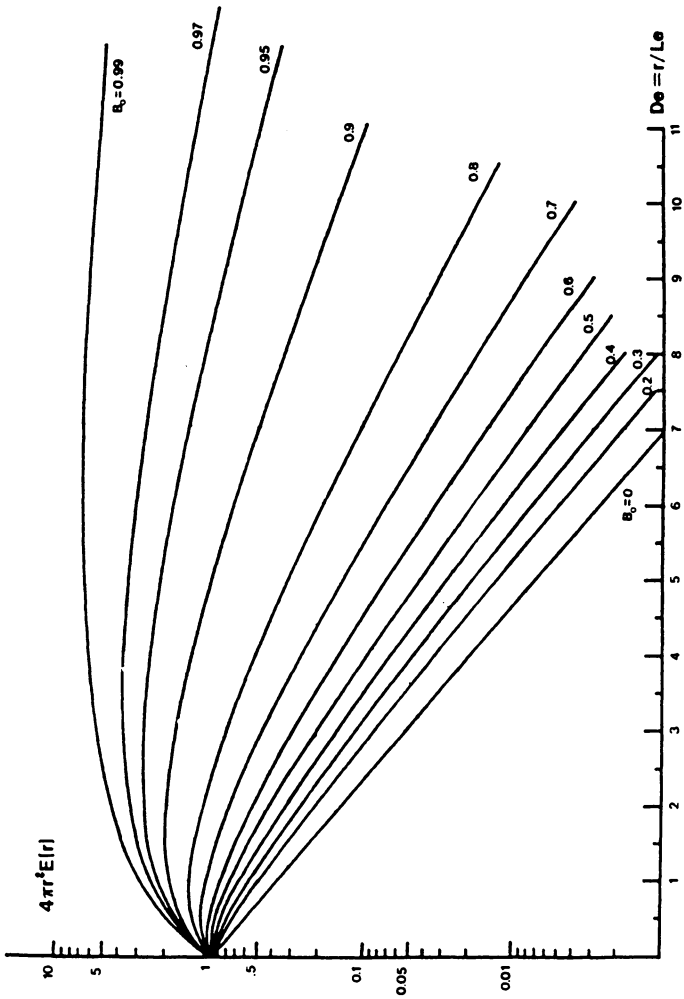

Figure 2. Normalized energy distribution curves corrected for spherical spreading, $4\pi r^2 E(r)$ as a function of normalized distance $D_e = r/L_e$ where L_e is the extinction length defined by Equation 6 in the text.

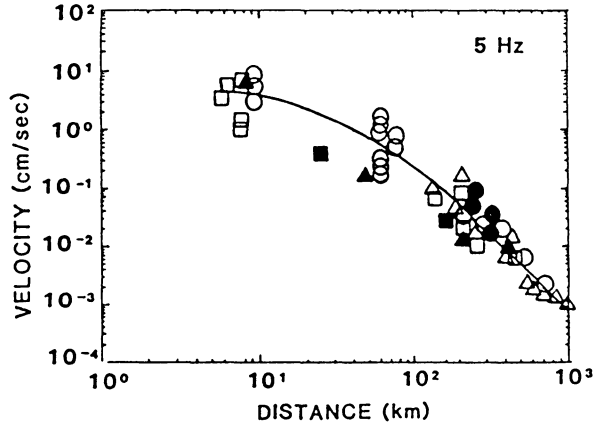

Figure 3a.

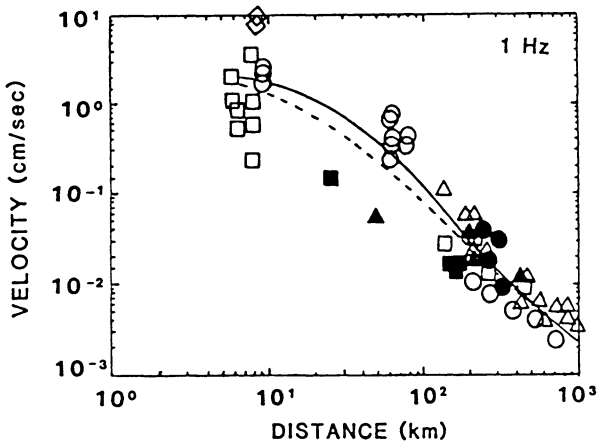

Figure 3b.

Figures 3a,b.
Ground velocity (PSV) at 5 Hz(3a) and 1 Hz(2a) as a function of distance for events in northeastern United States and Eastern Canada. Values normalized to a common magnitude. Data are from compilation of Risk Engineering, Inc., under EPRI sponsorship. The solid line in each case is a "best" fit to data.

△ 11-1-82, New Brunswick, M_b = 5.5, ECTN data

○ 19-1-82, New Hampshire, M_b=4.8, strong motion data and ECTN

□ 31-3-82, New Brunswick, M_b=4.8, strong motion data and ECTN

◇ 6-5-82, New Brunswick, M_b = 4.0, strong motion data

▲ 16-6-82, New Brunswick, M_b=4.6, strong motion data and ECTN

● 7-10-83, Adirondacks, New York, M_b=5.6, ECTN

■ 11-10-83, Ottawa, Canada, M_b = 4.1, ECTN

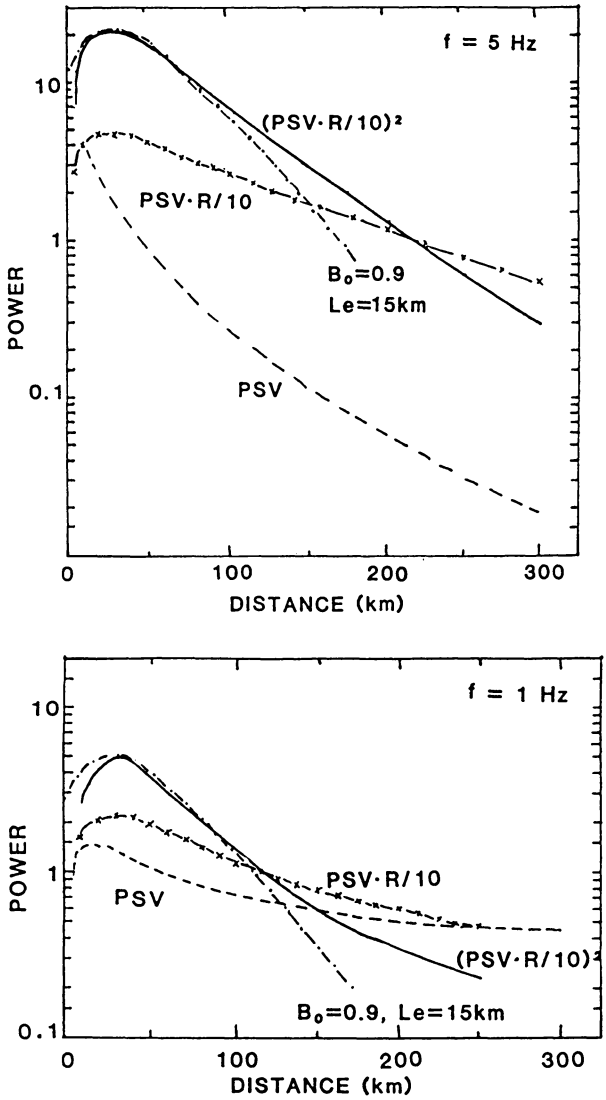

Figure 4a,b. Match between the multiple scattering model (B_o=0.9 and L_e = 15 km) and the observed ground motion data as function of radial (epicentral) distance R, at frequencies 5 Hz(4a) and 1 Hz(4b). PSV curves are the "best" fit curves of Figures 3a,b.(PSV.R/10) and $(PSV.R/10)^2$ are calculated from PSV curves. Note the goodness of fit between the model and data curves in the distance range of R = 10 to 100 km where model approximations are valid.

Table 1

Medium paratemers at f=1 and f=5 Hz based on multiple scattering theory.

Parameter	f = 1 Hz	f = 5 Hz
L_e	15 km	15 km
B_0	0.9	0.9
η_s	0.06/km	0.06/km
$L_s(=1/\eta_s)$	16.7 km	16.7 km
η_a	0.0067 km	0.0067 km
$L_a(=1/\eta_a)$	150 km	150 km
$Q_s(=kL_s)$	30	150
$Q_a(=kL_a)$	270	1350

In Figure 5 we plot the theoretical curves of PSV-distance relation for different seismic albedo B_0 when the extinction length is fixed at 15 km. A smaller albedo means a smaller intrinsic Q and therefore has a steep decrease of amplitude with distance. Figure 6 shows different curves of different albedos when the intrinsic Q is fixed at Q_a=1350. We can see that the strong scattering will make the apparent attenuation much bigger than the intrinsic attenuation when the distance is larger than the absorption extinction length, L_a. However, the amplitude change is not exponential for small distances.

Results given in Table 1 give a good fit to the data with a consistent set of parameters at f=1 Hz and f=5 Hz. They suggest a frequency dependent anelastic Q with Q_a=270 at 1 Hz and Q_a=1350 at 5 Hz. As it was discussed in the first section while reviewing the laboratory data, such variation of Q with frequency cannot be explained without a relaxation mechanism. In the crust, the fluids may provide such a mechanism.

3. EFFECTS OF FLUIDS ON ATTENUATION

A fracture medium can be viewed as a fully saturated porous material of low porosity and relatively high permeability. Following Biot (1956a,b; 1962), such a finite porosity rock is modeled as a statistically isotropic material composed of a solid elastic matrix permeated by a network of interconnected pores saturated by a compressible viscous liquid. The liquid phase is then continuous and the wavelength of the signal is considered to be large compared to the characteristic pore dimension. As it allows the analysis of the propagation of a total wavefield, this model has been the basis of numerous studies in various fields. However, it was not until recently that Plona (1980) and Plona and Johnson (1980) experimentally demonstrated the validity of the theory. It predicts the

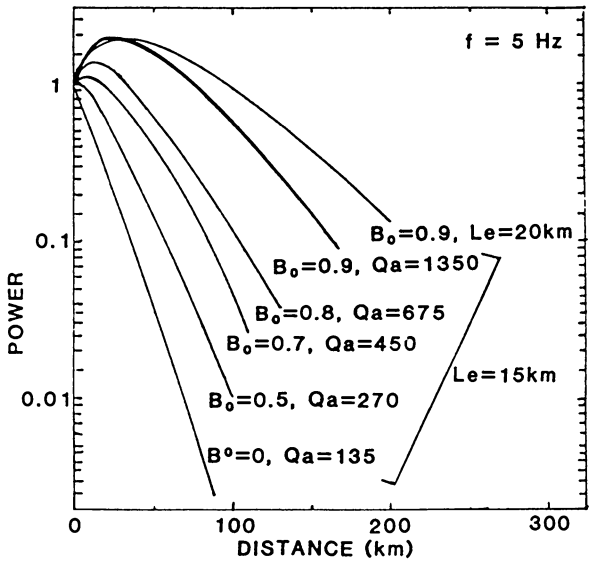

Figure 5. Sensitivity of theoretical curves (Power versus radial distance) at f = 5 Hz, to different model parameters. The model that fit the data best is shown as a "heavy" line.

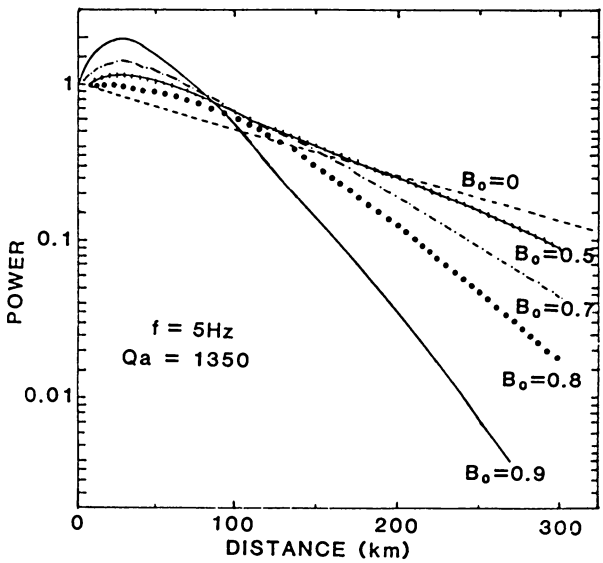

Figure 6. Sensitivity of theoretical curves to albedo (B_o) values at f = 5 Hz as a function of distance. Fixed parameters are L_e = 15km, Q_a = 1350. The model that fit the data best is shown as a solid line.

existence of three types of body waves: a compressional wave of the first kind (P_1), which displays high velocity and quasi elastic properties; a compressional wave of the second kind (P_2), associated with low velocity and quasi viscous characteristics, and a shear wave. All three body waves are dispersive and dissipative: their velocities and attenuations are frequency dependent. In this study, we will focus on the traditional P (i.e, P_1) and S waves.

Energy dissipation due to fluid flow is related to the relative motion of the two phases which are coupled through inertial and viscous forces. These are characterized by a vicous ($b(\omega)$) and a mass ($\alpha_{22}(\omega)$) coupling coefficients which can be expressed as functions of the imaginary and real parts (respectively) of the spectral signature of the material which is itself function of the pore shape and the pore geometry (Auriault et al., 1985; Schmitt, 1985). These forces are of the same order of magnitude for a so-called critical frequency f_{ci} given by:

$$f_{ci} = \frac{b(o)}{2\pi\, \rho_{22}(0)} = \frac{\nu\tilde{\phi}}{2\pi\tilde{k}\rho_f\theta} \tag{8}$$

where ν is the dynamic viscosity of the fluid, $\tilde{\phi}$ is the porosity, ρ_f is the fluid density θ is a coefficient characteristic of the pore shape and pore geometry and $\tilde{k}$ is the intrinsic permeability of the porous material.

Below the critical frequency, i.e. in the low frequency range, the viscous forces are dominant and the fluid flow follows Poiseuille's law. The attenuation (Q^{-1}) of P and S waves is then proportional to frequency. In the high frequency range, i.e. above the critical frequency, the viscosity effect takes place in a very thin boundary layer close to the pore wall and the inertial forces become dominant. The attenuation of both P and S waves is then proportional to the inverse of the square root of the frequency. The attenuation is maximum at the critical frequency for both the P and S waves. The theoretical prediction of the behavior of the attenuations above the critical frequency approximates quite well the observed frequency dependence (i.e., Q is proportional to $f^{0.4}$ in the Northeast and to $f^{0.45}$ in the West). It implies that the critical frequency is $f_{ci} \leq 1$ Hz.

In addition to the fluid flow attenuation, the P and S waves are attenuated due to Coulomb friction between grains of the rock. This attenuation is independent of frequency (Walsh, 1966). In a porous material, elastic constants can be expressed as functions of the bulk moduli of the constitutive grains K_s, the skeleton K_b and the fluid K_f, the shear modulus of the skeleton μ_b and the porosity ϕ (see Appendix B). The constant Q of the solid can be introduced through equation B-4.

To calculate attenuation due to fluid flow, we take a crustal crystalline rock model saturated with water. The physical parameters of the medium are given in Appendix B. The viscosity used for the fluid is 0.2 centipoise. This value corresponds to water viscosity at a temperature of 100°C.

The critical frequency defined by equation 8 is a function of the pore geometry, the permeability and the porosity. To obtain a critical frequency close to 1 Hz, using cylindrical ducts in two perpendicular

directions, typical values of permeability and porosity are: 50 darcies, 0.5%; 100 darcies, 1%; and 200 darcies, 2%. These sets of parameters give a critical frequency of 1.21 Hz. If instead of ducts we use fractures of equivalent permeability, we obtain fracture apertures of 20 to 800 μm. With increasing porosity, this leads to fracture densities of 0.6, 1.2 and 2.5 per meter. Although the fracture widths and densities are not unrealistic for the shallow part of the crystalline crust where drillings core and borehole studies have been done, it is necessary to do more detailed modelling to evaluate the effects of interconnected fractures systems.

Figures 7a, b display the velocity dispersion and attenuation for P and S waves between 0.1 and 100 Hz due to fluid flow. For both waves, the velocity dispersion is small. The maxima of attenuation decreases with decreasing porosity because of smaller volume of fluid. The attenuation of the S wave is much greater than that of the P wave. For shear waves Q values at successive maxima are equal to 700, 1400, and 2800. At 5 Hz, we obtain shear Q values of 1100, 2000 and 4000, in the range of Q values given in Table 1.

Adding the attenuation in the solid as constant Q raises the total attenuation values. Figures 8a,b display the results obtained with addition of constant quality factors of 500. For the S wave, the attenuation maxima now obtained corresponds exactly to the sum of the inverse of both quality factors (this rule does not hold for the P waves because of the presence of the P_2 wave). For shear waves, the Q values at 1.2 Hz for the three models are 290, 370 and 420, respectively. These fall in the range of Q values given in Table 1. For a higher Q, any Q=2000, shear Q values will more nearly approximate those given above. If we accept anelastic Q values given in Table 1(Q=270 at 1 Hz and Q=1350 at 5 Hz), then we need to combine the fluid flow mechanism with a constant Q value of 500 to 2000 in order to explain the attenuation. The upper limit of 2000 is obtained from the minimum plausible solid attenuation (Clark et al., 1980).

These simple calculations show that a combination of attenuation due to solid friction (constant Q) and fluid flow can explain the attenuation values after removing the scattering effects. The importance of fluid flow contribution is that it can explain the frequency dependence of observed intrinsic Q values of S waves.

4. DISCUSSION AND CONCLUSIONS

In this paper, we proposed three mechanisms to explain the attenuation of earthquake ground motion in the distance range of 10 to 100 km. These include multiple scattering due to heterogeneities in the crust, Coulomb friction in rocks and viscous dissipation due to fluid motions in cracks. In order to determine the relative importance of these mechanisms, we considered the Q measurements made in the laboratory, determined by the decay of coda waves of local seismograms and the amplitude decay of strong motion records in northeastern United States and Canada.

Laboratory data suggest that in rocks where there is no fluid flow Q is constant over a wide range of frequency. Fluid motion in pores and

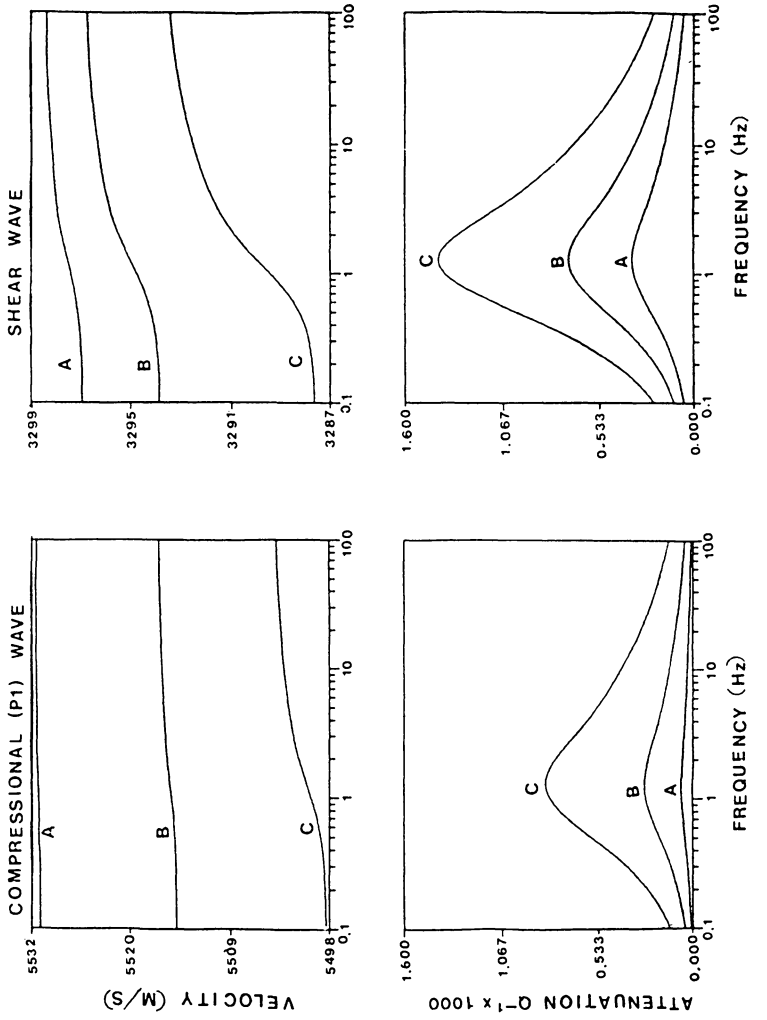

Figure 7. Velocity and attenuation (Q^{-1}) of P and S waves, as a function of frequency, due to fluid flow. The three models are for different porosity (ϕ) and permeability ($\tilde{k}$) values of fractured rock. A:ϕ = 0.5%, $\tilde{k}$ = 50 darcies; B:ϕ = 1%, $\tilde{k}$ = 100 darcies; C:ϕ = 2%, k = 200 darcies. The rock anelasticity is assumed to be zero. Note that velocity dispersion is small, but changes in attenuation are significant.

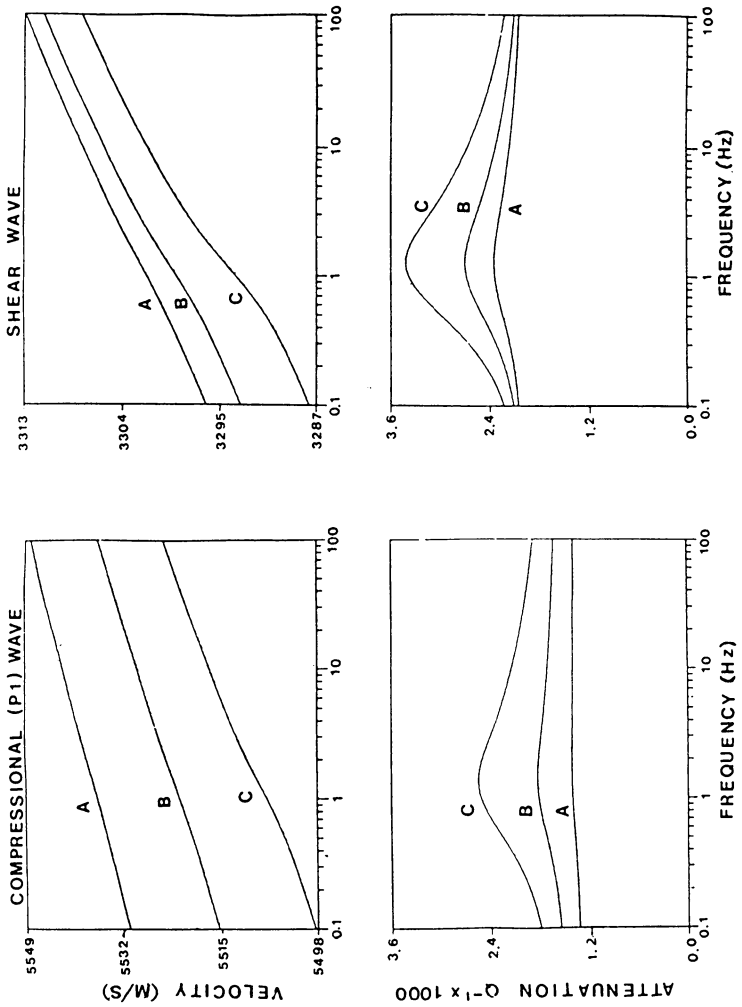

Figure 8. Velocity and attenuation of P and S waves due to fluid flow and rock anelasticity (Q_0=500). All other parameters are the same as those of Figure 7.

cracks introduces a frequency dependent Q. Frequency dependence is strongly controlled by a critical frequency which is a function of crack or pore geometry, porosity, permeability and fluid viscosity. Below the critical frequency Q decreases with frequency and above the critical frequency, Q increases with frequency. This increase is proportional to the square root of frequency.

The increase of Q with frequency and proportionality constant ($Q \propto f^{0.5}$) is very close to values determined for the crust from the coda wave analysis. Since coda decay provides a measure of the intrinsic attenuation in the crust, it is reasonable to assume that, in addition to constant Q, fluid flow plays an important role in attenuation in the crust. For the Northeast, we find the intrinsic constant Q to be high ($500 \leq Q \leq 2000$). The fluid flow effects on attenuation are as large or larger than that of the intrinsic attenuation in the frequency range of 1 to 10 Hz.

The scattering analysis of strong motion records at 1 Hz and 5 Hz in the distance range of 10-200 km gives a large albedo (B_0=0.9), implying strong scattering. In addition to albedo the only property of the scatterers that can be determined is the scattering extinction length. We obtain an extinction length of about 17 km for f=1 Hz and 5 Hz. The scatterers could be geologic fractures such as individual plutons, rock type changes, shear zones, dikes, sills or, most likely, a combination of all these.

It is important to state that the above discussions are based on a limited amount of data and theoretical models that make simplifying assumptions. It is necessary to analyze additional near-field data and to improve the models in order to draw firm conclusions.

5. ACKNOWLEDGEMENTS

We would like to thank Dr.Anton M.Dainty for critical discussions and his valuable suggestions. This work was supported by the United States Geological Survey under contract number 14-08-0001-G1092 and by the Advanced Research Project Agency of the Department of Defense and monitored by the Air Force Geophysical Laboratory under contract number F19628-86-K-0004.

6. REFERENCES

Aki, K., and Chouet, B.,(1975),Origin of coda waves: source, attenuation and scattering effects, J.Geophys. Res., 80, 3322-3342.

Aki, K.,(1980),Attenuation of shear waves in the lithosphere for frequencies from 0.05 to 25 Hz, Phys. Earth Planet. Inter., 21, 50-60.

Aki, K., and Richards, P.G.,(1980),Quantitative seismology. Theory and methods. W.H. Freeman and Co., San Francisco.

Auriault, J.L., Borne, L., and Chambon, R.,(1985), Dynamics of porous saturated media, checking of the generalized law of Darcy, J.Acoust.Soc. Am., 77, 1641-1650.

Birch, F., and Bancroft, D.,(1938), Elasticity and internal friction in a long column of granite, Bull. Seism. Soc. Am., 28, 243-254.

Bradley, J.J., and Fort, A.N.Jr.,(1966), Internal friction in rocks in Handbook of Physical constants, S.P.Clark, Jr., Ed., GSA Publ., p.175-193.

Brown, R.J.S., and Korringa, J.,(1975), On the dependence of the elastic properties of a porous rock on the compressibility of the pore fluid, Geophysics, 40, 608-616.

Biot, M.A.,(1956a), Theory of propagation of elastic waves in a fluid saturated porous solid. I.Low frequency range, J.Acoust. Soc.Am., 28, 168-178.

Biot, M.A.,(1956b), Theory of propagation of elastic waves in a fluid saturated porous solid. II.Higher frequency range, J.Acoust. Soc. Am., 28, 179-191.

Biot, M.A.,(1962), Mechanics of deformation and acoustic propagation in porous media, J.Appl. Phys., 33, 1482-1488.

Clark, V.A., Spencer, T.W., Tittmann, B.R., Ahlberg, L.A., and Coombe, L.T.,(1980), Effect of volatiles on attenuation Q^{-1} and velocity in sedimentary rocks, J.Geophys. Res., 85, 5190-5198.

Dainty, A.M., Goins, N.R., and Toksöz,M.N.,(1976), Seismic investigation of the lunar interior, in Lunar science VII:Houston Lunar Science Institute, p.181-183.

Dainty, A.M., and Toksöz,M.N.,(1977), Elastic wave propagation in a highly scattering medium. A diffusion approach, J.Geophys., 43, 375-388.

Dainty, A.M., and Toksöz,M.N.,(1981), Seismic codas on the Earth and the Moon: a comparison, Phys. Earth and Plan. Int., 26, 250-260.

Dunn, K.J.,(1985), Acoustic attenuation in fluid saturated porous cylinders at low frequencies, J.Acoust.Soc.Am, 79, 1709-1721.

Gao, L.S., Lee, L.C., Biswas, N.H., and Aki, K.,(1983a), Comparison of the effects between single and multiple scattering on coda waves for local earthquakes, Bull.Seism. Soc. Am., 73, 373-389.

Gao, L.S., Lee, L.C., Biswas, N.H., and Aki, K.,(1983b), Effects of multiple scattering on coda waves in three-dimensional medium, Pure and Applied Geoph., 121, 3-15.

Gardner, G.H.F., Wyllie, M.R.J., and Droschack, D.M. (1964), Effects of pressure and fluid saturation on the attenuation of elastic waves in sands, J.Petr.Tech., 189-198.

Gupta, I.N., Burnetti, A., McElfresh, T.W., von Seggern, D.H., and Wagner, R.A. (1983), Lateral variations in attenuation of ground motion in the eastern United States based on propagation of L_g.NUREG/CR-3555, U.S. Nuclear Regulatory Commission, Washington, D.C.

Hermann, R.B. (1980), Q estimates using the coda of local earthquakes, Bull. Seism. Soc. Am., 70, 447-468.

Johnston, D.H., and Toksöz, M.N. (1980), Ultrasonic P and S wave attenuation in dry and saturated rocks under pressure, J.Geophys. Res., 85, 925-936.

Klima, K., Vanek, J., and Pros, Z. (1964), The attenuation of longitudinal waves in diabase and greywacke under pressure up to 4 kilobars, Studia Geoph. et Geod., 8, 247-254.

Knopoff, L. (1964), Q, Rev. Geophys., 2, 625-660.

Kopnichev, Y.F. (1977), The role of multiple scattering in the formation of a seismogram tail, Izv. Acad. Sci., USSR, Phys. Solid Earth, 13, 394-398.

Mason, W.P., Beshers, D.N., and kuo, J.T., (1970), Internal friction in Westerly granite: Relation to dislocation theory, J.Appl. Phys., 41, 5206-5209.

Nur, A., and Winkler, K. (1980), The role of friction and fluid flow in wave attenuation in rocks (abst.), Geophysics, 45, 591-592.

O'Doherty, R.F., and Anstey, N.A., (1971), Reflections on amplitudes, Geophys. Prospect., 19, 430-458.

Pandit, B.I., and Savage, J.C. (1973), An experimental test of Lomnitz's theory of internal friction in rocks, J.Geophys. Res., 78, 6097-6099.

Peselnick, L., and Outerbridge, W.F. (1961), Internal friction in shear and shear modulus of Solenhofen limestone over a frequency range of 10^7 cycles per second, J.Geophys. Res., 66, 581-588.

Plona, T.J., Observation of a second bulk compressional wave in a porous medium at ultrasonic frequencies, Appl. Phys. Lett., 36, 256-261.

Plona, T.J., and Johnson, D.L. (1980), Experimental study of the two bulk compressional modes in water saturated porous structures, Ultrasonic Symposium, 864-872.

Pulli, J. (1984), Attenuation of coda waves in New England, Bull. Seism. Soc. Am., 74, 1149-1166.

Rautian, T.G., and Khalturin, V.I. (1978), The use of the coda for the determination of the earthquake source spectrum, Bull. Seism. Soc. Am., 1809-1827.

Richards, P.G., and Menke, W. (1983), The apparent attenuation of a scattering medium, Bull. Seism. Soc. Am. 73, 1005-1021.

Roecker, S.W., Tucker, B., King, J., and Hatzfled, D. (1982), Estimates of Q in central Asia as a function of frequency and depth using the coda of locally recorded earthquakes, Bull. Seism. Soc. Am., 72, 129-149.

Schmitt, D.P. (1985), Simulation numérique de diagraphies acoustiques. Propagation d'ondes dans des formations cylindriques axisymétriques radialement stratifiées incluant des milieux élastiques et/ou poreux saturés. Ph.D. thesis. Grenoble Univ.

Singh, S. (1985), L_g and coda wave studies of Eastern Canada, Ph.D. thesis Saint Louis University, Missouri.

Singh, S., and Hermann, R.B. (1983), Regionalization of crustal coda Q in the continental United States, J.Geophys. Res., 88, 527-538.

Spencer, J.W., Jr. (1981), Stress relaxations at low frequencies in fluid saturated rocks: attenuation and modulus dispersion. J.Geophys. Res., 86, 1803-1812.

Tittmann, B.R., Housley, R.M., Alers, G.A., and Cirlin, E.H. (1974), Internal friction in rocks and its relationship to volatiles on the moon, in Lunar Science Conf., 5th Proc., Geochim. et Cosmochim. Acta, suppl. 5, v.3, 2913-2918.

Tittmann, B.R., Nadler, H., Clark, V.A., Ahlberg, L.A., and Spencer, T.W. (1981), Frequency dependence of seismic dissipation in saturated rocks, Geophys. Res. Lett., 8, 36-38.

Toksöz, M.N., Johnston, D.H., and Timur, A. (1979), Attenuation of seismic waves in dry and saturated rocks. I.Laboratory measurements, Geophysics, 44, 681-690.

Toksöz, M.N., and Johnston, D.H. (1981), Seismic wave attenuation. Editors. Geophysics reprint series No.2. Society of Exploration Geophysicist.

Wallsh, J.B. (1966), Seismic wave attenuation in rock due to fracture, J.Geophys. Res., 17, 2591-2599.

Winkler, K., and Nur, A. (1979), Pore fluids and seismic attenuation in rocks, Geophys. Res. Lett., 6, 1-4.

Wu, R.S. (1984), Multiple scattering and energy transfer of seismic waves and the application of the theory to Hindu Kush region, in "Seismic wave scattering and the small scall inhomogeneities in the lithosphere", Chapter 4, Ph.D.thesis, Mass. Inst.Tech., Cambridge, M.A.

Wu, R.S., Multiple scattering and energy transfer of seismic waves. Separation of scattering effect from intrinsic attenuation. I.Theoretical modelling., Geophys. J. R.Astr. Soc., 82, 57-80.

Wu, R.S., and Aki.K. (1985), Multiple scattering and energy transfer of seismic waves. Separation of scattering effect from intrinsic attenuation. II.Application of the theory to Hindu Kush region, submitted to J.Geophys. Res..

APPENDIX A

The elastic wave energy received by an isotropic point receiver in a random heterogeneous medium can be represented by the average energy density $E(\underline{r})$ at that point. The energy density in radiative transfer theory is defined as (see Wu, 1985):

$$E(\underline{r}) = \frac{1}{C} \int_{4\pi} I(\underline{r},\hat{\Omega}) d\Omega \tag{A-1}$$

where C is the wave velocity, and $I(\underline{r},\hat{\Omega})$ is the specific intensity or directional intensity. It gives the power flowing within a unit solid angle in the direction $\hat{\Omega}$($\hat{\Omega}$ is the unit vector) received by a unit area perpendicular to $\hat{\Omega}$, in a unit frequency band. The specific intensity is defined for a frequency ω, which is omitted in the notation. Since the P wave energy is much smaller than the S wave energy for earthquakes, we consider here $I(\underline{r},\hat{\Omega})$ as only the S wave energy by neglecting the mode converted energy from P waves. We assume here also that the wave energy described by $I(\underline{r},\hat{\Omega})$ is depolarized, i.e. the energy is equally partitioned between the two orthogonal components of S waves. This agrees generally with the observations.

From the radiative transfer equations we can obtain the equation for the transfer energy density:

$$E(\underline{r}) = E_{in} e^{-\eta_e l} + \int_V \left[\eta_s E(\underline{r}_1) + \varepsilon(\underline{r}_1,\hat{\Omega})\right] G_0(\underline{r} - \underline{r}_1) dV_1 \tag{A-2}$$

where E_{in} is the incident field and,

$$\varepsilon(\underline{r}_1,\hat{\Omega}) = \frac{4\pi}{C} W(\underline{r}_1,\hat{\Omega}) \tag{A-3}$$

is the source energy density function, where W is the source power spectral density, and

$$G_0(\underline{r}_1 - \underline{r}) = \frac{e^{-\eta_e R}}{4\pi R^2} = \frac{e^{-\eta_e |r-r_1|}}{4\pi |r - r_1|^2} \tag{A-4}$$

In (A-2), suppose the incident field $E_{in}=0$ and the isotropic point source is located at $\underline{r} = 0$, radiating total power P_0. Then

$$\varepsilon(\underline{r}) = \frac{P_0}{C} \delta(\underline{r}) = E_0 \delta(\underline{r}) \tag{A-5}$$

and Equation (A-2) becomes:

$$E(\underline{r}) = E_0 \frac{e^{-\eta_e r}}{4\pi r^2} + \int_V \eta_s E(r_1) \frac{e^{-\eta_e |\underline{r}-\underline{r}_1|}}{4\eta |\underline{r} - \underline{r}_1|^2} dV_1 \tag{A-6}$$

Assuming $E_0 = 1$, the solution can be written as:

$$E(\underline{r}) = \frac{\eta_e P_d}{4\pi r} \exp(-\eta_e d_0 r) + \frac{\eta_e}{4\pi r} \int_1^\infty f(s, B_0) \exp(-\eta_e r S) d_s$$

$$= E_d(r) + E_c(r) \tag{A-7}$$

where

$$P_d = \frac{2d_0^2(1 - d_0^2)}{B_0(d_0^2 + B_0 - 1)} \tag{A-8}$$

and d_0 is the diffuse multiplier determined by:

$$\frac{B_0}{2d_0} \ln \left\{ \frac{1 + d_0}{1 + d_0} \right\} = 1; \tag{A-9}$$

and

$$f(s, B_0) = \left\{ \left[1 - \frac{B_0}{s} \tanh^{-1}\left(\frac{1}{s}\right) \right]^2 + \left(\frac{\pi}{2} \frac{B_0}{s}\right)^2 \right\}^{-1} \tag{A-10}$$

The first term in Equation (A-7) is the diffuse term E_d and the second term is the coherent term E_c.

Note that the diffuse multipler d_0 is always less than 1. When distance r is large, especially for large B_0, the diffuse term becomes dominant, and E(r) will be approximately an exponential decay with an apparent attenuation coefficient $d_0\eta_e$, which is less than the extinction coefficient η_e. The degree of reduction depends on the albedo B_0. Figure 1 shows the energy density distribution with distances for different albedo values.

APPENDIX B

EXPRESSIONS OF THE ELASTIC COEFFICIENTS

The elastic coefficients A and N are equivalent to Lamé's coefficients. $\tilde{R}$ is a measure of the fluid pressure needed to move a given fluid volume into the porous aggregate, the total volume being constant. T is related to the fluid and solid volume variations. These coefficients can be easily expressed as functions of the bulk moduli of the solid K_s, the skeleton K_b and the fluid K_f, the shear modulus of the skeleton μ_b and the porosity $\tilde{\phi}$. Following Plona and Johnson (1980), one has:

$$\left\{\begin{aligned} A &= \frac{(1-\tilde{\phi})(1-\tilde{\phi}-\frac{K_b}{K_s})K_s + \tilde{\phi}\frac{K_s}{K_f}K_b}{1-\tilde{\phi}-\frac{K_b}{K_s}+\tilde{\phi}\frac{K_s}{K_f}} - \frac{2}{3}N \\ T &= \frac{(1-\tilde{\phi}-\frac{K_b}{K_s})\tilde{\phi}K_s}{1-\tilde{\phi}-\frac{K_b}{K_s}+\tilde{\phi}\frac{K_s}{K_f}} \\ \tilde{R} &= \frac{\tilde{\phi}^2 K_s}{1-\tilde{\phi}-\frac{K_b}{K_s}+\tilde{\phi}\frac{K_s}{K_f}} \\ N &= \mu_b \end{aligned}\right. \tag{B-1}$$

In the above expression, it is assumed that the porosity does not vary with the pore pressure (Brown and Korringa, 1975; Dunn,1985).

Denoting α_m and β_m, the compressional and shear wave velocities of the dry rock, one can write:

$$\begin{aligned} K_b &= (1-\tilde{\phi})\rho_s(\alpha_m^2 - 4\beta_m^2/3) \\ N &= (1-\tilde{\phi})\rho_s\beta_m^2 \end{aligned} \tag{B-2}$$

and for the fluid

$$K_f = \rho_f\alpha_m^2 \tag{B-3}$$

If one assumes an anelastic attenuation for the P and S waves in the skeleton characterized by quality factors Q_{α_m} and Q_{β_m} and a frecuency dependence $e^{i\omega t}$, it implies a velocity dispersion of the form (e.g. Aki and Richards, 1980):

$$c(\omega) = \frac{c(\omega_0)}{(1 - \frac{1}{\pi Q} \operatorname{Log}(\frac{\omega}{\omega_0}))(1 - \frac{i}{2Q})} \qquad \text{(B-4)}$$

where

- ω_0 is a reference angular frequency
- $c(\omega)$ is the body wave velocity (α_m or β_m) at angular frequency ,
- Q is the corresponding quality factor (Q_{α_m} or Q_{β_m}).

In these conditions, α_m and β_m become complex and frequency dependent as well as K_b and the coefficients A, N, T and $\tilde{R}$.

The parameters chosen for the formation are α_m=5500 m/s; β_m=3300m/s, $K_s = 4.5\ 10^{10}$ Pa, and $\rho_s = 2700$ kgm^{-3}. When introduced, the quality factor is identical for both body waves of the skeleton and is equal to 500.

Section 3

Acquisition and Interpretation of Strong Motion Data (Including Case Histories)

DATA ACQUISITION AND PROCESSING IN STRONG MOTION SEISMOLOGY

Mauro Basili
Laboratorio Ingegneria dei Siti
ENEA
S.P. Anguillarese, 301
00100 Rome
ITALY

ABSTRACT. Intent of this paper is to describe the steps in the acquisition and processing of strong motion data. This is done referring to the Italian experience in this field. Particular emphasis in given to the problems of the management of the network and of the analog to digital conversion of data. The numerical processing of accelerograms is introduced as an important but not crucial step in the formation of data. Some comparisons between Italian and North American strong motion data are presented.

1. INTRODUCTION

The aim of this treatise is to describe the process of acquisition and processing of the accelerometric data that provide the time-history of the ground acceleration during an earthquake. The acquisition and processing of accelerometric data has to do with the following activities:

- the design of the network,
- the choosing of the instrument,
- the installation of the network set up by the selected accelerographs,
- the management of the network,
- the data collection,
- the data processing.

These activities began more than fifty years ago in the USA, the first accelerogram in the world is the one collected in Long Beach on the 10th of March 1933. Since then more than 6000 accelerographs have been installed providing many significant records.

The most adopted methodology for the formation of strong motion data is the one developed in California in the '70s; every country that used it has however had to fit it to its local facilities. I intend to point out the phases of the strong motion data formation with reference to what has been done in this field in Italy. The subject matter of this paper is organized in the following way:

M. O. Erdik and M. N. Toksöz (eds.), Strong Ground Motion Seismology, 251–331.
© 1987 by D. Reidel Publishing Company.

1. Introduction
2. Characteristics of Italian strong motion network.
3. Strong motion instrumentation.
4. Italian and American Strong Motion Data.
5. Analog to digital conversion of accelerograms
6. Accuracy of the A/D Conversion.
7. Numerical processing of strong motion data.
8. Caltech procedure.

2. CHARACTERISTICS OF THE ITALION STRONG MOTION NETWORK

In the framework of the activities carried out by the ENEA[1] - ENEL[2] Joint Commission a network consisting of 240 accelerographs has been installed and extended over the whole country, excluding Sardinia (see map in Fig. 1). This network fulfils the requirement of recording all the major earthquakes that will occur in Italy, the site for each station was selected on the basis of a statistical analysis of historical earthquakes.

As a rule, the accelerographs were installed in ENEL transformer stations (Fig. 2).

The choice of this kind of building was made for obvious economic and practical reasons and because it also meets the basic requirement of providing records that are practically not affected by soil-structure interactions thanks to the small dimensions of their enclosure.

The transformer stations selected for instrument installation,were to meet the following requirements:

- Sufficient space
- Easy access
- Sufficient distance from heavy traffic roads and railroads
- Segregation from other buildings
- Absence of filling material for the foundations
- Absence of adverse morphological conditions that could locally modify the features of the seismic event.

In a larger regional context, transformer stations built both on rocks and on loose soils were selected, whenever possible. In each station the instrument was solidly fixed to a concrete post directly anchored to the station foundation soils, but disengaged from the floor and from the loose rock foundation (Fig. 3).

Fig. 4 schematically illustrates the two types of post construction adopted depending on the nature of the foundation soil. In the case of loose soils, the post base was obtained by means of one concrete post "directly on the soil" into a trench at least 1 m deep. In the case of rock, the connection between the base and the foundation was obtained by means of four iron bars embedded in concrete.

---

[1] ENEA is the Italian Commission for Nuclear and Alternative Energy sources

[2] ENEL is the Italian Electricity Generating Board.

Figure 1(a). Italian Strong Motion Network

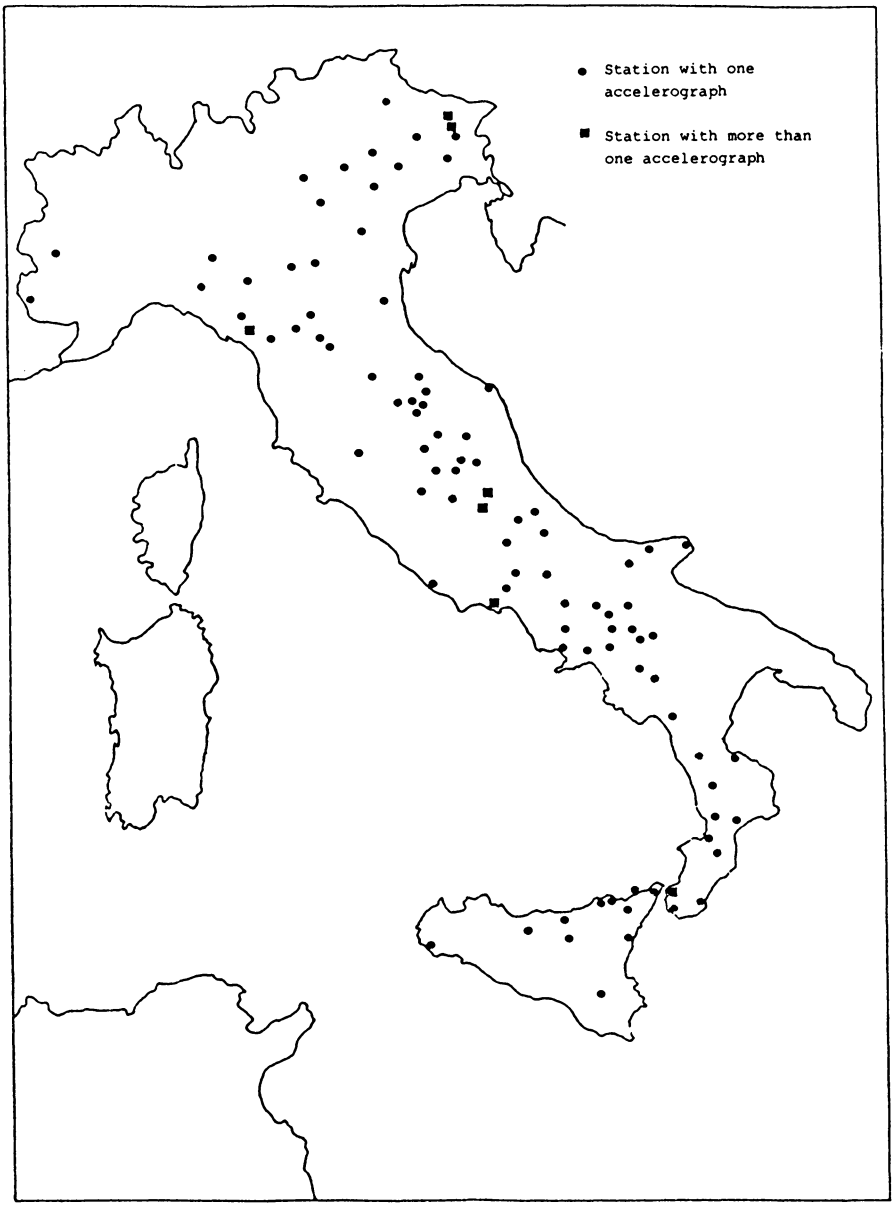

Figure 1(b). Stations triggered by seismic events

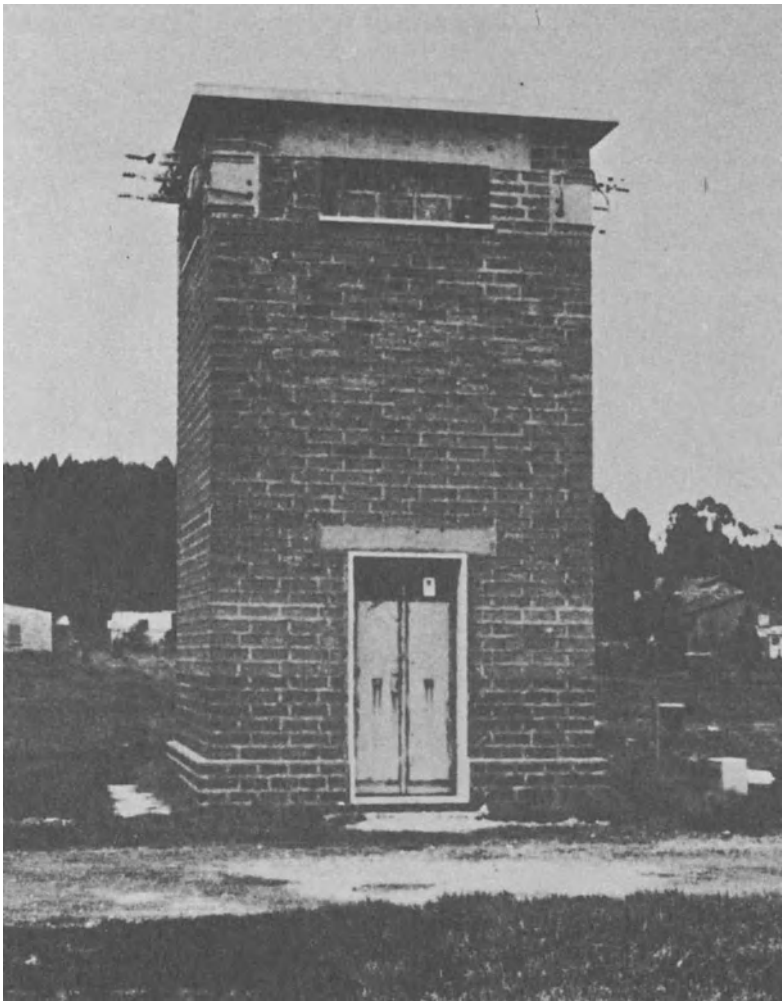

Figure 2. One of the Transformer Stations Usually Utilized to House the Accelerographs.

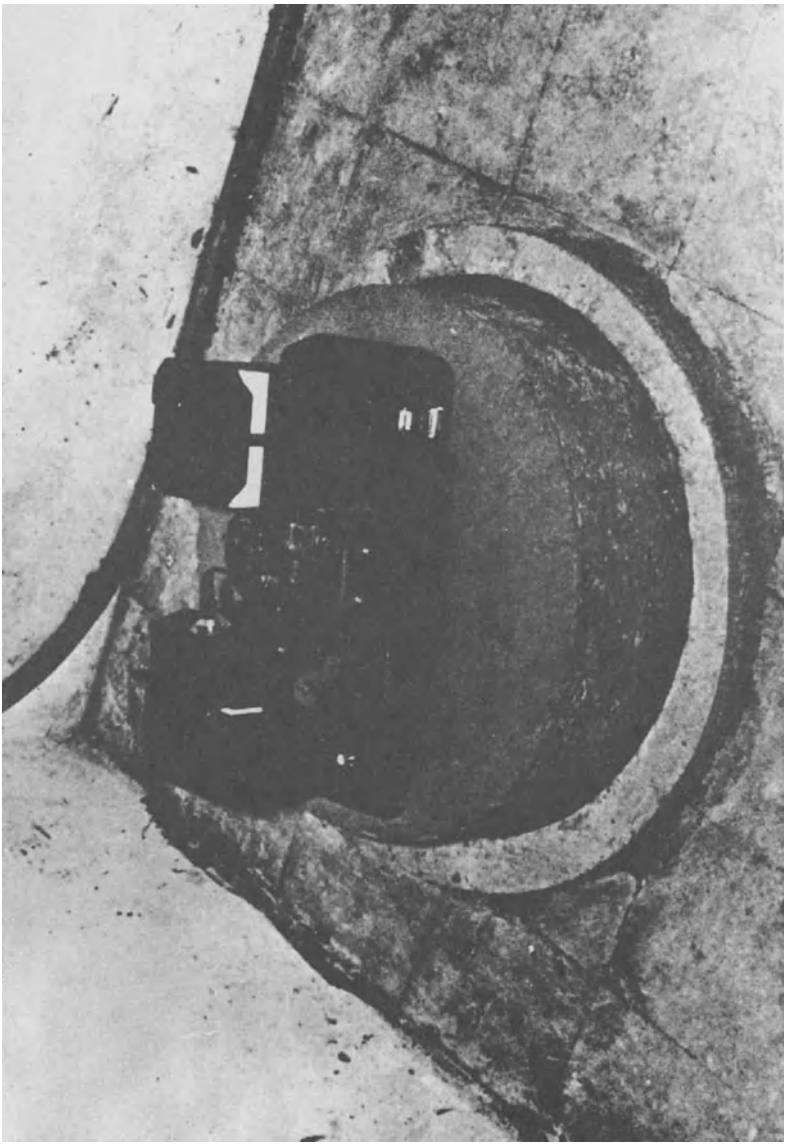

Figure 3. Accelerograph Installation

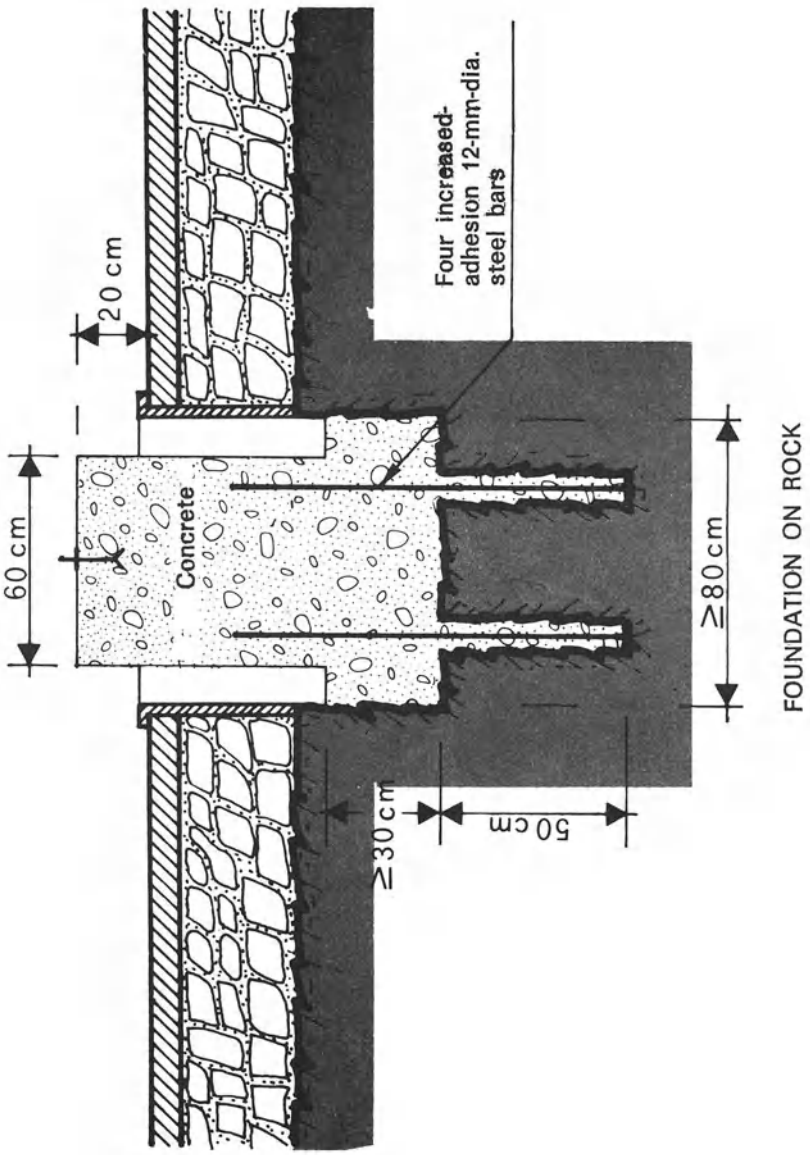
20 cm
60 cm
Concrete
Four increased-adhesion 12-mm-dia. steel bars
≥30 cm
50 cm
≥80 cm
FOUNDATION ON ROCK

Figure 4(a)

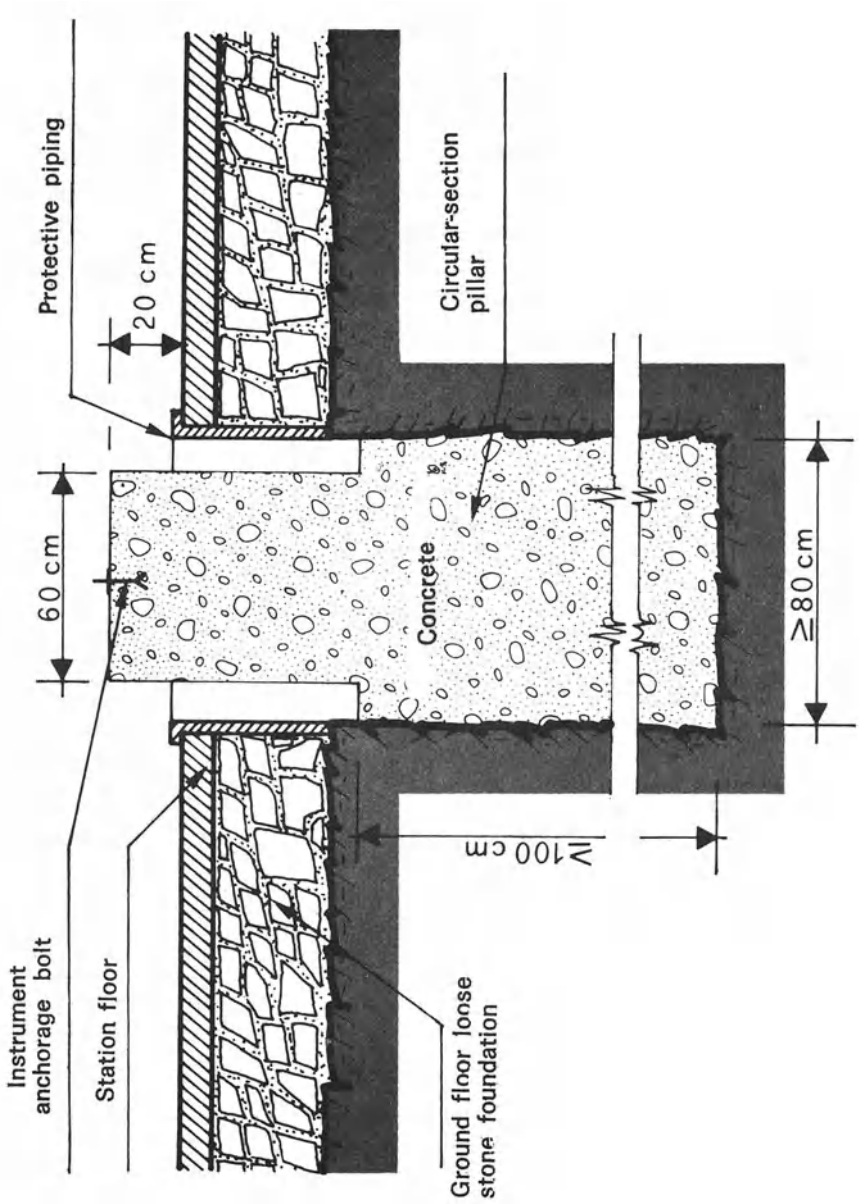

Figure 4. Foundation of the Accelerograph Anchorage Pillar

In order to prevent flexion of the abutting part of the post from altering the recordings of the instrument anchored to the post itself, the installation of each post was carried out with great care so that the length of the abutting part never exceeded 1.5 times its diameter.

The calculation of the vibration frequency for a standard post designed to the above mentioned limitation gave a value exceeding 200Hz and thus the post can be considered totally rigid or such, however, as not to affect the recording.

Recently Hudson (1983) pointed out that: "the design of strong motion systems depends very much on whether the devices were primarily individual stations, or part of a network or an array.

A network may be defined as any group of instruments having some common feature, such as management, maintenance, or data processing. Each station of the network can independently produce information of value, but the total information from the network is greater than the sum of the parts, since relationships can be established between measurements at various sites".

Greater are the common features of the strong motion system, more significant are the benefits coming from the information of the network as a whole. In the Italian network the common features are:

- same accelerographs
- same instrument housing
- same management
- same maintenance
- same data processing.

From 1973, year in which the first accelerographs were installed, to 1980 the management of the network was performed by a laboratory located in Rome. Centralized management is not convenient nor very practical. This is mainly due to the concurrence of two important factors: the considerable distance between the instruments, and the need for frequent action on the instruments both to collect the recording and to control the operating conditions of each accelerograph. Recently this activity has been taken over in part by personnel of regional offices of ENEL, 19 local centers (one in each region) have been established under the coordination of the main laboratory in Rome. These centers fulfill weekly the preventive maintenance on field following a checking list scheduled in a form such as that in Figure 5. The on field maintenance is carried out in each center by a technician 50 working days per year, while in Rome three technicians are involved full time in repairing, testing procedures and data storage. Every four months they visit each station in order to complete the checks on the instrumentation and to perform the calibration test.

Since the installation of the first accelerographs, valuable experience has been acquired on the installation and operation of these instruments and on the management criteria. It may be useful to illustrate the main aspects of this experience starting from the list of problems that arose during instrument installation and the start-up phase of network management:

- Anchorage of the accelerograph by means of expansion bolts supplied by the instrument manufactures was often unsatisfactory. Therefore, all the original bolts were replaced with

ENEL - DCO - SETTORE SITI E AMBIENTE Rete Nazionale di Rilevamento Sismico **SCHEDA DI MANUTENZIONE PROGRAMMATA**				Firma del Verificatore / DATA
POSTAZIONE DI _____				Sigla strumento installato _____
CONTROLLO TEMPORIZZATORE		fuori passo		Sigla nuovo strumento installato _____
		avanti (sec)		NOTE
		indietro (sec)		
TENSIONE DI RETE			V	
CARICA BATTERIE	Tensione di uscita con accellerografo e batterie disinserite		V	
	Tensione di uscita con carico di 200 mA		V	
BATTERIE	Tensione senza carico		V	
	Tensione finale con carico di 3A dopo 2 minuti		V	
	Data sostituzione batterie			
FUNZIONAMENTO SEGNALATORI		ACCELLEROGRAFO	regolare	
			non regolare	
		ALIMENTATORE	regolare	
			non regolare	
Valore di accellerazione di avviamento			mg +	
			mg −	
Partenza automatica			reg. / non reg.	
TENSIONE LAMPADA	PRIMA DEL CONTROLLO		V	
	DOPO IL CONTROLLO		V	
ALLINEAMENTI	REGOLARI	L	si / no	
		V		
		T		
	RETTIFICATI	L	si / no	
		V		
		T		
POSIZIONE BOBINA STARTER			reg. / non reg.	
Pellicola utilizzata per il controllo			cm.	
Rimanenza pellicola			cm.	
DATA SOSTITUZIONE PELLICOLA				

Figure 5. Checking List For the on Field Maintenance

clamps embedded in the post concrete or with more reliable espansion bolts.

- The main trouble experienced in instrument operation was mainly due to malfunctioning of the original supply system consisting of a small battery-charging system that was clearly unfit to supply the charging current required for the batteries on a continuous basis. The irregular feeder performance often caused variations in the light intensity of the projection lamp, and sometimes gave rise to faulty operation of the on-off relays of a few accelerographs. This trouble, which appears to be the most serious one, was overcome by supplying each accelerograph with a "stabilized" battery-charging system specially designed by the battery manufacturer.

- Lightning often caused accelerograph outages; besides blowing up the feeder protection fuses, they seriously damaged the feeders. The study of an a.c. supply filtering system is in progress to eliminate or, at least reduce considerably this trouble.

- Many spurious accelerograph activations followed by as many spurious recordings are to be imputed to high-frequency electric signals caused by lightning, to electric discharges associated with the opening of switches along the high-voltage lines, and to other sources not yet well identified. To eliminate this trouble, a conveniently sized filter will be installed on the trigger input amplifier.

- A very serious event, fortunately without consequences, was the explosion of an instrument, probably caused by hydrogen generation in the batteries which were originally placed inside the instrument. After this explosion the batteries were removed from the accelerograph and housed in an external container in which the stabilized feeder is also placed.

- The other failures and minor trouble fall under the normality of instrument operation; it should be mentioned however that a few of these failures can be imputed to impact and strong vibration to which the instruments were subjected in transit.

The foregoing list is sufficient to emphasize the need of frequent and accurate operability checks on the accelerographs to ensure network efficiency.

The experience in the United States on maintenance capability is approximately summarized by Figure 6 (from Matthiesen, 1976). The zero service time ordinate indicates that come of the instruments must be expected to be defective immediately after installation. With the four-month service period adopted in USA, about 95% of the accelerographs should obtain usable records, although perhaps only 60% of the records would be expected to be perfect in all respects. In Italy there has been

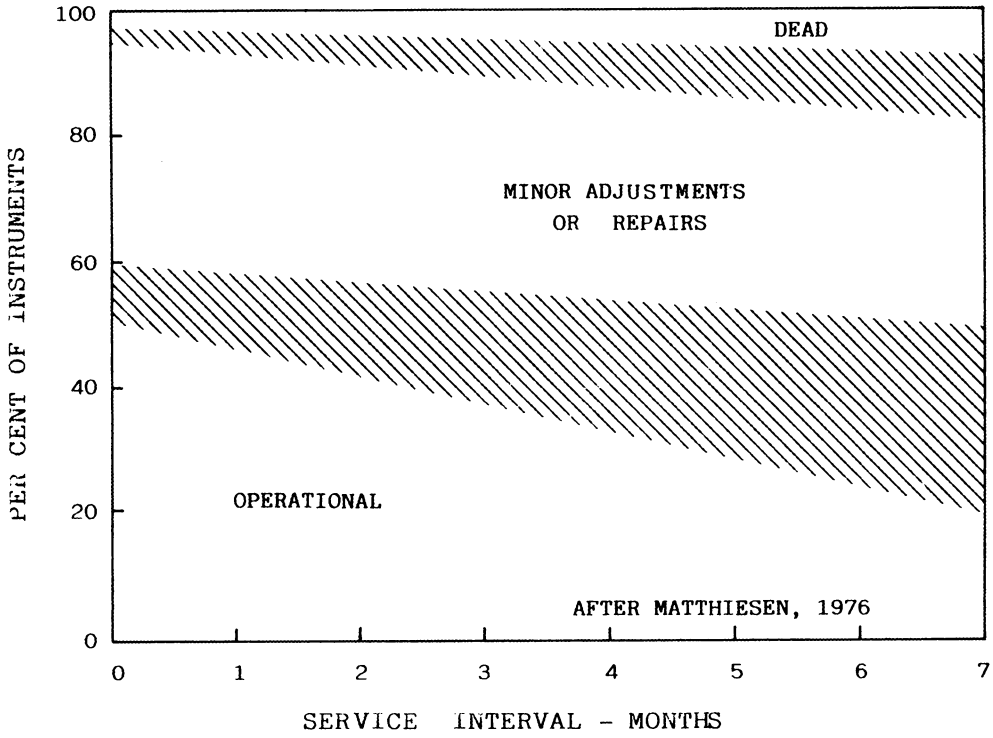

Figure 6. Operational characteristics of U.S. strong motion network.

only one case of detective working, this was for the Irpinia earthquake in 1980: an instrument was triggered by the shock but did not produce any record. More frequent are the cases of inconveniences that produce bad recordings.

The ENEA-ENEL Joint Commission has also designed a plan in order to install soon after a destructive earthquake, 20 accelerographs for a better recording of the aftershock sequence.

This sequence provides a unique opportunity to acquire experimental data needed for studying various engineering and seismological aspects of the ground motion.

The primary value of aftershock data in ground motion research is to complement the strong motion accelerograph data sample recorded from the main shock and to reduce the gaps in information which are always present. In fact the aftershock sequence provides an opportunity to deploy specially designed seismic arrays to acquire information about specific earthquake effects such as:

- ground motion variability,
- site amplification,
- effect to topography,
- soil-structure interaction,
- duration of shaking.

The aftershock data are also used to estimate ground shaking at sites where no ground motion records are obtained during the main shock.

In Italy, during the 13 years of activity in this field, 962 accelerograms have been recorded by 267 accelerographic stations (including the instruments installed in temporary arrays for collecting aftershock records). The cumulative distribution of the recorded peak ground acceleration (PGA) values is shown in Figure 7.

The cumulative expenditure, up-to-date to 1985, of the activities for the formation of the 962 accelerograms collected so far, is more than 6 million US dollars, details of the costs are shown in Figure 8. If this expenditure is considered in relation to the about 60 accelerogram components with PGA greater than 0.2 g, each component costs 100.000 US dollars. The cost involved with the realization of the network (instrumentation, installation, maintenance) is 53.2% of the cumulative expenditure, while the data processing is only the 14% of the total. The cost of the production of the accelerograms makes evident that a considerable effort in data processing is highly justified and economically convenient and dictates network systems which place the maximum simplicity in the field, with sophisticated facilities and computer codes in the laboratory.

When an earthquake triggers the instruments and consequently records are produced, the activities scheduled for the collection, storage, processing and dissemination of the data are activated. The logic scheme of the operations is shown in Figure 9.

3. STRONG MOTION INSTRUMENTATION

Figure 10, from Hudson (1983), shows in a schematic way the most used strong motion instrumentation systems. The diagram in(a) is the simplest:

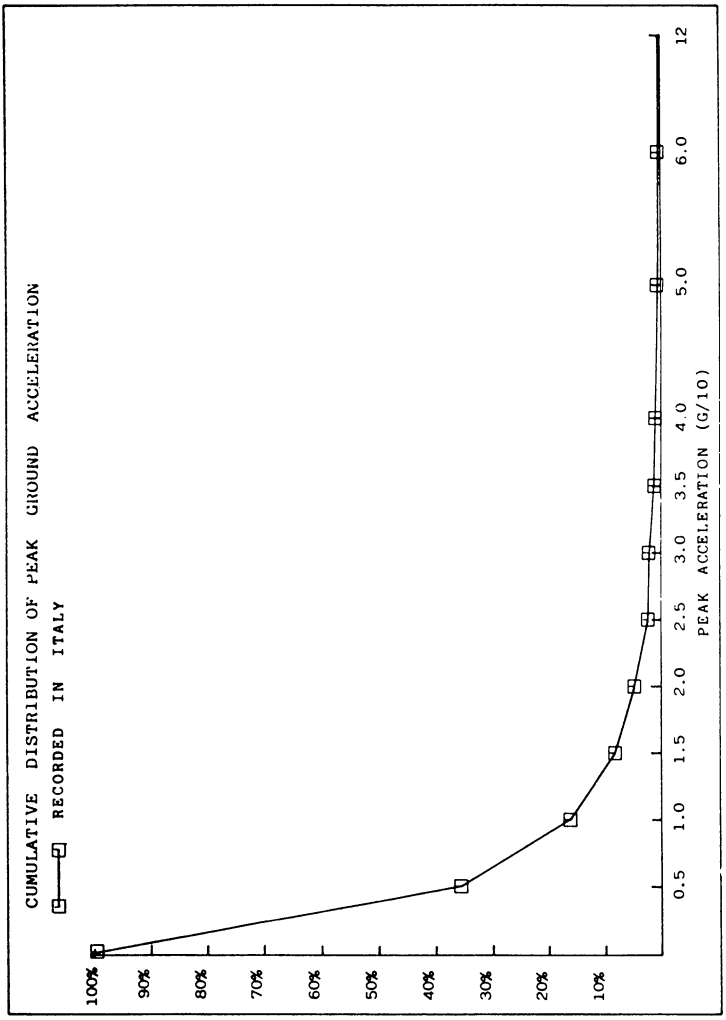

Figure 7. Cumulative distribution of peak ground acceleration recorded in Italy.

EXPENDITURE FOR THE FORMATION OF THE ITALIAN STRONG MOTION DATA

(1985 U.S. Dollars)

		% of Total
a) Cost instruments ENEL 240 SMA1 Kinem.	720,000	10.8
b) Spear parts ENEA+ENEL	50,000	0.7
c) Cost instruments 25 Mobile stations ENEA+ENEL	75,000	1.1
d) Cost site preparation, instrument housing, installation ENEL+ENEA	600,000	9.0
e) Cost of site investigation 25 triggered stations ENEA+ENEL	1,250,000	18.8
f) Cost of maintenance and management ENEA+ENEL	2,100,000	31.6
g) Cost of team expedition in occasion of destructive earth. ENEA+ENEL	600,000	9.0
h) Data storage (film proc., inventory, etc..) ENEA+ENEL	48,000	0.7
i) Autom. digit.	240,000	3.6
l) Numerical data processing	967,500	14.5
TOTAL	6,650,000	100.0

Figure 8. Cost breakdown for Italian strong motion network in US Dollars.

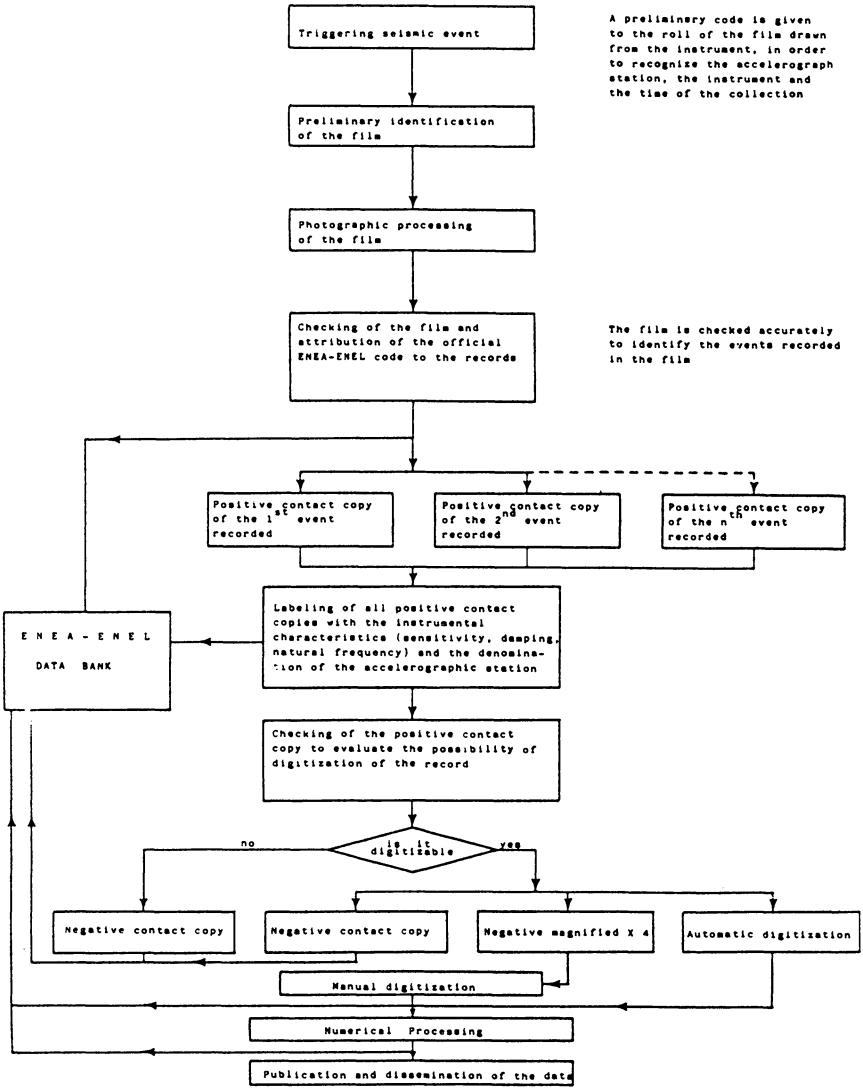

Figure 9. Activities for the Collections, Storage Processing and Dissemination of the s.m. data

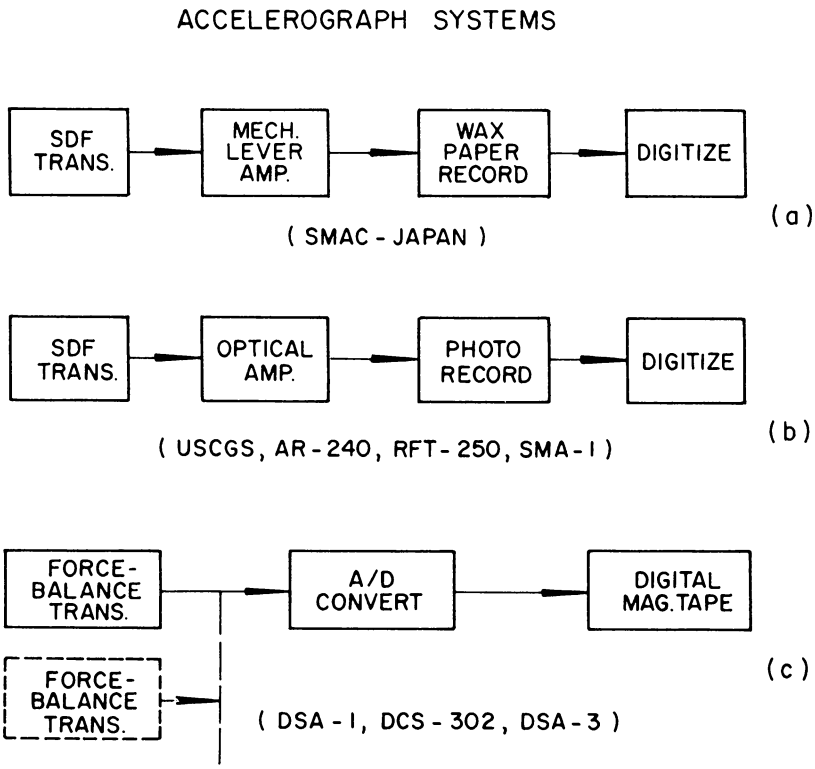

Figure 10. Accelerograph Systems (After Hudson, 1983)

the transducer is a mechanical single-degree-of-freedom (SDF) system, the magnification is obtained by mechanical levers, and the recording is by stylus on wax paper. The Japanese SMAC belongs to this type of instrumentation.

The diagram in(b), shows the most adopted type of accelerograph. The SMA-1 accelerograph, produced by Kinemetrics, belongs to this strong motion instrumentation system; this is the accelerograph adopted to set up the Italian network.

The diagram in (c) illustrates the first generation of digital recording system. Several instruments of this type have been deployed in the field. In the south of Italy, for example, an array of 10 DSA-1 Kinemetrics has been installed by ENEA on an experimental basis. Some records coming from a DSA-1 accelerograph have been collected during the aftershock sequence of the Irpinia earthquake (1980). The instrument was installed in an accelerograph station together with one of the SMA-1 type in order to compare the performances of the instruments and the records collected for the same events. The records are shown in Figure 11(a), (b).

In these last years many new types of strong motion instruments have been designed. They all tend to a massive use of digital devices giving undeniable advantages in the quality of the recording and in the speed of numerical processing but at the same time with undeniable disadvantages dealing with higher instrumentation costs, a higher level of competence and training of the field technicians, more maintenance problems.

Figure 12 shows a diagram of one of these new kinds of digital accelerograph. It has been produced by Contraves Italiana under the frame of a cooperative research program ENEA-Contraves Italiana. The system is based on MOS technology and is made of:

1) a microprocessor,
2) 12 bits A/D converter multiplexed,
3) solid state memory from 256 kbytes to 1 Mbytes,
4) standard interface for external personal computer, small display and for keyboard for checking and installation procedure,
5) wide dynamic settable gain operational amplifiers for matching impedance for remote recording.

Instrumentation of similar characteristics are available in other countries. The microprocessor is the device that makes this kind of instrument very different from the previous generations. They are capable to fit almost all the needs in engineering seismology. An array set up by 9 ENEA - Contraves instruments will be installed in the next months in archeologic areas of Rome for collecting records from possible ground motion induced by far seismic events that can be felt in the city or from weak events that occur in the southeastern Roman contryside. The data collected will give valuable information about the input motion to very old and fragile monuments.

The SMA-1 accelerographs will still give for many years significant records that need to be processed accurately and it will be necessary to back process the old records when there will be substantial improvement in the way that such analog records can be treated.

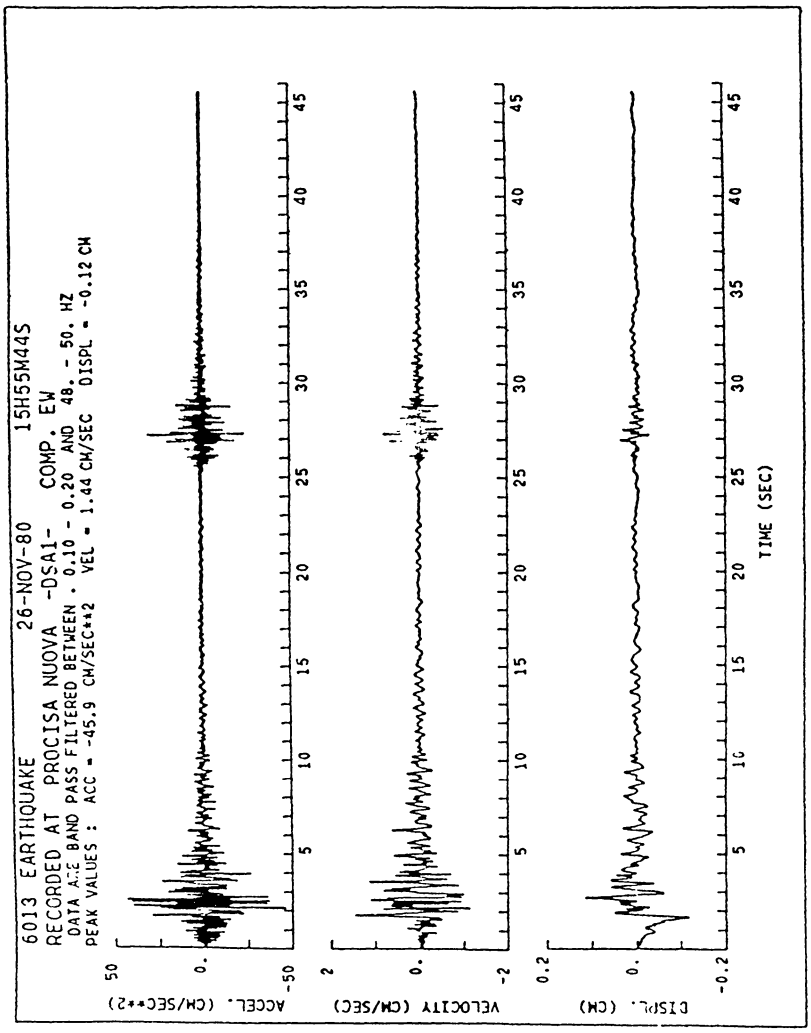

Fig.11 a

Figure 11(a). DSA-1 Record.

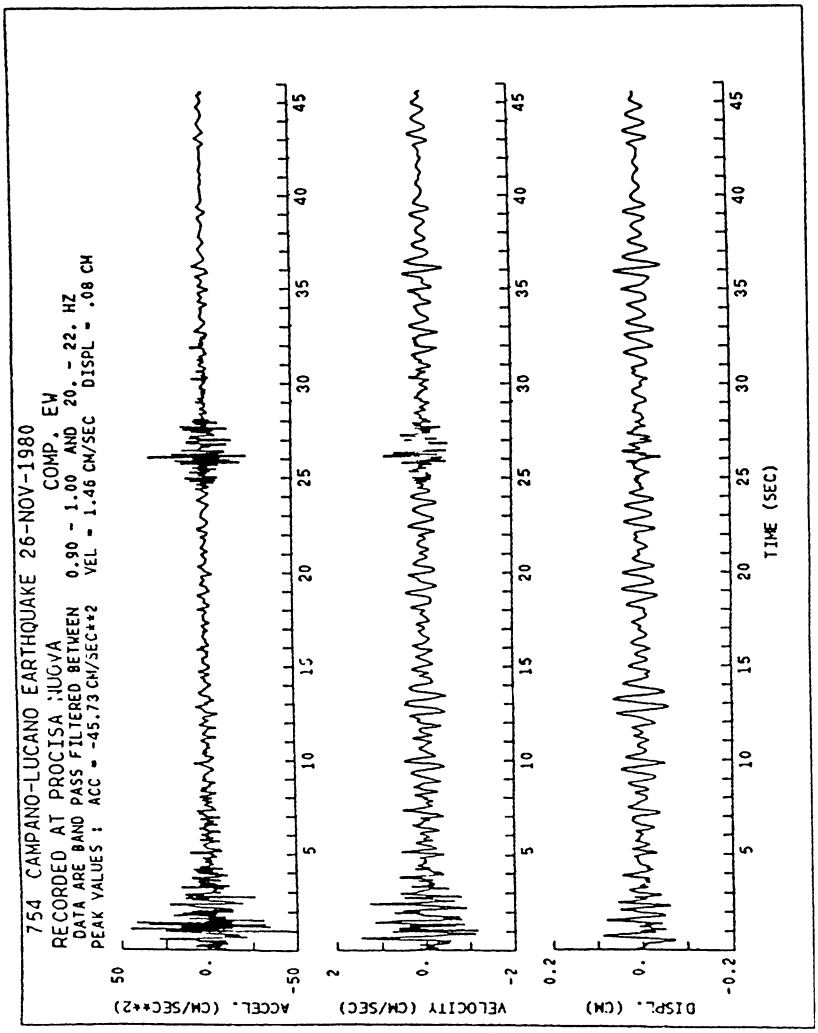

Figure 11(b) . SMA-1 Record.

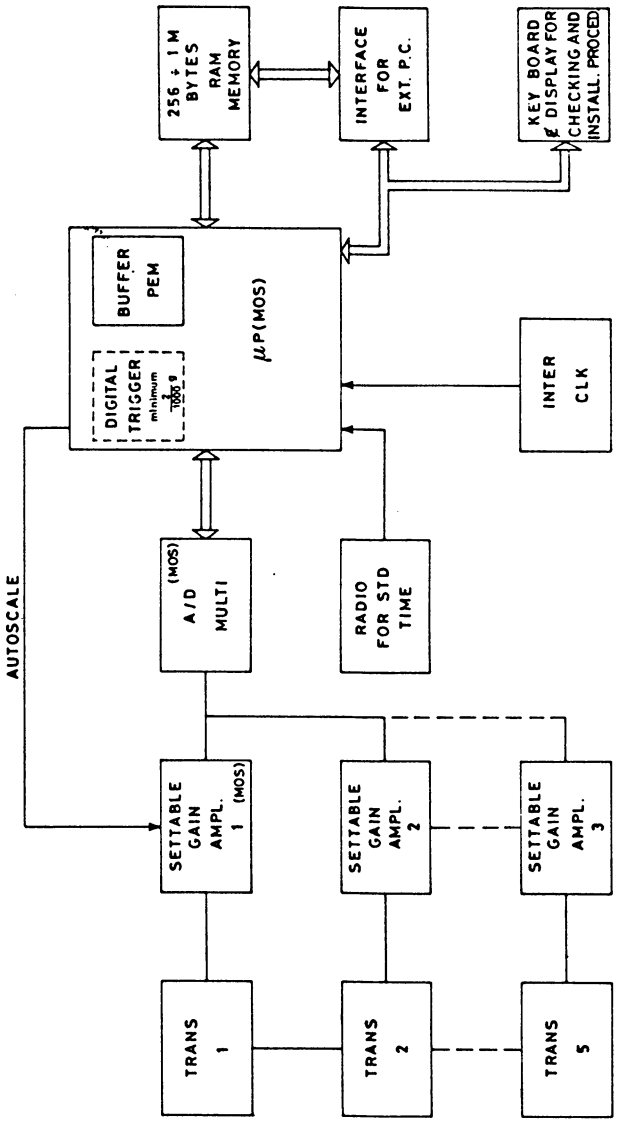

Figure 12. Solid State Accelerograph System

More in details, as shown in Figure 13, the instrument is constitued by:

a) Transducers

They are oriented in three orthogonal directions coinciding with the instrument axes.

In Figure 14 it is shown a schematic representation of one SDF transducer.

The relative motion y of the transducer mass is described by the differential equation:

$$\ddot{y} + 2\,\omega_o\,\zeta_o\,\dot{y} + \omega_o^2\,y = -\,\ddot{x} \qquad (1)$$

where ζ_o is the fraction of critical damping, ω_o is the natural frequency ($\omega_o = 2\pi\,f_o$), and $\ddot{x}$ is the absolute ground acceleration. For acceleration transducers the largest possible ω_o is chosen so that the term $\omega_o^2\,y$ dominates on the left-hand side of the equation. Furthermore, for input frequencies ω that are several times smaller than ω_o, $\ddot{y}$ and $2\,\omega_o\,\zeta_o\,\dot{y}$ are small, and $\omega_o^2\,y$ is, therefore, nearly the same as $-\ddot{x}$. For higher input frequencies, both amplitudes and phases are modified, and the correction terms involving $\ddot{y}$ and $2\,\omega_o\zeta_o\,\dot{y}$ may not be neglected.

The three components of ground motion are recorded by three transducer elements each of which is primarily sensitive to ground motion in one of the three mutually perpendicular directions. The influence of the ground accelerations in the other two directions on the transducer's motion in the primary direction is referred to as "cross-axis sensitivity' Erors caused by cross-axis motions would depend upon the acceleration levels involved in the other two directions and the amplitude of oscillations in the primary direction. For large accelerations these effect can be significantly more than about 5 per cent of the recorded amplitudes (Wong and Trifunac, 1977).

b) Trigger system

It is a unidirectional device, designed to respond to vertical motion. Basically, it is an overdamped spring-mass accelerometer. Its natural frequency is 4 Hz, and its damping is set at 1.5 critical. Its output voltage is generated by the mass, a coil of wire, moving in a magnetic field. This voltage is amplified by 1000, and fed through a single-stage, low-pass filter having a corner frequency of 15 Hz.

c) Timing system

The time-axis of the record is defined by means of two traces at the borders of the film, the traces provide time marks at equal intervals of 0.5 sec, with an accuracy within 0.2 percent of the rated interval.

In 1984 in all the instruments of the network one time mark generator has been switched to an external timing system that provide the absolute time in binary code directly on the trace.

The time on the film is the instant in which the instrument started to record the event.

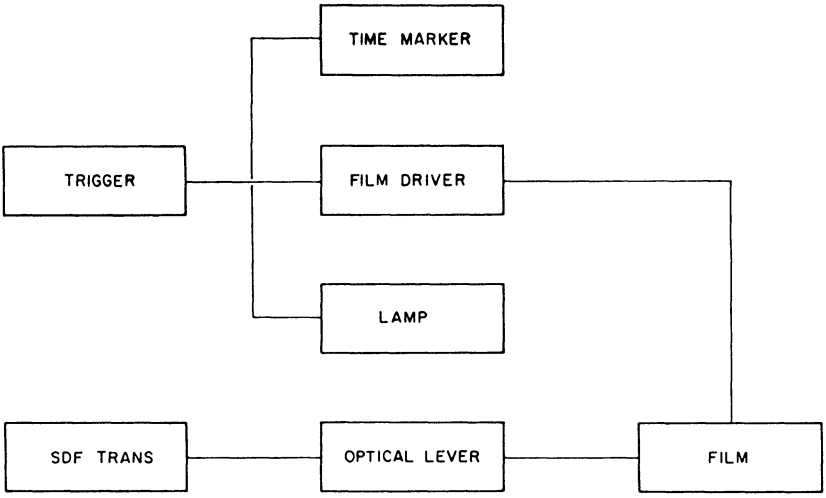

Figure 13. Schematic Representation of the SMA-1 Accelerograph

SCHEMATIC REPRESENTATION OF TRANSDUCER

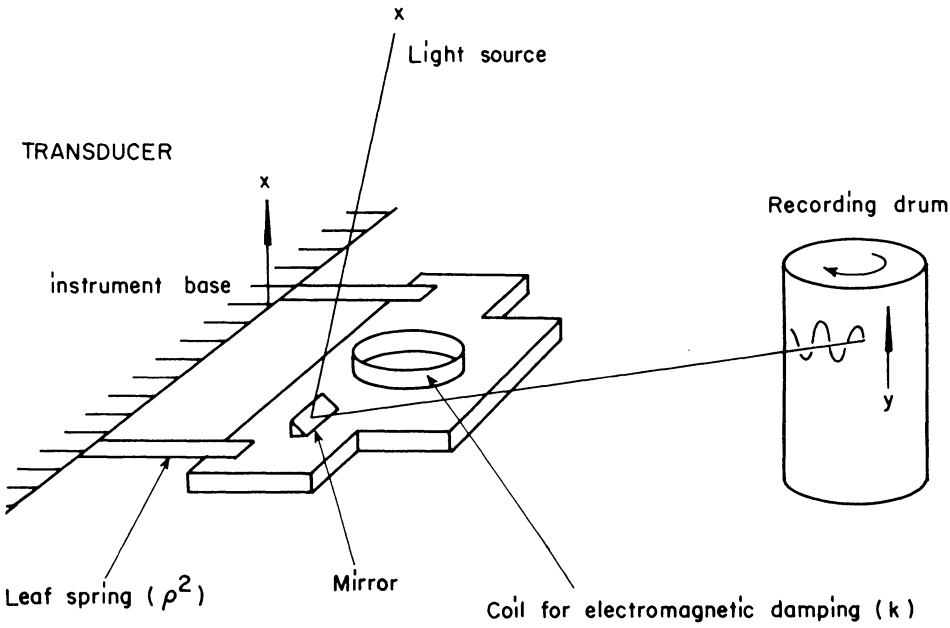

Figure 14. Schematic representation of transducer (After Brady, 1983)

d) Film driver

The film is confined in a light-proof roll, the driver moves the film with velocity 1 cm/sec.

e) Light beam generator

It is made of a special lamp with a linear filament.

The lamp intensity can be adjusted: the trace width should be less than 0.2 mm,sharp and clear.

f) Power supply

At present the system consists of a stabilized power supply with a 13.8 V d.c. output and current limited at 0.8 A, to which 12 V - 10 A/h buffer accumulator is connected. Where the time code generator is installed inside the accelerograph a lightning charge protection is inserted between the above mentioned group and the 220 V a.c.

Figure 15a shows a typical recording af a SMA-1 accelerograph triggered by a seismic event. Seven traces are clearly visible: the third, fourth and sixth correspond to the longitudinal (direction of the accelerograph main axis), vertical and transversal (direction of the accelerograph smaller axis), components, respectively. The first trace indicates the instant in which recording started: the second and fifth traces are fixed in respect to the ground, the seventh is the time-recorder trace, whose period is 0.5 seconds. According to the manufacturer, the optimal width of the photographic trace is about 0.10 cm, which, with a typical sensitivity of 0.5 g/cm, corresponds to an accuracy of about 5 thousandths of g.

Figure 15b gives an example of the illustrative label attached to each recorded accelerogram for classification purposes. The label gives the following information:

- name and geographic coordinates of the station where the accelerograph is installed;
- identification number and type of the accelerograph, name of the maker;
- date, hour, minute and second of the event, when possible;
- epicentral coordinates and magnitude, when possible;
- time recorder period.

Furthermore, for each component the label indicates:

- sensitivity expressed in cm/g;
- natural frequency;
- damping of the mobile equipment.

When the accelerograph starts recording the ground motion the film is transported at a constant speed of 1 cm/sec, but the moisture, the thermal variations, and the age might cause warping in the film, and the film-transport mechanism might undergo such modifications as to cause irregularities in the film transport speed. These irregularities can be either limited and occur during the whole recording, or sudden and localized.

The effects due to variations in the transport speed and to warpings in the film are:

- variable width of the trace;

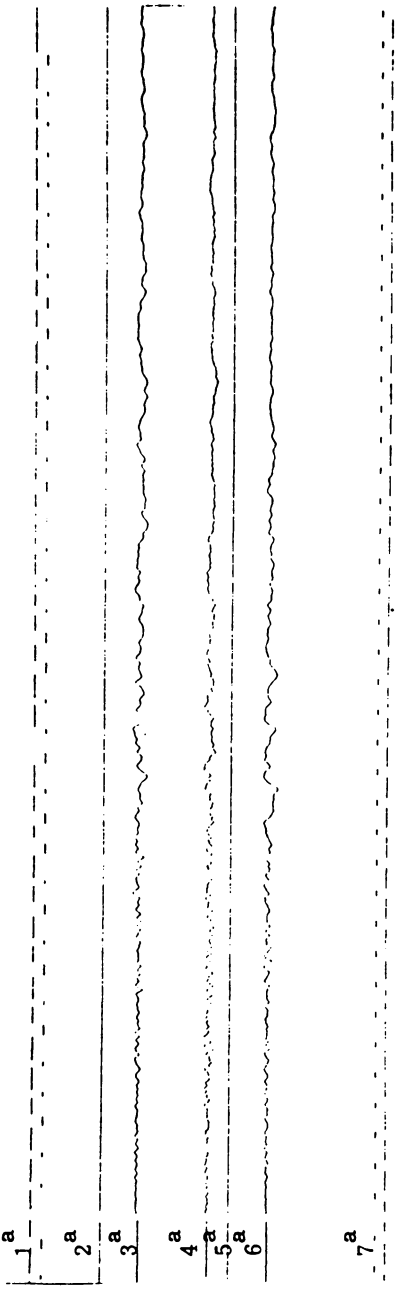

Figure 15(a).Typical Accelerogram Produced by an SMA-1

ENEL DCO - SETTORE SITI E AMBIENTE - SERVIZIO FISICA DEL TERRITORIO

POSTAZIONE DI .....

ACCELEROGRAFO No. .....TIPO .....

SCOSSA DEL .....

EPICENTRO ..... M=.....

DATA PRELIEVO ..... N.S. .....

CODICE ENEA-ENEL .....

	L	V	T
Sensibilità(cm/g)	.....	.....	.....
Frequenza(hz)	.....	.....	.....
Smorzamento	.....	.....	.....

Figure 15(b).Illustrative Label Attached to the Accelerogram

- non homogeneity in the time axis;
- fluctuations of the zero-acceleration trace.

The instrument sensitivity can also vary, owing to atmospheric agents. With time, the sensitivity values of the accelerograph might differ greatly from the manufacturer's rated values, sometimes with a variation around 10%. Therefore, the instrument should be calibrated periodically.

Warning lights of different colours were added to the segregated supply system of the instrument to indicate the occurrence of the recording and to signal faulty operation of the stabilized feeder. The lights relating to the instrument start-up are turned off by means of a switch, the key of which is only in the possession of the technician in charge of picking up the film.

Every four months the stations are inspected carefully by the technicians of the main laboratory in Rome, to ascertain the conditions of the instruments, which have been exposed to atmospheric agents for such a long period. Actions are carried out to check:

a) calibration and position of each trace on the film;
b) film speed;
c) damping and natural frequencies of the three mobile sections of the accelerograph;
d) threshold value of the trigger.

The accelerographs are manufactured so as to perform the inspections under b) and c) with only one operation, called "calibration". Fig. 16 shows the recording of a calibration procedure, and how the natural frequencies of the transducers and their damping, expressed as a fraction of critical damping, are determined. Once determined the X_2/X_1 ratio (Fig. 16), the actual damping is obtained with the diagram shown in Fig. 17, which is supplied by the accelerograph maker.

4. ITALIAN AND AMERICAN STRONG MOTION DATA

In the United States 2700 accelerographs have been installed by several Agencies and Universities, the management of the networks costs about 3.5 million dollars per year. The location of the instruments are shown in Figures 18 and 19 except for the accelerographs installed on the basis of the Uniform Building Code or in nuclear power plants. The instruments are of several types (SM, SM-D, MO-2, AR-240, RFT-250, SMA-1, DSA-1) and have been installed for different purposes.

A great part of the stations cannot be considered in free-field condition, because they are set up in buildings and on relevant structures such as dams, bridges, pumping and filter plants. The agencies that are managing the greater number of accelerographs are (Iwan, 1981):

- Los Angeles City Hall (486 instruments)
- California Division of Mines and Geology (384 instruments)
- U.S. Army Corp of Engineers (356 instruments)
- U.S.G.S. (250 instruments).

As already mentioned the first strong motion record was produced in 1933. Since that year the number of accelerograms collected in Western United States has become so large to put in evidence, at the end of '60s, the need for a standard processing of the records. In fact

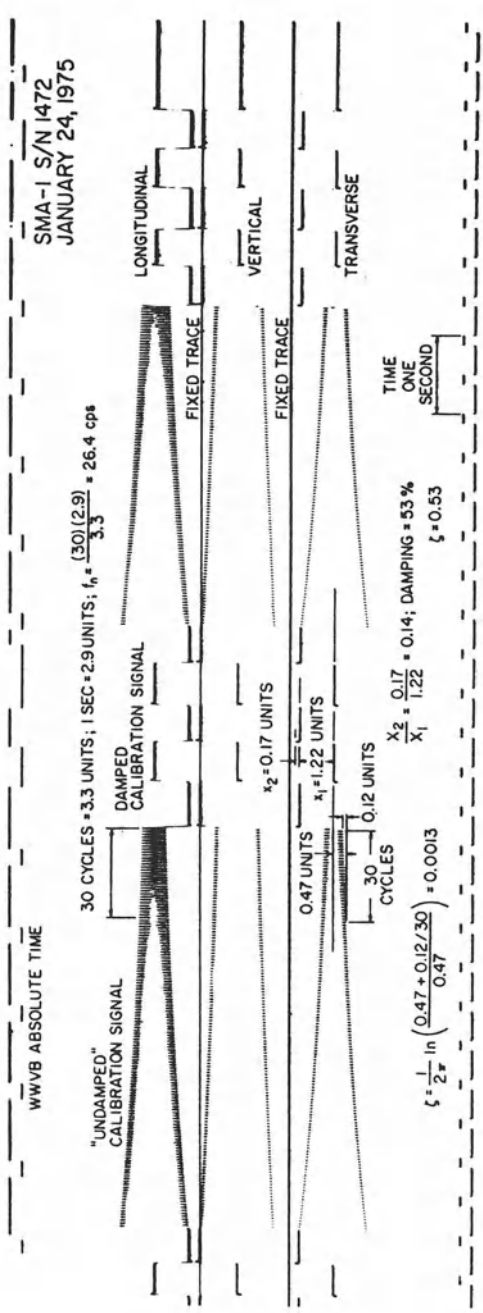

Figure 16. Calibration Record of an SMA-1 Accelerograph

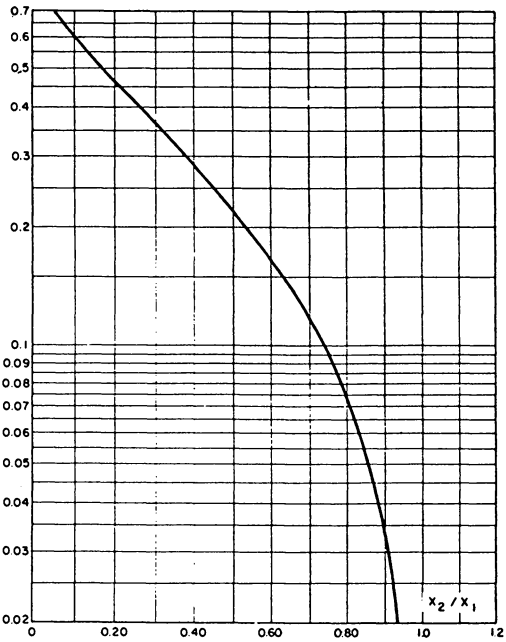

Figure 17. Damping Factor vs Overshoot Ratio

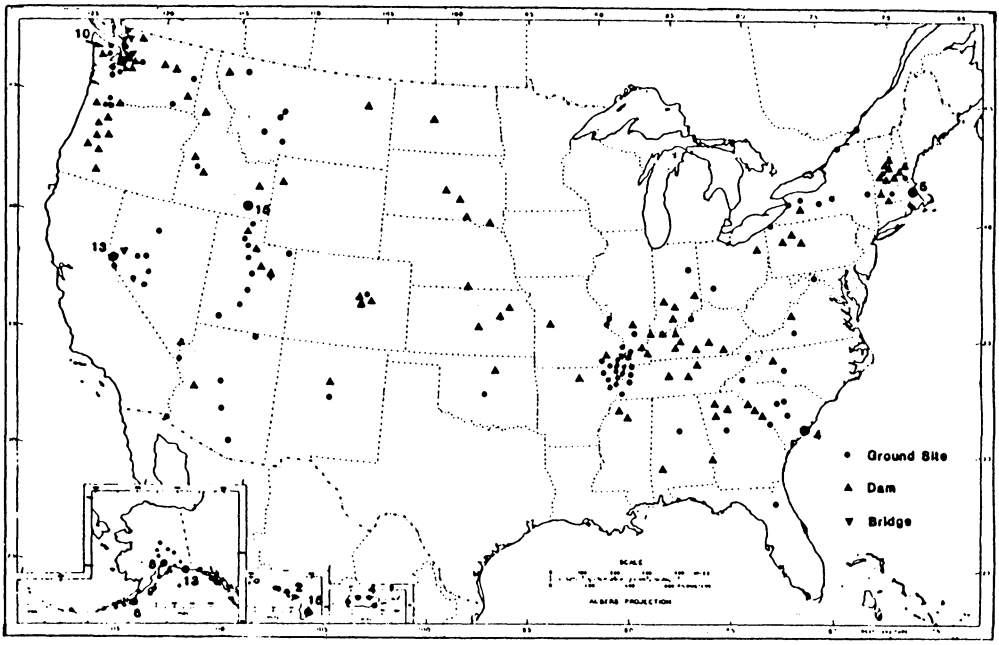

Figure 18. Accelerographic Stations in the U.S. Outside of California Excluding Commercial Nuclear Power Plants (After Iwan, 1981)

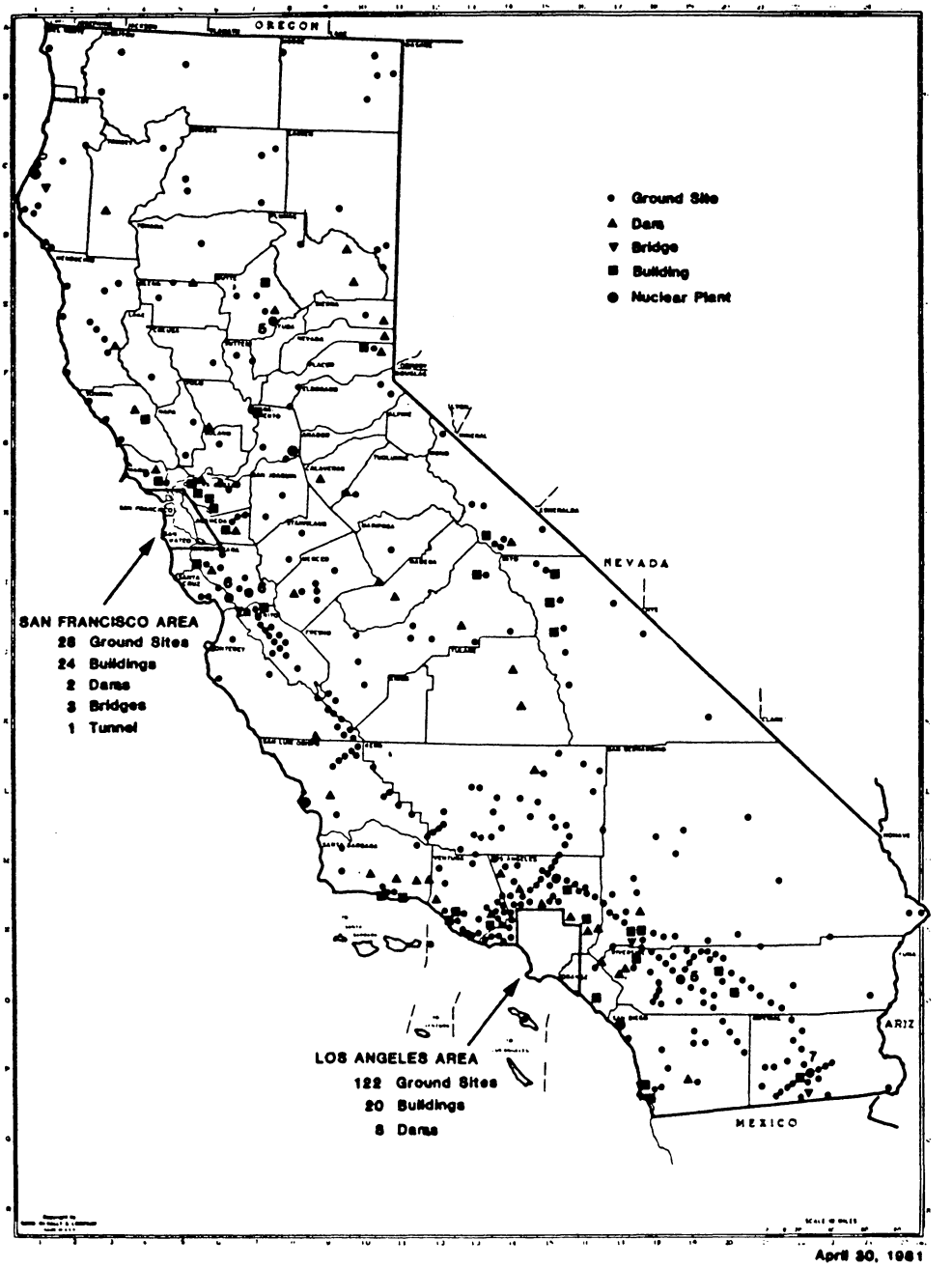

Figure 19. Accelerographic Stations in California, Excluding Instruments Required by Building Codes (After Iwan, 1984)

during those 30 years the kinds of instrumentation, the methodology of processing, the quality of the recordings were drastically changed. For this in 1968 the Earthquake Engineering Research Laboratory of the California Institute of Technology undertook a program for the digitization and numerical processing of the almost 100 records collected so far. The San Fernando earthquake occured in 1971 soon after the beginning of the project, and it produced 241 records, the largest number of records ever collected for one earthquake. The Caltech project was over in 1976. During its lifespan it introduced in Earthquake Engineering the most known and diffused methodology for processing accelerograms on analog format.

It is interesting to show a preliminary comparison of the characteristics of Italian and American strong motion records from a statistical point of view (Sabetta 1984). The American strong motion records taken in consideration are only those of the Caltech project, the reasons of this limitation are two:

a) in the years following the Caltech project several accelerograph stations in free field condition were installed referring to the seismotectonic characteristics of the selected areas. The data collected from these accelerographs are biased with respect to the statistical distribution of the ground motion parameters under comparison, the Italian network has been designed in fact taking into account the spatial distribution of the historical epicenters, in other words the data so collected are independent from the pattern of the seismotectonic structures

b) the Caltech data set is extremely important because it has been analyzed in many relevant scientific works in Geophysics (Aki, 1968; Boore and Zoback, 1974; Trifunac and Brady, 1975a; Archuleta and Day, 1977; Bouchon, 1978; Vanmarcke and Lai, 1980; etc.), in Engineering Seismology (Donovan, 1973; Trifunac and Brady, 1975b; McGuire and Barnhard. 1977; Campbell, 1981; etc.) and in Earthquake Engineering (Schnabel and Seed, 1972; Newmark et al., 1973; Perez, 1974; Seed et al., 1974; Newmark et al., 1976; Chang and Krinitzsky, 1977; etc.). Besides, the Building Code and the Nuclear Regulatory Guide of many countries have been developed with these data.

Figure 20 sums up some characteristics of the Caltech and Italian strong motion data sets. The total number of accelerograms digitized and processed by Caltech is 329 relating to 57 seismic events that took place in Western United States from 1933 to 1971 (Hudson, 1976; Chang and Krinitzskiy, 1978); 63% of these recordings refer to the San Fernando earthquake.

The accelerograms were recorded by 262 instruments having quite different characteristics, especially for what concerns natural frequency and damping: 82 instruments (31% of the total) are of the type AR-240; 58 (22%) are RFT-250 type, 44(17%) are USGS type, 43 (16%) are MO-2 and 35 (13%) are SMA-1 (Hudson, 1976). The instruments correspond to 197 stations all located in California except for 2 that are in Washington State and one in the State of Montana. More than 50% of the stations are located in Los Angeles and San Francisco because of the "Uniform Building Code". The station located in El Centro in South

	n° of record	n° of seismic events	n° of triggered accelerographs	n° of free field rec.	n° of records with PGA greater than .1 g
CALTECH DATA SET	329 (208 San Fernando)	57 (1933/71)	262 AR 240 31% RFT 250 22% USGS 17% MO 2 16% SMA 1 13%	187	103 (23 events)
ITALIAN DATA SET	315	117 (1972/81)	78 SMA 1 88% RFT 250 10% DSA 1 2%	315	62 (34 events)

Figure 20. Some Characteristics of the U.S. and Italian Strong Motion Data Set

California is the one that recorded the greatest number of events. The earthquakes that have provided the most records are, besides the San Fernando one, the Borrego Mountain one in 1968 (15) and the Lytle Creek one in 1970 (9).

Not considering the records obtained in the higher storeys of the buildings (142), 187 accelerograms remain (Chang, 1978, Trifunac and Brady, 1975) classified as in "free field" conditions. These accelerograms, corresponding to 49 seismic events with a magnitude between 3.8 and 7.7.

The total number of accelerograms obtained up to 1981 by the ENEA-ENEL network is 315 relating to 117 events starting from 1972. Differently from the Caltech data, all the records, for the previously mentioned characteristics of the Italian accelerogram stations, were obtained in free field conditions.

The instruments that provided records are 78: most of them of the SMA-1 type (88%), only a small percentage (10%) is represented by RFT-250 instruments and (2%) by digital instruments of the type DSA -1.

The Tolmezzo station in Friuli with its 26 accelerograms is the one that provided the greatest number of records while the seismic event that provides the most records is the Irpinia one (November 1980) with 16 accelerograms.

Figure 21 shows, for the Italian and Caltech data sets, the cumulative distribution of the record length (RL), that is the percentage of data having RL greater or equal to the actual value. Evident is the greater duration of the American accelerograms compared to the Italian ones, probably due to the greater magnitude and epicentral distance of the corresponding seismic events; less than 10% of the Italian data for example have an RL greater than 30 seconds against the 84% of the American data and moreover no Italian datum has an RL greater than 90 seconds against the 10% of American data.

Figure 22 shows the cumulative distribution of the epicentral distance (ED) for the accelerograms for which this datum is available.

The epicentral distances at which the American accelerograms have been recorded are definitely superior to those referring to the Italian acceleorgrams: only 10% of the Italian data have an ED bigger than 30 Km against the 77% of the American data and no Italian datum has an ED bigger than 50 Km against the 40% of the Caltech data; moreover almost the 20% of Americam accelerograms were recorded at epicentral distances greater than 100 Km.

Figure 23 shows the cumulative distribution of the peak ground acceleration (PGA) relating to the horizontal components of the Italian and Caltech accelerograms. The PGA of the American accelerograms are greater than the Italian ones: 16% of the Italian data have a PGA higher than 1 g/10 against the 42% of the American data.

The difference becomes smaller for higher values of the PGA: for both the Italian and American data only two horizontal components (corresponding respectively to the 0.3% and the 0.5% of the whole number) have a PGA higher than 6 g/10; in the first case it is the NS component of the accelerogram recorded in Ancona - Rocca (June, 14 1972), 6.21 g/10, and the WE component of the accelerogram recorded at Norcia-Mulino (September 1979), 6.74 g/10; in the American case the two components are

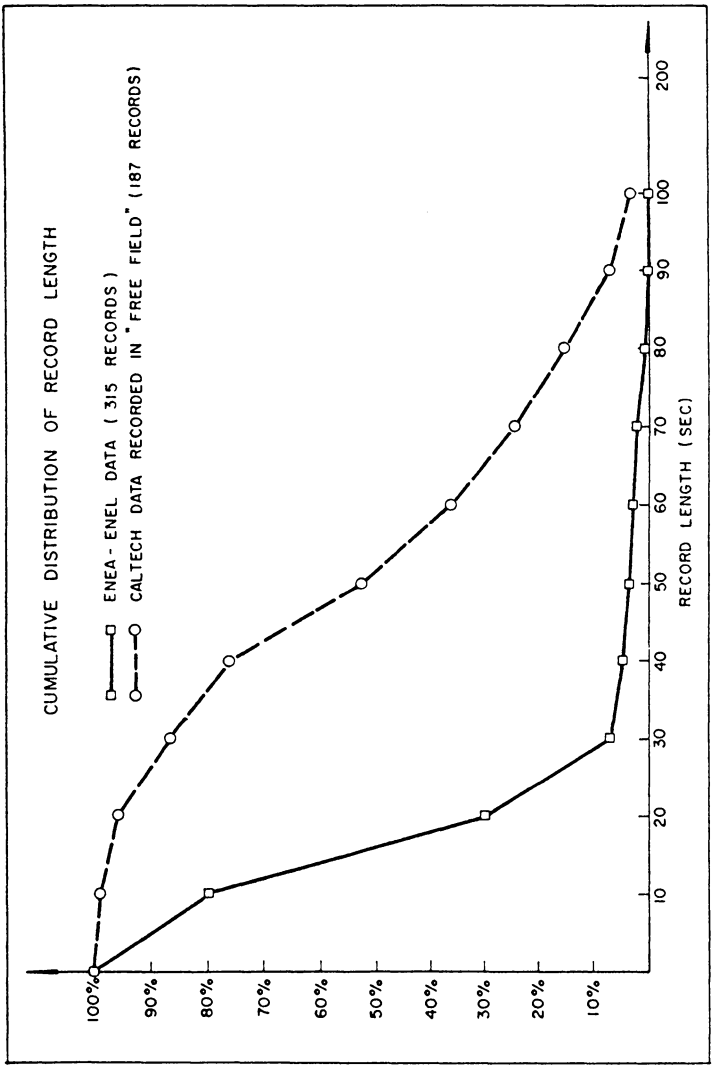

Figure 21. Cumulative distribution of record length (After Sabetta, 1984).

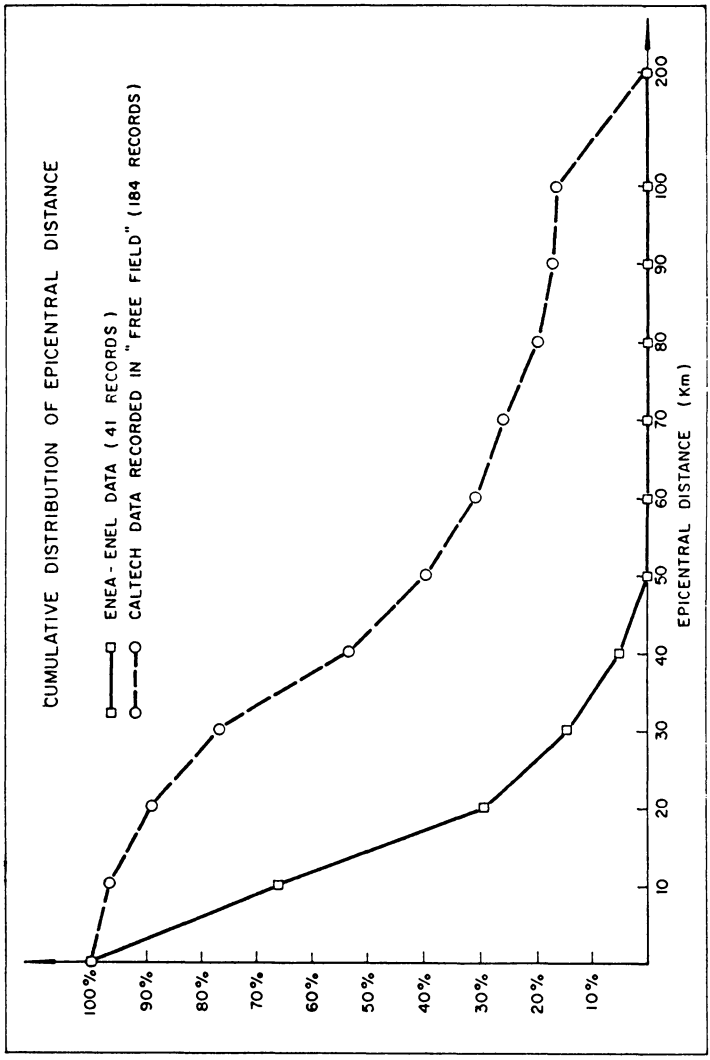

Figure 22. Cumulative distribution of epicentral distance (After Sabetta, 1985).

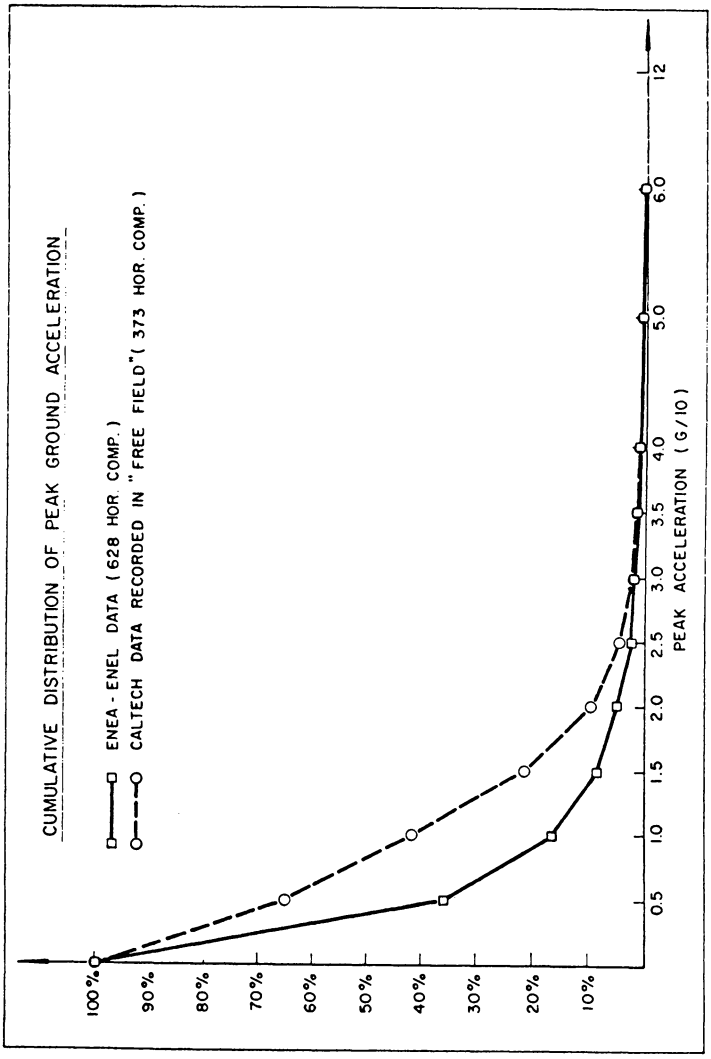

Figure 23. Cumulative distribution of peak ground acceleration (After Sabetta, 1984).

those of the accelerograms recorded at Pacoima Dam in February, 9, 1971 (respectively 12.4 and 12.5 g/10).

The difference in the distribution of the PGA is even more significant if we consider the distribution of the epicentral distances shown in Figure 22.

These few statistics point out not only some important differences in the characteristics of the vibratory motion in the U.S.A. (at least in California) and in Italy but also how necessary it is to be careful when using for engineering applications strong motion data relating to other countries.

5. ANALOG TO DIGITAL CONVERSION OF ACCELEROGRAMS

The processing of the accelerograms is performed to obtain the acceleration, velocity and displacement of the vibratory motion during the earthquake, and to evaluate the response and Fourier spectra. Therefore, it is necessary to transform the analog signals into a numerical sequence that can be processed with a digital computer, that is, to perform an analog-to-digital (A/D) conversion of the traces recorded on the film.

In general end-users of accelerograms do not care too much to know what they call "the details of the digitization". In several cases they use the strong motion data for analysis that do not take into account the confidence with which the information is available, this can produce misinterpretations of the final results.

The digitization of a signal consists of two separate operations: sampling and quantization.

Sampling defines the time instants at which the signal is to be observed, while quantization is the conversion of continuous signal amplitudes, at the sampled points, into a sequence of numbers.

Referring to Figure 24 an ideal sampler has the following properties (Kulanek 1976):

1) the sampler can open and close instantly;
2) the pulse duration, when the switch is closed, is small compared to the sampling period.

For the moment we limit our considerations to a sampler operating with constant sampling period Δt.

The sampler performs only the first operation of digitization. Quantization is carried out by an additional device called quantizer, not shown in Figure 24, that will be introduced further on. To introduce the sampling theorem we will follow the exposition of Kulanek (1976).

Let $x(t)$ be the analog input signal and $x_s(t)$ the sampler output. Furthermore, let $\delta_{\Delta t}(t)$ be the ideal sampling function representing an infinite train of equidistant unit impulses. The sampling function can be written

$$\delta\ \Delta t(t) = \sum_{m=-\infty}^{\infty} \delta(t-n\Delta t) \qquad (2)$$

where Δt = constant is the time interval between two impulse functions.

The output of the sampler is:

$$x_s(t) = x(t)\ \delta_{\Delta t}(t) = x \sum_{n=-\infty}^{\infty} \delta(\ t - n\ \Delta\ t\ ) \tag{3}$$

$$= \sum_{n=-\infty}^{\infty} x(n\Delta t)\ \delta(t - n\Delta t)$$

In terms of Fourier series $\delta_{\Delta t}(t)$ becomes:

$$\delta_{\Delta t}(t) = \frac{1}{\Delta t} \sum_{n=-\infty}^{\infty} \exp\ (j\ n\ \omega_s\ t\ ) \tag{4}$$

The frequency ω_s is the sampling angular frequency:

$$\omega_s = 2\Pi f_s = 2\Pi/\Delta t$$

The input-output relation of an ideal sampler, given by (3), can now be rewritten in a form:

$$x_s(t) = (1/\Delta t) \sum_{n=-\infty}^{\infty} x(t)\ \exp\ (j\ n\ \omega_s\ t\ ) \tag{5}$$

Applying the frequency-shifting theorem we have a Fourier transform pair:

$$x(t)\ \exp\ (j\omega_s\ \ t\ ) \leftrightarrow X(\omega - \omega_s)$$

and finally, the transform of (5) gives:

$$X_s(\ \omega\ ) = (1/\Delta t) \sum_{n=-\infty}^{\infty} X(\ \omega - n\omega_s\ ) \tag{6}$$

where $X(\ \omega\ )$ is the Fourier transform of the sampler input:

$$X(\ \omega\ ) = \int_{-\infty}^{+\infty} x(t)\ e^{-j\omega t} dt$$

Equation (6) demonstrates the fundamental consequences of sampling. While the frequency spectrum of the analog input of the sampler is a nonperiodic function, the spectrum of the sampler output is <u>always</u> a periodic function. That is:

$$X_s(\omega) = X_s(\omega + n\ \omega_s) \tag{7}$$

where n is an integer.

Equations (3) and (4) must be interpreted in the sense of

distribution theory, an elementary discussion of this theory will be given further on.

Figure 25 from Kulanek (1976), shows the spectrum of the signal input to the sampler and the spectrum of the output following eq. (7).

The output spectrum consists of primary and complementary components. Each component is identical to the input spectrum except for the normalizing factor $1/\Delta t$; the complementary components are displayed with respect to the primary by $\pm n\,\omega_s$ units.

If the input spectrum is band limited, as in Figure 25, from

$$-\omega_c \text{ to } \omega_c \text{ , i.e. } |X(\omega)| = 0, \text{ for } |\omega| > \omega_c \text{ ,}$$

it is then possible to recover the input signal from the spectrum of the sampler output, provided that $\omega_s/2 > \omega_c$. In other words the digitized signal is then equivalent to its analog form, and by digitizing we do not lose any information carried by the signal. The quantity $\omega_s/2 = \Pi/\Delta t$ in radians/sec is called the folding angular frequency or Nyquist angular frequency.

The influence of the length of Δt on the behaviour of the spectrum (ω) may be demonstrated following an example taken from Kulanek (1976) and shown in Fig. 26. Consider a continuous real and even time function, x(t), which has a band-limited spectrum $X(\omega)$ diagrammed in Fig. 26a.

The function x(t) is digitized with a sampling frequency $\omega_s = 2\Pi/\Delta t$ such that $\omega_s/2 > \omega_c$ (Fig.26b). Then, apart from the normalizing factor $1/\Delta t$, the primary and complementary components are separate perfect copies of the input spectrum. Therefore, the full recovery of the input signal in terms of the sampler output spectrum is possible.

When increasing the sampling period Δt up to the limit length when $\omega_s/2 = \omega_c$ (Fig. 26c) the picture will be similar. Any further increase of Δt will result in overlapping, so-called aliasing, of primary and complementary components (Fig. 26d).

The recovery of the input signal from the distorted output spectrum is then no longer possible. In other words, the highest frequency which can be reproduced from data sampled with the sampling period is:

$$f_N = \frac{f_s}{2} = \frac{\omega_s}{4\pi} = \frac{1}{2\Delta t} \qquad (8)$$

In agreement with the quantity $\omega_s/2$, f_N, in cps, is called the folding frequency or Nyquist frequency. Equation (8) represents an important result, commonly known as the sampling theorem. It says that at least two samples per cycle are required to define a frequency component in the original signal.

In many countries the digitization of the accelerograms is performed with digitizer tables. The Italion Joint Commission used, until 1981, the D-MAC2 digitizer table. The resolving capability of this table is 1/10 milimeter. The photographic enlargement facilitates sampling. The table characteristics require an enlargement factor 4.

A/D conversion of an accelerogram by means of a digitizer table calls for the following operations:

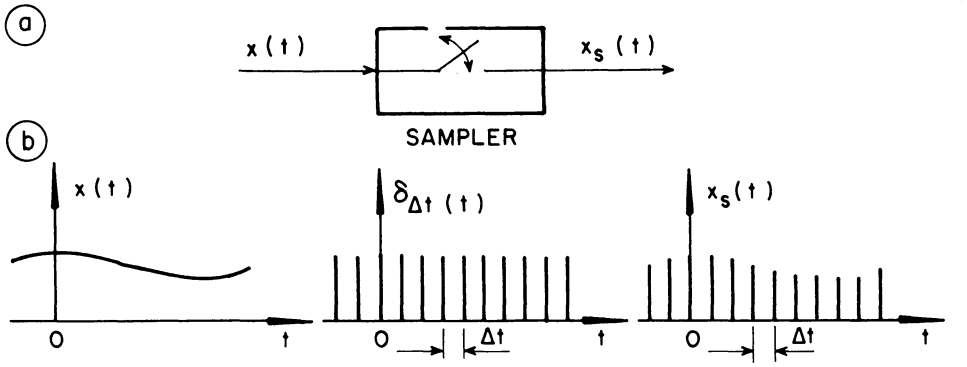

Figure 24. Schematization of an Ideal Sampler (After Kulanek, 1976)

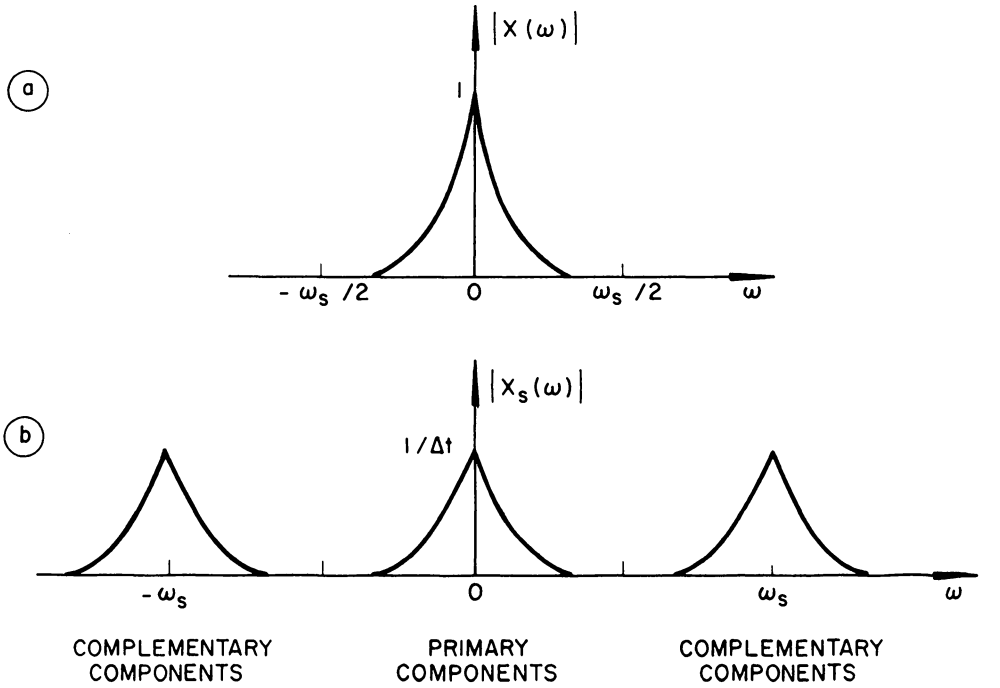

Figure 25. Input and output spectra of the signal (After Kulanek,1976).

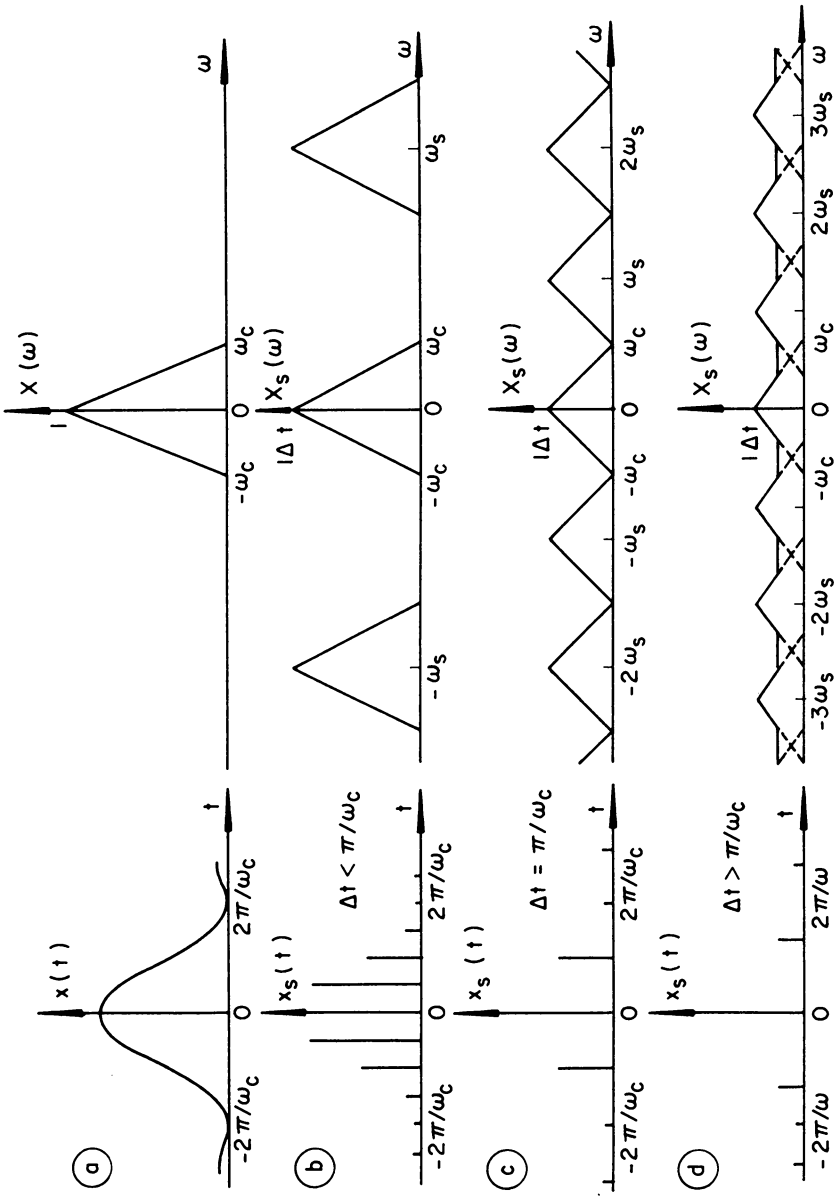

Figure 26. Influence of the signal duration on spectrum (After Kulanek, 1976).

- arrangement of the accelerometric trace on the table plane;
- selection of the origin;
- transfer of the sampled data on an adequate format for subsequent processing.

With regard to the first operation, the following expedients should be adopted: the x and y axes of the trace should be parallel to the x and y axes of the digitizer table as much as possible, in order to avoid misalignment of the sampled trace. Therefore, the recording should be arranged so that two extreme points of the same trace (generally the time-recorder trace) have the same ordinate value. The table is 1.2 x 1.2 m^2; if the enlarged trace is longer than 1 meter, the trace is to be sampled in two or more operations.

The table is equipped with a device that allows zero setting of the x-y coordinates, thus making it possible to select any point as the axes origin.

As the trigger threshold of the accelerograph is fixed at 1/100 of g, the first arrivals of the seismic waves are not recorded because the ground acceleration does not exceed the threshold. For these reasons the beginning of the recording, and thus of sampling, never coincides with the beginning of the ground motion.

Manual digitization is a difficult operation that requires great concentration and attention, and should therefore be performed by many operators to ensure acceptable levels of accuracy. It is essential to evaluate the digitation accuracy of each operator and their average performances.

To this aim, Trifunac et al. (1971) developed a procedure whose results are briefly illustrated below.

The authors decided to digitize a straight line impressed on a film, with a non-zero derivative, so as to obtain variable abscissae and ordinates during digitization. Five digitizations of the straight trace were performed, and before carrying out further analyses, the digitized data (Zij, i=1---5; j=1---N_{tot}, where N_{tot} is the number of points linearly interpolated) were translated and rotated with least square fit on the abscissae axis. The five sets of data thus obtained are given in Fig. 27.

The figure clearly shows two types of errors; one related to intermediate and high frequencies, the other related to long-period components present in each trace and thus common to the five digitations. The long-period components are due to systematic errors introduced by the digitizer table and photographic enlargement.

The difference (Zij-$\bar{Z}$j), where $\bar{Z}$j is the mean trace points out the high-frequency components due to casual errors of the operators.

For each difference (Zij-$\bar{Z}$j) the following standard deviation was determined:

$$\delta_i = \frac{1}{N_{tot}} \sqrt{\sum_{1}^{N_{tot}} j(Zij - \bar{Z}j)^2} \qquad (9)$$

and the histogram of Fig. 28 was drawn, with the amplitudes of the Zij-Zj differences (measured in fractions of standard deviations)

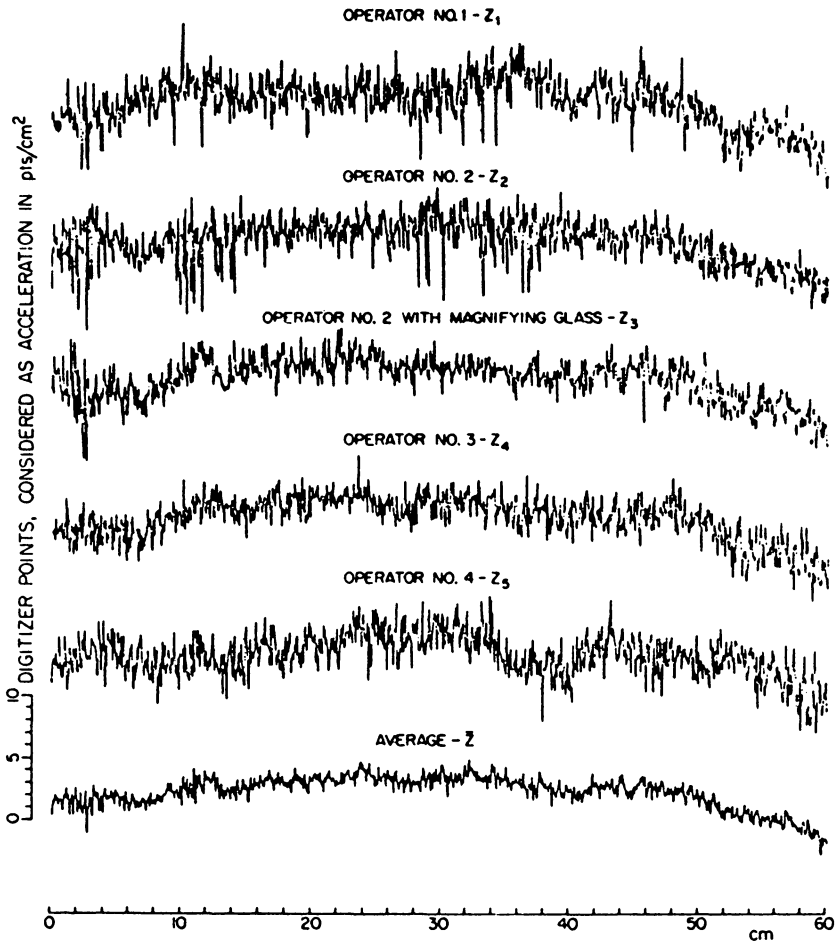

Figure 27. Digitization of a straight line (After Trifunac et al. 1971).

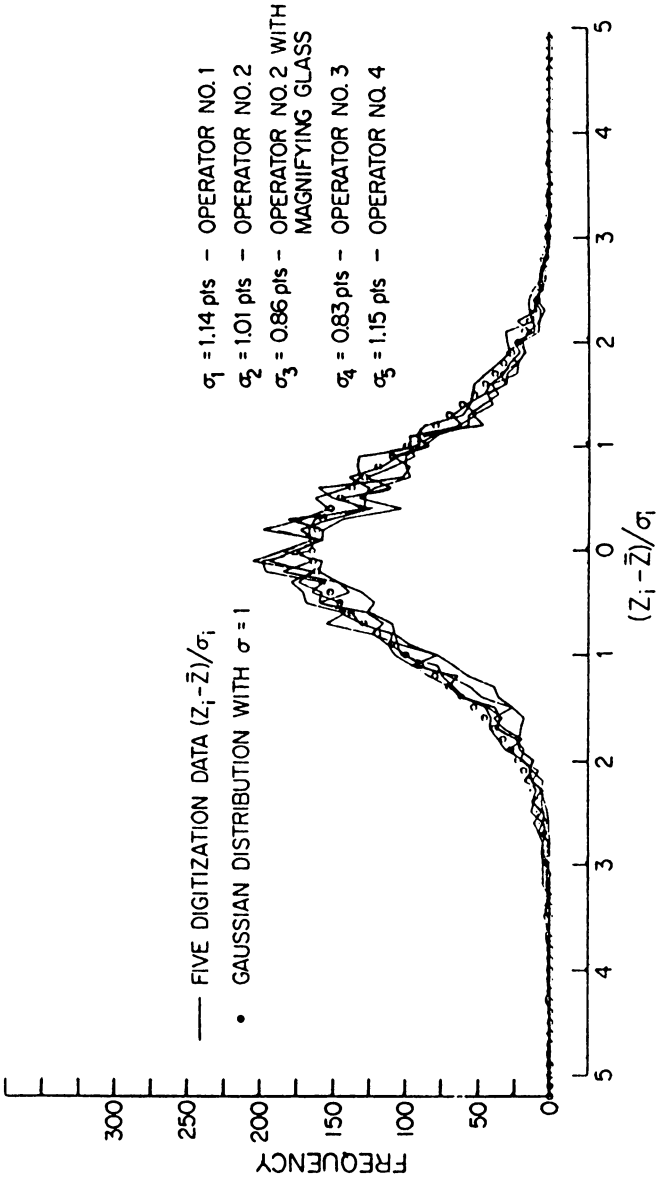

Figure 28. Histogram of Fig.27 data (After Trifunac et al. 1971)

plotted on the abscissa, and the recurring frequency, of a predetermined interval of these amplitudes, on the ordinates.

Figure 28 shows also the normal distribution with zero average value and unit standard deviation.

A comparison of the five histogram and the Gaussian distribution leads to two important conclusions: the random errors during digitization are normally distributed; the mean deviation of the distribution is one unit of the digitizer. The foregoing result proves that the digitization errors are mainly of the same order of magnitude as the digitizer table resolving power, that is, 0.10 mm in the case of the D-MAC2 table used by the ENEA-ENEL Commission.

Actually, there are sound reasons to believe that in digitizing a trace with a constant slope, the operator unconsciously introduces autocorrective factors that do not intervene in the case of waveforms with sharp and continuous slope variations.

Furthermore in the Trifunac's method the $Z_{ij}-Z_i$ differences are not affected by the time-axis uncertainties faced when the method is applied to real accelerograms.

Basili and Mariano (1980) applied Trifunac's method to ten different digitizations of the same accelerogram. The selection of the sampling rate was left to the operator.

The method developed by Trifunac et al. was used also to analyze the waveforms of velocity and displacement, which has been obtained by integrating the data from the ten digitizations of the first accelerogram.

An alaysis of the results led to the following considerations:

a) the sampling rate adopted by each operator can vary by a factor three, that is, from 27 to 80 points per second.

b) the maximum peak acceleration is recovered exactly in the manual A/D conversion and is not affected by the operator's sampling procedure,

c) in the manual A/D conversion of a real accelerogram, the random error distribution is <u>not</u> Gaussian, as can be seen in Fig.29, where an histogram obtained with the same method as those in Fig. 28 is shown,

d) The hand digitizing error is due to the following components:

$E_{sist\ 1}$;

$E_{sist\ 2}$;

E (f, Ampl., thick.).

E_{sist1} is the systematic error present in all the digitized versions of the accelerogram;

E_{sist2} is the systematic error present in each digitized version of the accelerogram and can be ascribed to systematic errors of each operator (for instance, parallax errors);

E(f, Ampl.thick) are random errors that depend on the frequency

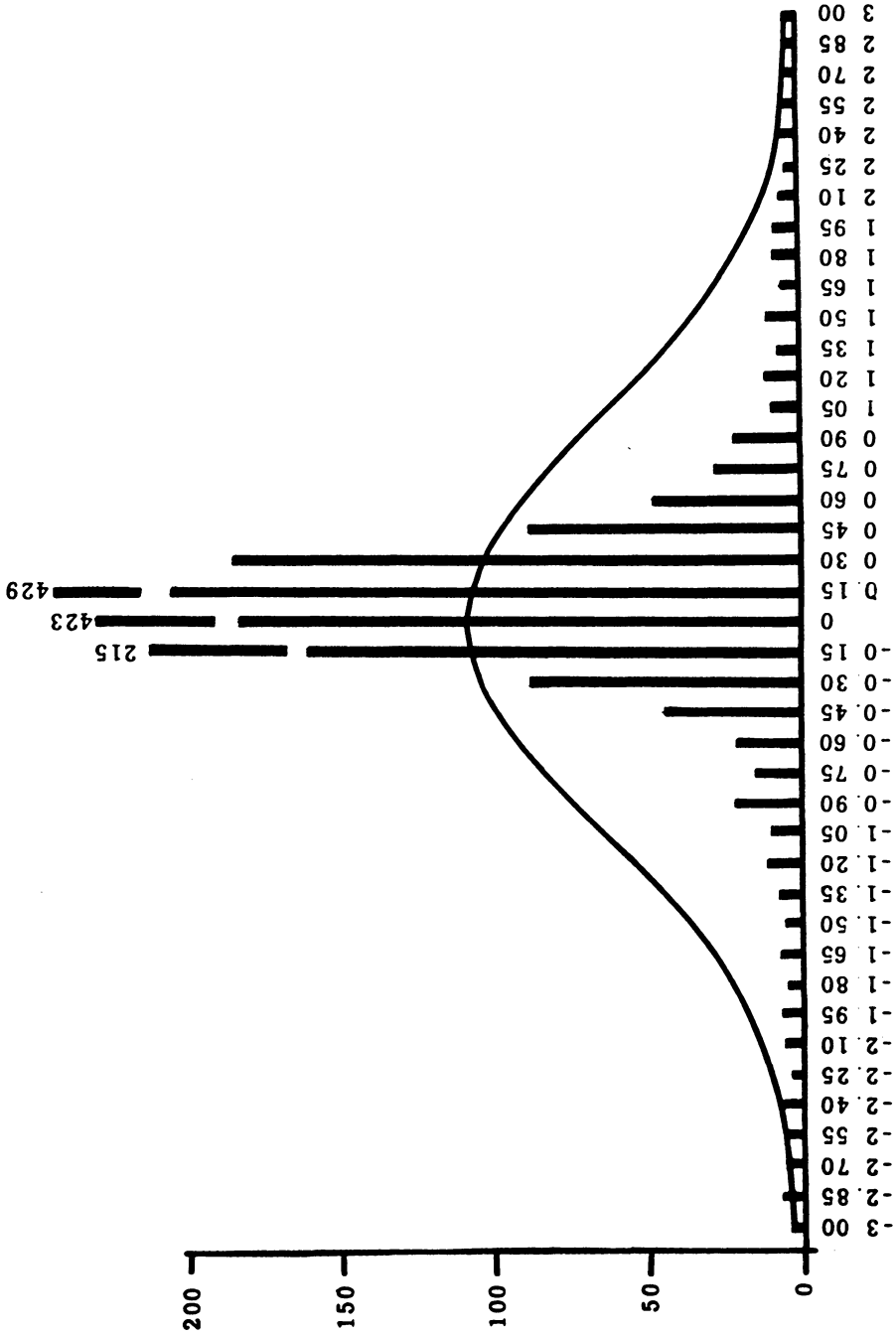

Figure 29. Histogram of a digitized straight line (After Basili and Mariano, 1980).

content of the signal, and on the amplitude and thickness of the trace; in this kind of errors participate the random ones pointed out by Trifunac, and those associated with the amplitude of the signal and the trace thickness.

e) The maximum random error $E_{(f,Ampl., thick.)}$ in the 10 digitizations is equal to 30% of the peak value in the acceleration waveform and 20% and 60% of the peak in the velocity and displacement waveforms, respectively.

The lowest error (in percentage respect to the peak value) is in the velocity waveform, this is due to the fact that in this waveform great importance has the intermediate frequency region of the original Fourier spectrum of the trace which the operators can recover with higher accuracy.

The acceleration waveform is strongly influenced by the high-frequency components; likewise, the displacement waveform is influenced by the low-frequency components.

Manual digitation acts as a passband filter on the trace, whose cutoff frequencies depend on the operator: the high-frequency cutoff value is substantially the same for all the operators, as the operator is "forced" to sample all the vertices to obtain the most accurate reproduction of the peaks.

The low-frequency cutoff value is on the contrary, extremely variable as no reference exists for the operator during the digitization; therefore, in sampling each operator tends to follow his own judgement. This fully justifies the high value (in percentage respect to the peak value) of the random error in the displacement waveform.

The random errors here discussed appear in contradiction with the conclusions reached by Trifunac et al., when they state that the standard deviation of the random error is equal to one unit of the table. These contradictions are due to the fact that the digitized data of the straight line do not present any problems of synchronization of the abscissae for calculating the differences (Zij-Zj), whereas, for the same calculation, digitized data of real accelerograms require synchronization of the recovered waveforms. Actually, owing to uncertainties in the time values, synchronization of the whole recording is impossible. Only one peak can be synchronized, and generally the highest peak is preferred.

During the digitization the operator selects points of the trace that in his opinion are the most appropriate to recover the character of the time-history. The digitized data will certainly include all the significant peaks and in general for an assigned total number of selected points, the non uniform digitization recovers the original trace with better approximation than the uniform one.

From a theoretical point of view the minimum wave length λ_{min} that is possible to resolve is:

$$\lambda_{min} = 2\Delta(cm)$$

where Δ is the resolving capability of the digitizer table. Assuming an

assigned film speed V_f and a photograhic magnification M of the original recording, the minimum period Tmin or the maximum frequency f_{max} that can be resolved in the accelerogram are expressed by:

$$T_{min} = \frac{\lambda}{M\ V_f} = \frac{2\Delta}{M\ V_f} = \frac{1}{f_{max}} \tag{10}$$

Considering the digitizing system adopted in Italy with $\Delta = 1x10^{-2}$cm and $M = 4$ we have:

$$f_{max} = 200 \text{ Hz}$$

This value does not take into account the random errors associated to the sampling of the trace, that is we assume to know exactly the coordinates of the selected points. Referring to Figure 30, from Arias and Sandoval (1979), the wavelenght of a sinewave, digitized in the points of maximum amplitudes, is known with a variance:

$$\text{var } \lambda = E(2(\varepsilon_2 - \varepsilon_1)^2) \tag{11}$$

where ε_1 and ε_2 are the errors in the digitizations of the abscissae of the peaks of the sinewave, assuming:

$$E\ (\varepsilon_1, \varepsilon_2) = 0$$

$$E\ (\varepsilon_1^2) = E(\varepsilon_2^2) = \delta\ x^2$$

ve have:

$$\text{var } \lambda = 8\delta\ x^2 \tag{12}$$

where δx is the standard deviation of the distribution of the random errors ε_1. For frequencies close to f_{max} (that is close to the limit of the resolving capability of the digitizer) it is not possible, following the (12), to know adequately the value of the frequency for which we have estimated the spectrum, the coefficient of variation, C.V., of f_{max} is in fact

$$\text{C.V.} \left(f_{max} \right) \frac{\delta f_{max}}{f_{max}} \quad 1{,}91 \tag{13}$$

Arias and Sandoval (1979) demonstrated that the random error ε of the time coordinate, $t = X/M\ V_f$, leads to an underestimation of the amplitude Fourier spectrum of the signal:

$$E\ \left[F(\ \omega;\ \varepsilon\ ) \right] = F(\omega)\ \exp \left(- \frac{\omega^2\ \delta_x^2}{2(M\ V_f)^2} \right) \tag{14}$$

Introducing the relative discrepancy, r_a, as:

$$r_a = \frac{F(\omega) - \varepsilon \left| F(\omega\,;\, E) \right|}{F(\omega)} = 1 - \exp - \frac{\omega^2 \delta_x^2}{2M^2 V_f^2} \tag{15}$$

it is possible to evaluate the limit in frequency of the resolving capability of the digitization system once given a certain value of r_a:

$$f_{max} \Big|_{r_a} = \frac{M V_f}{2\Pi\, \delta_x} \sqrt{2 \log_n \frac{1}{1-r_a}} \tag{16}$$

The following table indicates the value of f_{max} for an assigned value of r_a. The parameters δ_x (10^{-2} cm), M(4) and V_f(1 cm/sec) are those of the Italian system for the manual digitization.

r_a	f_{max} (hz)
0.01	11.78
0.02	16.64
0.05	26.62
0.10	38.14
0.20	55.51
0.40	84.00
0.50	97.84
0.75	138.37
1.00	∞

The non uniform digitization is followed by the operating of an interpolation of the sampled data in order to make available data equally spaced for the further numerical elaborations. In practice the interpolation is linear in most of the cases.

The modulus of the transfer function of the linear interpolation was determined by Trifunac et al (1973). Several cycles of a sine function were defined by equally spaced data connected with straight lines. The Fourier amplitude spectrum was then calculated for this continuous function and was divided by the Fourier amplitude spectrum for the exact sine function.

The result is shown in Figure 31 in which the transfer function is plotted versus the number of digitized points per cycle. The authors performed the same operations to evaluate the transfer function of the linear interpolation in case of sine functions defined by using unequally spaced data of various densities. The results are shown in Figure 31 by triangular points Trifunac at al.concluded that the transfer function of the linear interpolation for data not equally spaced can be described with good approximation by the theoretical function obtained in case of data equally spaced at the same sampling rate.

From the analysis of the results shown in Figure 31 the following considerations arise:

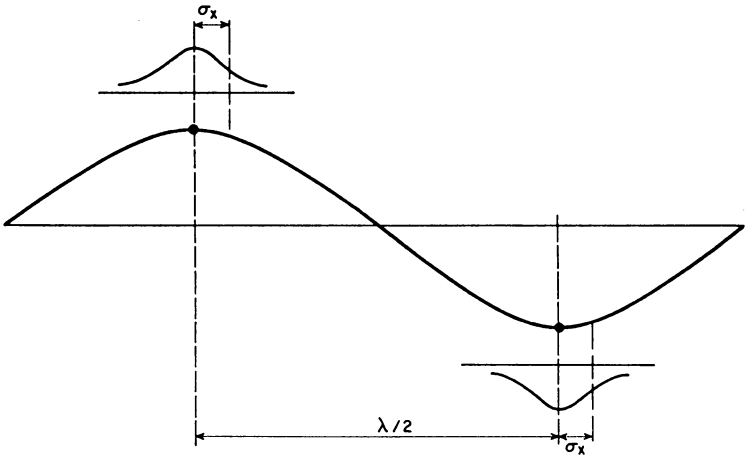

Figure 30. The wavelength of a sinewave digitized at maximum amplitudes

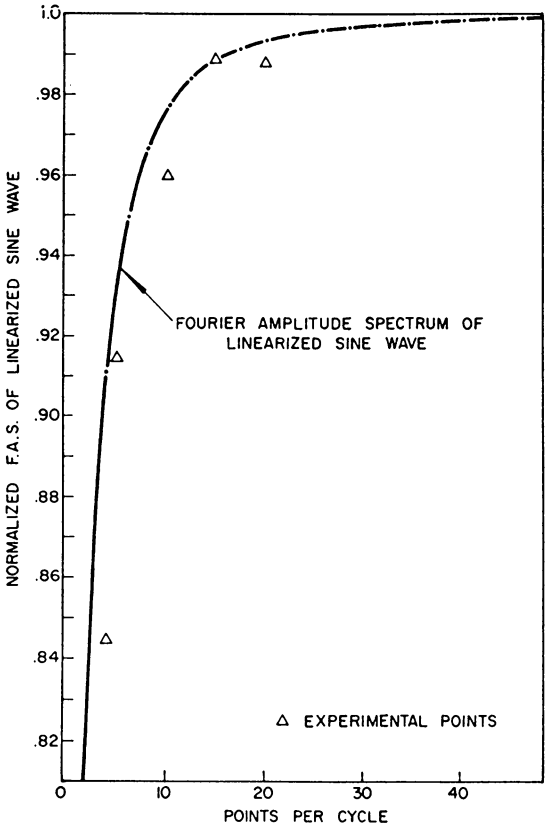

Figure 31. Fourier amplitude spectrum of linearized sine wave (After Trifunac et al. 1973).

- adopting a mean sampling rate of 2 pts/cycle the optimal value of the transfer function is 0.81, that is 19% of the amplitude spectrum of the signal is lost at that frequency;
- in order to maintain a 5% approximation in the Fourier amplitude spectrum, not less than 6 pts/cycle are required;
- once selected the mean sampling rate $\bar{f}_s$ and the approximation in the Fourier amplitude spectrum, the maximum frequency, f_{max}, for which such level of approximation is possible, is fixed and it is

$$f_{max} = \frac{\bar{f}_s}{n} \tag{17}$$

where n is the number of points per cycle given by the curve in Figure 31 for the selected approximation (Arias and Sandoval 1979). So for example if $f_s = 50$ pts/cycle and a level of approximation of 5% is requested, from Figure 31 we have $n = 6$, then

$$f_{max} = \frac{50}{6} = 8.33(\mathrm{Hz})$$

In the last years some systems for the automatic digitization of the analog signals recorded on film have been introduced in this field.

The IOM-TOWILL (Santa Clara, California) is using an automatic laser line follower. Figure 32 shows schematically the configuration for the sampling of the signal: a laser beam is rapidly revolving in a circle. The orbital center is positioned near the trace. "The angle in its orbit where the beam crosses the line and the line width, along with the position of the orbital center and the relative transmission of the line, are all accessible to the computer. Based on this information and knowledge of the orbital radius, the computer calculates the position of the point and determines where the next orbital center should be." (Roseman, 1979).

Operator intervention is required for decisions at trace intercepts, and for selecting visually located points when the trace is too pale for aitomatic detection. The machine has a limited measuring area 120 mm x 80 mm, therefore the accelerograms have to be cut in 12-cm sections. The digitized frames are reassembled mathematically. The digitization is not uniform at sampling rate greater than 600 points/sec. Then a linear interpolation is performed to obtain uniformly sampled time history of 600 pts/sec.

Fletcher et al. (1980) evaluated the accuracy of the system analysing the sampled data coming from the record of a small event (M=2) which occured soon after a major event that triggered the instrument. The sampled data are plotted at large scale, most of the points fall within ± 10 μm of the median line (Figure 33).

As the real accelerogram on the film has a trace width of about 0.2 mm, the digitizer is capable to define a median line that is 1/10 the visible trace thickness. A 2Hz component is evident in the displacement time-history. Fletcher et al. impute this periodicity to the

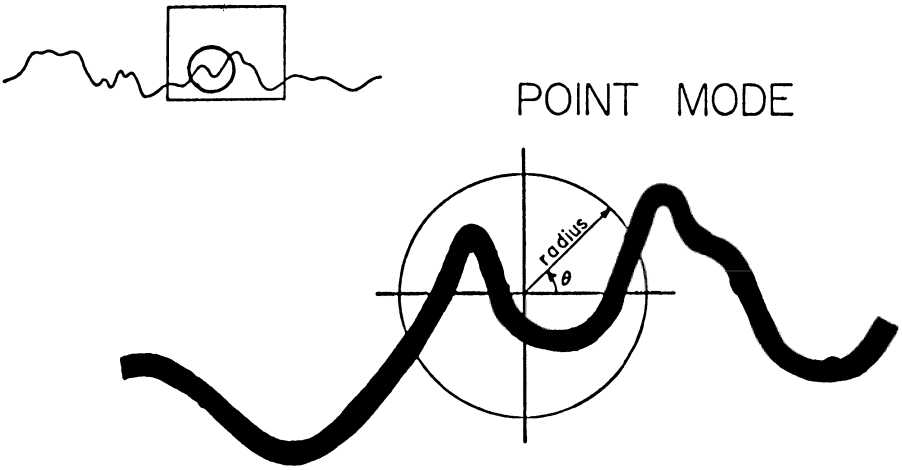

Figure 32. Configuration for sampling the signal (After Roseman, 1980).

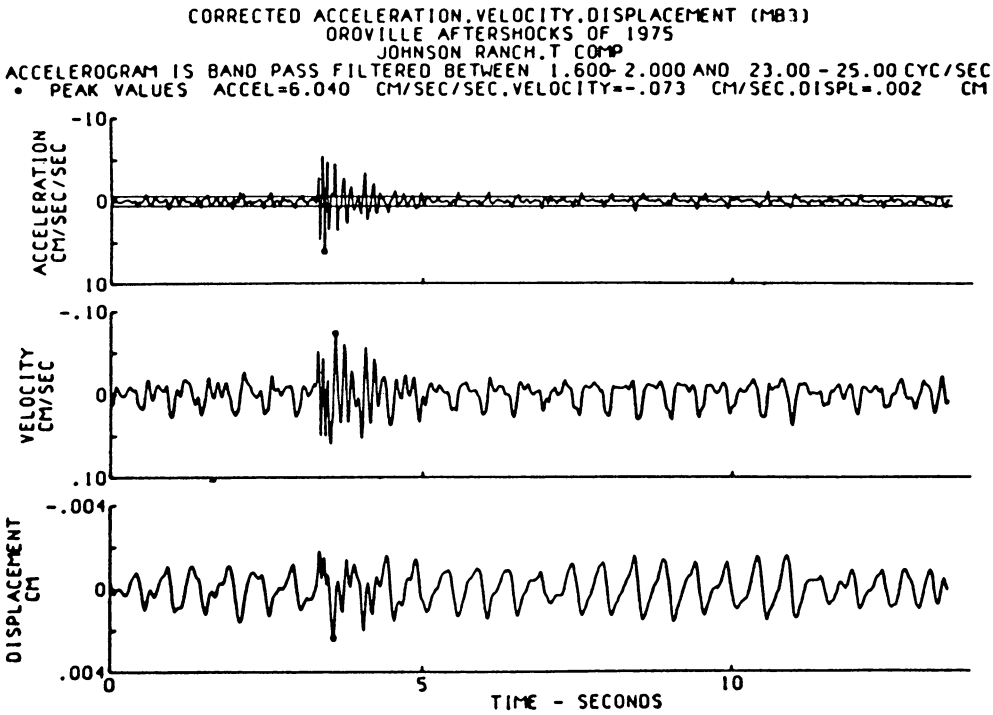

Figure 33. Corrected acceleration, velocity and displacement tracess (After Fletcher et al. 1980).

transverse shift (10 μm of amplitude) on the trace caused by the time-marker. As the digitizing system is capable of recovering this noise effect on the trace, the authors conclude that: "the accuracy of digitization using this laser system is close to the capability of the recording system.

Another automatic digitizer is available at the University of Southern California. Basically it consists of a rotating drum on which the film is fastened. The light source is inside the drum and the light transducer is below the drum. The transducer converts the light intensity transmitted through the film into digital count ranging from 0 to 256 (Trifunac, 1980). The light beam size in 50 μ m x 50 μ m. While the drum is rotating the transducer reads, at equal time intervals, the light intensity along the y-axis of the film. After one rotation of the drum the carriage, supporting both the light source and the transducer, moves to the right a multiple of 12.5 μm, tye system is than ready for another scan of the film. The drum scanner can accomodate at most 10 x 10" film. For this the record has to be reduced in square sections to be fasten on the drum. A software reassembles the digitized accelerogram.

Since 1981 the Italian Contraves has developed a system for the automatic digitization of the records. The system originally used for the sampling of contour curves has been adapted to the sampling of accelerograms on behalf of the ENEA-ENEL Joint Commission. The system in made of:

- a light source below a transparent plan on which the film is fixed,
- a photoscanner that measures the light intensity crossed though the film during the exposition time, t_e, usually 50 m sec.,
- a mobile carriage supporting the photoscanner that moves along the x-axis with constant velocity varing from 500 to 2000 μm/sec:
- a computer system for the acquisition of the data;

the system is shown in Figure 34.

The light transducer, 1 inch long, is made of an array of 1024 photodiodes, the array is perpendicular to the x-axis. It converts the light intensity into 1024 levels of voltage, one level for each photodiode. These levels are then compared every 50 msec, with a threshold level and converted into 1024 binary values. The logic value "0" is assumed for a photodiode obscured by the trace totally or in a good percentage (depending of the assumed threshold level) of its reading area; if this is not the case, the signal coming from the photodiode is higher than the threshold level and the logic value "1" is assumed. The photoscanner allows the digitization of the entire film without any cut of the record or distortions due to the photographic enlargment usually adopted for the manual digitization. The display of the digitized data allows the operator intervention for recovering the portion of signal in which the trace is too pale are absent and for removing spurious readings due to black spots that can be present in the film. A schematic view of the acquisition of the sampled data is shown in Figure 35.

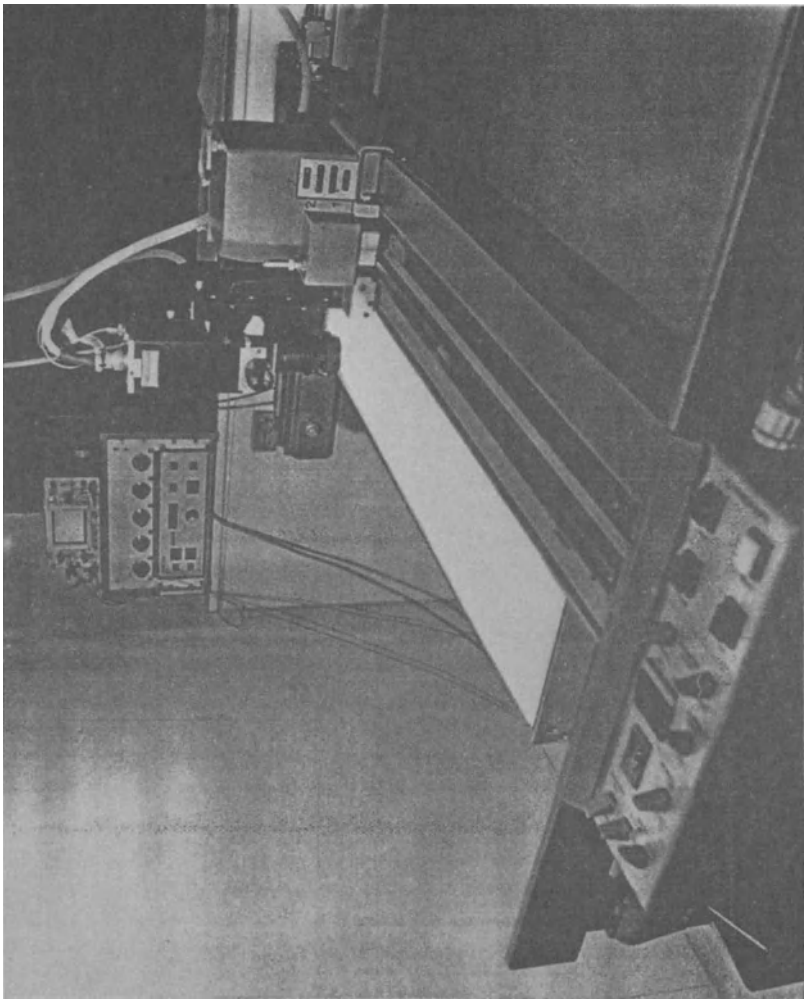

Figure 34. Italian Contraves Automatic Digitizer (After Santese, 1984).

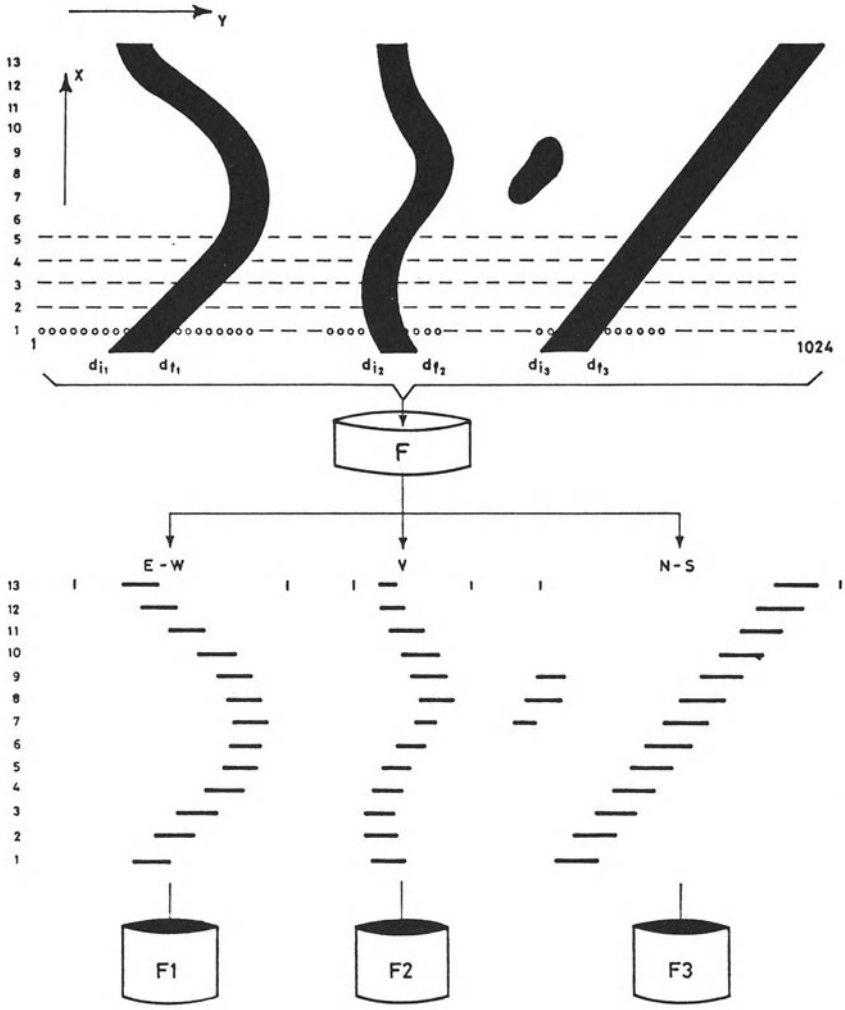

Figure 35. Schematic view of the sampled data from Contraves System (After Santese, 1984).

6. ACCURACY OF THE A/D CONVERSION

The manual A/D conversion of accelerograms requires the sampling of the trace along its center line. Two sources of errors can be associated with this operation, they are mainly related to the human limit in the capability of sampling the exact center line (positioning error) and to the quantization effects of the digitizer table (discretizing error).

The positioning error, ε , is the distance, on the Y-axis, of the sampled point from the center line. When the trace is thin and with very sharp boarders the probability distribution is that in Figure 36a. When the trace in thick and the boardes are shaded, the operator is in condition to realize the position of the center line. In this case the probability distribution should be that in Figure 36b.

There are several kinds of quantization operated by digital measuring devices: truncation, rounding, sign-magnitude truncation, the kind operated by the table is the rounding one, that is it approximates the signal by the nearest quantization level. Figure 37 shows the quantization levels of the table. The rounding effect can be described mathematically (Trifunac et al. 1973) as an operator N, such that

$$N(y) = \text{int}\ (y) + H\left[2\ (y - \text{int}\ (y)\ ) - 1\right] \qquad (18)$$

where int (y) denotes the integer part of y and H [ ] is equal to zero if its argument is negative, and equal to one if its argument is positive. Considering the rounding effect the probability distribution of ε is discrete and it is shown in Figure 36c and 36d . This the case when the center line coincides with a certain quantification level. If the center line, as in Figure 37, does not coincide with a quantification level and it is at distance δ from the closest level, a further error is introduced in the digitization process. In fact the total error in this case is

$$E = N(\varepsilon + \delta) - \delta$$

The distance δ can be considered a random, uniformly distributed variable. Figure 38 and 39 show respectively the distribution of P $(N(\varepsilon+\delta))$ and P (E).

The variance associated with these distributions show (Trifunac et al, 1973) that the rounding effect is not significant as the positioning error due to the operator. This is evident taking into account that the width of the trace is usually 0.2 mm and since a magnification 4 of the original film is adopted for facilitating the digitization there are tipically 7 - 8 quantization levels in the thickness of the trace.

Passing to consider positioning error and rounding effect of the automatic digitization, Figure 40 shows the trace of the record and the Contraves photoscanner. At first we suppose the arrays of photodiodes orthogonal to the trace and standing at a certain point. The trace is all black and the boards are well defined, its thickness is known exactly.

The quantization levels of the system cross the protodiodes at their baricenter, the dotted lines delimitate the region of the trace where the photodiodes have the logic value "0". We refer to these lines

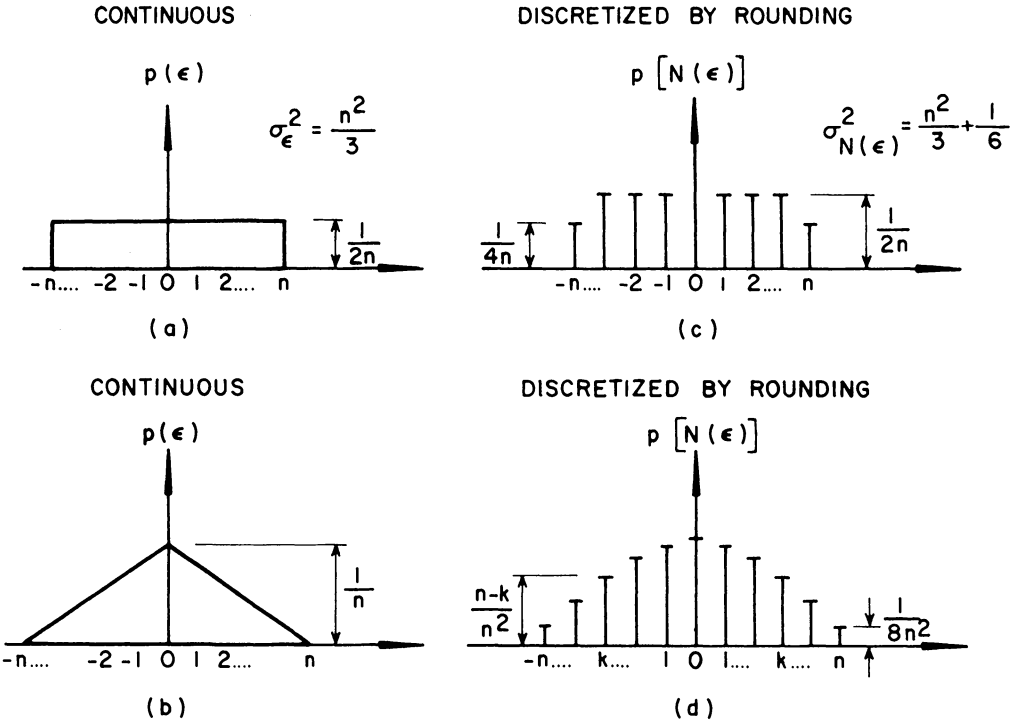

Figure 36. Probability distribution in digitization (After Trifunac et al.1971).

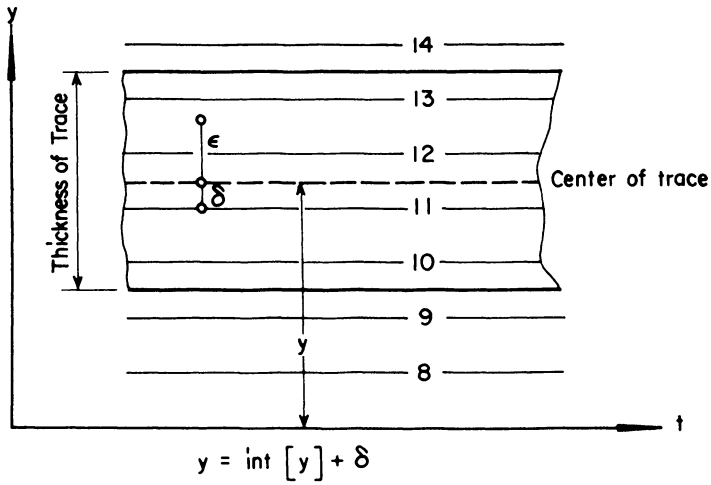

Figure 37. Quantization levels of the table (After Trifunac et al.1971)

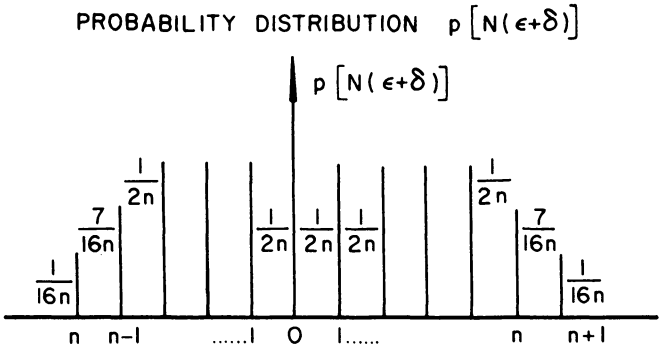

Figure 38. Probability distribution of P[N(ε+δ)].(After Trifunac et al. 1971).

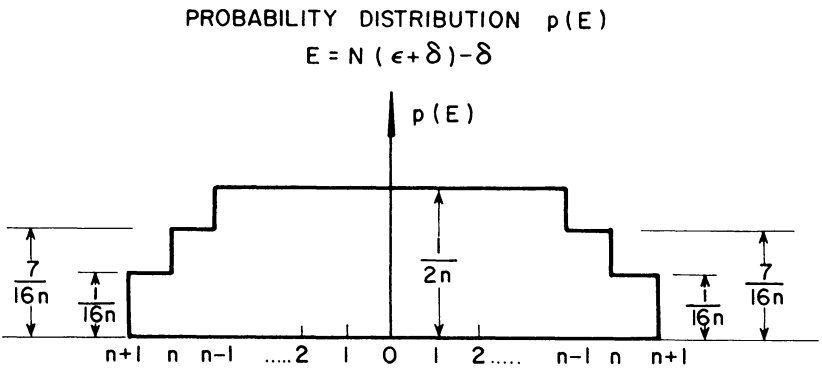

Figure 39. Probability distribution of P[N(ε+δ)].(After Trifunac et al. 1971)

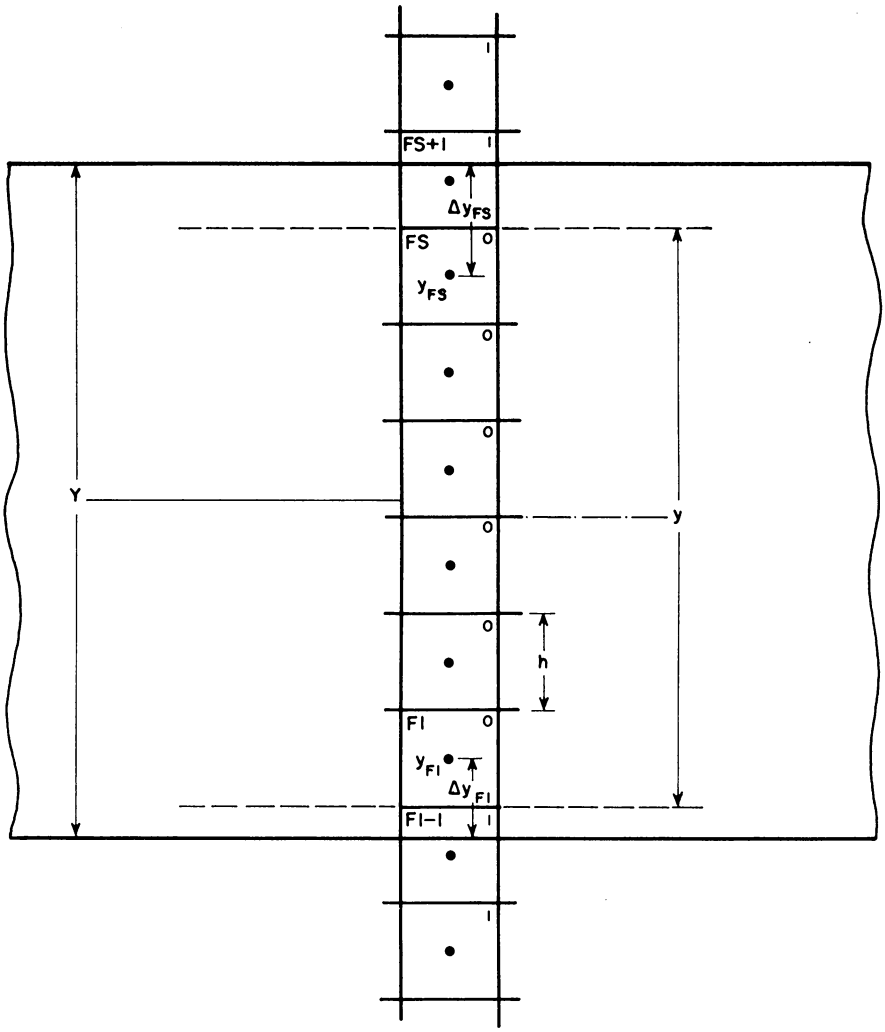

Figure 40. Trace of the record and contraves Photoscanner.

as the "logic boarders" of the trace.

Their position for an assigned thickness of the trace depends on the threshold Vs. For each scan the system provides a tern of integer values n, FI, FS that correspond respectively to the number of the scan and to the numerical order in the array of the first and the last photodiodes obscured by the trace. From this tern it is possible to know the coordinates of the sampled point. The time coordinate is:

$$t_n = K_1 \cdot n.\Delta_x \tag{19}$$

where K_1 is a scaling factor, if the film used for the digitization is the original $K_1 = 1$, and Δx is the sampling interval in the x-axis, the typical speed adopted for the carriage in 500 μ m/sec, the typical value of Δx is therefore 25 μ m.

The first and last photodiodes obscured by the trace have respectively ordinates

$$\begin{aligned} (y_{FI})_n &= h \cdot FI_n \\ (y_{FS})_n &= h \cdot FS_n \end{aligned} \tag{20}$$

where h, referring to Figure 40, is the height of one photodiode. The ordinate of the sampled point is assumed to be that of the center line of the trace that is

$$y_n = \frac{(y_{FI})_n - (y_{FS})_n}{2} \tag{21}$$

The positioning error is given by the difference

$$\varepsilon = Y_n - y_n \tag{22}$$

where Y_n is the true center line and y_n is evaluated with the (21). Referring to Figure 40, the positioning error is also defined by

$$\varepsilon = \frac{(y_{FI} + \Delta y_i + y_{FS} + \Delta y_s) - (y_{FI} + Y_{FS})}{2} \tag{23}$$

where Δy_i and Δy_s measure the distance from the real border and the logic one of the trace.

The maximum positioning error is:

$$\varepsilon_{max} = (y_{FI} + h + y_{FS} + h) - (y_{FI} + y_{FS}) = h \tag{24}$$

ε_{max} is equal to the dimension of a photodiode, that is 25 μ m. The distribution function of ε is constant in the range (0,h) because

the distribution function of Δy_i and Δy_s are independent and ranging from (0,h).

It is easy to recognize that these results are valid for any position of the trace respect to the array of the camera. For components of the accelerograms that have wavelength greater than 50 μm, that is frequency less than 200 Hz, ε_{max} is also independent from the motion of the photoscanner.

The rounding effect due to the quantization levels of the photoscanner is of the same order of magnitude of the positioning error.

Comparing the values of the positioning error and of the rounding effect of the automatic digitization to those of the hand digitization we have that:

- the rounding effect of the quantization levels is similar in both system, if the film is enlarged by a factor 4 in the case of manual digitization;
- the maximum positioning error ε_{max} of the automatic digitization is independent from the thickness of the trace and is 25 μm.
- the maximum positioning error in the manual digitization is strictly dependent from the thickness of the trace, and can be, in the case of the adoption of enlarged copies of the record, even twenty times larger than that of the automatic digitization.

Some comparisons have been performed between automatic and manually digitized data of accelerograms. We selected for the comparisons two records: the first from the Ancona earthquake (1972), recorded at Rocca, and the second from the Irpinia one (1980) recorded at Bagnoli Irpino. Both records were produced by SMA-1 Kinemetrics accelerographs.

For the hand digitization the D-MAC 2 table digitized was utilized, the automatic digitization was performed with Contraves system. Figures 41 and 42 show respectively the amplitude Fourier spectrum of the manual and automatic digitized data of the Rocca record. It is evident that the high frequency region of the two spectra has the same content while there are great differences in the low frequency region. In this region the amplitude spectrum of the manual digitized accelerogram is a factor 10 higher in the range 0.1 - 0.3 Hz. The two spectra begin to be identical at frequencies greater than 0.8 Hz.

The similarities of the spectra in the high frequency region could seem in contrast with the fact that the automatic digitization has an higher sampling rate than the manual one, but in case like the Ancona earthquake where very high frequency content is evident in the record, the human operator performs a very accurate digitization thanks to the presence of many peaks that he is able to recover very easily.

In Figure 43a, b are shown the acceleration, velocity and displacement time histories of the record for both digitizations. They have been calculated adopting the same cut-off frequencies for the passband filtering of the accelerograms. Because of the noise present in the manual digitized accelerogram in the low frequency region, there are great differences in the velocity and displacement waveforms spacially in the last part of the time-histories.

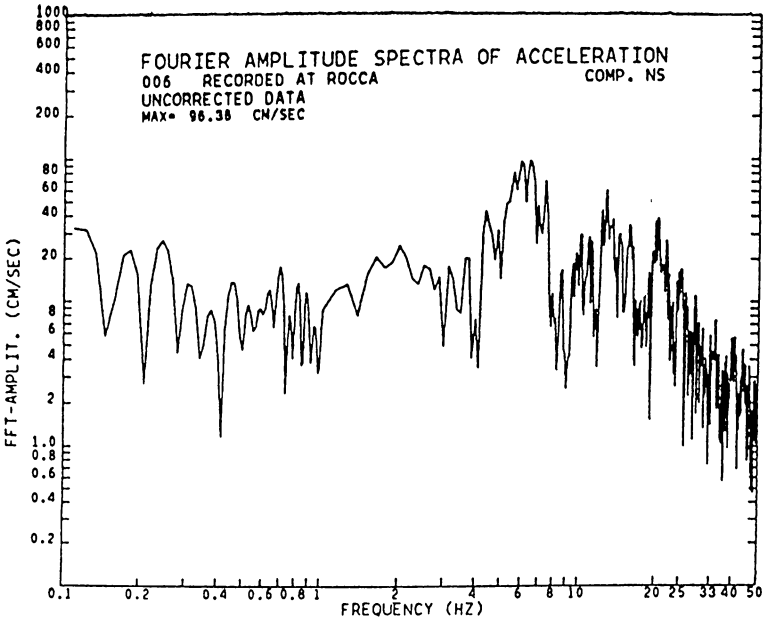

Figure 41. Fourier amplitude spectrum of the manually digitized data.

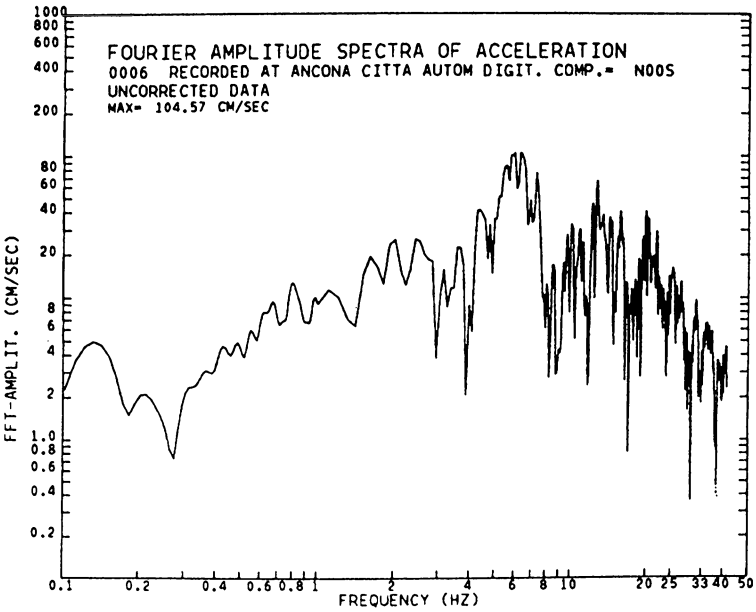

Figure 42. Fourier amplitude spectrum of the automatically digitized data.

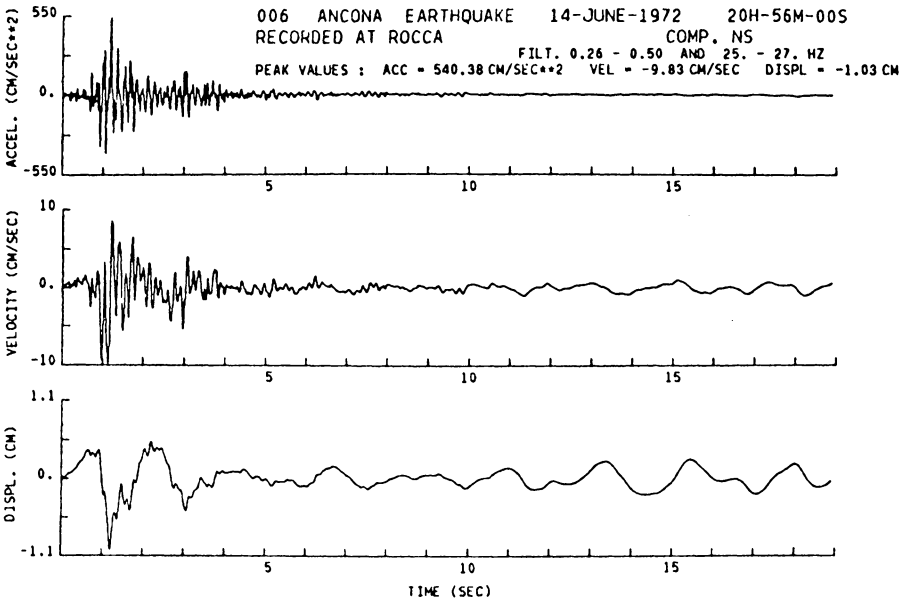

Figure 43 (a). Acceleration, velocity and displacement traces based on manually digitized data.

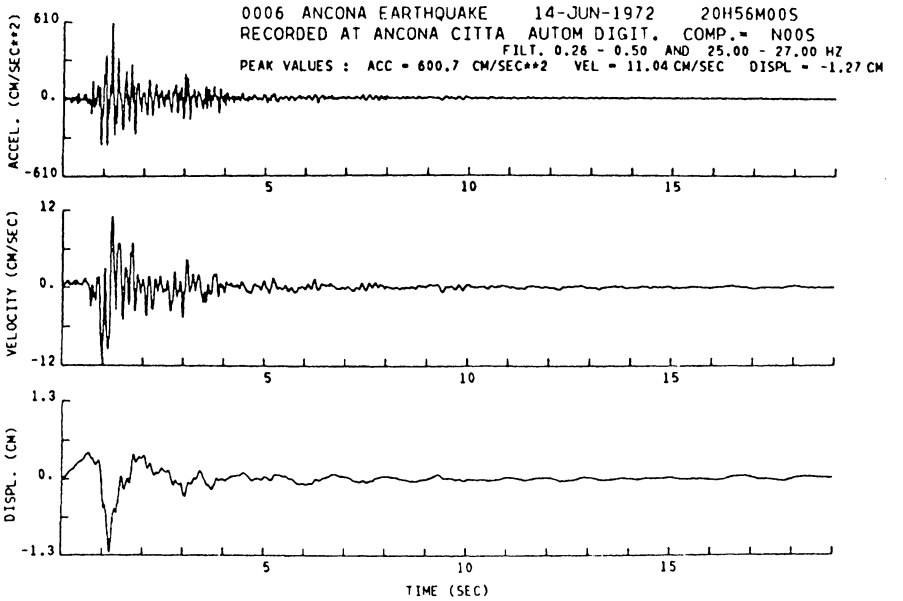

Figure 43 (b). Acceleration, velocity and displacement traces based on automatically digitized data.

Figures 44 and 45 show the Fourier amplitude spectrum of the record of Bagnoli Irpino, this record is very long (more than 80 seconds) and has lower frequency content at high frequency compared to the particularly evident in the high frequency region (f greater than 20 hz) where the spectrum of the manual digitization presents a plateau due to the noise of digitization. The human operator is not in condition of recovering accurately the high frequency components because of their small amplitudes. The acceleration, velocity and displacement waveforms shown in Figure 46 do not point out the noise at high frequency because of the limit of the analysis in time domain.

As already mentioned soon after the earthquake in Irpinia, one accelerographic station was set up installing, in the same place (Procisa Nuova), a SMA1 and a DSA1 accelerographs. Figure 47a, b,c shows the Fourier amplitude spectrum of one aftershock recorded in this station. The spectrum in 47a is that obtained adopting a manual digitization of the WE component recorded by the SMA1, the spectrum in 47b is that obtained adopting and automatic digitization of the same component and finally the spectrum in 87c is obtained directly from the accelerogram recorded by the DSA1 that provides equally digitized accelerograms sampled at 100 pts/sec. From the analysis of the spectra is evident an important difference in the frequency content of the low frequency range between the accelerogram recorded with the DSA1 and the one recorded with the SMA1. The spectrum below 1Hz of the automatic digitized accelerogram is lower than that of the accelerogram digitized manually, but it is still very high compared to that recorded by the DSA1. In the high frequency region the spectrum of the manual digitized accelerogram presents the plateau due to the random errors introduced by the human operator, while the spectra in 47b and 47c are very similar except for a spike at 40 Hz in the spectrum of the accelerogram recorded by the DSA1.

The automatic digitization of analog accelerograms allows the analysis the Fourier spectrum of the fixed trace without any sort of interpolation.

Figure 48, shows the Fourier amplitude spectrum of the fixed trace of the accelerogram recorded in Procisa Nuova with the SMA1. It is reasonable to assume this Fourier spectrum as the amplitude spectrum of the noiseof the instrument and to consider the signal to noise ratio for the selection of the cut-off frequencies for the pass band filtering for the accelerograms. Figure 49 shows this ratio for the record of Procisa Nuova automatically digitized. Fixing as reference line the value of 10 db, the cut-off frequencies are about 0.9 Hz and 20 Hz.

Figure 49 shows results of the numerical processing for the calculation of the acceleration velocity, displacement waveforms adopting these cut off frequencies for the pass band filtering of the record automatically digitized.

Figure 50 and 51 shows the results of the same calculation adopting the same pass band filtering respectively in the case of the manual digitization and the digitized data coming from the DSA1.

The DSA1 accelerograph has a pre event memory that allows the recording of the first motions of the seismic events.

Figures 49 and 11a look very much the same except for the first

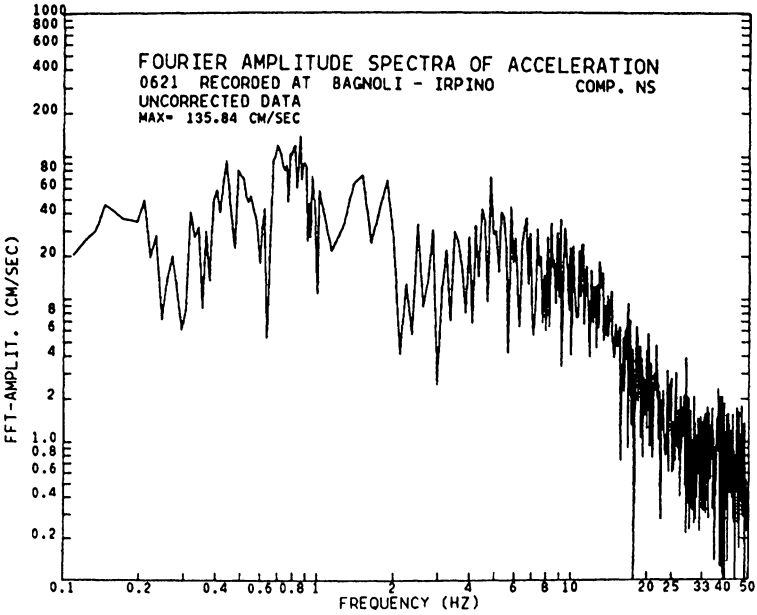

Figure 44. Fourier amplitude spectrum based on manually digitized data.

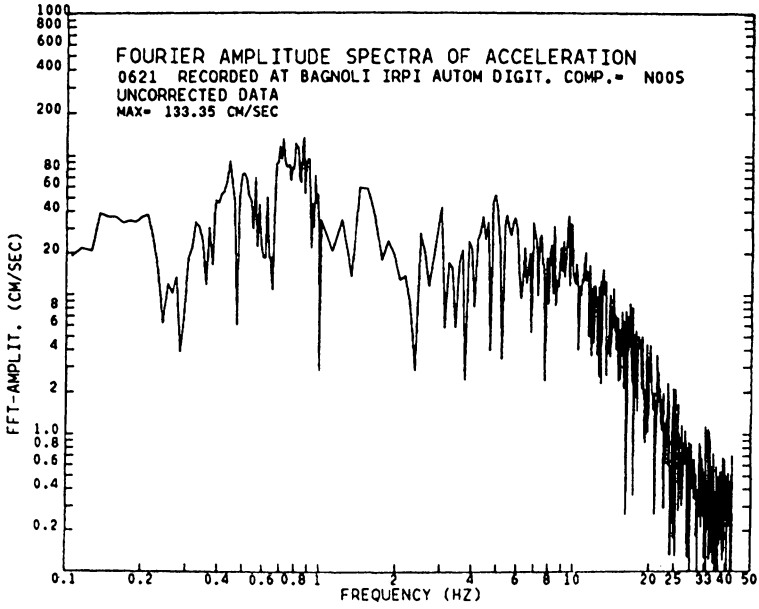

Figure 45. Fourier amplitude spectrum based on automatically digitized da

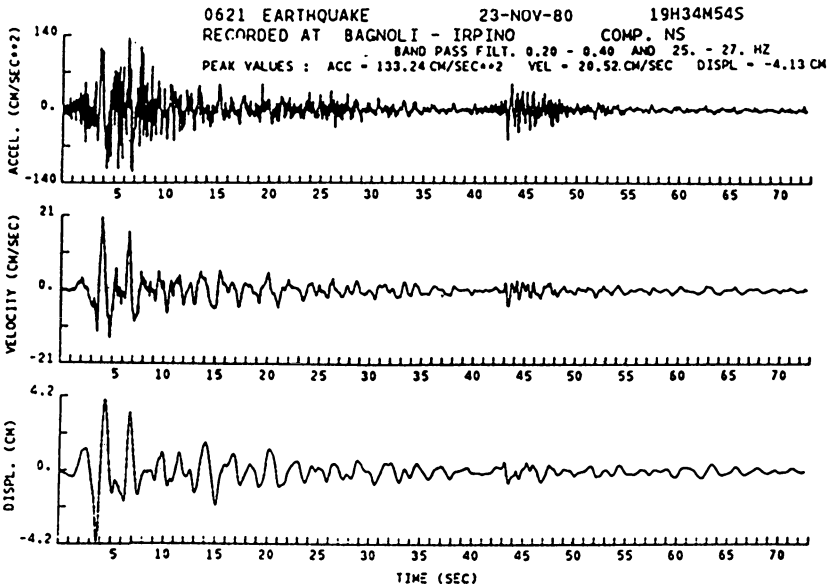

Figure 46 (a). Acceleration, velocity and displacement traces based on manual digitization.

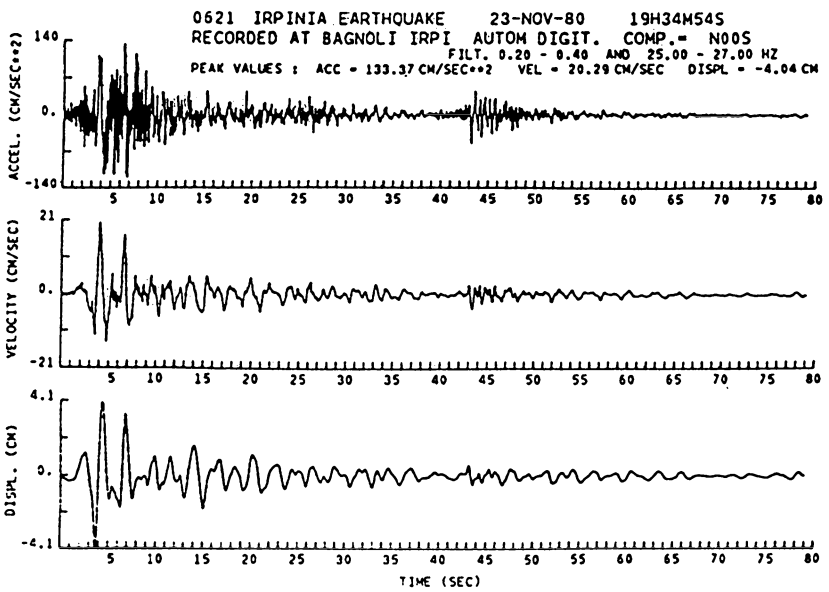

Figure 46 (b). Acceleration, velocity and displacement traces based on automatic digitization.

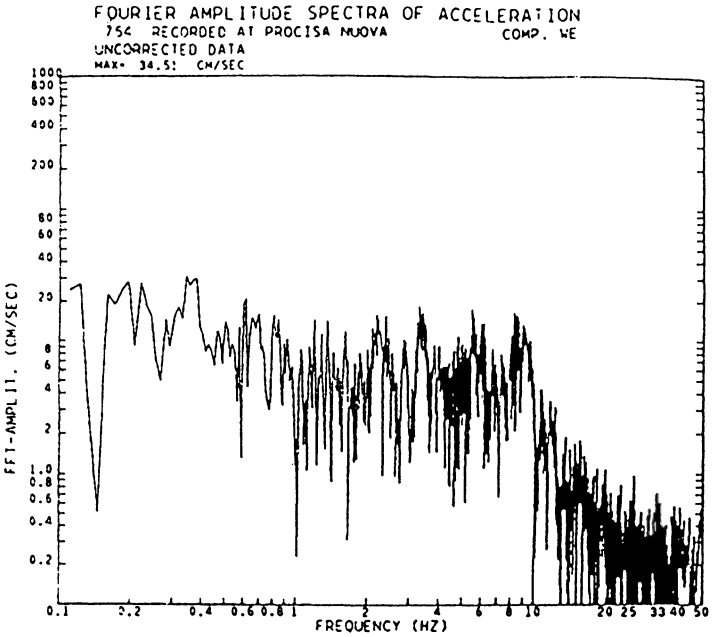

Figure 47 (a). Fourier amplitude spectrum based on manually digitized data.

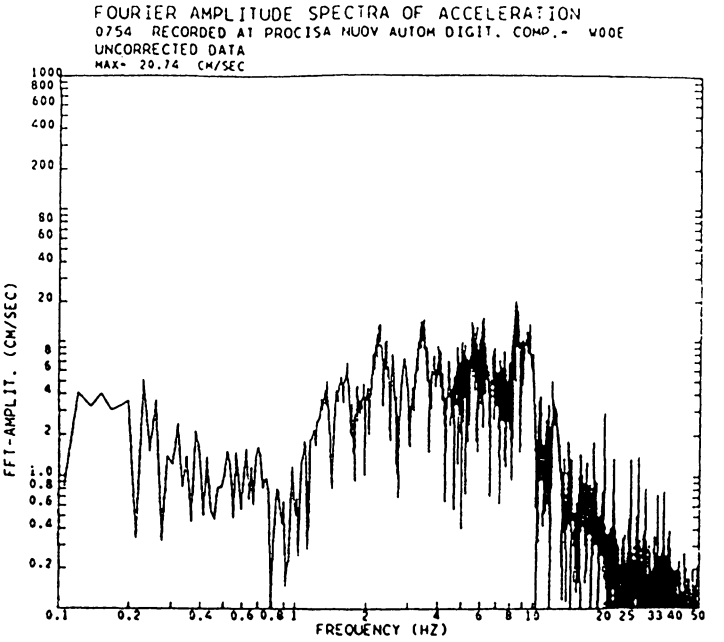

Figure 47 (b). Fourier amplitude spectrum based on automatically digitized data.

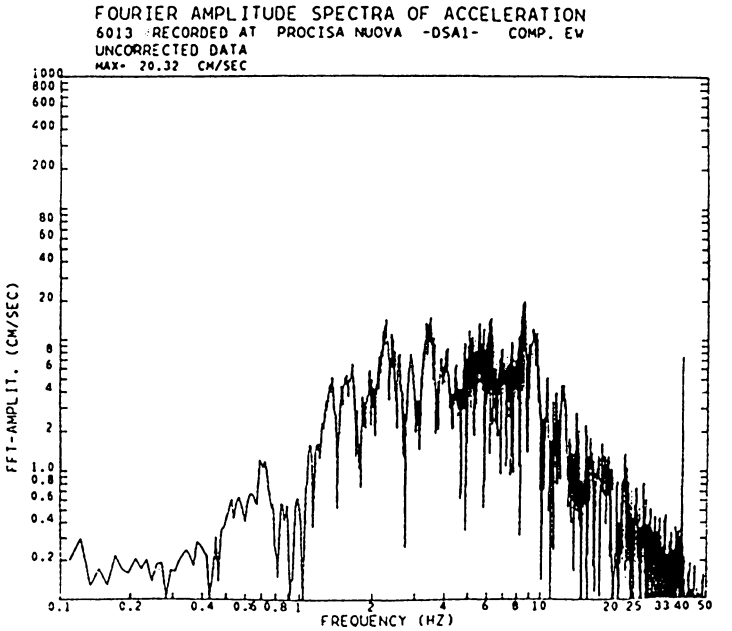

Figure 47 (c). Fourier amplitude spectrum based on digitizally recorded data.

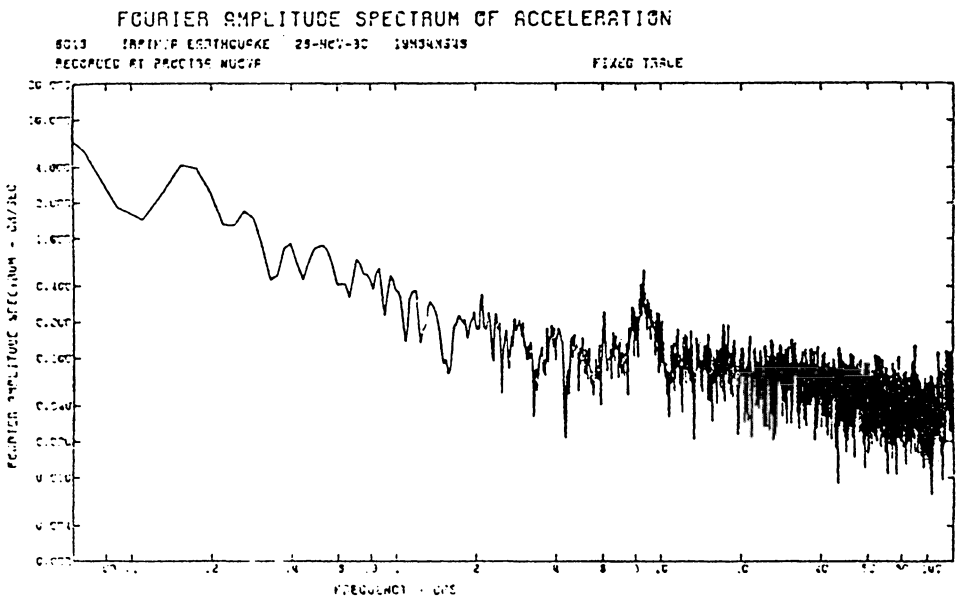

Figure 48 (a). Fourer amplitude spectrum of the fixed trace.

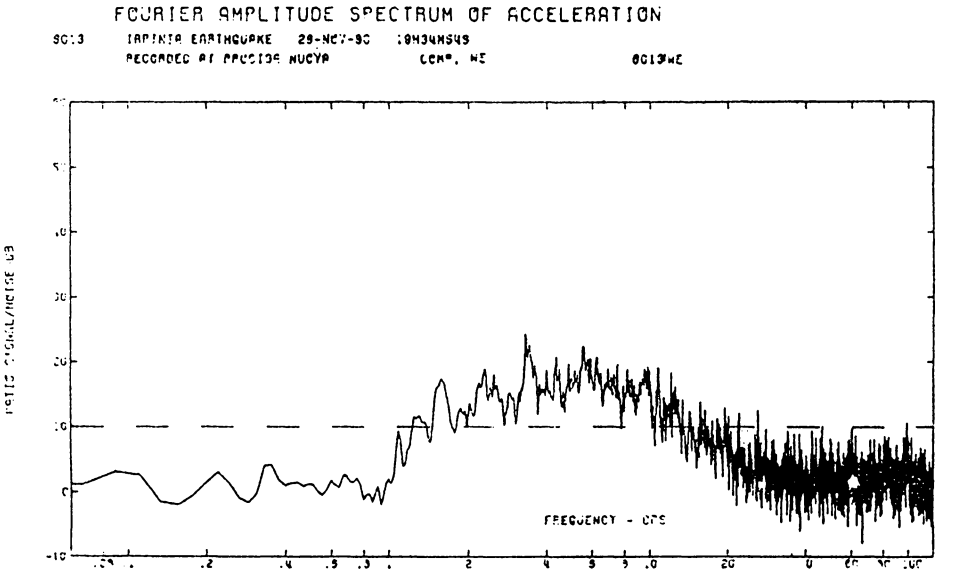

Figure 48 (b). Fourier amplitude spectrum of the fixed trace.

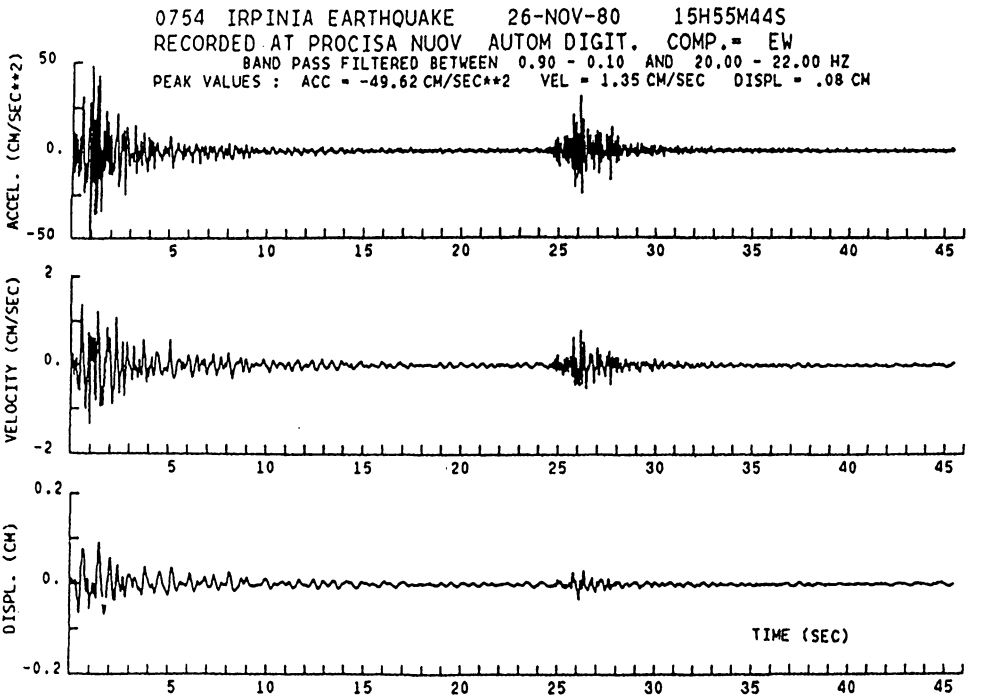

Figure 49. Acceleration, velocity and displacement traces (automatic digitization)

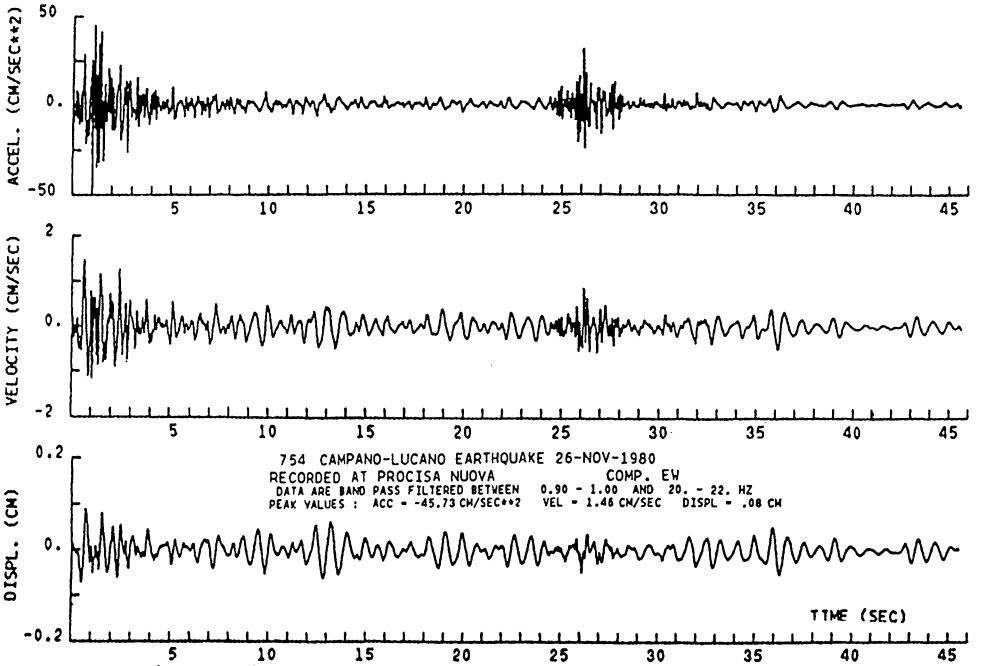

Figure 50. Acceleration, velocity and displacement traces (manual digitization)

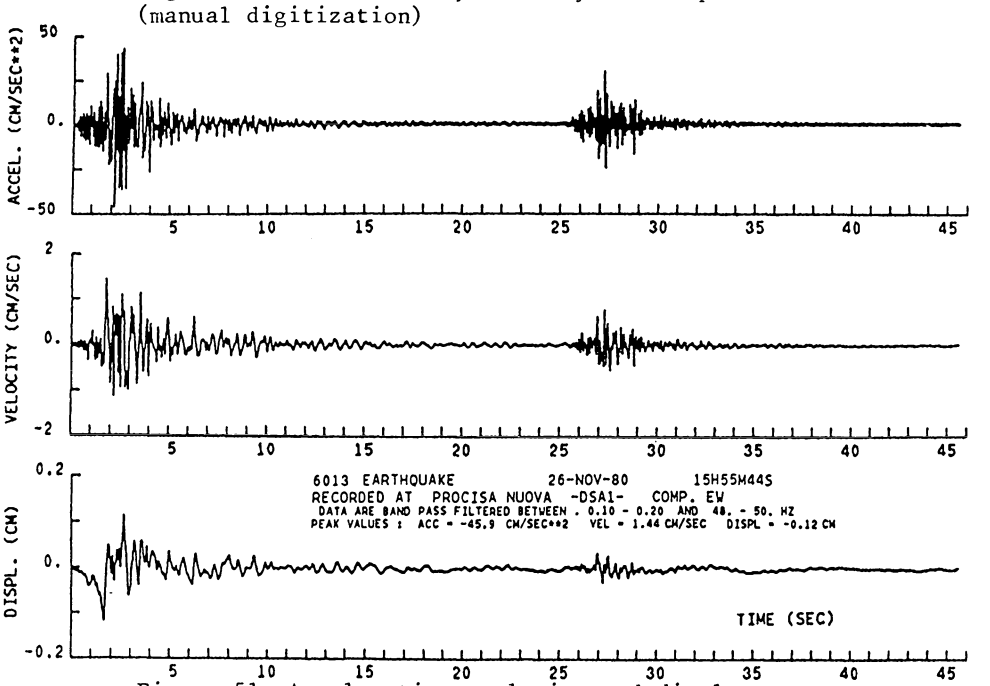

Figure 51. Acceleration, velocity and displacement traces from digitially recorded data.

portion of the signal (about 1 second) recorded by the DSA1. The time histories of Figure 11b on the contrary are heavily affected by the noise of digitization that cannot be removed by the filtering.

The results of Figures 49 and 11a are very important because they demonstrate that with an accurate analog to digital conversion it is possible to recover practically the same information obtained by a digital accelerograph of the type DSA1 Kinemetrics.

7. NUMERICAL PROCESSING OF STRONG MOTION DATA

Numerical processing of an accelerogram is performed to extract as much information as possible from it. Earthquake ground motion is very complex. The qualification and quantification of the key ground motion parameters, as they may be recorded by an accelerograph, are essential for engineering applications.

Starting from the digitized accelerogram, the ground acceleration, velocity and displacement, and the Fourier and response spectra of the ground motion are calculated.

The computation of velocity and displacement time-histories from the direct integration of digitized accelerograms, produces results utterly unrealistic, owing to distorsions of the acceleration time-history caused by several factors like: mechanical imperfection of the instrument, warping of the film, photographic process and digitization. All these factors contribute to alter uncontrollably the level of the baseline of the accelerogram, that is, the zero acceleration line all along the record.

Although the error in the numerical integration of the original accelerogram, may be very small in computing the acceleration time-history, the corresponding errors in velocity and displacement may be very large.

The first studies and techniques for the correction of the effects due to the unknown level of the baseline were developed in the time domain. They envisaged the adoption of a second-degree polynominal to be subtracted to the original accelerogram, that is, the baseline $a_o(t)$ is assumed to have a parabolic trend:

$$a_o(t) = C_1 + C_2 \ (t - t_o) + C_3 \ (t - t_o)^2; \ t_o < t < t_d \qquad (25)$$

in the interval $(t_o \ , \ t_d)$.

The method of least squares is then used to determine the coefficients $C_{1,2,3}$. Thus

$$\frac{\partial}{\partial C_i} \int_{t_o}^{t_d} \left[V(t)\right]^2 dt = 0 \qquad i = 1,2,3 \qquad (26)$$

where v(t) is the corrected velocity time-history.

Although no physical justification exists for the adoption of a parabolic trend for the baseline of the accelerograms this approach generally produces good results for record of short and medium duration. However, the effectiveness of the parabolic correction is affected by the length of the record, and is inadequate for the analysis of long-period components of the ground motion.

The adoption of a parabolic baseline for the acceleration entails for the velocity a baseline that can be described with a cubic equation.

An improvement of the parabolic correction is the method developed by Newmark (1973). The record is divided into several segments of adequate lenght, and the parabolic correction is applied to each segment, which is short enough to render the parabolic correction adequate.

To illustrate this point, the velocity time-history for the North-South component of the El Centro, 5-18-40, is presented in Figure 52. This record was corrected using a second degree polynomial and minimizing the error in square of the velocity within the first 30 seconds of the record. The velocity baseline for the simple parabolic correction underestimates the correction in the initial portion of the record (0 to 10 seconds), and overestimates the correction for the subsequent portion (10 to 30 seconds). In order to further reduce the error in the adjustment procedure, the baseline correction was applied in several segments of the record. Three segments of approximately 10 seconds each were selected.

The segmented correction is more flexible and allows a better fitting of the baseline to the record characteristics.

Figs 53 and 54 show respectively the velocity and displacement obtained using the simple and the segmented parabolic corrections. However, the correction procedure followed by Newmark has its limits due to subjectivity in the selection of the length of the segments, and hence in the waveform of the resulting baseline, and to the discontinuities introduced in the corrected acceleration at the points of contact of the parabolae. These discontinuities determine remarkable effects mainly in the periods over 10-15 secs.

8. CALTECH PROCEDURE

Trifunac (1970) developed a new method for the correction of the baseline of the accelerograms. The great merit of Trifunac's work is that it interprets the problem of the correction in terms of the analysis of the signal/noise ratio, that is, it selects and defines the frequency ranges where the distortion of the accelerogram and of its baseline are more significant.

The distortions that might affect the records are shown in following table (Trifunac et al; 1971). They are divided into two groups: distortions whose effects are evident mainly at low frequencies (below 1 Hz), and distortions whose effects are evident mainly at high frequencies (over 10 Hz).

As regards the contents of the table, the problem posed by the baseline correction becomes the problem of filtering from the accelerogram

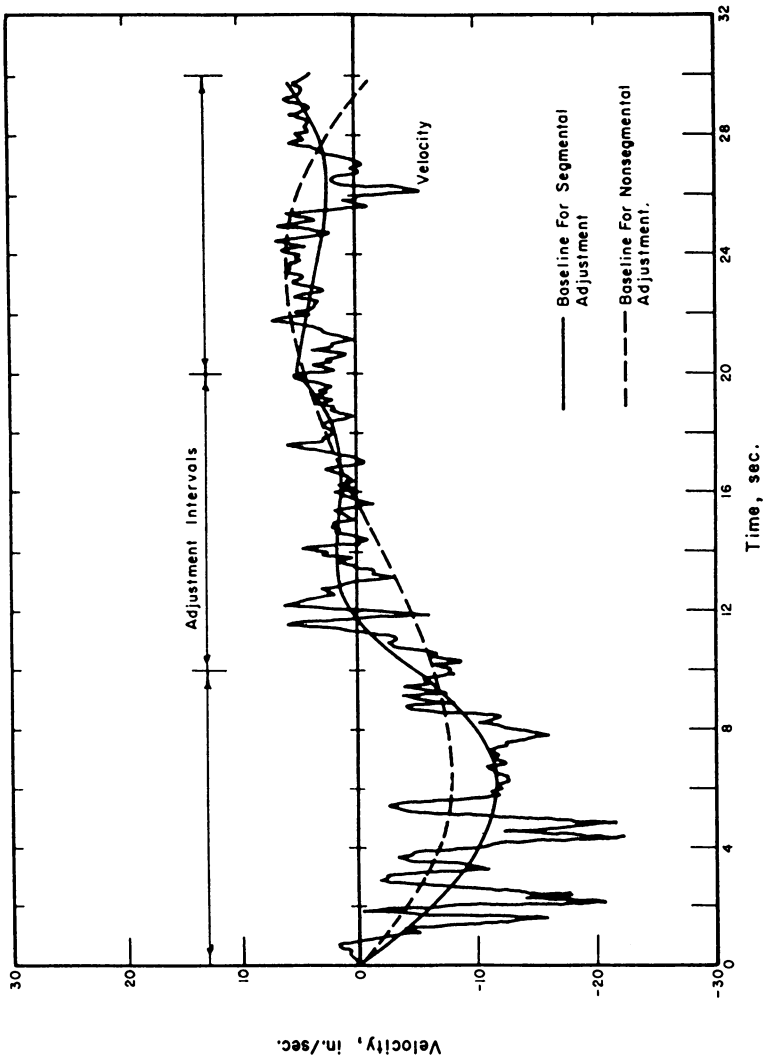

Figure 52. Segmental versus nonsegmental parabolic adjustment (After Newmark, 1973).

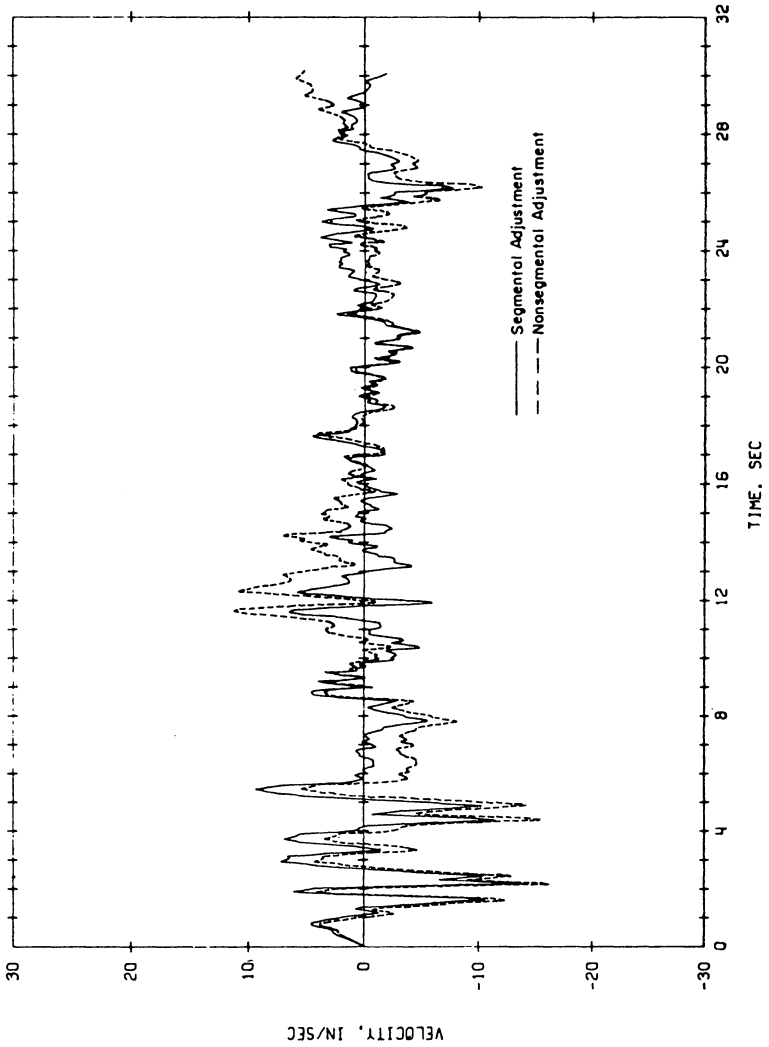

Figure 53. Segmentally adjusted velocity trace (After Newmark, 1973).

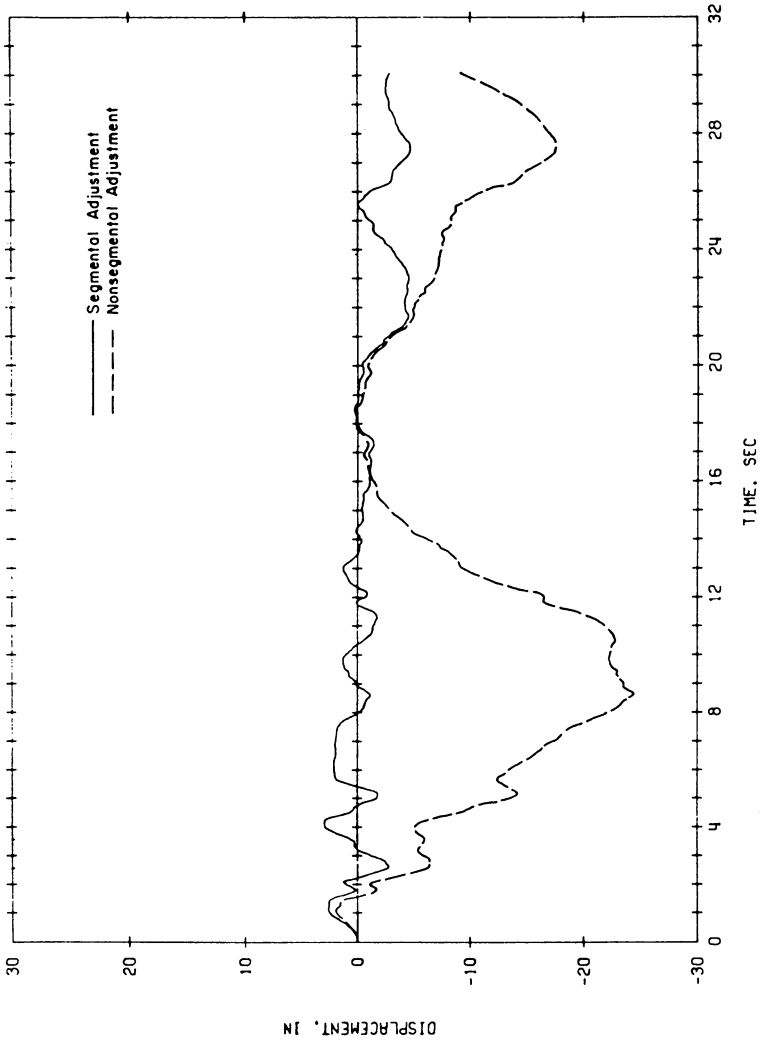

Figure 54. Segmentally adjusted displacement trace (After Newmark, 1973).

the components whose distortion irremediably compromises reliability of the final data.

Long Period Distortions
(Low Frequency Distortions)

Distortions caused by the transverse play of the recording film in the drive mechanism.

Distortions due to the warping of records, caused by aging, and distorsions introduced by photographic processing.

Systematic distortions due to imperfect mechanical transverse mechanisms of the cross-hair system on the digitizing table.

Random errors generated during the digitization process.

High Period Distortions
(High Frequency Distortions)

Modification by harmonic amplitudes and shift of phases caused by the finite natural frequency of the accelerograph transducer.

Disortions resulting from the imperfections in the transducer design (higher modes).

Random digitization errors.

Errors caused by inadequate resolution of the digitizing equipment.

Low-pass filtering effects in the optical mechanical digitization.

The test on the raliability of the photographic processing of strong-motion accelerograph films and of the manual digitization process done at Caltech, led to fix the cut-off frequencies for the passband filtering respectively to 0.07 and 25 Hz.

Beyond this frequency range, (0.07-25 Hz) the true signal is so affected by distortions as to render its discrimination impossible.

For the correction of the baseline at low frequencies the scheme used by the Earthquake Engineering Research Laboratory at Caltech is shown in Figure 55.

The basic concept consists in to subtract from the initial accelerogram a low-pass filtered version of it from which all frequencies higher than 0.07 Hz have been removed.

The removal of long-period Fourier components is performed in the

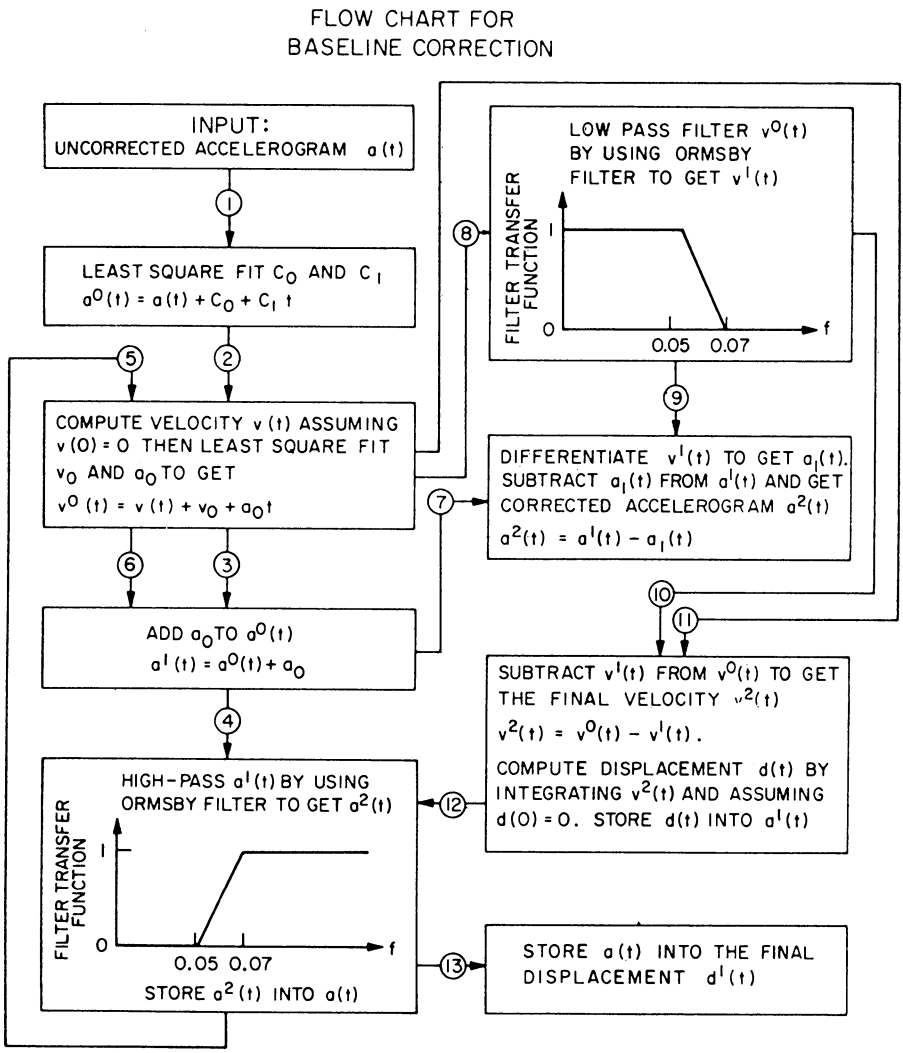

Figure 55. Caltech base line correction routine.

time domain by passing a filter, with specified shape and duration, along the time series, adjusting each point of the time series in turn. In the Caltech's scheme the filtering is performed with the Ormsby's filter (1961).

Ormsby's filter belongs to a closs of digital filers characterized by a transfer function with unit gain and zero phase shift in the pass-band, and a pth order roll-off in the transition zone between the pass-band and the rejection-band.

With p=1, the weighting function becomes:

$$h(t) = \frac{1}{2\pi} \int_{-\infty}^{\infty} e^{i\omega t} H(\omega)\, d\omega \tag{27}$$

is reduced to:

$$h(t) = \frac{\cos \omega_c t - \cos \omega_T t}{\pi(\omega_T - \omega_c)\, t^2} \tag{28}$$

The precision of the filter is given by the error of filtering defined as :

$$\varepsilon(\omega,N) = \hat{H}(\omega) - H(\omega) \tag{29}$$

where $H(\omega)$ is the transfer function of the ideal filter obtainable only with an infinite number of weights:

$$H(\omega) = \sum_{n=-\infty}^{\infty} h_n e^{i\, 2\pi n\omega/\omega_s} \tag{30}$$

and $\hat{H}(\omega)$ is the transfer function of the real filter, using the finite number of weights, N:

$$\hat{H}(\omega) = \sum_{n=-N}^{N} h_n\, e^{i2\pi n\omega/\omega_s} \tag{31}$$

ω_s and h_n are respectively the sampling angular frequency and the nth weight of the filter. Since $H(\omega)$ is hermitian, i.e., $H(-\omega) = H^*(\omega)$, it follows that Ormsby's filter is symmetric, and the following equality of weights holds:

$$h_n = h_{-n} \tag{32}$$

Ormsby gives an empirical expression for ε obtained from experimental curves :

$$\varepsilon = \frac{0.012}{\Delta f . N . \Delta t} \tag{33}$$

where Δf is the difference between the roll-of frequency and the cut-off frequency and Δt is the time sampling interval, i.e., the reciprocal of the sampling frequency, f_s . A value of around 1% is reasonable and makes it possible to simplify (33), which then becomes a relationship between Δf, N and Δt

$$\Delta f \cong 1/N.\Delta t \tag{34}$$

The product $N \cdot \Delta t$ corresponds to half the length of the filter window, L:

$$L = 2\ N.\Delta\ t \tag{35}$$

From (34) and (35) we obtain a relation between Δf and L:

$$\Delta f = 2/L \tag{36}$$

The values of Δf (0.07 - 0.05 = 0.02) and of ε (1.2%) chosen in the Caltech routine are such that the direct application of Ormsby's filter on the input time-history with constant Δt = 0.02 sec. would have been an uneconomic use of computer time. From (34), N = 2500 for the number of filter weights, that is, 5001 effective weights to apply for each of the input points.

To avoid this, referring to Fig. 55 the initial accelerogram is at first low-pass filtered with a running mean filter, or box-car filter. The time window of the box-car filter is fixed at 0.4 seconds so that the Nyquist frequency $1/(2 \cdot \Delta t)$, of the initial accelerogram is altered from 25 Hz. to 2.5 Hz., filtering out, approximately, the higher frequencies. At this point there is no reason to keep Δt equal to 0.02 seconds and it is possible to decimate the points of the digitized accelerogram so that Dt is equal to 0.2 seconds. In this way the number of weights of Ormsby's filter is decreased, for the same Δf and the same ε , from 2500 to 250, applied to only a tenth of the initial number of points.

REFERENCES

Aki K., (1968). Seismic displacement near a fault. J. Geophys. Res.73, p.5359-5376.

Archuleta R., Day S. M., (1977). Near field particle motion resulting from a propagating stress relaxation over a fault embedded within a layered medium. EOS Trans. AGU, 58, 445.

Arias A., Sandoval H. (1979). Muestreo e interpolacion de accelerograms obtenidos en instrumentos de registro optico o mecanico. Universidad Nacional Autonoma de Mexico, Instituto de Ingenieria, 416.

Basili M., Brady AG., (1978). Low frequency filtering and the selection of limits for accelerogrmas corrections. ENEA-RT|FIMA (78)2.

Basili M. Mariano A. (1980) Caratterizzazione delle distorsioni introdotte in un processo di conversione analogico/digitale manuale di una registrazione accelerometrica, Rapporto Tecnico CNEN.

Boore D.M., Zoback M. D., (1974). Two-dimensional kinematic fault modelling of the Pacoima Dam strong motion recordings of the February 9, 1971, San Fernando earthquake. Bull. Seism. Soc. Am., v. 64, p. 555-570.

Bouchon M., (1978). A dynamic model for the San Fernando earthquake. Bull. Seism. Soc. Am. v. 71, n.6, p.2039-2070, December 1981.

Brigham E. (1974). The Fast Fourier Transform, Prentice Hall Inc.

Campbell K.W., (1981). Near-source attenuation of peak horizontal acceleration. Bull. Seism. Soc. Am., v. 71, n. 6, p. 2039-2070, December 1981.

Chang F. K., Krinitzky E. L., (1977). Duration, spectral content and predominant period of strong motion earthquake records from Western United States. U.S. Army Engineer Waterways Experiment Station Report n. 8.

Cooley J.W., Tukey J.W. (1965). An Algorithm for the Machine Calculation of Complex Fourier Series, Math. Comput., 19, 297-301-

Donovan N. C., 1973. A statistical evaluation of strong motion data including the Feb. 9, 1971 San Fernando earthquake. Proc. World Conf. Earthquake Eng., 5th Rome.

Fletcher J.B., Brady A.G., Hanks T.C., (1980). Strong-motion accelerograms of the Oroville, California, aftershocks: data processing and the aftershock of 0350 August 6, 1975, Bull. Seism. Soc. Am., 70, 243-267.

Hudson D. E. (Ed.), 1976. Strong motion earthquake accelerograms index volume. Report No. EERL 76-02, Earthquake Engineering Research Laboratory, California Institute of Technology. Pasadena August 1976.

Hudson D.E. (1983). Strong Motion Instrumentation System. Proc. Golden Anniversary Workshop on Strong Motion Seismometry, March 30-31, 1983, Dep. of Civil Engineering. University of Southern California Los Angeles, California.

Laccarino E., Zaffiro C.(1973). Studies on a Network of Strong Motion Accelerographs to be installed in Italy, Proceedings of the Fifth World Conference on Earthquake Engineering, 25-29 giugno 1973, Rome, Italy.

Iwan U.D. (1960). Digital Calculation of Response Spectra and Fourier Spectra, Unpublished Note, California Institute of Technology, Pasadena.

Iwan W. D. (Ed.), 1981. Proceedings of the U.S.National Workshop on Strong-Motion Earthquake Instrumentation. April 12-14 1981, Santa Barbara, California.

Kulhanek O. (1976). "Introduction to Digital Filtering in Geophysics", Elsevier Scientific Publishing C.

McGuire R. K., Barnhard J.A., 1977. Magnitude, distance and intensity data for C.I.T. strong motion records. U.S. Geological Survey Journal of Research, v.5 n.4, p. 437-443.

Newmark N.M. (1973). A study of vertical and horizontal earthquake spectra, WASH - 1255 U.S. A.E.C. Washington, D.C.

Newmark N.M., Blume J. A., Kapur K.K., (1973). Seismic design spectra for nuclear power plants. J. Power Div., ASCE, 99, PO2, Proc. Paper 10142.

Newmark N. M., Mohraz B., Hall W. J., (1976). Statistical studies of vertical and horizontal earthquake spectra. U.S. Nuclear Regulatory Commission, Contr. n. AT(49-5)-2667.

Nigam N.C., Jennings P.C. (1968) Digital Calculation of Response Spectra from Strong-Motion Earthquake Records, Earthquake Eng. Res. Lab., California Institute of Technology, Pasadena.

Ormsby J.F.A., (1961). Design of Numerical Filters with Application to Missile Data Processing, Association for Computing Machinery, Jour., 8, 440-466.

Perez V., (1974). Time dependent spectral analysis of thirty-one strong motion records. U.S. Geological Survey, Open-File Report, November 1974.

Schnabel P.B., Seed H.B., (1972). Accelerations in rock for earthquake in the Western United States. Earthquake Engineering Research Center, Report EERC 72-2, University of California Berkeley.

Seed H. B., Ugas C., Lysmer J., (1974). Site dependent spectra for earthquake resistant design. College of Engineering. Report EERC 74-12, University of California Berkeley.

Shapiro H.S., Silverman R.A. (1960). Alias-free sampling of random noise, Journal Society Ind Appl. Mat, 8 - 255-248.

Trifunac M.D. (1970). Low-frequency digitization errors and a new method for zero base-line correction of strong-motion accelerograms, Earthquake Engineering Research Laboratory EERL 70-07, Calif. Inst. of Tech. Pasadena, California.

Trifunac M.D. (1971). Zero base-line correction of strong-motion accelerograms, Bull. Seismic Soc. Am. 61, 1201-1211.

Trifunac M.D., Udwadia F.E., Brady A.G. (1973). Analysis of errors in digitized strong-motion accelerograms, Bull. Seism. Soc. Am. 63, 157-187.

Trifunac M.D., Lee V. (1973). Routine Computer Processing of Strong Motion Accelerograms. Earthquake Engineering Laboratory, California Institute of Technology, Pasadena, California.

Trifunac M. D., Brady A.G., (1975a). A study on the duration of strong earthquake ground motion. Bull. Seism. Soc. Am., v.65, n.5, p.581-626.

Trifunac M. D., Brady A.G., (1975b). On the correlation of seismic intensity scales with the peaks of recorded strong motion. Bull. Seism. Soc. Am., v.65, n. 1.

STRONG GROUND MOTIONS IN ITALY: ACCELEROGRAM SPECTRAL PROPERTIES AND PREDICTION OF PEAK VALUES

Antonio Rovelli
Instituto Nazionale di Geofisica
Rome, Italy

ABSTRACT. In view of the paucity of data for strong earthquakes numerical techniques for simulating ground motion are being increasingly utilized. Two important aspects from the standpoint of accurate modelling are : a good knowledge of the seismotectonics of the region and the wave propagation mechanisms in the crust. This paper elaborates on the strong motions in Italy with special emphasis on the accelerogram spectral properties and prediction of peak values.

1. INTRODUCTION

Italy has always been a country characterized by high seismic activity. Thousands of data referring to its seismic activity have been preserved for centuries in contemporary chronicles, convent diaries and municipal archives. For years these data represented the only available source of information concerning the seismic activity of the territory. They are still extremely important because of the long period of time they span (more than twenty centuries!). Over the past two decades or so, in addition to macroseismic data, another important data base has become available to seismologists, engineers and geologists dealing with problems connected with seismic risk, i.e. seismometric and accelerometric instrumental records, in digital form. Six strong earthquake sequences, with a maximum magnitude exceeding 5, which occurred in Italy over the past fifteen years, have been particularly well monitored by instruments (see Fig.1). The most significant seismological characteristics of the main even of each of these sequences are shown in Table I. All the Italian sequences listed in Table I are accompanied by a large amount of data, collected in Italy by the ENEL-ENEA Joint Commission (accelerometric) and by university institutes and research agencies (seismometric). Included among the latter is the Istituto Nazional di Geofisica with its on-line network of teletransmitted data memorized in digital Form. As can be seen, in addition to the Italian sequences, also the Montenegro event of 15 April 1979 has been included in Table I. This particular event occurred off the Yugoslavian coast in front of the Central Italian regions on the Adriatic coast and was very accurately monitored by the

M. O. Erdik and M. N. Toksöz (eds.), Strong Ground Motion Seismology, 333–354.
© 1987 by D. Reidel Publishing Company.

TABLE 1. THE MOST SIGNIFICANT SEISMOLOGICAL CHARACTERISTICS OF THE MAIN EVENT

Event	Date	Magnitude	Seismic Moment (dyne.cm)	References
Ancona	14 June 1972	4.7	$1\ 10^{23}$	Console et al., 1973
Friuli	6 May 1976	6.3	$3\ 10^{25}$	Cipar, 1980; Bonamassa et al., 1983; Zonno and Kind, 1984
Montenegro	14 April 1979	6.7	$1\ 10^{26}$	Boore et al., 1981; Console and Favali, 1981
Valneria	19 September 1979	5.6	$6\ 10^{24}$	Deschamps et al., 1984
Irpinia	23 November 1980	6.5	$6\ 10^{25}$	Deschamps and King, 1983
Gubbio	29 April 1984	5.3	$3\ 10^{24}$	NEIS
Abruzzo National Park	7 May 1984	5.6	$8\ 10^{24}$	NEIS

stations of the Italian National Seismic Network and by the Yugoslavian Accelerometric Network.

Now that these data are available, it has become possible in Italy to make a start on studying the laws of attenuation, the scaling laws of ground motion and trends in the peak values of motion in relation to the seismotectonic characteristic of each of the above regions.

The acquisition of instrumental data, particularly for strong earthquakes, for several Italian or neighbouring seismogenetic regions has led to a turning point, to a change of method with respect to the stage in which only macroseismic data were used. It is now possible to make direct quantitative evaluations of the parameters defining the dangers of seismic excitation (e.g. the peak values of velocity and acceleration). Although this was an important breakthrough, there is still not enough information available to set up a large data base referring to strongest possible ground motions, and too little is still known about strong earthquakes at this preliminary stage of the project. In these conditions, one possible approach consists of using the information contained in low and medium magnitude earthquakes to predict to behaviour of the stronger earthquakes on the basis of more reliable theoretical models. The availability of data referring to the strength of the seismic excitation only after strong earthquakes have occurred in regions with high seismic activity means that what we know is restricted to a small number of seismic areas. Unfortunately, since the highly seismic zones in Italy vastly outnumber the six mentioned, the problem of predicting future hazards in terms of the size of the seismic input also in the other seismic areas is thus high on the list of priorities of those concerned with seismic risk.

In view of the spaucity of data for strong earthquakes in Italy, in recent years numerical techniques for simulating ground motion have been applied with increasing interest. Two important review studies illustrate the state of the art and the potential offered by the various numerical modelling techniques (Aki, 1982; Boore, 1983a). Two particularly important aspects from the standpoint of accurate modelling are: a good knowledge of the seismotectonic characteristics of the region in which the earthquakes are assumed to occur, which is necessary in order to make a correct evaluation of the source dynamics: a preliminary study to be made of the propagation and attenuation mechanisms in the crust and, above all, in the upper layers. The latter are those which have been observed to have the greatest effect on the size of the seismic input at a given site. In this sense, the recording and study of medium magnitude earthquakes in seismically active areas has proved just as useful for the acquisition of all the fundamental information required for correctly predicting strong ground motions.

2. NUMERICAL TECHNIQUES

Strong-motion recordings are used to monitor the high-frequency component of the motion ($\gtrsim$ 1Hz). They thus allow an investigation to be made of that part of seismology which borders on earthquake engineering (see Fig.2) The collection of acceleration time histories allows seismologists and

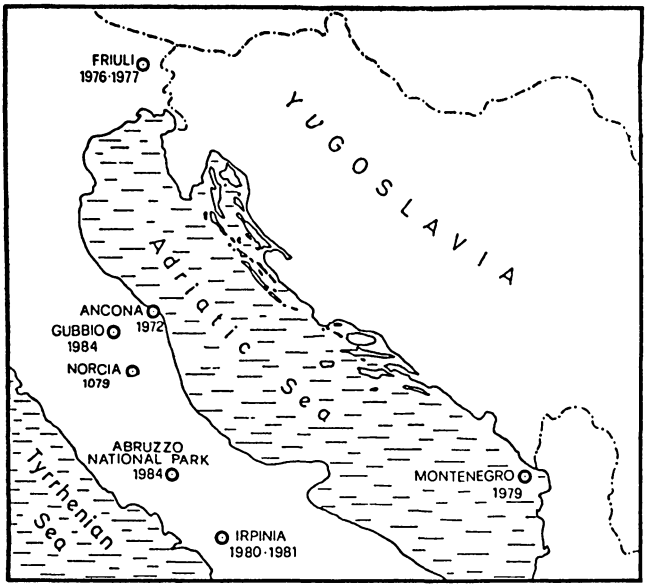

Figure 1. Seismogenic areas where earthquakes occurred over the past fifteen years, with a maximum magnitude exceeding 5

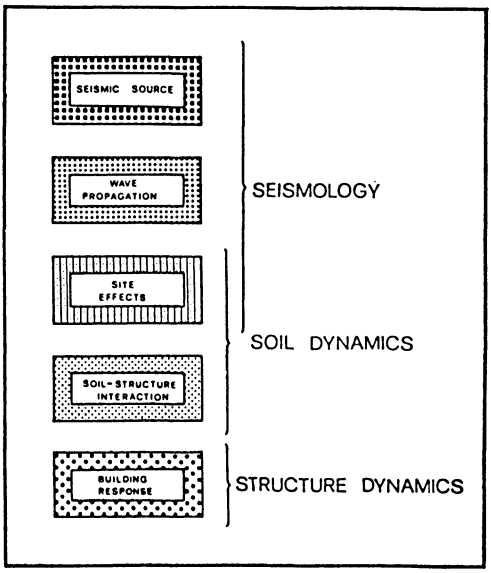

Figure 2. Seismology and earthquake engineering: topics of interest for seismic risk studies.

engineers to predict, in terms of earthquake size, the seismic excitation to be resisted by the structures at different frequencies and in environments with different geological and topographic characteristics. Mention has already been made of the importance of computer simulations of motions in those regions in which no significant data has even been recorded or, even when data do exist regarding events of interest, the events themselves are smaller in magnitude than maximum expected. Boore (in the present volume) has shown that two approaches to the problem of numerical simulation are generally made. In one of these, the deterministic approach, a study is made of the displacement field generated in the surrounding space by the propagation of the rupture along a fault of given size and direction. Even though these techniques offer the advantage of being able to use readily available information on strong-motion earthquakes (i.e. fault location, source mechanisms, etc.) and allow sufficiently accurate predictions to be made concerning the low-frequency component of the motion (< 1 Hz), their limitations are unfortunately not negligible as far as the high-frequency band is concerned (e.g. extreme complexity of the computer codes, lack of information usually available about the details of the rupture, high costs, etc...).

The second, or stochastic, approach neglects seismological considerations and consists in the generation and treatment of discrete sequences having the characteristics of, often Gaussian, white noise, to simulate the randomness of the rupture and the scattering of the seismic waves inside the Earth. Despite its limited physical basis, this approach offers the advantage of lower costs.

Up to only a few years ago, these two different approaches were considered as alternatives. However, there has been an increasing awareness in recent years of the importance of developing mixed simulation techniques. It has been attempted to develop procedures that, starting from mathematical artificies of a statistical nature, make it possible to take into account the physical characteristics of the earthquakes to be simulated, for instance, by manipulating sequences of random numbers according to seismological models of the seismic radiation spectrum.

An important role is played in this category by simulations using ARMA (autoregressive - moving average) processes. The time-evolution of this type of linear process can be represented by the equation

$$\begin{aligned} Xt = a_o + a_1 X_{t-1} + a_2 X_{t-2} + \cdots + a_r X_{t-r} + \\ + b_o \ell_t + b_1 \ell_{t-1} + b_2 \ell_{t-2} + \ldots + b_q \ell_{t-q} \end{aligned} \qquad (1)$$

where t represents the discrete index corresponding to successive increments of the time sampling Δt and e_t is a Gaussian white noise sequence. The a_j ($j = 0,1,2,3\ldots, p$) and b_k ($k = 0,1,2,\ldots,q$) are the coefficients of linear regression and are estimated from the data. In particular, a type (1) process is denoted as ARMA (p,Q) in order to indicate that the degree of the regressive portion (AR) is p and of the moving average portion is Q. One example of an accelerogram obtained using this type of procedure is shown in Fig.3.

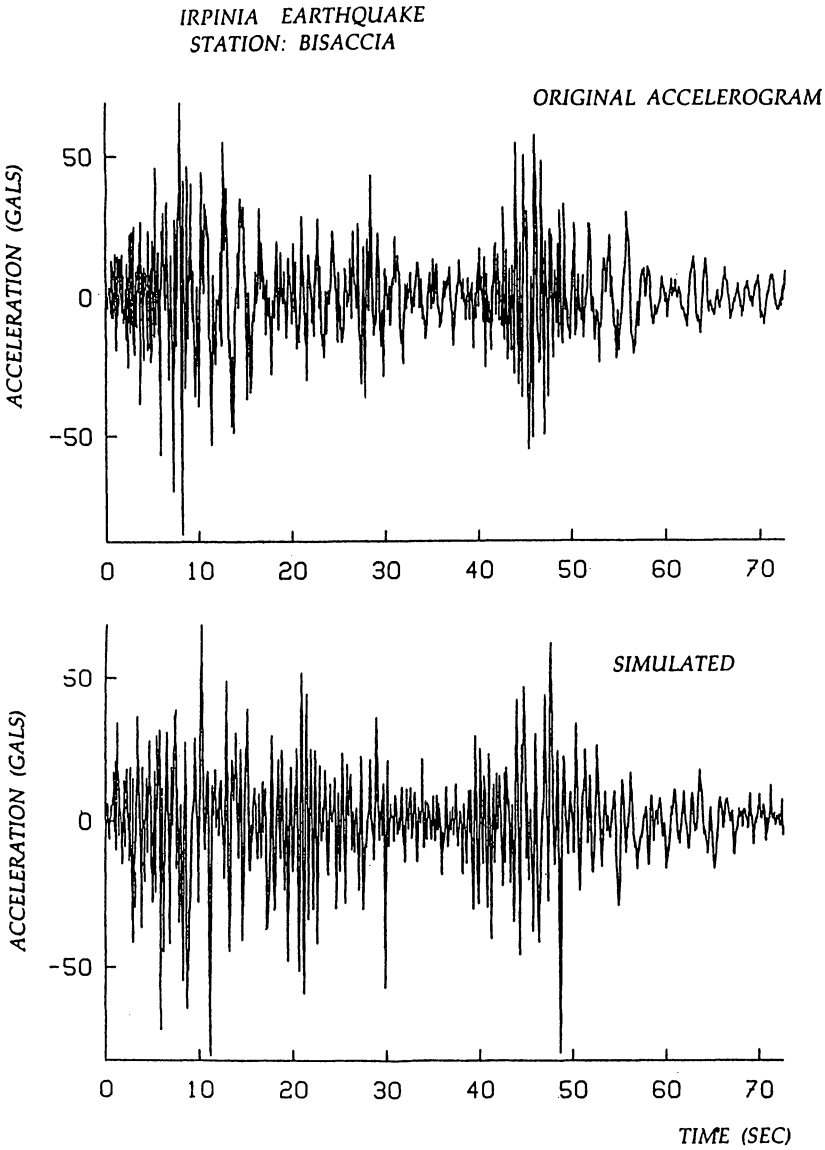

Figure 3. A specimen of numerical simulation of the ground motion using ARMA techniques.

ARMA Techniques, initially of a typically mathematico-statistical nature, gradually developed in the direction of mixed techniques. Several authors (of.Jurkevics and Ulrych, 1978 and 1979; Rovelli, 1983; Rovelli and Bonamassa, 1985) have stressed the fact that the simplest way (and the one easiest to relate back to a clear physical interpretation) of writing (1) is

$$xt = a_1 X_{t-1} + a_2 X_{t-2} + e_t \qquad (1')$$

i.e. as an ARMA(2,0) or simply AR(2) process. In fact, this is the case of a damped harmonic oscillator excited by a Gaussian white noise e(t). The coefficients a1 and a2 are directly related to the two spectral parameters characterizing the process, the dominant frequency (fo) and the band width (Δf). Indeed, it is a known fact that, by writing the differential equation of the oscillator for the continuous process, x(t)

$$\ddot{X}(t) + \frac{c}{m}\dot{X}(t) + \frac{k}{m}X(t) = e(t)$$

and processing do discretize it, we obtain (1') provided that

$$\frac{c}{2m} = \frac{1}{\Delta t}\ \frac{1 + a_2}{1 - a_2}$$

and

$$\frac{K}{m}\ \frac{2}{\Delta t^2}\ \frac{a_1 + a_2 - 1}{a_2 - 1}$$

Recalling that

$$f_o = \frac{1}{2\Pi}\sqrt{\frac{k}{m} - \left(\frac{c}{2m}\right)^2}$$

and

$$\Delta f = \frac{c}{2m}$$

the dependence of f_o and Δf on a1 and a2 can be expressed. Equation (1') can thus be used to generate synthetic signals have the desired spectral characteristics: this is ensured by suitably selecting the pair of values a1 and a2 can be extremely useful in obtaining an accurate description of the non-stationarity of the motion in the domain of time and frequency simultaneously.

Emphasis must be laid from the outset on the importance of knowing the spectral behaviour of the motion when applying statistical simulation techniques established on a physical basis. Another powerful simulation technique that has come to the fore in recent years is that developed by

Boore (1983b). The physical basis in this case consists of the parametrization of the scaling laws of motion in the domain of frequency. The advantage of Boore's technique is that it can be used to obtain highly realistic predictions (statistically speaking, of course) of the time-evolution of many physical quantities widely used in seismology, as a function of a small number (usually one, the seismic moment) of parameters characterizing the size of the earthquake. For instance, for a hypothetical recording point, it becomes possible to predict the acceleration, velocity and ground displacement, or else the output of a Wood-Anderson or any other kind of instrument. This particular simulation technique seems to offer the greatest potential at the present state of art. The scheme in Fig.5 outlines the algorithm used in this type of approach. The physically determinant point for the entire procedure is the one indicated as (4) in Fig.5 during the phase of generating the acceleration time sequence: the choice of the correct parametrization for the motion spectrum as a function of earthquake size and the focal distance. In order to describe source and crustal structure effects (and possibly those of a suitable recording instrument), following Boore (1983b), it was postulated that

$$S(f) = C\, f^{n}\, \dot{M}O(f)\, D(f) \qquad (2)$$

where f is the frequency, S(f) the motion spectrum at a focal distance R and n has the value 0,1,2 according to whether it is intended to indicate displacement, velocity or acceleration, respectively. C has the value of

$$C = \frac{\langle R_{Q,\psi} \rangle\, F_s}{4\Pi\, \rho_s\, C_s^{3}}$$

$\langle R_{Q,\psi} \rangle$ indicates the rms value of the radiation pattern, F_s is a free surface factor ρ_s and C_s are, respectively, the density and the velocity of the seismic waves of the crust in the vicinity of the source. $\dot{M}O(f)$ describes the seismic radiation emitted by the focus at frequency f. I(f) is the frequency response of any instrument it is intended to simulate (assuming I(f) = cost = 1 the ground motion is obtained directly). D(f) is the attenuation due to the crustal structure effects with regard to the entire path followed by the seismic waves and to the site effects.

In accordance with Boore (1983b), it was assumed that

$$\dot{M}O(f) = \frac{M_o}{1 + \left(f/f_c\right)^2} \qquad (3)$$

and

$$D(f) = \exp\left(-\frac{\Pi f\, R}{C_s\, Q}\right) \left[1 + \left(f/f_{max}\right)^8\right]^{-\frac{1}{2}}$$

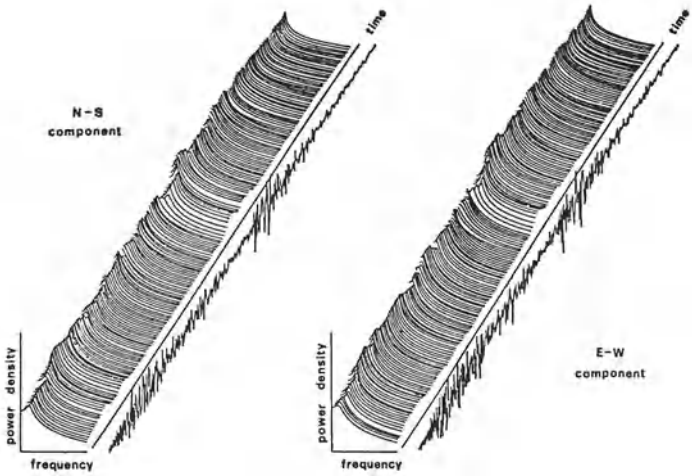

Figure 4. Time-frequency analysis of the ground motion using AR(2) techniques. The accelerograms shown in this figure have been written by the Irpinia earthquake of 23 November 1980 at the station of Calitri (about 30 km from the focus).

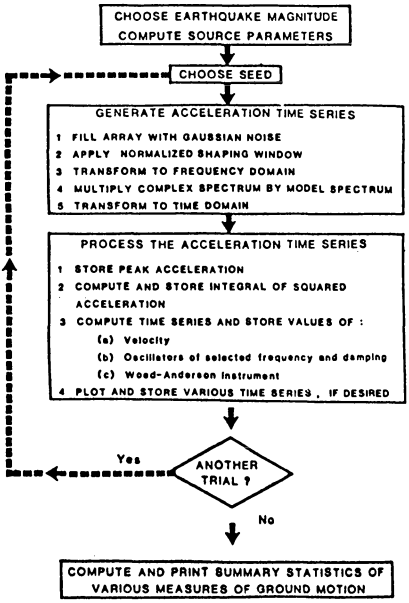

Figure 5. Flow chart showing the algorithm for the numerical simulation of the motion in the time domain (from Boore, 1983b).

where Mo is the (static) seismic moment, f_c is the Brune corner frequency, Q is the quality factor, which generally displays a high degree of dependence on the seismic wave frequency. f_{max} is a cutoff frequency (Hanks, 1982) observed to drastically limit the high-frequency spectrum, probably because of the dissipation due to the upper layers of the crust.

If the parameters in expression (2) are known, it becomes possible to simulate ground motion or the recording of any instrument whatsoever in the time domain, using the scheme illustrated in Fig.5. The following dependency on Mo was used for the corner frequency

$$f_c = 4.9\ 10^6\ C_s \left(\frac{\Delta\sigma}{M_o} \right)^{1/3}$$

where the stress drop $\Delta\sigma$ was assumed to be constant at 100 bars, according to the indications given by numerous authors (Hanks, 1979; Hanks and McGuire, 1981; Boore, 1983b; Hanks and Boore, 1984; amongst others).

Fig.6 shows the results obtained from about 200 simulations for peak values of acceleration and velocity with varying earthquake size. As already known (Boore, 1985), the most striking result is that, for strong earthquakes, the peak velocity increases more rapidly with increasing seismic moment than does the acceleration peak. On the other hand, for low values of Mo, both velocity and acceleration have the same rate of increase, which is much higher than for strong-motion earthquakes. This may be summed up quantitatively by writing

$$\log \begin{pmatrix} a_p \\ v_p \end{pmatrix} \propto \begin{pmatrix} 1.0 \\ 1.0 \end{pmatrix} \log M_o \quad \text{for Mo} \lesssim 10^{22} \text{dyne.cm} \qquad (4)$$

$$\log \begin{pmatrix} a_p \\ v_p \end{pmatrix} \propto \begin{pmatrix} 0.22 \\ 0.37 \end{pmatrix} \log M_o \quad \text{for Mo} \gtrsim 10^{23} \text{dyne.cm} \qquad (4')$$

As clearly explained by Boore (1985), the relations (4) and (4') are a direct consequence of the spectral limitations imposed in the frequency domain. In particular, the greater the extend to which the corner frequency exceeds the value of f_{max}, the more the seismic input will tend towards a simple pulse of amplitude propertional to Mo: the time sequence of the motion, or the output from any kind of instrument, will have a similar form quite independently of the seismic moment, and an amplitude proportional to it. This is of particular interest with regard to the simulation of Wood-Anderson recordings, from which the Richter magnitude (ML) is calculated, since the peak values can be used to obtain a theoretical moment-magnitude relation (Hanks and Boore, 1984) In fact,even very contradictory experimental values have been found for the coefficients of the linear type of empirical relations between log Mo and ML estimated for various different regions. These differences have often been given a seismotectonic or geostructural interpretation,

i.e. they have been expressed in terms of a different type of seismic activity of the various active areas. Fig.7a shows, however, that these differences can be explained in terms of variations in the curvature characterizing the synthetic moment-magnitude curve, since the linear type of relations are valid only over narrow magnitude ranges and the coefficients vary with the magnitude itself.

Another interesting physical quantity which can be usefully simulated as a function of seismic moment is the apparent stress, defined as

$$\sigma_a = \frac{\mu E}{M_o}$$

where μ is the modulus of rigidity and E is the energy irradiating from the source, which is calculated from the integral in the phase S of the square modulus of the velocity, and corrected for the effects due to the distance from the focus. The results of the simulation (see Fig. 7b) reveal a strong dependence of apparent stress on the seismic moment for low Mo values, despite the facts that a constant stress model is being used. This apparent contradiction is fully explained by Boore (1985).

3. COMPARISON WITH OBSERVED DATA

For the purpose of checking the reliability of these preliminary simulations obtained using a constant-stress Brune model, and in order to verify the extent to which it can reasonably be expected to describe the various Italian seismo-tectonic situations, it is necessary to make a series of comparisons between the patterns obtained from the numerical simulations shown in Figs. 6 and 7, and the experimental results referring to the same physical quantities obtained fron the Italian data. Figs. 8 and 9 show the comparisons between the synthetic curves obtained using the constant-sizes Brune model and the experimental values. Even if the agreement does not appear completely unsatisfactory, the desirability of making further trials using more complex source models clearly emerges. Brune's constant-stress model, which represent the most simplistic model of a source spectrum to be used in (4), can be replaced by more complex models. Gusev (1983) suggests that regional differences in the various seismotectonic structures (e.g. the space scale of the heterogeneities of the lithosphere or stress concentrations on a fault plane) can produce a narrower bandwidth in the acceleration spectra than that predicted by Brune's model; the data analysed by Gusev actually show this effect. Luco (1985) remarks that simple models having a single corner frequency, such as that of Brune, are insufficient for adequately describing the complexity of the spectral behaviour of motion over a wide frequency range. He postulates that the use of spectral models characterized by two characteristic frequencies can reduce the gay often observed between theoretical predictions and experimental values. Faccioli and Rovelli (1985) have shown the possible advantages to be gained by using spectra limited by two frequency characteristics when predictions of the peak values of the motion are made by applying the

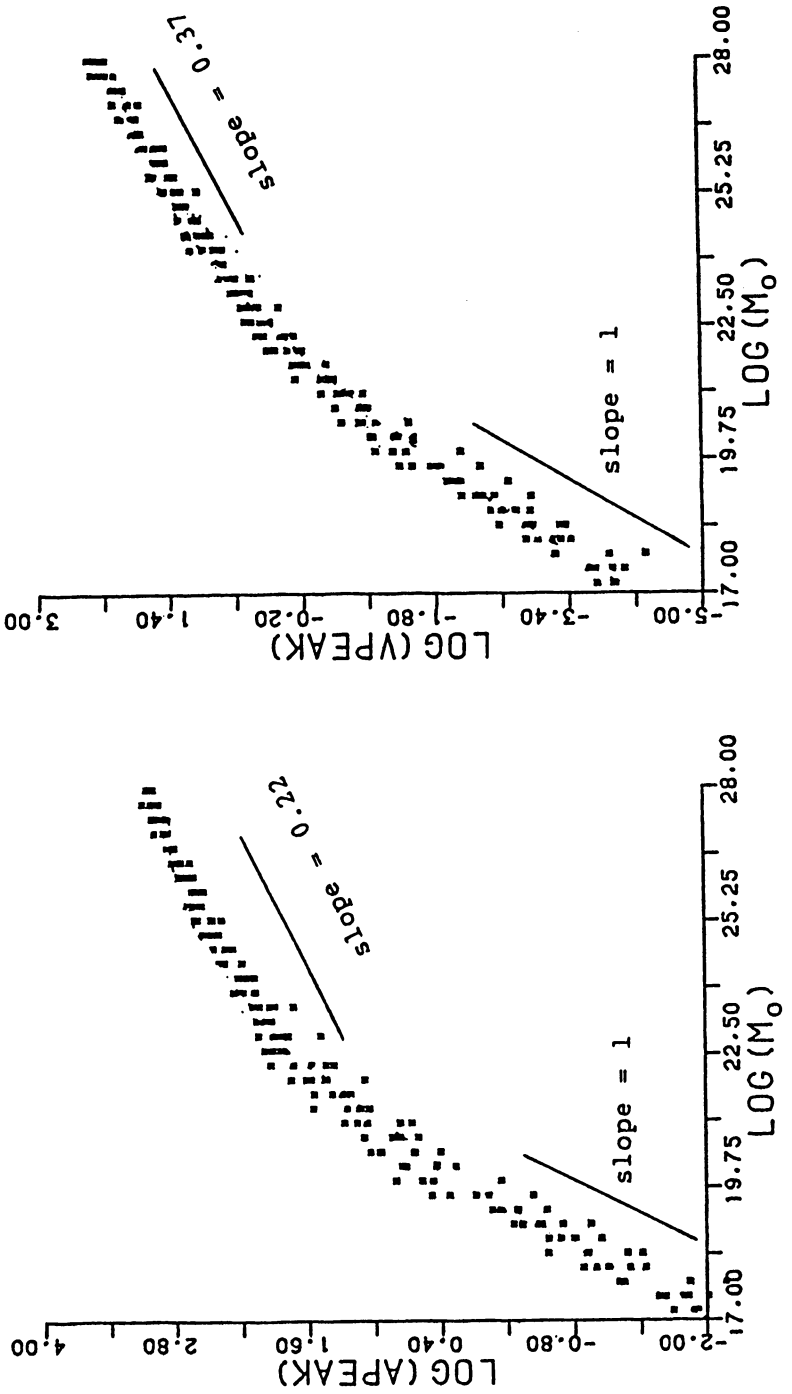

Figure 6. Prediction of peak motion values using the constant-stress Brune (1970) model (with $\rho_s = 2.8$ g/cm, $c_s = 3.5$ Km/sec, $\langle R_{\theta,\psi} \rangle = 0.63$, $F_s = 2$, $Q(f) = 80\,f$, $f_{max} = 10$ Hz).

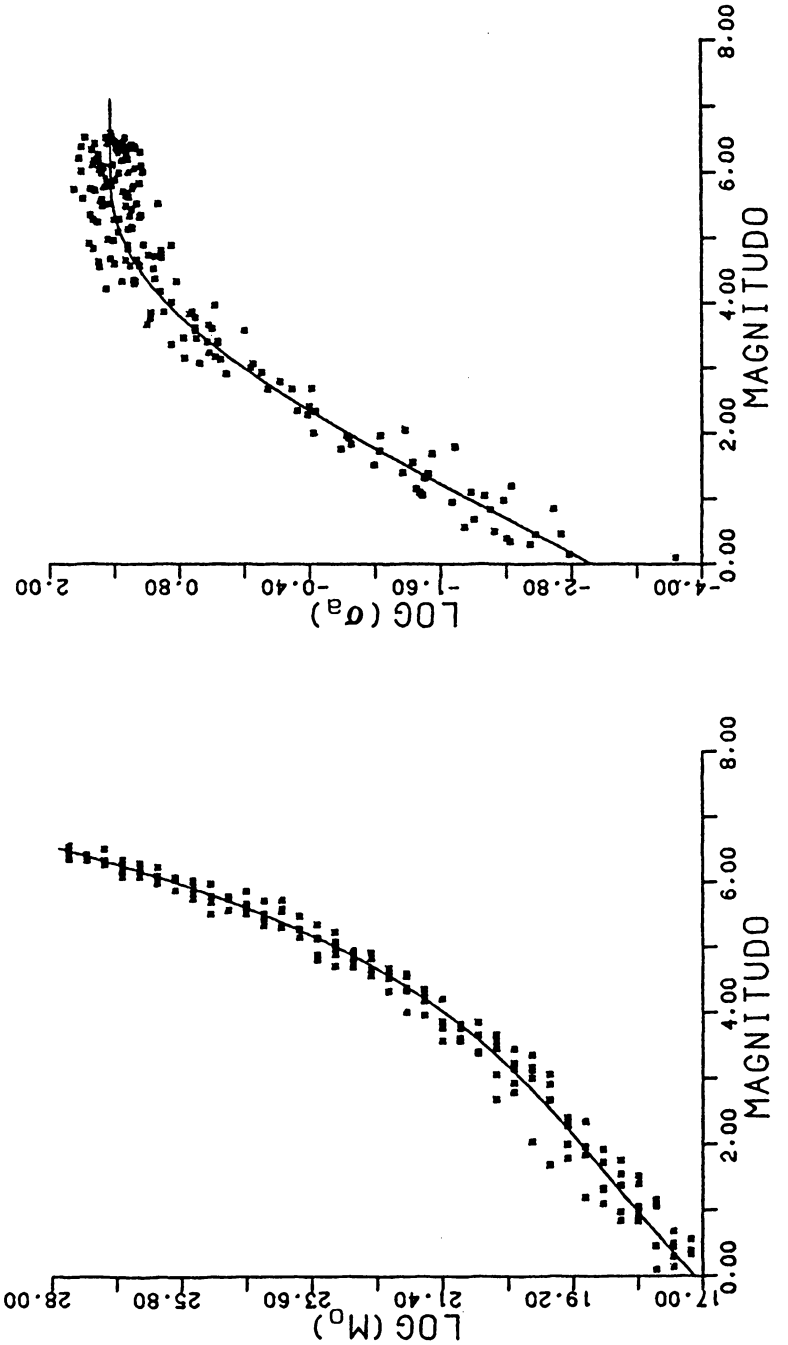

Figure 7. Synthetic curves for the moment-magnitude and apparent stress-magnitude relations, obtained using the constant-stress Brune (1970) model.

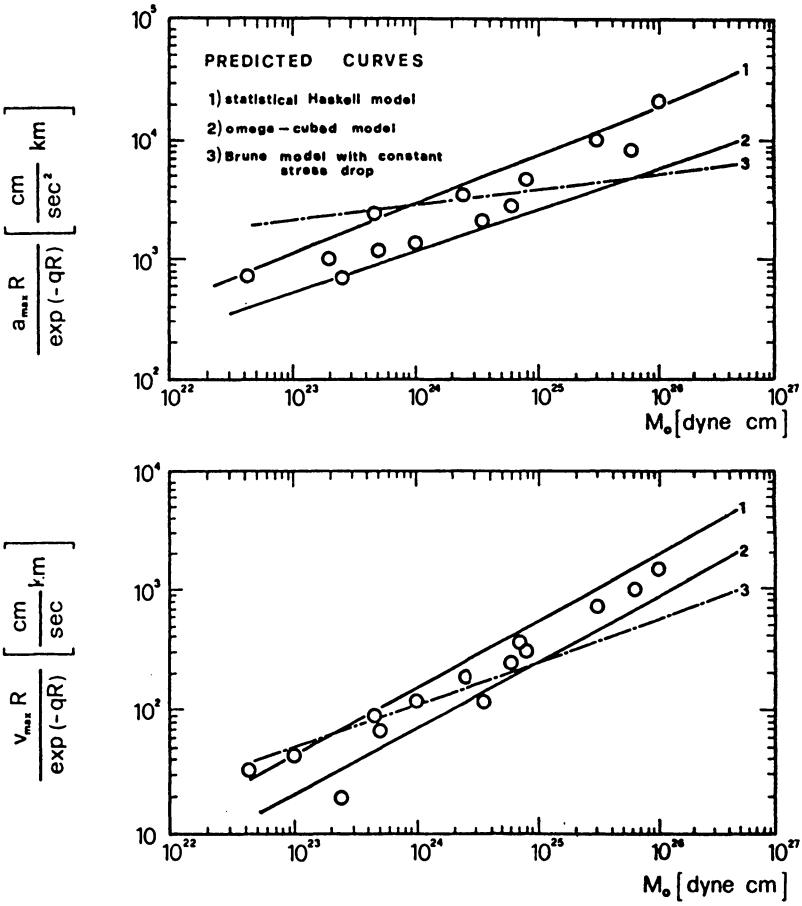

Figure 8. Comparison between synthetic curves obtained using different spectral models and observational data.

theory of random vibrations in the case of high-magnitude earthquakes. These authors describe the source by means of the statistical model proposed by Haskell (1966), in which the slipping of the fault is treated as a random process in space and time, and as being characterised by an autocorrelation function such that a high precentage of the irradiated energy is associated with a small fraction of the total length of the fault (L) and of the total duration of the rupture (T). In other words, it is postulated that the propagation of the rupture, although irregular in its details, occurs unilaterally at a mean velocity v, and is governed by two coefficients of correlation, a spatial one (kl) and a temporal one (kt). It this case we get

$$\dot{M}o(f) = \frac{M_o}{\sqrt{1 + (f/f_1)^2}\left[1 + (f/f_2)^2\right]} \qquad (5)$$

where f1 and f2 are the two characteristic frequencies of the model. They are given respectively by

$$f1 = \frac{\nu K_1}{2\pi(1-m\cos\theta)} \quad \text{and} \quad f_2 = \frac{K_T}{2\pi}$$

where m is the ratio v/c_s and θ is the angle lying between the direction of propagation of the rupture and the seismic radius. f1 and f2 have been calculated by analysing the acceleration spectra of some seventy or so of the more significant accelerograms referring to the Ancona, Friuli, Valnerina, Montenegro and Irpinia earthquakes. The relations found as a function of seismic moment for these events are (Facioli and Rovelli, 1985)

$$f_1 = 7.3 \cdot 10^3 \quad Mo^{-0.12}$$

and

$$f_2 = 3.5 \cdot 10^5 \quad Mo^{-0.23}$$

Using the source spectrum (5) instead of spectrum (3), repeating the procedure described in Fig. 5 above, and taking the dependence of f_1 and f_2 on Mo as given above, the results shown in Figs. 10 and 11 are obtained, which certainly display better agreement with observed data than the simulations carried out using Brune's model (Figs. 8 and 9). Using the theoretical spectra referring to Haskell's model we obtain

$$\log \begin{pmatrix} a_p \\ \nu_p \end{pmatrix} \propto \begin{pmatrix} 0.80 \\ 0.85 \end{pmatrix} \log M_o \quad \text{for } Mo \lesssim 10^{22} \text{ dyne.cm.} \qquad (6)$$

and

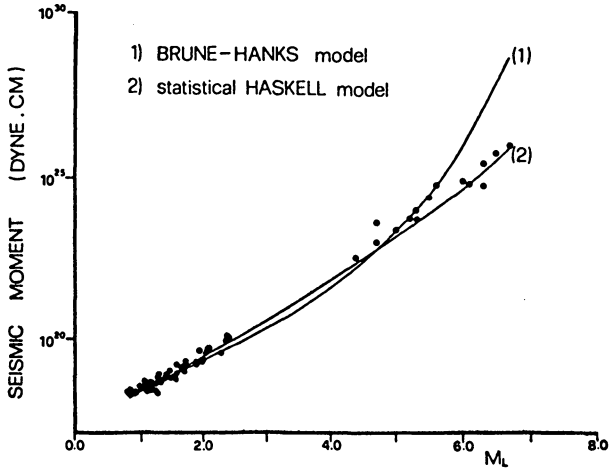

Figure 9. As figure 8.

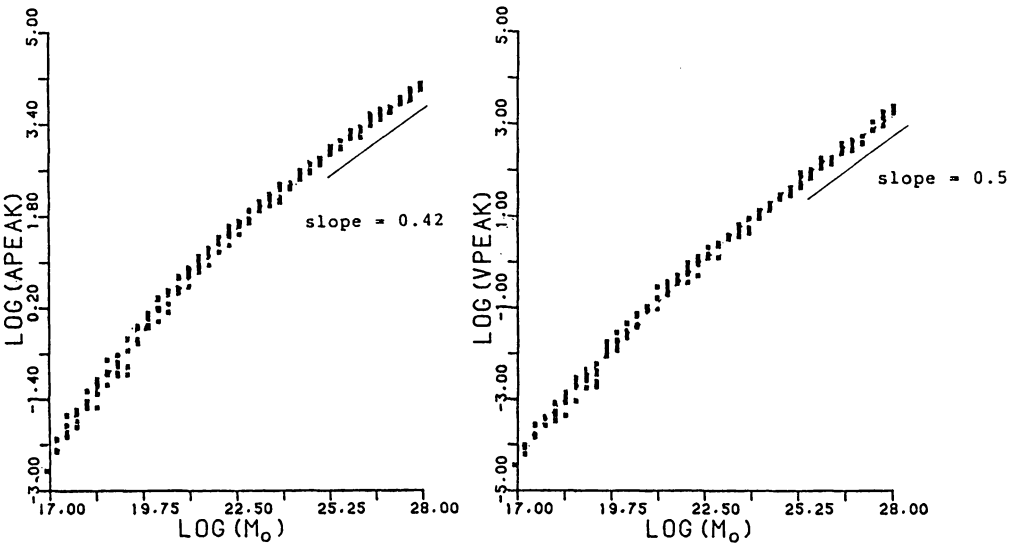

Figure 10. Prediction of peak motion values using the statistical Haskell (1966) model.

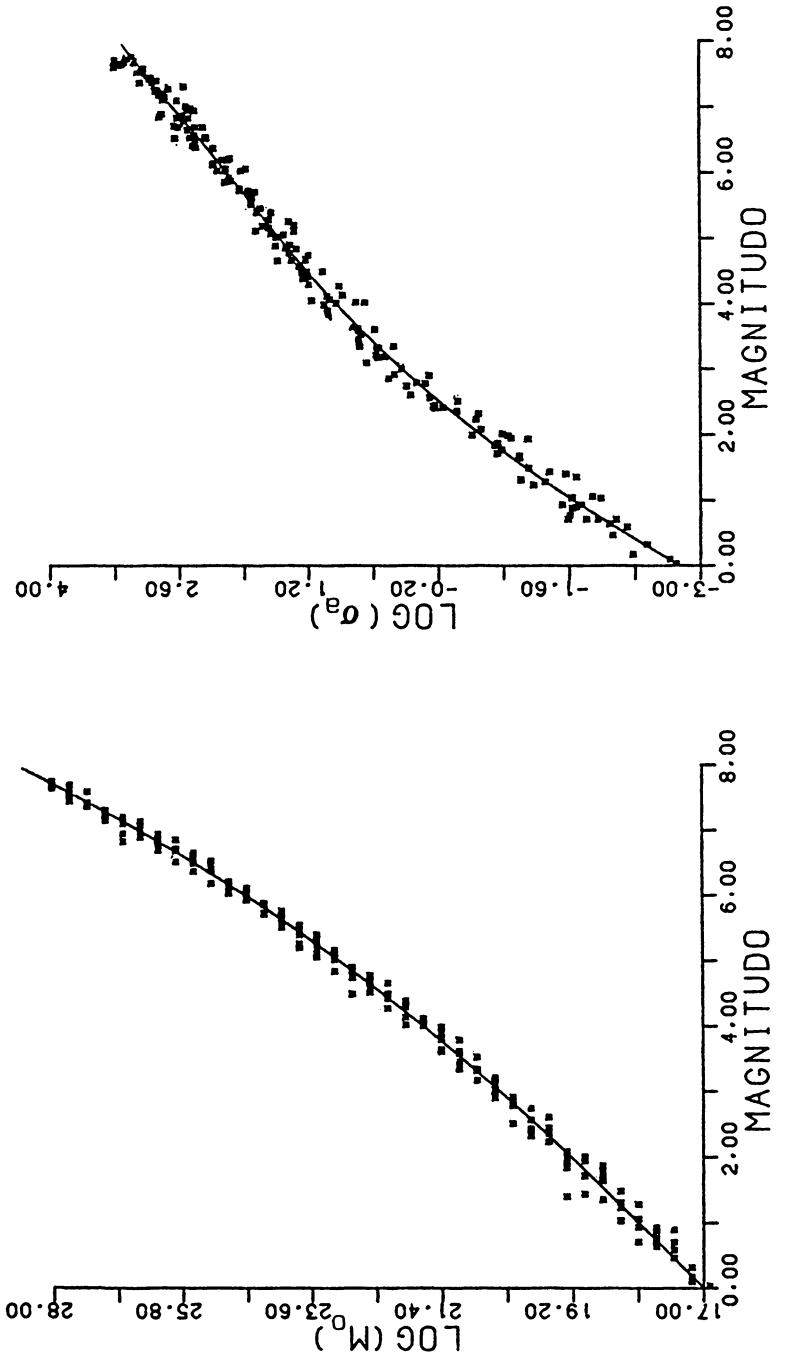

Figure 11. Synthetic curves for the moment-magnitude and apparent stress-magnitude relations, obtained using the statistical Haskell (1966) model.

$$\log \begin{pmatrix} a_p \\ \nu_p \end{pmatrix} \propto \begin{pmatrix} 0.42 \\ 0.54 \end{pmatrix} \log M_o \quad \text{for } Mo \gtrsim 10^{23} \text{ dyne.cm} \qquad (6')$$

Coinciding as they do with those found previously for high magnitudes using the random vibration theory of Faccioli and Rovelli (1985), the relations (6') for a_p and ν_p versus M_o show a better agreement with observed data than the previous simulations using Brune's constant-stress model. Fig. 8 shows that the two synthetic curves obtained using the value of f_1 calculated from the data and with the value $f_1 = f_2$, represent respectively lower and higher limits within which practically all the experimental values lie. Also the moment-magnitude relation (see Fig. 9) is fairly well simulated with respect to the real data for strongest events if a more complex spectral model is used.

The important conclusion which emerges from these applications is that the increase in peak values predicted as a function of seismic moment using a statistical model with two characteristic frequencies obtained empirically from the data, is considerably higher than that predicted using Brune's model, for seismic moments. The aforegoing warrants a number of careful considerations being made.

4. CONCLUSIONS AND FURTHER DEVELOPMENTS

The theoretical prediction of the peak values of motion in particular seismotectonic situations is highly dependent on the choice of spectral model used. By means of Boore's (1983b) technique it is possible, using seismic moment as the only scale parameter, to calculate several different theoretical curves (see Figs. 8 and 9) as a function of different spectral models. For the Italian data it has been seen, for instance, that a model with two characteristic sequences (probably connected with the dimension of the sub-events and with the spacing between successive barriers) produces theoretical curves which fit the experimental data better than a constant-stress Brune type model. However, a further series of tests must be carried out before any conclusions of a general nature can be reached concerning the absolute superiority of a Haskell type statistical model. One could, in fact, erroneously conclude that, in view of the agreement between the theoretical model and the observed data, a Haskell type source model is the only key to a correct interpretation of the spectra observed. However, this can be stated with any certainty only after carefully evaluating the various assumptions related to (2). While it is certainly true that the power of these simulation techniques comes from the fact that the predicted peak values of the motion is all the more accurate the greater the extent to which the spectral information used in (2) is consistent with the data themselves (see Fig. 8 and Fig. 9), this does not mean that it is possible to derive arguments in support of one seismological interpretation rather than another for one only of the terms appearing in (2), since their product is physically determinant. The preference for an expression of

type (5) rather than (3) is still an open problem: the difficulty is the physical interpretation of the observed high-frequency special limitations. As Boore (1985) points out, the correct description of the spectral cutoff observed in the high-frequency band is a physically very important point for predicting the behaviour of numerous quantities of seismological interest. In this connection, Boore (1985) points out that it is practically impossible at the present state of the art of anelastic attenuation. For instance, in the light of the results obtained by Faccioli and Rovelli (1985), the dependence also of f_1 on M_0 would seem to favour an interpretation of both characteristic frequencies in terms of source effects, as well as the gradual spectral impoverishment of the high-frequency radiation emitted at the focus observed, with a slope of the f^{-1} type, observed in the acceleration spectra of the Italian earthquakes studied by Faccioli and Rovelli (1985). It actual fact, this is not the only possible interpretation of these data. The procedure adopted involves two points which must be discussed carefully. The first of these is that a Haskell model produces less satisfactory results at low magnitudes (6) compared with Brune's model (4); this is not unrealistic and could be interpreted in the sense that simple (Brune) rupture models work for small earthquakes better than complex rupture models. The second point is that, although the agreement between observed spectra and theoretical spectra is generally very good, there are some exceptions which could point to a need to reappraise some of the formulae used to parametrize the spectral shape. For instance, Fig.12 referring to the accelerogram of the station of Somplago situated in a tunnel some 300 meters below the surface, shows no high-frequency attenuation, at least up to 25 Hz. Instead of the function $[1+(f/f_{max})^8]^{-1/2}$ is would therefore appear to be more useful to use an expression of the type $e^{-\pi kf}$ (see Anderson and Hough, 1984), where k can generally be a function of the site and fo the focal distance. One important fact is that if k is calculated from the data, the value obtained experimentally in Italy ($k \simeq 0.1$) is seen to produce spectral shapes with slopes similar to that observed in the spectra described by Faccioli and Rovelli in terms of the source using a Haskell statistical model. Therefore, comparison with the experimental data alone in no way allows any conclusions to be drawn concerning the superiority of one model over the other; using different values of k in the numerical simulations means that equally appreciable variations in the slope of the curve the peak values of the motion occur as a function of M_0, as previously shown by Boore (1985). The attribution to the site or the source of certain effects observed in the data will remain controversial (McGarr et al., 1985; Boore, 1985; Aki, 1985; Anderson, 1985). Probably only the use of recordings using sensors situated at varying depths will allow these doubts to be resolved in the future.

One point that stands out in particular is the interpretation of the cutoff frequency at low frequencies in the acceleration spectra (f_2 in Haskell's model) in terms of patch corner frequency, i.e. in terms of a quantity linked to the size of the sub-events rather than to the total size of the fault, as in Brune's model.

The scale relation obtained

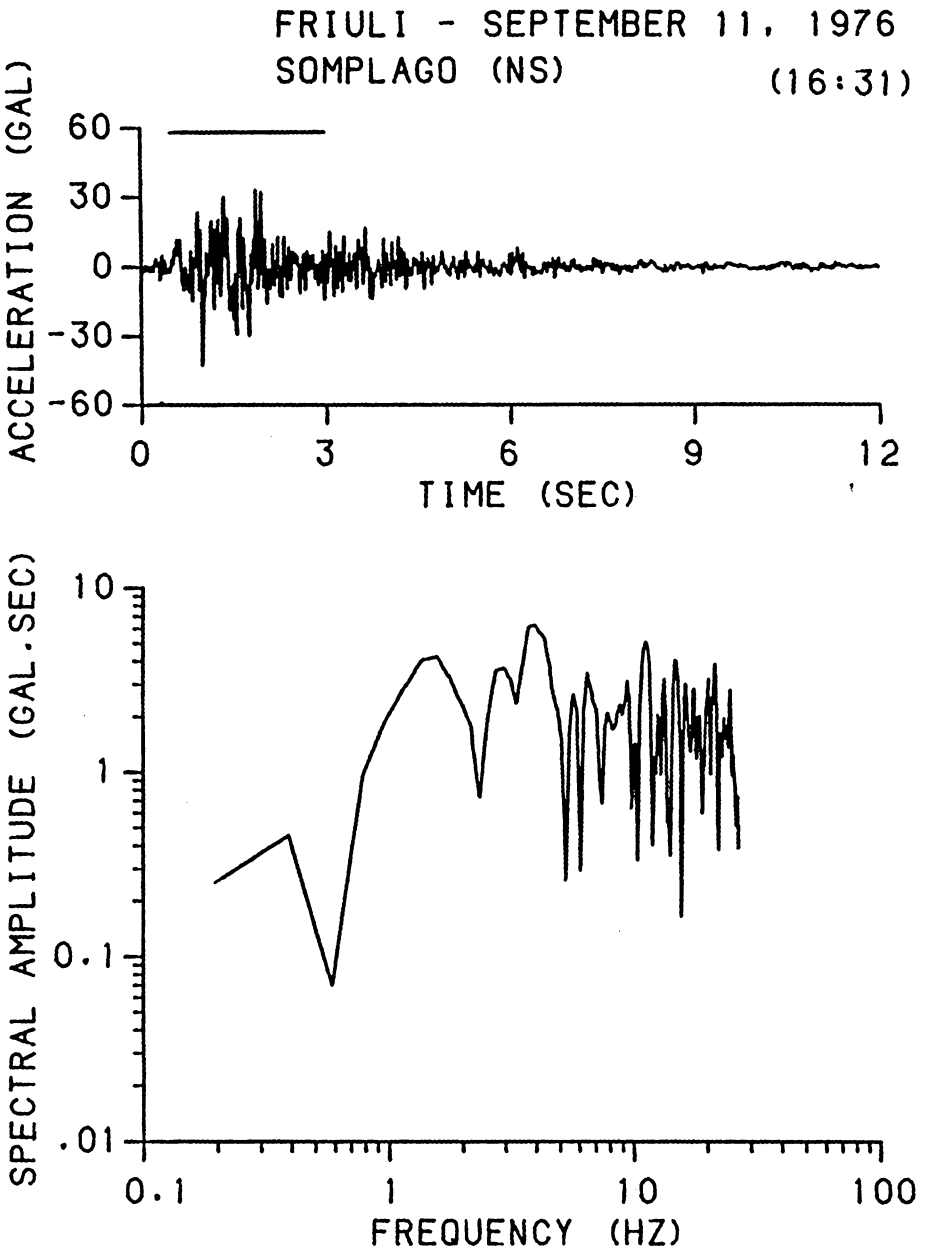

Figure 12. Acceleration spectrum for the recording of the station of Somplago (Friuli), situated in a tunnel some 300 m below the surface, showing no high-frequency attenuation in the band in analysis.

$$M_o \; f_2^4 \sim \text{const} \qquad (7)$$

involves a breakdown in the condition of similarity, which seemed to be guaranteed by Brune's constant-stress model (for which Mo $f^3 \sim$ const), at least starting from a limiting value of Mo $\gtrsim 10^{23}$ dyne.cm. Even if the seismological interpretation of the scaling law (7) is not univocal (see Nuttli, 1983), it is confirmed by the results of Aki (1985) for the Japanese earthquakes, and by Cocco and Rovelli (1985) by means of the numerical simulation of highly complex random rupture events.

The problem of the correct scale relation is by no means of merely academic interest. The use of a patch corner frequency scaling as in (7) instead of a Brune corner frequency can lead to appreciable differences in the predicted behaviour of peak values of high-magnitude motion and have important repercussions at the applicational level.

5. REFERENCES

Aki, K., B.S.S.A., Vol.72: S29-S41, 1982.

Aki, K., presented at "V Symposium on Earthquake Source Mechanics ", Ewing, 20-24 May 1985.

Anderson, J.G., presented at "V Symposium on Earthquake Source Mechanics ", Ewing, 20-24 May 1985.

Anderson, J.G. and S. Hough., B.S.S.A., Vol.74: 1969-1994, 1984.

Bonamassa, O., R. Console, A. De Santis and A. Rovelli, Annales Geophysicae, Vol.2: 17-22, 1984.

Boore, D.M., Rev. Geophys. Space Phys., Vol.21: 1308-1318, 1983(a).

Boore, D.M., B.S.S.A., Vol.73: 1865-1994, 1983(b).

Boore, D.M., presented at "V Symposium on Earthquake Source Mechanics", Ewing, 20-24 May 1985.

Boore, D.M., J.D. Sims, H. Kanamori and S. Harding, Phys. Earth Planet. Int., Vol.27: 133-142, 1981.

Brune, J.N., J. Geophys. Res., Vol.75: 4997-5009, 1970.

Cipar, J., B.S.S.A., Vol.70: 963-983, 1980.

Cocco, M. and A. Rovelli, 1985 (in preparation).

Console, R. and P. Favali, B.S.S.A., Vol.71: 1233-1248, 1981.

Console, R.,F. Peronaci and A.Sonaglia, Annali di Geofisica, suppl.1973.

Deschamps, A.G. Iannaccone and R. Scarpa, Annales Geophysicae, Vol.2: 29-36, 1984.

Deschamps, A. and G. King, Earth Planet.Sci Lett., Vol.62: 296-304, 1983.

Faccioli, E. and A. Rovelli, B.S.S.A. (submitted for publication), 1985.

Gusev, A.A., Geophys. J. of the R.A.S., Vol.74: 787-808, 1983.

Hanks, T ., J. Geophys. Res., Vol.84: 2235-2241, 1979.

Hanks, T., B.S.S.A., Vol.72: 1867-1879, 1982.

Hanks, T. and D.M. Boore, J. Geophys. Res, Vol.89: 6229-6235, 1984.

Hanks, T. and R.K. McGuire, B.S.S.A., Vol.71: 2071-2095, 1981.

Haskell, N.A., B.S.S.A., Vol.56:125-140, 1966.

Jurkevics, A. and T.J. Ulrych, B.S.S.A., Vol.68: 781-801, 1978.

Jurkevics, A. and T.J. Ulrych, B.S.S.A., Vol.69: 2025-2036, 1979.

Luco, J.E., B.S.S.A., Vol.75: 641-649, 1985.

McGarr, A., C. Mueller, J.B. Fletcher and M. Andrews, presented at " V Symposium on Earthquake Source Mechanics ", Ewing, 20-24 May 1985.

Nuttli, O.W., B.S.S.A., Vol.73: 519-535, 1983.

Rovelli, A ., Phys. Earth Planet. Int., Vol.33: 94-110, 1983.

Rovelli, A. and O. Bonamassa, 1985 (in preparation).

Zonno, G. and R. Kind, B.S.S.A., Vol.74: 1645-1659, 1984.

ANALYSIS OF STRONG-MOTION DATA FROM THE NEW HAMPSHIRE EARTHQUAKE OF 18 JANUARY 1982

F. K. Chang
USAE Waterways Experiment Station
P.O. Box 631
Vicksburg, MS 39180-0631

ABSTRACT. This paper presents an analysis of the strong-motion data from the New Hampshire earthquake of 18 January 1982 which occurred at latitude 43.5°N, longitude 71.6°W. Thirty-six accelerograms, mainly on Corps dams, were recorded, digitized, corrected, and processed. The earthquake records were obtained by the US Army Corps of Engineers (CE) Strong-Motion Instrumentation Program (SMIP). The attenuation curves of the three orthogonal components for peak acceleration, peak velocity, peak displacement, and velocity spectrum intensity on the crest, abutment, and downstream sites of the five earth dams were plotted and compared. The transverse component shows the highest energy at the Franklin Falls Dam (FFD). However, its attenuation rate is faster than the vertical and longitudinal components. The transverse component of the accelerograph located on the right abutment of FFD recorded a maximum acceleration of 0.55 g's, which is the highest acceleration ever recorded in the eastern United States. The integrated maximum velocity is 5.59 cm/sec, which is very low in comparison with other earthquake records in the western United States.

1. INTRODUCTION

An earthquake occurred at 19:14:42 EST on 18 January 1982 (UT 00:14:42, 19 January 1982) north of Tilton (near Franklin), New Hampshire. The geographic coordinates of the epicenter are 42.5°N and 71.6°W. Slight damage, Modified Mercalli (MM) Intensity VI, was observed at Bristol, Canaan, Danbury, New Hampshire, and North Hartland and White River Junction (WRJ), Vermont. The shock was felt throughout most of New England, northern New York, and as far away as southern Quebec and northeastern Ontario. The Richter magnitude was determined by the US Geological Survey (USGS) (USGS, 1982) to be 4.7 (m_b = 4.4, m_{bLg} = 4.5). The focal depth was between 4.5 and 8.0 km (personal communication, John E.Ebel, Weston Observatory).

The US Army Engineer Division, New England (NED), had strong - motion accelerographs at 12 dams in New England. Eleven three-component accelerographs at five of the dams, plus one instrument at a Veterans

M. O. Erdik and M. N. Toksöz (eds.), Strong Ground Motion Seismology, 355–367.
© 1987 by the U.S. Government.

Administration (VA) hospital, recorded this earthquake. All of these instruments are maintained by the US Army Engineer Waterways Experiment Station (WES) Under the US Army Corps of Engineers (CE) Strong-Motion Instrumentation Program. This is the first time 36 accelerograms were recorded in a single earthquake in the eastern United States. Figure 1 shows the locations of the six recording stations and distances from the epicenter. Table I provides further information on the recording sites.

The uncorrected peak accelerations recorded at the abutment, crest, and downstream sites are listed in Table II. At Ball Mountain Dam (BMD) useable records were observed only from the crest and not from instruments at the abutment and downstream sites. The records at the abutment and downstream sites show very small amplitudes from which meaningful digital values could not be obtained.

The FFD is an earth dam at a distance of about 8 km from the epicenter. Only minor damage to the gatehouse at this dam has been reported. At this location nine channels of acceleration data were recorded. The predominant frequency recorded at Franklin Falls (11 to 21 Hz) is higher than those typical of the West Coast (4 to 6 Hz). The frequency range of 11 to 21 Hz can be significant to the response of many nuclear power plant systems and structures.

2. PURPOSE

The purpose of this paper is to present the corrected digitization of the 36 accelerograms, the integrated velocities , and the displacements. A collection of 108 response spectra of accelerations, velocities, and displacements will be published in a WES report.

3. DATA DIGITIZATION AND PROCESSING

3.1. Digitization

The 36 accelerograms were digitized with a laser line digital machine by IOM-Towill (I/O Metrics and R.M. Towill Corporation) of Santa Clara, California. The accelerograms were measured to a centerline occuracy of better than 3 micrometers (0.0001 in.) with a spacing between points of 20 micrometers (0.0007 in.). The three accelerograms (Figure 2) recorded at the right abutment of the FFD were digitized at 600 points per second, the remainder (Figures 3 and 4) at 200 points per second. The 36 uncorrected accelerograms were stored on a magnetic tape which is kept in the Branch of Engineering Seismology and Geology (BES & G), USGS, Menlo Park, California, with the original 35-mm records.

3.2. Baseline Corretion

The basic concept of baseline correction is to subtract from the raw accelerogram a low-pass filtered version of the accelerogram, using Ormsby's filter (Ormsby, 1961) in which all frequencies higher than 0.7 Hz have been removed. The result is a high-pass filtered accelerogram

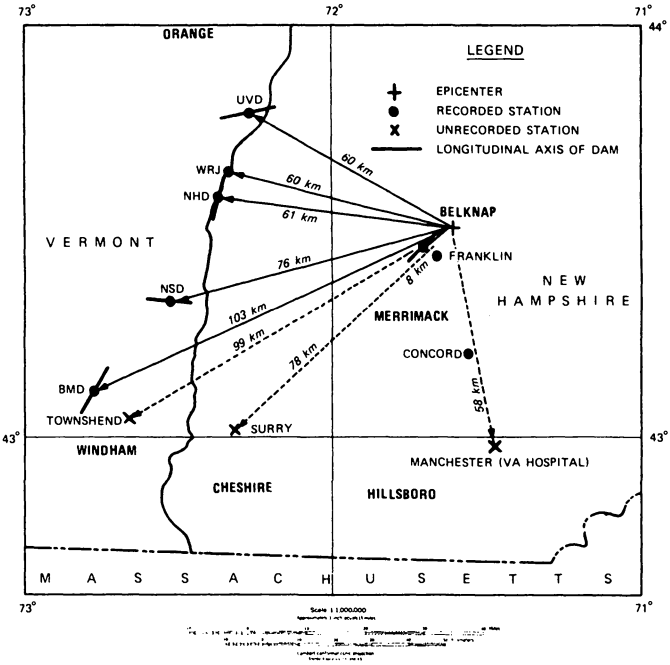

Figure 1. Location of epicenter and recording stations

TABLE I. SITES OF STRONG-MOTION RECORDS

Owner	Recording Site	Epicentral Distance km	Height of Dam, m	Top Elevation of Crest msl, m	Location of Recording Instrument	Number of Records	Type of Structure
NED	Franklin Falls Dam (FFD)	8	45	130	Crest, right abutment, downstream toe	9	Earth dam
NED	North Springfield Dam (NSD)	76	38	178	Crest, downstream	6	Earth dam
NED	Ball Mountain Dam (BMD)	103	81	329	Crest	3	Earth dam
NED	Union Village Dam (UVD)	60	53	183	Crest, left abutment, downstream	9	Earth dam
NED	North Hartland Dam (NHD)	61	58	179	Crest, left abutment	6	Earth dam
VA	White River Junction (WRJ)	60	--	--	Basement	3	Three-story building
					TOTAL	36	

TABLE II. RESULTS OF CE ACCELEROGRAPH RECORDS OBTAINED FROM NEW HAMPSHIRE EARTHQUAKE OF 18 JANUARY 1982.

Station	Site Location	Azimuth of Component	Azimuth* deg	Uncorrected Accelerations cm/sec^2	Maximum Acceleration (a), cm/sec^2 (Corrected)	Maximum Velocity (v) cm/sec (Corrected)	Maximum Displacement (d) cm (Corrected)	Velocity Spectrum Intensity 5%, ζ	$\frac{a \cdot d}{v^2}$ Hori.	$\frac{a \cdot d}{v^2}$ Vert.	$\frac{v}{a}$ Hori.	$\frac{v}{a}$ Vert.	(v/a) vert. / (v/a) hori.	$\frac{a_{vert}}{a_{hori}}$
Franklin Falls Dam	Downstream	L-225°	234.5	111.68 (21 Hz)	140.70 (0.143 g)	2.03	0.16	9.53	5.464		0.0144		0.443	1.926
Epicenter Distance =		Up		208.34 (21 Hz)	271.00 (0.276 g)	1.73	0.08	7.29		7.251		0.0064		
8 km		T-135°		267.94 (16 Hz)	377.86 (0.385 g)	2.87	0.17	13.23	7.798		0.0076		0.842	0.717
	Right Abutment	L-45°		282.52 (14 Hz)	287.70 (0.293 g)	2.68	0.25	13.08	10.017		0.0093		1.150	0.601
		Up		171.89 (20 Hz)	172.89 (0.176 g)	1.86	0.41	11.61		20.487		0.0107		
		T-315°		565.05 (14 Hz)	539.96 (0.550 g)	5.59	0.43	22.39	7.432		0.0103		1.039	0.320
	Crest	L-45°		102.79 (11.4 Hz)	123.96 (0.126 g)	2.67	0.36	12.09	6.259		0.0215		1.176	0.922
		Up		111.38 (11.4 Hz)	114.31 (0.116 g)	2.89	0.47	13.15		6.432		0.0253		
		T-315°		243.46 (14 Hz)	306.83 (0.312 g)	4.06	0.33	17.12	6.143		0.0132		1.916	0.372
Union Village Dam	Crest	L-245°	300.0	24.08	22.46	0.46	0.04	2.32	4.246		0.0205		0.883	1.031
Epicenter Distance =		Up		23.31	23.17	0.42	0.04	2.19		5.254		0.0181		
60 km		T-155°		25.73	25.07	0.50	0.005	2.67	0.501		0.0199		0.909	0.924
	Left Abutment	L-245°		9.05	9.49	0.15	0.03	0.95	12.653		0.0158		1.727	0.654
		Up		6.00	6.21	0.17	0.05	1.04		10.744		0.0273		
		T-155°		7.17	6.73	0.23	0.06	1.39	7.633		0.0341		0.801	0.922
	Downstream	L-245°		38.15	37.01	0.82	0.08	3.54	4.403		0.0221		0.706	0.781
		Up		27.02	28.90	0.45	0.07	2.37		9.990		0.0156		
		T-155°		22.96	22.58	0.47	0.05	2.45	5.111		0.0208		0.750	1.279
North Hartland Dam	Left Abutment	L-15°	178.5	6.66	11.08	0.20	0.05	1.24	13.850		0.0180		2.072	0.338
Epicenter Distance =		Up		3.56	3.75	0.14	0.04	0.95		7.653		0.0373		
61 km		T-285°		6.35	6.84	0.22	0.06	1.45	8.479		0.0321		1.162	0.548
	Crest	L-15°		33.57	37.34	0.76	0.12	3.74	7.757		0.0203		1.354	0.448
		Up		17.12	16.73	0.46	0.09	2.40		7.116		0.0275		
		T-285°		29.39	38.19	0.86	0.13	3.86	6.712		0.0225		1.222	0.438
North Springfield	Crest	L-275°	255.5	26.05	24.38	0.56	0.06	2.38	4.664		0.0229		0.659	0.921
Dam, Epicenter		Up		22.61	22.45	0.34	0.06	1.91		11.652		0.0151		
Distance = 76 km		T-185°		21.55	21.54	0.41	0.09	2.59	11.532		0.0190		0.795	1.042
	Downstream	L-275°		24.88	31.08	0.41	0.07	1.74	12.942		0.0132		1.159	0.439
		Up		14.20	13.66	0.21	0.05	1.39		15.487		0.0153		
		T-185°		20.72	22.59	0.29	0.06	1.76	16.116		0.0128		1.195	0.605
Ball Mountain Dam	Crest	L-30°	245.6	8.75	8.80	0.37	0.08	2.15	5.142		0.0420		0.676	1.360
Epicenter Distance =		Up		11.97	11.97	0.34	0.07	1.92		7.248		0.0284		
103 km		T-300°		10.38	10.03	0.37	0.07	2.27	5.128		0.0369		0.769	1.193
White River Junction	Basement	L-270°	285.0	14.80	15.00	0.33	0.06	2.04	8.264		0.0220		0.791	1.454
(VA Hospital)		Up		21.34	21.81	0.38	0.08	2.40		12.083		0.0174		
Epicenter Distance =		T-180°		29.04	31.00	0.57	0.12	3.23	11.449		0.0184		0.946	0.703
60 km														
								Data No.:	24	12	24	12	24	24
								Mean:	7.903	10.116	0.0204	0.0203	1.047	0.830
								SD:	3.678	4.387	0.0086	0.0088	0.400	0.403
								Mean & SD:	11.581	14.403	0.0290	0.0291	1.447	1.233

* Azimuth is from epicenter to the recording site. Azimuth is also related to geographical north.

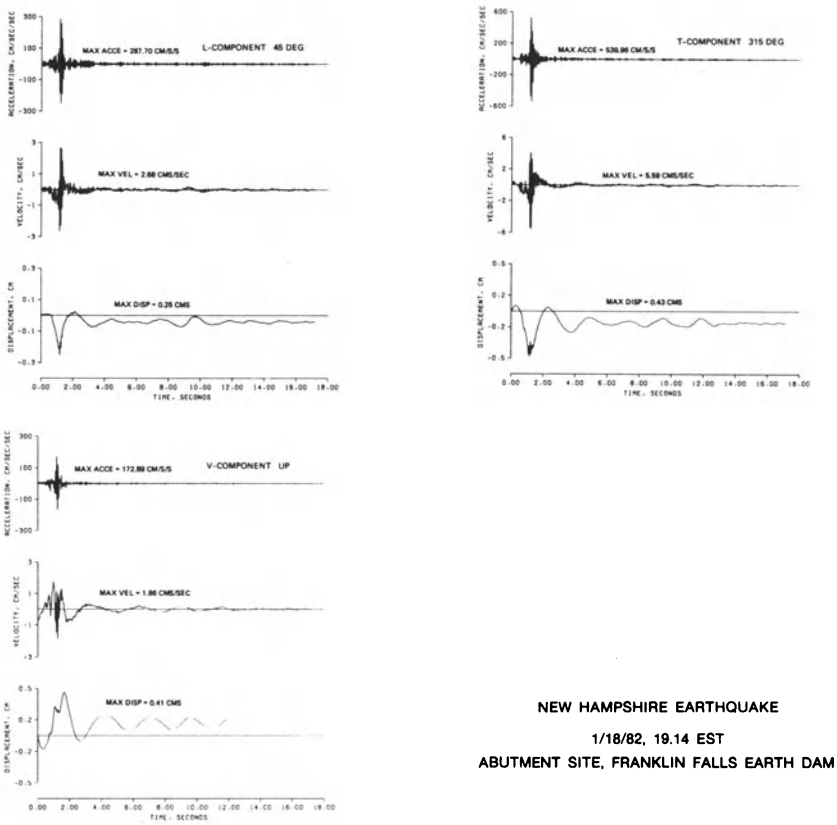

Figure 2. Corrected accelerogram and integrated velocity and displacement curves of the L, T, and V components at abutment site, Franklin Falls Dam.

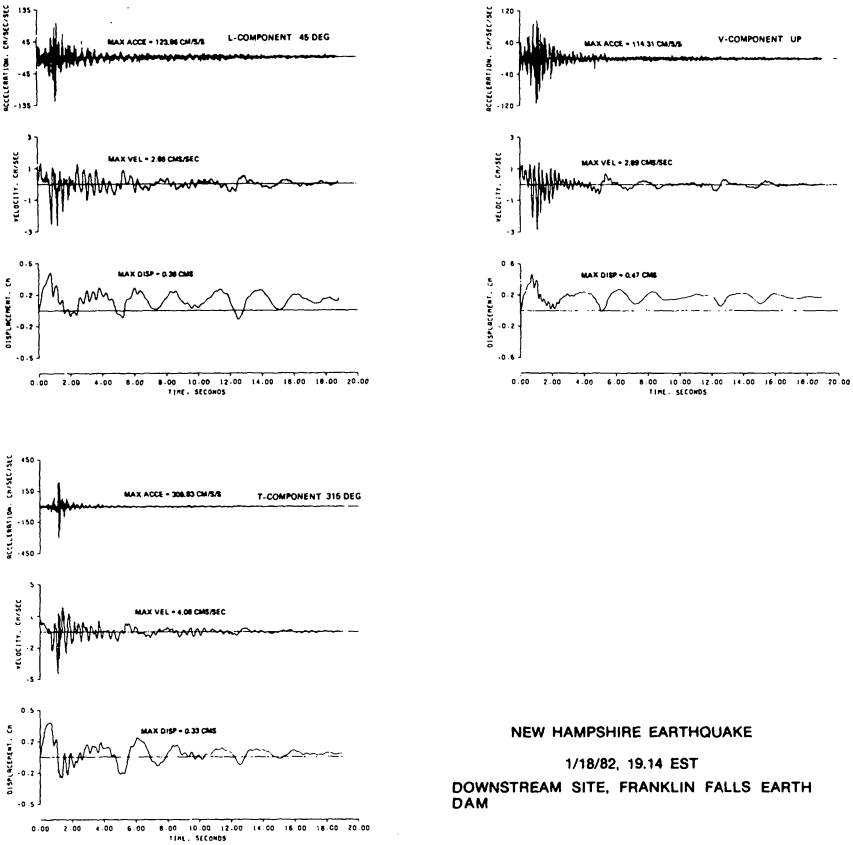

Figure 3. Corrected accelerogram and integrated velocity, and displacement curves of the L, T, and V components at downstream site, Franklin Falls Dam.

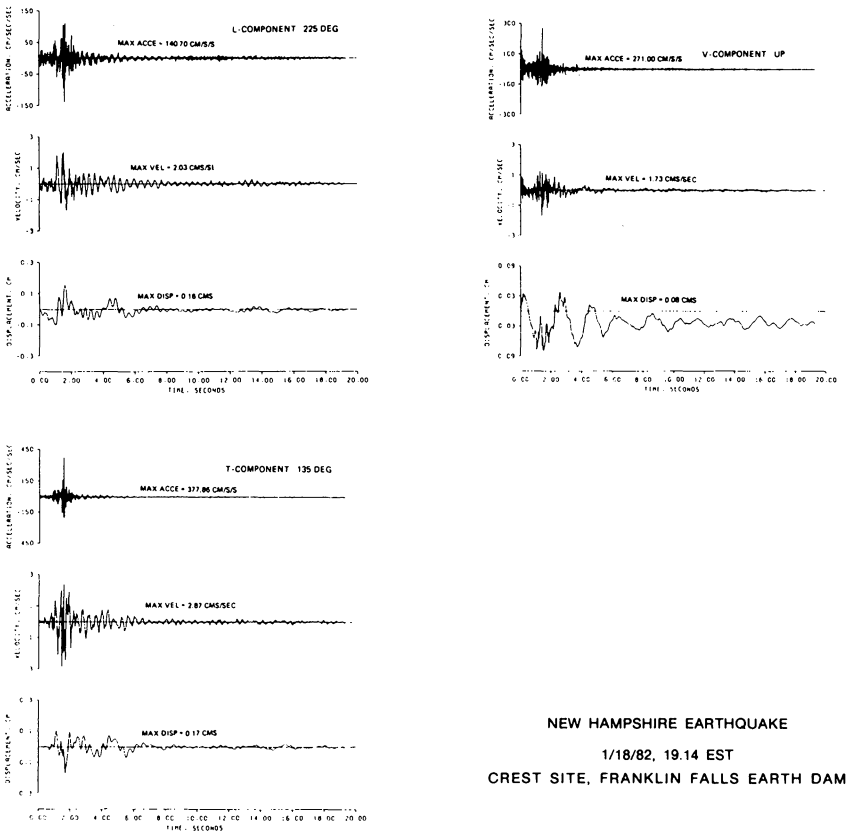

Figure 4. Corrected accelerogram and integrated velocity, and displacement curves of the L, T, and V components at crest site, Franklin Falls Dam.

from which low frequency noise is eliminated. This is part of the standard routine processing of accelerograms (Hudson and others, 1971; and Trifunac and Lee, 1973). The general procedure of baseline correction for this report is the same as mentioned above except that Ormsby's filter had been replaced by an equivalent Butterworth filter (USGS,1976) and some minor changes. Details of these and other data processing procedures are discussed in a User's Manual for the computer code AGRAM by Converse (USGS, 1983).

3.3. Data Processing

The 36 corrected accelerograms, velocities, displacements, and their response spectra were processed by the BES &G using their standard routine computer program AGRAM. Plots showing the corrected acceleration, velocity, and displacement curves (Figures 2, 3, and 4) in this paper were prepared by WES.

The spectra of absolute response acceleration, relative response velocity, and relative response displacement will be published in a separate Nuclear Regulatory Commission (NRC) report.

4. DATA PRESENTATION

Station, site location, coordinates, epicentral distances, azimuth from source to accelerograph site, instrument component, uncorrected maximum acceleration, corrected maximum acceleration, maximum particle velocity, maximum displacement, velocity spectrum intensity, and ratio of $a \cdot d/v^2$, v/a, and a_v/a_h are listed in Table II. By definition, the spectrum intensity is the area under the velocity spectrum curve, of 5 percent critical camping, between 0 and 4.0 sec.period.

$$SI_{\zeta} = \int_{0}^{4.0} S_v(\zeta,T)dt$$

where ζ is the amount of damping. In this report, ζ = 5 percent. The area under a curve is a measure of the intensity of the ground motion for the range of periods and that amount of damping.

5. DATA ANALYSIS

The 27 records from Union Village Dam (UVD), North Hartland Dam (NHD), WRJ VA Hospital, Nort Springfield Dam (NSD), and BMD were all obtained at sites located in Vermont, to the west of the epicenter, at distances between 60 and 103 km as shown in Figure 1. The VA Hospital accelerograph at Manchester, New Hampshire, about 57.5 km south of the epicenter, was not triggered by the earthquake. The strong-motion stations, at CE dams located near Townsend, Vermond, and Surry, New Hampshire, about 99 km and 79 km, respectively, from the epicenter also did not record any

values. No strong-motion instruments in Massachusetts were triggered by the earthquake. The ground motion was evidently strongest westward from the source. The direction of the horizontal resultant peak ground acceleration at FFD was in the range between N64°W to N74°W as shown in Figure 5, which was determined from the two horizontal maximum accelerations at the downstream, crest, and abutment sites, i.e.,

$$(a_L)\ \max \mathbin{+\!\!\rightarrow} (a_T)\ \max$$

where $+\!\rightarrow$ = addition of two vectors L and T

(a_L) max = maximum acceleration of longitudinal component

(a_T) max = maximum acceleration of transverse component

The best way to determine the direction of the ground motion is to use the first motion of the records. However, this was not done in this case due to the trigger level of the strong-motion instrument.

The corrected maximum acceleration of 0.55 g's recorded on the transverse component of the accelerograph at the right abutment (rock) of FFD is the highest acceleration ever recorded in the eastern United States. However, the corresponding integrated maximum velocity is 5.59 cm/sec (Figure 2). In comparing this value with the Melendy Ranch (M = 4.7) with maximum acceleration of 506.12 cm/sec^2 and a velocity of 13.72 cm/sec on the N29°W component, the particle velocity for FFD is much less than the Melendy Ranch record. This difference is probably caused by the predominant frequency content, 11 Hz for the former and 5 Hz for the latter.

It is noted from Table II that the laximum acceleration recorded on the crest (Figure 4) of the FFD did not amplify due to the height of the 45-m earth dam. Actually, the peak ground acceleration recorded at the downstream site (Figure 3) was even somewhat higher than that on the crest.

Because of the lack of the strong-motion data in the eastern United States, the attenuation of ground motion is always a problem. For the first time, 36 accelerograms have been recorded for one earthquake in the eastern United States. Even though the data are not sufficient or not evenly distributed with distance and it would be better to make an analysis for the attenuation of ground motion using data for different site conditions, the analysis was performed because these are the first data from this region. The 36 records were recorded on the crest, abutment, and downstream sites of five eart dams and at one basement of the VA Hospital, i.e., FFD, UVD, NHD, NSD, BMD, and VA Hospital at WRJ (Figure 1). The location distribution of the 36 records is shown in Table I.

All five earth dams are located in different valleys and their geometrical boundaries are certainly critical to the ground motion. Generally, the two horizontal components of an accelerograph on the crest of a dam are oriented parallel to the dam axis (longitudinal component) and perpendicular to the dam axis (transverse component). For the purpose of comparison, the accelerographs located on the abutment and

downstream are oriented the same as on the crest. Thus, in terms of site topography the longitudinal component is approximately the motion perpendicular to the axis and the transverse component the motion parallel to the valley axis. Figure 1 shows the direction of the longitudinal axis of each earth dam and the orientation is also given in Table II. If desired, the transverse and longitudinal components can be resolved into the radial and tangential components with respect to ray path from the focus.

Figures 6a, b, c, and d show the attenuation curves of the three orthogonal components for peak ground accelerations (PGA), peak ground velocity (PGV), peak ground displacement (PGD), and velocity spectrum intensity (VSI) on the crest, abutment, and downstream sites for the five CE earth dams.

The general attenuation characteristics of the ground motion are shown as follows. The attenuation rate of PGA, PGV, and VSI on the crest site is about the same as on the downstream site. Attenuation is naturally faster on the abutment (rock) than on the crest and downstrem sites. The energy or amplitude of the transverse components at the FFD is higher than the other two components. However, the rate of attenuation for the transverse component is faster than for the longitudinal and vertical components. The attenuation trend of PGV and VIS is similar, because both are based on the same concept of energy. The PGD for the downstream site is somewhat lower than the crest site and overall the presentation is not as unique as PGA, PGV, and VSI curves due to the double integration of the long-period waves.

Based on the statistical analysis of the peak ground motions, a, v, and d, it has been found that the average ratio of v/a for the 36 components of the earthquake is 0.024 sec. The average ratio of v/a for the 110 components of the western United States is about five times higher than for this earthquake. The average ratio of a_v/a_h (vertical maximum acceleration to horizontal maximum acceleration) for this earthquake is 0.83. Uwabe* and others (1977) found the average ratios of a_v/a_h for Japan and the western United States are 0.33 and 0.48, respectively. The cause of this difference needs further investigation.

The average ratio of ad/v^2 for 189 vertical components of the strong-motion records in the western United States is 6.62 $\pm$ 4.30 and for 382 horizontal components 5.30 $\pm$ 3.84. The former is about 25 percent higher than the latter. However, in the eastern United States, the average ratio of ad/v^2 for the 12 vertical components of this New Hampshire earthquake is 10.116 + 4.387 and for the 24 horizontal components is 7.903 $\pm$ 3.678. The former is about 28 percent higher than the latter. For most earthquakes of practical interest, Newmark and Rosenbluth (1971) give ad/v^2 = 5 to 15. This is in agreement with the present study.

---

* Uwabe, T. 1979. "Comparison of Vertical Components of Strong-Motion Accelerograms for Western United States and Japan," unpublished report, U.S. Army Engineer Waterways Experiment Station, Vicksburg, Mississippi 39180 - 0631

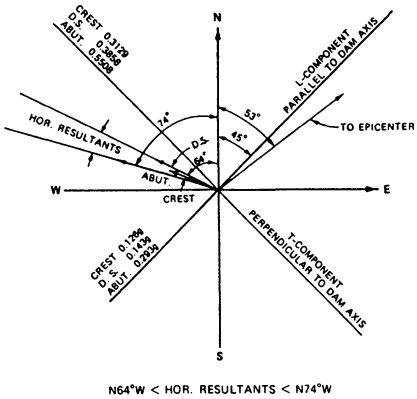

Figure 5. Resultant force direction of horizontal peak ground acceleration of crest, downstream, and abutment at Franklin Falls Dam

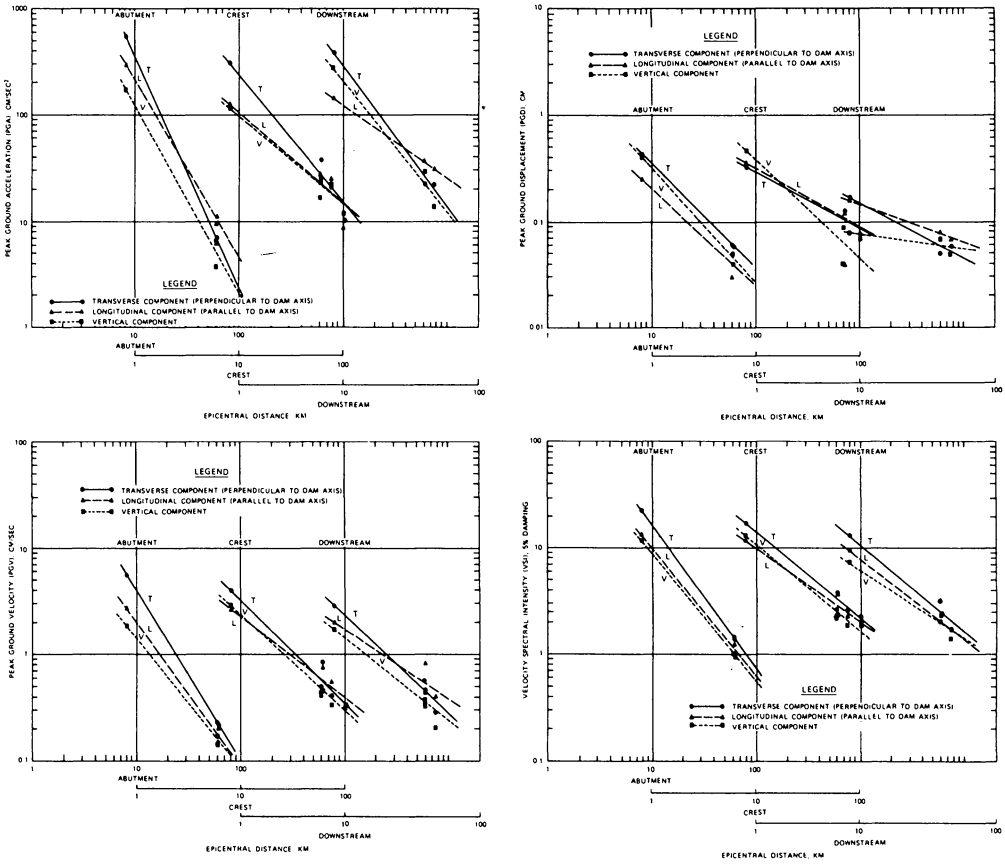

Figure 6,a,b,c, and d. Attenuation of PGA, PGV, and VSI versus distance at abutment, crest, and downstream of the earth dam.

6. SUMMARY

Thirty-six analog accelerograms of the New Hampshire earthquake of 18 January 1982, which occurred at latitude 43.5°N, longitude 71.6° W were digitized, corrected, and integrated.

Results of the 36 accelerograph records such as uncorrected maximum accelerations, corrected maximum acceleration (a), velocity (v), and displacement (d), velocity spectrum intensity, and the ratio of ad/v , v/a , v/a , $(v/a)_{vert}/(v/a)_{hori}$, and a_{vert}/a_{hori} are listed in Table II.

Eleven accelerographs on the five earth dams of the CE and one accelerograph in the basement of the WRJ VA Hospital in Vermont recorded the earthquake. The five earth dams are Franklin Falls in New Hampshire and Union Village, North Hartland, North Springfield, and Ball Mountain in Vermont. No strong-motion instruments in the Massachusetts were triggered by the earthquake. The direction of the horizontal resultant force was within the range of N64°W and N74°W.

The maximum acceleration of 0.55 g's recorded on the transverse component at the right abutment (rock) of the FFD is the highest acceleration ever registered in the eastern United States. However, the corresponding integrated maximum velocity is 5.59 cm/sec, which is much lower than is typical at the same acceleration level and earthquake magnitude for the western United States.

It is noted that the maximum acceleration on the crest of the FFD was not amplified by the height of the 45-m earth dam.

The attenuation curves of the three orthogonal components for PGA, PGV, PGD, and VIS on the crest, abutment, and downstream sites of the five CE dams were plotted and compared. The transverse components show highest energy in almost every site except for the downstream site of the UVD, but the rate of attenuation is faster than the rates of the other two components. The attenuation rate for the crest and downstream sites is similar and is slower than on the abutment (rock) sites.

The average ratio of v/a for the western United States is about five times higher than this for the New Hampshire earthquake. The average ratio of a_v/a_h for this earthquake is 0.83, which is higher than the 0.48 for the western United States and 0.33 for Japan. The ratio of ad/v^2 for the vertical component is higher than for the horizontal component.

7. ACKNOWLEDGEMENT

This paper is extracted from the report published by NRC under Contract No.Res-79-111 MOD 2. The work was monitored by Dr.Andrew J.Murhphy, Seismologist, Earth Sciences Branch, NRC. The tests described and the resulting data presented herein, unless otherwise noted, were obtained from research conducted under the SMIP of the CE by WES. Permission was granted by the Chief of Engineers to publish this information.

8. REFERENCES

Converse, A.M. 1983 User's Manual for the Computer Code AGRAM US Geological Survey Open File Report.

Hudson, D.E., Brady, A.G., Trifunac, M.D., and Vijayaraghavan, A. 1979. Strong-Motion Earthquake Accelerograms, Vol II, Part A, Corrected Accelerograms and Integrated Velocity and Displacement Curves, Earthquake Engineering Research Laboratory Report No. EERL 71-57, California Institute of Technology, Pasadena.

Newmark, N.M., and Rosenbluth, E. 1971. Fundamentals of Earthquake Engineering, Prentice Hall, Englewood Cliffs, N.J.

Ormsby, J.F.A. 1961. "Design of Numerical Filters with Applications to Missile Data Processing," Association for Computing Machinery, Journal 8, pp 33-466.

Trifunac, M.D., and Lee, V. 1973. Routine Computer Processing of Strong-Motion Accelerograms, Report No. EERL 73-03, California Institute of Technology, Pasadena.

US Geological Survey. 1976. "Seismic Engineering Data Report, 1971 Records," Open File Report 76-609, July, Menlo Park, California.

US Geological Survey. 1982. "Preliminary Determination of Epicenters, Monthly Listing," January, 1982, National Earthquake Information Service, Golden, Colorado.

Uwabe, T., Noda, S., Kuvata, E., and Hayashi, S. 1977. "Characteristics of Vertical Component of Strong-Motion Accelerograms," 9th Joint Meeting of US-Japan Panel of Wind and Seismic Effects, UJNR.

SEISMIC INTENSITY AND ITS APPLICATIONS TO ENGINEERING : A STUDY IN JAPAN

Yutaka OHTA, Hiroshi KAGAMI, Shigeyuki OKADA
and Hitomi OHASHI
Department of Architectural Engineering,
Faculty of Engineering,
Hokkaido University, Sapporo 060, JAPAN

ABSTRACT. Motivated by a belief that qualified seismic intensity data should have wider application capability in engineering seismology and earthquake engineering, we have been continuing a series of investigations in Japan, based essentially upon a questionnaire method advanced in both of survey scheme and subsequent data processing. Briefly in this paper we first describe the survey procedure, and then demonstrate a few applications to drawing minute isoseismal maps, to exploring seismic source and path characteristics, and further to elucidating microzoning characteristics in urban and rural areas. The exemplified are 1981 Off-Urakawa and 1983 Central Japan Sea earthquakes. The obtained results are well examined through various comparisons with instrumental and other data.

1. INTRODUCTION

For more than a decade we have been conducting a dense survey on seismic intensity for almost all the moderate-to-large earthquakes occurred in and around Japan. The major reasons are as follows. The officially announced seismic intensities by JMA (Japan Meteorological Agency) have serious demerits that its determination is made in a limited number as 2-3 locations per prefectural unit with the average area of ca. 10,000 km^2 and that its accuracy is rather low due to the summary determination. Therefore the announced intensities are insufficient so as to be basic data for succeeding studies in seismology and engineering. High-precision and dense survey has long been desired in this respect.

Incidentally, it is needles to say that the best way for determining seismic severity is due to the instrumental data by, say , a strong motion seismometer. But, in Japan the total number of such seismometers is at most 1500 in the year of 1985 and it is rare that we have 10-20 strong motion records good for analysis even in a large earthquake. Yet the installation is biased in man-made structures because the strong motion observation started mostly aiming at engineering use. Added to this, the areal distribution is also inhomogeneous as is seen most of them are installed in major cities, along national

M. O. Erdik and M. N. Toksöz (eds.), Strong Ground Motion Seismology, 369–384.
© 1987 by D. Reidel Publishing Company.

railways, and in important structures. Because of this historical background, Japan is too far to be ideal in strong motion data availability as for evaluate spatial distribution of seismic severity in an earthquake. But not rapid progress in strong motion observation network is relizable. The other countries than Japan seem to be in the similar or rather worse situation. This is why we consider that an urgent task is to introduce a good substitute for instrumental data. The long continuing study in our group is to provide a better substitute of indexing seismic severity by developing a field survey techniques of " Seismic Intensity".

In this paper, major subjects covered and results obtained through this series of studies are summerized first on the procedure of seismic intensity survey and then on its applications to engineering seismological and earthquake engineering problems, demonstrating the significance of dense and qualified seismic intensity data.

2. DENSE SURVEY OF SEISMIC INTENSITY

There are several ways for determining seismic intensity. A field inspection of damaged structures is one of the most popular techniques in the present world and most of the isoseismals due to the past earthquakes are drawn based upon thus obtained seismic intensity data. This method seems advantageous because the field survey is made in direct reference of texts by which seismic intensity scale is defined. But, judging from the fact that we often encounter plural numbers of isoseismals for an earthquake, drawn by different researchers, this method is not so ideal as is expected. The obtained intensities by means of field inspection are not only limited in number but also subjective , depending upon where to inspect and how to interprete structural and other damages, since no all-round and detailed investigation is far incapable. Although one recognizes the importance of this way of intensity determination, the more objective and less troublesome method is desired to be introduced. Another one which is also popular is so - called questionnaire method. This method has long been performed in Japan, USA and other countries, because of its brevity in survey. As is also called a mail survey a simple questionnaire sheet,mostly printed in a postal card, with several to 10 questions are mailed to the residents in the affected area due to an earthquake, and collected so as to estimate seismic intensities where the questionnaire cards are returned. The dominant merit in this method is its simplicity and objectivity at intensity determination, if the survey is made appropriate enough, and the data processing is performed reasonably. But, the previous surveys in this kind were somewhat insufficient in these respects. Therefore all the intensity data in this manner were considered merely auxiliary material. What we wanted to develop in Japan is essentially a questionnaire method. But, the developed one is significantly different from the previous ones in both of survey scheme and subsequent data processing. In the affected areas by an earthquake there are significant numbers of residents, if its magnitude is moderate-to-large. We regard such people as the earthquake-observers whose individual responses may

be somewhat scattered but statistically processed responses in a certain bounded area are qualified. Then by performing an intensive survey we can expect that the conventional questionnaire method will be renewed from both in density and precision of seismic intensity determination.

2.1. Questionnaire

Prepared questionnaire for evaluating seismic intensity at a site contains 34 items of questions. Several items are for asking the respondent's physical situations of residential house, house plan, floor number etc and the non-physical situation in which state he or she encounters a shock. The items directly related to seismic intensity are around 20 in number from people's perception to forced behavior under shaking, and to damages to structure and nonstructure elements and also to physical deformation of indoor and nearby environs. All of the items in the questionnaire are made in reference with the texts in JMA intensity scale (See Appendix). The answers to be checked are arranged in ascending order of seismic severity and composed of categoric manner. Special attention paid are to prepare duplicate questions in a certain range of intensity so as to improve the accuracy of respondents. According to JMA scale in a range of intensity V, for example, there is no description about any structural damages, in spite that intensity VI brings collapsed house of 10-30%. This suggests that the JMA scale is too rough to be applied to advanced damage analysis. The corresponding acceleration to the intensity V is considered 80-250 gals and, if so, it is too wide to be condensed in a class from engineering point. One of our major objectives in this study is to develop a way of dividing an intensity class into several sub-classes. Namely it is to improve the number of significant figure which the JMA intensity has from one to two. Arrangement of order of item-categoric questions, number of categories for a question, and, layout and format of the questionaire etc are carefully decided in consideration of respondent's convenience. A set of questionnaire is composed of 4 pages by A-4 size sheet.

2.2. Survey scheme and processing

The actual procedure differs depending upon the objective of survey. If we want to grasp the general pattern of isoseismals covering all the areas affected by an earthquake, the areal size to be surveyed should be in concordance with earthquake magnitude. If a shallow earthquake with magnitude around 7 occurs in around Japan, generally several hundreds of municipalities (of city, town or village unit) are included in the so-called felt area. Therefore, 5,000 - 10,000 questionnaires are delivered to residents in the affected area usually via local governmental offices so as to get 20-50 collections by a unit area. Depending upon the earthquake magnitude, the numbers to be delivered are adjusted from at least 1,000 to 20,000. In case when we have a special objective of elucidating near-distant isoseismals a more dense survey is carried out in the area including epicenter. If the survey is concentrated in a moderate-to-large city, it gives considerable data to assess microzoning characteristics of urban area. In such a way we have been conducting for more than 20 earthquakes in Japan.

The collected questionnaires are analysed so as to get raw intentisies first, in the manner as one intensity by one questionnaire, and then by use of several tens of raw intensity data in a unit area, statistically processed so as to improve its accuracy with two significant figures. The actual conversion to JMA intensity was made through several times of comparative survey in special areas where JMA regional observatories locate. The relation of our intensity, I_Q, of JMA intensity, I_{JMA}, is written as

$$I_{JMA} = \mathrm{IFIX}\left[I_Q + 0.5 \right].$$

From several points of view , verifications were tested. Fig. 1 is an example. The upper two maps show the topographical features by means of collected questionnaires and the lowest map does actual one in a surveyed city. This comparison suggests that people's answers are conceivable and therefore reproduction capability by this method is rather well. Another example listed in Table 1 is a numerical comparison among I_Q, I_{JMA} and maximum ground accelerations measured in a specific site.

TABLE 1. COMPARISON AMONG I_{JMA}, I_Q, AND ACCELERATION AT A SITE

I_{JMA}	I_Q	Acc (gal)
V	4.5	213
V	3.9	88
V	3.8	90

From this we know our intensities are much more sensitive to delicate changes of seismic severity at a site. More detailed explanations on this dense and precision intensity survey will be made in the following sections. The exemplified are two recent major earthquakes occurred in Japan.

3. 1982 OFF-URAKAWA EARTHQUAKE

On March 21, 1982 a large earthquake with M = 7.1 occurred off Urakawa, Hokkaido district in northern most Japan and suffered significant amount of damage in several towns along the Pacific coast and a few inland cities. Although the maximum intensity by the JMA was VI at Urakawa, no continuation to V was reported at any affected areas. The second maximum intensity of IV was reported at several cities in considerable epicentral distances. Such an unusual event seems mostly due to that in Hokkaido district of the total area 1,100 km^2 there are only 17 JMA stations at which the intensities are determined. For the purpose to overcome such contradiction, and to draw precise isoseismal maps including epicentral region, a survey was carried out distributing 6325 questionaires to 212 municipalities in Hokkaido. On the other hand in Sapporo,

with a population over one million, various damages of grounds and dwellings and of interruption of life line systems were observed differently from place to place, although the formally announced intensity is merely IV. This suggests that a solitary observation of intensity IV as for such big city is too inappropriate and give no useful information to the subsequent areal damage analysis.

Therefore, we performed dense questionnaire surveys for this earthquake with special objectives of getting precise isoseismal map, of elucidating intensity distribution along the coastal line passing through epicentral area, and of characterizing microzoning of Sapporo city.

3.1. Isoseismal map

The delivery of 6,325 questionnaires was made in relation of population as 100 for a city with 100,000 population or higher, 50 for the other cities and 25 for a town or a village, and we got 86.5% answers. Fig.2 illustrates 0.25 increment-isoseismal maps drawn by use of obtained intensities by municipalities. The actual drawing was made automatically by Ohta and Kagami's technique (1982). The observed isoseismals are somewhat irregular than circular. Contour lines seem extended in E-W direction, but contracted in N-S direction. This is a common character of isoseismals due to earthquakes in Hokkaido district. To know more detail about this peculiarity, the deviation from the standard intensity attenuation with distances was deduced and its anomaly map was drawn as is shown in Fig. 3 and compared with the so-called Bouguer anomaly map compiled by Hagiwara (1983). As is seen in this figure we find a significant correlation between two maps. It is evidence that in the region where intensity anomaly is positive deep seated soft soils deposit widely and in its negative region geologically old or volcanic rocks distribute. This clearly shows that the obtained isoseismal map reflects well regionality in seismic wave propagation.

3.2. Epicentral region

A dense questionnaire survey was performed in several towns locating Pasific coastal line in epicentral region. Fig 4 summarizes observed and calculated intensity distributions, together with the other physical data. The upper most curve shows relative ground deformation between this earthquake. The second one is PGA (peak ground acceleration) distribution curve derived by Kobayashi et al (1982). The lowest ones are our calculation and observation. The calculated intensities are based upon the empirical equation proposed by us previously (Ref. Ohta et al 1983). All the distributions cited here are in remarkable agreement. A comparison of the ground deformation curve with that of observed intensity tells that the occurrence of dominant ground failures is limited within the region where the intensity is equal to or higher than the lower bound of VI, which is in good agreement with the description in JMA intensity scale.

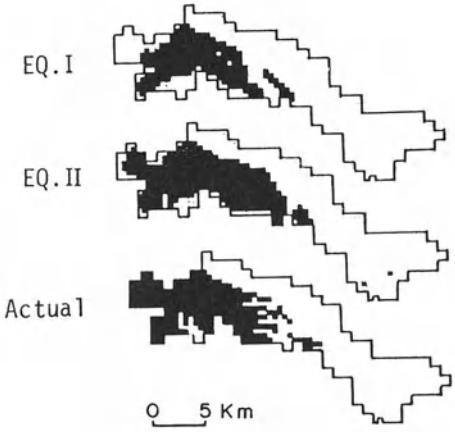

Figure 1. Comparison of deduced and actual topography.

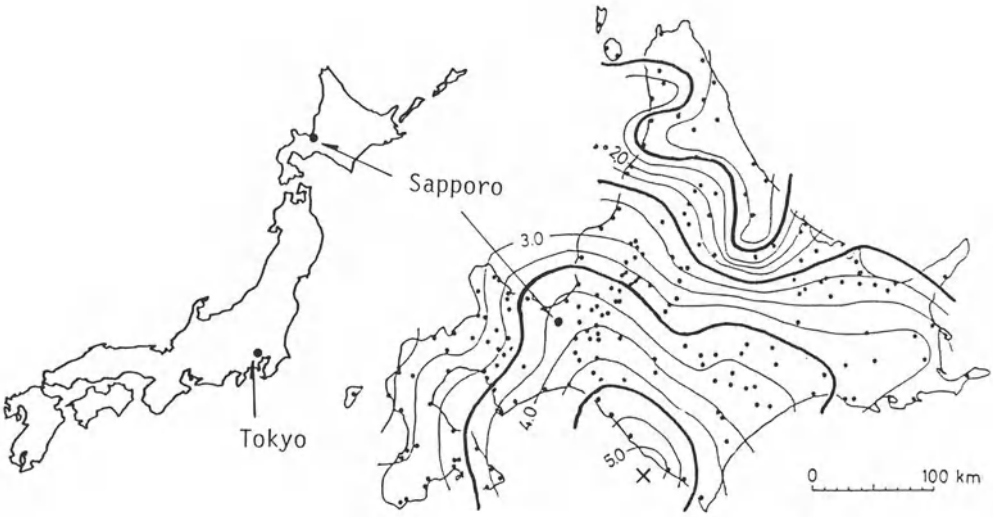

Figure 2. Obtained isoseismal map.

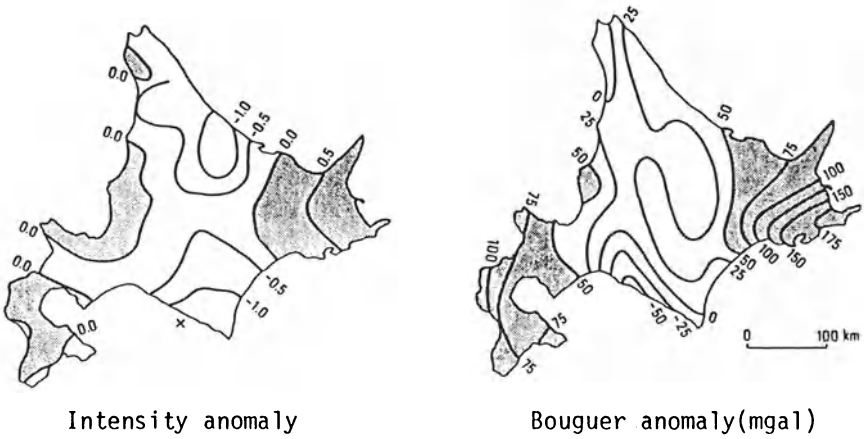

Figure 3. Comparison between intensity and Bouguer anomalies.

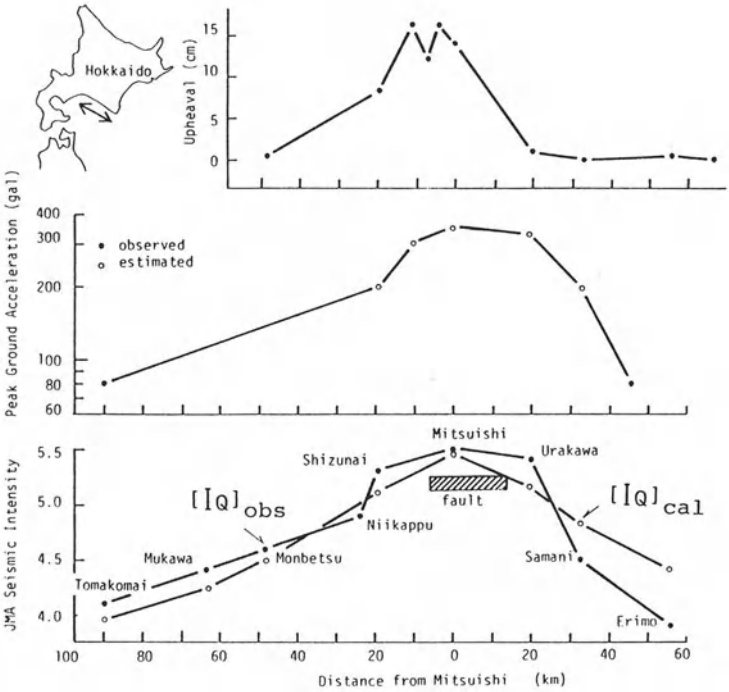

Figure 4. Comparison of intensity with other physical data.

3.3. Urban area

Similar but more dense survey was performed in Sapporo city distributing 10,000 questionnaires so as to cover whole the residential area, and got 83% answers. Fig.5 shows the histogram through which one can see the observed intensities spreads from II to V in JMA scale, through the average intensity of 3.8 is in good agreement with that by JMA Sapporo station. Areal distribution of intensities are shown in Fig.6 together with site plots where considerable damages occurred. Thus obtained microzoning characteristic reflects well the seismic severity distribution due to this earthquake.

Next, we examined a physical reason of such microzoning characteristics. Since Sapporo city is in an epicentral distance range of (145 $\pm$15) km, distance effect seems small. Source and path effects are also less influential because, in this distance, source fineteness can be out of consideration and all the paths to Sapporo are approximately identical. If these are true, only the physical possibility of such spatial intensity distribution should be explored in so-called site effect due to surface soils. Fig. 7 illustrates a line-up of histograms of intensity deviation (δI) from the average value by surface soil types. The upper 4 histograms are for alluvial soils, which indicates rather large intensities, and the remainder ones are mostly for older soils and rock sites The soil layer thickness is effective up to 10 m but after that it seems saturated.

Based upon this preliminary analysis we can develop an empirical equation to estimate seismic intensities in Sapporo city. The intensity at a given site, I_i, is written as

$$I_i = f(M,\Delta) + \left(\begin{array}{ll} 0.256 & \text{silt} \\ 0.182 & \text{peat} \\ 0.050 & \text{volcanic ash} \\ 0.040 & \text{sandy silt} \\ -0.051 & \text{sandy and clayey silt} \\ -0.156 & \text{river deposit} \\ -0.278 & \text{gravel} \\ -0.396 & \text{andesite (weathered)} \\ -0.406 & \text{talus} \end{array} \right) + 0.04\, H_i$$

where

$$f(M,\Delta) = 2M - 4.601 \log\Delta - 0.00166\Delta - 0.32 \quad \text{(Kawasumi, 1954)}$$

and M is the JMA magnitude, Δ is the epicentral distance in km and H is the thickness of surface soil in m.

Fig. 8 summarizes various disasters observed in this city in relation with seismic intensities.

4. 1983 CENTRAL JAPAN SEA EARTHQUAKE

A great earthquake occurred on May 26, 1983 and brought serious damages to northern districts in mainland Japan. Because of its large magnitude

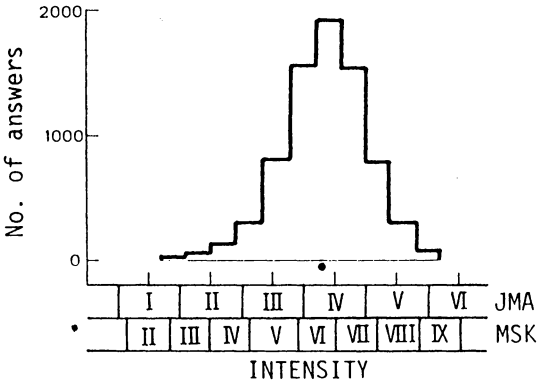

Figure 5. Histogram of intensities obtained in Sapporo city.

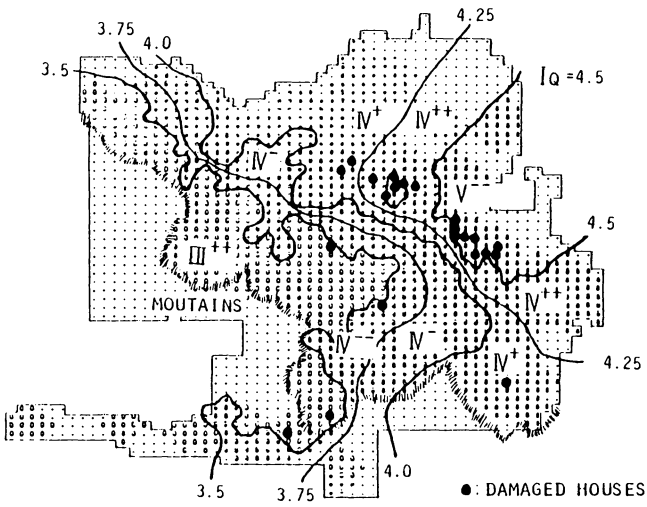

Figure 6. Intensity microzoning map in Sapporo city.

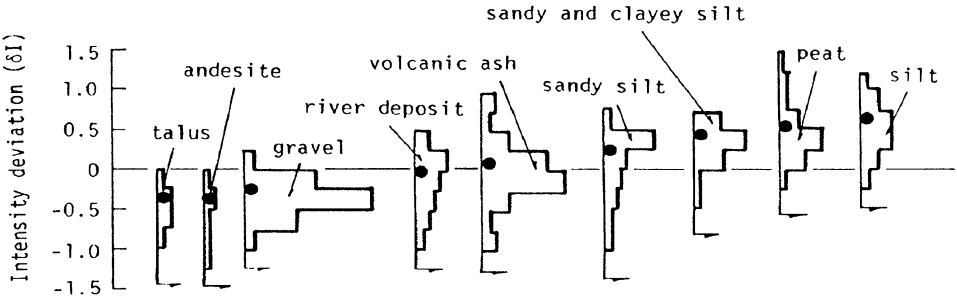

Figure 7. Histograms of intensity deviation by soil types.

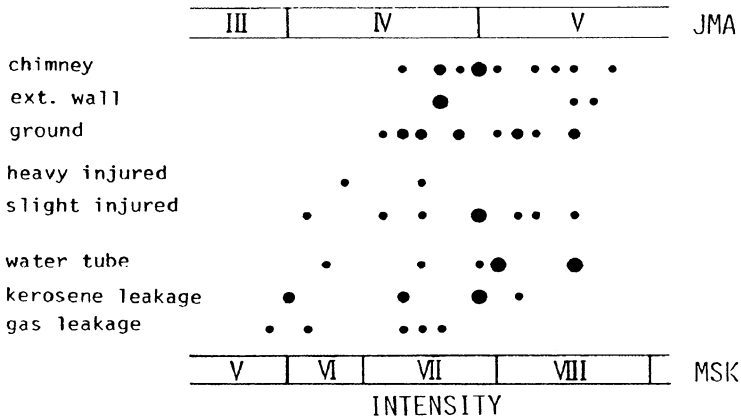

Figure 8. Various disasters in relation with intensity.

of 7.7, the affected areas were so wide covering Hokkaido, Tohoku and Kanto districts of nearly 10 prefectures. For this earthquake a dense survey was performed similarly to the 1982 Off-Urakafa earthquake, including 435 municipalities. The total number of questionnaires delivered exceeds well 10,000, by which almost all the areas with intensity of III and higher were investigated. The answers arrived at about 80%. By use of these data several analyses were conducted. Those are general pattern of isoseismals, source and path effects, and, regional and local effects etc.

4.1. Isoseismal pattern

The actual intensity determination was made at 403 unit areas (The JMA stations were official intensities were reported are around 20 among these areas). Although the maximum intensity by JMA is reported as V at 3 stations, we could reveal that there are several areas where it arrived at VI. The isoseismal map drawn 0.25 increment is illustrated in Fig. 9. From this we find several significant features. One is that area with intensity V and higher spreads widely in NS direction than in EW direction. This seems due to configurational characteristics of the earthquake fault. The other contours have also the similar tendency of extending NS direction. And this tendency is rather common to most isoseismal maps for shallow earthquakes occurred in northern part of Japan.

4.2. Source and path effects

The N-S directionally extended isoseismal contours in Fig. 9 can not be explained by a simple attenuation equation assuming a point source and seems to reflect well the finiteness of seismic source. We have already proposed an empirical equation appropriate for near-distant intensity distribution enclosing seismic source area (Ohta, 1983). Let us apply the same equation to this earthquake. According to the equation, the intensity at any point on the ground is expressed as

$$I = C_1 \log D^k \int^L \int^W \frac{1}{F(R^{-P})} \, d\xi \, d\eta ,$$

where D is the average resultant slip measured by the cordinate system (ξ , η) on the fault surface, k is the coefficient relating to slip contribution upon intensity, and p is the coefficient relating to the attenuation due to the distance, and the appropriate values are empirically derived for k and p as 0.25 and 2-3 respectively. Here, we perform the following examinations. That is, through numerical comparison of calculated and observed intensities in near-distances we try to find out the optimum configurational solutions in terms of fault length and strike direction. The ranges we examined are for fault length L from 40 to 200 km and for strike direction from N30°W to N30°E, assuming that fault width is known as W = 40 km and dip angle as 30°E. Actual

calculation was done so as to evaluate the correlation between observed and calculated intensities in ranges higher than III. Fig. 10 illus - trates contours of thus obtained correlation coefficient. From this we know that the optimum values are L = 120 km and N20°E, though the probable values for fault length and strike direction are in a little wider range. These values are in quite agreement with those derived from instrumental data. This clearly tells that the obtained isoseismals ref - lect well the source finiteness and configurational characteristics. A few more examinations to know the effect of different source models upon near-distant seismic intensity distribution were performed. We changed fault width and dip angle to some extent and found no significant effect appears upon intensities. Since it has been insisted that this earthquake is composed of multiple shocks with two major events, we checked the dependency of seismic intensity due to such events and found no recognizable difference. Careful statistics give no indication of so-called Doppler effect due to faulting directivity upon the observed intensities. All these findings teach that the physical quantity of "seismic intensity is a rather good index to bring important information on seismic source but it is somewhat insensitive to delicate faulting processes.

As is seen above the intensity distribution in its higher ranges is in close relation with configurational characteristics of earthquake fault. Such effect, however, should decreases with increasing distances and then the isoseismals in lower intensity range become homogeneous and circular. But, the isoseismal map in Fig. 9 does not indicate such character so sharply. This suggests that we should consider another effect of, say, path effect. The path effect is divided into two major parts of regional and local effects. We tried to separate path effect from the obtained intensities. However, the path effect we can deal with is, in this data set, only the regional effect because of insufficient questionnaire distribution. Actual procedure to deduce the regional effect, I_r, is made as

$$I_r = I_{obs} - I_{cal},$$

where I_{cal} means the estimated intensity considering seismic source finiteness. Fig. 11 shows thus deduced residual intensities in comparison with the spatial distribution map of Quaternary soils. Both are in remarkable correlation.

4.3. Local site effect : A case study

In a town locating along the Japan Sea coastal line with a population of ca.10,000, a whole survey for all the families was performed and compared with damage and other data in order to elucidate local changes of seismic effect. Fig. 12 illustrates the observed intensities by 18 subareas in comparison with structural damage rate and periods necessary for recovery of daily life and for restoration of dwelling. We understand that all of them in sub-areal distribution are in dominant correlation and therefore the seismic severity measured in terms of seismic intensity is the most fundamental factor on direct and indirect eartquake

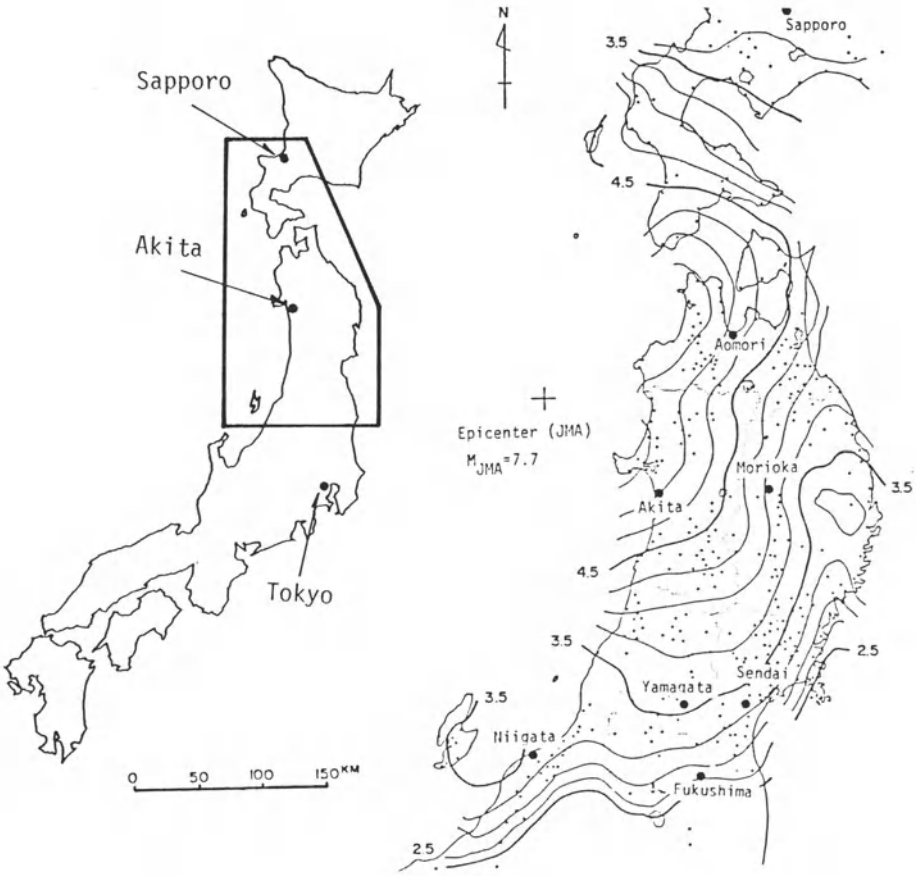

Figure 9. Obtained isoseismal map.

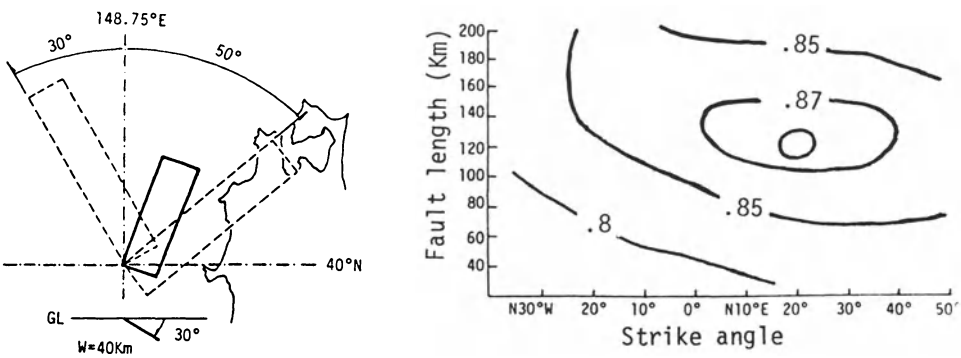

Figure 10. Estimation of fault length and strike direction.

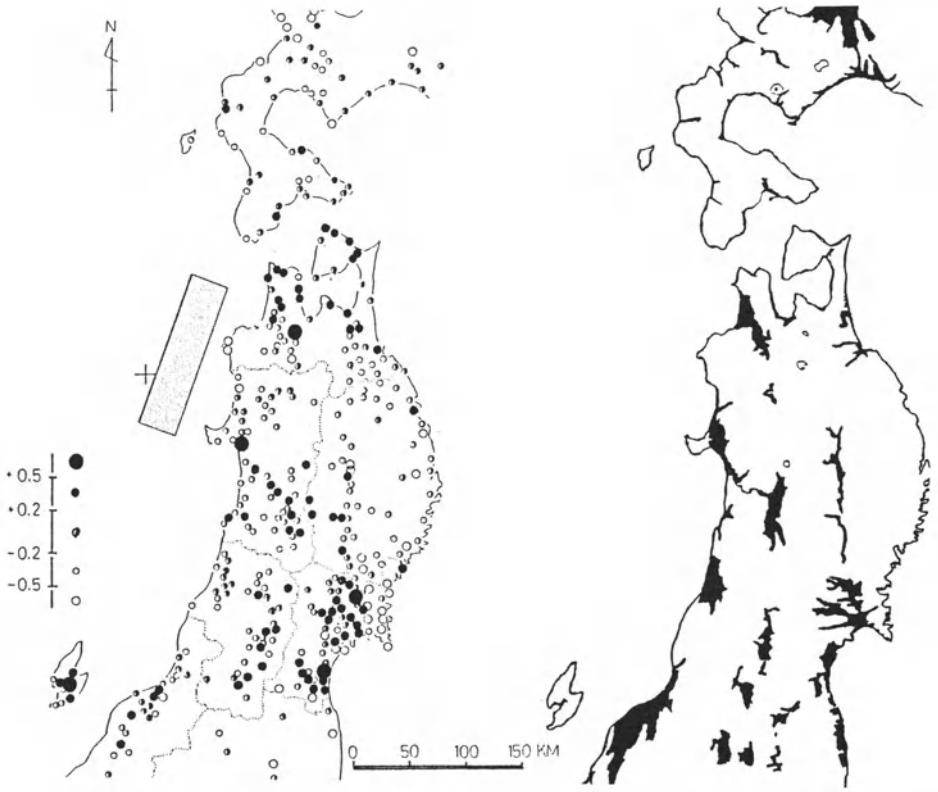

Figure 11. Comparison intensity deviation with surface geology.

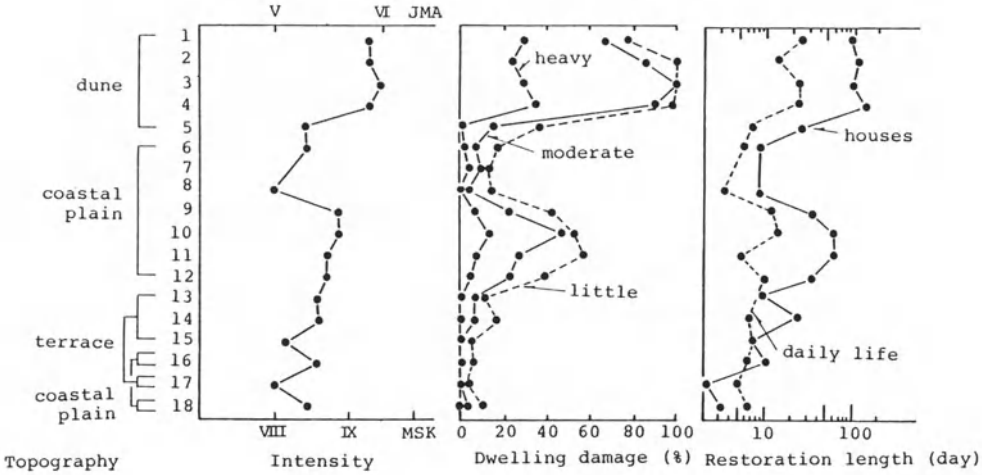

Figure 12. Comparison of intensity with damage and aftermath.

disasters. If we compare this intensity change with local geological data, we find that the sub-area with highest intensity is composed of the latest sand dunes and the second highest areas are of alluvial soils and in the areas with surface soil older than alluvium the intensities are clearly low.

5. CONCLUDING REMARKS

5.1. Summary of results

Through this series of studies for developing seismic intensity survey by means of questionnaire method we found that dense and qualified intensities are rather easily obtained and such intensity data are well applied for advanced analysis on seismic source and path characteristics and for comparative study with damage and other data. In conclusion we would like to say that, since this questionnaire method is simple and systematic enough to be performed with no much special technique, it should have wider application capability to any other countries than Japan.

5.2. Further problems

There are at least two major problems to be solved relating to "seismic intensity". One is to continue this series of studies so as to widen its application capability in engineering seismology as well as in earthquake engineering. The other important problem is to develop a way of understanding physical background of seismic intensity in the manner far precise than is expressed simply as a function of acceleration only. Qualitatively it has long been said that seismic intensity is also a function of the duration time of ground shakings and so-called Peak Ground Acceleration can not be the primary factor which governs seismic severity. But, in the present there is no equation sufficient enough to define seismic intensity in terms of physical parameters. As a first step for overcoming this difficulty we have been making a special effort for simultaneous observation of seismic intensity, and, acceleration and other instrumental data. The forthcoming analysis of these data will surely bring useful information to explore a better way of solving this long-desired problem.

6. REFERENCES

Hagiwara, Y.(1983) "Seismic intensity of the 1982 Urakawa-oki earthquake as related to the Bouguer gravity anomaly", Jour. Geodetic Soc. Japan, 29, 164-65 (in Japanese).

Kawasumi, H.(1954) "Intensity and magnitude of shallow earthquakes", Travaux Scientifique, Publ. BCSI, Ser. A, 19, 99-114.

Ohta, Y. and H. Kagami(1982)" An automatic drawing technique of contour

maps of seismic intensity and other spatially distributed earthquake engineering data", Proc.Inter.Microzonation Conf., 3, 1405-1416.

Ohta, Y.(1983, editor) "A comprehensive study on earthquake disasters in Turkey in view of seismic risk reduction", Hokkaido Univ., Sapporo, Japan.

APPENDIX
JMA INTENSITY SCALE (Abbreviated)

0. No feeling : Registered by seismographs only: not felt by any people.

I. Slight : Felt by some individuals at rest, or by some especially sensitive to earthquakes.

II. Weak : Felt by most people, with slight rattling of doors and paper sliding screens.

III. Rather strong : Shaking of houses and buildings ; strong rattling of doors and paper sliding screens, swinging of chandeliers and other hanging objects; perceptible movement of liquids in containers.

IV. Strong : Strong shaking of houses and buildings ; unstable objects fall over; liquids spill out from open containers at least four-fifths full.

V. Very strong : Cracking of plaster walls; heavy objects such as tombstones and stone lanterns fall over, damage to masonry chimneys and mud-plastered warehouses (or godowns).

VI. Disastrous : Collapse of up to 30% of wooden houses; numerous land slides and embankment failure; fissures on flat ground.

VII. Very disastrous : Collapse of more than 30% of wooden houses ; falling of objects; wavy deformation observed in horizon.

SEISMIC INTENSITY AND ITS APPLICATIONS TO ENGINEERING: A STUDY IN TURKEY

Yutaka OHTA and Hitomi ŌHASHI
Department of Architectural Engineering,Faculty of Engineering,
Hokkaido University, Sapporo 060, JAPAN
Oktay ERGÜNAY and Ahmet TABBAN
Earthquake Research Division, Ministry of Public Works
and Housing, Yüksel Caddesi, 7/B, Yenişehir, Ankara, TURKEY

ABSTRACT. First, based on earthquake data in Turkey two kinds of seismic intensity equations are derived. One is for the rough estimation in which a relation of the area with a given intensity to earthquake magnitude is obtained in the least squares sense. Configurational characteristic of isoseismals is also considered in regard of earthquake fault length. The other equation is for the precise evaluation of intensities at near epicentral distances. For this purpose an advanced model considering seismic source parameters such as fault size and slip displacement etc. is developed starting from a conventional model. Second, combining these with structural damage and human victim data, empirical vulnerability functions and casualty rate functions are constructed. Finally, a way to seismic risk assessment due to a future earthquake is proposed.

1. INTRODUCTION

In Turkey a great earthquake with magnitude 7 or higher occurs in every 3 or 4 years and causes significant amount of damage to man-made structures as well as to human lives. Due to several tens of earthquakes which occurred in the period of 1900-1976,58 thousand persons were killed and 392 thousand buildings were destroyed. The earthquake disaster prevention planning has, therefore, been dealt with an important and long-term project. As a part of this project we have been conducting a joint research on why and how Turkey has suffered such serious disasters in earthquakes (Ohta, 1981 and 1983). This paper describes partial results obtained through this series of studies, demonstrating engineering importance of seismic intensity.

Most of major earthquakes in Turkey have occurred as inland and shallow events along North Anatolian fault zone and in western graben region so that structural damages as well as human casualties are extremely severe in the epicentral region. This suggests that more effort for elucidating influence of an earthquake fault upon spatial damage distribution is necessary. Another conspicuous feature is that earthquake disasters in Turkey are rather severe compared with earthquake

M. O. Erdik and M. N. Toksöz (eds.), Strong Ground Motion Seismology, 385–401.
© 1987 by D. Reidel Publishing Company.

magnitude. To know more detail about these phenomena much data for the past earthquakes should be first of all accumulated. One of the most essential materials are doubtlessly instrumental data on seismic severity measured in terms of physical quantity such as acceleration and others. In Turkey such advanced data are quite insufficient because an effort to spread strong motion observation network has been made at most in recent 10-15 years. Instead, significant amount of field data on seismic intensity in MSK scale (almost equivalently to MM scale) as well as on structural and other damages has been collected since the beginning of this century. Thus our study started by finding out a better way of using those data. A field survey was also carried out paying attention to earthquake fault tracing, inspection of damaged and undamaged structures, investigation of house plan and family constitutent for residents, and so on, at the regions affected by major earthquakes in recent decades. Combining these field data with those from previous surveys and observations, a variety of analyses have been conducted. Those are i) general trend analysis of isoseismals, ii) empirical derivation of seismic intensity attenuation equation in consideration of source finiteness, and iii) construction of vulnerability functions and casualty rate functions etc. Combining all these findings, effective techniques for assessing seismic risks were proposed. Seismic intensity used in this paper is mostly unified in MSK scale.

2. SEISMIC INTENSITY ANALYSIS

2.1 Macro Trend Analysis

Since a seismic intensity distribution is characterized by a lot of factors such as fault parameters, propagation path and local conditions of geology and topography, its estimation is not a simple matter. A macro trend analysis on isoseismals would therefore be most appropriate as for an initial stage of estimation of spatial distribution of seismic severity due to an earthquake. From this point of view areal and configurational characteristics of intensity isoseismals are first examined by use of the past earthquake data. A catalogue of earthquakes for Turkey and surrounding region by Ergin et.al. (1967, 1971) is the most dominant data source. This catalogue compiles 36 isoseismal maps for shallow earthquakes occurred from 1928 to 1970, redrawn with a unified scale of 1/2,000,000. Isoseismal maps due to the earthquakes after 1970 were supplemented with data set provided by the Earthquake Research Institute in Ankara. In Fig.1 location map of these earthquakes is illustrated with number of victims. Areas enclosed by various isoseismals are measured by use of planimeter. In case of coastal isoseismals,areas are obtained by an extrapolation under an assumption that more than half is on land.

Average intensity attenuation curves of thus chosen several tens of earthquakes are illustrated in Fig.2 Taking for x-axis a radius of an equivalent circle which has the same area, it is found that intensity is dominantly controlled by earthquake magnitude and it attenuates from IX to V approximately in inverse proportion to logarithm of epicentral

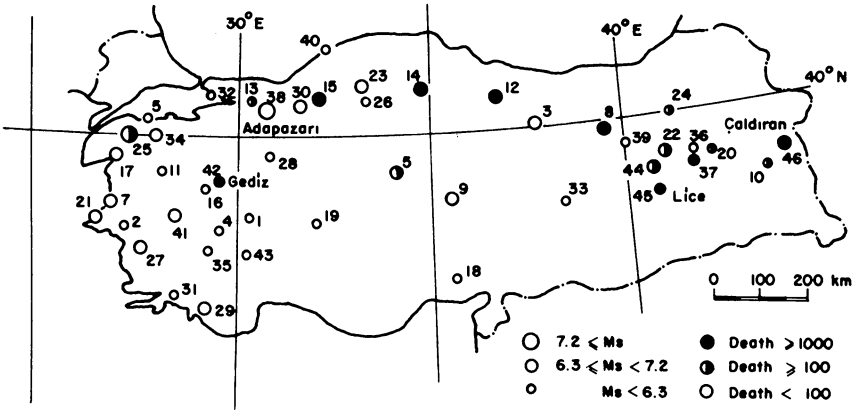

Figure 1. Location map of disastrous earthquake in 1925-1976.

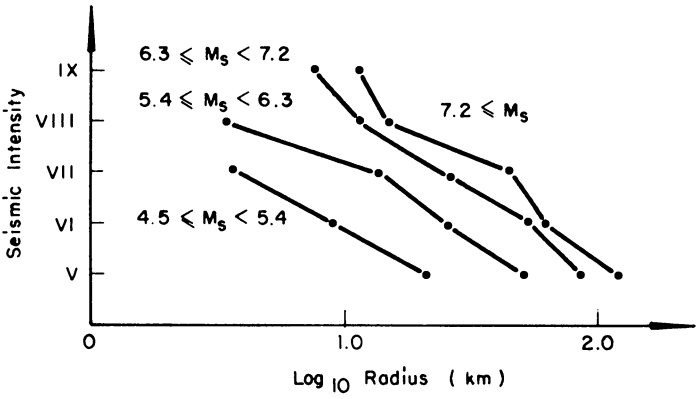

Figure 2. Averaged intensity attenuation in relation with magnitude.

distance. Maximum intensity becomes larger than IX for $M > 7.2$, from VIII to IX for $6.3 < M < 7.2$, from VII to VIII for $54. < M < 6.34$, and around VII for $M < 5.4$. From this we know that the simplest way of expressing areal characteristic of isoseismals is to perform regression analysis as a function of earthquake magnitude on areas enclosed by isoseismal lines of intensities V, VI, VII and VIII respectively. Obtained empirical equations are

$$\log A_{v} = 0.52M + 0.73 \qquad \log A_{vi} = 0.65M - 0.62$$
$$\log A_{vii} = 0.76 - 1.81 \qquad \log A_{viii} = 0.84M - 3.20 \qquad (1).$$

A comparison of these with similar equation for a different region is necessary for understanding attenuation characteristic of seismic intensity in Turkey. Toppozada (1975)'s result for California and Western Nevada is suitable for this purpose, because San Andreas fault is of strike-slip type as is in North Anatolian fault, most active region in Turkey. As illustrated in Fig.3, areas for California are in general larger than those for Turkey. The discrepancy between the two is apparent at lower intensities of V and VI, though the difference is smaller at VII and VIII. This indicates the attenuation in Turkey is much sharper in short distances. The result obtained here is in accordance with Chandra et al (1979) who insist attenuation in Iran is slightly higher than that in California.

Another important factor to be considered is the configuration of isoseismals. Since an earthquake fault of a considerable length appears on the ground, it should make some influence on intensity distribution. If geological structure of region is relatively homogeneous, an isoseismal line of an elliptical or circular form would be expected. Therefore measuring lengths of major and minor axes, the ratio of the two can be regarded as a simple index of a configurational characteristic of isoseismals. Plots of length of major axis in relation with fault length indicate that isoseismal lines of intensity VII are in general longer than faults and those of intensity VIII or IX correspond to the fault length. This fact agrees with the definition of MSK intensity scale which says "cracks in ground up to width of several centimeters" for VIII. Another thing to be noted is that ratios of major axis to minor axis are almost constant as =3 for intensity VII and =4 for intensity VIII. As seismic waves attenuate and intensities get smaller, this ratio becomes smaller so that isoseismal lines look more circular. This tendency of changing forms is illustrated in Fig.4 by use of a simple track model. As is seen here configurational characteristic of isoseismals for moderate-to-large earthquakes are strongly affected by the existence of fault, namely by the areal finiteness of seismic source.

2.2. Semi-empirical Equation

The derived intensity equation could get its simplicity at the sacrifice of accuracy and thus of limitation in engineering application capability. A more profound intensity equation is necessary to be developed for wider applications. Especially in Turkey an equation by which seismic

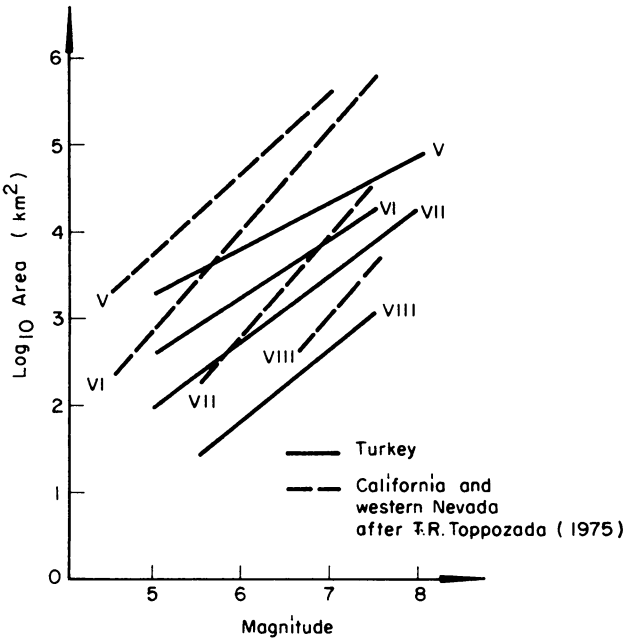

Figure 3. Comparison of attenuation trends with other region.

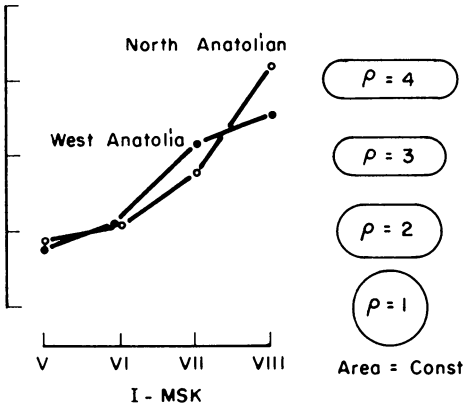

Figure 4. Changes of isoseismal patterns by intensities.

intensities in near distances can be well evaluated is highly desired because most of disastrous earthquakes occur shallow and inland. Nowadays there are numbers of empirically derived equations. But, most of them are constructed assuming simply a form of $I=f(M, R)$ or $I=f(I_{max},R)$, and little attention has been paid to the seismic source finiteness. Besides, the majority of those equations aim at evaluating regional attenuation characteristics with distances as far as several hundreds kilometers. Only a limited number of studies can apply their results to seismic risk assessment in near distances. Evernden et al. (1973)is a representative example of such studies and is noteworthy for an improvement by introducing a line source model explicitly. Here, in a manner somewhat similar to Evernden we extend a new model by which observed intensities in short-to-moderate epicentral distances can be well interpreted.

The basic idea is as follows. First, under the assumption that an earthquake fault as "finite area source" is an aggregate of numbers of segmental faults, the effective ground acceleration is evaluated by the constructive interference of an acceleration originating from each segmental fault. Second, a conversion from thus obtained acceleration into intensity is performed by a well-known relationship between these two quantities (For details of derivation, see Ohta et al. 1983). Parameters considered at derivation are length L, width W, and dip angle θ , of the fault, resultant slip D on the fault surface and focal distance R etc (See Fig.5). The general equation for effective acceleration at a point on the ground a(x,y) is therefore given as

$$a(x,y)=B\int^{L}\int^{W}\frac{[D(\xi,\eta)^{k}]}{F(R^{-p})}\,d\xi\,d\eta \qquad (2)$$

Hence, (ξ , η) is a coordinate system defined on the fault surface and $d\xi\,d\eta$ is a segmental area. Slip D is expressed as a function of (ξ , η). $F(R^{-p})$ is a formal expression of attenuation effect. Factor p of the equation (2) reflects the effect due to the constructive interference as well as geometrical and other attenuations. That is, as for an index to express the interference, smaller p results in simultaneous contribution from the greater part of the whole fault and reversely bigger p tends to weight the contribution from the fault segment nearest to a given point. Assuming $D(\xi,\eta)=\bar{D}=$ const. and a relationship between acceleration and intensity as $I=C_1 \log a+C_2$ we have

$$I=C_1 \log \bar{D}^{k}\int^{L}\int^{W}\frac{1}{F(R^{-p})}\,d\xi\,d\eta \qquad (3)$$

and if site amplification characteristic is known as $[Z_1,Z_2,..Z_m]$ by geological conditions of m kinds respectively

$$I = C_1 \log \bar{D}^k \int^L \int^W \frac{1}{F(R^{-p})} d\xi \, d\eta + [Z_1, Z_2, \ldots, Z_m] \quad (4)$$

can be used. Here, unknown coefficients (C_1 , C_2 , Z_i) are obtained by the requirement that the sum of mean squares of residual between observed and calculated intensities should be minimized, while changing the parameters (k,p) by inspection. For a more complicated fault such as with plural number of planes, this model is also applicable after a small modification. Rupture velocity is also an influential factor, however, approximately constant value is known for different shocks so that it is not considered here. Nor is source time function taken into consideration in this model, since its effects upon seismic intensity is not yet understood well in short period range. Fig.5 illustrates an outline of intensity analysis procedure in this manner. As is seen in Fig.6 as an example of comparison, the observed and calculated isoseismals are in good agreement. Finally derived equation good for moderate-to-large earthquakes in Turkey is

$$I = 1.320 \log \left[\bar{D}^{-0.25} \int^L \int^W \frac{1}{R^3} d\xi \, d\eta \right] + 8.04 \quad (5)$$

Two kinds of empirical equations for evaluating spatial intensity distribution were constructed by use of earthquake data in Turkey. The simple one will be useful in a rather approximate estimation of the areal size of a certain intensity due to an earthquake with given magnitude, and the advanced one will work in precise intensity evaluation and in empirical determination of vulnerability and casualty rate functions.

3. DAMAGE ANALYSIS

3.1. Vulnerability functions

There is a large variety of structures especially in rural areas in Turkey depending upon environmental conditions such as regional climate, topography, available building materials and degree of economic development. Timber frame structures are dominant in the western part while adobe or rubble stone masonry with flat earthern roof structures covers and extensive area in the eastern Turkey. The aseismic strengths should be examined by a careful analysis of structural damages due to past earthquakes. Here, we selected 7 earthquakes as is seen in Fig.7, considering both of seismic regions and structural types. Based on the damage distribution data for the 7 earthquakes, heavy damage percentages are examined in relation with seismic intensity and consequently aseismic strength of local type of structures is evaluated. Here we must recall that conventional seismic intensity scales are not sharp enough to distinguish delicate differences of earthquake phenomena,

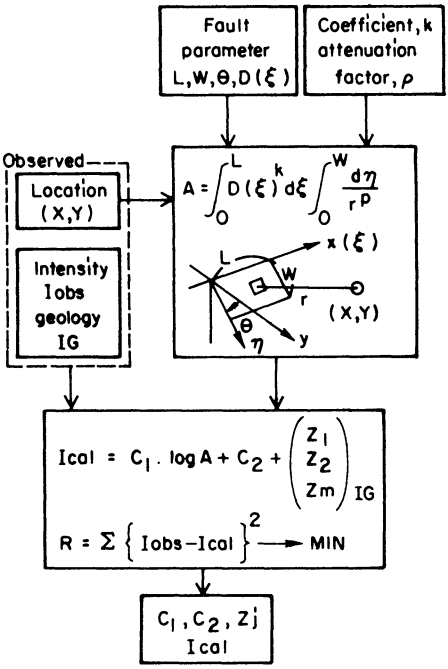

Figure 5. Flow diagram for derivation of advanced intensity equation.

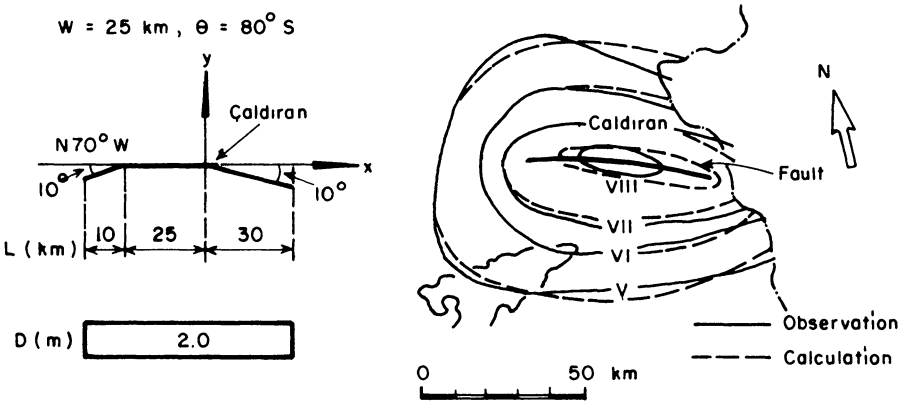

Figure 6. Comparison between observed and calculated isoseismals

since those are composed of a set of discrete and rough one digit values. In this paper two-digit and thus accurate intensities in villages were estimated tentatively by use of the advanced empirical attenuation equations derived in the manner stated above. In Fig.8 percentage of structural damage as a function of thus determined intensity is indicated. From this we find that the average strength of structures in Çaldıran is the weakest and those in Lice, Gediz and Adapazarı follow in this order. That is, dwellings made of rubble stone or adobe masonry in Çaldıran and Lice regions are extremely weak and brittle while those in Gediz and Adapazarı regions are of timber frame with higher strength and ductility.

Now let us consider which type of structures among A, B and C in MSK scale corresponds to each of local dwellings in Turkey. As for Adapazarı region the structures appear to be similar to type C (reinforced buildings, well-built wooden structures). In the same manner, it seems that those in Gediz region are between type A and B and those in Burdur region are type A (rural structures). Here is another question of what type A actually means. In Balkan countries where MSK scale was originally proposed, even adobe or field stone constructions generally have timber frame roofs (Georgescu, 1979) which are quite different from flat and earthern roofs in the eastern Turkey in view of aseismic performance. Therefore a possible adjustment will be to raise the intensities of Lice and Çaldıran cases by one unit, and to evaluate dwellings in the eastern Turkey as being little weaker than type A. Average aseismic strengths evaluated are 7.0 or a little weaker than structure A of MSK scale for the adobe or rubble stone masonry, 7.8 or comparable to structure B for brick masonry, 9.2 for reinforced concrete buildings and 9.5 for Bağdadi (high quality wooden) type. Thus derived vulnerability functions for typical structures in rural Turkey are summarized in Fig.9.

3.2. Relation of Structural Damage to Human Casualty

Now, we can show death ratios in relation with intensity for the 7 respective earthquakes as is illustrated in Fig.10. Let us compare this with Fig.8. Things characteristic here are that both heavy damage ratio and death ratio are highest for the eastern Turkey, higher at Gediz and smallest at Adapazarı of northwest. Maximum percentage of life loss at the Çaldıran earthquake reaches about 20% at intensity IV (MSK), which means that most of the people indoors were devastated. However, in case of the Adapazarı earthquake, the ratio was nearly 0% at the same intensity. Interesting here is that the Lice earthquake shows the trend similar to Çaldıran, while other events such as Varto, Bingöl and Gediz have often casualty occurrence before heavy damage percentage reach the maximum (100%). It is also true that death ratio is not proportional to heavy damage ratio. If we take a look at casualty rate functions in Fig.11, which is derived in the similar manner for structures, and compare with Fig.9, we understand the above difference in death ratio is mostly due to the structural types.

Incidentally in Turkey most of earthquake damage statistics do not classify heavy damage and collapse separately because it is difficult to

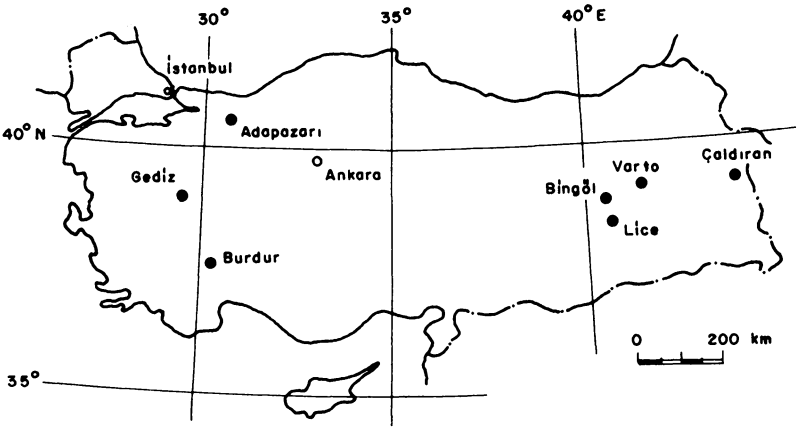

Figure 7. Location map of 7 selected earthquakes.

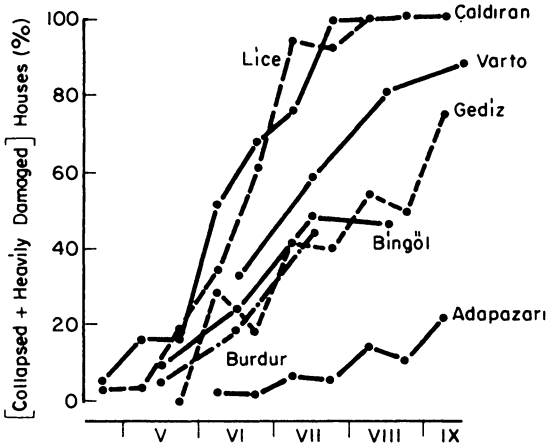

Figure 8. Percentages of heavily damaged houses vs. intensity.

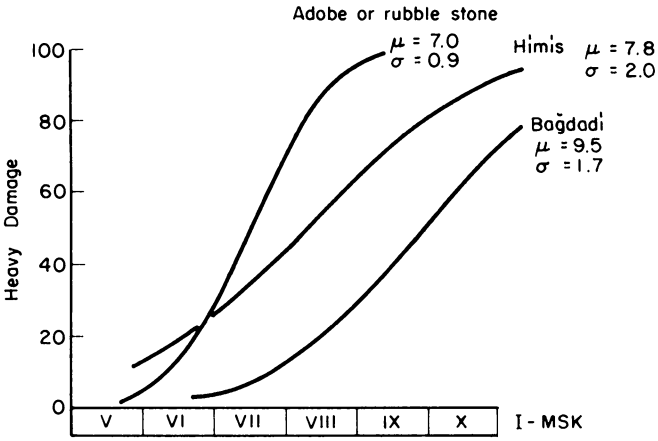

Figure 9. Derived vulnerability functions by structure types.

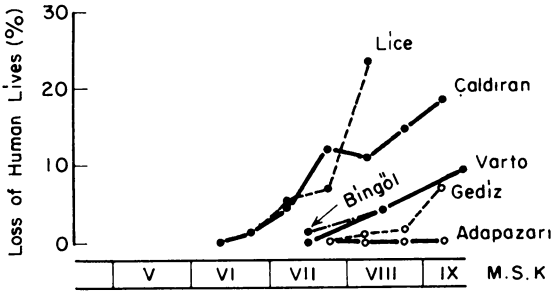

Figure 10. Percentages of loss of human lives vs. intensity.

distinguish the difference in the field in a short time. But as casualty rate functions by structure types Fig.11 tells us, phase of failure is obviously in progress from the damage degree which does not expose occupants to an danger to the degree which can be a direct threat to people. Here let us simply assume that "collapse" is such a damage grade as to kill every occupant's life. Probability of death (P_d) can be approximated in linear relation with probability of collapse (P_c) as $P_d = k\ P_c$, where k is the ratio of people who stay at home in an earthquake. Under the condition that all kinds of damage are mostly dependent upon seismic intensity, distribution functions of heavy damage and collapse are fixed for a certain village as Fig.12 illustrates. Accordingly a point(P_c,P_h) or (P_d, P_h) will proceed the unique locus as seismic intensity increases, where P_h is probability of heavy damage. The most extreme case is the locus A($P_h = P_c$) which means that I)structures are extremely brittle so that they proceed from heavy damage to collapse almost at once. Another extreme case is the locus B($P_d = 1.0 - P_h = 1.0$), which means whether II) structures are ductile and not very inhomogeneous or III) they are so homogeneous that heavy damage and collapse do not overlap. The moderate locus C, which is intermediate of A and B, is also probable when structural strength is inhomogeneous and distribution is partially overlapped. In this case there are some dwellings with moderate damage left, while some may be already collapsed causing casualty.

4. WAY TO SEISMIC RISK ASSESSMENT

4.1. Intensity Estimation

In order to practice seismic risk assessment of a certain region, a consideration on seismic hazard should first of all be ahead. That is to say, it is necessary to know the size and the location of an anticipated earthquake and then to estimate ground motion severity distribution over the concerned area properly. An analysis on macro tendency of isoseismals and a trial to generalize empirical intensity equation have confirmed that the ground motion severity can be estimated in terms of "seismic intensity" to a certain extent of reliability. This offers a sufficiently practical method of deterministic seismic hazard evaluation. Besides, an output as precise and minute as desired can be estimated by giving required amount of input information on the regional society and by choosing equations according to the purpose. Here, the relation between input information and output result of the evaluation will be briefly summarized.

Rough Estimation: Using a set of simple empirical equations on intensity area, isoseismal contours can be drawn for each discrete intensity. If only epicentral coordinates and magnitude of a future earthquake are known or estimated most simply, output by this estimation brings mere circular isoseismals. If the strike direction can be also informed, elliptical isoseismals with improved reliability are drawn by use of major and minor axis ratio. In Turkey the earthquake mechanism is highly in order from tectonic viewpoint in the most of seismically active regions. Therefore we will not encounter much difficulty when

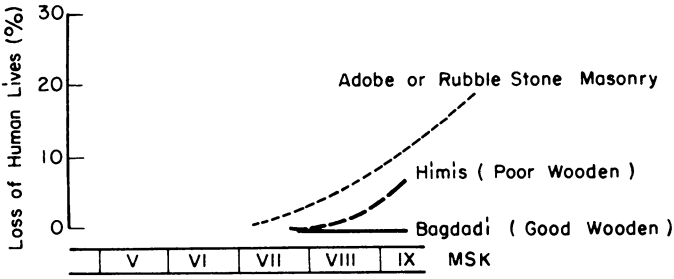

Figure 11. Derived casualty rate functions.

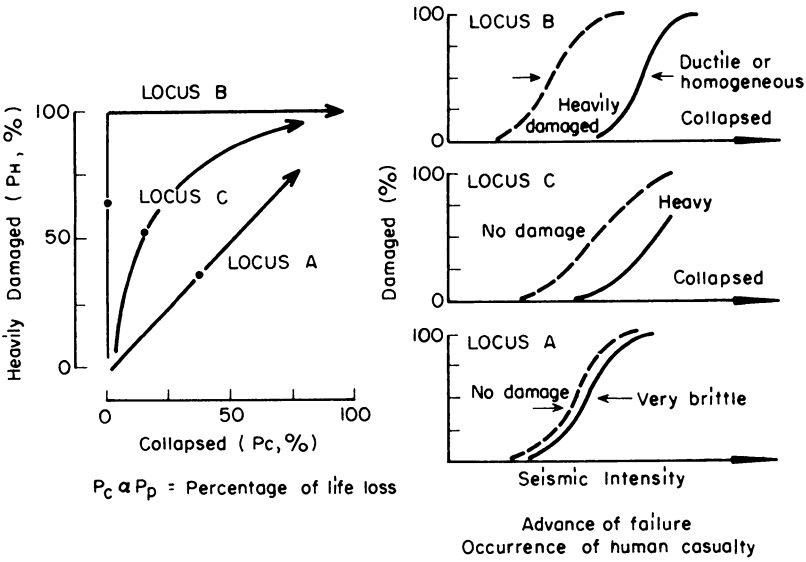

Figure 12. Schematic relation of casualty to structural damage.

characterizing an anticipated earthquake, at least in this level of seismic intensity estimation.

Precise estimation. This method uses the equation based on the finite area source model. Seismic intensity can be easily estimated as a continuous quantity at any given point. When epicentral coordinates, strike direction and magnitude M or fault length L are given, fault parameters are estimated from M by known scaling laws and by assuming initially a vertical fault. In Turkey relationships, $\log L = 0.95M-4.97$ and $\log D = 0.76M-5.27$, are well established(Tabban, 1979). For an estimation of fault width W, one can simply employ an well-known empirical equation, $W = 1/2L$, since deeper part on the fault plane than 1/2L does not contribute much to the intensity at any point on the ground. If it is possible to predict fault parameters independently based on regional tectonic conditions as well as data of past earthquakes, the result would more reflect regional characteristics. Further adding local conditions of geology and soils and evaluating intensity increment for each category of geology, would make more realistic distribution available.

4.2. Vulnerability and population data

Another important factor at an assessment is vulnerability of structures and danger of casualty as a function of, say, seismic intensity. Population and number of houses within a region considered are also important local information. Now, let us classify social information tentatively into three levels according to coarseness of local population data, structural types and their strength existent in the area. At coarse level, population density, aseismic strength of structures and risk to human life are known only as regional average. Since this level is suitable to grasp regional characteristics of disasters and to make comparison among different regions, application to national scale planning and decision making is conceivable. At medium level, population of towns and villages are known and regionally averaged percentages of structural types and their vulnerability functions are considered. This level would be effective for regional planning of disaster prevention especially in the extension of area where a single earthquake will cause some damage. At fine level ,further detailed data such as percentages of structural types within a city is prepared, so that application to local disaster prevention programs is practical. But, one must remind that in this case the data on spatial distribution of local geology is of importance as well.

4.3. Risk evaluation

It should be emphasized that the balance between hazard information and knowledge on social conditions is important. We should remind that,even if detailed local information is given precisely, this only does not make any risk assessment possible. Total damage lists are obtained by means of rough estimation, while detailed estimation produces lists containing division by various categories as well as various maps on structural and other damages.

The following are brief description for a standard assessment and

consequent output to be obtained. Quantities to be assessed are total number, H_k, of houses heavily damaged and total number of casualty, D_k, in a region. They are expressed as

$$H_k = \Sigma\ (A_i - A_{i+1})\ \frac{d_i}{h_i}\ \Sigma\ t_{jk}\ r_{ij}$$

$$D_k = \Sigma\ (A_i - A_{i+1})\ d_i\ \Sigma\ t_{jk} u_{ij}$$

with

A_i = area where intensity is equal to or greater than i and in Turkey it is obtained empirically in simple and precise ways.

$d_i = P_i/(A_i - A_{i+1})$ = average population density of i intensity zone

P_i = sum of population in i intensity zone

h_i = average size of household in i intensity zone

t_{ij} = percentage share of j-th category of structure

r_{ij} = structural damage ratio of j-th category of structure at intensity i

u_{ij} = casualty ratio of j-th category of structure at intensity i.

It is also possible to make microzoning within a town or a village. Estimations in any level will surely be improved, if the intensity after modification in regard with local site geology is provided and is combined with regional and/or local information.

Seismic risk assessment techniques as explained are expected to be useful to examine various earthquake disaster prevention measures such as land use regulations, building code and strengthening of existing structures. It is effective also for somewhat extended applications of I)pre-earthquake planning for post-earthquake rebuilding, II)urgent countermeasures in case of earthquake prediction, and III)rapid estimation of damage immediately after an earthquake etc.

5. CONCLUDING REMARKS

Despite of such success of using seismic intensity to engineering application it is yet obvious that there remain several problems to be solved. Some are as follows.

i) Precision and dense measurement of seismic severity. In the situation that there does not exist any sufficient strong motion observation network, it is common to employ a seismic intensity as the scale to measure the earthquake severity. We have used consistently the MSK intensity scale as the most important index in our study, and found its usefulness and convenience in describing and analysing earthquake disasters. But, because of its wide application capability it is inevitable that there arise several problems related to this scale. Althoug the MSK scale has the most refined line-up of descriptions among the seismic intensity scales in the present world, the field determination by use of this scale is not so distinctive nor reliable as expected from the definition itself. The fact that plural numbers of isoseismal maps for a single earthquake have not scarcely been drawn is mostly due to the difficulty in the field determination of seismic intensity. The most

important directions for determining seismic intensity are two;one is to develop a precision and dense determination technique and the other is to publish the unified result. Among several institutions dealing with earthquake problem in Turkey the Earthquake Research Institute in Ankara has a responsibility of the determination of seismic intensity and of publishing the formal isoseismals. It is a matter of course that a study for correlating seismic intensity with other physical quantities deduced from the instrumental records is very important. This is to be more emphasized together with further development in the installation of seismic strong motion observation network.

ii) Consideration from direct to indirect disasters Earthquake disasters in Turkey have a majority in the so-called primary (or direct) disasters such as damages to structural and other constructions and human casualty, and therefore the subsequent (or indirect) disasters seem less important as far as learned from the past experiences in Turkey. However no one can expect this favorite situation will continue forever, if taking account of a gradual increase in population and of rather abrupt urbanization in West Turkey from Ankara to Istanbul through which the North Anatolian fault as the generating sources of major earthquakes runs. Many of the important cities in industry and commerce locate near to and in parallel with the North Anatolian fault. When a large earthquake might attack one of those cities, not only direct but also indirect disasters will be serious: in case of major city of Ankara to Istanbul its impact effect upon social and economical circles would become enormous. It will become an essential subject to develop a soft engineering technique for assessing seismic risks including indirect disasters. In such a situation a variety of empirical vulnerability functions in relation with seismic intensity would become more the object of earthquake engineering attention.

REFERENCES

Chandra, U., J.G.G.McWhorter and A.A.Nowroozi(1979)'Attenuation of intensities in Iran', Bull.Seism.Soc.Amer., 69,237-250.

Ergin, E., U.Güçlü and Z.Uz (1967)'A catalogue of earthquakes for Turkey and surrounding area (11 AD to 1964 AD)', Technical Univ. of Istanbul.

Ergin, E., U.Güçlü and G.Aksay (1971)'A catalogue of earthquakes of Turkey and surrounding area'. ditto.

Evernden, J.F., R.R. Hibbard and J.F.Schneider (1973)'Interpretation of seismic intensity data', Bull.Seism.Soc.Amer., 63, 399-422.

Georgescu, E.S. and M.M.Crainicescu (1979)'Low-cost traditional dwellings for rural areas in Romania', Lecture Notes, 7th Regional Seminar on Earthquake Engr., Istanbul, Turkey.

Ohta, Y.(1980, editor)'Engineering seismological studies on the 24 November 1976 Çaldıran earthquake in Turkey', Hokkaido Univ., Sapporo, Japan.

Ohta, Y. (1983, editor)'A comprehensive study on earthquake disasters in Turkey in view of seismic risk reduction', Hokkaido Univ., Sapporo, Japan.

Tabban, A. (1979)' Deprem ve sorunları', Jeoloji Mühendisleri Odası, Ankara, Turkey (in Turkish).

Toppozada, T.R. (1975)'Earthquake magnitude as a function of intensity data in California and western Nevada', Bull.Seism.Soc.Amer., 65, 1223-1238.

UNESCO (1976)' Country monograph of Turkey on assessment and mitigation of earthquake risk', Ankara, Turkey.

Section 4

Hazard Assessment

PROBABILISTIC MODELS FOR ASSESSMENT OF STRONG GROUND MOTION

Carlos S. Oliveira
Structures Department, Laboratorio Nacional de Engenharia Civil
Av. do Brasil
1799 Lisboa Codex
Portugal

ABSTRACT. We present a method for idealizing strong ground motion using a complex stochastic process decomposed in two parts: the first, related to the phenomenon of occurrence, is represented by a Point process; the second, describing ground motion for a given occurrence, is represented by a Continuous Time-dependent process. The convolution of both processes leads to the probabilistic definition of ground motion.

In this review paper we present the three-dimensional space-time-size occurrence model based on geologic and tectonic environment and on historical and instrumental seismicity. In defining ground motion, we identify first and second-order-of-importance parameters and discuss their dependence on source mechanisms and travel path. We endeavor to incorporate all available information, microseismic as well as macroseismic. Finally, we briefly discuss the convolution of the Point process and the Continuous Time-dependent process and the influence of parameter uncertainties on final probability distributions.

1. INTRODUCTION

Defining strong ground motion, either in frequency or time domain, is of great importance in designing and checking safety of structures. The glory epoch of indiscriminately using the N-S component of the El Centro 1940 acceleration time-history as recorded has given place to more refined models that consider not only the hazard exposure to scale the amplitudes, but also the physical phenomena of generation and attenuation of seismic waves.

Even though we still use peak ground acceleration (PGA) as the major parameter of ground motion, most assessment studies also address complementary aspects such as frequency contents and duration.

Since the early 1950s, two approaches to ground motion representation have been used. The deterministic approach favors the use of recorded time-histories, and the stochastic approach uses "prior" probabilistic models. The advantage of the latter is that it can better represent the great variability in the characteristics of ground motion and the uncertainty of expected intensity levels during a given interval

M. O. Erdik and M. N. Toksöz (eds.), Strong Ground Motion Seismology, 405–460.
© 1987 by D. Reidel Publishing Company.

of time. Each of these two methods of handling individually the problem leads, however, to large uncertainties, the first because it does not allow randomness in the process and the second because it disregards the deterministic features of earthquake phenomenon.

Refinements in the theory of seismic wave propagation, especially in the near-field, together with an increase of strong motion data records, has made it possible to elaborate on models that incorporate what is known in the field of geophysics-seismology with what is unknown and so stochastically described. This mixed scheme will certainly lead to much more reasonable estimates of ground motion and significantly decrease the associated uncertainties.

We describe here the alternative methods of representing ground motion, and make use of all available data to reduce the uncertainty level on final estimates.

1.1. The Earthquake Process

The objective of assessing strong ground motion is to evaluate the motion expected within a given time period at a given site or group of sites. The motion can be represented either in the time domain by a set of time-series or in the frequency domain by a power spectral density function.

We consider that strong ground motion can be idealized by a complex stochastic process decomposed in two subprocesses (Figure 1). The first is a point process to describe the phenomenon of earthquake occurrence, and deals with location of focus, time and size of the earthquake. This three-dimensional (3-D) model makes use of all available information for the region under study: tectonic and geologic environment with emphasis on neotectonic structures; historical seismicity considering well-documented events of all kinds and epochs; and instrumental seismicity, which in most regions comprises two periods of development: the first (1900-1950) with sparse information both in time and space, and the second (1950-present) associated with the modern high-resolution network systems (since 1970).

The second subprocess, to describe ground motion at a site for a given event of known epicentral location and size, is a continuous time-dependent process that defines the sequence of amplitudes u(t) based on (1) the phenomena at the source - type of fault and its kinematic and dynamic properties, and (2) on the distance and azimuth of the site in reference - path and local geology. Other type of information such as sparse intensity evaluations or isoseismal maps of intensities from past epochs, strong ground motion records of the region or regions with similar tectonic and geophysical environment, and data from standard seismographic stations should also be considered.

The need for simple analytical models has modified the proposed methodology in the following terms. In a first task called the seismic hazard analysis one considers that the ground motion produced by a given earthquake at a site can be represented by a single parameter (y), generally the peak ground acceleration, and generates its probability distribution function when the randomness of occurrence is allowed. In Figure 2 we present the outcome of hazard analysis in the form of annual

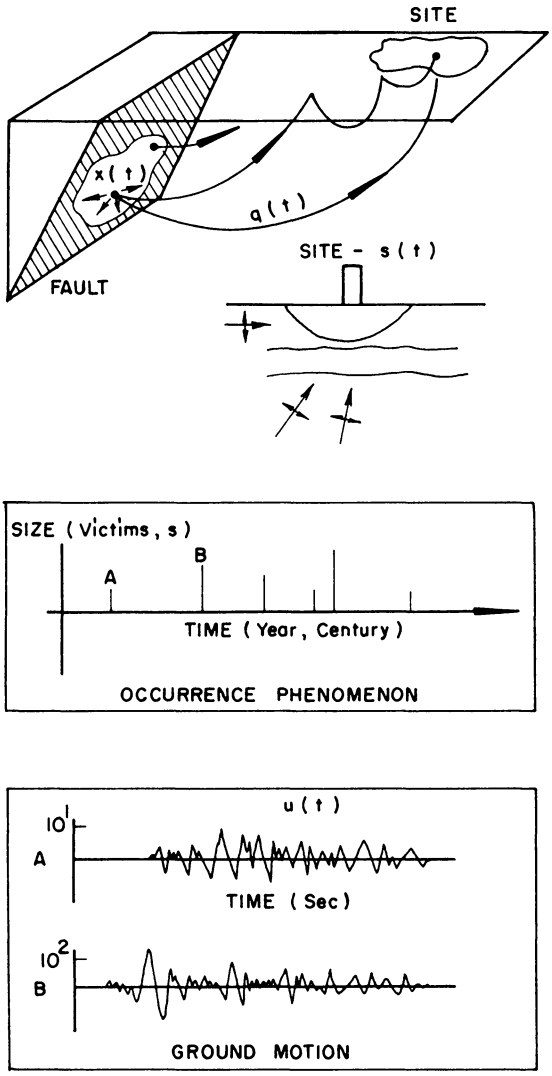

Figure 1 - Schematic representation of earthquake generation and propagation of seismic waves. Decomposition of the complex stochastic process for strong ground motion at a site into a point process and a continuous time-dependent process.

probability of exceedence of y (1-prob ($Y \leq y$)): the center curve corresponds to the "best estimate" and the other two to the upper and lower bounds. Figure 2 also shows the tranformation of current annual probabilities of exceedence into probability of exceedence during time intervals of 20, 50, 100 and 500 years.

In a second task, one generates the ground motion compatible with existing source-path-soil characteristics and scale the values to the results obtained in the hazard analysis.

The decision on the probability level to use in the hazard studies is complex and depends on final risks that the structure under analysis may undergo. The probabilities of exceedence currently used in the design of structures are approximately as follows:

- standard buildings - 2×10^{-2} to 10^{-3} per year
- important structures - 2×10^{-3} to 10^{-4} per year
- nuclear power plants - 10^{-4} to 10^{-6} per year.

These probabilities increase significantly when the period of interest extends to the life time of the structure (Figure 2).

1.2. Topics under Discussion.

After enumerating existing data in section 2, we discuss in section 3 the main parameters of the 3-D model for the occurrence of earthquakes, giving special emphasis to the importance of historical seismicity and its qualification. An analysis of the interrelationships between space-time and size of events is also discussed.

Section 4 characterizes the continuous time-dependent process. After describing the main features of recorded acceleration time histories, we study first-order-of-importance parameters such as peak ground acceleration (PGA), peak ground velocity (PGV) and peak ground displacement(PGD), response spectra, power spectra and duration. We then describe second order-of-importance parameters to be those related to the variability of ground motion both time and space. Discussion on how information on intensities can be used to derive attenuation curves and analyse the existence of anisothropy is also referenced.

In section 5 we analyse the complex stochastic process of strong ground motion, refering to the current hazard analysis methods, and discussing the influence of model uncertainties on final probability distribution functions. The section concludes with the presentation of simplified methods for generating the ground motion time-series compatible with the results of the complex model.

2. EXISTING DATA

The types of existing data needed to assess strong ground motion varies considerably from region to region as shown in the comparison between three countries in the Ibero-Mogrebi (Table I). The data can be organized according to the following categories.

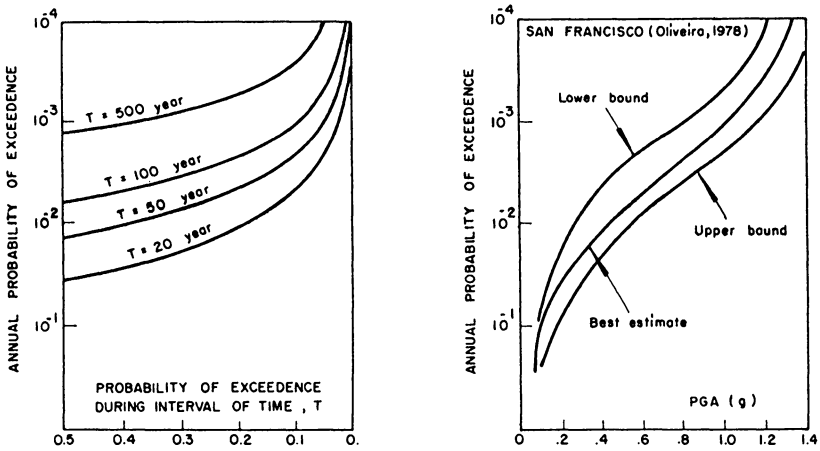

Figure 2 -
Output of seismic hazard analysis for a site: probability distribution function of ground motion parameter Y; "best estimate", and upper and lower bounds. Conversion of annual probabilities of exceedence into probability of exceedence during time intervals of 20, 50, 100, and 500

TABLE 1. SUMMARY OF DATA EXISTING IN THREE COUNTRIES OF THE IBERO-MOGREBI REGION.

	PORTUGAL	SPAIN (South)	ALGERIA (North)
Geological and Tectonic Setting.	Average knowledge on recent Quaternary geology for the entire country	Average knowledge on recent Quaternary for the entire country. Good investigation in few individual sites.	Poor knowledge on recent Quaternary for the entire country. Detailed investigation in the zone of Ech Cheliff with the identification of fault activity.
Historical seismicity.	Catalogue of events since 216 A.C under revision.	Catalogue of events since 800 A.C.; revised.	Catalogue of events since 1790
Large earthquakes.	Large MMI (IX-X) in earthquakes clustered in time and space.	Large MMI (IX-X) in singular spots. No repetition of events	Large MMI (X) in earthquakes clustered in time and space with high rate of occurrence.
Instrumental seismicity	Network with good coverage since 1975. Moderate knowledge of outer crust. Shallow earthquakes in land and in the sea. Low activity nowadays.	Network with good coverage since 1950. Moderate knowledge of outer crust. Shallow earthquakes Moderate activity.	Network with good coverage does not exist. No knowledge of outer crust. Suspicion of heterogeneous formations. Shallow earthquakes. Moderate activity.
Strong motion instrumentation	Poor in the near future. One record	Medium in the near future.	Good in the near future
Studies of individual earthquakes.	A good number of intensity evaluations (maps of isosseismals) - MMI.	Large number of intensity evaluations -MSK-	Very few evaluations -MMI-

2.1. Geological and Tectonic Data

Geological and tectonic information is viewed at two levels. The first is the tectonic evolution of plate configurations and the second is the identification of regional and local fault structures that are potential sources of events. While the first type informs us of long term slip rates, the second, observing the neotectonic evolution in recent Quarternary epochs, may quantity the seismic activity in recent geological times (the past 10000 years). Both are important, but the second one is much more critical as it informs us of an epoch much closer to our times. The other is important for evaluating stationarity patterns for time occurrences.

The search for active faults or systems of fault structures is very difficult, especially in areas for which we have little geological knowledge or where seismic slip rates are very small. One should expect this search to identify fault traces and access their rate of activity for the near future. This implies the complete characterization of fault properties such as length, width, dip, etc. (see section 4.4), the quantification of size of possible events and their respective recurrence rate.

2.2. Historical Seismicity

The catalogue of historical events in a region is based on descriptions of damage inflicted to people and property, and on general human behavior. This information is used to determine the following earthquake parameters:

- time of occurrence;
- epicentral location;
- maximum intensities in different locations.

Many factors, including the size of the earthquake, the epoch of occurrence, and the population in the region affect the accuracy of these evaluations (Muñoz et al.1982). The importance of the epoch is stressed by Van Gills (1983), who identifies five historical periods in Europe for which the record of earthquakes with MM intensity above a certain value is considered complete:

- up to 1300 - (Int > VIII)
- 1300 to 1600 - (Int > VII)
- 1600 to 1750 - (Int > VI)
- 1750 to 1900 - (Int > IV-V)
- 1900 to present - (Int > III-IV)

To establish a measure of accuracy of the information, we propose assigning quality factors to each event. First, the information is analysed at its original source, without any prior treatment. Translation from old into current language introduces errors which are always difficult to correct. Second, the information for each parameter under analysis is classified according to the number of existing

elements, extent of description, number of recurrent observations, and reliability of source. A factor of 1 (low), 2 (average) or 3 (high) is attributed to each parameter, according to the quality of information. The score obtained by the product of the factors, on a scale 1 to 81, constitutes the basis for an objective assignment of quality factors. It is obvious that the quality factor is very large in recent epochs when macroseismic data is used in conjunction with instrumental data.

The information is then interpreted at several levels, and finally transformed into catalogue parameters. For a detailed treatment see Mendes-Victor et al.(1985); an example of application of this system from an open-file tentative catalogue for Portugal is presented in Figure 3.

Historical seismicity, summarized as a catalogue, is very important in characterizing events of moderate to large intensity, precisely those that are most critical to our studies. The introduction of quality factors permits the use of all historical data, even those that, due to great uncertainties, have been disregarded in the past. The quality factor applies also to drafting isoseismal maps, a major source of information for studying attenuation of ground motion with distance.

2.3. Instrumental Seismicity

Instrumental seismicity was initiated with the development of seismographic networks. Use of data first generated by these networks around the turn of the century yields good determination of occurrence time and long period-spectra but poor estimations of epicentral locations (sometimes uncertainties of the order of several tens of kms). A second period beginning between 1950 and 1970 is marked by the installation of many short-period instruments, which allowed the detection of smaller events and greater accuracy in focal mechanism determinations. Local networks and a better knowledge of the crustal properties permit the determination of focal location with high resolution. This important evolution of networks has enabled good correlation between seismic activity and the presence of fault structures. The innovation is taking place all over the world and is of capital importance for the definition of seismic source zones, not only for obtaining their geometry, but also to help in defining the rate of occurrence of earthquake events. However, extreme caution should be exercised when extrapolating from small-magnitude event and short periods of observation to large magnitude- events and long time periods. As we will discuss in section 3.2, stationarity and linearity are generally not present in earthquake processes.

2.4. Strong Motion Seismicity

The increasingly widespread use of strong motion instruments since 1970 and earthquake ground motion data gathered under various tectonic and geological conditions (faults, soils, source-site situations) has yielded the most useful information on the characteristics of the time-history records. Unfortunately, many seismic regions still have

	DATE	HOUR	LAT	LONG	MAG	MMI	LOCAL
31	1504-04-05(a)	00-00(d)	38.7	05.6(b)	7.0(c)	8.5(b)	Carmona
32	1512-01-28(a)	00-00(d)	38.7	09.2(b)	6.3(c)	8.0(a)	Lisboa
33	1522-09-22(a)	00-00(d)	43.4	05.8(b)	5.0(c)	6.0(b)	Almaria
34	1528-03-12(a)	08-30(b)	39.7	08.9(c)	5.0(c)	6.0(c)	Alcobaca
35	1531-01-26(a)	01-15(b)	38.9	09.0(a)	7.0(a)	8.5(a)I	V.F.Xira
36	1568-04-17(a)	00-00(d)	38.5	08.0(c)	5.0(c)	6.0(c)	Evora
37	1575-06-07(a)	16-30(b)	38.7	09.2(b)	4.3(c)	5.0(b)	Lisboa
38	1587-11-00(b)	00-00(d)	37.1	08.0(b)	6.0(c)	7.5(b)	Loule
39	1597-07-22(d)	23-00(a)	38.7	09.2(b)	5.7(c)	7.0(b)	Lisboa
40	1598-07-28(a)	17-30(b)	38.7	09.2(b)	4.3(c)	5.0(a)	Lisboa

a) correct
b) ± one day
c) ± one month
d) occurence doubtfull

a) correct
b) ± one hour
c) ± quarter day
d) no informotion

a) ± 0.5 MMI
b) ± 1.0 MMI
c) > ± 1.5 to 2.0 MMI

$$\varepsilon_{earthquake} = f(\varepsilon_{date} * \varepsilon_1 * \varepsilon_2)$$

ε : error function

$\varepsilon_{earthquake}$: error on earthquake parameter characterization (location of focus, size, perceptibility pattern)

ε_{date} : error on date of occurrence

ε_1 : error on intensity scale interpretation from historical descriptions

ε_2 : error on interpolation for establishment of isos-seismal curves

Figure 3. Earthquake catalogue having quality factors. Propagation of errors in the assessment of earthquake parameters.

poor or no coverage for strong motion and, consequently, other sources of information are required:

- Earthquake records from regions with similar tectonic environments can be used. However, this requires a great knowledge of the kinematics and dynamics of the seismic sources in both regions, which implies expertise rarely available.
- Simulation models based on either simple models of stochastic processes or kinematic models of the sources that consider wave propagation are needed. These models must be calibrated in regions where records are available.
- Analytical and experimental models of simple structures subjected in the past to earthquakes must be developed to determine the most important characteristics of ground motion. Some work has succeeded recently in predicting peak ground parameters and frequency content from observations of rocking of tombstones (Yim et al.1980) and ringing church bells (Oliveira et al.1983).

The study of strong ground motion has been greatly enhanced with the recent deployment of dense arrays of instruments (Bolt et al.1983). These arrays permit the study of variability of ground motion over short distances and of coherence of seismic waves in space. They also permit us to identify other important features of seismic propagation, such as the influence of source path and soil on wave characteristics.

The distinction between seismographic instrumentation and strong motion instrumentation will disappear in the future as the dynamic range of seismographic instruments increases until they can record both teleseismic and nearby earthquake motions. These improvements would show up in more accuracy strong motion records, especially in displacement estimates.

3. OCCURRENCE MODELS

Earthquake generation of an event i can be represented by stochastic processes in a 3-dimensional space-time-size continuum (L_i, T_i, M_i), where L_i is the location of focus, which itself is a 3-component vector characterized by latitude, longitude and depth, T_i is the time of occurrence, and M_i is the Richter or local magnitude. For small epicentral distances, the characterization of the earthquake size requires a vector quantity representing the mechanism of generation at the source and the radiation pattern, adding at least one more dimension to the problem.

The complete statistical analysis of the earthquake process must consider the probability distribution (and correlations) of these three parameters. This involves handling a 3-D continuum which generally constitutes a very complex model due to the scarcity of available data. First we will analyse each one of the processes separately, then groups of two, and finally all three together.

3.1. Location of Earthquakes

The first task is to characterize the space (volume, area, line, or point) where earthquakes have taken place in the past and define the source-zones where they will occur in the future.

It is well accepted that earthquakes are related to the energy release in the contact of the two surfaces defining the fault plane. However, to define such geographic structures, it is necessary that all elements discussed in previous sections converge to the same solution. This is not the general case: geological and tectonic evidence very often does not agree with the historical and instrumental seismicity. The same can be said of historical and instrumental seismicity. In fact, as each scans different periods of time and a different levels of accuracy, it is not surprising that the earthquake process might be different from period to period. Also, in many regions with very low rates of earthquake occurrence, tectonic rupture mechanisms are much more difficult to predict.

The development of dense seismographic networks in recent years has resulted in great progress in defining structural alignments, both in plan view and in depth. We can now accuratly describe the active seismic zones in a few regions of the world.

In many regions, however, historical seismicity is probably the only available information for identifying earthquake source-zones. In these cases, earthquake source-zones must be diffuse to overcome not only all uncertainties of epicentral locations, but also the subjective nature of historical information. When more precise information is available, historical seismicity should be given the weight it deserves; but it must always be taken as a standard value for comparison. Obtaining tectonic information, as mentioned before, is generally difficult and requires great expertise. This is excellent information to guide revisions of epicentral locations of events not previously correlated with any given structure, or can serve as a constraint in selecting possible computer solutions.

Convergence of all available information will definitely decrease uncertainties related in this topic. Usually, at the very end of this task we are confronted with various alternative hypotheses for earthquake source-zones. If information is vague, the source-zones should have uniform distribution of epicenters and we expect large associated uncertainties. When local tectonics and historical seismicity studies are available, the zones are much more delimited and there is less uncertainty. Figure 4 shows an example of the evolution of earthquake source-zones after refined tectonic studies were performed.

Different experts may propose quite different solutions using the same data. The alternative solutions should be analysed, conveniently weighted, and used to carry out the other tasks. This point is very important as the selection of source-zones will most probably influence the final hazard results.

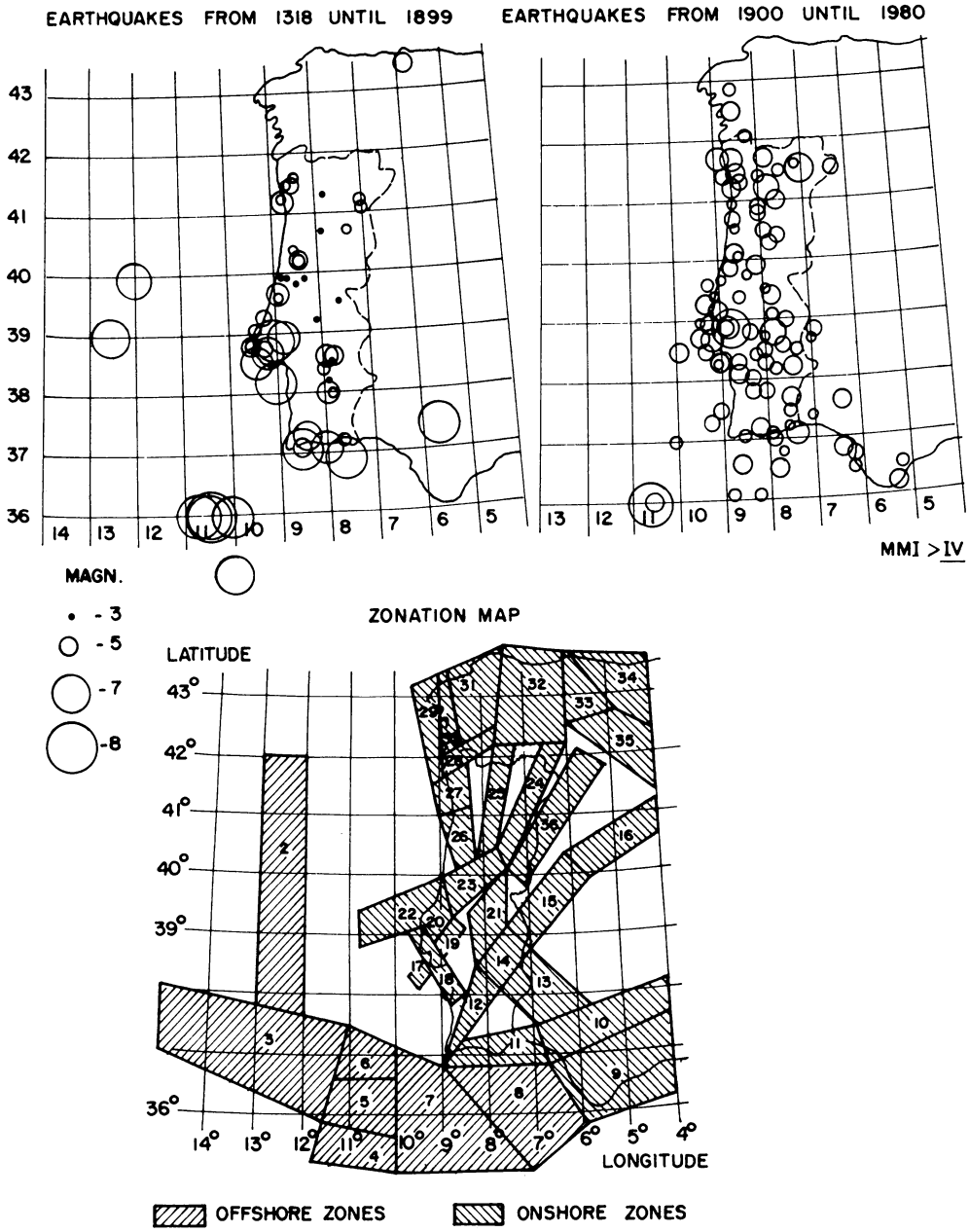

Figure 4. Improvements in epicentral locations based on macroseismic information and updating earthquake source-zones in a region.

With the continuous updating of earthquake data, the source-zones should be revised regularly. We expect that these updating studies will not lead to completely different results, but instead will decrease the margins of uncertainty on final estimates (Figure 2). These are, of course, a function of the total investment made.

3.2. Time of Occurrence

The second task is to characterize rates of occurrence of events of source-zones defined in the previous section.

The most widely used model of large-event occurrence is the Poisson model (Cornell 1971). However, we strongly recommend validation of this assumption in the face of historical and geological data, as well as the check of time dependence of small to mid-size events. Analysing the interarrival times of historical earthquakes IMM>IV in Northern California and in Portugal, we found in both cases that the empirical distribution does not fit the negative exponential distribution (corresponding to the Poisson model), demonstrating the existence of a much larger number of small intervals than expected (Figure 5a). Also, by plotting interarrival time IT(i) versus the previous one IT(i-1) (Costa et al.1985) one can see that data in Portugal shows a time dependence for small events (Figure 5b). The last representation strongly suggests studying the stationarity of the time process as it allows the determination of conditional probabilities. This dependence is mostly related to the mechanism of energy dissipation and readjustment of crustal stresses for small events.

Estimating mean rate of occurrence of large events in a given source-zone, using either historical or geological data, should yield consistent values. This consistency has been observed in a few areas such as California and Algeria, where detailed geological prospection has identified the occurrence of several large events within a certain time horizon.

If the characterization of time of occurrences has to be based only on poor-quality historical data and short periods of time (less than 100 years), as in many regions, large uncertainties in final hazard estimates are expected.

3.3. Magnitude

The distribution of magnitude for an entire region or for a given earthquake source-zone (third task) is generally an exponential negative form with truncations both at the lower magnitude level, M_o, and at the upper level, M_1. This distribution is compatible with the so-called Richter linear law relating the logarithm of the number of events above a certain magnitude threshold to the magnitude.

Quality of data is a crucial issue. In analysing the earthquake catalogue for Portugal since the year 250 B.C., we found the unexpected results presented in Figure 6a: the time window 1500-1755 shows higher occurrence frequencies in the class M<4.5 than any other selected time window. One of the explanations for this anomaly is the deficient measure of magnitude for that particular period of time. The

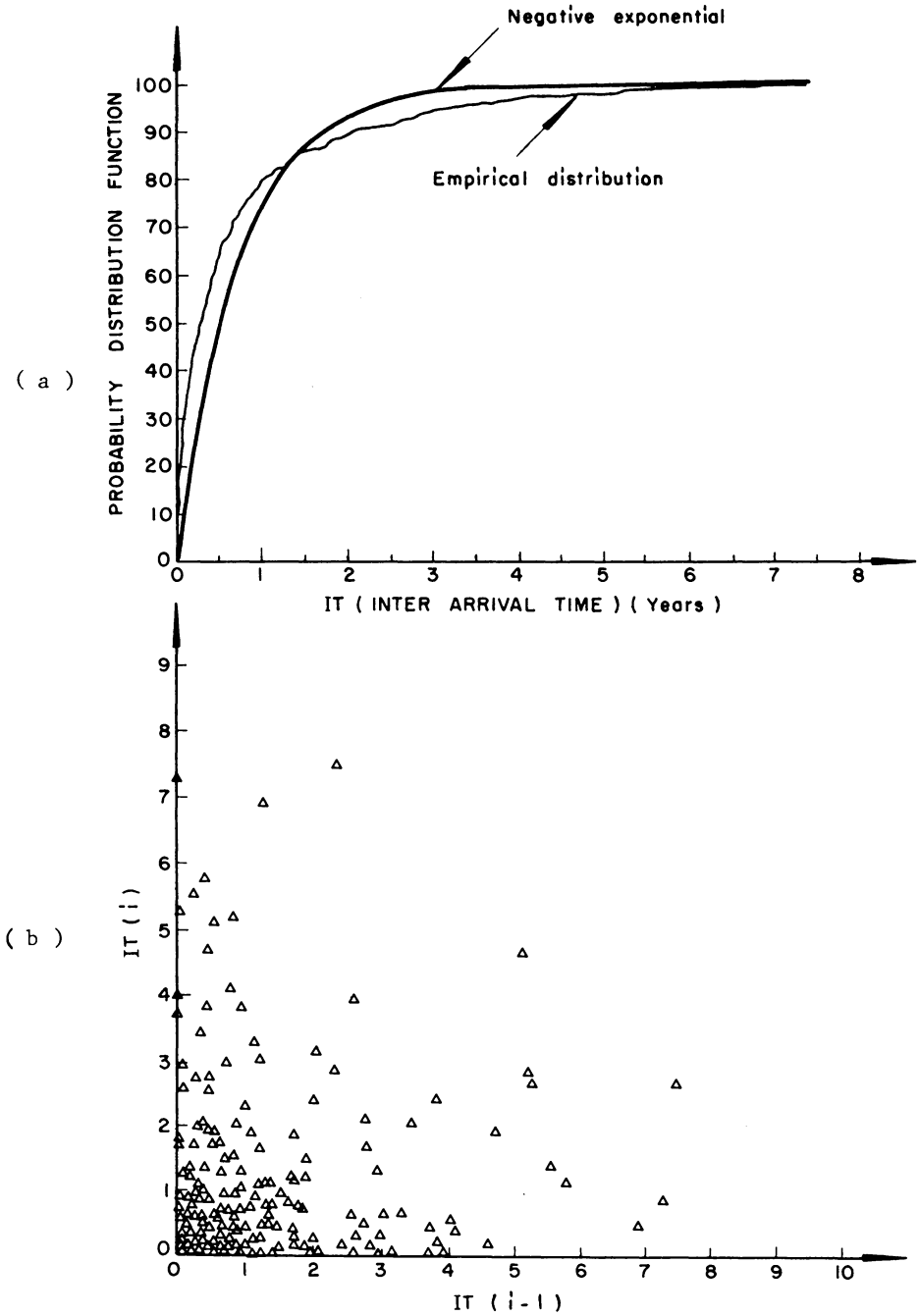

Figure 5 - Statistical analysis of interarrival times between consecutive events: a) probability distribution function; b) IT(i) vs IT(i-1).

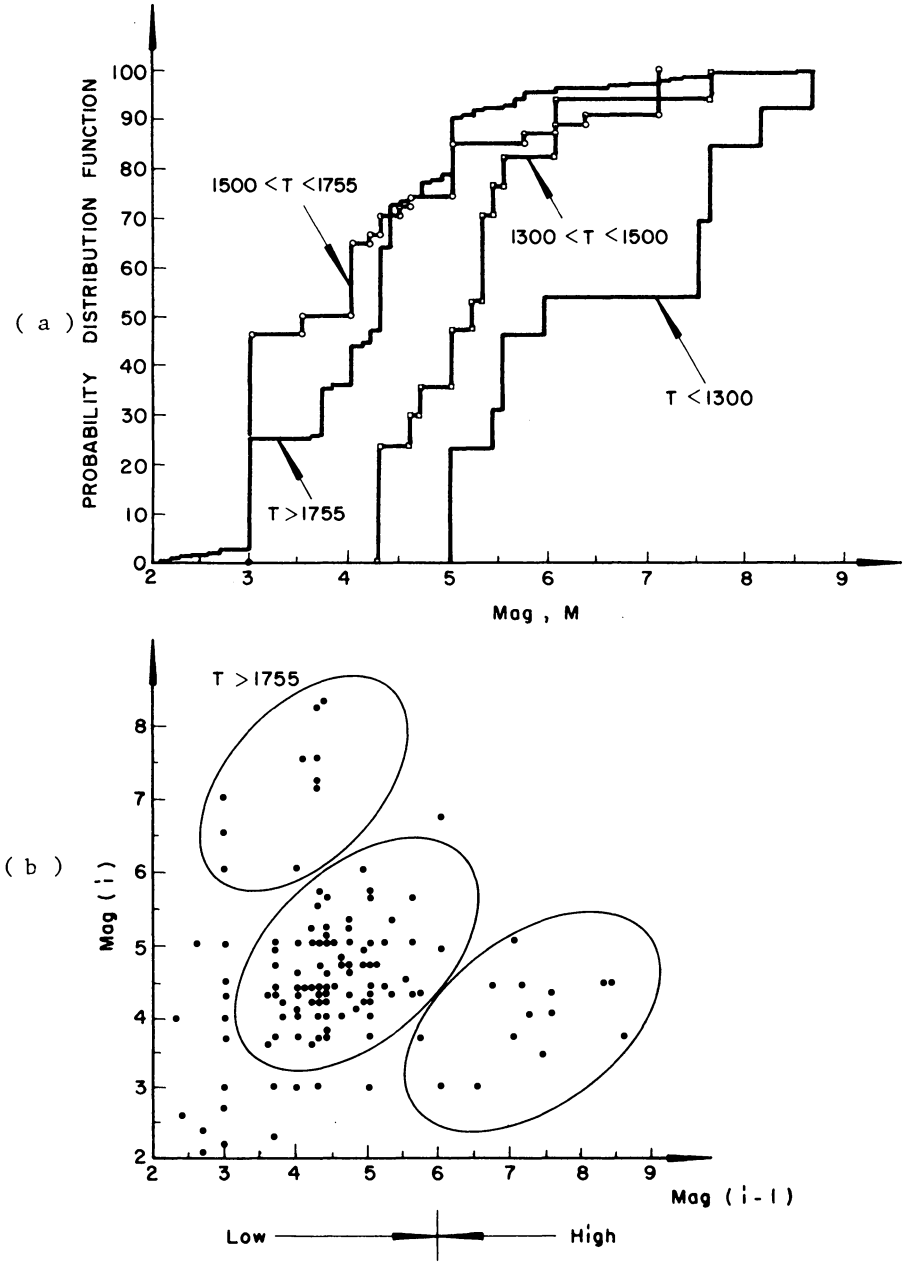

Figure 6 - Statistical analysis of magnitudes: a) probability distribution function; b) Mag(i) vs Mag(i-1).

small-to-moderate seismic events are very difficult to classify from historical descriptions. In the present case, a few events in this period corresponding to magnitudes 4<M<6 may have been misplaced in the class 3<M<4.

Lower and upper-magnitude values are influenced by incomplete of information and the physics of earthquake generation at the source, respectively. We have mentioned the role of data quality in establishing M_o; assessment of M_1 is very complex and depends on the method of analysis. Using either the concept of fault length from tectonic consideration (Slemmons, 1977) or a function of the extreme value statistics of the combined historical plus instrumental data (Oliveira et al.1984), the degree of uncertainty on M_1 should always be objectively quantified.

We used the plot M(i) versus M(i-1) to check the magnitude dependence of sucessive events (Figure 6b) and it became clear that events could be grouped into two categories, the high M>6 and the low M<6, with significant interdependences as measured by the following transition matrix:

$$\begin{array}{c} \\ L \\ H \end{array} \begin{array}{c} \begin{array}{cc} L & H \end{array} \\ \begin{bmatrix} 95.9\% & 4.1\% \\ 92.9\% & 7.1\% \end{bmatrix} \end{array} \qquad \begin{array}{l} L \text{ - Low event category} \\ H \text{ - High event category} \end{array}$$

These results support the assertion that the earthquake process can be represented by the superposition of two individual processes, each having a different mechanism of generation. Figure 7 presents the magnitude distributions for the two above-mentioned processes.

3.4. Correlations Among Occurrence Processes

The phenomenon of occurrence cannot, in fact, be separated into its several components as these components are indeed correlated with each other. We can use two techniques to visualize and quantify these dependences: 1) plot IT(I) vs Mag(i) to determine the conditional probabilities; and 2) identify classes within each process and establish transition matrices. The major problem with this analysis is the spatial dependence, which itself is a two-parameter process. In order to simplify the treatment, one must reduce the dimension of the problem. The easiest way is to consider the concept of source-zone, by combining the latitude, longitude, and depth into a single scalar quantity. We use this technique to analyse the data in Portugal: a strong dependence between space and size was observed but no clear dependence between space and size or time and space was found (Costa et al.1985).

Instead of studying dependences between pairs of processes we can determine the principal components of the entire 4-D process, time-lat-long-magnit, which informs on main components of the process and how they relate to each other. The following results were obtained:

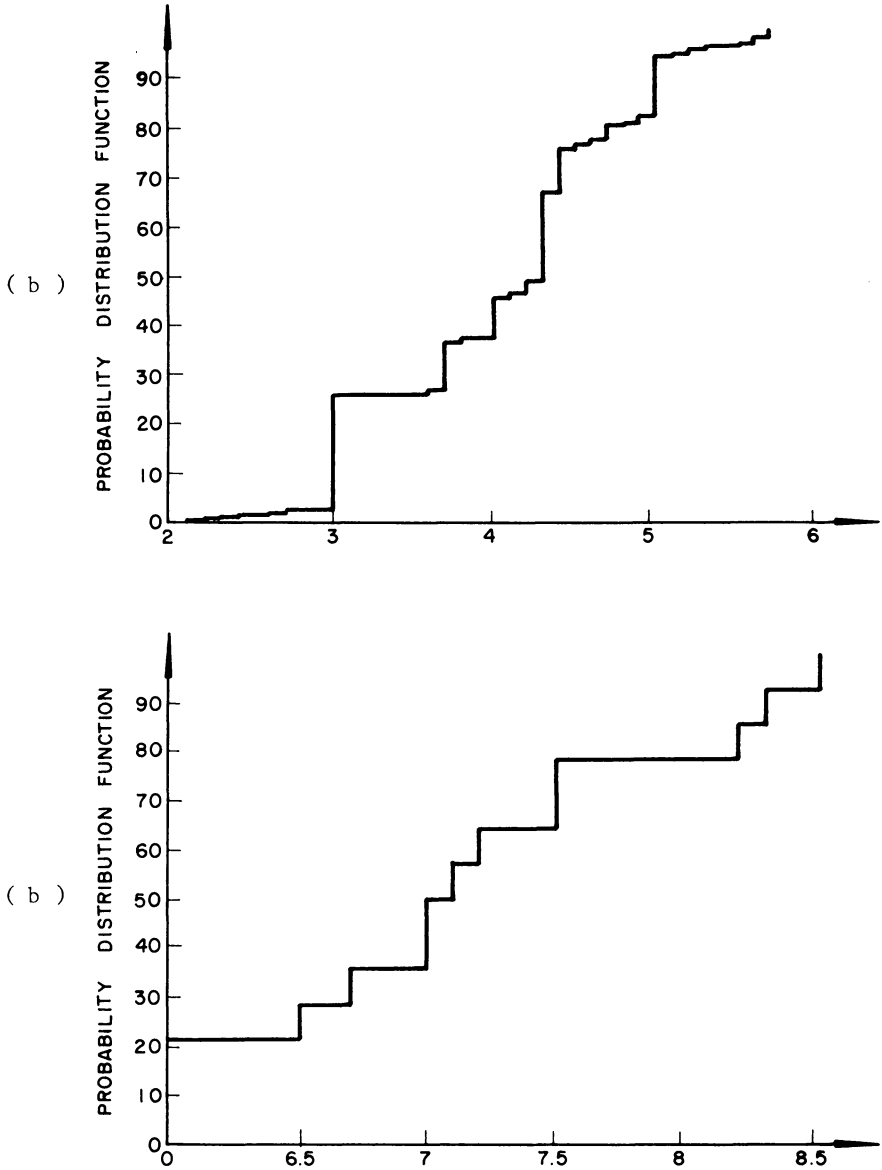

Figure 7 - Probability distribution function of magnitudes for separate processes: a) M<6; b) M>6.

Eigen value	Eigen vector			
	IT	Mag	Long	Lat
1.375	0.534	1.000	0.986	-0.849
1.024	1.000	-0.507	-0.456	-0.498
0.852	0.714	-0.002	0.476	1.000
0.748	0.228	1.000	-0.905	0.270

This technique showed consistency with the two-dimensional analysis presented in section 3.3.

The concepts briefly presented in the previous sections constitute a first step towards the global characterization of the stochastic process of occurrences. When implemented it can be applied as a major tool to be used in 1) the simulation of other series of events exhibiting similar properties to the ones observed in the existing historical record, and/or 2) to the refinement of analytical models.

4. STRONG GROUND MOTION

Dynamic analysis of structures requires the specification of earthquake loads in time or/and frequency domain, or at least the knowledge of some parameters characterizing those records, such as peak ground acceleration (PGA), the peak ground velocity (PGV), the peak ground displacement (PGD), and duration. Studies of ground motion records produced at different sites during different earthquakes have shown statistical correlations among those peak values, and peak values and earthquake magnitude and site-source distances. These correlations, however, present very large scatter.

As the record from any strong motion instrument is the final product of a complex mechanism of generation and propagation, the signal has been treated as a time-dependent stochastic process obtained by the superposition of random arrivals of different types of waves generated at the source. The first representations considered the process as Gaussian stationary and ergotic. Gathering new earthquake records, however, permitted a continuing improvement of the models by successively introducing the concepts of stationarity, non-stationarity, and envelope time-dependent processes.

Earthquake records present some common deterministic features that reflect the mechanism at the source and the influence of the travel path. They correspond to different phase arrivals and are not so easily identified as in teleseismic recordings. Nevertheless, in many strong motion records, it is possible to refer certain wave trains to the arrivals of the P and S pulses. Recent analytical studies on simulation of ground motion close to fault zones have shown the possibility of predicting the motion with great success in the spectral region up to 1 or 2 Hz. Many other features, still present in all accelerograms, especially in the higher frequency range cannot be associated with wave arrivals or any other vibratory properties related to the propagation phenomenon and so far should be considered as random noise with certain properties. They result essentially from the combination of multiple

perturbation of the simple phenomenon, site reverberation, transient vibrations, etc., and should be superimposed on the basic skeleton of the main wave phase arrivals.

Selection of strong ground motion at sites in the proximity of fault traces has been a very difficult problem, due to the complexity of the Earth phenomenon and the lack of reliable near-field data. Dispersion in the empirical attenuation curves is very large and consequently design criteria based on upper values may lead to unreasonably large estimates. This is particularly relevant in the assessment of ground motion exhibiting very low probability of exceedence as it is the case of nuclear power plants, dams, and long bridges that might be located near active faults.

We will first describe the ground motion and its main properties, then look briefly into the elastodynamics of generation and propagation of seismic waves, and finally discuss the correlation between ground motion parameters and characteristics of the source and path. We will generally emphasize engineering applications.

4.1. Descriptions of Earthquake Ground Motion

The motion generated by the passage of seismic waves at a site (Figure 8a) can be decomposed into 6 components, three in translations, u_x, u_y, u_z, and three rotations Θ_x, Θ_y, Θ_z. The axes of reference are x, y, and z, and u may represent either acceleration, velocity or displacement. Both time u(t) and frequency $U(\omega)$ representations (Figure 8b) are complete descriptions of the motion at a site. Since the wave phenomenon is also a function of space, we need other relationship to define dependence among the of motion recorded at any number of sites, 1, 2,...,i,...j, close to one another.

Newmark et al.(1971) grouped time descriptions of ground motion into four categories (Figure 9):

- 1) The impulse type, recorded nearby the epicenter, is of short duration (5-10 sec), and has high frequency content and a peak acceleration of much large amplitude than all the others.
- 2) The more stable record, with duration 15 to 30 sec, originated from moderate magnitude, 30 to 50 km epicentral-distance events, shows a constant property description between instants t_1 and t_2, an initial zone with increasing amplitudes, and decreasing frequency content, and a final zone exhibiting attenuation of amplitudes and frequency content dislocated even further towards the lower frequencies. In phenomenological terms , the first part of the record corresponds to the arrival of the P-wave train, the second zone to the S-waves and sometimes also the surface waves, and the third part to the coda and represents the natural damping of the main wave phases.
- 3) Very long duration records, greater than 30 sec, exhibit a remarkably consistent character throughout the entire record, and correspond to very large epicentral distances and moderate to large-magnitude events. Multiple shocks may also produce this type of ground motion. Amplitude tends to stay fairly constant and frequency content peaks at the lower side of the spectrum.

N-S COMPONENT

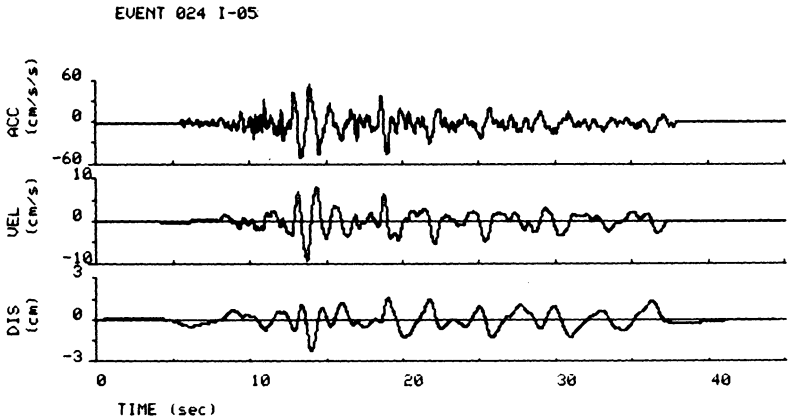

VERTICAL COMPONENT

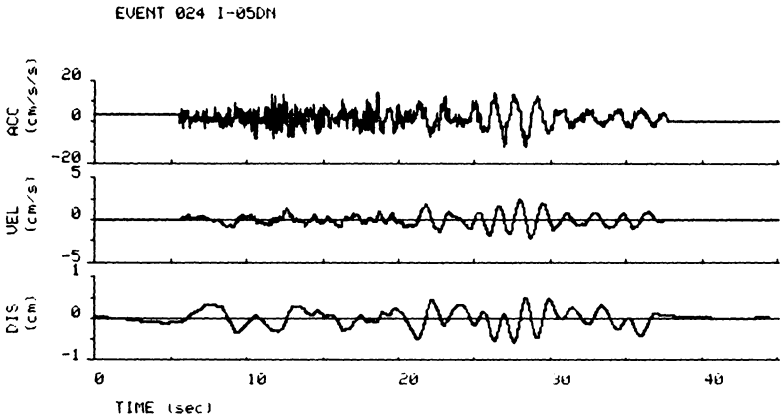

Figure 8(a)

N-S COMPONENT

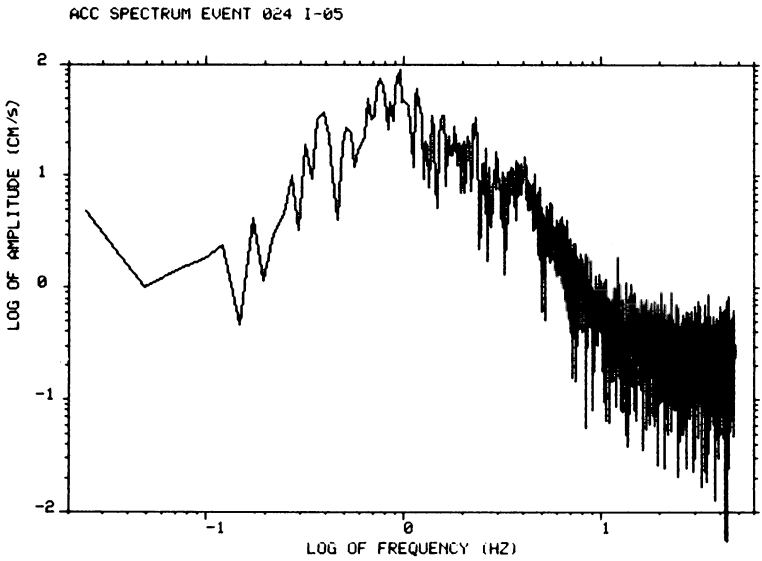

(b)

VERTICAL COMPONENT

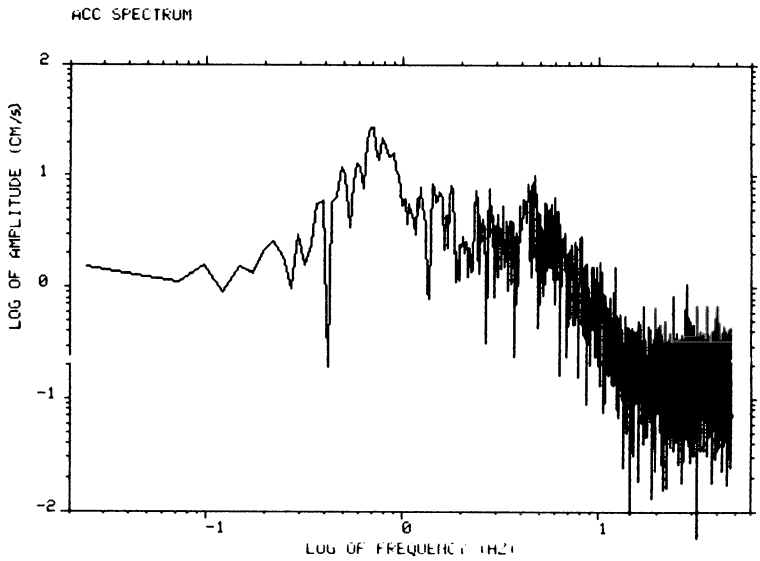

Figure 8. Ground motion at a site: a)time-histories of acceleration, velocity, and displacement; b)Fourier amplitude spectrum. Comparison between horizontal and vertical component (Event # 24 recorded at SMART-1 Array, Oliveira et al., 1985).

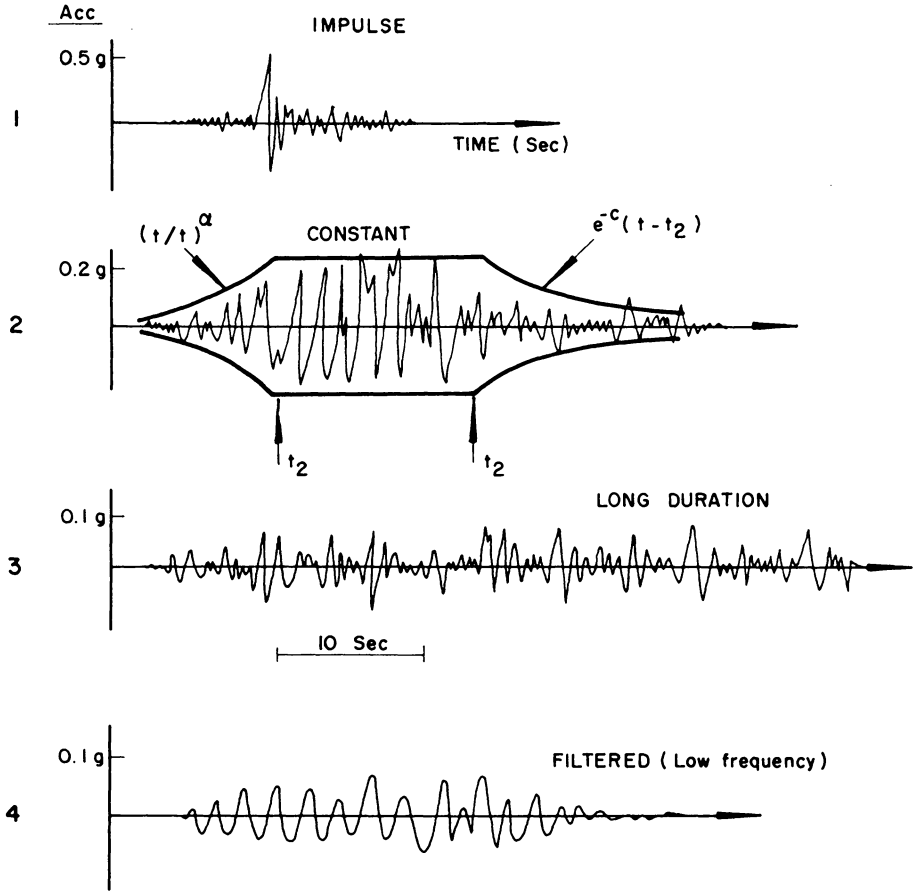

Figure 9 - Typical envelope shapes (categories) for ground motion records, after Newmark and Rosenblueth (1971).

• 4) Motion recorded at very peculiar soil or topographical conditions, usually in a valley with thick layers of soft soils. These records are greatly influenced by the dynamic properties of the valley and tend to exhibit predominance of some discrete frequencies.

Recent studies of records of strong motion arrays (Oliveira et al.1985) show that this classification system does not reflect other possible envelope patterns such as the existence of more than one portion of the record exhibiting large-amplitude wave trains. Further studies should be pursued to generalize the ground motion wave form concept.

Frequency representations are essentially based on the Fast Fourier Transform algorithm (FFT), which computes the discrete numerical analog of Fourier transform of time signal $\ddot{u}(t)$:

$$U(i\omega) = 1/2\pi \int_{-\infty}^{\infty} \ddot{u}(t) \exp(-i\omega t)\, dt \ . \qquad (1)$$

The complex quantity $U(i\omega)$ is usually presented in the amplitude and phase spectra (Figure 9), the first indicating the differences among the amplitude of sinusoidal components, and the second the phases among themselves. The phase spectrum is generally ignored in practical applications, but is very important for studying variability of ground motion and may play an important role in simulation of earthquake motion.

A related frequency representation is the power spectral density function, (S_o) defined as (Figure 10)

$$S_o(\omega) = \lim_{T\to\infty} \left[\int_{-T/2}^{T/2} \ddot{u}(t)\, e^{-i\omega t} \cdot \int_{-T/2}^{T/2} \ddot{u}(t)\, e^{+i\omega t}\, dt \right] / \ 2\pi T \ . \qquad (2)$$

S_o is a measure of the distribution of the amplitudes throughout the frequency domain, and is obviously related to the Fourier amplitude spectrum. S_o has been found to be very important in studying response of structures.

One should be aware of the limitations, both on theoretical and numerical grounds, of applicability of Eqs. 1 and 2 (e.i. stationarity, existence of limit), and to the errors introduced by the algorithm (Kanasewich 1981). In some cases, other techniques of analysis have produced better results than the FFT. That is the case of the entropy methods (Barrodale et al.1980) very useful tools to analyse short signals.

The concept of response spectrum (RS), first introduced by Housner, $S_v(\omega,\xi)$ is another frequency representation of ground motion that has been used with great success. $S_v(\omega,\xi)$ is defined as the maximum response of a single degree of freedom system having unit mass, frequency ω_o, and damping ratio ξ, when subjected to a given ground motion u(t) (Figure 10),

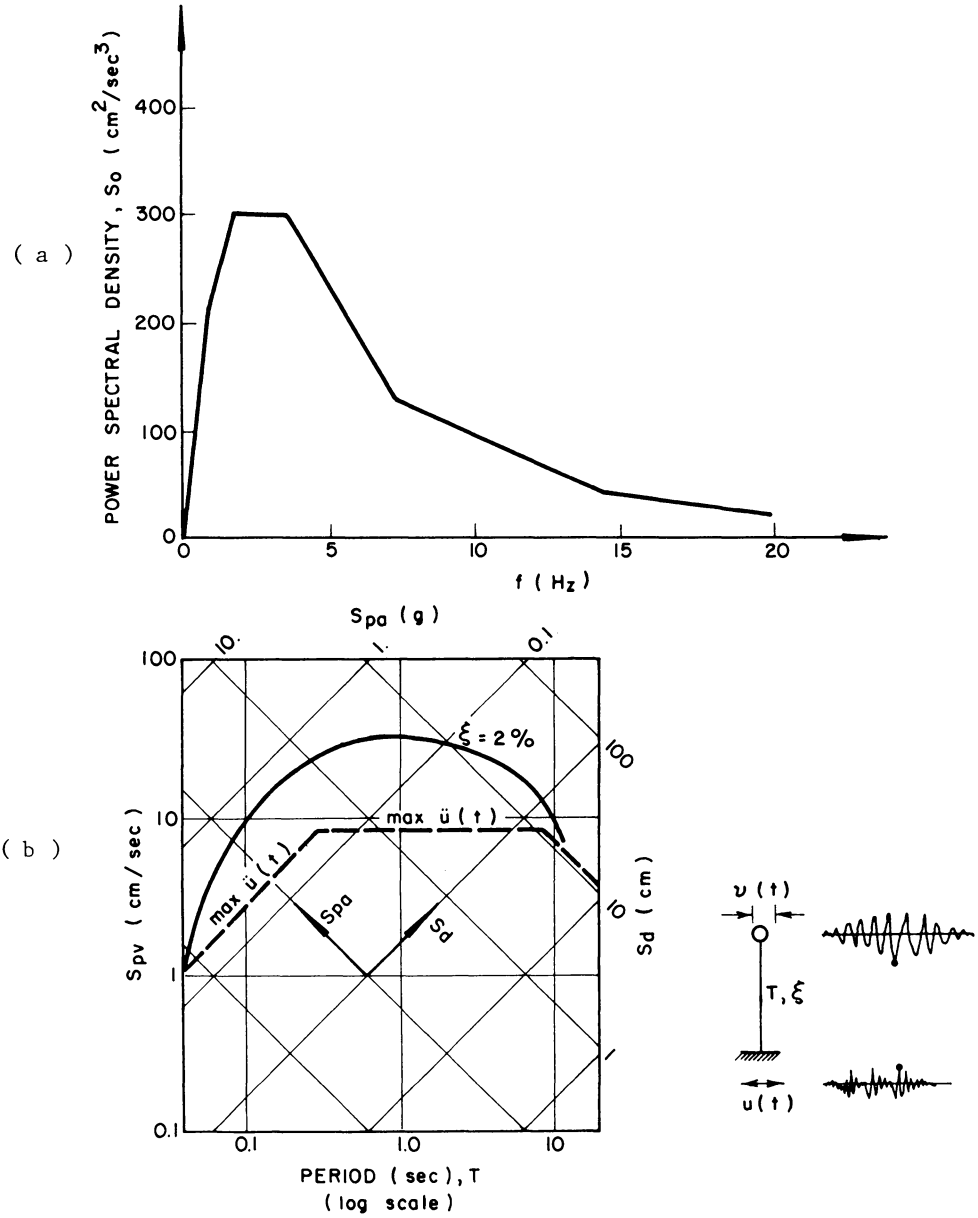

Figure 10 - The concepts of: a) power spectral density function and b) response spectrum.

$$S_{pv}(\omega,\xi) = \max \left[\int_0^t \ddot{u}(\tau).\ \exp\ [\xi\omega(t-\tau)]\ \sin\ \omega_d(t-\tau)\ d\tau \right] \qquad (3)$$

($\omega_d=\omega_o(1-\xi^2)^{1/2}$; for pratical purposes, $\omega_d \approx \omega$).
Note that S_{pv} is a pseudo-velocity RS as it is obtained from the true relative displacement RS multiplied by ω_d. The exact true relative RS has a much more complex expression, but for low damping ratios and away from the long periods, both expressions yield about the same values. An elegant and simple form of presenting the RS is by means of a four-way log plot S_{pv} versus period (T_o) or ω in log-log paper (Figure 10); the lines at 45° represent constant pseudo-absolute acceleration values, S_{pa}, when the slope equals 1, and constant relative displacement, S_d, when slope is -1. It can be shown that the asymptotic values of RS are given by

$$\lim_{\omega \to 0} S_d = \max \left[u(t) \right]$$
$$\lim_{\omega \to \infty} S_{pa} = \max \left[\ddot{u}(t) \right] .$$

Because of its simple physical meaning and its immediate applicability to the study of response of complex structures to seismic loads, the RS is by far the most widely used representation of earthquake ground motion. We will see in the next section how to relate peak ground motion values to the main features of RS through the concept of power spectrum.

Several representations of ground motion are intended to express the total 'energy' contained in the record by a single valued parameter. This can be obtained by integrating the power spectrum, S_o (mean square value), or the RS, S_{pv} over a large frequency band (Arias Intensity SI)

$$SI = \int_{0.1}^{2.5} S_{pv}\ (\xi,T_o)\ dT_o \qquad (T_o \text{ is period in sec}) \quad ; \qquad (4)$$

or by using the concept of root mean square (RMS) intensity of either the acceleration or velocity, defined as the integral

$$RMS^2 = \int_0^T \ddot{u}(t)^2 dt/T \quad => \int_{-\infty}^{+\infty} S_{o\ddot{u}}\ (\omega)\ d\omega \qquad (5)$$

RMS of acceleration has been used to measure the amount of work produced by the passage of seismic waves on different one degree of freedom systems with unit mass and spanning frequencies 0 to infinity; RMS of velocity is directly related to the flux of energy of the travelling waves.

The clear image that, in most cases ground motion is a non stationary process, has led to refinements in data treatment. The following models have been considered:

- stationary white noise;
- band-limited white noise;
- shot-noise (with constant filter parameters);
- filtered white noise (with time-dependent filter parameters)
- arbitrary shape (both in time and frequency).

A time window or moving window technique used prior to applying the Fourier Transform permits the study of frequency content evolution with time, according to the representation:

$$\ddot{u}(t) = \sum_{k}^{m} \zeta_k(t)\, \ddot{b}_k(t) \qquad (6)$$

where $\zeta(t)$ is a deterministic intensity function and $\ddot{b}(t)$ the stationary stochastic part; the sum takes place over m different time-windows, each one having its own frequency content. Figure 11 presents the evolutionary spectrum of the 1940 El Centro earthquake as computed by Tilliouine et al.(1984), and a sketch of how main wave phases are organized in a record.

4.2. First-Order-of-Importance Parameters

Although ground motion is most comprehensively characterized by frequency content, it can be described, in simplified form, by the following parameters:

- Peak ground motion values - acceleration (PGA), velocity (PGV), and displacement (PGD).
- Duration of motion - there is no unique definition of duration; roughly speaking it corresponds to the intense phase of shaking and is commonly measured by the amount of time for which the amplitudes of motion are kept above a certain threshold, taken as a standard value or as a percentile in the statistical distribution of amplitudes.

To illustrate the most important features of ground motion records, we selected the events recorded at the SMART-1 array (Bolt et al.1982) and (Oliveira et al.1985), as they cover major tectonic and morphological (source-site) situations with interesting engineering applications.

Reverse and strike-slip with some reverse component fault mechanisms; M magnitudes ranging from 3.2 to 7.2; epicentral distances between 3 and 200 km; and depths between 4 and 116 km are the important characteristics of these earthquakes. At least one event has a propagating fault rupture mechanism; several events have their focii right beneath the array, causing near-field motion associated with small and shallow faults.

4.2.1. Time analysis. Time analyses of earthquake records made at several stations for the same event show great differences in wave aspects, including peak ground motion values, envelope shapes, and

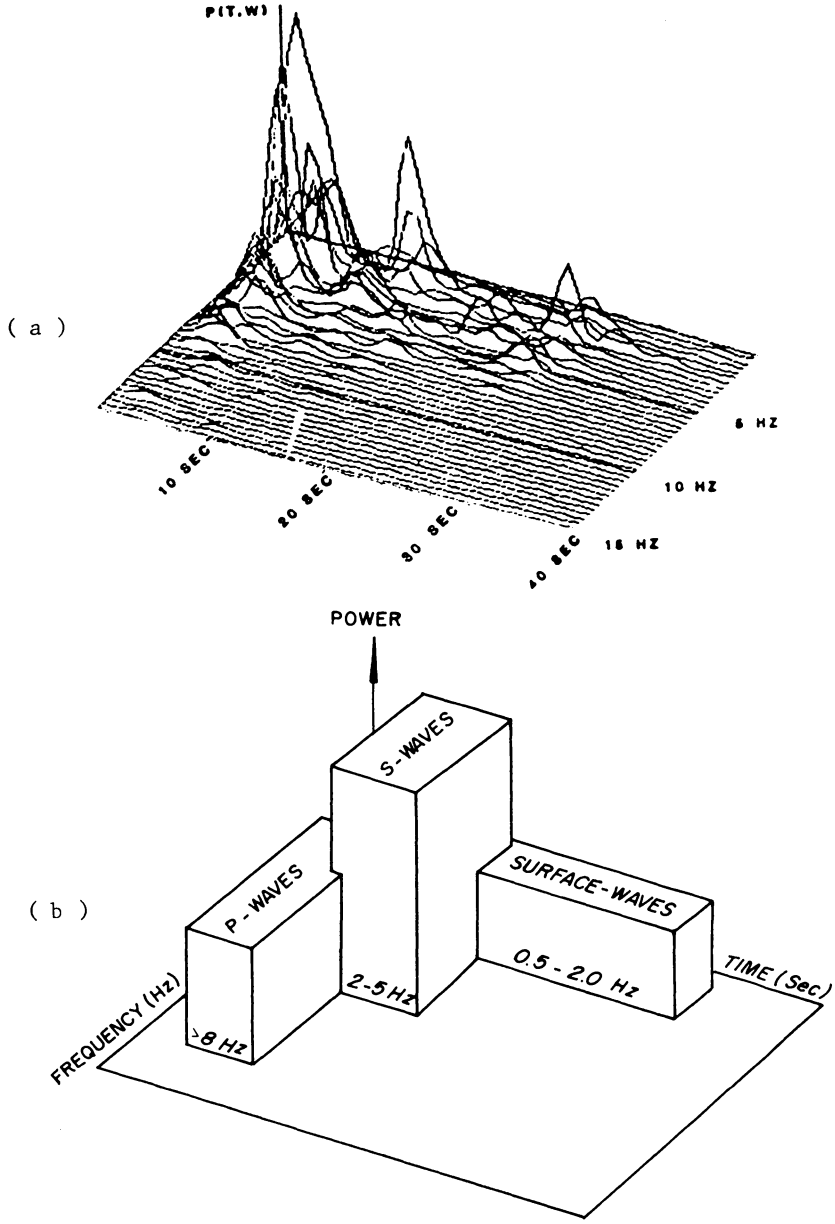

Figure 11 - Non-Stationary processes: a) evolutionary spectrum of the 1940 El Centro earthquake (after Tilliouine et al., 1982); b) time and frequency organization of main wave phases.

frequency content (Figure 9). Differences are greater when comparing records from different events and even greater for events of different source-site situations.

Even though records of other events not related to SMART-1 may show quite different features, the following comparisons constitute valuable information on ground motion characterization.

1-PGAs values obtained from the array for several recorded events vary widely. The largest PGA for each event range from values barely above the triggering threshold (≈ 10 gal) to 244 gal for the horizontal component and from 2 to 69 gal in the vertical component. Very few records can be considered as representative of large acceleration samples. Computed PGVs and PGDs for the horizontal components are in the range 0.5 to 15 cm/sec and 0.1 to 2.5 cm, respectively.

2- The mean ratio of PGAs in the two horizontal components approaches one with a coefficient of variation in the range 0.11-0.24; they usually tend to be localized in the same time window.

3- The vertical component shows a tendency for constant amplitude throughout the duration, especially for the distant-epicenter earthquakes. The mean ratio between PGA of any horizontal component and the vertical component for moderate to distant-focus events varies from 2.0 to 4.0 with the coefficient of variation in the range 0.3-0.4. Usually horizontal and vertical peaks are far apart in time. For nearby focus, the horizontal-to-vertical ratio approaches one with a large coefficient of variation of 0.7.

4- Hardsoil sites recorded PGAs 1.6 to 3.2 times smaller than the average in the array. The largest reduction was observed for the larger events.

5- Duration of ground motion varies from event to event in the range 10 to 40 sec, showing dependence on epicentral distance and magnitude. The larger the magnitude the larger the duration.

4.2.2. Frequency analysis. The following observations can also be depicted from analysing different events or station components of the same event (Figure 9b):

1 - Differences between the two horizontal components for the same station are not significant, for either NS-EW or radial and transversal components; the vertical component, however, has much more energy in the higher frequency bands.

2 - For almost all records there is a remarkable change of frequency content time. Three main regions can be defined for the horizontal components, the first corresponding to the P-wave train, with higher frequencies, the second corresponding to the S-wave train, with lower frequencies and higher amplitudes and sometimes mixed with P-waves, and the third corresponding to surface waves, usually with a very well defined lower frequency train. These features may explain why peak values for acceleration, velocity, and displacement do not coincide in time. Usually PGDs occur toward the end of record with large monochromatic coda waves.

3 - Predominant frequencies of motion change with the epicentral distance and magnitude. The distant, large-magnitude events contain much

more energy in the longer periods than the nearby, moderate-magnitude events.

One should add to this illustration the important situations of moderate-to-large magnitude small epicentral distance event, and large magnitude moderate-to-large epicentral distance event. The first causes high accelerations (> 500 gal), high displacements (> 20 cm) and high frequency content; durations are short (< 15 sec) and the vertical component exibits very large peak ground values. The first situation was observed in a few recent earthquakes such as the 1979 Imperial Valley earthquake which produced a large amount of important records. The second situation differs from the cases already reported, because it causes very long durations and the predominance of coda waves with very low frequency content ($0.3 < f < 0.7$ Hz)

4.2.3. Comparing Models The variability in ground motion records points to the use of statistical models for their study and characterization. This can be achieved in two different ways (Figure 12): 1) analyse a collection of data in its various aspects and obtain statistical estimates for its main parameters; 2) define "a priori" a theoretical model whose parameters fit the observed data. An example of the first method is obtained by superimposition of RP from different time-histories to determine mean values, draw confidence intervals, smooth the results, etc. The stochastic method as second approach, considers that each time-history is representative of a family of realizations (time-series that can be generated) with a given power spectral density function. Both treatments should yield similar results if the number of time-histories for the same source and path conditions become very large.

The stochastic approach has the great advantage of being able to predict, under certain conditions, the distributions of maxima and peak values (Figure 13a). In fact, considering that u(t) is a stationary Gaussian process, these distributions can be derived from the moments, m_i, of the process S_o

$$m_i = \int_{-\infty}^{\infty} \omega^i \, S_o(\omega) \, d\omega \tag{7}$$

and the duration T, of motion. The distribution of first peak is sharply peaked, with approximately the same mean, median, and mode. The mean is given by

$$\eta_e = [(2 \ln \nu T)^{1/2} + 0.5772/(2 \ln \nu T)^{1/2}] \, m_o \tag{8}$$

where $\nu = 1/2\pi(m_1/m_o)^{1/2}$ is the number of zero crossings during the motion. For engineering applications the term in brackets is approximately equal to 3, meaning that as a simple rule of thumb, PGA can be computed as 3 times the area under $S_o(\omega)$. This theory enables us to establish a direct correspondence between $S_o(\omega)$ and RS (Pereira et al.1976). In fact, the power spectral density of response, $S_{ov}(\omega)$ in

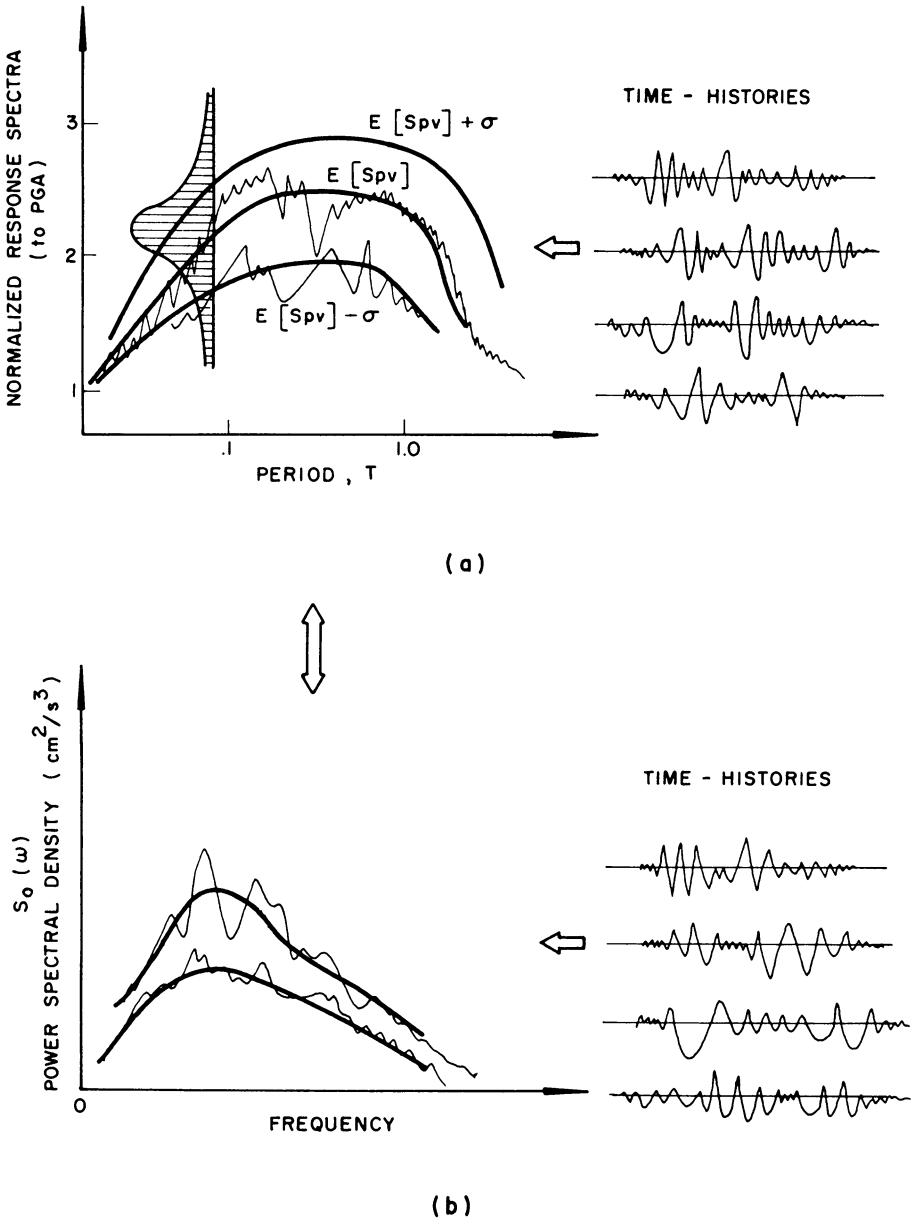

Figure 12 - Models to account for the variability in ground motion records: a) direct statistical analysis of different time-histories; b) power spectral density function.

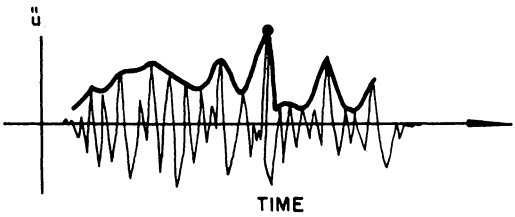

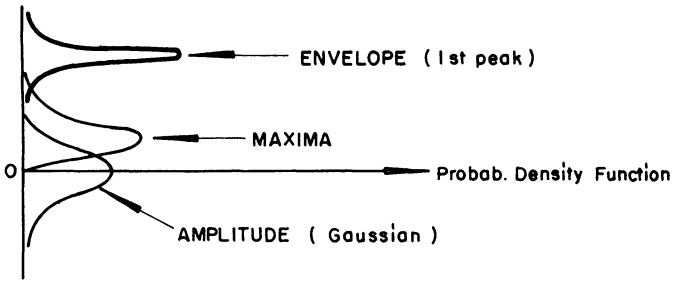

(a)

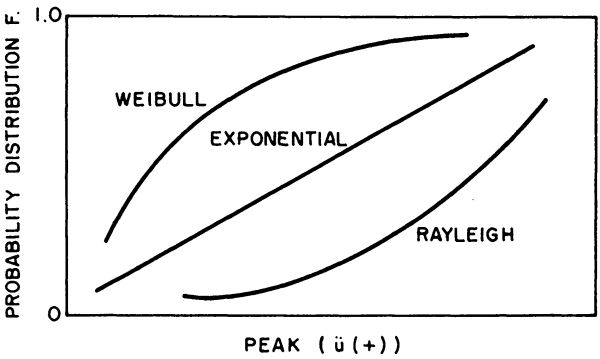

(b)

Figure 13 - a) Relations among probability distributions of amplitudes, maxima (peaks), and largest peak derived from the theory of stochastic analysis and order statistics; b) statistical distribution of maxima, 1st, 2nd, ..., nth peak, observed in real accelerograms, adapted from DeHerrera (1980).

terms of relative velocity, v(t) of one degree of freedom system characterized by ω_o, ξ and having the transfer function

$$H(i\omega) = \frac{-i}{\omega} \cdot \frac{(\omega/\omega_o)^2}{[1-(\omega/\omega_o)^2 + 2i\xi\omega/\omega_o]} \tag{9}$$

and subjected tothe power spectral density of input acceleration $\ddot{u}(t)$, $S_{o\ddot{u}}(\omega)$ is

$$S_{ov}(\omega) = S_{o\ddot{u}}(\omega)\,[\,H(i\omega)\,]^2 \tag{10}$$

Eqs. 7 and 8 will then allow for the computation of max $[\,v(t)\,]$.

Using similar means, it is possible to obtain the distributions of the 2nd, 3rd,... peaks. Statistical observation of peak values in a given accelerogram shows that they fit either the Exponential, Rayleigh or Weibull distributions (class of Extreme Type I, Borges et al.,1971). Figure 13b presents the general trend of these three distributions plotted on exponential probability paper. In Rayleigh distribution the peaks are concentrated in the high acceleration part, whereas in the Weibull distribution they concentrate in the lower acceleration portion.

Using the theory of order distributions (extreme type), the mean values of any peak, X_k is given by

$$\frac{X_k}{X_1} = \left[\frac{-\ln(\,k/(N+1))}{\ln(\,N+1\,)}\right]^n \qquad \begin{array}{ll} n=1 & \Rightarrow \text{Exponential} \\ n=2 & \Rightarrow \text{Weibull} \\ n=1/2 & \Rightarrow \text{Rayleigh} \end{array} \tag{11}$$

where N is the standard number of peaks, (DeHerrera et al.1982), defined as twice the number of upper median exponential peaks for the total length of the record. As an example taken from soft soil data in California, the third peak averages 1.30 below the first peak for the Exponential distribution, 1.52 for the Weibull and 1.18 for the Rayleigh.

The distribution of peaks beyond the first one is very important in establishing rules for determining effective peak acceleration, giving some insight on how high peaks are organized. The highest peak may not be significant for engineering purposes, especially if it is an isolated value associated to high frequency pulse. Second and third peaks would be more appropriate. According to the previous values we expect an average of 30% off PGA for 3rd peak.

This concept is also of interest in studying source parameters, as there seems to be some correlation between type of distribution and directivity effect as we will see in section 4.4.

4.2.4. Variability for close-distance sites. Arrays are especially important in the study of variability of ground motion for stations located close to each other. In Figure 14a we present the geographical distribution of PGA for the N-S component of a distant event. Plots of this kind can be made for all types of parameters and reflect the complex nature of wave propagation. In-plan representations are most

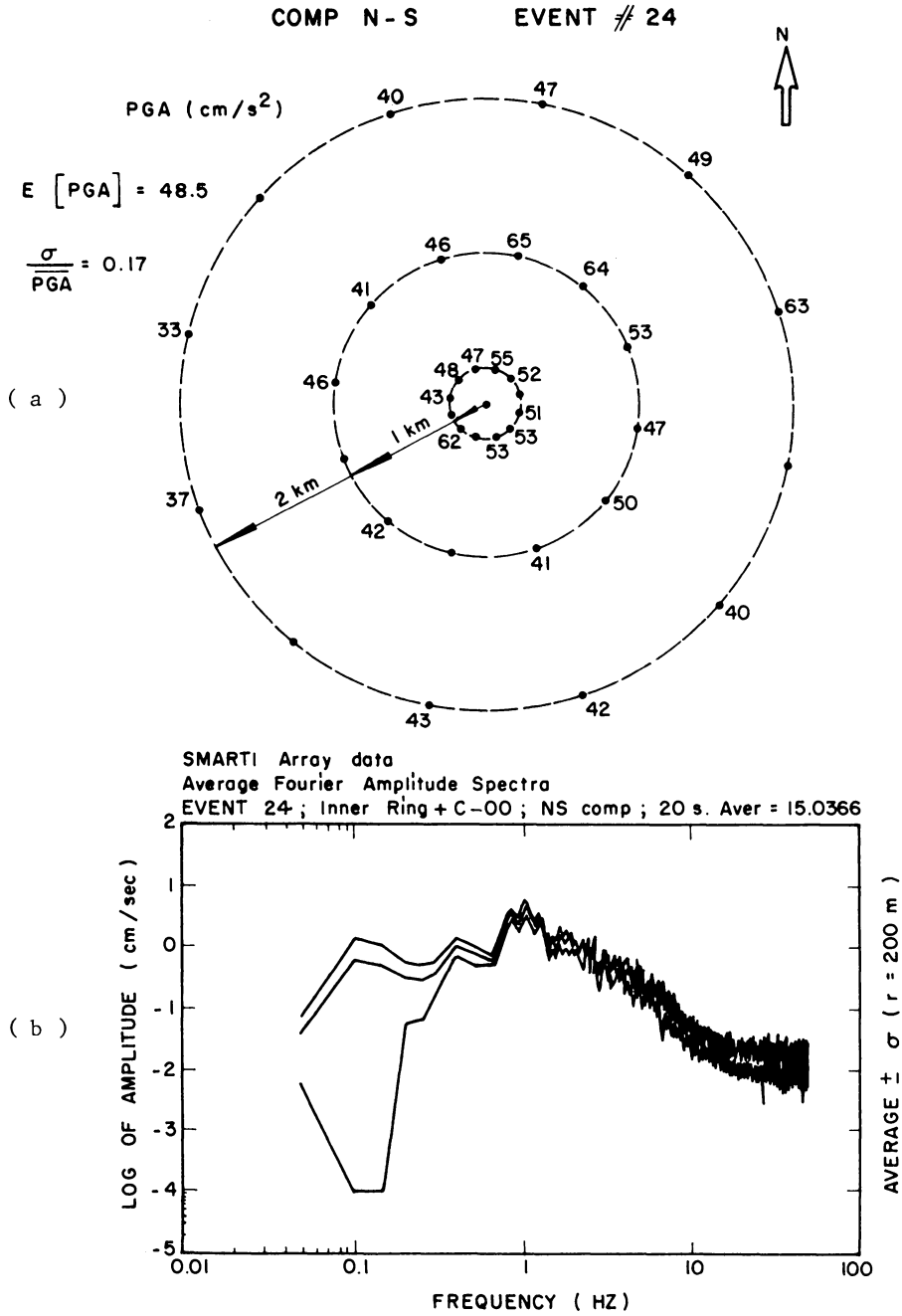

Figure 14 - Variability in ground motion for close-distanced sites: a) in PGA; b) in frequency (Event #24 recorded at SMART-1 array, Oliveira et al., 1985).

useful; for example, they can be used to recognize soil behavior differences across the array and separate them from source mechanism patterns.

Variations in PGA within the array for a given event, measured as the ratio of high to low value, varies from 2:1 to a maximum of 6:1. The coefficient of variation σ/x vary from a minimum of 0.17 to a maximum of 0.49. The largest variations are observed in nearby earthquakes and are caused by one or two stations out of 20. If these extreme cases are excluded, variations fall immediately to (2.5-3.0):1 with coefficient of variation on the order of 0.20. Figure 14b presents an average Fourier spectra $\pm\sigma$ for stations with an average separation of 200 m; these variations that can go to 1:2 increase with increasing distance between stations.

As the variability of ground motion parameters is quite large, even over short distances, it is very difficult to predict ground motion using representations based on properties recorded at a single station. Once more we emphasize the important role of strong motion array instruments in estimating, on one hand, the variability of strong motion records, and on the other hand, their average values. Further studies on this subject are in progress.

4.2.5. Correlation among components. The extension of 1-component analysis of ground motion to the 2-horizontal components and 3-components cases implies the establishment of appropriate cross spectral density functions or corresponding cross correlation functions.

For a stationary random process, the cross power spectrum of any two components $\ddot{u}_i$ and $\ddot{u}_j$ is

$$S_{ij}(i\omega)= \lim_{T\to\infty} \left[\int_{-T/2}^{T/2} \ddot{u}_i(t)\, e^{-i\omega t} . \int_{-T/2}^{T/2} \ddot{u}_j(t) e^{+i\omega t}\, dt \right] / 2\pi T , \quad (12)$$

and the cross correlation:

$$R_{ij}(\tau)= \lim_{T\to\infty} \frac{1}{T} \int_{-T/2}^{T/2} \ddot{u}_i(t)\, \ddot{u}_j(t+\tau)\, dt \quad . \quad (13)$$

It can be shown that:

$$R_{ij}(\tau) \Rightarrow FFT^{-1}(S_{ij}(i\omega)) \quad (14)$$

If i=j we get the autocorrelation function $R(\tau)$ and the power spectrum $S(\omega)$. Due to the nature of the process, $S_{ii}(\omega)$ is a real quantity, $Re(S_{ij})=Re(S_{ji})$ and $Im(S_{ij})=-Im(S_{ji})$. This means that $S_{ij}(i\omega)$ is a Hermetian matrix.

The correlation R_{ij} leads to the concept of correlation coefficient ρ_{ij} between two signals

$$\rho_{ij}(\tau)= \frac{R_{ij}(\tau)}{\sqrt{R_{ii}(\tau)}\sqrt{R_{jj}(\tau)}} \tag{15}$$

whereas S_{ij} leads to the concept of coherence function γ_{ij}

$$\gamma_{ij}(\omega)= \frac{[S_{ij}(i\omega)]^{1/2}}{\sqrt{S_{ii}(\omega)}\sqrt{S_{jj}(\omega)}} \tag{16}$$

Penzien et al.(1976) have shown that the available strong ground motion records support the idea that the components of the 3-D model are not statistically related if the system of reference coincides with the principal axes of ground motion. These are defined by the eigen vector of the correlation matrix,

$$R_{ij} = E[\ \ddot{b}_i(t)\ddot{b}_j(t+\tau)\ ]$$

where $b_i(t)$ is the stationary stochastic part of ground motion u(t), given by eq.(6) when m=1

$$\ddot{u}_i(t) = \zeta(t)\ \ddot{b}_i(t) \qquad i=x,y,z$$

and $\zeta(t)$ is the deterministic intensity function. Under certain conditions that are observed in pratical applications, R_{ij} has the same eigen vector as the correlation matrix of the original time-history. In physical terms, Penzien et al.(1976) found that the major principal axis of ground motion fluctuates during the motion around the direction towards the expected epicenter and the minor principal axis remains vertical; the ratio of minor to major principal variances (eigen values of R_{ij}) is approximately 0.5, which is in agreement with the 2:3 ratio between PGAs for vertical and horizontal components. This conclusion, however, may not be extended to more general time-dependent cases as the ones defined by eq.(6), for which peak envelope functions coincide. SMART-1 data shows that the peaks of the two horizontal components rarely occur simultaneously, but for events of category 1 (section 4.1), this phenomenon was observed. Scherer et al.1982 arrived to similar conclusion when studying evolutionary spectra.

4.3. Second-Order-of-Importance Parameters

Directly associated with the phenomenon of wave propagation are the spatial dependence of ground motion recorded at two different sites, and rotational components. Even though the theory of elasticity studies these concepts, only with the recent development of strong motion accelerograph array networks has it been possible to progress in this field. The results are of great importance for the definition of seismic input in 1) extended structures such as long bridges, dams, which will be subjected to differential movements at the foundation level; 2) structures with rigid base-mat foundations, like some nuclear power plants; and 3) tall structures, such as high-rise buildings, towers, and

chimneys, which are very sensitive to rotational components (torsion and rocking).

The first of two ways to look at this problem considers that waves propagate with a predominant monochromatic wave train with a given apparent velocity, V_{app} (Figure 15). The semblance of wave forms, measured through the cross correlation-coherence coefficient defined by eqs.(15,16), where indexes i and j represent a given component recorded at stations i and j, attenuates with the separation distance between stations. The second approach considers the entire spectrum of frequencies decomposed into several frequency bands and associates an apparent velocity and a loss of coherency to each of them.

4.3.1 Rotational Components. We concentrate here on only the first approach. Following Newmark (1964), we can compute the rotational components produced by a monochromatic wave as

$$\Phi\ (t) = \frac{du}{dt} / V_{app} \tag{17}$$

where du/dt is the ground velocity in the direction perpendicular to the propagation. Using this simple formulation, the response spectra for rotation can be derived from the RS for acceleration as

$$\max\ [\ \ddot{\Phi}\ ] = \max\ [\ d^3u/dt^3\ ]\ /\ V_{app}\ . \tag{18}$$

Lines of equal angular acceleration in the tri-logarithm response representation corresponds to a slope of ω^2. Recent analytical and experimental studies indicate that this approach (Bouchon et al.1982), which leads to an upper bound estimative, requires V_{app} to be the shear velocity at the base rock or the rupture velocity at the fault zone and not the shear velocity at the surface layers.

The problem, however, based on data on the three translational components measured at closely located stations (no direct measurements of torsion have been done so far), is much more complex than the previous simplified model would anticipate. Rotational components, decomposed in torsional, and rocking in relation to two horizontal perpendicular axes, are a function of frequency band and rapidly attenuate with distance to the rupturing fault. Peak values decreased from 10^{-3} radians (distances < 5 km, Niazi 1985) to 10^{-5} radians (distances > 30 km, Bouchon et al.1982), indicating their importance in engineering application for sites near the fault zone and probably for large magnitude events at moderate distances.

4.3.2 Spatial correlations of ground motion. The dynamic analysis of a structure subjected to multi-support excitation requires the knowledge of both acceleration and displacements at all n support points as a function of time (Oliveira et al.1985). This implies the development of a (3n)x(3n) matrix of cross power spectral density function $S_{i,j}(i\omega)$ - considering only the acceleration components and taking for displacements

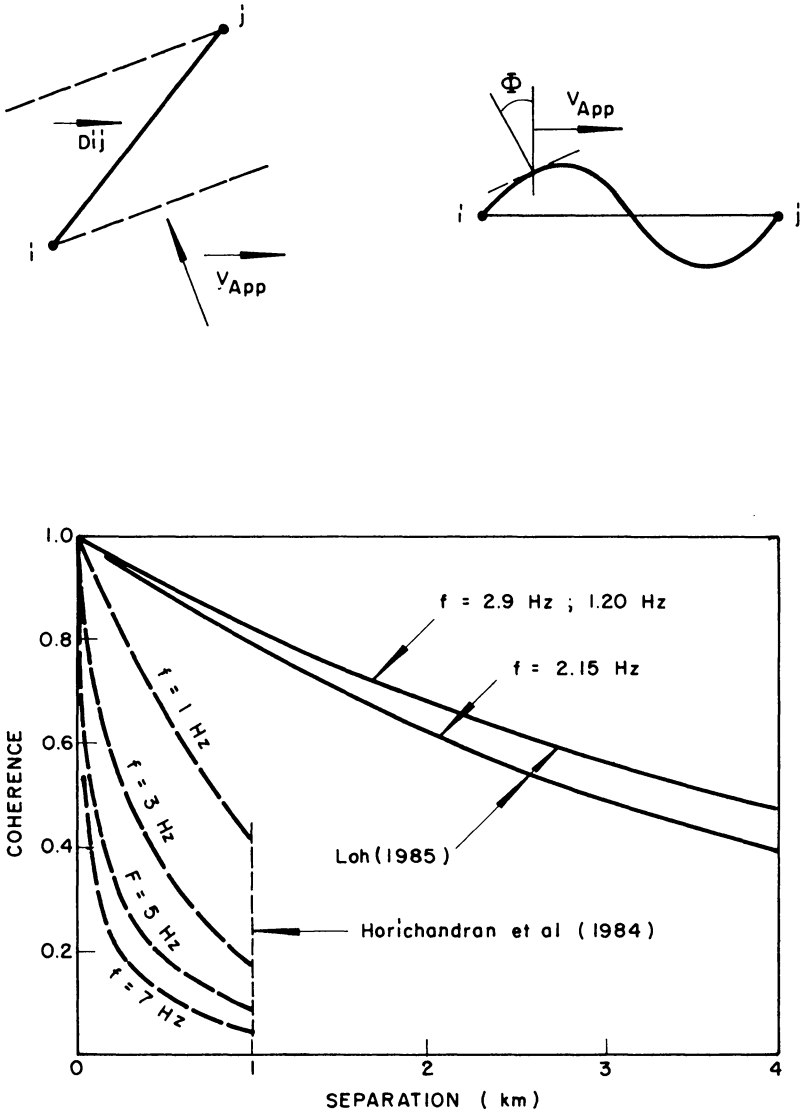

Figure 15 - Wave propagation and its consequences on ground motion. Attenuation of cross power spectral density function (after Loh, 1985 and Harichandran et al., 1984).

$$S_u\ (i\omega) = S_{\ddot{u}}\ (i\omega)\ /\ \omega^4 \quad . \tag{19}$$

Data from the SMART-1 array support the idea that the cross spectrum attenuates with the distance between sites and suffers a phase shift due to the traveling waves (Loh 1985, Harichandran et al.1984):

$$S_{ij}(i\omega) = S_o(\omega)\ \exp(-\lambda[\overrightarrow{D_{ij}}])\ \exp(i\omega\ \overrightarrow{V_{app}}.\overrightarrow{D_{ij}}/\overrightarrow{V_{app}}^2) \tag{20}$$

where $\overrightarrow{D_{ij}}$ - position vector for stations i,j;
λ - constant depending on frequency, to obtain from data;
$\overrightarrow{V_{app}}$ - apparent velocity of wave train with center frequency ω
$S_o(\omega)$ - power spectrum for the entire array.

Based on Eq.20 one can directly compute the response of any dynamic system using the theory of stochastic processes or generate artificial ground motion time-series.

4.4. Mechanisms of Generation and Attenuation of Seismic Waves

In the preceeding sections, earthquake generation has been characterized in terms of occurrence time, epicentral location, and magnitude. It is now necessary to quantify the earthquake action at a site located at a given distance from the focus.

The signal recorded at the site u(t) is the result of the convolution of the original source signal, x(t), with the impulse functions representing the path, q(t), the site response, s(t) and the instrument response i(t),

$$u(t) = x(t)*q(t)*s(t)*i(t) \tag{21}$$

where s(t) includes both geological and topographic influences. We will briefly discuss the most important features of x(t) and q(t) to include their influence in the assessment of strong ground motion. We will not discuss s(t) and i(t).

When the dimensions of the surface rupture are of the same order the distance to the site under consideration (near-field), magnitude is not enough to characterize the earthquake at the source. The effect of other parameters connected to the elastodynamics of the system might be of great importance. Magnitude becomes increasingly dominant for larger epicentral distances (far-field).

Among the geometrical, material, kinematic, and dynamic variables (Brune 1976, Bolt 1981) related to the the source function (Figure 16a), the seismic moment (M_o), the dynamic stress drop ($\Delta\sigma$), and the rupture velocity (V_r) greatly influence x(t) and should be considered when predicting the ground motion at a site. The first two are directly related to the Fourier far-field amplitude ground displacement spectrum ($\Omega(\omega)$) as can be seen in Figure 16b: the seismic moment is related to the fairly flat portion in the range 0.1 to 1.0 Hz; beyond about 2 Hz, spectra from different earthquakes show a pronouced decrease, typically with one or more slopes γ which in a log-log plot are proportional to ω^{-2} - ω^{-3}. The changes in slope, designated by corner frequencies (ω_c),

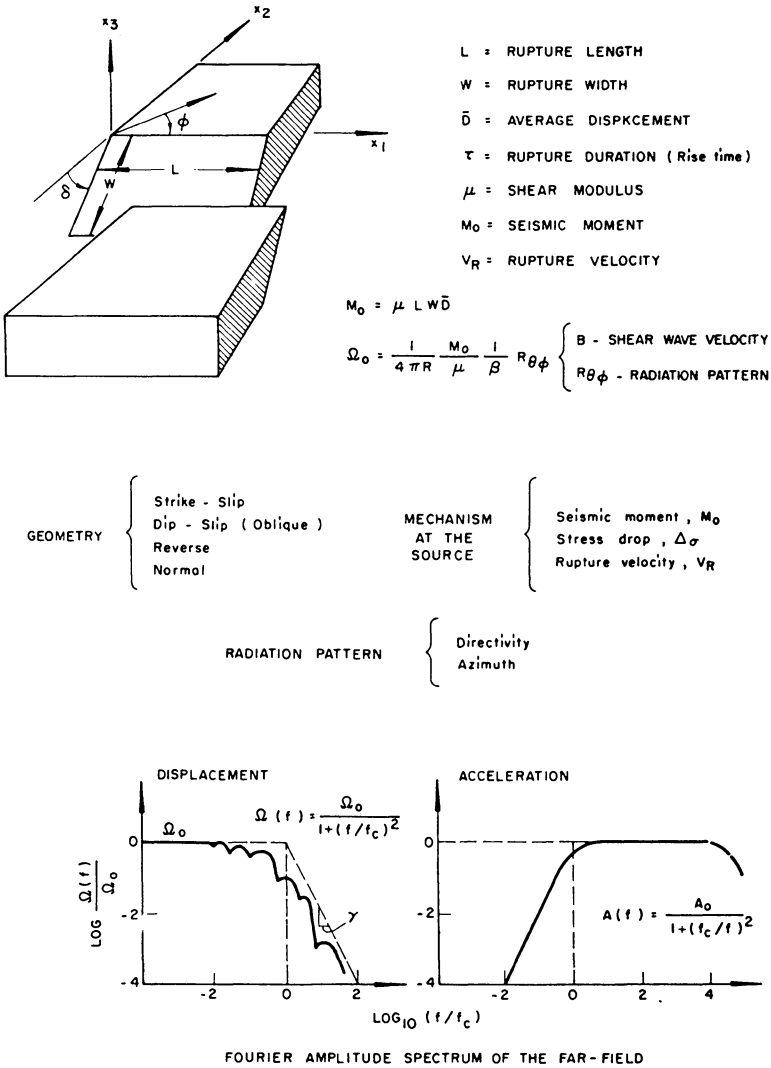

Figure 16 - a) Main parameters describing the geometry, mechanic properties and source-function of an active fault; b) typical shape source displacement and acceleration Fouries spectrum for the far-field.

seem to be related to the different characteristics of rupture phenomenon, such as rising time, initiation and termination of phases of rupture, etc., and are different for P and S waves,

$$\Omega\ (\omega) = \frac{\Omega_o}{1+\ (\omega/\omega_c)^{\gamma}} \quad . \tag{22}$$

There are several formulae to relate Ω_o to the fault characteristics (Bolt 1981).

For the near-field, the Fourier spectrum exhibits an asymptote proportional to ω^{-1} in the lower frequency range, and is much more sensitive to the rupture stopping phases.

Rupture velocity, affecting the frequency content and the duration of motion at a site, is the main cause for directivity effects. From theoretical considerations, there is a change in corner frequency (ω_c) of the displacement spectra for the ω^2 model given by

$$\omega_c = \frac{2\beta}{L}\ (\frac{\beta}{V_r} - \cos\Theta\ )^{-1} \tag{23}$$

where β is the shear wave velocity, L the fault rupture, V_r the rupture velocity, and Θ the azimuth of the epicenter-site direction in relation to the fault. The duration of motion at the site is L/β times the second term in the Eq.(23). From the equation we see that these two parameters may be greatly affected by the rupture phenomenon.

Azevedo (1984), studying a few California earthquakes, observed that the records within an angle of 20° to each side of the fault line measured from the epicenter and up to 50 km (Figure 17), have a clear Weibull distribution, whereas the records for the complementary sectors and distances to the epicenter greater than 50 km have a clear Rayleigh distribution. For the other regions of the space, a mixed situation develops. This conclusion emphasizes the influence of distance and azimuth over frequency content and duration of ground motion as mentioned in section 4.1.

The seismic waves generated at the fault, propagate in all directions, attenuating with distance and azimuth. The attenuation comprises two main parts:

1) One resulting from the geometrical spreading - P and S waves at large distances compared to the source dimensions are attenuated as R^{-1}; surface waves are attenuate as $R^{1/2}$. At short distances the geometric attenuation is function of the source parameters and mechanisms of generation, and the amplitudes decay in proportion to R^{-2}.

2) And the other resulting from internal dissipation and travel path, and approximately represented by the model

$$\Omega(\omega,R) = \Omega(\omega,0)\ \exp\ [-a(\omega)\ R] \tag{24}$$

where $$a(\omega) = \frac{\omega}{2Qc}$$

c is the phase velocity; 1/Q is the specific attenuation coefficient; $\Omega(\omega,R)$ the Fourier displacement amplitude at distance R and $\Omega(\omega,0)$ the Fourier amplitude at R=0.

The model presented (Eq.22 to 24) should be applied to the most important phases that will influence the ground motion at a site. This simple method to obtain earthquake motion at a site, starting from a source model with at least two independent parameters, such as seismic moment and stress drop, and attenuating the source spectrum with distance, can keeping track at the same time of the different phase arrivals. Much more complex models have been developed and successfully used in specific situations.

4.5. Simplified Model for Attenuation and Spectral Shapes.

To be of practical use in the engineering profession we need some simplified models of attenuation and to be able to associate the main tectonic environment to certain spectral properties and to peak ground motion parameters.

The present state of knowledge of seismic loads and their effect on structures suggests that PGA, PGV, PGD and duration are suitable parameters to define earthquake ground motion. PGA and PGD are fairly good indicators of the response of structures possessing, respectively, high (>2 Hz) and very low (<0.5 Hz) natural frequencies. In the intermediate range of natural frequencies PGV correlates better with the response but the correlation is less precise than that of the former parameters.

These parameters are not all independent. $PGA*PGD/PGV^2$ and PGV/PGA were proposed as two important parameters controlling the construction of RS. They are somehow related to the transitions PGA->PGV and PGV->PGD in the spectrum. Without going into details it can be said that they both increase with distance, but while the former decreases with magnitude the latter increases.

4.5.1. Categories of Seismic Scenarios. From analysing various conditions in a region, several seismic scenarios yielding specific ground motion records can be considered. As an example, we describe three distinct situations (Oliveira et al.1984, Oliveira 1985b) that are encountered quite often (Figure 18):

- 1 - Nearby shallow small-magnitude earthquakes (M in the range 3-4), originated most probably at small shallow faults.
- 2 - Shallow moderate to large-magnitude events at intermediate distances from the site (20 to 50 km). The tectonic mechanism should be similar to the one referred to 1, above.
- 3 - Distant (more than 100 km) moderate to large-magnitude events at moderate to intermediate depths.

4.5.2. Attenuation Relationships. In current practice, however, peak ground motion values are computed with simple empirical formulae such as

$$y = a_0 + a_1 \exp(a_2 M) (R + a_3 \exp(a_4 M))^{a_5} \varepsilon \qquad (25)$$

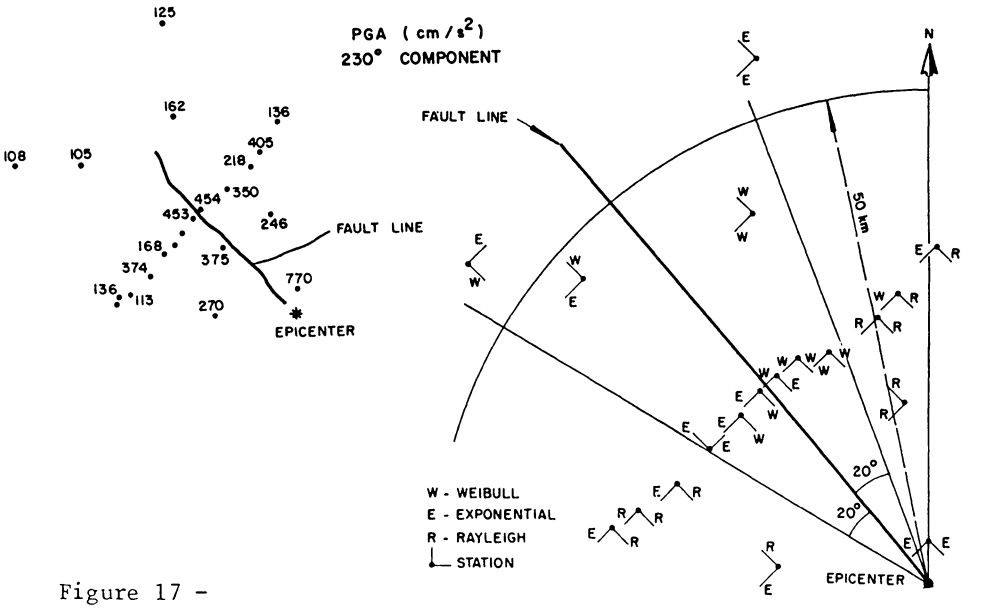

Figure 17 -
Source-directivity influence on type of peak distribution: the 1979 Imperial Valley earthquake, adapted from Azevedo (1984).

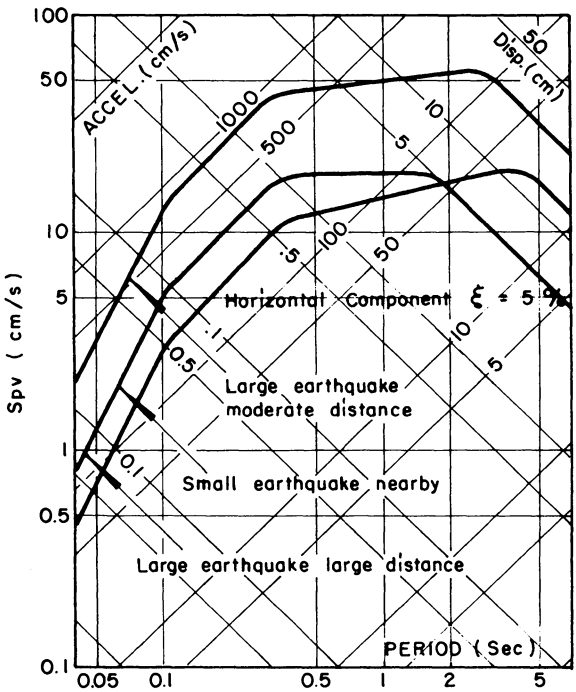

Figure 18 - Influence of site-source in response spectra: typical situations.

where y represents PGA, PDV, PGD, or any spectral ordinate; a_0, a_1,a_2,a_3,a_4 and a_5 are constants obtained from data; R is the epicentral distance or some function of the azimuthal distance; and ε is an error function that takes into consideration the dispersion between the data and the computed values using the Eq.(25). Uncertainty about the values obtained with this equation are very large as they have to account for many different features not explicitly considered.

Many different attenuation formulae have been devised throughout the world, based on ground motion parameters. The most thorough treatments try to separate the various tectonic environments, the effect of soil conditions, and the directivity effect, and to determine intervals of confidence through sophisticated regression analysis. Figure 19 presents a typical attenuation curve obtained from instrumental data (Bolt et al.1982, Joyner et al.1981). As presented in a separated sketch, uncertainties vary with distance and are higher for larger events due to scarcity of data. Other attenuation formulae include the cases of duration, effective peak acceleration, predominant frequencies and RMS as a function of R and M.

As already mentioned, closely located stations show great variability in peak ground motion parameters. To take this effect into consideration in the assessment of ground motion characterization, an additional probability distribution function should be added to the average value obtained through the attenuation laws.

4.5.3. Macroseismic data and the assessment of attenuation functions. Wave attenuation is another important field of engineering seismology that cannot be solved nowadays by instrumental measurements only. In fact there are many seismic regions in the world with no instrumental strong motion data; sometimes not even microseismic data. But some may have a good historical record of macroseismic data which can inform on earthquake mechanisms and wave attenuation. This is particularly important when strong motion data is not available.

Quality of data plays an important role in establishing attenuation curves from isoseismal intensity maps. These constitute the final product of a long chain of information based on the elements discussed in Section 2.2. The uncertainties in the rough data are carried through the chain, increasing or decreasing the intervals of confidence. Quality of data helps define these intervals.

A further source of uncertainty, causing perhaps greater problems, is translation of intensity measurements into ground motion parameters. There have been several tentative efforts to correlate damage (and consequently intensity) with ground motion parameters, but all show great scatter. One way to reduce the scatter is to separate historical buildings that went through earthquake motion, the destroyed as well as the ones that survived, into different classes, according to their dynamic properties. At least two classes can be considered: the short period, small, and more stiff structures such as small chapels, low-rise massive houses, and the long period structures, such as the larger palaces, slender aquaducts, etc. Dynamic analysis of old well-documented structures under seismic loads will inform us quite accurately, not only

(a)

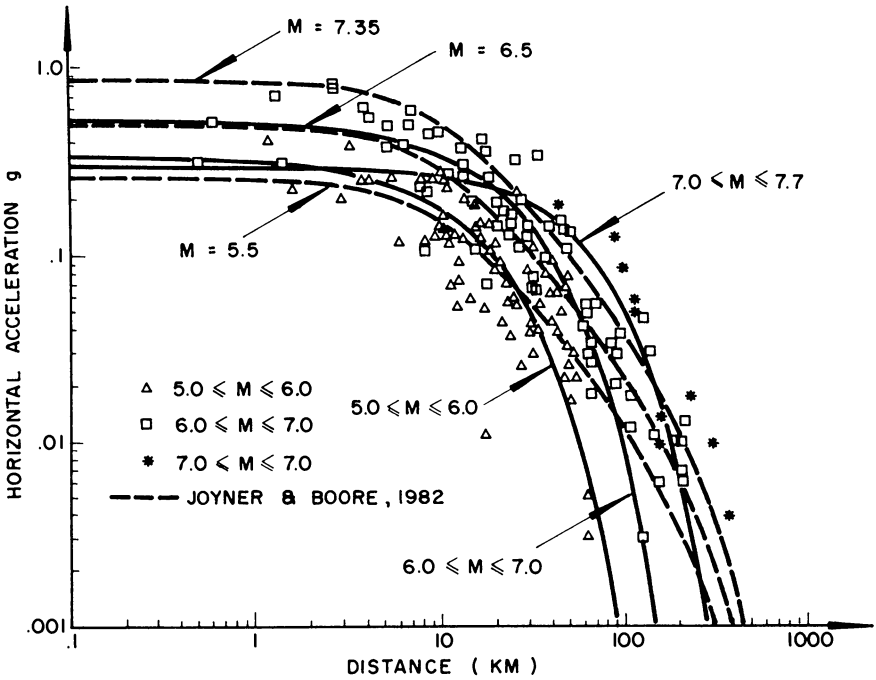

(b)

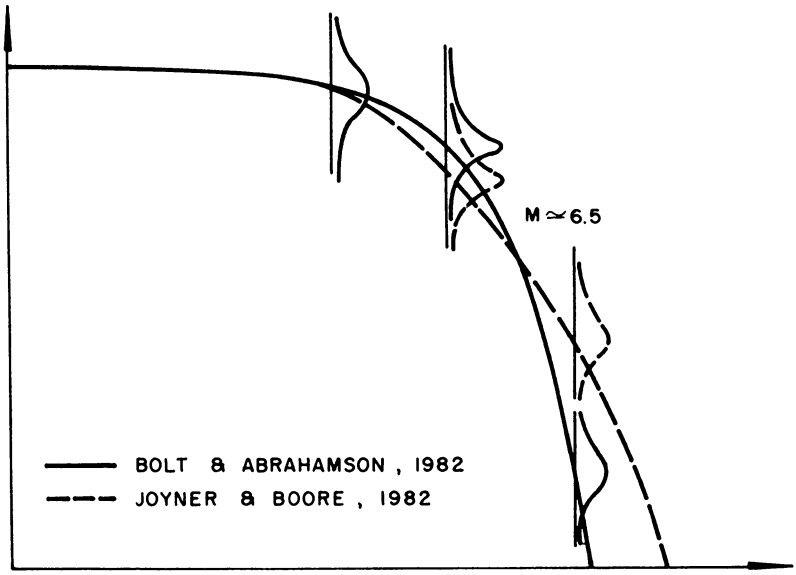

Figure 19. Typical attenuation curves derived from instrumental data (from Bolt et al.1982 and Joyner et al.1981)

on the ability of similar structures to survive future motion, but also on the upper and lower bounds of seismic motion in the past.

The earthquake record from the first epoch of the instrumental network, 1900 to 1950, also deserves careful study. There are European teleseismic records (Wiechert T=10sec) for distances of 500 to 2000 km corresponding to waves trapped in the stratified upper crust. Due to high attenuation of first arrivals and the scarcity of stations, standard earthquake parameter assessment does not work in these cases. But Goula et al.(1985) used synthetic seismograms very successfully to explain the source parameters of the Provence, June 11, 1909 (France) earthquake; the results are also in good agreement with the macroseismic data.

Though intensity measurements to evaluate attenuation features should be used cautiously, isoseismal maps have the great advantage of informing other aspects of propagation. One of them deals directly with the anisothropy. Figure 20 presents two examples of this effect, the first of them used as a basis to derive one attenuation for Portugal

$$I= c_0 + c_1 M_L + c_2 \ln (R+R_0 + c_3 [\sin\Theta]) \qquad (26)$$

where c_0, c_1, c_2, and c_3 are constants to be adjusted to each source zone and Θ is the angle between the azimuth of a site and the azimuth of a specific point, both in relation to the center of mass of that zone. Eq.(26) takes into account the phenomenon of wave diffraction in the transition rom oceanic to continental crust.

5. MODELS INCORPORATING BOTH STOCHASTIC MODELS: OCCURRENCE AND GROUND MOTION

We can now obtain the final probability distribution of ground motion parameters, considering the occurrence and the ground motion processes. We make use of Eqs.(25 or 26) as the linking element between the two processes.

The material in the subsequent sections is presented in a summarized form refering the reader to the most important points, and aims at giving an integrated view of the entire probabilistic assessment of ground motion. More detailed work can be found elsewhere (Oliveira, 1978 and Oliveira et al.1984).

5.1. Hazard Studies

There are three categories of mathematical models to compute the probability density function of a site-parameter $G_Y(y)$ defined by Eq.(25), as the result of randomness in occurrence and propagation (first column Table III):

- 1 - The analytical methods consider different earthquake source zones characterized by the probability density of occurrence and use standard probability techniques of transformation of random variables to transform the 3-d space-time-magnitude process into nx(1-d) ground motion parameters (n is in general 1 or 2 - PGA, PGV).

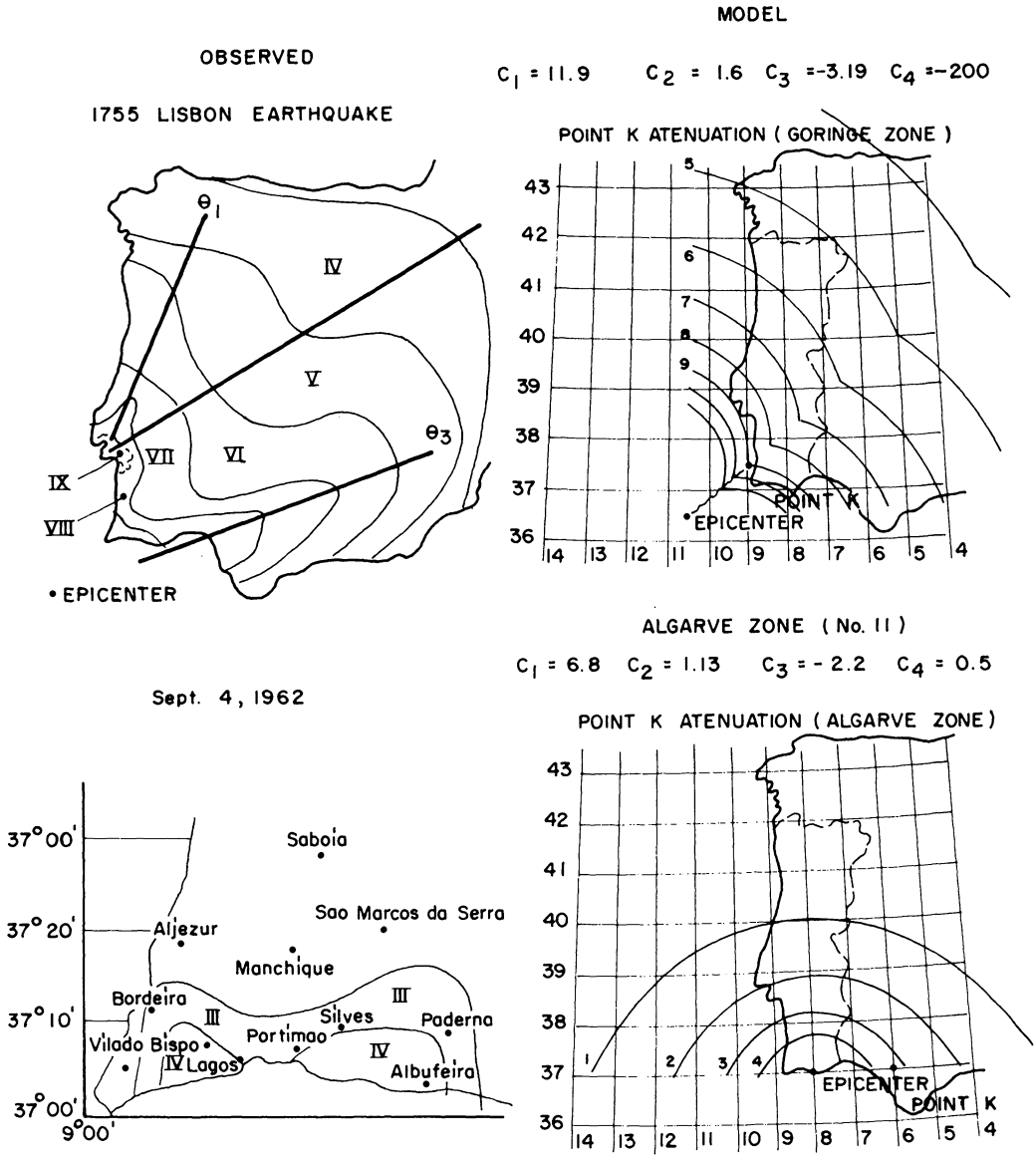

Figure 20 - Anisotropy effects depicted from isoseismal maps.

• 2 - The experimental or empirical method considers the simple family of earthquakes that have occurred in the past; then, transform each event into ground motion parameters at a site using Eq.(25); and performs a statistical analysis of extreme type (Martin Martin et al.1984).
• 3 - The method based on simulation generates a set of occurrences according to the techniques mentioned in Section 3.4 and then applies the extreme value technique referred in 2).

While the analytical method may include all uncertainties on parameter estimations and yield the final distribution of site-parameter Y on its entire range, the experimental method considers only what has happenned in the recent past. The simulation, however, may well replace the analytical method, even though it may take more computer time. The experimental method has the advantage of referring to an actual past, and should always be used as a standard distribution for comparison.

In order to understand the influence of parameter uncertainties on final probability distributions of Y, the following methodology based on Bayes's theorem can be used:
1- Select a group of hypotheses, such as one given source-zone geometry, one rate of occurrence, one attenuation formulae, etc, and name it alternative i, A_i.
2- Compute the probability distribution of Y for the group of hypotheses. Uncertainty in the most important parameters, such as in a given attenuation function, and on upper magnitude values, can be included in the analysis.
3- Assign a weighting factor, w_i, to each of n alternatives A_i, according to the degree of confidence (section 2) attributed by the experts who provided the information.
4- Use the theorem of total probability,

$$P_r (Y > y) = \sum_{i}^{n} P_r (Y > y \mid A_i) w_i \qquad (27)$$

to compute the final probability distribution of Y.

The final results can be presented in two different forms: first form considers separately the mean value of the final distribution on Y and upper and lower bounds on the estimations (Figure 21); the second considers the final distribution function with all uncertainties included. Data refer to hazard studies made for Portugal (Oliveira et al.1984). The first one has the advantage of showing the intervals of confidence on the "best estimate".

5.2. Analysis of Uncertainties and Hazard Evaluation for Low Probability of Exceedence

The several algorithms for hazard analysis which may explicitly compute the influence of some uncertainties in the final distributions (McGuire 1976, Kulkarni et al.1984, and Bender 1984), usually yield probability distributions of Extreme type II with large coefficient of variation.

Studies of sensitivity done in several places show that the relative importance of parameter uncertainties on final results depend

on the specific situation under analysis. Intervals of confidence show a general trend of widening towards the smaller probabilities of exceedence. Figure 21 presents the hazard results for a site in Portugal showing an interval of confidence with variations 1:4.

Updating hazard studies is of great importance and should take place whenever new significative elements become available. Figure 22 summarizes the important steps for updating hazard studies in Portugal in the last 15 years, and presents a comparison of results obtained. As we would expect, these updating studies will not lead to completely different results, but instead decrease the margins of uncertainty on final estimates.

To illustrate the influence of some of the problems discussed in Sections 3 and 4 when estimating the hazard in a region, we refer to the studies made in three countries of the Ibero-Mogrebi region. Table II presents a summary of the main characteristics of earthquake generation and attenuation, Table III the methodologies of analyses, and Table IV the main final results obtained. As it can be seen in these Tables, even though the countries exhibit some common tectonic and morphologic features, final results differ quite significantly from one another (in average as well as in intervals of confidence). Comparisons suggest that homogeneization of data treatment and methodologies may eventually contribute towards a reduction on final hazard estimations for that region.

Extrapolation for the zones of very low probability of exceedence as it is required in the study of important structures, is very delicate. Usually intervals of confidence wide considerably in those zones. The matters discussed in Section 2., making use of all available information, are critical to reduce these uncertainties, in particular:

- Geological prospection to inform on events occurred in the last 10^3 to 10^5 years and on the extend of fault rupture length.
- Historical records to inform on events covering periods of 200 years or more.
- Mechanics of generation and propagation to set some bounds on upper values to expect at a site.

5.3. Convolution of Processes

We obtain the final probability distribution function of strong ground motion parameters, convoluting the random variable for strong motion given the process of occurrence with the random variable representing the occurrence, using the continuous version of eq.(27). As the distribution of the first variable (ground motion parameter or spectral value) is of extreme type I, section 4.3.3., with much smaller coefficient of variation than the second variable (closer to extreme type II), for probabilities of exceedence greater than 10^{-3} per year, the second distribution tends to control the final distribution, (Borges et al.1971). In this case the selection of ground motion parameters can be obtained using the hazard results for a given probability of exceedence and the average spectral values (50% percentile); there is no reason to use average $+\sigma$. If risk studies require a probability of exceedence smaller than 10^{-3}, then the above simple rule may not apply

	A	B	C	D	E
1958	1	1	1	3	2
1972	1	2	2	1	1
1976	2	2	2 + 3	1 + 4	1
1979	3	2	2 + 3	1 + 4	1
1983	3	1 + 2	3	3	2 + 3

CODE

CODE

A - Tectonics
1 - Geologic units
2 - Alignments
3 - Active structures

B - Earthquake catalogues
1 - Historical seismicity (up to 1900)
2 - Instrumental seismicity (1900 - 1980)

C - Mathematical Modelling
1 - Deteministic
2 - Experimental or empirical
3 - Source zones

D - Attenuation
1 - Accel. val
2 - Int MM (radial)
3 - Int. MM (non-radial)
4 - Instrumental

E - Seismic zoning
1 - Accel (ISO)
2 - Intensity MM (ISO) - inland earthquake
3 - Intensity MM (ISO) - dist earth

Figure 22(a). Updating seismic hazard studies in Portugal.

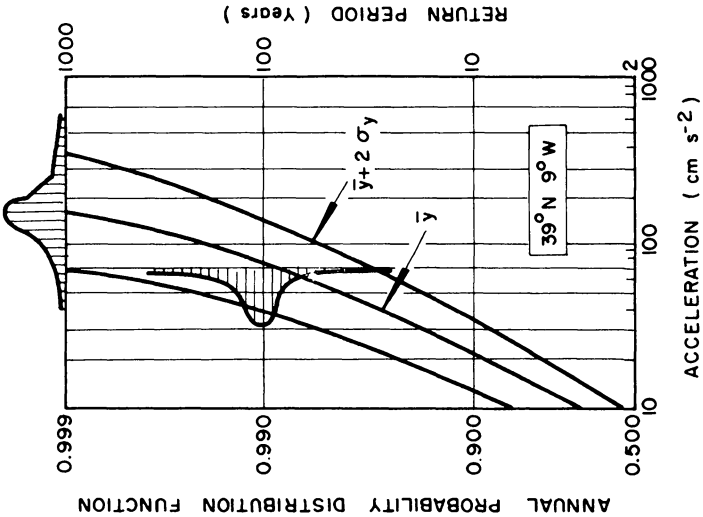

Figure 21. Influence of parameter values and uncertainties in final hazard estimates.

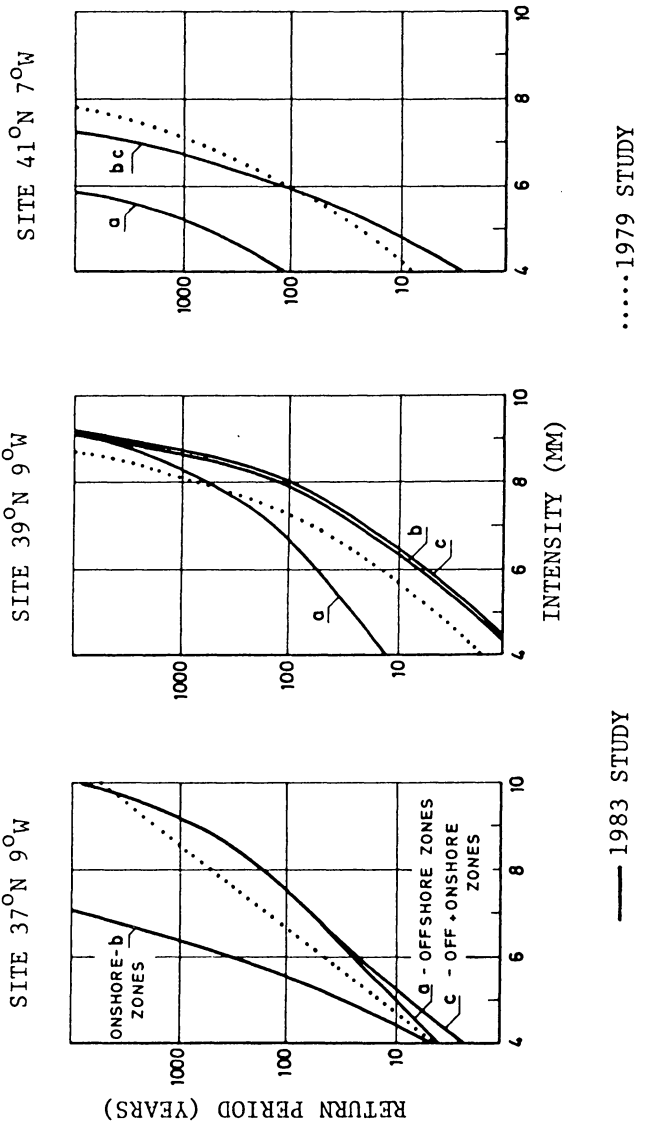

(b)

Figure 22(b). (Cont.)

TABLE 2. MAIN CHARACTERISTICS OF EARTHQUAKE OCCURRENCE AND ATTENUATION OF WAVES IN THE IBERO-MOGREBI REGION.

	PORTUGAL	SPAIN (South)	ALGERIA (North)
Quality of data	Varies quite considerably with historical epoch. Difficulty in assigning intensities for ancient earthquakes.	Idem	No data available until 1800. Very good information on geological dating of large events (1000 years).
Mecanism of generation.	Two types of earthquakes: 1) large magnitude, distant offshore epicenter, in the Atlantic; 2) moderate magnitude generated inland at normal and reverse fault systems.	The large offshore magnitude still influence the southwest coast. Moderate earthquake in reverse faults inland	Large inland earthquake generated in abundant reverse faults.
In time	Non-stationary in time and space. Clustering phenomenon. Characteristic earthquake. With large number of after shocks.	Non-stationarity in time. Large magnitude in the past. Very active with small events, nowadays	Great activity this century. Tectonic evidence in the last 1000 years in agreement with seismicity data, assigning a 500 years time interval between large events. Long term slip rates indicates much longer intervals.
In space	Difficult to correlate earthquakes with given fault traces. Shallow focus (0 - 15 Km)	Idem (0 - 15 Km)	Idem except for very large earthquakes (0 - 15 Km)
Attenuation of waves from data on intensities	Anisothropy in offshore earthquakes. Near field data with saturation (MMI =X) Fast attenuation for inland earthquakes.	Some anisothropy. Fast attenuation with distance but great variability from zone to zone.	Poor data, some anisothropy; fast attenuation.

TABLE 3. SUMMARY OF METHODOLOGIES USED IN HAZARD ANALYSES FOR THE IBERO-MOGREMI REGION.

	PORTUGAL	SPAIN (South)	ALGERIA (North)
Definition of source zones	Historical Seismicity and considerations on tectonics of Quaternary. A few different sets of source areas were used Very detailed	Historical seismicity and considerations on large geological units. Different authors use different sets of source areas.	Historical seismicity and detailed Quaternary investigations for the Ech Cheliff area One single skeme defining source-lines (identified active faults) and source areas
Characterization of seismic activity in each zone	Recurrence relations obtained with historical and instrumental data using various time periods; upper magnitude obtained from extreme value of seismicity data. Sensitivity analysis on fitting techniques and on grouping several zones together	idem Upper magnitude judged on historical seismicity.	Recurrence used historical seismicity and dating geological evidence of earthquakes occurrences. Upper magnitude based on length tectonic structures. Several alternatives were weighted according to prior expert opinion.
Wave attenuation	Transformation of MMI values into peak acceleration and used linear square fitting of smooth isosseismals. Use direct MMI values and allow some degree of anisothropy in attenuation compare with formulae in other regions.	Idem. Attenuations always taken with radial symmetry. Both MSK and peak acceleration were used. Fitting was made through the individual points not having any previous smoothing.	No use of local information. Attenuation formulae taken from instrumental values in California
Mathematical modeling	Method of source zones; method of extreme value analysis of observed events at a given site Several alternatives. Comparison with observed seismicity.	Idem; used also a combined method of source zones where the source is represented only by the extreme occurrence observed inside.	Method of sources only, using a bayesion approach or a logic tree concept to direct incorporate parameter uncertainties.
Presentation of results	Maps for acceleration, velocity, displacement and MMI. Intervals of confidence.	Idem. Several alternative maps. No interval of confidence.	Maps for acceleration; response spectra for isolated sites

TABLE 4. MAIN RESULTS OBTAINED IN THE HAZARD ANALYSES FOR THE IBERO-MOGREBI REGION, ERRORS INVOLVED.

	PORTUGAL	SPAIN (South)	ALGERIA (North)
Mean upper values, $\bar{y}$ Prob>0.002	High intensities, (IX) Low acceleration (0.15g)	Idem: (IX) (0.2g)	High accelerations (0.5g)
Regional variations	1:3	1:2	1:4
Uncertainties in acc.	1:4 $(\bar{y}+2\sigma)$: $(\bar{y}+2\sigma)$	-	25% - 35% (?)

and the convolution has to be carried out for the specific site hazard distribution. And the smaller the probability of exceedence the larger the influence of distribution asymptotic behavior in the tail.

5.4. Simulation of Time-series

Dynamic analysis of important structures and research studies involving experimental or nonlinear behavior requires the ground motion in the form of a time series compatible with given a spectral shape as derived in previous sections. The procedures to obtain the desired accelerograms are essentially summarized in the following (Penzien 1985): 1) use real accelerograms; 2) use spectral compatible accelerograms; and 3) use stochastically generated accelerograms (Duarte, 1984).

The first procedure requires the access to a large variety of recorded motions and its selection should consider the tectonic and morphologic similarities referred in 2.4. Unfortunatly, it is common practice to use just the one single record, the one available at the moment. The increased attention given to the creation of strong motion data centers (Coffman et al.1985) will facilitate the application of this methodology. The second procedure starts off with one given accelerogram adequate to the site and, using the concepts described by eqs.(7 to 10), adjust its FFT amplitudes until matching the desired response spectrum. The convergence of this iterative algorithm depend on the initial time history, but in general good results are obtained in two or three iterations. The third procedure is identical with the second one but requires the generation of a first time-series. And this can be performed in more or less sophisticated ways as referred previously. Caution should be exercised when generating three components of ground motion: start with independent time-series in the reference system of principal directions and then rotate the system to a necessary direction.

In all cases filtering is needed to provide adequate control of accelerations, velocities and displacements.

If the ground motion to expect at a site is originated at completely different source-mechanism, exhibiting different spectral shapes, each source should be treated separately. Superposition can only be done within the concept of RS.

6. CONCLUDING REMARKS

The knowledge on the phenomenon of occurrence of earthquakes has improved quite significantly in the last decade and one can rely on good estimates of the probability distributions for a few regions in the world. In others, the estimates show large uncertainties.

The earthquake ground motion has a random character due to the complex phenomenon of generation and propagation of seismic waves. Many variables contribute to this randomness, and consequently the representation of ground motion cannot contain all those features. Only the most important ones must be contemplated:

- arrival of main phases, such as P, S, and surface waves, in all three components;

- the previous feature should be satisfied in both frequency and amplitude;
- attenuation of waves should be carried out separately for frequency bands, higher frequencies attenuating faster;
- directivity effect should be included in situations of clear understanding of propagating rupture;
- other anisothropies that are specific to some particular seismic environment should also be brought into the model.

The combination of uncertainties existing in both processes increases the confidence intervals on final estimations, especially towards the zones of low probability of occurrence.

The random character of the representations will tend to decrease when the knowledge on mechanisms of occurrence, generation, and propagation are better understood. But still a long way to go before one can rely on just a complete deterministic analysis.

Acknowledgements

The material presented is included in the Earthquake Engineering course that the author teaches at the Instituto Superior Tecnico, Lisbon, and is based on the experience gained at LNEC. Some examples taken from SMART-1 Project were obtained during a sabbatical leave at the Seismographic Station, University of California, Berkeley, in 1985. Erica Orvis edited an early version of the manuscript.

REFERENCES

Azevedo, J. J. (1984) - 'Characterization of Structural Response to Earthquake Motion', PhD Dissertation, Dept. Civil Eng., Stanford University.

Barrodale, I.; Erikson, R. E. (1980) - 'Algorithm for Least Square Linear Prediction and Maximum Entropy', Geophysics, Vol 45, No 3, pp 420-446.

Bender, B. (1984) - 'Incorporating Acceleration Variability into Seismic Hazard Analysis', Bulletin Seismological Society of America, Vol 74, No 4, pp 1451-1462.

Bolt, B. A. (1981) - 'Interpretation of Strong Ground Motion Records', Miscellaneous Paper S-73-1, Report 17, State-of-the-Art for Assessing Earthquake Hazards in the United States, U.S. Army Engineer Waterways Experiment Station, Vicksburg.

Bolt, B. A.; Abrahamson, N. A. (1982) - 'New Attenuation Relations for Peak and Expected Accelerations of Strong Ground Motion', Bulletin Seismological Society of America, Vol 72, No 6, pp 2307-2321.

Bolt, B. A.; Loh, C. H.; Penzien, J.; Tsai, Y. B.; Yeh, Y. T. (1982) - 'Preliminary Report on the SMART1 Strong Motion Array in Taiwan', Report UBC/EERC-82/13, University of California, Berkeley.

Borges, J. F.; Castanheta, M. (1971) - 'Structural Safety', Laboratorio Nacional de Engenharia Civil, Lisboa.

Brune, J. N. (1976) - 'The Physics of Earthquake Strong Motion' in Seismic Risk and Engineering Decisions, chapter 5, pp 140-177, C. Lomnitz and E. Rosenblueth (editors), Elsevier, Amsterdam.

Bouchon, M.; Aki, K. (1982) - 'Strain, Tilt, and Rotation Associated with Strong Ground Motion in the Vicinity of Earthquake Faults', Bulletin Seismological Society of America, Vol 72, No 5, pp 1717-1738.

Coffman, J. L.; Godeaux, S. (1985) - 'A Catalogue of Strong Motion Accelerograph Records', Report SE-38, World Data Center A for Solid Geophysics, US Dept. Commerce, NOAA, Boulder.

Cornell, C. A. (1971) - 'Probabilistic Analysis of Damage to Structures Under Seismic Loads', in Dynamic Waves in Civil Engineering, pp 473-494, D. A. Howells, I. P. Haigh and C. Taylor (editors), Wiley Interscience, London.

Costa, R. A.; Oliveira, C. S. (1985) - 'Models of the Seismic Stochastic Process of Occurrences in Portugal Considering the Time-Space-Size Interrelations', Abstract submitted to the 8th Europ. Conf. Earthq. Eng., Lisbon, Sept 1986.

DeHerrera, M. (1980) - 'A Time Domain Analysis of Seismic Ground Motions Based on Geophysical Parameters', PhD Dissertation, Dept. Civil Eng., Stanford University.

Duarte, R. T. (1984) - 'Spatially Variable Ground Motion Models for the Earthquake Design of Bridges and Other Extended Structures', 8th World Conf. Earthq. Eng., Vol II, pp 613-620, Prentice Hall, Englewood Cliffs, NJ.

Goula, X.; Bouchon, M. (1985) - 'The Earthquake of June 11, 1909 (France), Part II - Focal Parameter Discrimination by Ground Motion Simulation', Abstract submitted to the 8th Europ. Conf. Earthq. Eng., Lisbon, Sept 1986.

Harichandran, R.; Vanmarcke, E. (1984) - 'Space-Time Variation of Earthquake Ground Motion', Research Report R84-12, Dept. Civil Eng., Massachussetts Institute of Technology.

Joyner, W. B.; Boore, D., M. (1981) - 'Peak Horizontal Acceleration and Velocity from Strong Motion Records from the 1979 Imperial Valley, California, Earthquake', Bulletin Seismological Society of America, Vol 72, No. 6, pp 2011-2038.

Kanasewich, E. R. (1981) - 'Time Sequence Analysis in Geophysics', The University of Alberta Press, Canada.

Kulkarni, R. B.; Youngs, R. R.; Coppersmith, K. J. (1984) - 'Assessment of Confidence Intervals for Results of Seismic Hazard Analysis', 8th World Conf. Earthq. Eng., Vol I, pp 263-270, Prentice Hall, Englewood Cliffs, NJ.

Loh, C. H. (1985) - 'Analysis of the Spatial Variation of Seismic Waves and Ground Movements for SMART1 Array Data', Journal of Earthquake Engineering and Structural Dynamics, in Press.

Martin-Martin, A. J.; Garcia-Yague, A. (1984) - 'Seismic Risk in the Iberia Peninsula', 8th World Conf.Earthq. Eng., Vol , pp 181-188, Prentice Hall, Englewood Cliffs, NJ.

McGuire, R. K. (1976) - 'Fortran Computer Program for Seismic Risk Analysis', US Geological Survey, Open-File Report 76-67.

Mendes-Victor, L. A.; Oliveira, C. S.; Matos, D. S.; Carvalho, A. M.; Almeida, J. M.; Nicolau, J. S.; Mendonca, M. E. (1985) - 'Bases for the Elaboration of a National Earthquake Catalogue', Abstract submitted to the 8th Europ. Conf. Earthq. Eng., Lisbon, Sept 1986.

Munoz, D.; Udias, A. (1982) - 'Historical Development of Spain's Catalogues of Earthquakes', Bulletin Seismological Society of America, Vol 72, No 3, pp 1039-1042.

Newmark, N. M. (1969) - 'Torsion in Symmetrical Buildings', Proc. 4th World Conf. Earthq. Engin., Vol , A3.19-A3.32, Santiago do Chile.

Newmark, N. M.; Rosenblueth, E. (1971) - Fundamentals of Earthquake Engineering', Prentice Hall, Englewood Cliffs, NJ.

Niazi, M. (1985) - 'Inferred Displacements, Velocities and Rotations of a Long Rigid Foundation at El-Centro Differential Array Site During the 1979 Imperial Valley Earthquake', Journal of Earthquake Engineering and Structural Dynamics , in Press.

Oliveira, C. S. (1978) - 'Seismic Risk Studies for San Francisco and for the Greater San Francisco Bay Area', Report No. UCB/EERC-78/16, University of California, Berkeley.

Oliveira, C. S.; Costa, A. C. (1983) - Analytical Studies of Old Church Towers under Seismic Loads', Poster presented at the Int. Assoc. Bridges Str. Eng., IABSE Symposium, Venice.

Oliveira, C. S.; Costa, A. C. (1984) - 'Updating Seismic Hazard Maps', 8th World Conf. Earthq. Eng., Vol I, pp 303-310, Prentice Hall, Englewood Cliffs, NJ.

Oliveira, C. S.; Penzien, P. (1985) - 'Spatial Variation of Seismic Ground Motion Based on SMART-1 Array Data', Paper presented at the Earthquake Engineering Lifeline Seminar, National Taiwan University, Taipei.

Penzien, J.; Watabe, M. (1975) - 'Characteristics of 3-Dimensional Earthquake Ground Motions', Journal of Earthquake Engineering and Structural Dynamics, Vol 3, pp 365-373.

Penzien, J. (1985) - 'Lecture Notes on Earthquake Engineering Analysis', University of California, Berkeley.

Pereira, J.; Oliveira, C. S.; Duarte, R. T. (1977) - 'Direct and Indirect Conversions from Power Spectra to Response Spectra', 6th World Conf. Earthq. Eng., Vol 2, pp 279-284.

Scherer, R. J.; Schueller, G. I. (1982) - 'On the Correlation Between xyz-components of Earthquake Accelerations', 7th Europ. Conf. Earthq. Eng., Vol 2 pp 169-177.

Slemmons, D. B. (1977) - 'Faults and Earthquake Magnitude', Miscellaneous Paper S-73-1, Report 6, State-of-the-Art for Assessing Earthquake Hazards in the United States, U.S. Army Engineer Waterways Experiment Station, Vicksburg.

Tilliouine, B.; Azevedo, J. J.; Shah, H. C. (1984) - 'A Computer Program for Nonstationary Analysis and Simulation of Stong Motion Earthquake Records', The John A. Blume Earthq. Eng. Center, Report no.63, Stanford University.

Van Gills, M. (1983) - 'The Earthquake Catalogue of the Europ. Econ. Commun. Countries', paper presented at the 2nd CSNI Specialist Meeting for Probabilistic Methods in Seismic Risk Assessment for Nuclear Power Plants, Livermore.

Yim, C-S.; Chopra, A. C.; Penzien, P. (1980) - 'Rocking Response of Rigid Blocks to Earthquakes', Report No. UBC/EERC-80/02, University of California, Berkeley.

SEISMIC SOURCE REGIONALIZATION

Vedat Doyuran
Earthquake Engineering Research Center
Middle East Technical University, Ankara
Turkey

ABSTRACT. Seismic source regionalization problem entails the full use of geologic, tectonic, historical, instrumental macro-seismic records, and micro-earthquake survey findings. The seismic sources are usually delineated on the basis of the uniformity of tectonic features, homogeneity of earthquake occurrences, and the consistency of focal mechanisms.

In seismic source regionalization studies large-magnitude shallow earthquake records of both historical and instrumental extending as far back in time as possible, provide the most valuable seismological data. The geological aspects of seismic source regionalization rely upon the sound knowledge of the late Quaternary history.

The plate tectonics concept coupled with the information on neotectonics provide a considerable insight to aid the understanding of major earthquake sources both of the global and the regional scales. Major seismic sources of the Anatolian peninsula include the North Anatolian Fault, East Anatolian Fault, Bitlis Suture Zone, and the West Anatolian Graben Complexes. These seismic sources account for most of the devastating earthquakes which took place in the Anatolian peninsula.

1. INTRODUCTION

Evaluation of the seismic hazard plays an important role in the site selection and in seismic design decisions of engineering structures. The seismic hazard analysis requires consideration of both local and regional aspects of earthquakes which involves the disciplines of seismology, geology, geophysics, geodesy, and engineering.

The more frequent occurrence of earthquakes in some areas than others is readily apparent from any review of seismological data. Few now doubt that earthquakes and surface faulting are related. The association of earthquakes with well defined faults throughout the world constitutes the basic philosophy behind seismic source regionalization.

The emerging field of plate tectonics has provided considerable insight to aid the understanding of major global courses of earthquakes. In recent years very detailed geological studies have been conducted in Turkey in conjunction with siting nuclear power plants. These studies,

M. O. Erdik and M. N. Toksöz (eds.), Strong Ground Motion Seismology, 461–476.
© 1987 by D. Reidel Publishing Company.

and others as well, have led to a better understanding of the seismicity and the structure of the Anatolian peninsula and subsequently have led to more detailed seismic source regionalization maps. The tools used to prepare such maps include studies of geologic history, current concepts of plate tectonics, in-situ stress measurements, seismic record, geophysical investigation, and geological mapping. The seismotectonic maps prepared in such a manner provide rather detailed assessment of the overall seismicity in a given locale. Where long term seismological data for some regions are very insufficient or not available at all, seismotectonics represent the only source of information required for defining seismicity, identification of the epicenters of future earthquakes and estimation of their expected magnitudes. The seismotectonics maps are thus indispensable for the delineation of seismic source regions.

In the following sections, the geological aspects of seismic source regionalization will be emphasized. The discussion on the fault activity will be followed by seismotectonic map preparation and neotectonic models proposed for Turkey.

2. DEFINITIONS

Although there are no universally accepted definitions for the following terms, for the purposes of this paper the following definitions will be sufficient to clearify certain points.

Active Fault : A fault that has slipped during the present seismotectonic regime and is therefore likely to have renewed displacement.

Capable Fault : A fault which has a significant potential for relative displacement at or near the ground surface (I.A.E.A., 1979).

Macroearthquake : Earthquakes having magnitudes equal to or greater than 3.0 (I.A.E.A., 1979).

Macroseismicity : Seismicity of a level such that it implies significant, coherent, sustained tectonic activity. With respect to individual faults or fault zones, macroseismicity is seismicity of a level that implies a significant and constant tectonic driving mechanism (I.A.E.A., 1979).

Microearthquake : Earthquakes having magnitudes less than 3.0 (I.A.E.A., 1979).

Neotectonics : The tectonics of the Quaternary period or more generally, the tectonics of the latest stages of the Alpine orogenesis. (I.A.E.A., 1979, Manfredini and Ventriglia, 1974).

Seismic Risk : The expected number of lives lost, persons injured, damage to property, disruption of economic activity due to a particular earthquake.

Seismically Active Structure : A structure or a fault which exhibits seismicity at a level which indicates significant coherent activity on structure or fault, regardless of whether or not geologically young movement on it can be demonstrated at the earth's surface (I.A.E.A., 1979).

Seismic Hazard : Is the probability of occurrence, at a given place or within a given period of time, of different levels of ground motion due to expected earthquakes.

Seismotectonic Province : A geographic area characterized by similarity of geological structure and earthquake characteristics (I.A.E.A., 1979).

Surface Faulting : The cracking or the differential displacement of the ground caused by the movement of fault at or beneath the surface (I.A.E.A., 1979).

Tectonic Structure : A large-scale structural feature resulting from deformation of the earth's crust (I.A.E.A., 1979).

3. SEISMIC REGIONALIZATION AND ZONING

Seismic zoning may be defined as the subdivision of a region into areas or zones that have relatively similar exposure to various earthquake - associated effects, such as surface fault rupture, ground shaking, ground failure, etc. In this context, consideration must be given to the geology, seismicity, soil type, groundwater level, and structure type (Kulhawy and Ninyo, 1977). The last three items refer to specific site conditions which require evaluation individually, while the first two refer to broader regional conditions which can be generalized to some degree.

Seismic regionalization, on the other hand, involves delineation or modeling seismic sources. The seismic sources may be modeled as point, line or area source. Where seismicity is diffused over a large area without identifiable active and/or capable fault, tectonic province approach is used, which delineates different provinces as area sources. All known active and/or capable faults are modeled by line sources. In some cases several line segments are used to model a single fault. The earthquakes associated with known faults are included with a band drawn around each source. Individual events that are not associated with line or area sources are modeled as point sources.

To develop a reasonable model a minimum of five types of inputs are generally needed. These include the location of all faults; behavior of all faults; geographical distribution of past earthquake data; focal depth characteristics for each fault, and maximum credible events for each fault.

Oborn (1974) argues that potential hazards from faulting differ from one fault to another depending upon their status (main, branch, secondary) and kind (thrust, normal, reverse, transcurrent). The local geology, tectonic history and seismicity all play a major part in determining potential risks to life and property.

The geological studies contribute data for the identification and delineation of earthquake sources, assessment of earthquake size, estimation of earthquake recurrence intervals, evaluation of the potential for surface fault rupture, the ground shaking hazard, and the ground failure hazard. Seismological studies on the other hand provide data on instrumental determination of the epicenters and/or hypocenters as well as some of the important physical properties of earthquakes.

The geological aspects of seismic source regionalization generally rely upon identification and delineation of earthquake sources, that is, the active and/or the capable faults.

3.1. Criteria For Identifying Active Faults

Generally accepted criteria for the recognition of active faults are well established and described by Allen (1975); Cluff and Brogan (1974), and Slemmons and McKinney (1977) and recognitions of them has proved to be the most fundamental tool in identifying and delineating potential earthquake sources. Five general types of criteria are used to evaluate whether or not a fault is active; these are geological, including geomorphic and stratigraphic; historical, including accounts of past historic earthquakes and surface faulting; seismological, which are considered in terms of the pre-instrumental historic record and the instrumental record; geophysical, considering various remote techniques used to obtain data; and geodetic, using data from two or more precise surveys.

3.1.1. Geological Criteria

Geological criteria provide the most reliable data upon which to make judgments about fault activity. The Quaternary period, especially the Quaternary (Holocene) is generally considered sufficient by most researchers for the evaluation of recent fault activity.

Geological criteria may be discussed under two main titles, namely, geomorphic and straighraphic. Geomorphic evidences include fault scarps, triangular facets, fault scarplets, fault rifts, shutterridges, offset streams, closed depressions (if small and containing water, they are known as sag ponds, otherwise fault-sags), fault valleys (i.e. graben valleys) fault troughs (rift zones), etc. Many of these geomorphic features are well observed along the North Anatolian Fault zone.

Stratigraphic evidence of active faulting include displaced rocks of Pleistocene and/or Holocene.

3.1.2. Historical Criteria

Historical criteria rely upon historical record of earthquakes and historic events of surface faulting. However, due to uncertainties involved in obtaining early historic records, evidence of parts earthquakes may or may not be indicative of past surface faulting. Some early accounts of surface faulting such as difference in elevation, open fissures, changes in spring activity, and so forth, are rather rare and they must be considered with great caution.

3.1.3. Seismological Criteria

Clusters of shallow earthquakes, especially those with Richter magnitudes greater than 5, commonly indicate the presence of potentially active geological structure (Albee and Smith, 1966). Small magnitude earthquakes, due to their generally random distribution, can be related to active faults less convincingly. Large magnitude (7 1/4 or greater) shallow earthquakes are nearly always accompanied by surface faulting; those with magnitudes 5 1/2 or smaller, only rarely. The extent of surface faulting is largely related to the magnitude and focal depth of an earthquake. The maximum magnitude earthquake that a fault is capable

of generating is in all probability a function of the length of the pre-existing fault (Oborn, 1974).

A seismically active fault may not always generate a surface faulting. For example, deep-focus earthquakes have not been associated with surface faulting (Cluff and Brogan, 1974).

The seismological data are most useful especially when it is not possible to identify a fault with conventional geological techniques due to heavy vegetation or water cover, and concealement with extremely young floodplain deposits.

3.1.4. Geophysical Criteria

Geophysical criteria depend upon identifying anomalies within geologically young sediments. Such anomalies may be identified using conventional seismic,electrical, geometric, and gravimetric techniques. However, geophysical data must be interpreted with other definitive evidences. Although geophysical techniques may be utilized to reveal the existence of a fault, they do not, however, give sufficient criteria in terms of its acitivity.

3.1.5. Geodetic Criteria

Precise geodetic surveys may be utilized to show if a seismic slippage along a fault (fault creep) is taking place or not. Geodetic data may also indicate an accumulation of strain. Due to difficulties involved in obtaining long term precise measurements the geodetical criteria are not as usable as other historical or geological criteria.

4. SEISMOTECTONIC MAPS

Delineation of seismic and related regionalization studies must be based upon reliable seismotectonic maps. The seismotectonic maps are prepared by plotting earthquake epicenters on a base map which contains well defined tectonic structures (mainly faults). Since macro-earthquakes generally provide a better and more reliable basis of correlation with the existing faults, it is thus recommended that large magnitude shallow earthquake epicenters should be plotted on the tectonic base map. Under certain circumstances records of micro earthquakes can be of considerable value in delineating certain ill-defined structures. For example, the epicentral distribution of after shocks of major earthquakes, if concentrate along well defined belts, may indicate the existance of active or capable faults. Therefore, it is required that the available records, both historic and instrumental, be collected extending as far back in time as possible.

For the Eastren Mediterranean region the plot of earthquake epicenters indicate rather well defined seismic zones (Figure 1). These zones can easily be correlated with major tectonic features of the region.

Delineation of seismic sources must be made with recognition of the associated geologic and tectonic information. Such information may be obtained from published sources, remote sensing data, such as satellite

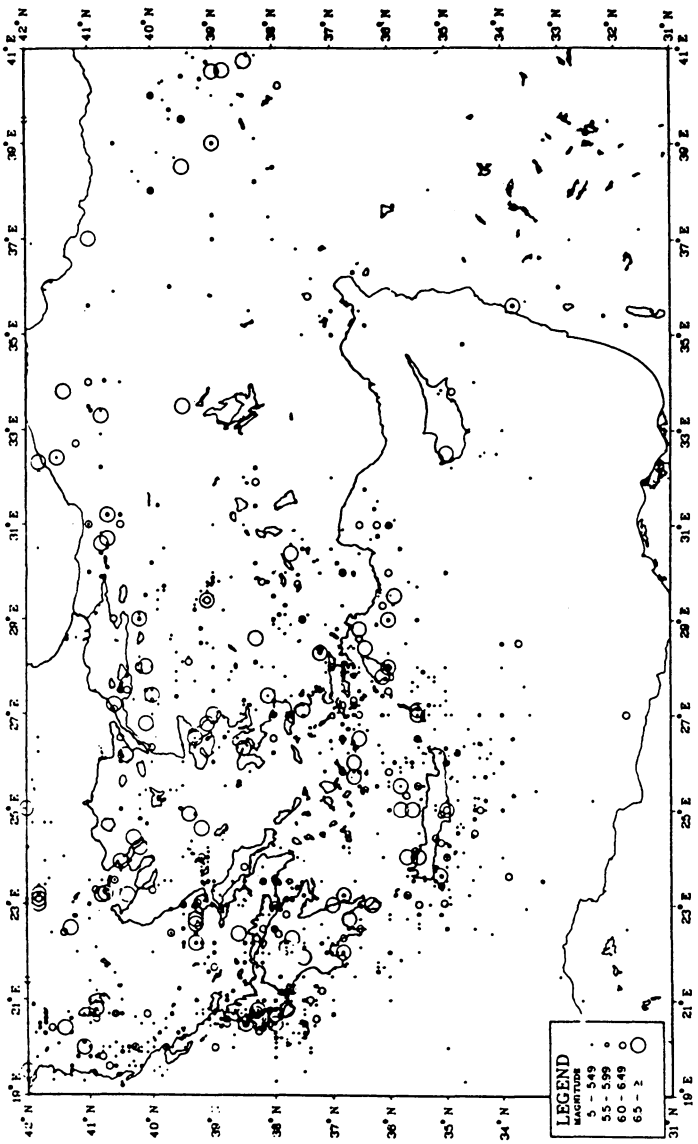

Figure 1. Distribution of Earthquake epicenters in the Eastern Mediterranean region

photographs, side-scan radar, aerial photographs, aeromagnetics, and gravimetrics. The structural features, or more specifically the faults, thus established are plotted on a base map. Where definite geological field evidences exist it is recommended to distinguish the faults as dead or active using appropriate symbols on the tectonic map.

According to Rast and Saegesser (1980) seismic source regionalization should follow the following principles:

1. Source boundaries should be defined with regard to the subsequently applied seismic hazard methodology.
2. Sources (or regions) should be defined as areas with seismic characteristices as homogeneous as possible.
3. Between sources (regions) of different seismic potential, the boundary should be located close around the "hard core" of the more active one.
4. In areas of statistically sufficient number of reliable events, boundaries should be mainly based on seismic data as expression of tectonic activity and backed up by tectonic arguments.
5. In cases of insufficient number of events or large uncertainties attached to them the existence of a boundary has to be proofed by arguments based on the most dominant tectonic or seismic features.

Usually, the purpose of seismotectonic studies is to define geographic regions within each of which similar earthquake potential exists. The seismotectonic provinces thus established provide the bases of seismic source regionalization studies. The seismotectonic map for Turkey, prepared by Erdik and Mathur (1979), is given in Figure 2. In this map, only the large events ($M \geq 5.9$) recorded within the period 1900-1977 are plotted. From figure 2 it is evident that the large events show an excellent correlation with major tectonic features of Turkey.

5. PLATE TECTONIC MODELS AND THE SEISMIC SOURCES

Concentration of earthquake epicenters around some of the major continental blocks and along the midocean ridges can readily be seen on any global seismicity map. These maps reveal major seismic sources on a global scale. In certain regions of the world, such as in the Eastern Mediterranean area the picture is somewhat complicated. This complication generally arises from the existence of smaller and rapidly moving plates.

Turkey lies within the Mediterranean sector of the Alpine-Himalayan orogenic system. The Alpine orogeny is produced as a result of compressional motion between Europe and Africa, whereas the Himalayan orogeny is resulted from India-Asia collision. The distribution of seismicity within the alpine-Himalayan systems is not homogeneous. The seismic activities are mostly concentrated along the plate margins. A number of plates, large or small, have been identified in the Eastern Mediterranean region on the basis of present-day seismicity at their margins. According to Morgan(1968), Le-Pichon (1968), and McKenzie (1970) only three plate boundaries of any importance enter the area and therefore only three major plates are involved in the tectonics of the Mediterranean region. These plates are the African, Eurasian, and Arabian plates.

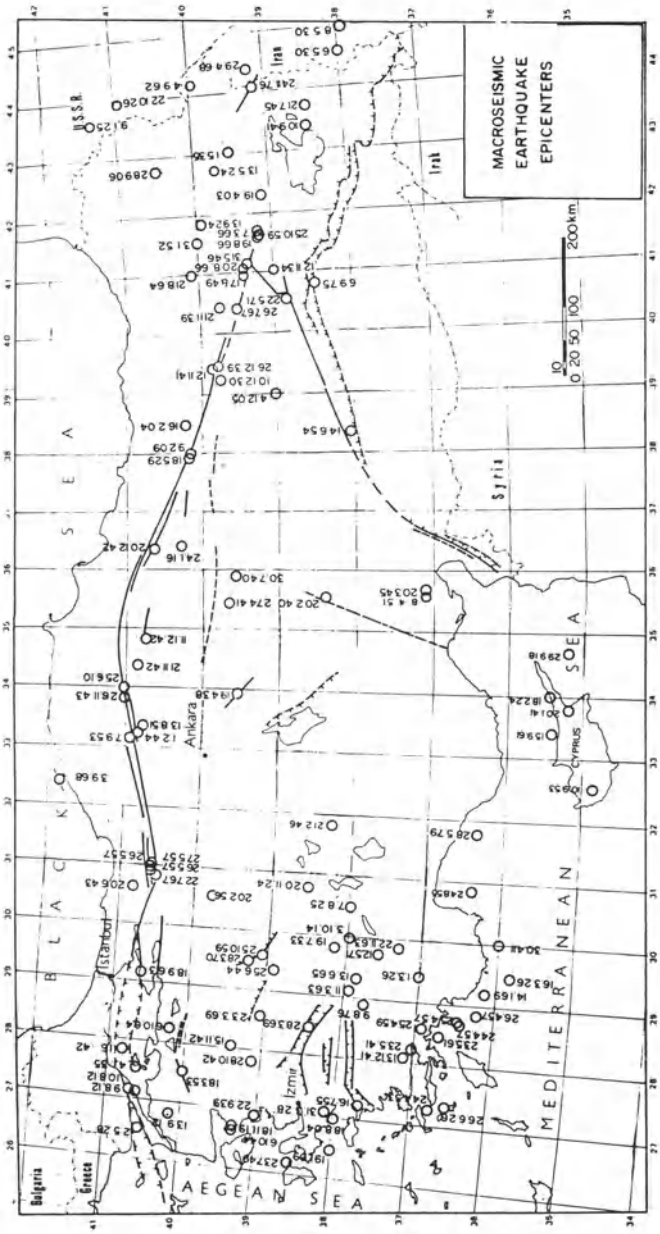

Figure 2. Seismo-Tectonic Correlation for Turkey (After Erdik and Mathur, 1979)

Although the boundaries of these three plates account for most of the tectonic and/or seismic activity the situation in the Eastern Mediterranean, however, is somewhat complicated. The cause of local increase in seismic activity of this region is attributed to the existence of smaller but rapidly moving plates (McKenzie, 1970 and 1972; Dewey et al., 1973). According to McKenzie (1970 and 1972) one of these plates contain the Aegean part of Greece, Crete, and part of Turkey (the Aegean plate), and the other contains most of Turkey and Cyprus (the Turkish or the Anatolian plate). He also introduced a third plate which contains the northern and central Greece as well as northern Aegean Sea for which no name was assigned (Figure 3).

In the McKenzie model the boundary between the Aegean and the Turkish plates is rather vaguely defined. Alptekin (1973) points out the shortcomings of this boundary by rejecting the mechanism with which such a boundary causes the graben systems in the western Anatolia and thus he combines the two plates and calls it "the Aegean-Turkish plate" (Figure 4). Dewey and Şengör (1979) suggest and alternative solution for Aegean tectonics. They do not seem to agree with McKenzie's (1972) Aegean plate and rather they propose Peloponnesian plate in the central Aegean and Cretan plate in the south. They, however, seem to agree with McKenzie's plate in the northern Aegean and they call it the "Macedonian plate". Dewey et al., (1973) introduced another plate in the eastern Anatolia called the "Van plate" (Figure 5).

The seismotectonic model proposed by Papazachos (1974), however, further complicates the picture. Based on geographic and vertical distribution of the foci of earthquakes occuring between 1901 and 1971 as well as on the fault plane solutions of earthquakes occuring between 1948 and 1969, Papazachos (1974) defined several other smaller blocks (plates) within the Aegean region. From north to south, these blocks include the Rhodopean, Olympus, Saros, Northern Anatolian, Western Turkey, Taurus, and Aegean (Figure 6).

5.1. Delineation of the Seismic Sources

Although the plate tectonics models given above bring out the fact that the regional tectonics is somewhat complicated, the proposed models and the associated seismicity, however, reveal that many seismic sources located at the plate boundaries are common in all models. Figure 7 depicts a synthesis and compilation of these common features to constitute the seismic source regionalization for Turkey. For the Anatolian peninsula, the seismic sources named as North Anatolian, Horasan-Narman, Çaldıran, Bitlis, East Anatolian, Cyprus, Cretan, and the Anatolian Trough encompass the micro-plate boundaries; the seismic sources named as Edremit-Bakırçay-Simav-Gediz, Küçük Menderes-Büyük Menderes-Kerme, and Cyclades are correlated with the intra-plate tectonics and seismicity; and the seismic source titled Fethiye stands for a stress concentration zone.

5.2. Description of Seismic Sources

North Anatolian : It corresponds to the North Anatolian Fault (NAF) ,

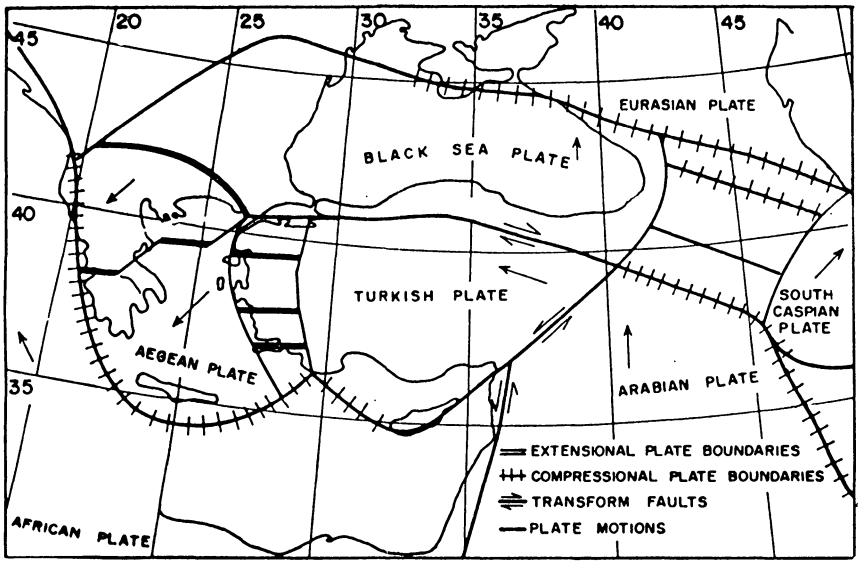

Figure 3. Plate Tectonics Model (After Mc Kenzie, 1972)

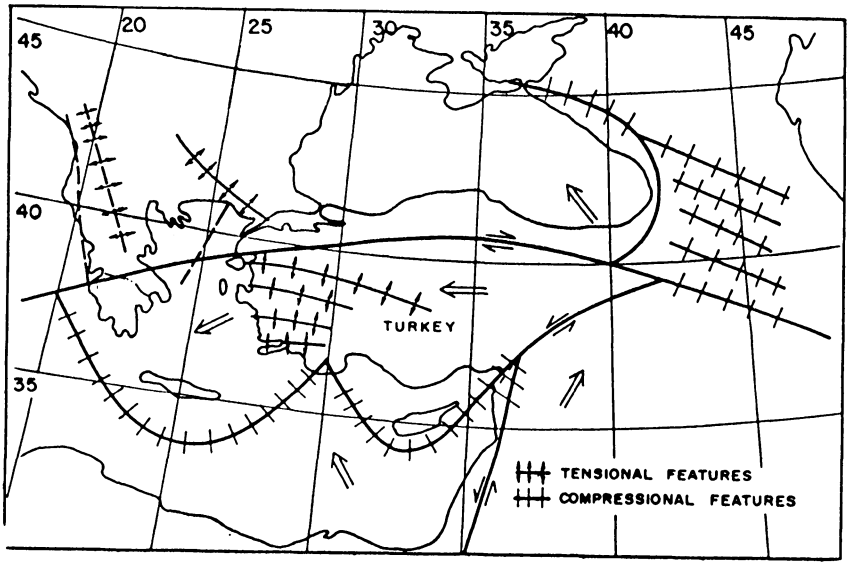

Figure 4. Plate Tectonics Model (After Alptekin, 1973)

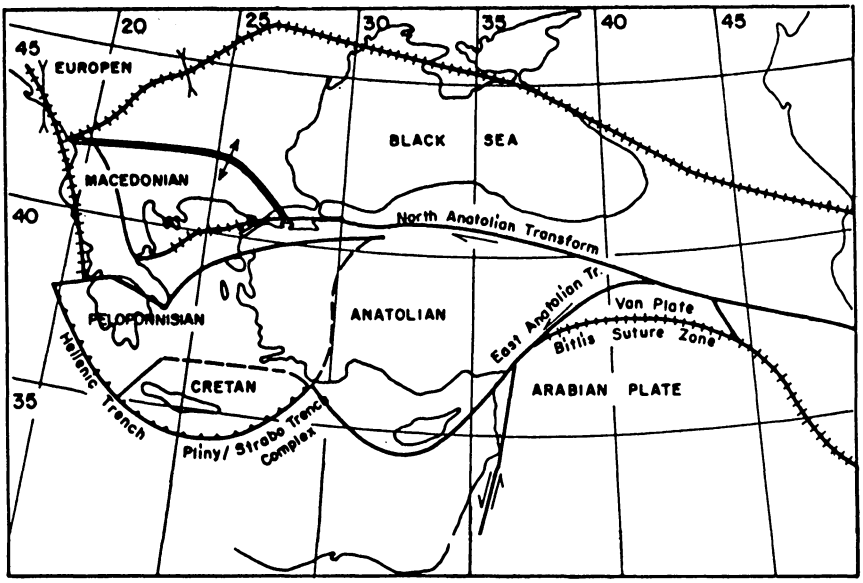

Figure 5. Plate Tectonics Model (After Dewey et.al.,1973,1979)

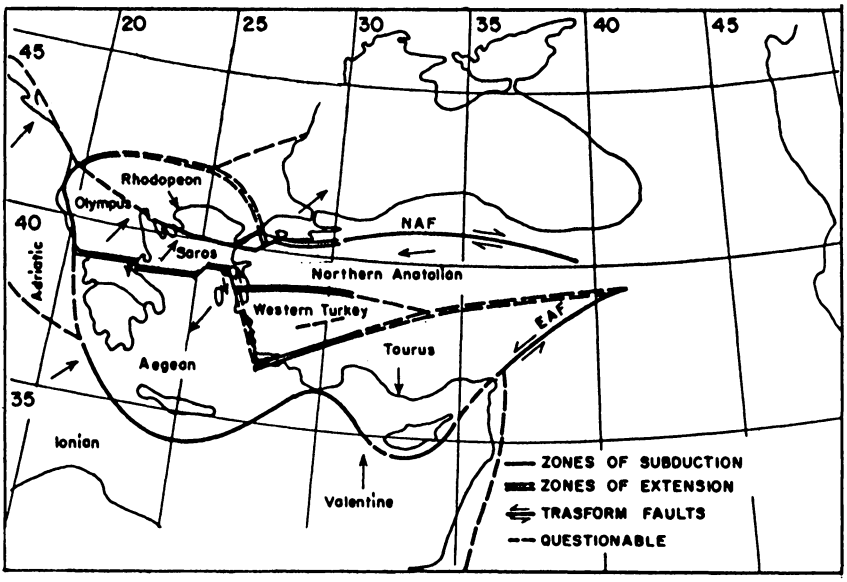

Figure 6. Plate Tectonics Model (After Papazachos, 1974)

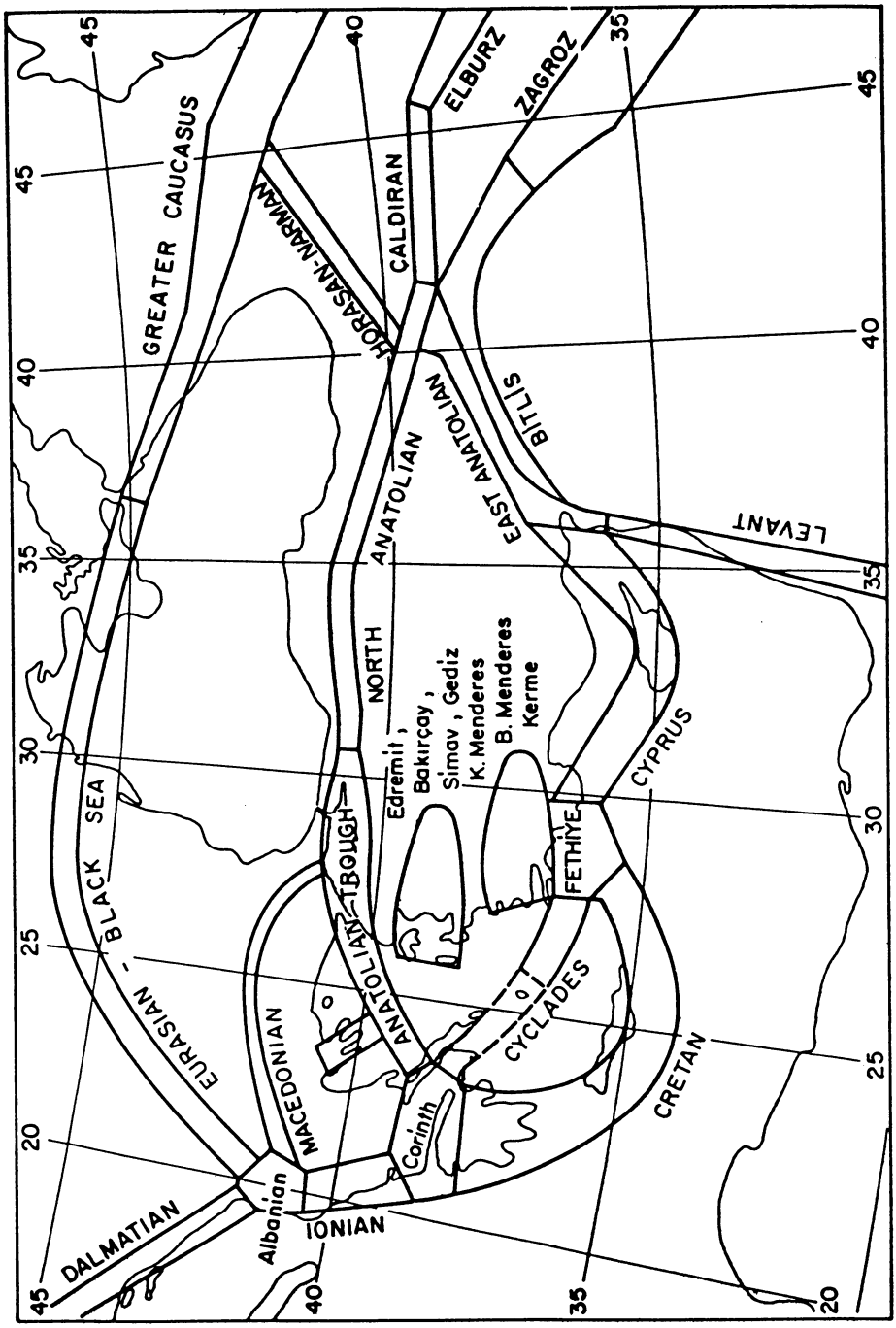

Figure 7. Seismic source for Turkey and its surroundings.(After Erdik et al. 1982)

which constitutes the boundary between the Anatolian and the Black Sea plates. NAF also takes up the relative motion between the two plates. It is a morphologically distinct and seismically active right lateral strike slip fault.

Horasan-Narman : The NE-SW trending seismic zone which seems to be forming a northern conjugate of the North Anatolian fault zone is referred to as Horasan-Narman after the destructive earthquake (M = 6.9,USGS) took place on 30 October 1983. The earthquake produced surface faulting of approximately 12 km long and characterized by left-handed strike slip motion. The zone probably corresponds to the Abul Samsar fracture zone also extending NE-SW and traversing the geological structures of the Caucasus. According to Nowroozi (1971) the Abul Samsar fracture zone accounts for most of the seismic activity represented by a transverse trend of epicenters within the Lesser Caucasus.

Çaldıran : Çaldıran seismic zone accounts for several earthquakes east of Karlıova (e.g. Varto and Çaldıran) which produced right-lateral surface ruptures but lacking the continuity and the uniformity of the North Anatolian Fault.

Bitlis : Bitlis suture zone marks the boundary between the Arabian and the Anatolian (or Van, according to Dewey et al., 1973) plates. Along this zone the Arabian plate dives underneath the Anatolian plate along a north sloping subduction zone indicating a north-south compression. The zone essentially consists of two thrust belts. The southern thrust belt extends westward until Cyprus (McKenzie, 1970) and eastward to join the Zagros Crush Zone (Dewey et al., 1973).

East Anatolian : East Anatolian Fault is a geologically distinct and seismologically active left-lateral strike slip fault which extends all the way from Antakya to Karlıova. In the northeast it joins with the North Anatolian Fault at the triple junction in the east of Karlıova and in the southwest with the Dead Sea Fault or Levant fracture, at the triple junction near Maraş.

Cretan and Cyprus : The seismic source referred to as Cretan accounts for the seismic activities associated with the subduction of African plate along Hellenic trench and Pliny/Strabo trench complex located south of Crete and Rhodes, respectively (McKenzie, 1970; Dewey and Şengör, 1979). The zone runs eastward through south of Cyprus into the Gulf of Iskenderun to join East Anatolian Fault and/or Bitlis suture zone.

Anatolian Trough : Anatolian Trough is a well established plate boundary in the northern Aegean including Saros and Sporades Troughs and terminating at the Gulf of Corinth (Morelli et al., 1975; McKenzie, 1972). The Anatolian Trough corresponds to the western continuation of the northern strand of the North Anatolian Fault. It also includes the Sea of Marmara, the İzmit-Sapanca graben, and the Gemlik-İznik graben north of Bursa.

Western Anatolian Grabens : The seismic sources shown in the western Anatolia refer to the broad region of scattered seismic activity associated with the east-west, occasionaly southeast-northwest, trending graben complexes. Edremit, Bakırçay,Simav, Gediz, Alaşehir, Küçük Menderes, Büyük Menderes, and Kerme are typical examples of these grabens. The grabens close eastward and also terminate westward shortly after the western coast line of Anatolia.

Cyclades and Fethiye : In the southern Aegean, a Tertiary-Quarternary volcanic arc produces a prominent feature. It stretches from Thebes in the northwest across the southern part of the Cyclades towards the Bodrum peninsula in southwestern Turkey. The eastward continuation of this arc has a higher seismic activity compared to its northwestern part. In the northwest and southeast the Cyclades arc terminates at the stress concentration areas referred to as Corinth and Fethiye, respectively.

6. CONCLUSIONS

In the seismic source regionalization studies knowledge of the seismotectonic characteristics of the region is indispensable. Geological record, and the late Quaternary history in particular, is a valuable tool in estimating seismicity and associated earthquake hazard. The geological history of late Quaternary faulting is the most promising source of statistics in frequencies and locations of large earthquakes. All major seismic sources in Turkey may easily be identified even in the absence of historic records by field studies of Quaternary faulting.

The one-to-one relationship between active faults and earthquakes in Turkey is so clear that a realistic seismic source model of the country may be made using the geological data. The combination of seismological and geological data (seismotectonicts) will produce even more realistic models.

7. REFERENCES

Albee, A.L., and Smith, J.L., 1966, Earthquake characteristics and fault activity in Southern California, in Engineering geology in southern California: Assoc. Engng. Geologists, Los Angeles Sec.Spec. Publ. 9-34.

Allen, C.R., 1975, Geological criteria for evaluating seismicity : Geol. Soc. Amer. Bull. 86, 1041-1057.

Alptekin, Ö., 1973, Focal mechanisms of earthquakes in western Turkey and their tectonic implications : Ph.D. Dissertation, New Mexico Institute of Mining and Technology, 190 (Unpublished)

Cluff, L.S., and Brogan, G.E., 1974, Investigation and evalutaion of fault activity in the U.S.A. : Proceedings of the Second Intrnl. Congress of the Internl. Assoc. of Engng. Geol., Sao Paulo, Brazil, 11-PC-4.1-11 PC-4.16.

Dewey, J.F., Pitman, W.C. III., Ryan, W.B.F., and Bonnin, J., 1973, Plate tectonic and the evolution of the Alpine system: Bull. Geol. Soc. America, 84, 3137-3180.

Dewey, J.F., and Şengör, A.M.C., 1979, Aegean and Surrounding regions: Complex multi-plate and continuum tectonic in a convergent zone: Bull. Geol. Soc. America, 90, 84-92.

Erdik, M., and Mathur, S.K., 1979, Evaluation of earthquake hazards-correlation of seismic activity and tectonic elements of Turkey : Bull. Intrnl. Assoc. Engng. Geol., 19, 145-151.

Erdik, M., Doyuran, V., Yücemen, S., Gülkan, P., and Akkaş, N., 1982, A probabilistic assessment of the seismic hazard in Turkey for long return periods : Proceedings. Third Internl. Earthquake Microzonation Conference, Seattle, U.S.A., 1-12.

International Atomic Energy Agency, 1979, Earthquakes and associated topics in relation to nuclear power plant Siting, A safety guide : Safety Series, 50-SG-51, Vienna, 69.

Kulhawy, F.H., and Ninyo, A., 1977, Earthquakes and earthquake zoning in New York State: Bull. Assoc. Engng. Geol., XIV, 2, 69-88.

Le Pichon, X., 1968, Sea floor spreading and continental drift : J.Geophys. Res., 73, 3661-3697.

Manfredini, M., and Ventriglia U., 1974, Seismic evaluation of an area: Proceedings of the Second Internl. Congress of the Internl. Assoc. of Engng. Geol., Sao Paulo, Brazil, 11-4.1-11-4.6.

McKenzie, D.P., 1970, Plate tectonics of the Mediterranean region : Geophys. J.R. Astr. Soc., 30, 109-185.

McKenzie, D.P., 1972, Active tectonics of the Mediterranean region: Nature, 226, 239-243.

Morelli, C., Pisoni, M., and Gantar, C., 1975, Geophysical studies in the Aegean Sea and the Eastern Mediterranean : Bollettiono Di Geofizic; XVIII, 66, 127-168.

Morgan, W.J., 1968, Rises, trenches, great faults and crustal blocks: Jour. Geophy. Research, 73, 1959-1982.

Nowroozi, A.A., 1971, Seismo-tectonics of the Persian plateau, eastern Turkey, Caucasus, and Hindu-Kush regions: Bull. Seism. Soc. Amer. 61, 2, 317-341.

Oborn,L.E., 1974, Seismic phenomena and engineering geology : Proceedings of the second Internl. Congress of the Internl. Assoc. of Engng. Geol., Sao Paulo, Brazil, II-GR.1-11-GR.41.

Papazachos, B.C., 1974, Seismotectonics of the Eastern Mediterranean area : Engineering Seismology and Earthquake Engineering, Ed. by J. Solnes . Nordhoff-Leiden, 1-32.

Rast, B., and Saegesser, R., 1980, On the systematics in defining seismic zones : Proceedings of the Seventh World Conference on Earthquake Engineering, Istanbul, Turkey, Geoscience Aspects, Part 1, 261-268.

Slemmons, D.B., and McKinney, R., 1977, Definition of active fault: U.S. Army Engineer Waterways Experiment Station Soils and Pavements Laboratory, Miscellaneous Paper 5-77-B, 1-22.

Section 5

Site Response and Engineering Application

SITE RESPONSE ANALYSIS

Mustafa Erdik
Earthquake Engineering Research Center
Middle East Technical University
Ankara, Turkey

ABSTRACT. In this report, a review of the site response assessment methhodologies in current use for engineering oriented investigations will be made. Emphasis will be on the treatments involving visco-elastic and non-linear material behavior. Simple applications based on SH-wave fields will be covered to illustrate the use of these methodologies. The theoretical findings will be evaluated through comparisons with the observational data.

1. INTRODUCTION

Ground motions during earthquakes are functions of source mechanics and dynamic characteristics of the propagation media. The local geologic and topographic conditions strongly affect the temporal and spatial behavior of the ground motion. Although it is accepted that the ground motions reflect the geodynamic characteristics of the underlying soil layers, the degree of this influence has been a controversial issue in earthquake engineering and strong ground motion seismology. There exist theoretical findings on the influence of local soil conditions successfully correlated with strong ground motion or other macro seismic data at a number of locations where the local subsoils are soft such as at Mexico City, Caracas, San Francisco and several locations in Japan including Tokyo (Kanai, 1961; Herrera et al., 1965; Idriss and Seed, 1968; Seed et al., 1972). On the other hand, it has also been shown that,with the exception of those recorded on deep and soft soil deposits, the peaks of the ground motion spectra do not show any correlation with the ground characteristics (Newmark et al., 1972) the Fourier Amplitude Spectra of the records obtained at different stations on rock and soil during the 1971 San Fernando earthquake do not differ in shape significantly with respect to the local soil conditions (Berril, 1975), and the local site conditions and the soil-structure interaction were neither the single nor the major contributors to the observed difference in the frequency domain characteristics of the basement motion observed on several buildings (Crouse, 1973).

Weak motion data from downhole and surface seismometer arrays

M. O. Erdik and M. N. Toksöz (eds.), Strong Ground Motion Seismology, 479–534.
© 1987 by D. Reidel Publishing Company.

indicate general agreement on the observations and theoretical findings based on local geotechnical conditions. (Dobry et al., 1971; Joyner et al., 1976; Johnson and Silva, 1981; Kudo et al., 1984 and Kinoshita and Mikoshiba, 1984). Similar findings on the significant effect of soil conditions have also been reported on the basis of the ground motion data obtained from nuclear explosions (Borcherdt and Gibbs, 1967; Hays et al., 1979 and Murphy, 1983). On the other hand, various statistical correlations of the strong motion data with the site soil conditions have indicated that, once the shallow soil and soft soil deposits are removed from the data set, the differences in accelerations recorded on soil and rock sites will not be statistically significant (Boore et al., 1980; Campbell, 1981).

Under the influence of these findings and issues the engineering question becomes to determine the circumstances under which significant local soil effects will be expected in a predictable manner and how predictive theoretical models will be in assessing the temporal and spatial characteristics of the design basis strong ground motions.

For the design of routine building type structures the effect of local soil conditions was introduced in the earthquake resistant design codes either in the form of a coefficient in the base shear calculations that depend on the "fundamental or predominant period" of the underlying soil formations or in terms of "site dependent spectra". For the design of important and critical structures, however, the engineers are faced with the problem of determining the temporal and spatial characteristics of strong ground motions that will be used in the design of the structure. Such problems are called "site response problem".

Site response problems involve the determination of the seismic motion at a prescribed location on the basis of a specified motion (control motion) at a specified location (control point). A typical application of the site response problem is shown in Fig.1. The control point is usually selected on the free field ground surface (Point A) or on the surface of an outcrop of the underlying half-space (Point B) where the information on the characteristics of strong motion records normally available. The determination of the motion at the layered soil medium-half-space interface, generally needed for soil-structure interaction analysis, and the motion, strains and stresses at a variety of points (D, E, G and F) from the control motion at either point A or B are the typical engineering problems. Another important class of site response problems deal with the determination of the spatial characteristics of ground motion at various support points of long structures affected by the so called "asynchronous multiple support excitation" phenomena.

Site response problems involve basic assumptions on the generic wave-pattern (seismic environment) of the control motion. The assumptions on the seismic environment may consist of vertically propagating or inclined body waves and surface waves. The assumed wave patterns also introduce restrictions on the location of control points. Since neither the type nor the relative composition of the seismic environment is known, site response studies are usually based on sensitivity analyses involving comparison of motions resulting from individual wave patterns.

In engineering practice most of the site response problems are

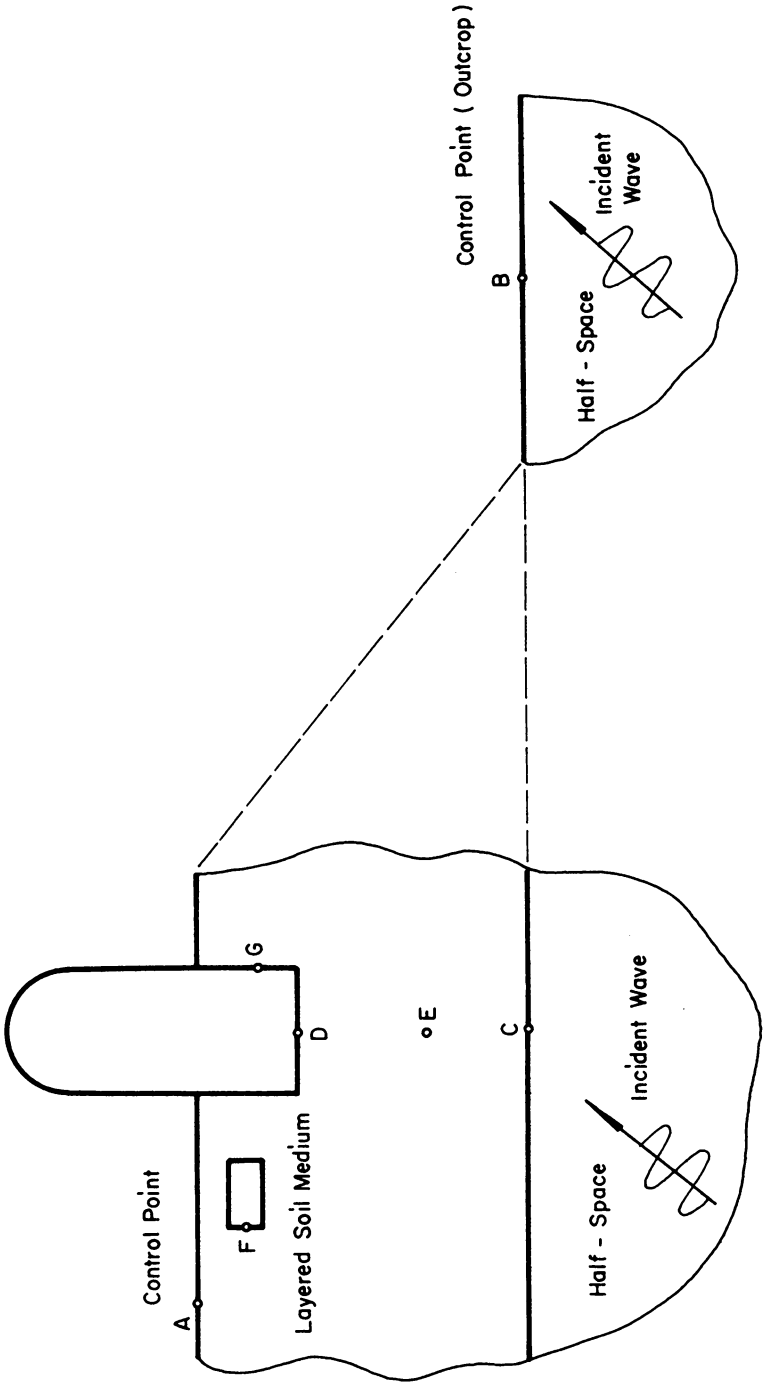

Figure 1. Typical Application of a Site Response Problem

being handled through the assumption of body-waves for the seismic environment. Even in studies where the surface waves are utilized as the generic wave pattern only one propagating mode, usually the fundamental mode with the shortest wavelength, is used due to the restrictions imposed by the control motion, which provides only one amplitude at a given frequency in the frequency domain (Chen et al., 1981). On the other hand investigations reported by Wolf and Obernhuber (1982) and Seed and Lysmer (1980) indicate that the displacement fields created in the shallow soil layers by assuming surface wave patterns involving fundamental and higher order modes can be simulated, at least in lower frequencies, by assuming vertical or inclined body-wave fields. Chen et al. (1981) also states that it will usually be more conservative to compute the maximum horizontal motions in soil layers based on an SH-wave assumption than a Rayleigh-wave assumption for a control motion specified at the free-field ground surface.

However, the importance of the asynchronous and low frequency excitation caused by the surface waves for long and/or flexible structures should not be overlooked especially since the investigations carried out by several researchers have shown that for shallow earthquake sources in typical earth structures surface waves dominate the ground motion at moderate distances (on the order of 10's of kilometers) and at frequencies less than 1-0.5 Hz (Swanger and Boore (1978)).

Although various computational procedures have been proposed for the site response problem, the problem remains mathematically ill-posed and unique solutions can only be obtained on the basis of restrictive assumptions regarding the soil or site geometry, boundary conditions and the generic wave pattern. The computational procedures can be classified to be continuum or discrete, time domain or frequency domain and linear or non-linear. Continuum solutions involve the analytical solution of the governing differential equation. Discrete solutions can be of finite element or finite difference type.

Practical applications of the non-linear site response analysis involve even more restrictive assumptions on the generic wave pattern, soil layer geometry, boundary conditions and constitutive relationships of the soil medium. The common computational procedures are the equivalent linear method (Schnabel et al., 1972; Lysmer et al., 1975), method of characteristic (Streeter et al., 1974), implicit discrete techniques based on the solution of a lumped parameter multi-degree-of freedom system (Idriss and Seed, 1967; Chen and Joyner, 1974; Martin and Seed, 1978) and explicit discrete techniques involving finite difference formulations (Joyner, 1977; Lam et al., 1978; Day et al., 1981; Joyner and Chen, 1975). Truly non-linear solutions with practical engineering applications are limited to soil media with parallel, homogeneous and isotropic layers overlying a half-space with wave patterns based on vertically propagating shear waves and with control motions specified on the outcrop of the half-space. (Chen et al., 1981; Martin and Seed,1982).

In this study, a review of the site response assessment methodologies in current use for engineering oriented investigations will be made. Emphasis will be on the treatments involving visco-elastic and non-linear material behavior. Simple applications based on SH-wave fields will be covered to illustrate the use of these methodologies. The

theoretical findings will be evaluated through comparisons with the observational data. Following the introductory first section, the second section is devoted to the available computational methods under two subsections for the continuum and discrete methodologies. Section 3 provides a simple application of the transfer matrix method to the assessment of the response of a single uniform layer over uniform half space. Dynamic material properties and non-linear constitutive relationships are covered in Section 4. Section 5 encompasses the non-linear treatments of the site-response problem on the basis of true-nonlinear and equivalent-linear methodologies.

2. COMPUTATIONAL METHODS

Computational methods involving continuum and discrete formulation of the site response problem will be reviewed. The soil medium will be a plane strain medium consisting of homogeneous, isotropic layers overlying a half space. Interfaces between the soil layers and between the layered medium and the-half space will be assumed to be in welded contact. The constitutive relationships will be covered in Section 4. The wave patterns will include plane harmonic waves.

2.1. Continuum Formulations

When a plane harmonic SV-or P-wave incident from the half space to the layered soil medium hits the half-space the remaining part will be transmitted to the ground surface through successive refractions and reflections in the layered soil medium as indicated in Fig.2. In plane particle motions (u, w) and stresses (σ, τ_{xz}) will result from the transmission of P-and SV-waves and Rayleigh-waves. Out-of-plane particle motions (v) and stresses (τ_{yz}) will result from the transmission of SH-and Love-waves. Assuming welded contact at the interfaces, the boundary conditions will be the continuity of displacements and stresses at the interfaces. The boundary condition at the ground surface can be met by specifying zero stresses. For given excitation frequency, the application of these boundary conditions to the governing wave-field equation yields the displacements and stresses at a given interface in terms of the subsequent one through the so called "transfer matrices" or "propagator matrices".

For the j th layer the displacements and stresses of the j+1 th interface, $\{z\}_{j+1}$, can be determined on the basis of the displacements of stresses of the j th. interface, $\{z\}_j$, through the transfer matrix, $\{H\}_j$, as a function of the excitation frequency.

$$\{z\}_{j+1} = \{H\}_j \quad \{z\}_j \tag{1}$$

In Eqn.1 $\{z\}_j$ is known as the "state vector" and consists of

$$\{z\}_j^T = \{|u_j|, |w_j|, |\sigma_j|, |\tau_{xzj}|\} \tag{2}$$

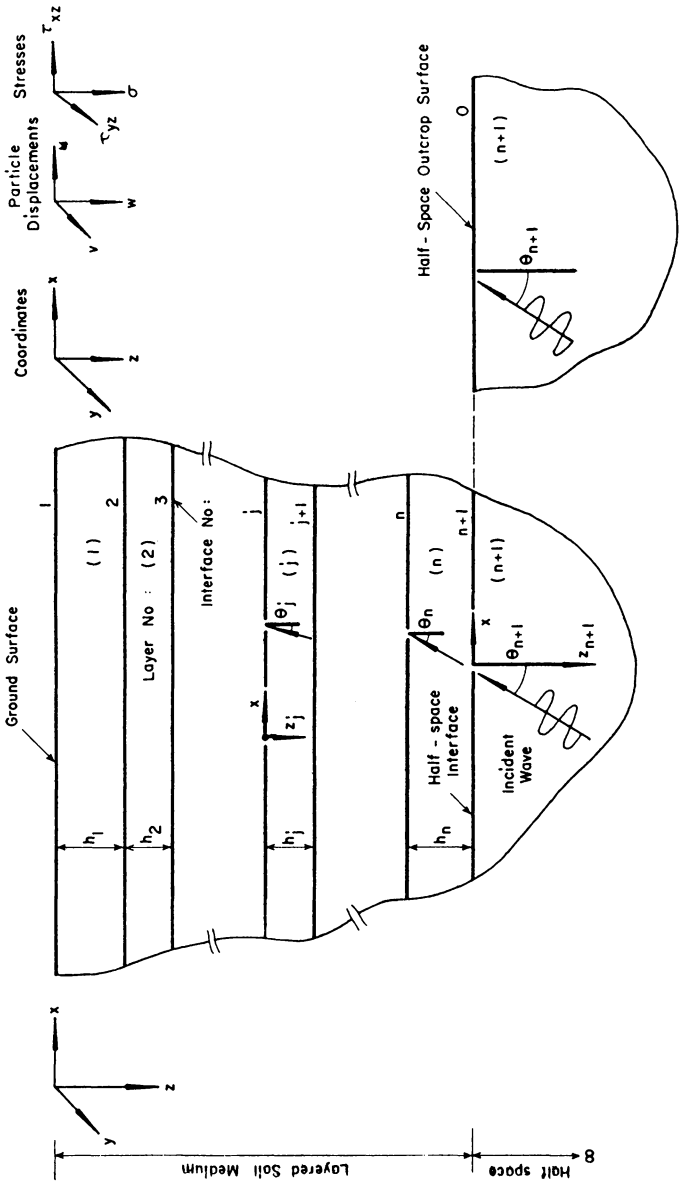

Figure 2. Soil Profile Geometry Considered

for P-, SV- and Rayleigh-waves, and

$$\{z\}_j^T = \{|v_j| \ , \ |\tau_{yzj}|\} \tag{3}$$

for SH- and Love-waves.

Through matrix algebra the "stiffness matrices" $[K]_j$ connecting the stresses of the upper and lower interfaces to the displacements of the upper and lower interfaces can also be obtained.

Consecutive application of the "transfer" or "stiffness" matrices yields the global "transfer" or "stiffness" matrix between the displacements and stresses of any two given interfaces; usually the half-space interface and the ground surface. The global transfer or stiffness matrix essentially provides the harmonic transfer function between the displacements and stresses of two given interfaces which can be utilized in the frequency domain analysis of the site response problem. Extensive treatments of this formulation are provided by Haskell (1953), Thomson (1950), Özgür and Gürpınar (1972), Silva (1976), Kenneth and Kerry (1979), Kausel and Roesset (1981), Wolf and Obernhuber (1982) and Huang (1983).

The treatment that will be considered in this report will be based on an inclined SH-wave type wave-pattern.

For an incident plane-harmonic SH-wave in the half-space (n+1 th layer) given by

$$v_{n+1}\ (z_{n+1},\ x,\ t) = \bar{v}_{n+1}\ (z_{n+1})\ \exp\ [i(\omega t - k_{sxn+1} x)\ ] \tag{4}$$

the displacement in the jth layer can be written as follows (Aki and Richards, 1980)

$$v_j(z_j,\ x,\ t) = \bar{v}_j(z_j)\ \exp\ [i(\omega t - k_{sxj}\ x)] \tag{5}$$

where

$$\bar{v}_{n+1}\ (z_{n+1}) = A_{n+1}\ \exp\ (i\ k_{szn+1}\ z_{n+1}) \tag{6}$$

and

$$\bar{v}_j(z_j) = A_j\ \exp\ (\ i\ k_{szj} z_j) + B_j\ \exp(-ik_{szj}\ z_j) \tag{7}$$

In Eqns. 4, 5, 6 and 7 k_{szj} and k_{sxj} are respectively the wave numbers in z and x directions and A_j and B_j are the wave amplitudes propagating in negative and positive z-directions.

$$k_{szj} = \frac{\omega}{\bar{V}_{szj}} = \frac{\omega}{V_{sj}/\cos\theta_j} = k_{sj}\cos\theta_j \tag{8}$$

$$k_{sxj} = \frac{\omega}{\bar{V}_{sxj}} = \frac{\omega}{\bar{V}_{sj}/\cos\theta_j} = k_{sj}\sin\theta_j \tag{9}$$

The angle of incidence measured from the z_j axis in the j th layer is θ_j. The frequency of excitation is denoted by ω and $\bar{V}_{sj}$ is the complex shear wave velocity in the j th layer. (See Section 4 for the complex material properties)

The shear stress, τ_{yzj}, in the j th layer is given by:

$$\tau_{yzj}(z_j, x, t) = i\,\bar{G}_j k_{szj}\,\bar{\tau}_{yzj}(z_j)\exp\left[i(\omega t - k_{sxj}x)\right] \tag{10}$$

where

$$\bar{\tau}_{yzj}(z_j) = A_j \exp(ik_{szj}z_j) - B_j(-ik_{szj}z_j) \tag{11}$$

$\bar{G}_j$ is the complex shear modulus for the viscoelastic medium given by,

$$\bar{G}_j = G_j(1 + 2\beta_j i) \tag{12}$$

For a Voight type viscoelastic model β_j is the hysteretic damping ratio as derived in Section 4.

$$\beta_j = \frac{\omega\eta_j}{2G_j} \tag{13}$$

where η_j is the coefficient of viscosity and G_j is the shear modulus. Assuming welded contact at the interfaces the boundary conditions will be :

$$v_j(z_j = h_j, x, t) = v_{j+1}(z_{j=1} = 0, x, t) \tag{14}$$

$$\tau_{yzj}(z_j = h_j, x, t) = \tau_{yz\,j+1}(z_{j+1} = 0, x, t) \tag{15}$$

and for the free ground surface :

$$\tau_{yz1}(z_1 = 0, x, t) = 0 \tag{16}$$

Application of these boundary conditions to Eqns.5 and 10 yields the following relationships also known as the Snell's Law ;

$$k_s = k_{sxj} = k_{sxn+1} \quad \text{or} \quad C = \frac{\bar{V}_{sxj}}{\sin\theta_j} = \frac{\bar{V}_{sn+1j}}{\sin\theta_{n+1}} \tag{17}$$

and the following recursion formula :

$$\begin{Bmatrix} A_{j+1} \\ B_{j+1} \end{Bmatrix} = [a]_j \begin{Bmatrix} A_j \\ B_j \end{Bmatrix} \tag{18}$$

where the transfer matrix between the wave amplitudes in the jth and j+1 th interface, $[a]_j$, is given by:

$$[a]_j = [b]_j \; [d]_j \tag{19}$$

$$[b]_j = \frac{1}{2} \begin{bmatrix} (1 + \gamma_j) & (1 - \gamma_j) \\ (1 - \gamma_j) & (1 + \gamma_j) \end{bmatrix} \tag{20}$$

$$[d]_j = \begin{bmatrix} \exp\,(ik_{szj}\, h_j) & 0 \\ 0 & \exp\,(-ik_{szj}\, h_j) \end{bmatrix} \tag{21}$$

γ_j denotes the impedance ratio between the j th and j+1 th layers.

$$\gamma_j = \frac{\rho_j\, \bar{V}_{sj}\, \cos\theta_j}{{}_{j+1}\bar{V}_{sj} \cos\theta_{j+1}} \tag{22}$$

The application of the boundary condition given by Eqn.16 to the ground motion yields $A_1 = B_1$ and, accordingly, the displacement at the ground surface becomes:

$$v_1\,(z_1 = 0,\, x,\, t) = 2\, A_1 \exp \quad i(\omega t - k_{sx1}\; x) \tag{23}$$

Beginning with the surface layer the repeated use of Eqn.18 will yield A_j and B_j at the j th interface as follows :

$$\begin{Bmatrix} A_j \\ \\ B_j \end{Bmatrix} = [a]_{j-1}\,[a]_{j-2}\cdots[a]_1 \begin{Bmatrix} A_1 \\ \\ A_1 \end{Bmatrix} = [H]_j \begin{Bmatrix} A_1 \\ \\ A_1 \end{Bmatrix} \tag{24}$$

for $j = 2, \ldots, n$

Defining the following transfer functions between A_j, A_1 and B_j, A_1 as.'

$$TA_j(\omega) = \frac{A_j}{A_1} \quad ; \quad TB_j(\omega) = \frac{B_j}{A_1}$$

the following matrix equation can be written :

$$\begin{Bmatrix} TA_j\ (\omega) \\ \\ TA_j\ (\omega) \end{Bmatrix} = |H|_j \begin{Bmatrix} 1 \\ \\ 1 \end{Bmatrix} \tag{25}$$

Accordingly the transfer function between the motions at the j th. and the ℓ th interface becomes :

$$T_{j,\ell}(\omega) = \frac{A_j + B_j}{A_\ell + B_\ell} = \frac{TA_j(\omega) + TB_j(\omega)}{TA_\ell(\omega) + TB_\ell(\omega)} \tag{26}$$

For j=1 and ℓ=n+1 we can obtain the transfer function between the motions of the ground surface and of the half space.

$$T_{1,\ n+1} = \frac{2A_1}{A_{n+1} + B_{n+1}} = \frac{2}{TA_{n+1}(\omega) + TB_{n+1}(\omega)} \tag{27}$$

Considering the same incident wave field, the motion at the surface of the half-space outcrop can be obtained as:

$$v_0 = (\ z_{n+1} = 0,\ x,\ t) = 2A_{n+1} \exp\ i(\omega t - k_{sxn+1}x) \tag{28}$$

The transfer function between the ground surface motion and the outcrop motion can then be given by the following expression :

$$T_{1,0}\ (\omega) = \frac{2A_1}{2A_{n+1}} \quad \frac{1}{TA_{n+1}(\omega)} \tag{29}$$

Same results can be obtained on the basis of the following layer stiffness matrices, $[K]$, provided in Kausel and Roesset (1981)

$$\{\bar{P}\} = [K]\ \{\bar{U}\} \quad \text{or} \quad \begin{Bmatrix} \bar{P}_1 \\ \bar{P}_2 \end{Bmatrix} = \begin{bmatrix} K_{11} & K_{12} \\ K_{21} & K_{22} \end{bmatrix} \begin{Bmatrix} \bar{U}_1 \\ \bar{U}_2 \end{Bmatrix} \tag{30}$$

Where considering an SH-wave field and for the j th layer the stiffness matrix, $[K]$, the external load vector, $\{\bar{P}\}$, and the displacement vector, $\{\bar{U}\}$, for the upper and lower interface can be given in the frequency domain by :

$$\{\bar{P}\} = \begin{Bmatrix} \bar{P}_1 \\ \bar{P}_2 \end{Bmatrix} = \begin{Bmatrix} \bar{\tau}_{yzj}(z_j = 0) \\ -\bar{\tau}_{yzj}(z_j = h_j) \end{Bmatrix} \tag{31}$$

$$\{\bar{U}\} = \begin{Bmatrix} \bar{U}_1 \\ \bar{U}_2 \end{Bmatrix} = \begin{Bmatrix} \bar{v}_j\ (z_j = 0) \\ \bar{v}_j\ (z_j = h_j) \end{Bmatrix} \tag{32}$$

$$[K] = \begin{bmatrix} K_{11} & K_{12} \\ K_{21} & K_{22} \end{bmatrix} = \frac{k_{sxj}\ s_j\ \bar{G}_j}{\sin k_{sxj} s_j\ h_j} \begin{bmatrix} \cos k_{sxj}\ s_j\ h_j & -1 \\ -1 & \cos k_{sxj}\ s_j\ h_j \end{bmatrix} \tag{33}$$

For the half-space the external forces and the displacements at the surface can be related through :

$$\bar{P}_{n+1} = \tilde{K}_{n+1}\ \bar{U}_o \tag{34}$$

where $\tilde{K}_{n+1} = i\ k_{sn+1}\ s_{n+1}\ \bar{G}_{n+1}$ (35)

is called the half-space stiffness matrix or, in this case, coefficient. In Eqns.33 and 35 the following definitions apply :

$$s_j = \cot\theta_j = \left[\left(\frac{\omega}{k_{sxj}\ \bar{V}_{sj}}\right)^2 - 1\right]^{\frac{1}{2}} \tag{36}$$

$$k_{sxj} = k_{sj}\ \sin\theta_j \tag{37}$$

such that $k_{sxj}\ s_j = k_{sj}\ \sin\theta_j\ \cot\theta_j = k_{sj}\cos\theta_j = k_{szj}$

For a multi-layered soil medium resting on a half space the global stiffness matrix can be assembled from the stiffness matrices of the individual layers (Kausel and Roesset, 1981). The global stiffness matrix between the ground surface and the half-space interface can be given as:

$$\{\bar{P}\} = [S]\ \{\bar{U}\} \tag{38}$$

where

$$\{\bar{P}\}^T = \{\bar{P}_1\ ,\ \bar{P}_2,\ \ldots\ldots,\ \bar{P}_n\ ,\ \bar{P}_{n+1}\} \tag{39}$$

$$\{\bar{U}\}^T = \{\bar{U}_1\ ,\ \bar{U}_2,\ \ldots\ldots,\ \bar{U}_n\ ,\ \bar{U}_{n+1}\} \tag{40}$$

and

$$[S] = \begin{bmatrix} [K_{11}]_1 & [K_{12}]_1 & & & & \\ [K_{21}]_1 & [K_{22}]_1 + [K_{11}]_2 & [K_{12}]_2 & & & \\ & [K_{12}]_2 & [K_{22}]_2 + [K_{11}]_3 & & & \\ & & \ddots & \ddots & & \\ & & & [K_{22}]_{n-1} + [K_{11}]_n & [K_{12}]_n & \\ & & & [K_{21}]_n & [K_{22}]_n + [\tilde{K}]_{n+1} & \end{bmatrix} \tag{41}$$

On the basis of the surface motions of the half-space outcrop, $\bar{U}_o$, the displacement vector $\bar{U}$ can be obtained in the frequency domain by using:

$$\bar{P}_j = 0 \text{ and } \bar{P}_{n+1} = \tilde{K}_{n+1} \bar{U}_o \tag{42}$$

such that $\{\bar{P}\}^T = \{0, 0, \ldots, \tilde{K}_{n+1} \bar{U}_o\}$ (43)

and

$$\{\bar{U}\} = [S]^{-1} \{P\} = [D] \{\bar{P}\} \tag{44}$$

where $[D]$ can be termed as the global flexibility matrix.

Same considerations also apply for the layer stiffness matrices of in-plane P-and SV-wave fields as provided in Kausel and Roesset(1981). For this wave field the stiffness matrix is 4x4 and there are 4 terms in the external load and displacement vectors.

The natural modes and frequencies of wave propagation (Rayleigh and Love-waves) are obtained from the eigenvalue problem which is obtained by setting the load vector $\{\bar{P}\}$ to zero. For practical applications the discretized form of the transfer matrix solutions is utilized (Udaka, 1975; Chen et al., 1981).

Theoretical findings based on the transfer matrix formulation have successfully correlated with the observational findings from vertical seismometer arrays, such as in Menlo Park and Richmond, California and in Tokyo, at least for weak ground motions. Probably the most successfull vertical array has been installed by the U.S. Geological Survey near Menlo Park, California (Joyner et al., 1976). Schematic sections are given in Fig.3. Fig.4 provides the observed horizontal spectral ratios (transfer functions) between the surface-and-12 m and the surface-and-186 m motions for different earthquakes. Also indicated on these figures are the theoretical transfer functions. As stated in Joyner et al. (1976) the good correlation between the theoretical and the empirical transfer functions "provide evidence that, under favorable conditions, simple plane-layer models are capable of giving reasonably good approximations of the effects of local soil conditions on low-amplitude ground motion".

2.2. Discrete Methods

Both the finite difference and the finite element methods can be used in wave propagation analysis. Detailed accounts of the applications can be found in Boore (1972) and Lysmer and Drake (1972). The type of applications faced in the strong ground motion studies necessitate the solution of nonlinear, transient structure-continuum problems. The governing equations for a discrete formulation can be expressed as :

$$[M] \{x\} = \{F_{ext}\} - \{F_{int}\} \tag{45}$$

subject to the initial and boundary conditions imposed on the problem.

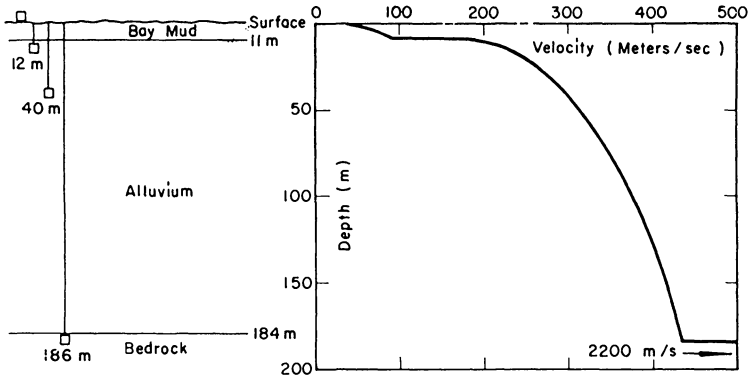

Figure 3. U.S.G.S. Menlo Park Vertical Array

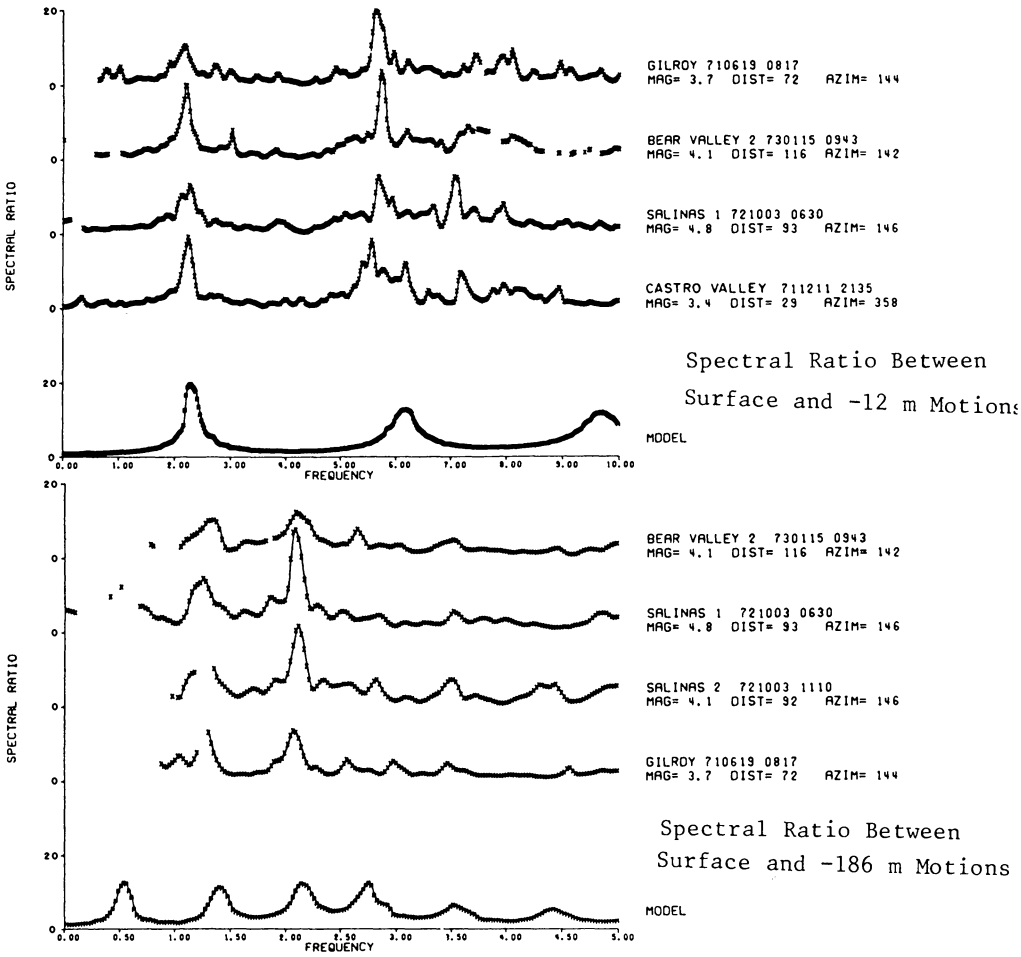

Figure 4. Observed and Theoretical (Model) Horizontal Spectral Ratios (After Joyner et al., 1976)

Eqn.45 is nothing but a matrix form of Newton's Second Law. The matrix $[M]$ includes the discrete masses, $\{\ddot{x}\}$ is a vector of absolute accelerations at the discretized nodal points, $\{F_{ext}\}$ is a vector of externally applied discretized forces and $\{F_{int}\}$ is a vector representing the discretized internal forces that develop in the continuum-structure system. For linear visco-elastic type constitutive relationship $\{F_{int}\}$ can be written as :

$$\{F_{int}\} = [K]\ \{u\} + [C]\ \{\dot{u}\} \tag{46}$$

where $[K]$ is the stiffness matrix, and $[C]$ is the damping matrix. $\{u\}$ and $\{\dot{u}\}$ are the vectors representing the nodal point relative displacement and velocities.

For continuum-structure models excited at the boundary synchronously by a motion, y(t), Eqn.45 can be written as:

$$[M]\ \{\ddot{u}\} = \{R\}\ \ddot{y}(t) - \{F_{int}\} \tag{47}$$

where $\{R\}$ is a coefficient vector that is related to the mass matrix $[M]$.

For solution in temporal domain various forms of integration methods (e.g. Newmark 1959; Wilson et al., 1973) are in use to obtain the nodal point displacements and velocities from the nodal point accelerations and initial conditions. In the temporal domain wave propagation problems are usually solved by explicit integration. In explicit integration the absolute and relative accelerations of the nodal points at each time step Δt are computed from Eqn.45 as

$$\{\ddot{x}\} = [M]^{-1}\ (\{F_{ext}\} - \{F_{int}\}) \tag{48}$$

and

$$\{\ddot{u}\} = \{\ddot{x}\} - \{I\}\ \ddot{y}(t) \tag{49}$$

where $\{I\}$ is a unit vector.

The basic calculation cycle can be given as follows :

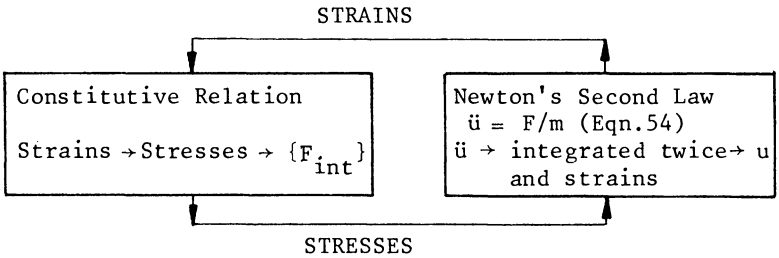

(50)

In the left box the stresses (or stress increments) in each element are evaluated from the strains (or strain increments) existing for the given spatial and temporal location. The right box indicates a time step where the nodal point displacements are updated. For a non-linear

hysteretic constitutive relationship this routine is straight forward. For visco-elastic constitutive relationship (e.g. Voight model) problems arise on the applications since to simulate the soil behavior the coefficients of viscosity in the damping matrix, $[C]$, has to be treated as a function of the excitation frequency, which is not "a priori" known in time domain computations . However there exist time-domain "equivalent linear" approaches where the $[C]$ matrix is formed from the damping matrix of individual elements on the basis of considering only a constant frequency, ω_1, (the first mode vibration frequency of the whole system) and updated at suitable intervals following the changes in element strains (Idriss et al., 1973).

Another time domain procedure is the so-called "modal superposition" method (Clough and Penzien, 1975). This method is based on the formulation of a transformation matrix, $[P]$, to diagonalize the matrices $[M]$, $[K]$ and $[C]$ of Eqns.45 and 46.

$$[\tilde{M}] = [P]^T [M][P], \quad [\tilde{C}] = [P]^T [C] [P] \text{ and } [\tilde{K}] = [P]^T [K][P] \tag{51}$$

through a coordinate transformation :

$$\{u\} = [P] \{z\} \tag{52}$$

In the above equations $[\tilde{M}]$, $[\tilde{C}]$ and $[\tilde{K}]$ are diagonalized matrices and $\{z\}$ is called the generalized displacement vector. In practice $[P]$ is found through the solution of characteristic equation

$$\left[[K] - \omega^2 [M]\right] \{\phi\} = \{0\} \tag{53}$$

yielding n eigen vectors (modal vectors), $\{\phi_j\}$, and n eigen values (modal frequencies), ω_j . The eigen vectors are usually normalized with respect to $[M]$ such that

$$\{\phi_i\}^T [M] \{\phi_j\} = \begin{cases} 1 & \text{for} \quad i=j \\ 0 & \text{for} \quad i \neq j \end{cases} \tag{54}$$

Defining the transformation matrix $[P]$ as the matrix whose columns are the normalized eigen vectors $\{\phi\}_j$ and a diagonal matrix $[\Omega^2]$ whose elements are ω_j^2 , it can be shown that :

$$[P]^T [K] [P] = [\Omega^2] \quad \text{and} \quad [P]^T [M] [P] = [I] \tag{55}$$

where $[I]$ is the identity diagonal matrix. Using the transformation given in Eqn.52 the following transformed equation can be obtained from Eqns.46 and 47.

$$\{\ddot{z}\} + [P]^T [C] [P] \{\dot{z}\} + [\Omega^2] \{z\} = [P]^T \{R\} \ddot{y}(t) \tag{56}$$

Eqn.56 yields a set of uncoupled differential equations of the form :

$$\ddot{z}_i + 2\omega_i\beta_i\dot{z}_i + \omega_i^2 z_i = r_i \ddot{y}(t) \tag{57}$$

provided that the damping matrix $[C]$ satisfis the Rayleigh condition.

$$[C] = a[M] + b[K] \tag{58}$$

Here β_i is the damping ratio in the i th mode and a and b are arbitrary constants. For site response problems with uniform damping ratio at all points of the model Rayleigh condition is satisfied, and a good approximate procedure will be to use superposition of modal responses obtained by assuming constant damping ratio, β, for all modes. However, as is the case with most site response problems, when damping ratio varies within the model the use of modal superposition can lead to significant errors (Whitman et al., 1972).

A feasible solution for such viscoelastic discrete formulation can be realized in the frequency domain on the basis of complex stiffness matrix formulation of Eqns.46 and 47. Assuming a unit harmonic the excitation, $y(t) = \exp(i\omega t)$, the output displacements will be also harmonic with

$$\{u\} = \{A(\omega)\} e^{i\omega t} \tag{59}$$

where $\{A(\omega)\}$ is called the harmonic response function given by

$$\{A(\omega)\} = \left[[K] - \omega^2 [M]\right]^{-1} \{R\} \tag{60}$$

Since superposition is applicable in linear visco-elastic systems, the nodal point displacements can be given by the following discrete inverse Fourier transform :

$$\{u(k\Delta t)\} = \mathrm{Re}\left[\sum_{s=0}^{N/2} \{A(\omega_s)\} \ddot{Y}(\omega_s) e^{i\omega_s k\Delta t}\right] \tag{61}$$

$$\omega_s = \frac{2\pi}{N\Delta t} s, \quad (s = 1, 2, \ldots\ldots, N/2) \tag{62}$$

where $A(\omega_s)$ is the harmonic response function at $\omega = \omega_s$, N is the total number of discrete time history values digitized at an interval Δt, and $\ddot{Y}(\omega_s)$ is the Discrete Fourier Transform of the discretized time domain record $\ddot{y}(k\Delta t)$ given by :

$$Y(\omega_s) = \begin{cases} \frac{1}{2}\sum_{k=0}^{N-1} \ddot{y}(k\Delta t)e^{-i\omega_s k\Delta t} & \text{for} \quad s = 0 \text{ and } s = \frac{N}{2} \\ \frac{2}{N}\sum_{k=0}^{N-1} \ddot{y}(k\Delta t)e^{-i\omega_s k\Delta t} & \text{for} \quad 1 \leq s < N \end{cases}$$

Such frequency domain solutions constitute the backbone of the so called "equivalent linear" solutions utilized in Lysmer et al.(1974)and (1975).

2.3. Treatment of the Boundaries

The usual method of excitation in the finite element models in wide engineering use (e.g.Lysmer et al. 1974 and 1975) is to assume that the lower boundary moves according to a specified motion in a rigid body fashion where all nodes on the boundary move synchronously. This is clearly an approximation. However it is justified (Seed and Lysmer, 1977) that there is a growing body of evidence that variations of motions with depth computed by such assumptions correlate with field observations and that, at least for soil-structure interaction analysis, such body wave field assumptions are conservative. The rigid base should be deep enough to account for the effects of so called "radiation damping"in the actual field system unless such a rigid bedrock boundary already exists at the site. Joyner and Chen (1975) have shown that if the layered soil medium is assumed to overlie a uniform elastic half-space at which outcrop (real or assumed) the control motion is specified, then the actual incident wave effects (i.e. interaction between the layered soil media and the halfspace) can be simulated if the layered soil media is supported on a Lysmer-Kuhlemeyer boundary at the half-space interface and excited with a shear force at this boundary proportional to the specified control motion at the half-space outcrop.

Nodes at the lateral boundaries are usually constrained to move only in the horizontal and/or vertical direction, depending on the soil geometry and the type of excitation, to simulate the existence of horizontal soil layers outside the vertical boundaries. Such infinitely extending soil media simulations can also be achieved through the use of transmitting boundaries (Lysmer and Kuhlemeyer, 1969).

The specification of the control motion at the half-space outcrop and then the application of this motion to the layered soil strata overlying the half-space through Lysmer-Kuhlemeyer type dashpots (viscous boundary elements) has been utilized by Joyner and Chen (1975). Simplified and limited applications of this method can also be found in Tsai (1969). The derivation of this methodology is as follows:

For a given soil media (layered or uniform, linear or non-linear) overlying a uniform elastic half space, as indicated in Fig.5, and assuming vertically incident S-waves, the horizontal motions in the half space can be given by :

$$u_b = u_I + u_R = U_I(z + V_{sb}t) + U_R(z - V_{sb}t) \tag{64}$$

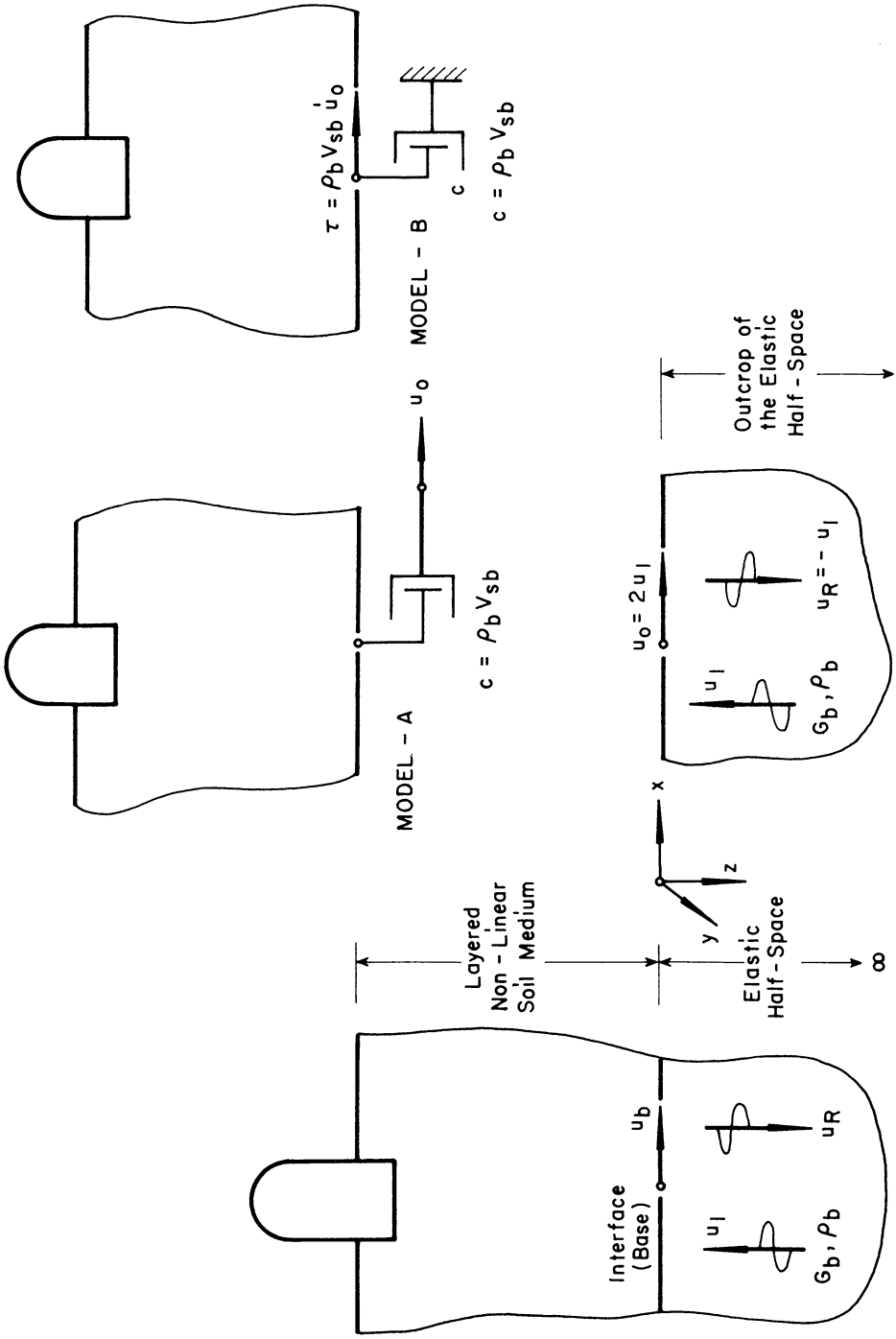

Figure 5. Control Motion at Outcrop Problem for Non-linear Media

where U_I and U_R are the amplitudes of the incident and reflected waves (u_I and u_R) and V_{sb} is the shear wave propagation velocity. The shear stress at the interface, τ_b, will then be :

$$\tau_b = G_b\left(\frac{\partial u_I}{\partial z} + \frac{\partial u_R}{\partial z}\right) = \rho_b V_{sb} (\dot{u}_I - \dot{u}_R) \tag{65}$$

where G_b and ρ_b are respectively the shear modulus and the mass density of the half-space and $\dot{u}_I$ and $\dot{u}_R$ are the particle velocities associated with the incident and reflected wave fields.

From stress free boundary conditions at the half-space outcrop surface it is evident that :

$$u_o = 2u_I \tag{66}$$

where u_o is the half-space outcrop surface displacement and u_I is the incident wave amplitude. Through the use of Eqns. 64, 65 and 66 the base shear can be given as :

$$\tau_b = \rho V_{sb} (\dot{u}_o - \dot{u}_b) \tag{67}$$

On the basis of the Eqn.67 two analogous models for base excitation of the layered soil media can be formulated as indicated in Fig.5. In Model-A the base is excited by the half-space outcrop motion, u_o, through the dashpot of coefficient of viscosity of $c = \rho_b V_{sb}$, whereas in the Model-B the base is excited by a shearing force of $\rho_b V_{sb} u_o$ against the fixed dashpot. It can be seen that in either case the correct base displacement u_b can be obtained following the Eqn.67.

Following the same methodology it is a simple exercise to show that for an inclined SH-wave field in the half-space incident to the interface at on angle θ_b with the vertical the coefficient of viscocity of the dasphot will be

$$c = \rho_b V_{sb} \cos \theta_b \tag{68}$$

Specification of the control motion at the half-space outcrop is a rational procedure since for viscoelastic systems and for control motions specified at the surface of the layered soil media the convolution process that needs to be carried to assess the appropriate rigid base motion provides only approximate results with significant uncertainties in the high frequency regions (Velera et al., 1977) and since for true non-linear formulations (i.e. non-linear hysteretic constitutive equations) such a deconvolution process cannot be carried out.

3. RESPONSE OF A SINGLE UNIFORM LAYER OVER UNIFORM HALF-SPACE

Wave propagation in a single uniform layer over uniform half-space problem has been the subject of several extensive studies (Wolf and Obernhuber, 1982a, b, Huang, 1983 and Chen et al., 1981) due to the relative ease of expressing different transfer functions between different motions in an explicit format on the basis of transfer (or stiffness) matrix formulation. The soil system considered is shown in Fig.6 together with the half-space outcrop. The following transfer functions between ground, interface, outcrop and incident wave motions can be described.

$T_{2,1}(\omega)$: Transfer function between the interface and ground motions which provides the interface motion for an assigned control motion at the ground and indicates the distribution of motion with depth within the layer.

$T_{1,0}(\omega)$: Transfer function between the ground and outcrop motions which provides the ground motion for an assigned control motion at the outcrop. Also known as the amplification function.

$T_{2,0}(\omega)$: Transfer function between the interface and the outcrop which provides the interface motion for an assigned control motion at the outcrop.

$T_{1,2}(\omega)$: Transfer function between the ground and interface motions also known as the amplification function.

$T_{1,A}(\omega)$: Transfer function between the ground motion and the incident wave amplitude in the half-space also known as the amplification function.

These transfer functions are obviously not independent from each other and not all transfer functions are applicable for all types of wave fields, including the surface waves.

On the basis of the formulation described in Section 2.1 for the transfer matrices involving SH-wave fields in visco-elastic media, the following transfer function can be obtained for the layering system considered in Fig.6.

$$T_{2,1}(\omega) = \frac{TA_2(\omega) + TB_2(\omega)}{2} \tag{69}$$

$$T_{1,0}(\omega) = \frac{1}{TA_2(\omega)} \tag{70}$$

$$T_{2,0}(\omega) = \frac{TA_2(\omega) + TB_2(\omega)}{2\ TA_2(\omega)} = T_{2,1}(\omega)\ \ T_{1,0}(\omega) \tag{71}$$

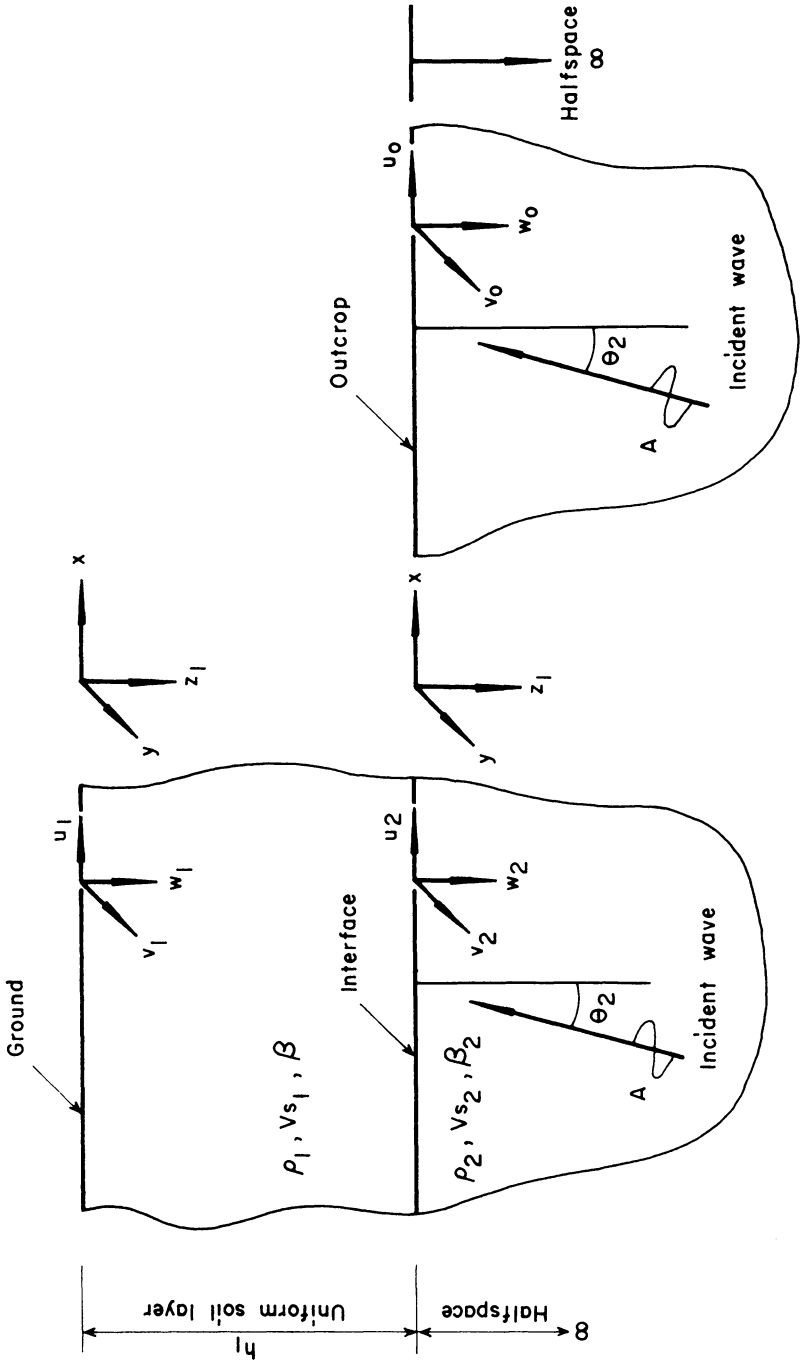

Figure 6. Single Uniform Layer Overlying Half-Space

$$T_{1,2}(\omega) = \frac{2}{TA_2(\omega) + TB_2(\omega)} = 1/T_{2,1}(\omega) \tag{72}$$

and

$$T_{1,A}(\omega) = \frac{2}{TA_2(\omega)} = 2\, T_{1,0}(\omega) \tag{73}$$

where the individual transfer functions TA_2 and TB_2, given by Eqns.18, 19, 20 and 21, are :

$$\begin{Bmatrix} TA_2(\omega) \\ TB_2(\omega) \end{Bmatrix} = \frac{1}{2} \begin{bmatrix} (1+\gamma_1) & (1-\gamma_1) \\ (1-\gamma_1) & (1+\gamma_1) \end{bmatrix} \begin{bmatrix} \exp(ik_{sz1}h_1) & 0 \\ 0 & \exp(ik_{sz1}h_1) \end{bmatrix} \begin{Bmatrix} 1 \\ 1 \end{Bmatrix} \tag{74}$$

yielding

$$TA_2(\omega) = \cos(k_{sz1}\, h_1) + i\gamma_1 \sin(k_{sz1}h_1) \tag{75}$$

and

$$TB_2(\omega) = \cos(k_{sz1}\, h\ ) - i\gamma_1 \sin(k_{sz1}h_1) \tag{76}$$

Where

$$\gamma_1 = \frac{\rho_1\, \bar{V}_{s1} \cos\theta_1}{\rho_2\, \bar{V}_{s2} \cos\theta_2} \quad ; \quad k_{sz1} = \frac{\omega}{\bar{V}_{s1}} \cos\theta_1 \tag{77}$$

$$\bar{V}_{s1} \cong V_{s1}\sqrt{1+2i\beta_1} \quad ; \quad \bar{V}_{s2} \cong V_{s2}\sqrt{1+2i\beta_2} \tag{78}$$

and where the angle of incidence, θ_1, in the top layer is given by the Snell's law as :

$$\sin\theta_1 = \frac{\bar{V}_{s1}}{\bar{V}_{s2}} \sin\theta_2 \tag{79}$$

In the above equations ω is the excitation frequency and θ_2 is the angle of incidence with the vertical in the half space. V_{s1} and V_{s2} are the shear wave velocities, β_1 and β_2 are viscous damping ratios and ρ_1 and ρ_2 are mass densities in their respective media as shown in Fig 6.

Equations for the transfer matrices same as those obtained above can also be derived on the basis of the layer stiffness matrices given in Section 2.1.

For vertical incidence the transfer functions for the horizontal motion resulting from SH-and SV-waves are the same. The transfer functions for the vertical motion resulting from P-waves are the same as

that for SH-waves once the respective values of the propagation velocities are introduced in the formulation. Huang (1983) has shown that for both inclined SV-and P-waves with angles of incidence below the critical on the transfer functions between the ground and the outcrop motions ($T_{1,0}(\omega)$) are similar to that obtained on the basis of SH-wave assumption, with the exception of small humps and dips near the natural frequency of vibrations of the layer for normally incident P-waves due to coupling effects.

In Figs. 7, 8 and 9 the transfer function between the ground and the interface motions, $T_{1,0}(\omega)$, is plotted against the dimensionless frequency $\omega h_1/V_{s1}$ for different angles of incidence, θ_2, mass density ratios, ρ_1/ρ_2, shear wave velocity ratios, V_{s1}/V_{s2}, and viscous damping ratios β_1 and β_2. As it can be assessed from the relevant formulation and can be seen in these figures, the transfer function reaches its maxima at :

$$\frac{\omega h_1}{V_{s1}} = (2n - 1)\frac{\pi}{2} \quad \text{or} \quad \omega_n = \frac{(2n - 1)\pi}{2}\frac{V_{s1}}{h_1} \tag{80}$$

and, neglecting the viscous damping ratio in the half-space, its maxima will be :

$$T_{1,0}(\omega_n) = \frac{2}{(2n-1)\pi\left[\beta_1 + \frac{2}{(2n-1)\pi}\frac{\rho_1 V_{s1}}{\rho_2 V_{s2}}\right]} \tag{81}$$

The second term in the brackets in the denominator of the above equation termed as the "equivalent damping" and provides a measure of the energy loss introduced by the different impedance values compared to that of a layer overlying a rigid half space.

As it can be seen from these figures, for near-vertical (i.e. $\theta_2 \leq 30^o$) angles of incidence, the most important factors determining the shape of the transfer function are the (V_{s1}/h_1) and (V_{s1}/V_{s2}) or $(\rho_1 V_{s1})/(\rho_2 V_{s2})$ ratios. The latter ratio is also known as the impedance ratio.

The first frequency, ω_1, at which the maximum of the transfer function reached is called the "fundamental frequency".

$$\omega_1 = \frac{\pi}{2}\frac{V_{s1}}{h_1} \quad ; \quad T_{1,0}(\omega_1) = \frac{1}{\frac{\pi}{2}\beta_1 + \frac{\rho_1 V_{s1}}{\rho_2 V_{s2}}} \leq \frac{\rho_2 V_{s2}}{\rho_1 V_{s1}} \tag{82}$$

The importance of the fundamental frequency can also be seen in the transfer function between the ground and the interface motions, $T_{1,2}$, provided in Fig.10. This function is the same as the transfer function between the ground and outcrop motions for a rigid half space.

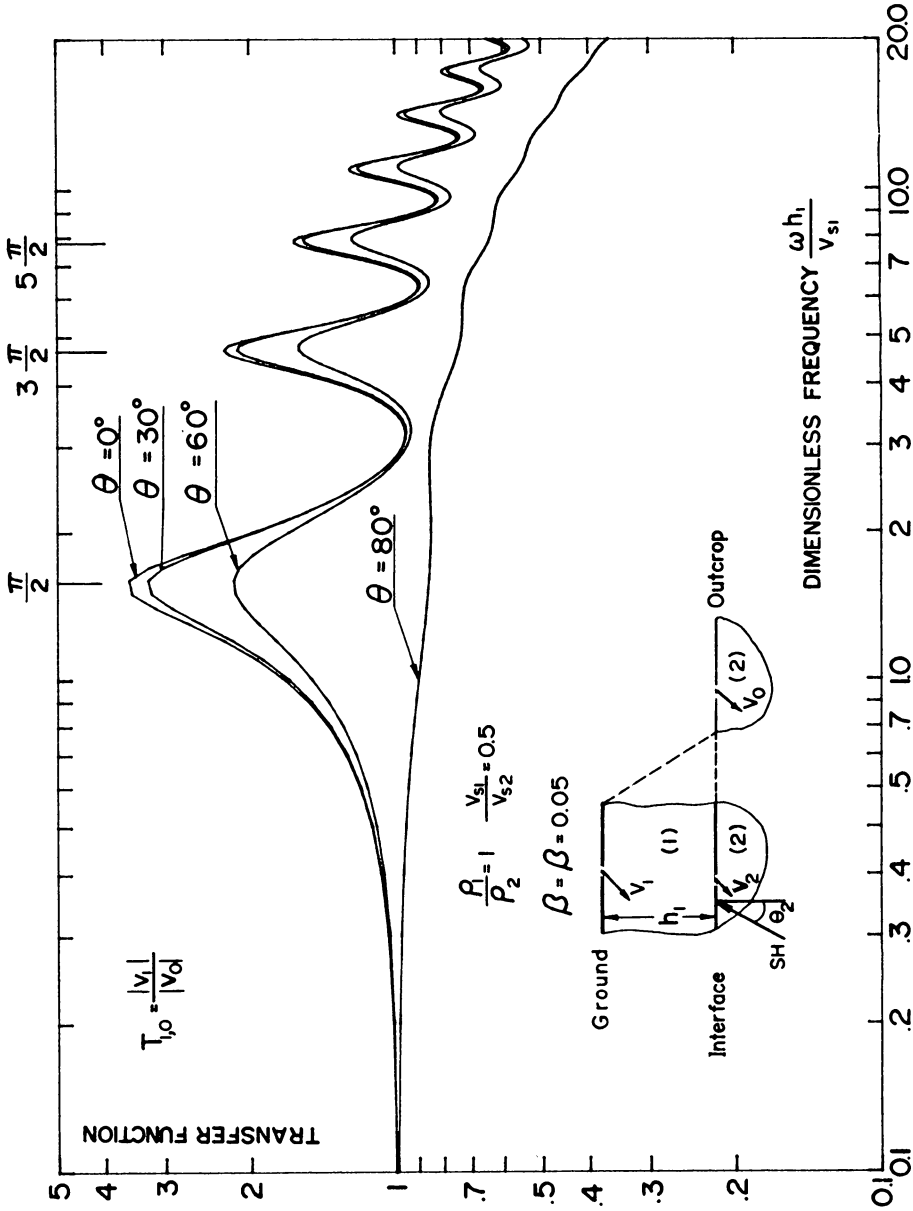

Figure 7. Transfer Function Between the Ground and Outcrop Motions

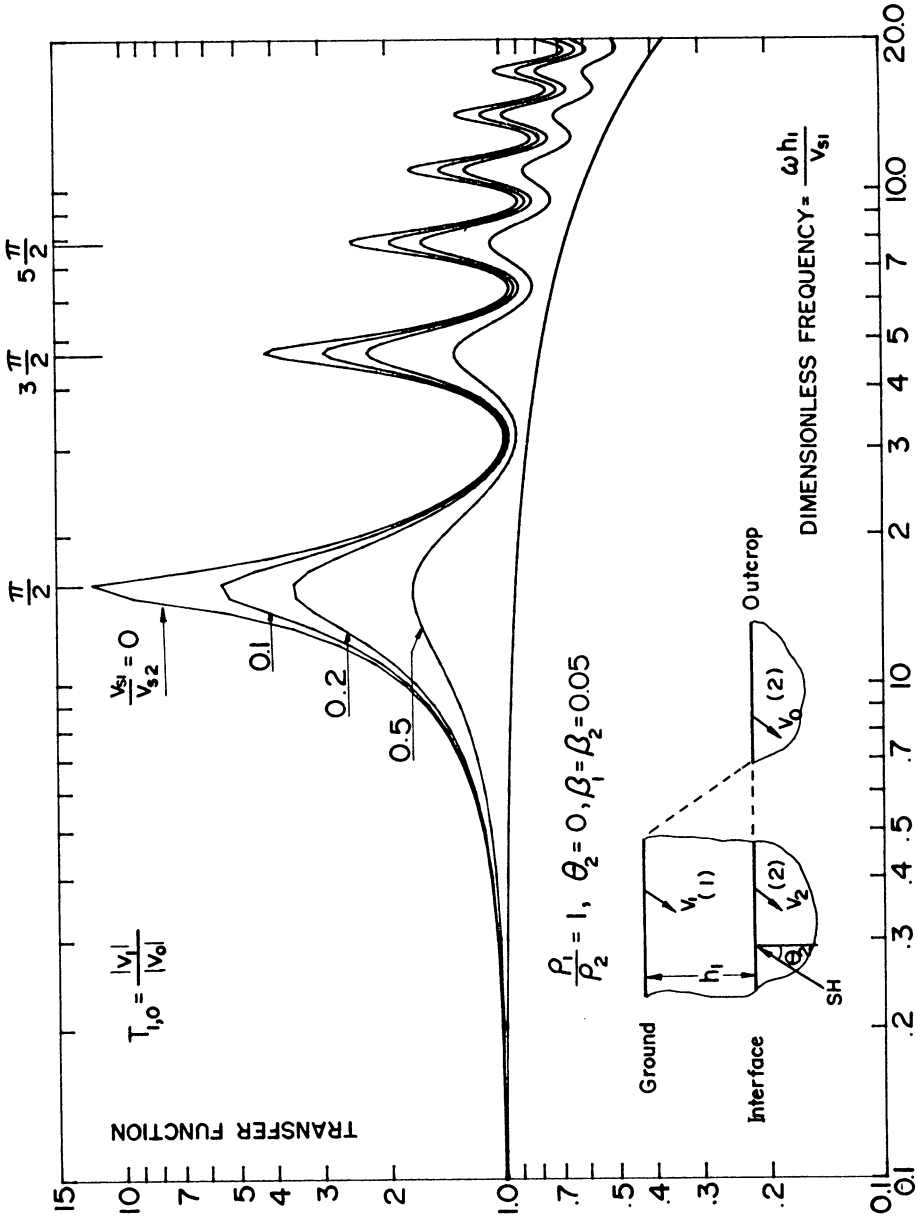

Figure 8. Transfer Function Between the Ground and Outcrop Motions

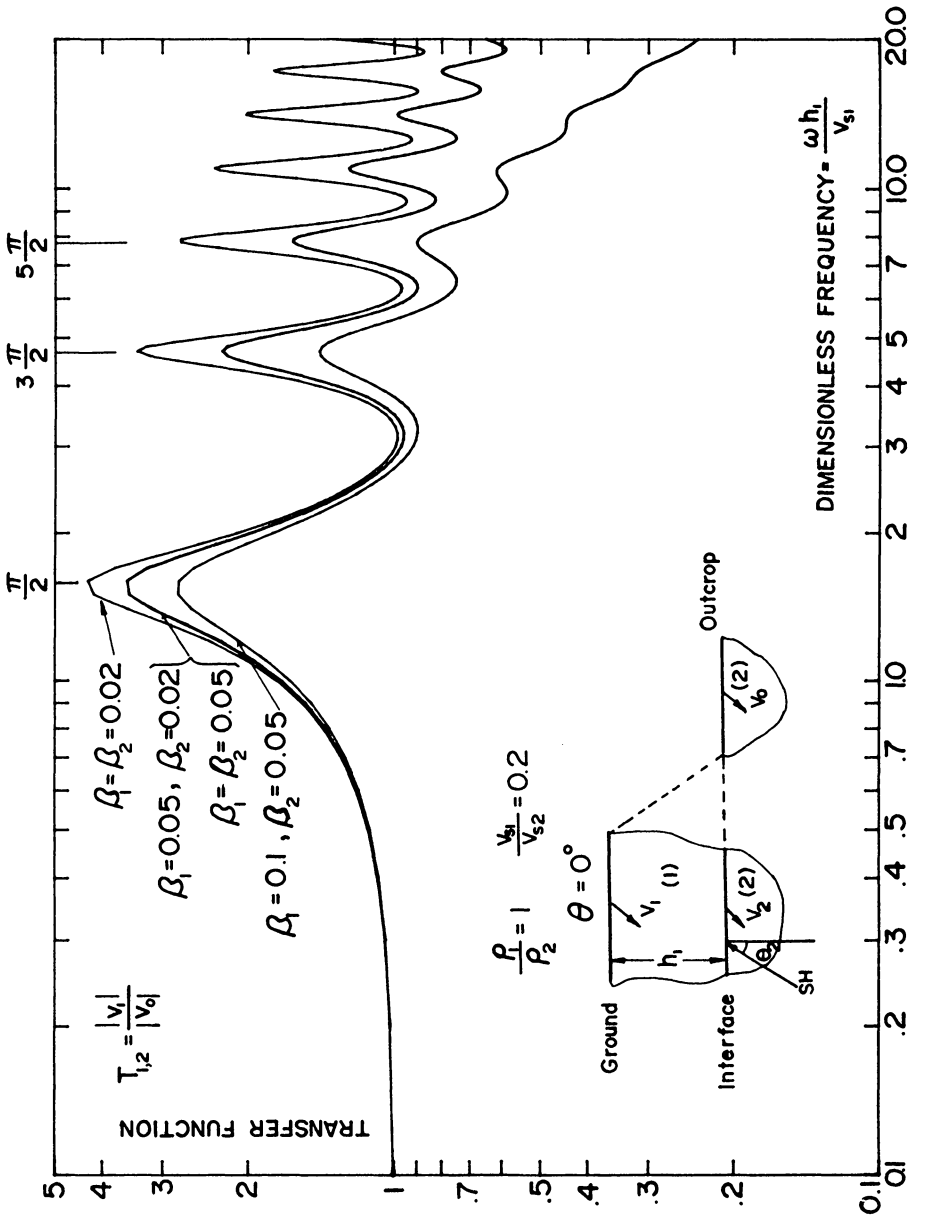

Figure 9. Transfer Function Between the Ground and Outcrop Motions

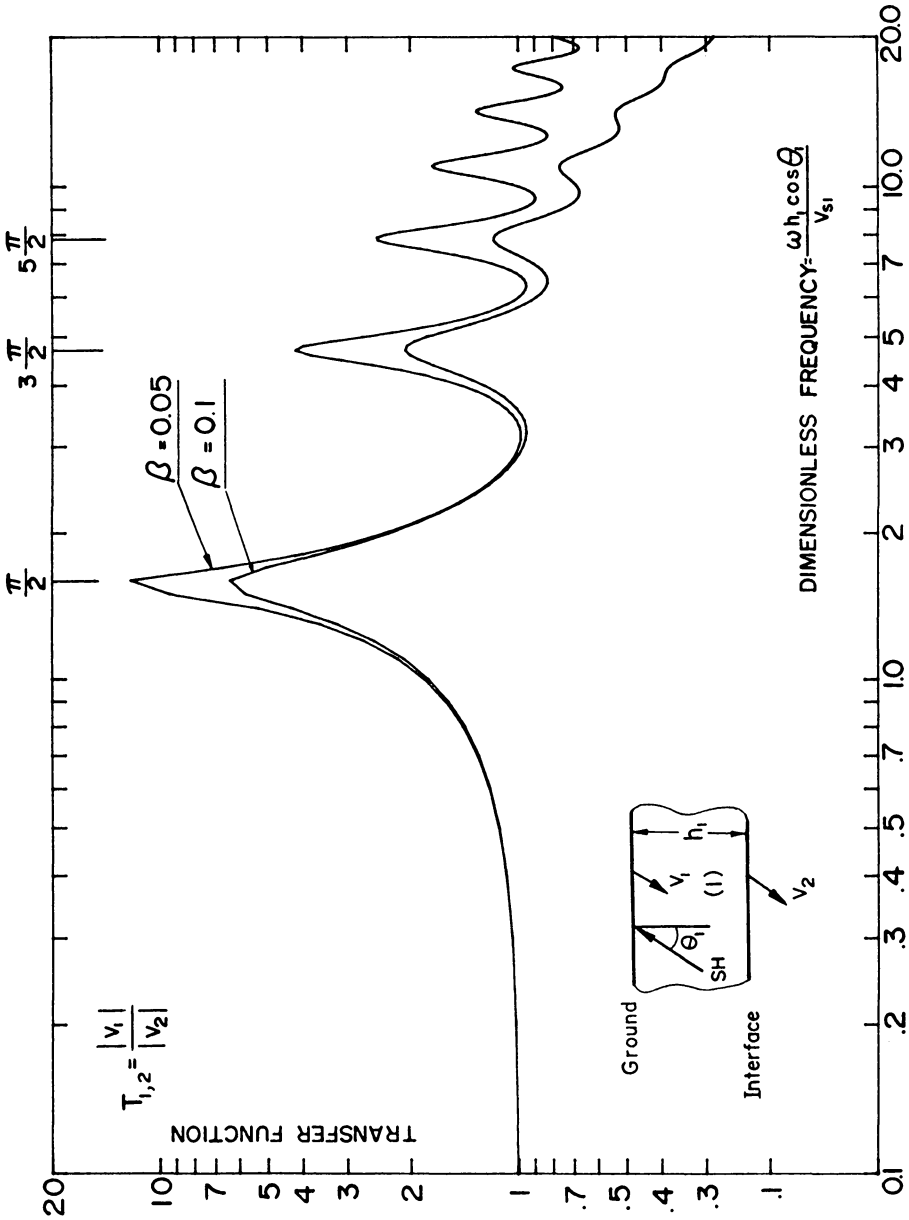

Figure 10. Transfer Function Between the Ground and Interface Motions

The dimensionless frequency defined by $(\omega h_1 \cos\theta_1)/V_{s1}$ is utilized in plotting $T_{1,2}(\omega)$. Note that $T_{1,2}(\omega)$ is independent of the properties of the underlying medium. The maxima of the transfer function is given by :

$$T_{1,2}(\omega_n) = \frac{2}{(2n-1)\pi\beta_1} \tag{83}$$

which can also be obtained by setting $\rho_2 V_{s2} = \infty$ in Eqn.(82). Eqn.(83) indicates substantial amplification of the ground motion with respect to the motion at depth. There exists observational evidence on the substantial variation of the motion with depth for rather low strain amplitudes. Fig.11 produced after Joyner et al.(1976) indicates the variation of seismogram for an earthquake with respect to depth as measured by the U.S.G.S. vertical array at Menlo Park (Fig.3). Fig.12 produced after Omote et al. (1984) indicates the distribution of maximum accelerations with depth at the Tomioka (TMK) vertical strong motion array. The variation of the peak accelerations observed at the ground and basement levels of buildings during 1971 San Fernando and 1968 Tokyo earthquakes also indicate up to 25% variation (Seed and Lysmer, 1980).

The fundamental soil frequency (or period) has for a long time constituted the backbone parameter for the description of site effects on the ground motion. Kanai's(1962) semi-empirical transfer function providing the ratio of the ground and incident wave motion amplitudes as a function of the fundamental frequency has found wide spread utilization particularly in Japan.

$$G(T) = 1 + \frac{1}{\sqrt{\left[\frac{1+\alpha}{1-\alpha}\left\{1-\left(\frac{T}{T_G}\right)^2\right\}\right]^2 + \left(\frac{0.3}{\sqrt{T_G}}\,\frac{T}{T_G}\right)^2}} \tag{84}$$

where $\alpha = \dfrac{\rho_1 V_{s1}}{\rho_2 V_{s2}}$ = impedance ratio

$G(T)$ = ratio of magnification $(T_{1,A} = 2\,T_{1,0})$

T = excitation period $(2\pi/\omega)$

T_G = predominant period of surface layer $(2\pi/\omega_1)$

Note that for $T = T_G$ Eqn.(84) goes to maximum given by

$$G(T_G) = 1 + \frac{\sqrt{T_G}}{0.3} \tag{85}$$

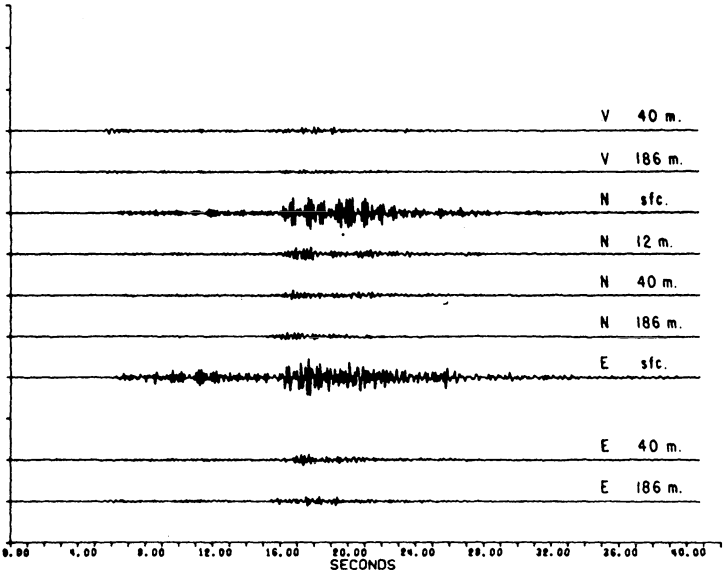

Figure 11. Seismograms at the Surface-12, -40 and -186 m (U.S.G.S. Menlo Park Array, Anzar Earthquake) (After Joyner et al.,1976) (See Fig.3 for Array Geometry)

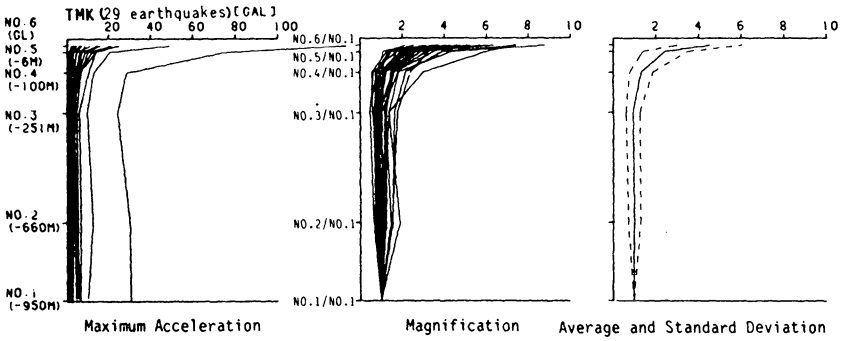

Figure 12. Vertical Distribution of Maximum Accelerations at TMK, Japan Vertical Array (After Omote et al., 1984)

regardless of the impedance ratio.

In the earthquake resistant design codes following SEAOC (Structural Engineers Association of California) recommendations the lateral force coefficient is varied between 1 and 1.5 depending on the degree of similarity between the fundamental mode period of the structure, T, and the socalled "characteristic site period", T_s, as follows :

$$\text{for} \quad \frac{T}{T_s} \leq 1 \qquad S = 1.0 + \frac{T}{T_s} - 0.5 \left[\frac{T}{T_s}\right]^2 \leq 1$$

$$\text{for} \quad \frac{T}{T_s} > 1 \qquad S = 1.2 + 0.6 \frac{T}{T_s} - 0.3 \left[\frac{T}{T_s}\right]^2 \leq 1 \tag{86}$$

The rationale behind this approach is given in the code commentary (SEAOC, 1980) by stating that "greater damage is likely to occur when the fundamental natural period of vibration of a structure is similar to that of the soil deposit on which it is constructed" and by citing the supporting evidence from the 1967 Caracas earthquake (Seed et al., 1970).

However the recognition of the fact that the strong dependence of the ground motion on the fundamental soil period phenomena can only be associated with special geological and geotechnical conditions and special excitations has recently led to the description of the site effects in the design codes in terms of the site-dependent-spectra (ATC,1978; Umemura, 1984).

Figures 13 and 14 provide respectively the transfer function between the ground and interface, $T_{2,1}$ and between the interface and outcrop, $T_{2,0}$, motions against the dimensionless frequency. These figures indicate that for white-noise type motions at the ground or at the outcrop the corresponding motions at the interface will be substantially deficient of the frequency components at frequencies equal to the eigen frequencies of the layer. In other words a white-noise type or a broadband control motion can not be applied if the control point is to be selected at the interface. Since the wave length associated with the fundamental frequency of the layer is $\lambda_1 = V_{s1}/(4f_1)$, one can also observe that, in a deposit with uniform properties, seismic motions will decrease with depth below the ground surface at least down to the depth $z = V_{s1}/(4f_{max})$, where f_{max} is the highest frequency considered in the analysis. This conclusion is of great importance for the soil-structure interaction analysis of embedded structures.

Supporting evidence of this phenomena has been established on the basis of low-strain data obtained from vertical seismograph arrays. Using the data from U.S.G.S. Menlo Park Vertical Array, Seed and Lysmer (1980) have found the ratio of the spectral accelerations recorded at -12 m to those recorded on the surface, $T_{2,1}$, for different earthquakes, as illustrated in Fig.15, indicate a suppression of frequency components corresponding to the fundamental frequency of the 12 m deep soil layer.

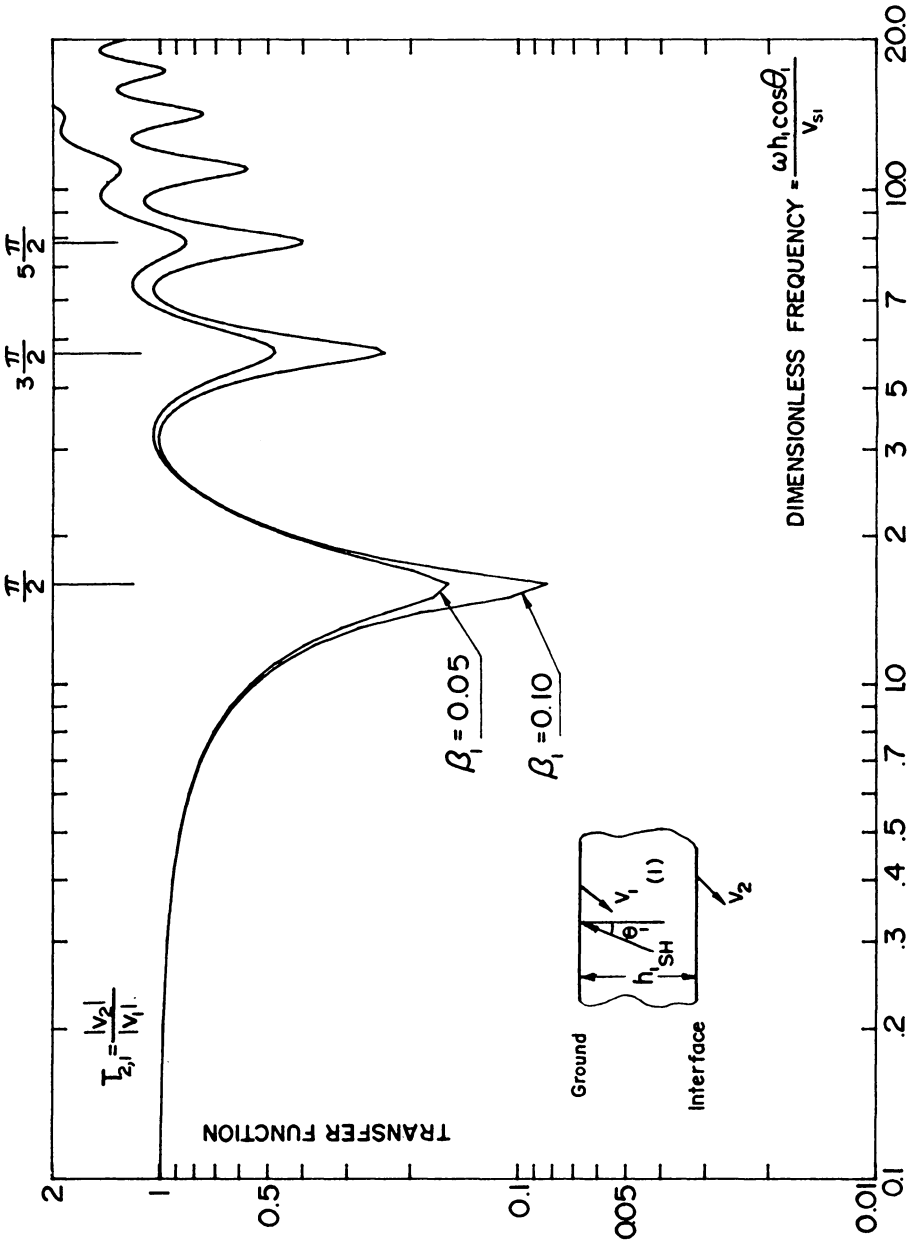

Figure 13. Transfer Function Between the Interface and the Ground Motions

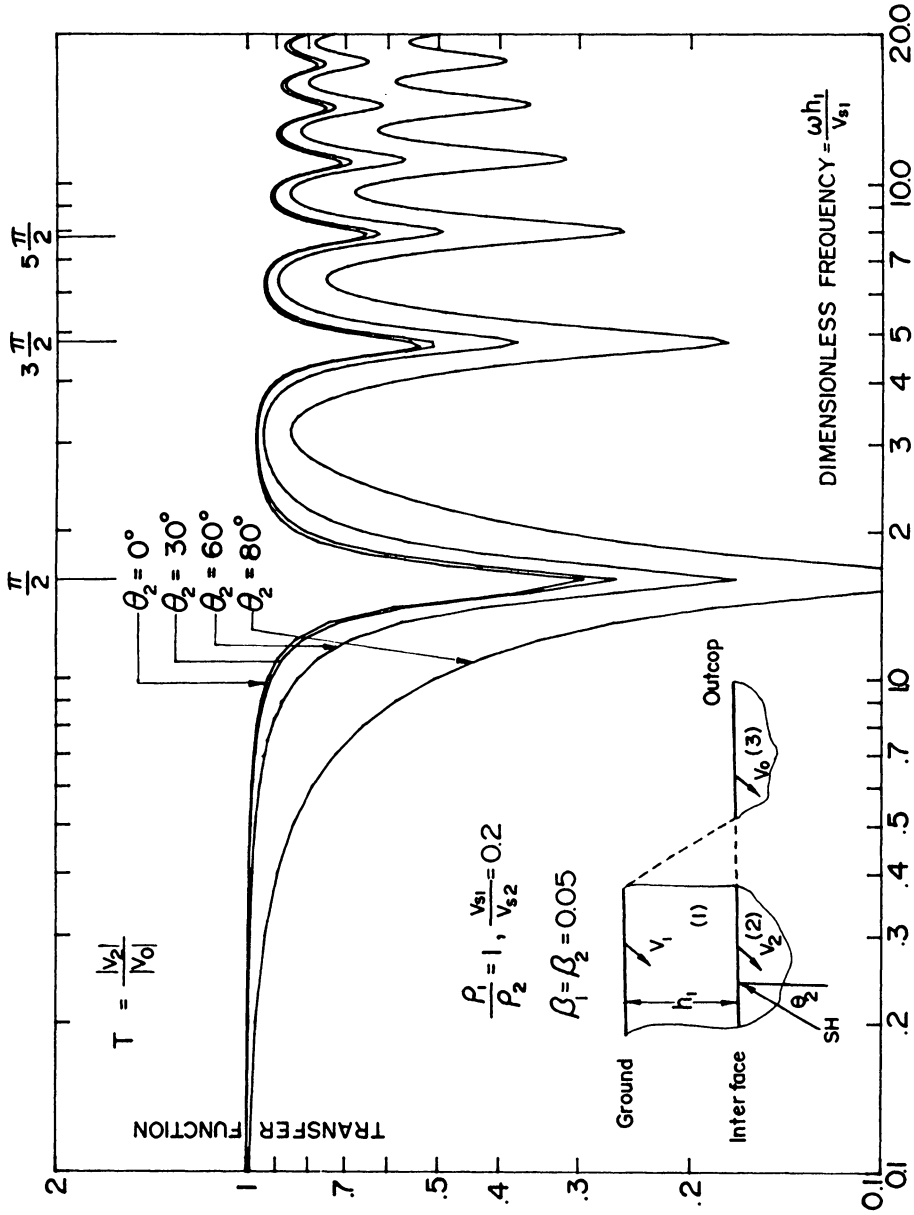

Figure 14. Transfer Function Between the Interface and the Outcrop Motions

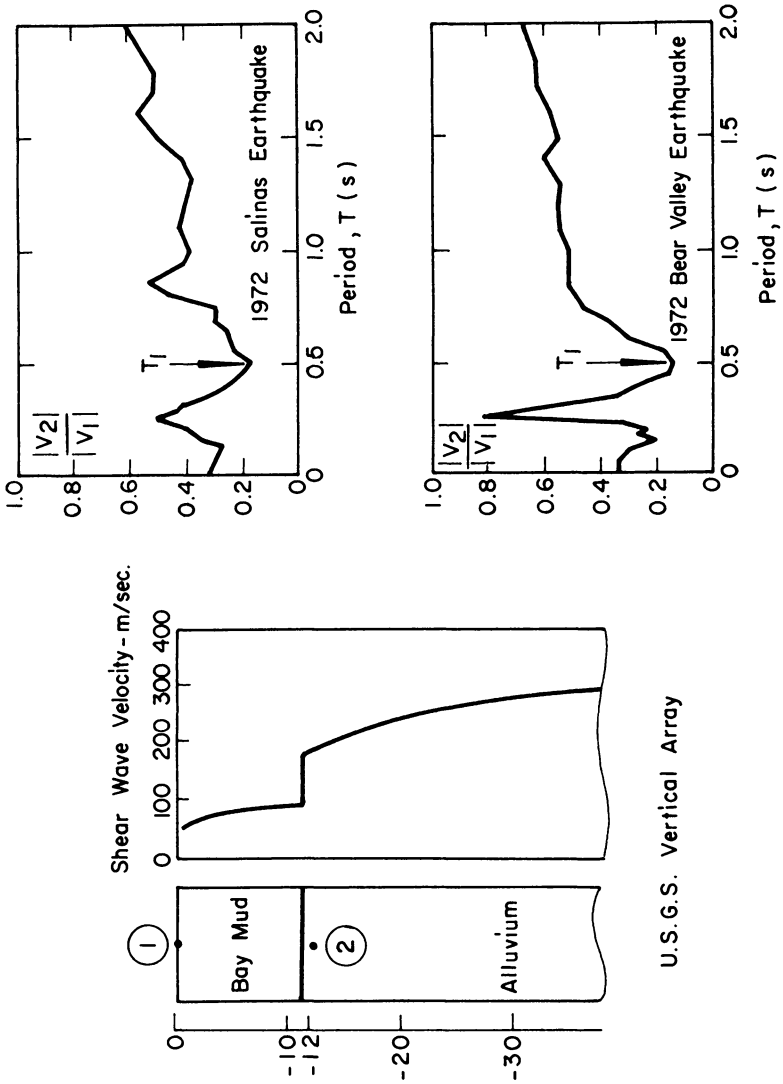

Figure 15. Relative Spectral Accelerations at Different Depths (U.S.G.S., Menlo Park Array, Fig.3) (After Seed and Lysmer, 1980)

4. DYNAMIC MATERIAL PROPERTIES

Most of the information on the dynamic material properties of soils are based on the experiments with harmonic excitation. Under cyclic excitation soils generally show non-linear hysteretic stress-strain relationship. Several researches have shown that the stiffness and the energy dissipation (damping)behavior of the soils strongly depend on the strain amplitude but can be considered to be generally independent of the excitation frequency (Hardin and Drnevich, 1970). Defining the shear modulus, G, as the slope of the line through the end (turning) points of the hysteresis loop and the damping ratio , β, as

$$\beta = \frac{1}{4\pi} \frac{\Delta W}{W} \tag{87}$$

where ΔW is the energy dissipated in one hysteresis cycle (i.e. area inside the hysteresis loop) and W is the energy stored during initial loading (i.e. area under the skeleton curve), several researchers have provided curves depicting the change of G and β with the cyclic strain amplitude. The average curves suggested by Seed and Idriss (1970) are provided in Fig.16 . It should be noted that these curves should only be interpreted as indicative since they are associated with substantial scatter of data.

4.1. Voight Model

Eqn.87 is originally suggested by Jacobsen (1960) to formulate and equivalent viscous damping ratio for the equivalent-linear analysis of a non-linear single-degree-of-freedom (S.D.F.) system and is based on the matching of the energy lost by the non-linear system in one oscillation cycle to that of the linear visco-elastic (Voight model) S.D.F. system responding at resonance. As indicated in Fig.17 the equivalent damping ratio (hysteretic damping ratio) for a Voight-type constitutive model can be derived as :

$$\beta = \frac{\omega\eta}{2G} \tag{88}$$

where η is the coefficient of viscosity. Since for soils β and G can be taken to be independent of frequency, for a Voight model to be adopted as a constitutive relationship for soil, the coefficient of viscosity, η, should be proportional to the inverse of the frequency. Such a model is called the linear hysteretic model. As shown in Fig.17 the frequency domain constitutive relationships of such a model can be given by:

$$\tau(\omega) = G\ (1 + 2i\beta)\ \gamma(\omega) \tag{89}$$

In "equivalent-linear" approximations to the true non-linear site response problems the parameters G and β of Voight model are updated following the changes of shear strain field on the basis of experimental curves such as those provided in Fig.16 (Schnabel et al., 1972).

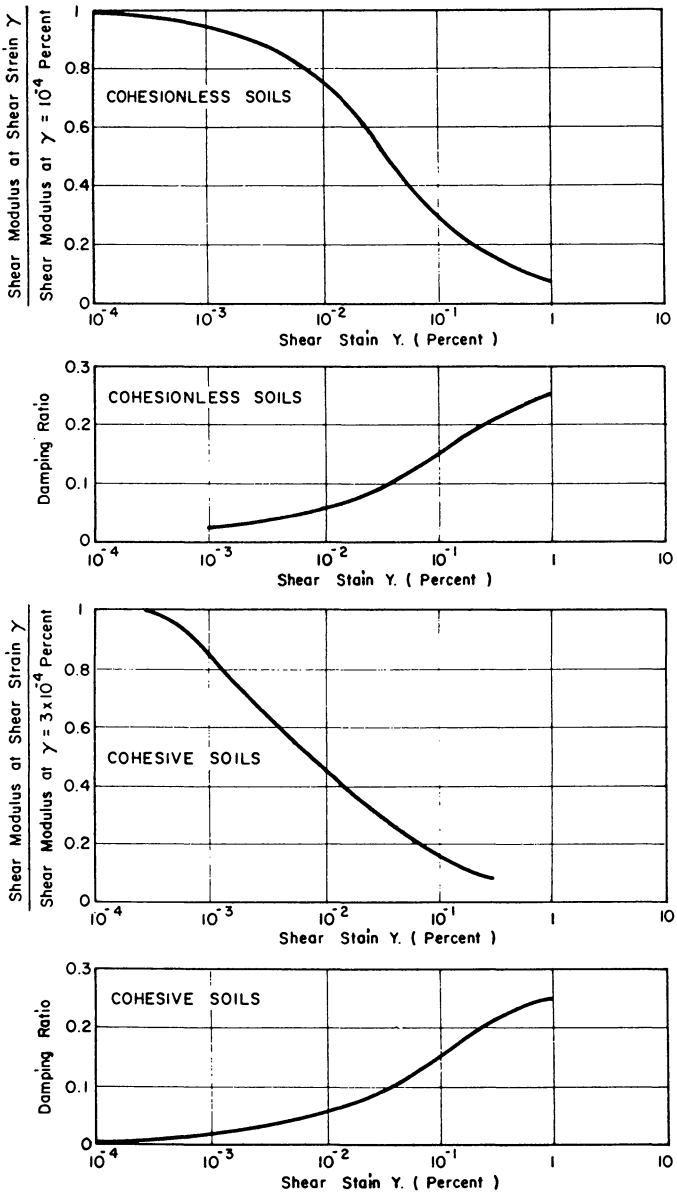

Figure 16a,b,c,d. Typical Curves Defining Strain-Dependent Soil Properties (After Seed and Idriss, 1970)

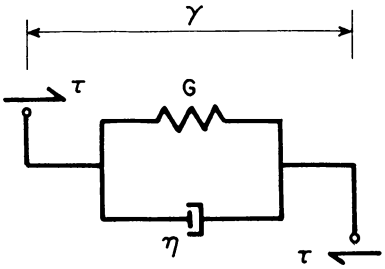

Stress - Strain Relationship : $\tau = G\gamma + \eta\gamma$

For Harmonic Excitation : $\gamma = \gamma_0 e^{i\omega t}$

$\tau = (G - i\omega\eta)\gamma$

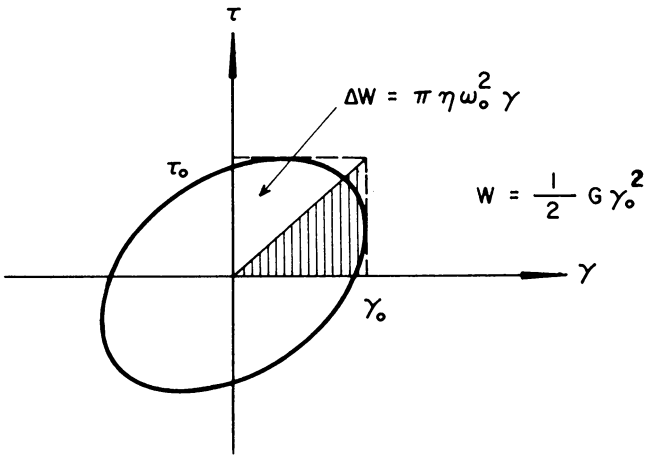

Hysteretic Damping Ratio : $\beta = \frac{1}{2\pi}\frac{\Delta W}{W} = \frac{\omega\eta}{2G}$

Frequency Domain Constitutive Relationship : $\tau(\omega) = \bar{G}\gamma(\omega) = G(1+2i\beta)\gamma$

Figure 17. Voight-Model Type Constitutive Relationship

The frequency domain constitutive relationship for the equivalent-linear approximation can be given as :

$$\tau(\omega) = G(\gamma_o) \left[1 + 2i\beta(\gamma_o)\right] \gamma(\omega) \tag{90}$$

where γ_o is the shear strain amplitude.

The particle displacements resulting from a one-dimensional harmonic plane shear wave propagating in the positive x-direction in a uniform viscoelastic media (Voight-model) can be given by:

$$u(x,t) = A \exp \left[i(\omega t - \bar{k}_s x) \right] \tag{91}$$

where $\bar{k}_s$ is the complex shear wave number expressed by:

$$k_s = \frac{\omega}{\bar{V}_s} = \frac{\omega}{\sqrt{\bar{G}_s / \rho}} = \frac{\omega}{\sqrt{G/\rho}\ \sqrt{1 + 2\beta i}} \tag{92}$$

and where $\bar{V}_s$, $\bar{G}_s$ are respectively the complex shear wave velocity and complex shear modulus. For $\beta << 1$ it can be shown that :

$$\bar{k}_s = \mathrm{Re}(\bar{k}_s) + i\ \mathrm{Im}(\bar{k}_s) = \frac{\omega}{V_s} - i\ \beta \frac{\omega}{V_s} \tag{93}$$

From Eqn. 91 and 93 one can obtain

$$u(x,t) = A \exp \left[i(\omega t - k_s x) \right] \exp \left[-\beta \frac{\omega}{V_s} x \right] \tag{94}$$

where $k_s = \omega / V_s$ is the real shear wave number. The first exponential term indicates propagation with real V_s in the + x direction and the second exponential term indicates decay (attenuation) which is analogous to the so called Q-attenuation in seismology. The relationship between the Q (quality factor) and the β (damping ratio) is given by:

$$\beta = \frac{1}{2Q} \qquad \text{for } \beta << 1 \tag{95}$$

4.2. One Dimensional Hysteretic Constitutive Models

Soil behavior under dynamic loading is frequency independent and highly non-linear involving plastic deformations. There exist several proposals for constitutive relationships that conforms with the observed experimental behavior of soils under cyclic loading. Two of the most utilized ones are the Ramberg-Osgood (Ramberg and Osgood , 1943) and the Martin-Davidenkov (Martin , 1975) models. Both of the models satisfy the so-called Massing's Hypothesis (Massing, 1926), namely, that the stress-strain curves associated with one-dimensional symmetrical closed

hysteresis loops should be of the same form as those of the initial loading curve except for an enlargement by a factor of two. These constitutive models can be used in the time domain either directly on the basis of their mathematical formulations or through the use of a collection of perfectly elastic and rigid-plastic or slip elements arranged in series-parallel combination as proposed by Iwan (1967).

In the Ramberg-Osgood model for the initial loading curve the shear strain (γ) normalized by the reference strain (γ_y) is given as a function of the shear stress (τ) normalized by the ultimate shear stress (τ_{ult}) and two dimensionless parameters $\alpha(>1)$ and $r(>0)$.

$$(\gamma/\gamma_y) = (\tau/\tau_{ult}) + \alpha(\tau/\tau_{ult})^r \quad ; \quad \gamma_y = \tau_{ult}/G_o \tag{96}$$

where G_o is the low strain shear modulus. In Eqn.96 r=1 signifies linear and $r = \infty$ signifies elasto-plastic type relationship.

In the Martin-Davidenkov model for the initial loading curve the normalized shear stress (τ/τ_{ult}) is given in terms of the normalized shear strain (γ/γ_y) and the two dimensionless parameters 2B and A.

$$(\tau/\tau_{ult}) = \left[1-\left(\frac{(\gamma/\gamma_y)^{2B}}{1-\left[\gamma/\gamma\right]^{2B}} \right)^A \right] (\gamma/\gamma_y) \tag{97}$$

By an appropriate choice of four parameters in either Eqn.96 or in Eqn.97 the two non-linear models can be made to fit approximately to the experimental one-dimensional cyclic stress-strain shape of soils.

A simple hyperbolic model for the initial loading curve has been used by several researchers (e.g. Hardin and Drnevich, 1972) to approximate the experimental behavior of non-cohesive soils. In this model the initial loading curve is expressed by :

$$(\gamma/\gamma_{ult}) = \frac{(\gamma/\gamma_y)}{1 + (\gamma/\gamma_y)} \tag{98}$$

which corresponds to assigning B = 0.5 and A = 1 in Eqn.97. The stress-strain curves resulting from such a hyperbolic constitutive model are plotted in Fig.18.

5. NONLINEAR SITE RESPONSE ANALYSES

Both time-domain and the frequency-domain analyses are used to account for the non-linear effects in site-response problems.

The so-called "true-nonlinear" and "equivalent-linear" methods are

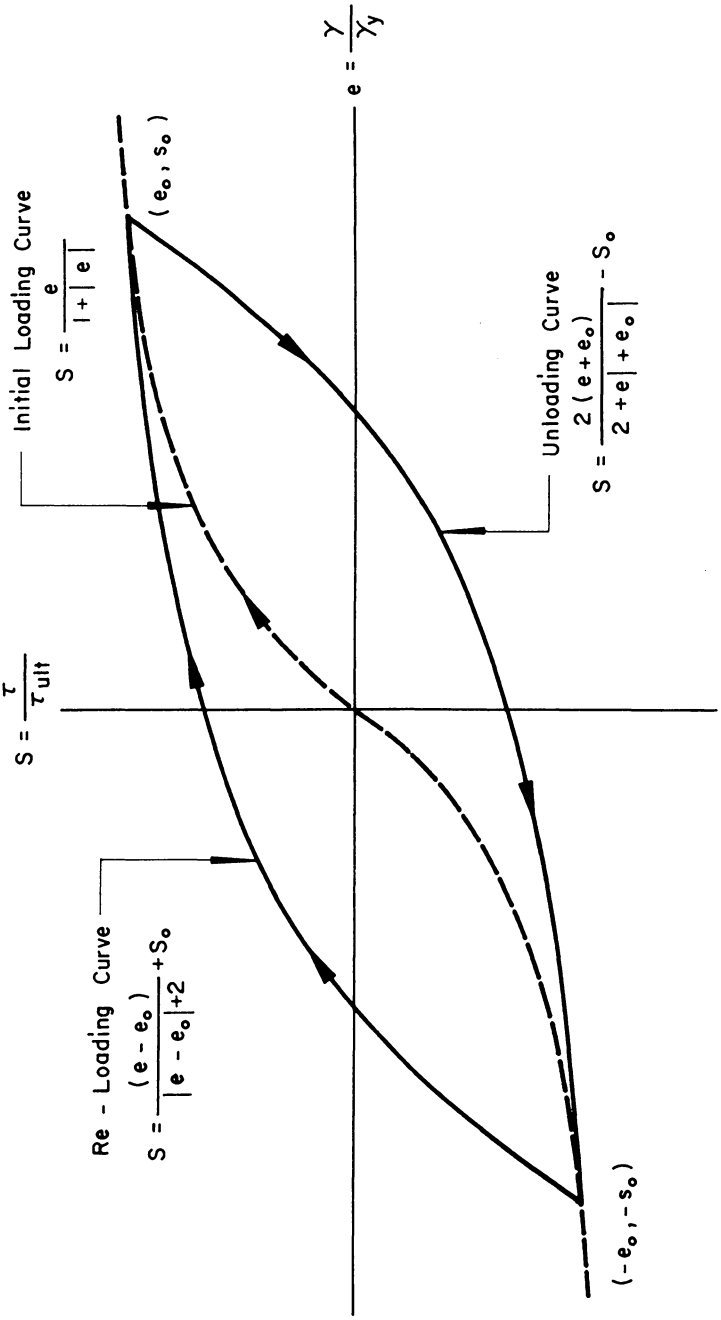

Figure 18. Hyperbolic Constitutive Relationship

utilized respectively in the time and frequency domain for the one-dimensional analyses of shear wave propagation in layered soil media.

5.1. True-Nonlinear Methods

The most common public-domain computer programs for the true-non-linear analysis are NONL13 (Joyner and Chen, 1975, CHARSOIL (Streeter et al., 1974a and b) and MASH (Martin and Seed, 1978).

The program CHARSOIL uses the Ramberg-Osgood type constitutive model with a time-domain solution technique based on the method of characteristics (Streeter et al., 1974). The program MASH uses the Martin-Davidenkov type constitutive model with the implicit time-domain solution based on the cubic inertia method (Argyris et al., 1973). The program NONLI3 models the hysteretic behavior of the soil by the composite elasto-plastic subelements (Iwan, 1967) with an explicit finite-difference time-domain solution. Both the CHARSOIL and MASH programs require a rigid boundary where the input seismic motion is defined. In NONLI3 a transmitting boundary is used to account for the finite rigidity of the underlying elastic half-space as described in Section 2.3. Extensive comparison of the techniques used in these programs on the basis specific site response problems have been conducted (e.g. Joyner and Chen, 1975; Lam et al., 1978; Martin and Seed, 1982).

Although there are some efforts (e.g. Joyner, 1975), the utilization of two-or three-dimensional true-nonlinear analysis in site response problems are not yet established for practical applications, mostly due to the inadequacy of available constitutive relationships.

As an illustration, one-dimensional vertical shear wave propagation in horizontally layered media will be covered utilizing a true-nonlinear approach similar to that proposed by Joyner and Chen (1975).

Consider a horizontally layered non-linear soil medium overlying a uniform linear half-space where a vertically incident S-wave is specified as indicated in Fig.19. The soil medium is discretized into n sub-layers with absolute displacements u_j, defined at the j th sub-layer, interface and with shear stress, τ_j, defined at the mid-points of each interface. On the basis of the Newton's Second Law the incremental equations (within a time step Δt) for the interface absolute accelerations can be written as :

$$\Delta\ddot{u}_j = \frac{1}{m_j}(\Delta\tau_j - \Delta\tau_{j-1}) \; ; \; m_j = \frac{1}{2}(\rho_j \Delta x_j + \rho_{j-1}\Delta x_{j-1}) \qquad (99)$$

where m_j is the lumped mass at the j th interface, ρ_j and Δx_j are, respectively the mass density and the thickness of the jth. sub-layer. For the first layer it is obvious that :

$$\Delta\ddot{u}_j = \frac{1}{m_1}(\Delta\tau_1) \; ; \qquad m_1 = \frac{1}{2}\rho_1 \Delta x_1 \qquad (100)$$

At the half-space interface one can write that

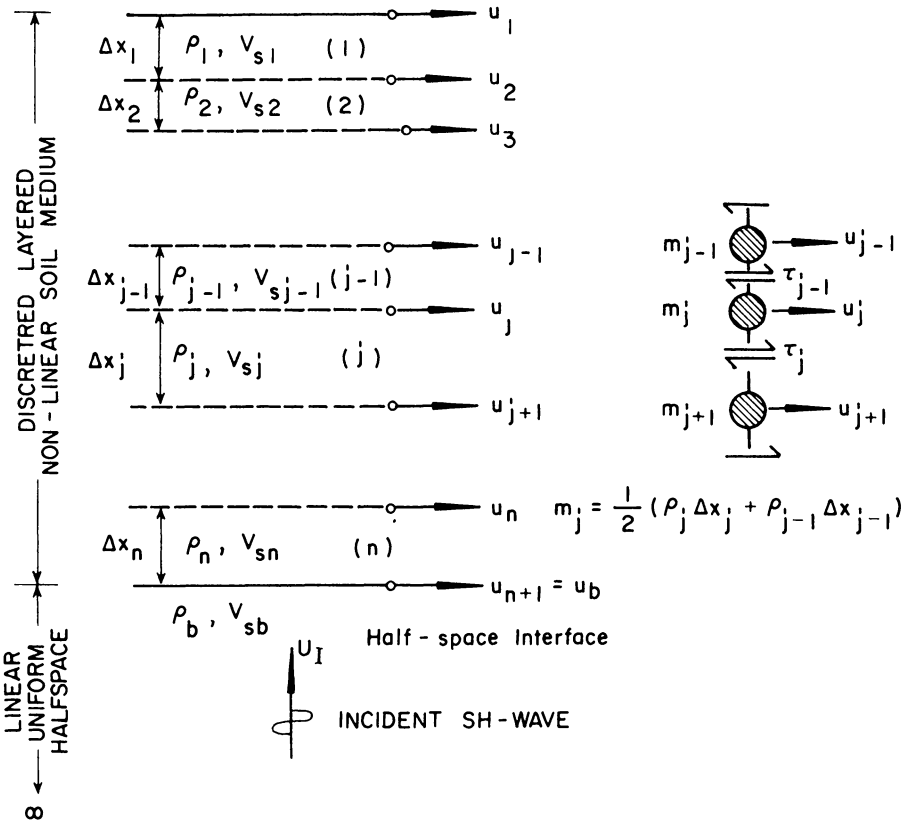

$$m_j = \frac{1}{2}\left(\rho_j \Delta x_j + \rho_{j-1} \Delta x_{j-1}\right)$$

Top Layer : $\Delta \ddot{u}_1 = \frac{1}{m_1} \Delta \tau_1$

j th Layer : $\Delta \ddot{u}_j = \frac{1}{m_j} \left(\Delta \tau_j - \Delta \tau_{j-1} \right)$

Half - space Interface :

$$\Delta \ddot{u}_b = \frac{1}{m_b + \frac{1}{2} \Delta t \rho_b V_{sb}} \left[\rho_b V_{sb} \left(2 \Delta \dot{u}_I - \ddot{u}_b(t) \Delta t \right) - \Delta \tau_n \right]$$

Figure 19. Explicit Discrete Formulation For One-Dimensional Shear Wave Propagation Problem

$$\Delta\ddot{u}_b = \Delta\ddot{u}_{n+1} = \frac{1}{m_b}(\Delta\tau_b - \Delta\tau_n) \quad ; \qquad m_b = \frac{1}{2}\rho_n \Delta x_n \tag{101}$$

where τ_b is the shear stress at the half-space interface defined by Eqn.66 and 67 and τ_n is the shear stress defined at the mid-point of the n th sub-layer. On the basis of Eqn.66 and 67

$$\Delta\tau_b = \rho_b V_{sb}\left[2\Delta\dot{u}_I - \Delta\dot{u}_b\right] \tag{102}$$

and assuming that the accelerations vary linearly during the time increment Δ

$$\Delta\dot{u}_b = \Delta t\left[\ddot{u}_b(t) + \frac{1}{2}\Delta\ddot{u}_b\right] \tag{103}$$

one can obtain by substituting Eqn.102 and 103 into 101 and rearranging:

$$\Delta\ddot{u}_b = \frac{1}{m_b + \frac{1}{2}\Delta t\,\rho_b V_{sb}} = \left[\rho_b V_{sb}\,(2\Delta\dot{u}_I - \ddot{u}_b(t)\,\Delta t) - \Delta\tau_n\right] \tag{104}$$

Note that $2\Delta u_I$ is equal to the Δu_o, where $u_o(t)$ is the motion associated with an outcrop of the half-space (c.f.Eqn.66).

Thus for known conditions at time $t, u_j(t)$, $\ddot{u}_b(t) = \ddot{u}_{n+1}(t)$ and $\tau_j(t)$ (for j=1 to n+1)) one can obtain the shear strain increments :

$$\Delta\gamma_j = \frac{\Delta t}{\Delta x_j}\left[\dot{u}_{j+1}(t) - \dot{u}_j(t)\right] \tag{105}$$

and the shear stress increments $\Delta\tau_j$ from the appropriate constitutive models enabling to compute $\Delta\ddot{u}_j$ from Eqns.99 and 100 and $\Delta\ddot{u}_b = \Delta\ddot{u}_{n+1}$ from Eqn.104 for specified $2\Delta\dot{u}_I$ (half-space outcrop motion). With known $u_j(t)$ various numerical integration techniques can be utilized to obtain $u_j(t+\Delta t)$, $\dot{u}_j(t+\Delta t)$ and $\ddot{u}_j(t+\Delta t)$.

The stability and the convergence of the numerical methods for such non-linear analyses have not been rigorously studied. For the linear analysis the stability is insured if the time step of integration is less than the transversal time of the wave access a discrete spatial step (Belytschko, 1976).

$$\Delta t \leq \frac{\Delta x_j}{V_{sj}} \tag{106}$$

For linear systems stability also implies convergence. Spurious high

frequency oscillations with frequencies related to the fundamental frequencies of the sub-layers (i.e. $V_{sj}/4\Delta x_j$) associated with such explicit numerical techniques may be needed to be suppressed either through the use of some small nominal amounts of viscous damping during the computation or through low-pass filtering after the computation. (Chen and Joyner, 1974).

This formulation together with a Martin-Davidenkov constitutive model and Wilson's θ type (Bathe and Wilson, 1975) numerical integration has been utilized in a computer program SITAMP (Erdik, 1981) and has been found to produce almost identical results with the test cases reported in Joyner and Chen (1975) and Martin and Seed (1978).

An intensive application of the one-dimensional true nonlinear site response analysis has been conducted by the Building Research Institute of the Ministry of Construction of Japan (Sugimura et al., 1984 and Ohsaki et al., 1984). In this true nonlinear analysis a Ramberg-Osgood type constitutive relationship is used with Wilson's θ (Bathe and Wilson, 1975) direct integration routine encompassing a 2% viscous damping ratio (presumably to suppress spurious oscillations). A simulated earthquake motion, specified at the bedrock with 0.1 and 0.3 g peak acceleration levels, is utilized for the site response analysis involving 948 soil profiles selected for the microzonation. The results of an interesting regression analysis between the peak ground accelerations, A_{max}, in g's and the fundamental period of the soil profiles, T_G, in sec's are as follows :

$$A_{max} = 0.08\ T_g^{-0.77} \quad \text{for 0.1 g peak base acceleration}$$

$$A_{max} = 0.14\ T_g^{-0.87} \quad \text{for 0.3 g peak base acceleration}$$

Although T is obviously not the only variable affecting the A_{max} the limited scatter of the data indicate very good correlation for the range of T_g is between 0.16 s and 1.6 sec.

Results of similar nature have also been reported by Erdik (1980) on the basis of a single-degree-of-freedom non-linear analog model of the true non-linear problem.

5.2. Equivalent-Linear Method

The so-called "equivalent-linear approach involving the iterative use of strain compatible soil properties in a frequencey-domain based analysis has been widely used by the engineering community. The most common public-domain computer programs conducting such site-response analysis are SHAKE (Schnabel et.al., 1972) for one dimensional analysis, LUSH (Lysmer et al., 1974) for two dimensional analysis and FLUSH (Lysmer et al., 1975) for approximate three dimensional extention of the two dimensional plane-strain analysis. For the two-dimensional analyses the shear, the constrained modulus and the damping ratio are adjusted with respect to the strain compatibility. Iteration process conducted only on the basis of the experimentally determined changes of the shear wave modulus and the associated damping ratio under uniaxial cyclic loading.

This is an approximation resulting from lack of data on strain-dependent P-wave properties and from the limitations of experimental results to describe such two-dimensional cases (Chen et al., 1981).

As an illustration, an equivalent-linear treatment of one-dimensional vertical shear wave propagation in horizontally layered media will be described in a similar manner to that used in SHAKE (Schnabel et al., 1972).

The analysis will be based on the transfer matrix formulation covered in Section 2.1 and Fig.2. The S-wave incidence is assumed to be vertical. The iterative methodology consists of the following steps carried out in the frequency domain:

(1) Transform the reference motion $v_{n+1}(t)$ specified at the reference interface (n+1) to obtain the Fourier Transform $\ddot{V}_{n+1}(\omega)$.
(2) Using small strain (10^{-3} -10^{-4}) soil parameters G_j^{n+1} and β_j compute the coefficients A_j and B_j for j = 1 to n
(3) Compute mid-point strain-to-base acceleration frequency response functions for all layers $H_{j,n+1}(\omega)$
(4) Compute strain time histories for all layers through the inverse Fourier-Transform of $\ddot{V}_{n+1}(\omega)$, $H_{j,n+1}(\omega)$
(5) Determine the maximum γ_j for all layers and the average strain through R.M.S. combination of maximum γ_j,
(6) Using $\bar{\gamma}$ find $G_j(\bar{\gamma})$ and $\beta_j(\bar{\gamma})$ from the experimental curves, such as those provided in Fig.16.
(7) Repeat steps (3) to (6) and check until the previous and current values of $\bar{\gamma}$ do not differ more than a previously established tolerance level.

With such an iterative scheme convergence (Step 7) is usually reached within several cycles. For control motions specified either at the surface or at the outcrop of the half-space the reference motion at the n+1 th. interface can be obtained through the use of appropriate transfer function with a similar iterative scheme in the frequency domain.

The applicability of the equivalent-linear techniques has been demonstrated on two well known case studies. One of them, as illustrated in Fig.20, involves the computation of the recorded ground motion at the base of the State Building starting from the ground motion recorded at the base of the Southern Pacific Building during the 1957 San Francisco earthquake (Seed and Schnabel, 1972). The other one, as illustrated in Fig.21 and 22, involves correlation of the computed and the recorded response at the Humbold Bay Power Plant. (Valera et al., 1977). The responses were recorded in the 1975 Ferndale earthquake and for computations a two-dimensional plane-strain equivalent linear approach, which approximates the third dimension effects through viscous element, is utilized.

Several researchers have compared the site-response analysis results based on the equivalent linear and true non-linear approaches. Conclusions reached by Martin and Seed (1982), Joyner and Chen (1975) and Öner et al., (1981) reveal that in the frequency domain the equivalent-linear method significantly and consistently underestimates the level of motion for frequencies above 2-5Hz. The equivalent-linear method may also predict high acceleration levels. For example in one of the

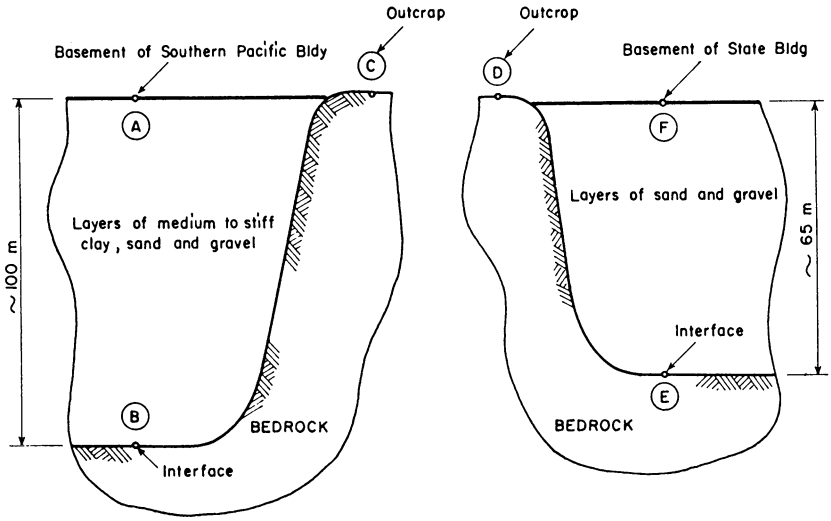

Recorded Motion at A = 0.048 g

(Equivalent Linear Analysis, Deconvolution)

Computed Motion at B = 0.032 g

Computed Motion at C = 0.039 g

(Emprical Attenuation Relationships)

Computed Motion at D = 0.048 g

(Equivalent Linear Analysis)

Computed Motion at E = 0.044 g

(Equivalent Linear Analysis)

Computed Motion at F = 0.093 g

Recorded Motion at F = 0.013 g

Figure 20. Response of one Site Computed from Motions Recorded at Another Site During 1957 San Francisco Earthquake (Seed and Schnabel, 1972).

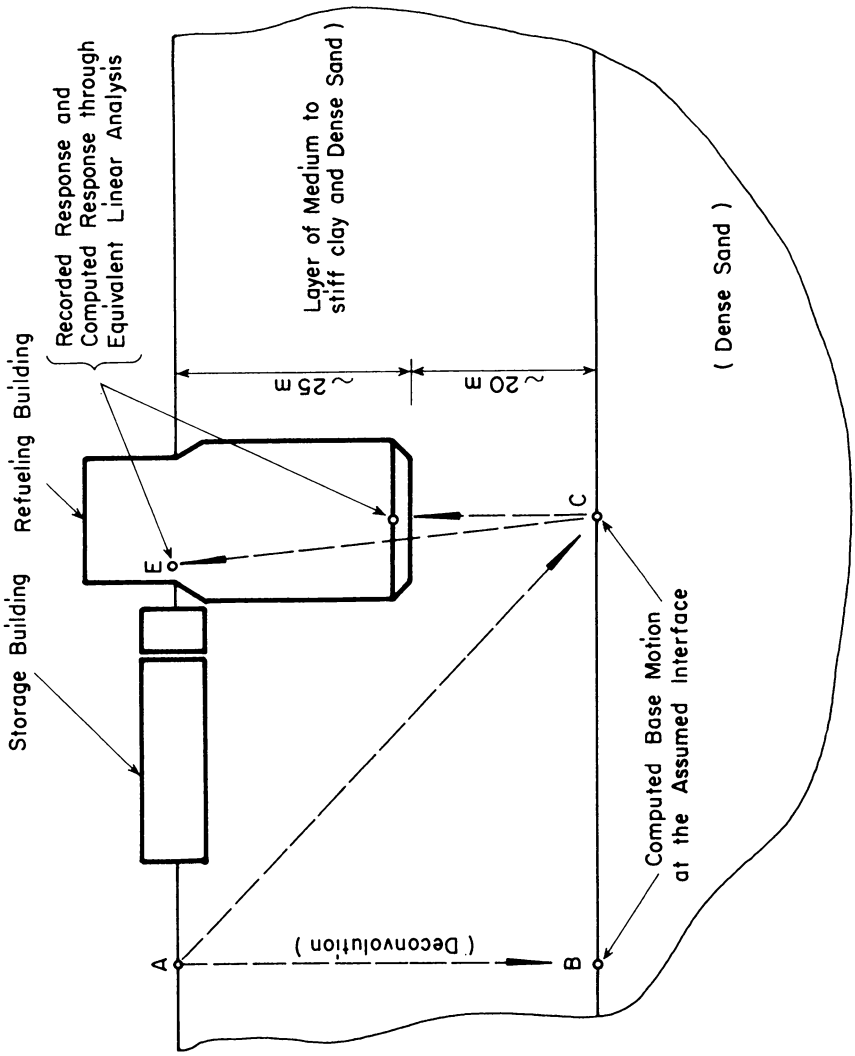

Figure 21. Ground Motion and **Response** Records and the Schematic Representation of the Computational Approach (Humboldt Bay Power Plant, Ferndale Earthquake (After Valera et al., 1977)

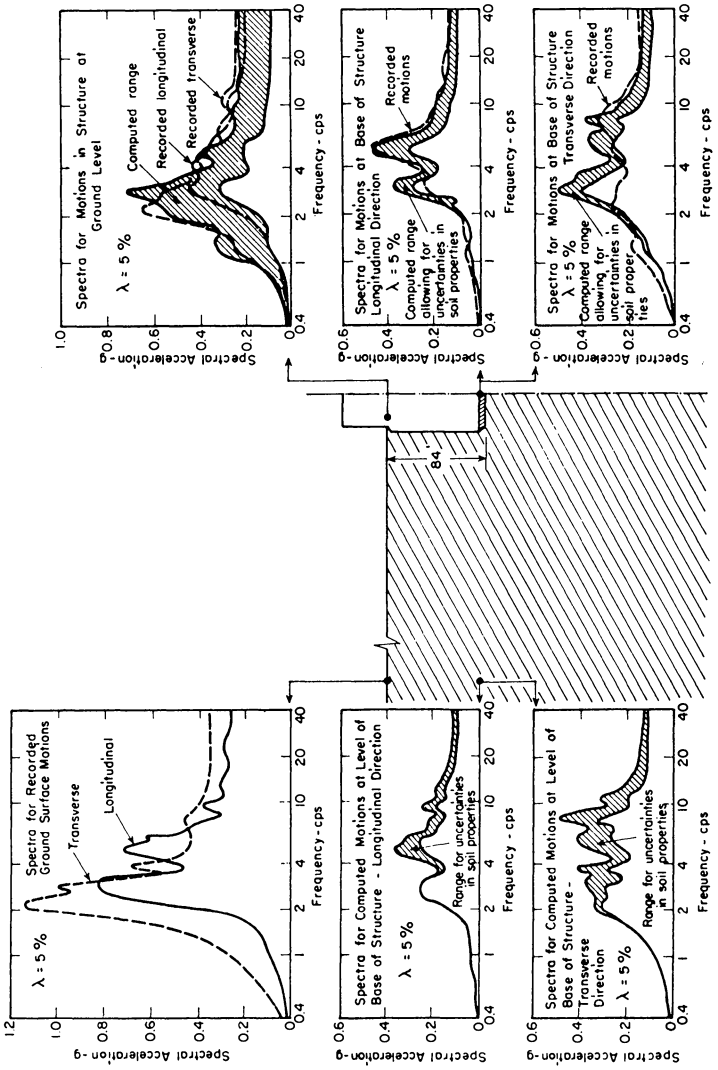

Figure 22. Comparison of Recorded and Computed Spectra in Refueling Building-Humboldt Bay Power Plant (After Valera et al., 1977)

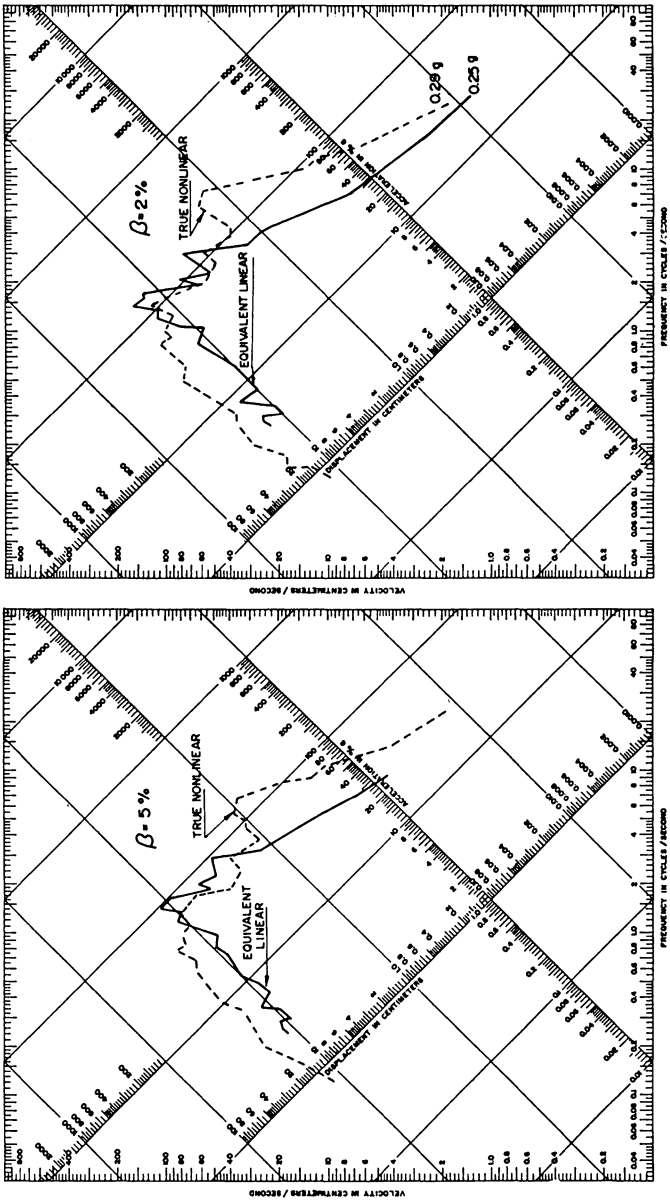

Figure 23. Response Spectra of Ground Motions (Karakaya Railway Bridge Site, Taft Accelerogram at Bedrock Outcrop) (After Öner et al., 1981).

comparisons presented by Martin and Seed (1982) the ground surface accelerations of 0.55 g, 0.22 g, an 0.27 g are obtained respectively through the applications of equivalent-linear and two true-non-linear methods to a site response problem involving 100 ft dry sand with a maximum base acceleration of 0.57 g. A comparison of the response spectra of the ground motion obtained on the basis of equivalent-linear and true-non-linear techniques is provided in Fig.23 for a specific site-response analysis (Öner et al. 1981).

REFERENCES

Aki, K. and P.G.Richards (1980). Quantitative Seismology, Theory and Methods, W.H. Freeman and Co., San Francisco, 1980.

Argyris, J.H., P.C.Dunne and T.Angelopoulos (1973), Dynamic Response by Large Step Integration, Journ. of Earth. Engrg. and Struct. Dyn., v.2, pp.185-203.

ATC (1978) - Applied Technology Council - Tentative Provisions for the Development of Seismic Regulations for Buildings, NBIS, Special Pulication No:510, Washington, D.C., USA.

Bathe, K.J. and E.L.Wilson (1976), Numerical Methods in Finite Element Analysis, Prentice-Hall, Inc., Englewood Cliffs, New Jersey.

Belytschko, T. (1976), A Survey of Numerical Methods and Computer Programs for Dynamic Structural Analysis, Nuclear Engineering and Design, 37, pp.23-34.

Berril, J.B. (1975), A Study of High Frequency Strong Ground Motion From the San Fernando Earthquake, Soil Mechanics Laboratory, California Institute of Technology, Pasadena, CA.

Boore, D.M. (1972), Finite Difference Methods for Seismic Wave Propagation in Heterogeneous Materials, in Methods in Computational Physics, Vol.11, Ed.by B.A.Bolt,Academic Press, New York and London.

Boore, D.M., W.B.Joyner, A.A.Oliver and R.A.Page (1980), Peak Acceleration Velocity and Displacement from Strong Motion Records, Bull.Seism. Soc. Am. 70, 305-321.

Borcherdt, R.D. and J.F.Gibbs (1976). Effects of Local Geological Conditions in the San Francisco Bay Region on Ground Motions and the Intensities of the 1906 Earthquake, Bull.Seism. Soc. Am., 66, 467-500.

Brekhovskikh, L.M. (1980), Waves in Layered Media, Academic Press Inc.

Campbell, K.W. (1981). Near-source Attenuation of Peak Horizontal Acceleration, Bull. Seism. Soc. Am., 71, 2039-2070.

Chen, A.T.F. and W.B.Joyner 1974, Multi-Linear Analysis for Ground Motion Studies of Layered Systems, Report No.USGS-GD-74-020, U.S.G.S., Menlo Park, CA.

Chen, J.C., J.Lysmer and B.Seed (1981), Analysis of Local Variations in Free Field Seismic Ground Motions, Earthq.Engrg.Res.Center, Univ. of Calif.,Berkeley, Report No.EERC 81-03, CA.

Clough, R.W. and J.Penzien (1975), Dynamics of Structures, McGraw-Hill, Inc., New York.

Crouse, C.B. (1973), Engineering Studies of the San Fernando Earthquake, Report No: 73-04, Earthquake Engineering Research Laboratory, California Institute of Technology, Pasadena, CA.

Day, S.M., Read, H.E., Swanger H.J. and K.J.Cheverton (1981), Simulation of Local Site Response to Earthquakes, U.S.G.S. Open File Report 81-85, Menlo Park, USA.

Dobry, R., R.V. Whitman and J.M.Roesset (1971), Soil Properties and the One-Dimensional Theory of Soil Amplification, Research Report No:R71-18, Depth.of Civil Engrg., Massachusetts Institute of Technology, Cambridge, MA.

Erdik, M. (1980), A Single Degree of Freedom Model for Non-Linear Soil Amplification, Proc. 7th. World Conf. on Earthq.Engrg., Istanbul, Turkey, V.2, pp.191-198.

Erdik, M.Ö. (1981), Finite Difference Solution for Non-Linear Wave Propagation in Soils (in Turkish), Proc.First National Congress of Soil Mechanics and Foundation Engineering, Ankara, Turkey, pp.189-213.

Hays, W.W., A.M.Rogers and K.W.King (1979), Empirical Data About Local Ground Response, Proc. 2nd.Natl.Conf. on Earthq. Engrg., pp.223-232, Stanford, CA.

Haskell, N.A. (1953). The Dispersion of Surface Waves on Multilayered Media, Bull.Seism.Soc. Am. 73. 17-34.

Hardin, B.O. and V.P. Drnevich (1972), Shear Modulus and Damping in Soils, ASCE, Jour. Soil Mech. and Fdtn. Div., 98, pp.603-624 and 667-692.

Herrera, I., E.Rosenblueth and O.Rascon (1965), Earthquake Spectrum Prediction for the Valley of Mexico, Proc. 2nd. World Conf. on Earthq. Engrg., New Zealand, V.I. pp. 1.61-1.74.

Huang, M. (1983), Investigation of Local Geology Effects on Strong Earthquake Ground Motions, Calif. Inst. of Tech., Earthq.Eng.Res.Lab., Report no: EERL 83-03. Pasadena, California.

Idriss, I.M. and H.B.Seed (1967), Response of Horizontal Soil Layers During Earthquakes, Department of Civil Engineering, U.C., Berkeley,CA.

Idriss, I.M. and H.B.Seed (1968), An Analysis of Ground Motions During the 1957 San Francisco Earthquake, Bull. Seism.Soc. Am., V.58, pp.2013-2032.

Idriss, I.M., J.Lysmer, R.Hwang and H.B.Seed (1973), "QUAD-4" A Computer Program for Evaluating the Seismic Response of Soil Structures by Variable Damping Finite Element Procedures, Earthquake Engineering Research Center Report No:EERC 73/16, Univ. of Calif., Berkeley CA.

Iwan, W.D. (1967), On a Class of Models for the Yielding Behavior of Continuous and Composite Systems,Trans. ASME, Journal of Applied Mechanics, pp.612-617.

Jacobsen, L.S. (1969), Damping in Composite Structures, Proc. 2nd.World Jonf. on Earthq. Engrg., Tokyo and Kyoto, Japan, pp. 1029-1044.

Johnson, L.R. and W.Silva (1981), The Effects of Unconsolidated Sediments Upon the Ground Motion During Local Earthquakes, Bull. Seism. Soc. Am., V.71, pp.127-142.

Joyner, W.B. and A.T.F. Chen (1975), Calculation of Non-Linear Ground Response in Earthquakes, Bull. Seism. Soc. Am., v.65, pp.1315-1336.

Joyner, W.B. (1977), A Fortran Program for Calculating Nonlinear Seismic Ground Response "NONLI3", U.S.G.S. Open File Report 77-761, Menlo Park, USA.

Joyner, W.B., R.E.Warrick and A.A.Oliver (1976), Analysis of Seismograms from a Downhole Array in Sediments near San Francisco Bay, Bull. Seism. Soc. Am., V.66, pp.937-958.

Kanai, K.(1961), An Empirical Formula for the Spectrum of Strong Earthquake Motions, Bull.Earthq. Res. Inst., v.39, pp.85-95.

Kanai, K. (1962), On the Spectrum of Strong Earthquake Motions, Bull.of Earthq. Res. Inst., v.40.

Kausel, E. and J.M.Roesset, (1981). Stiffness Matrices for Layered Soils, Bull. Seism. Soc. Am. 71, 1743-1761.

Kennett, B.L.N. and N.J. Kerry (1979). Seismic Waves in Stratified Half Space, Geophys. J.R. astr. Soc. 57, 557-583.

Kinoshita, S. and T.Mikoshiba (1984), Observation of Earthquake Response of Thick Sedimentary Layers, Proc. 8th. World Conf. on Earth. Engrg., v.2. pp.753-760, San Francisco.

Kudo, M., E.Shima and Y.Sawada (1984), Comparative Observation of Ground Motions at Different Soil Conditions from Moderately Large Earthquakes, Proc.8th. World Conf. on Earthq. Engrg., V.2. pp.769-776., San Francisco.

Lam, I., Tsai, C.F., and G.R.Martin (1978), Determination of Site Dependent Spectra Using Non-Linear Analysis, Second Int. Conf. on Microzonation, Vol.2, San Francisco, USA.

Lysmer, J. and R.L. Kuhlemeyer (1969), Finite Dynamic Model for Infinite Media, Journal Engrg. Mech.Div., ASCE, Vol.95, pp.859-877.

Lysmer, J. and L.A.Drake (1972), A Finite Element Method for Seismology, in Methods in Computational Physics, Vol.11, Ed.by B.A.Bolt, Academic Press, New York and London.

Lysmer, J., T.Udaka, H.B. Seed and R.Hwang (1974). "LUSH" a Computer Program for Complex Response Analysis of Soil-Structure Systems, Earthq. Engrg. Res. Center, Univ. of Calif., Berkeley, Report No: EERC 74-4.

Lysmer, J., T.Udaka, C.F. Tsai and H.B.Seed (1975), FLUSH-A Computer Program for Approximate 3-D Analysis of Soil Structure Interaction Problems, Earthq.Engrg. Res.Center, Report No:EERC 35-30, University of Calif., Berkeley, CA.

Martin, P.P. (1975), Non-Linear Methods for Dynamic Analysis of Ground Response, Ph.D. Thesis, Univ. of Calif., Berkeley.

Martin, P.P. and H.B.Seed (1978), "MASH", A Computer Program for the Non-Linear Analysis of Vertically Propagating Shear Waves in Horizontally Layered Deposits, Report No.EERC 78-23, U.C., Berkeley, CA.

Martin, and H.B. Seed (1982), One-Dimensional Dynamic Ground Response Analysis, Journal of Geotechnical Engrg., ASCE, G77, pp.935-952.

Massing, G. (1926), Eigenspannungen und Verfestigung beim Messing, Proc. 2nd. Int. Congress of Appl. Mech., pp.323-335.

Murphy, J. (1983), Site Effects on Strong Ground Motion Observed From Underground Explosions, in Proc. of a Workshop on Site Specific Effects of Soil and Rock and Ground Motion and the Implications for Earthquake Resistant Design, U.S.G.S., Reston, VA .

Newmark, N.M., A.R.Robinson, A.H. - S.Ang, L.A.Lopez, W.J.Hall (1972), Methods for Determining Site Characteristics, Proc. the Int. Conf. on Microzonation for Safer Const., Res. and Application, pp.113-129, Seatle, Washington.

Newmark, N. (1959), A Method of Computation for Structural Dynamics, J.Eng. Mech.Div., Proc. of ASCE, 67-94.

Ohsaki, Y. (1975), Dynamic Characteristics and One-Dimensional Amplification Theory of Soil Deposits, Int. Inst. of Seism. and Earthq. Engrg., Tokyo, Japan.

Ohsaki, Y., M.Watabe, M.Tohdo and I.Ohkawa (1984), Characteristics of Surface Ground Motions Considering The Various Property Combinations of Subsoils and Earthquakes, Proc. 8th. World Conf. on Earthq. Engrg., San Francisco, U.S.A.

Öner,M.,M.Erdik and G.Özcebe (1981), A Cases Study of Soil Amplification Analysis by Equivalent-Linear and True Nonlinear Methods, Earthquake Engineering Research Center, Report No: 81-03, Middle East Technical University, Ankara, Turkey.

Omote, S. et al.(1984), Observation of Earthquake Strong Ground Motion with Deep Boreholes-An Introductory Note for Iwaki and Tomioka Observation Station in Japan, Proc. 8th.World Conf. on Earthq. Engrg., v.1, p.p.739-746, San Francisco, CA.

Özgür, D. and A.Gürpınar (1972). Modeling of the Earthquake Acceleration Spectrum (in Turkish), Scientific and Technical Research Institution of Turkey, Project No: MAG 302, Ankara, Turkey.

Ramberg, W. and W.R.Osgood (1943), Description of Stress-Strain Curves by Three Parameters, Technical Note 902, NACA.

Roesset, J.M.(1970), "Fundamentals of Soil Amplification", in Seismic Design for Nuclear Power Plants, editör, R.J.Hansen, p.p.183-244.

Schnabel, P.B., Lysmer, J. and H.B.Seed(1972), "SHAKE" A Computer Program for Earthquake Response Analysis of Horizontally Layered Sites," Report No.EERC 72-12, U.C.Berkeley, CA.

SEAOC (1980), Recommended Lateral Force Requirements and Commentary, Seismology Committee, Structural Engineers Association of California, San Francisco, USA.

Seed, H.B. and I.M.Idriss (1970), Soil Moduli and Damping Factors for Dynamic Response Analysis, Report No: EERC 70-10, Univ. of Calif., Berkeley, CA.

Seed, H.B. and Per.B.Schnabel (1972), Soil and Geologic Effects on Site Response During Earthquakes, Proc.First Int.Conf. on Microzonation, Seattle, Washington, U.S.A.

Seed, H.B., R.V. Whitman, H.Dezfulian, R.Dorey and I.M.Idriss(1972),Soil Conditions and Building Damage in 1967 Caracas Earthquake, J.Soil. Mech. and Found. Div., ASCE, 98, 787-806.

Seed, H.B. and J.Lysmer (1977), Soil Structure Interaction Analysis By Finite Element Methods, State-of-the-Art, Trans.Structural Mechanics in Reactor Technology, San Francisco, CA.

Seed, H.B. and J.Lysmer (1980), Site Response and Soil-Structure Interaction Analysis, Lecture Notes, Short Course on Earthquake Engineering, University of California, Berkeley, June 16, 1980.

Silva, W.(197). Body Waves in a Layered Anelastic Solid, Bull. Seism. Soc.Am. 66, 1539-1554.

Streeter, V.L., Wylie, E.B. and F.E.Richart (1974a), Soil Motion Computations by Characteristic Method, Journal of Geotech. Eng.Div., ASCE, Vol.100, GT.

Streeter, V.L., Wylie, E.B. and F.E.Richart (1974b) "CHARSOIL", Available through NISEE, Univ. of Calif., Berkeley, USA.

Sugimura, Y. and I.Ohkawa (1984), Seismic Microzonation of Tokyo Area, Proc. 8th. World Conf. on Earthq. Engrg., San Francisco, USA.

Swanger, H.J. and D.M.Boore (1978),Simulation of Strong-Mation Displacements Using Surface-Wave Model Superposition, Bull. Seism.Soc. Am.,68, pp.247-263.

Thomson, W.T.(1950). Transmission of Elastic Waves Through a Stratified Soil Medium, J.Appt. Phys. 21, 89-93.

Tsai, Nien-Chien (1969), Influence of Local Geology on Earthquake Ground Motion, Ph.D.Theis, California Institute of Technology, Pasadena, CA.

Umemura, H., M.Wataba, Y.Ishiyama, T.Fukuta (1984), Follow-up of New Earthquake Resistant Design Regulations for Buildings in Japan, Proc. 8th. World Conf. on Earth. Engrg., v.1,pp.739-746, San Francisco, CA.

Valera, J.E., H.Seed, C.F.Tsai and J.Lysmer (1977), Soil Structure Interaction Effects at the Humboldt Bay Power Plant in the Ferndale Earthquake of June 7, 1975., Earthquake Engineering Research Center, Reports No:UCE/EERC-77/02, University of California, Berkeley, CA.

Whitman, R.V., J.M.Roesset, R.Dobry and L.Ayestaran (1972), Accuracy of Model Superposition for One-Dimensional Soil Amplification Analysis. Proc. First Conference for Microzonation, Seattle, Washington.

Wilson, E.L., I.Farhoomand and K.J.Bathe (1973), Nonlinear Dynamic Analysis of Complex Structures, Int.Journal of Earthquake Engrg. and Struct. Dyn. v.1, 241-252.

Wolf, J.P. and P.Obernhuber (1982a), Free Field Response From Inclined SH-Waves and Love-Waves, Earthq.Engrg. and Struct. Dyn., 10, 823-845.

Wolf, J.P. and P.Obernhuber (1982b), Free Field Response From Inclined SV-and P-Waves and Rayleigh Waves, Earthq.Engrg. and Struct.Dyn.10, 847-869.

CONSTITUTIVE RELATIONSHIPS FOR SOIL DYNAMICS

Atilla M.Ansal
Civil Engineering Faculty
Istanbul Technical University
Ayazaga - Istanbul

ABSTRACT. The main intention in this paper is to give a brief overview of the constitutive relationships developed to model cyclic behavior of soils. In doing this, the constitutive equations formulated and implemented in various numerical analysis methods are classified under two categories; nonlinear elastic and elasto-plastic. In the last section of the paper, as an example to the elasto-plastic constitutive relationships, a brief description and an application of an endochronic constitutive equations developed to model cyclic simple shear behavior of cohesive soils is presented.

1. INTRODUCTION

During the last decade, the requirements imposed in the analysis and design of the important engineering structures such as large dams, nuclear power plants and offshore structures justified the use of more sophisticated methods to evaluate the response of these structures under cyclic and transient loads. In the meantime the advances accomplished in the computer technology with respect to memory capacity and computation speed increased the feasibility of these sophisticated analysis procedures. In addition, it was observed for some engineering structures that conventional pseudo-static methods of analysis may give erroneously high safety factors.

As a result, there was an eminent demand for realistic constitutive relationships in the field of soil dynamics to model the behavior of a soil element under cyclic loads. In actuality this demand has arisen mainly from the increasing use of numerical methods such as finite elements, in analyzing the response of soil layers and earth structures. Initially most of these methods are formulated based on the concept of linear elastic stress-strain relationship, however, in the case of soils the use of linear elasticity has a very limited applicability in analyzing the response of various structures under cyclic loads such as earthquakes. Therefore most of the efforts was directed towards the implementation of more realistic constitutive relationships into these numerical analysis methods so that the results obtained would have some

M. O. Erdik and M. N. Toksöz (eds.), Strong Ground Motion Seismology, 535–544.
© 1987 by D. Reidel Publishing Company.

significance in the engineering evaluation of the response of the structure investigated.

The constitutive relationships thus developed may be considered in two groups. The first group of relationships are based on visco-elastic or nonlinear elastic expressions developed mostly in a semi-emprical manner from the observed cyclic behavior of soil samples in the laboratory. The second group of constitutive relationships evolved basicly from the theory of plasticity or based on elasto-plastic concepts used for modelling soil behavior. As an example to this second group of constitutive relationships an endochronic model developed for cyclic behavior of clay will be briefly summarized.

2. NONLINEAR ELASTIC RELATIONSHIPS

The experimental investigations conducted on cyclic behavior of soils have shown a strong dependence of dynamic modulus and damping ratio on the strain amplitude as shown in Figure 1 and 2. This nonlinearity of dynamic soil parameters may simply be taken into account by adopting an equivalent linear analysis method. In this approach an iterative procedure is utilized to obtain modulus and damping values compatible with the effective strain. The variation of modulus and damping values with respect to strain amplitude is determined based on laboratory and field cyclic testing.

The most widely used constitutive relationships in the field of soil dynamics are based on the concept of nonlinear elasticity. Among these relationships which involve different semi-emprical expressions to define various aspects of cyclic soil behavior, the most frequently used ones are bilinear, Ramberg-Osgood and Hardin-Drnevich models.

In the bilinear model the histeresis loops observed during cyclic behavior of a soil element are modelled with piecewise linear relationships for stress and strain where

$$\tau = G_o \gamma \qquad \text{for} \qquad \gamma < \gamma_y \tag{1}$$

and

$$\tau = \tau_y + G_y (\gamma - \gamma_y) \qquad \text{for} \qquad \gamma \geq \gamma_y \tag{2}$$

In the Ramberg-Osgood model the stress-strain relationship can be expressed as

$$\gamma = \frac{\tau}{G_o} \left(1 + \alpha \left| \frac{\tau}{\tau_y} \right|^{\beta}\right) \tag{3}$$

and in the Hardin-Drnevich (1972) model as

$$\tau = G_o \gamma / (1 + G_o \gamma / \gamma_f) \tag{4}$$

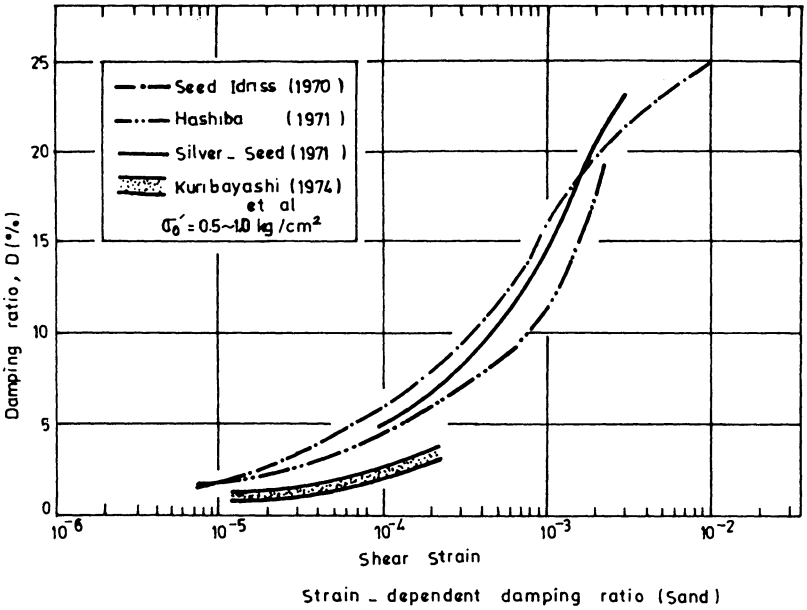

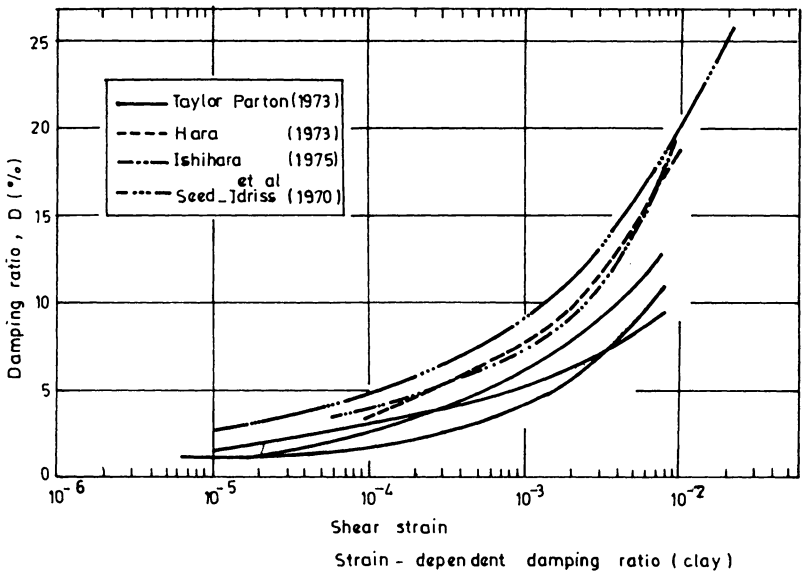

Figure 1. Strain-Depentent Damping Ratio

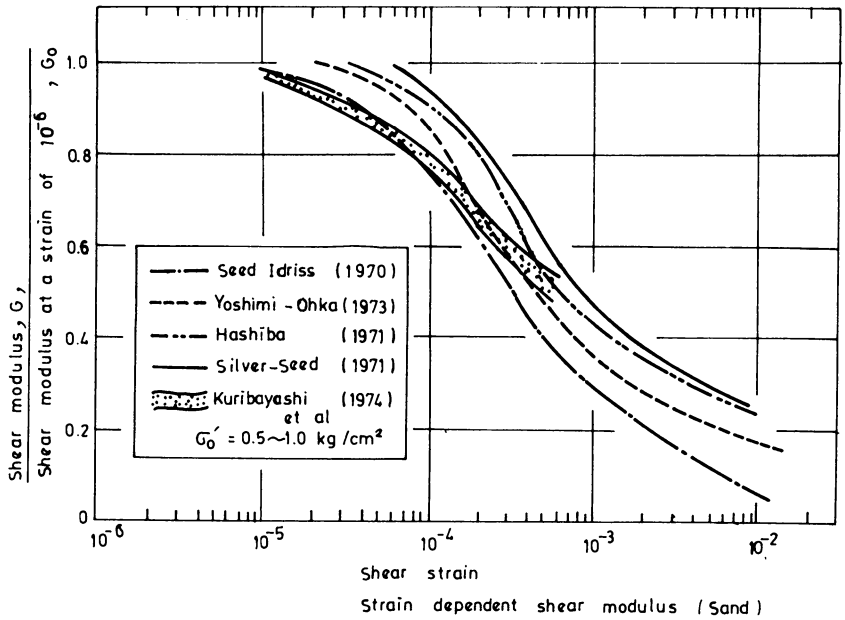

Strain dependent shear modulus (Sand)

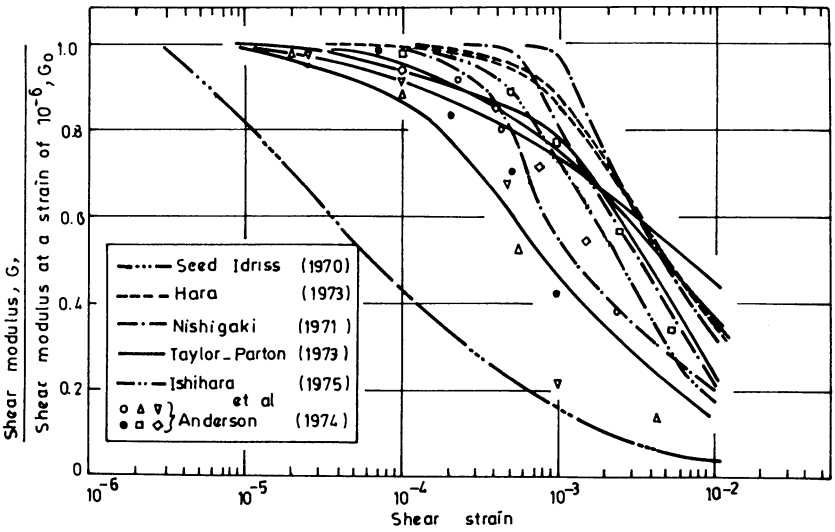

Strain - dependent shear modulus (clay)

Figure 2. Strain-Dependent Shear Moduli

where τ_y is the yield stress, G_y is the shear modulus after yield, γ_y is the yield strain, G_o is the initial tangent modulus, τ_f is the shear strength and α, β are material constants.

An example to an application of Hardin-Drnevich type constitutive model has been reported by Finn, Lee, and Martin (1976). In this application the shear stress shear strain relationship for initial loading is formulated as

$$\tau = G_{mo}\gamma \Big/ \left(1 + \frac{G_{mo}}{\tau_{mo}}\gamma\right) \tag{5}$$

where τ is the shear stress at strain amplitude γ, G_{mo} is initial maximum tangent modulus and τ_{mo} is the initial maximum shear stress that can be applied without failure.

The stress-strain curve for unloading and reloading is defined in accordance with the Masing rules as

$$\frac{\tau - \tau_r}{2} = f\left(\frac{\gamma - \gamma_r}{2}\right) \tag{6}$$

where (τ_r, γ_r) is the last load reversal point.

In the proposed constitutive relationship which was originally formulated to model the cyclic shear behavior of sand layers, a semi-emprical expression is introduced to evaluate the pore pressure response for saturated layers.

The increase in the pore water pressure is considered as the product one dimensional rebound modulus of sand, E_r, and volumetric compaction strain increment, $\Delta\varepsilon_{vd}$ as

$$\Delta u = E_r \, \Delta\varepsilon_{vd} \tag{7}$$

The volumetric strain increment and the magnitude of rebound modulus is determined from the laboratory test results. In addition the effect of hardening and pore pressure change was considered and the magnitudes of initial modulus and maximum shear stress were re-evaluated at each cycle.

3. ELASTO - PLASTIC RELATIONS

A major group of constitutive relationships developed to model the cyclic behavior of soils are based on the concept of elasto-plasticity. Considering the existence of elastic recoverable and plastic irrecoverable and plastic irrecoverable strains from the very onset of loading in soils it appears more realistic to adopt such an approach in the evaluation of the response of soil layers under cyclic and transient loads. A large number of constitutive relationships thus developed are derived from the theory of plasticity utilizing different formulations in defining the yield surface or yield function, plastic potential or loading function, isotropic and kinematic hardening rules.

Am important example to this group of constitutive relationships is the multi-surface plasticity model developed by Prevost (1977). It was assumed that the elasticity of the material is linear and isotropic and nonlinearity and anisotropy is a result of plastic straining. The effects of cyclic loading on the soil behavior are taken into account with isotropic or kinematic hardening or both depending on the type of soil and the nature of the loading. The concept of plastic moduli proposed by Mroz (1967) introducing a collection of nested yield surfaces is adopted to define the region of constant plastic moduli in the stress space. The model parameters are obtained from conventional triaxial tests in the laboratory.

3.1. An Endochronic Model For Cyclic Behavior

The soil response is considered as composed of elastic deformations resulting from the compression of soil particles and particle structure and inelastic deformations from the very onset of loading due to relative movements between particles. Thus a stress-strain relationship can be expressed in terms of elastic and inelastic components. However, it is necessary to adapt an incremental relationship that may be solved utilizing a step-by-step integration procedure due to the dependence of inelastic strains on stress and strain path followed. The endochronic constitutive equations formulated in this study are based on this concept and the basic shear stress, τ, and shear strain γ, relation is expressed as :

$$d\gamma = d\tau/G - \tau dz/G \tag{8}$$

where G is the elastic shear modulus and z is defined as the intrinsic time. The first term represents the elastic strains and the second term represents the elastic strains and the second term represents the inelastic strains in Eq(8) where intrinsic time increment is treated as an inelasticity coefficient which would yield the inelastic strain increment when multiplied with the total elastic strain. In addition to handle the sudren change of soil response a kinematic hardening scheme is introduced in Eq.(8) as suggested by Ansal, Krizek, and Bazant (1980).

The endochronic approach implemented is based on the assumption of the existence of internal state variables which monitor the inelastic behavior of soils. One such variable incorporated in Eq.(8) is the intrinsic time which is a nondecreasing scalar formulated to account for the effects of changes in the particle structure along a loading path.

In modelling stress-strain behavior of soils it appears necessary to consider the influence of microstructural changes and the strain rate. In the proposed approach assuming that the contribution from these two factors can be expressed separately, the intrinsic time increment, dz, is as (Bazant and Bhat, 1976) :

$$(dz)^2 = (d\tau/z_1)^2 - (dt/t_1)^2 \tag{9}$$

In this equality τ is defined as rearrangement measure, dt represents the period of cyclic loading, and z_1 and t_1 are material constants. The implementation of the second term in this equation is to account for the effect of the loading rate or frequency. The first term is introduced to evaluate the effects of micro-structural changes in the particle structure and fabric of the soil element on the inelastic strains. A set of relationships similar to ones developed by Ansal, Bazant, and Krizek (1979) is used to define the rearrangement measure as,

$$d\tau = d\eta/f(\eta) \tag{10}$$

and

$$d\eta = F(\varepsilon,\sigma)d\xi \tag{11}$$

where η is used as a deformation variable composed of strain softening function, F, and distortion measure, ξ. f (η) defined as the strain hardening function is included to account for isotropic hardening. In modelling the soil behavior under shear stresses, since the controling factor is the shear strain, the increment of distortion measure may be taken as :

$$d\xi = |d\gamma| \tag{12}$$

In the formulation of the strain softening, F, two main parameters (a) effective stresses expressed as the first invariant of stress, I_1^σ, (b) accumulated shear strain expressed as the second invariant of deviatoric strain, J_2^ε, was found to be sufficient to establish a realistic model for cyclic behavior of clay samples. The relationship utilized in this study is taken as

$$F(\varepsilon,\sigma) = a_1 - (1.0 - a_2 J_2^\varepsilon)/(1.0 - a_3 I_1^\sigma) \tag{13}$$

where a_1, a_2, and a_3 are material constants.

The pore pressure behavior is modelled based on the concept of two phase medium (Biot, 1956) considering the compessibility of pore water and volumetric strains due to shear stresses. Unlike other materials, soils exhibit dilatancy or densification depending upon the initial density even under pure shear stresses. One way of evaluating this phenomena, adopted in the endochronic approach, is based on the formulation of a densification-dilatancy function defined as :

$$d\lambda = \{ c_1(1.0 - c_2 J_2^3)/(1.0 - c_3\lambda) \} d\xi \tag{14}$$

In this expression λ is the inelastic volume change and c_1, c_2, and c_3 are material constants. It is assumed in this relationship that the inelastic volume changes are only due to the shear strains and the consolidation process is not considered. The pore pressure increment is determined utilizing the increment of inelastic volume change and the compressibility of the pore water.

The elastic shear modulus, G, in Eq.(8) is assumed dependent only on the effective stresses. A strain controlled integration procedure is used along with a nonlinear least squares algorithm to determine the values of material constants that would give the best fits for cyclic test results conducted under different shear amplitudes.

Cyclic simple shear tests are performed on the kaolinite specimens prepared in the slurry consolidometers. They were consolidated under isotropic stresses in the shear cell and cyclic tests are conducted at a frequency of 0.1 Hz. The main intention in this investigation was to demonstrate the applicability of the endochronic approach in modelling cyclic behavior of soils. Total of 11 material constants are used in material functions and cyclic shear stress-shear strain loop for two tests performed are modelled. The behavior calculated for the first test with a relatively large shear stress amplitude is shown on Figure 2. The stress-strain loops for the second test with a smaller stress amplitude is shown on Figure 3. It is possible to see from these data that cyclic stress-strain behavior modelled is very similar to observed behavior in cyclic simple shear tests. In addition to stress-strain behavior the variation of the pore pressure in the second test is shown on Figure 4 with respect to the shear strain. It is also possible here to see the similarity between calculated and observed pore pressure behavior. These results as well as the others obtained in the previous investigations (Krizek, Ansal, and Bazant, 1978; Bazant, Ansal and Krizek, (1982) indicate clearly the flexibility of endochronic constitutive models.

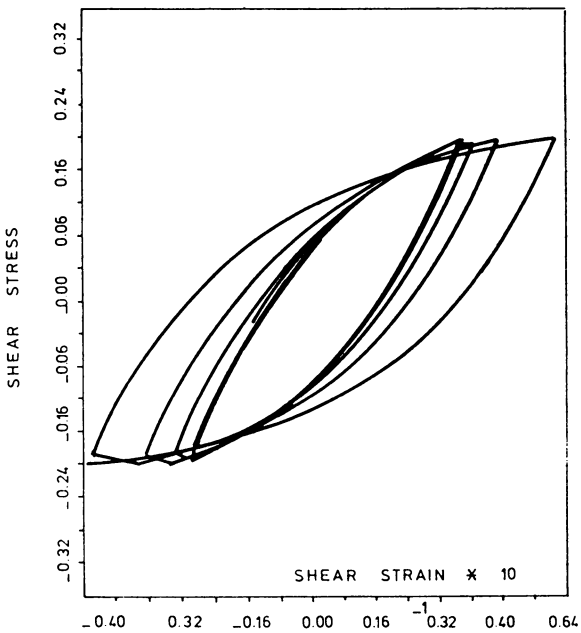

Figure 3. Cyclic Shear Stress-Shear Strain Behavior Calculated

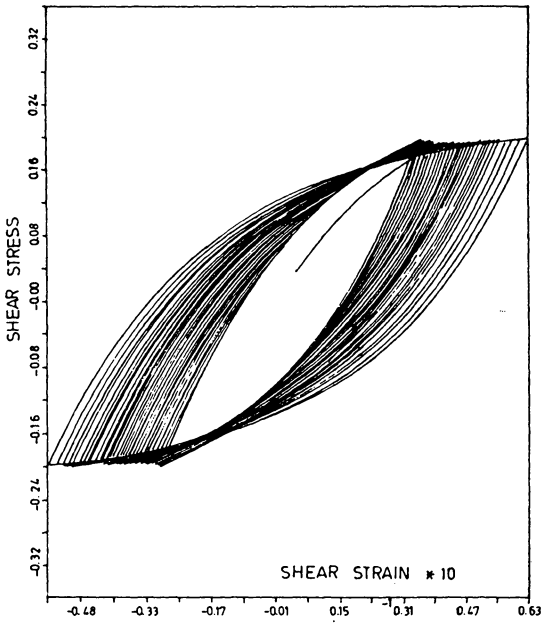

Figure 4. Shear Stress-Shear Strain Response Modelled

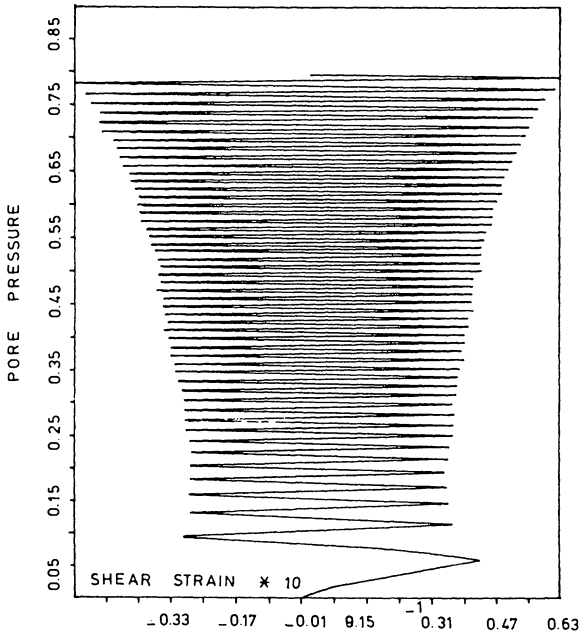

Figure 5. Variation of Pore Pressure Modelled with Respect to Shear Strain

4. REFERENCES

Ansal,A.M., Bazant,Z.P., and Krizek,R.J.(1979). Viscoplasticity of Normally Consolidated Clays. ASCE J.Geotechnical Div. (105), GT4, pp.519-537.

Ansal,A.M.,Krizek,R.J., and Bazant, Z.P.(1980). Prediction of Soil Behavior by Endochronic Theory. Proc.Workshop on Limit Equilibrium Plasticity and Generalized Stress-Strain in Geotechnical Engineering, pp. 286-327.

Bazant,Z.P., Ansal,A.M., and Krizek,R.J. (1982). Endochronic Models For Soils. Soil Mechanics Transient and Cyclic Loads Ch.15, pp.419-438, Wiley, New York.

Bazant,Z.P. and Bhat,P.D. (1976). Endochronic Theory of Inelasticity and Failure of Concrete. ASCE J.Engineering Mechanics Div. (102), EM4, pp.701-722.

Biot,M.A.(1956). Theory of Deformation of a Porous Viscoelastic Anisotropic Solid. J.Applied Physics. (27), 5, pp.459-467.

Finn, W.D.L. Lee, K.W., and Martin, G.R. (1976) "Constitutive Laws for Sand in Dynamic Shear" Proc. 2nd Int.Conf. on Numerical Methods in Geomechanics. Vol. pp.270-282.

Hardin,B.O. and Drnevich, V.P. (1972) "Shear Modulus and Damping in Soils Design Equations and Curves", ASCE Journal of Soil Mechanics and Foundations Division. Vo.95, No.SM7, pp.667-692.

Idriss, I.M. and Seed, H.B. (1968) "Seismic Response of Horizontal Soil Layers" ASCE, Journal of Soil Mechanics and Foundations Division, Vol.94, No.SM4, pp. 1003 - 1031.

Krizek,R.J., Ansal,A.M., and Bazant,Z.P. (1978). Constitutive Equations for Cyclic Behavior of Cohesive Soils. Proc. ASCE Spec.Conf. Earthquake Engineering and Soil Dynamics (2), pp.557-568, Pasadena, Calif.

Prevost,J.H. (1977) "Mathematical Modelling of Monotonic and Cyclic Undrained Clay Behavior " Publ. of NGI No.117

Ramberg, W. and Osgood, W.R. (1943) "Description of Stress-Strain Curves by Three Parameters , Technical Note 902, NACA.

SOURCE AND LOCAL SITE EFFECTS - PRELIMINARY RESULTS BASED ON THE FRIULI EARTHQUAKE SEQUENCE 1976

Dr.-Ing.Raimar Scherer
c/o Dyckerhoff & Widmann AG
8000 München 81
West Germany

ABSTRACT. The source and local site effects are studied by comparing the records of the two largest aftershocks (M ~ 6.0) of the Friuli Earthquake Sequence 1976, obtained at 10 stations with an epicentral distance of less than about 30 km. Additionally for one station the recorded spectra are compared with the theoretical one using the model of a horizontal layered halfspace.

1. INTRODUCTION

For the aseismic design of structures an important fact is whether the strength, the time shape and the frequency content of the acceleration on the surface of the earth is determined by the local site or the source. Whereas the characteristics of the source, i.e. the location, the orientation and the rupture process, are very random parameters, which could be forecast only with a high uncertainty, the local site is a fixed and nearly unalterable fact. The complexity of the local site system nearly vanishs compared to the complexity of the macroseismic system. Therefore it is possible to forecast the influence of the local site on the acceleration time history very precisly.

Since it can be forecast with a high statistical confidence, the structure can be adjusted to the local site effects, leading to a higher probability of survival of seismic hazards in connection with lower costs for the aseismic design of the structure.

The source and local site effects are studied by comparing the records of the two largest aftershocks (M ~ 6.0) of the Friuli Earthquake Sequence 1976, obtained at 10 stations with an epicentral distance of less than about 30 km. Additionally for one station the recorded spectra are compared with the theoretical one using the model of a horizontal layered halfspace.

2. THEORETICAL RESULTS ON THE GROUND ACCELERATION OF BODY WAVES

2.1. Acceleration on Bedrock

In the definition we use, bed rock means soil with an S-wave velocity of

M. O. Erdik and M. N. Toksöz (eds.), Strong Ground Motion Seismology, 545–558.
© 1987 by D. Reidel Publishing Company.

about 2 km/s and a depth below the surface of the ground great enough that no resonance occurs. This is the case if the depth H is

$$H > \frac{T_B \, v_S}{4} \tag{1}$$

where T_B is the duration of the direct body waves, i.e. direct s-waves, and v_S is the corresponding velocity. As long as the two criteria are fulfilled we can write - separately for every wave type - the power spectrum of the acceleration on bed rock S_B (Scherer, 1984 a,b) as

$$S_B(f,t) = S_S(f) \; I(t) \; H_G^2(f) \; H_D^2(f) \; H^2_T(f) \tag{2}$$

In Eq. 2 S_S is the source spectrum and the H_S, which are only weakly frequency dependent, are the transfer function of the geometrical attenuation (G), the damping (D) and the transmission at significant soil interfaces (T). For convenience the transfer functions are computed for a mean or a minimum distance between source and station, whereas the time-dependent scaling effects, caused by the varying distance, are collected in the time-dependent intensity function I(t), which also contains the directivity effect. The directivity effect can be described by a rectangular window with a unit area and a window width (duration) of

$$T_B = T_R(1 - \frac{v_R}{v} \cos \psi) \tag{3}$$

where T_R means the rupture duration, v_R the rupture velocity, v the wave velocity and ψ the angle between the source plane and the ray path. Following (Papageorgiou and Aki, 1983) the source spectrum $S_{S,f}$ can be approximated by a stationary spectrum for the far field term. The corresponding source spectrum of the intermediate field term $S_{S,m}$ which has to be considered for shallow earthquakes in the epicentral regions has the form (Scherer, 1984b).

$$S_{S,m}(f) \propto \frac{1}{f^2} \tag{4}$$

In the above formulation the radiation pattern is incorporated in the source spectrum.

The main features are that for the mean intensity $\overline{I}$ and the duration of the direct body waves, T_B, the following relation holds:

$$\overline{I} \propto 1/T_B \tag{5}$$

and that, outside the epicentral region only, the source spectrum of the far field term is relevant, which is a white noise spectrum. Following Eq. 2 the bed rock spectrum S_B has to be a white noise spectrum, too.

Both hypothesis, the relation between the mean intensity and the duration (Eq.5) and the spectral form at the acceleration on bed rock (white noise spectrum) will be tested by the Friuli data in Section 3.

2.2. Acceleration on the Earth Surface

Assuming that the soil overlying the bed rock can be modeled with a sufficient accuracy as a horizontal layered medium over a half space, the Haskell-Thomson-Algorithm (Aki, 1980) can be used to establish the transfer function of the layered soil and to compute the acceleration on the surface of the earth from the acceleration on bed rock. If the approximation of a layered half space fails, which may be the case at the edge of a sedimentary valley, more elaborated methods, such as the Boundary or the Finite Element Method, can be used in order to incorporate the real 2- or 3- dimensional geometry of the local soil.

3. EMPIRICAL RESULTS OF ACCELERATION RECORDS

3.1. Spectral Shape of the Acceleration on Base Rock

Power spectra from records (Scherer and Schuëller, 1984) measured:a) on rock overlayed by a thin soil layer (Tarcento), b) on outcropping rock (San Rocco, Robic, Somplago) and c) in a cavern about 300 m below the surface of earth (Somplago Turbin), are simplified by three straight lines in order to predict the second corner frequency, (called f_{max} by Hanks, 1982), and the exponent of the spectral shape between the two corner frequencies f_{c1} and f_{c2} . The parameters are defined in Fig.1 and Eq.6

$$a(f) \sim f^{-\gamma_a} \qquad (6)$$

The first corner frequency f_{c1} is almost always smaller than the lower cut off frequency for the base line correction and could not be estimated out of the computed spectra.

The minimum/maximum values for the exponent γ_a (Table 1) show a high scattering reaching from -0.7 to +0.5 for all rock-like stations. Going more into detail and seperating the values for each station we get more significant results: Tarcento, a station situated on a thin layer overlaying the bed rock, shows half of the scattering of all rock like stations and a non-positive γ_a value, which means that in most cases the spectral shape increases up to the second corner frequency. The second corner frequency is probably the highest, dominant resonance frequency of the thin layer.

San Rocco, which is situated on strongly weathered outcropping rock, also shows a high scattering of the exponent γ_a, but with a mean value of zero. Again the spectral shape and the second corner frequency are determined by resonance frequencies of the soil, however the resonance peaks are not so much pronounced as in the spectrum of the records from Tarcento. Both, the less pronounced resonance peaks and the mean value of the exponent γ_a, point to a very random transfer function of the rock layers, which indeed is expected by from a strongly weathered rock.

TABLE 1. EXPONENT γ_a OF THE SIMPLIFIED ACCELERATION SPECTRA

Station	Min γ_a	Max γ_a	No. of Records
All rock like stations	-0.7	+0.5	33
Tarcento	-0.6	0.0	5
San Rocco	-0.5	+0.5	7
Robic	-0.3	0.0	3
Somplago (all)	-0.7	+0.1	18
Somplago Turbin (all)	-0.7	+0.1	8
Somplago Turbin (best)	0.0	+0.1	3

Robic, which is situated on weakly weathered outcropping rock, shows a much smaller scattering of the exponent and a stable second corner frequency of about 12 Hz. Again, the second corner frequency is probably the greatest, dominant resonance frequency of the soil.

Somplago is a small network of three stations situated at a hydro power plant, one station is installed at the entrance of the tunnel, one some hundred meters inside the tunnel and one beside the turbin about 300 m below the surface of the earth. The scattering of the exponent is again very high for all records from Somplago. Focusing our attention on the turbin station and picking out only those records which contain the whole direct incident S-wave and some of the P-waves we get the very interesting result that the exponent γ_a is zero and the second corner frequency is greater than about 22 - 25 Hz. The Nyquist frequency of the records is about 25 Hz. No doubt the power spectrum of the body wave field on bed rock (below the surface of the earth is a white noise spectrum as it is predicted by the theoretical model.

The second corner frequency which is drawn over the magnitude for Tarcento, San Rocco and Somplage Turbin (Fig. 2) shows a slight dependency on the magnitude for the two stations situated on the earth surface. The same degree of dependency can be achieved between the second corner frequency and the maximum horizontal acceleration. Taking into consideration that the dependency for the records from Tarcento is much stronger than for those from San Rocco and no dependency at all can be found for the records from the compact rock stations, Robic and Somplago, we have to suppose that the second corner frequency is determined by the soil layers. If we call to mind the relations between the resonance frequencies of the layered soil f_i, the shear modulus G, the strain ε and

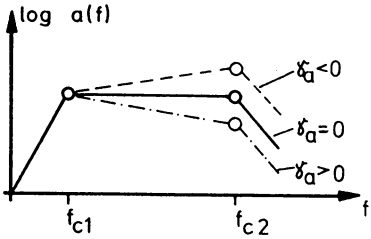

Figure 1. Simplified Fourier Spectrum of the Acceleration

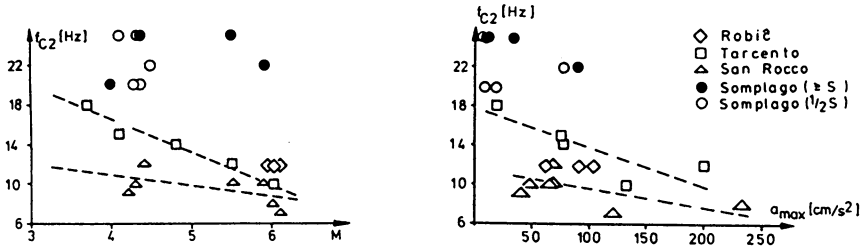

Figure 2. Second Corner Frequency f_{c2}

the acceleration a, such that:

$$f_i = g_1 \quad (\sqrt{G}) \qquad (7a)$$

$$G = g_2 \quad (1/\varepsilon) \qquad (7b)$$

$$\varepsilon = g_3 \quad (a) \qquad (7c)$$

and if we identify the second corner frequency as the highest dominant resonance frequency of the layered soil we can state that the second corner frequency is a local site parameter.

3.2. The Time Shape of the Acceleration Process

Two greater aftershock with nearly equally located epicenters and magnitudes of 5.5 - 6.0 are well recorded by several stations showing epicentral distances between 2 and 30 km. The orientation of the focal mechanism of both shocks is quite different, which is indicated in the upper left corner of Fig.3 and 4 (Cipar, 1981), and therefore systematic differences in the records of both aftershocks can be expected to be source dependent.

The time dependent RMS (root mean square functions) of the acceleration time histories,

$$a_{RMS}(t) = \left[\frac{1}{\Delta T} \int_{t-\Delta T/2}^{t+\Delta T/2} a^2(t)dt \right]^{1/2} \qquad (7)$$

with $\Delta T = 0.4$ s

which are simplified by straight lines, are shown in Fig. 3 and 4 for the two horizontal components. The outlined RMS-functions are limited to the duration of the direct S-waves, which is more or less identical to the part of strong shaking in the horizontal direction. The estimated duration of the S-wave, T_S, is given on top of the RMS- curves. The max. value of the simplified RMS-function is indicated on the ordinate and the estimated second corner frequency is outlined on the abscissa. In order to get a better insight into the results of Fig. 3 and 4, the three values: T_S, max. a_{RMS} and f_{c2} are given in Table 2 for the two aftershocks.

The arrows indicate whether the values of the 3h15 shock are increasing or decreasing compared to those of the 9th21 shock. The values of the 3h15 shock measured at Gemona are interchanged (indicated by an asterix) in order to achieve an equal componental orientation for both shocks concerning the epicenter. The station of Conegliano (CON) has to be excluded from the comparison because of two reasons:

a) very large epicentral distance which leads to a small and therefore very uncertain measured acceleration and
b) the seismogram probably is dominated by surface waves which is supported by an overestimated duration T_S and the geological information.

From the remaining 10 stations, 9 stations show an opposite dependency between the S-wave duration T_S and the max. RMS acceleration, which

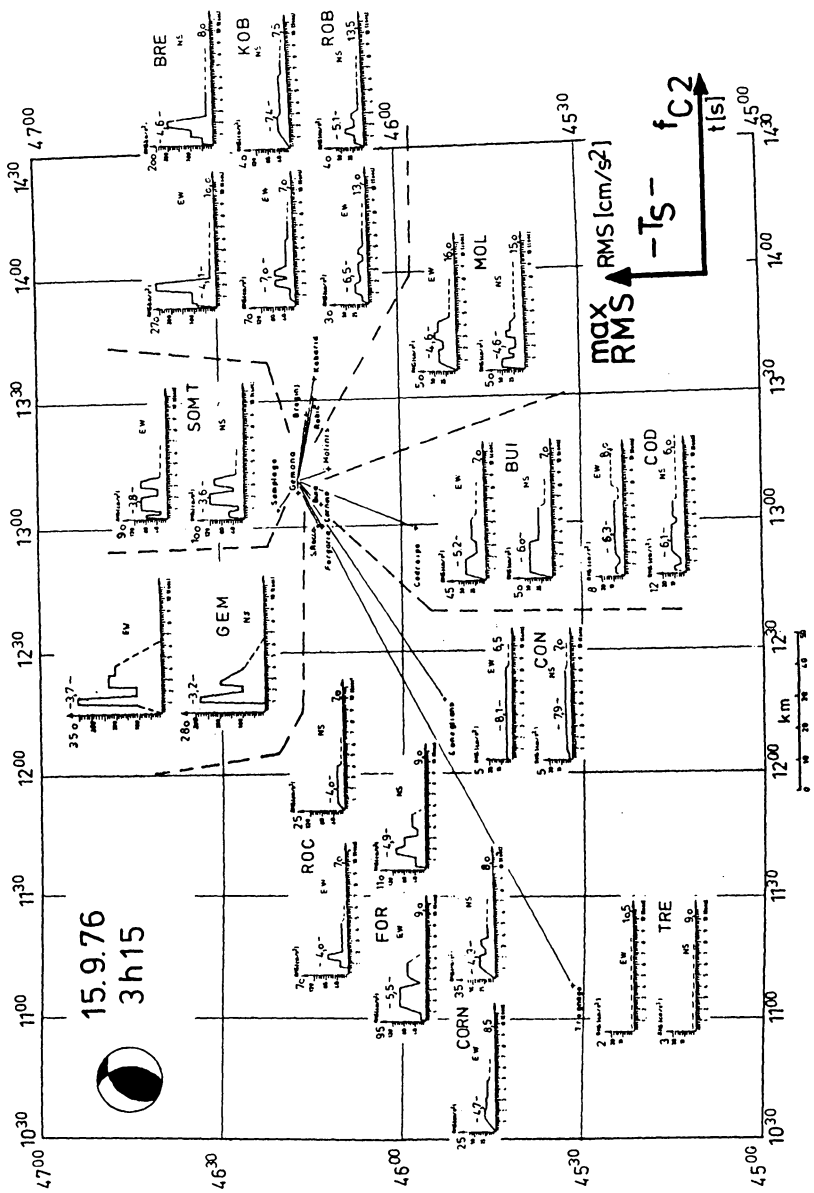

Figure 3. Temporal shape of the acceleration process.

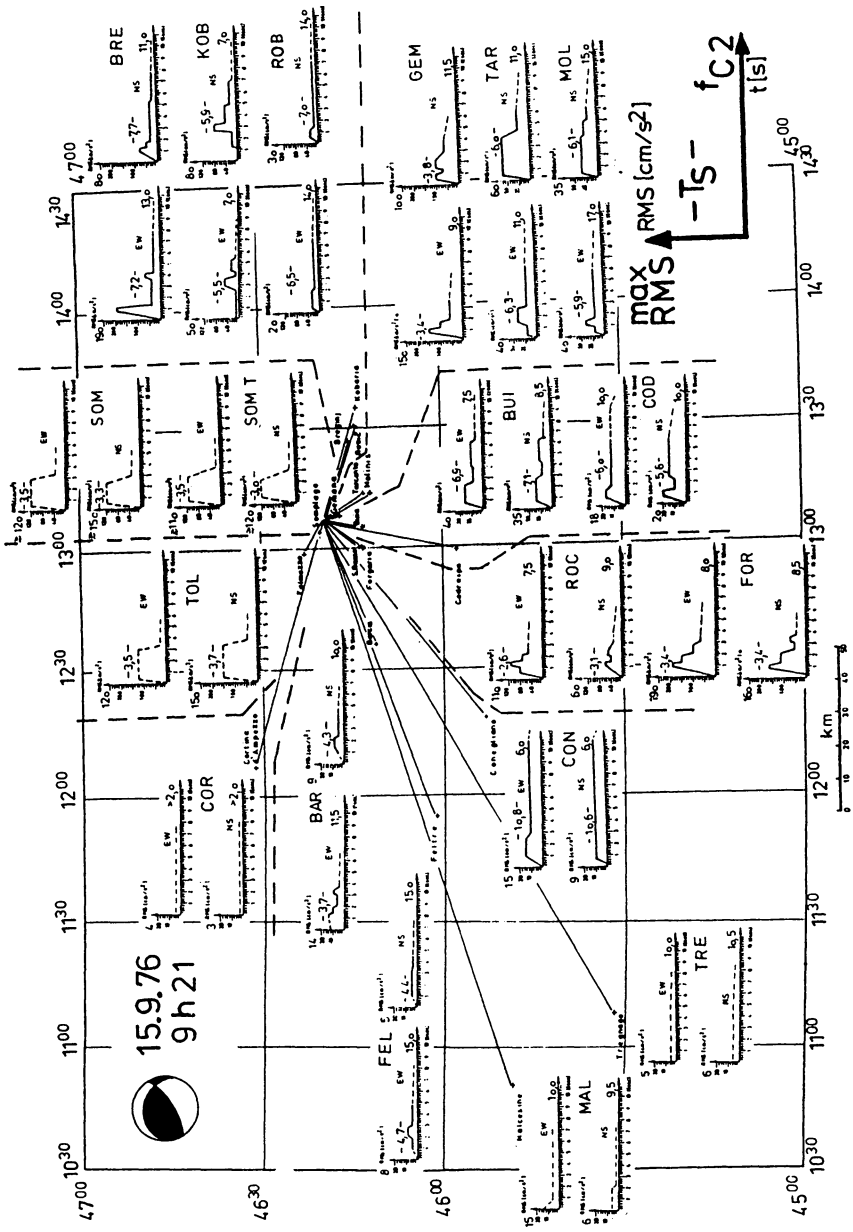

Figure 4. Temporal shape of the acceleration process.

TABLE 2. S-WAVE DURATION T_S; MAXIMUM RMS-ACCELERATION MAX. a_{RMS} AND SECOND CORNER FREQUENCY f_{c2} FOR TWO AFTERSHOCKS ON SEPT.15th, 1976.

Station		T_S (s) 9h21	T_S (s) 3h15	max.a_{RMS} (cm/s²) 9h21	max.a_{RMS} (cm/s²) 3h15	f_{c2} (Hz) 9h21	f_{c2} (Hz) 3h15
BRE	EW	7,2	4,1 ▼	190	270 ▲	13,0	10,0 ▼
	NS	7,7	4,6 ▼	80	200 ▲	11,0	8,0 ▼
KOB	EW	5,5	7,0 ▲	50	70 ▲	7,0	7,0 –
	NS	5,9	7,4 ▲	80	40 ▼	7,0	7,5 ▲
ROB	EW	6,5	6,5 –	20	30 ▲	14,0	13,0 ▼
	NS	7,0	5,1 ▼	30	40 ▲	14,0	13,5 ▼
GEM	EW	3,4	3,2* ▼	150	280* ▲	9,0	-
	NS	3,8	3,7* ▼	100	350* ▲	11,5	-
MOL	EW	5,9	4,6 ▼	40	50 ▲	17,0	16,0 ▼
	NS	6,1	4,6 ▼	35	50 ▲	15,0	15,0 –
BUI	EW	6,9	5,2 ▼	40	45 ▲	7,5	7,0 ▼
	NS	7,1	6,0 ▼	35	50 ▲	8,5	7,0 ▼
COD	EW	6,0	6,3 ▲	18	8 ▼	10,0	8,0 ▼
	NS	5,8	6,1 ▲	20	12 ▼	10,0	6,0 ▼
ROC	EW	2,6	4,0 ▲	110	70 ▼	7,5	7,0 ▼
	NS	3,1	4,0 ▲	60	25 ▼	9,0	7,0 ▼
FOR	EW	3,4	5,5 ▲	190	95 ▼	8,0	9,0 ▲
	NS	3,4	4,9 ▲	160	110 ▼	8,5	9,0 ▲
CON	EW	10,8	8,1 ▼	15	5 ▼	6,0	6,5 ▲
	NS	10,6	7,8 ▼	9	5 ▼	6,0	7,0 ▲
SOM,T	EW	3,5	3,8 ▲	≥120	90 ▼	-	-
	NS	3,0	3,6 ▲	≥120	100 ▼	-	-

supports on the one hand the directivity effect and on the other hand the fact that the duration of the incidence of direct S-waves is also equal to the apparent duration of the rupture. The second corner frequency is independent of both, the S-wave duration and the max. RMS acceleration. More than that, the second corner frequencies measured during both shocks do not alter very significantly. Because of this we have to conclude again that the second corner frequency is a local site parameter. Comparing the simplified RMS-function of both shocks no significant dependency can be noted which leads to the conclusion that the rupture process may determine the RMS-function and therefore the envelope of the acceleration time-history during the incidence of the direct body waves.

3.3. Transfer Function of the Local Site

The systematic investigations of the power spectra of several selected stations on soft soil and the above mentioned stations show that the spectral peaks for the same station but for different shocks are located more or less at the same frequencies, which points out that the spectral shape is determined by the local site conditions. For the station located nearby Forgaria excellent cross-hole measurements of the P- and S-wave velocities are available which provides the computation of the transfer function of the local soil (Fontanive et al., 1981).

Fig. 5 shows two different degrees of the simplified velocity profiles used in the computation. In the first stage a damping value of $\zeta = 10$ % is used, which means a quality factor of $Q = 5$. The cross-hole measurement was limited to a depth of 43 m. This leads to the first model, the 7-layers-model. Compared with the power spectra of the records it is realized that the two spectral peaks of the transfer function of normally incident SH-waves, show more or less the same frequency as the 2nd and 3rd peak in the measured spectra. (Fig. 6) Extending the model by an additional layer limited to a depth of 100 m the model fits very precisely to the resonance peaks of the local site (see 8-layer-model). The simplification of the soil profile to a 3-layer-model does not alter very significantly the location of the resonance peaks which indicates that every dominant change in the velocity profile procedures one spectral peak. The fit of the spectral values for the peaks is still very poor for the 3-layer-model, but for the 4-layer-model, where the layer with a lower wave velocity is added to the model, the spectral values for the peaks fit the measured ones quite satisfactorily. The influence of the damping values is studied by using the 8-layer-model. For small damping, 2% were choosen for every layer, a very pronounced transfer function is obtained, showing also higher resonance frequencies for every sub-layer.

The medium damped model ($\xi = 2 - 10$ %) with a higher damping value in the surface layer and decreasing damping values for the deeper layers leads to a 3-peaked transfer function. However the spectral amplitudes increase with an increasing resonance frequency. The stronger damped model ($\xi = 5 - 20$ %) fits very satisfactory with the measured spectrum in both the location of the resonance frequencies and the spectral amplitudes.

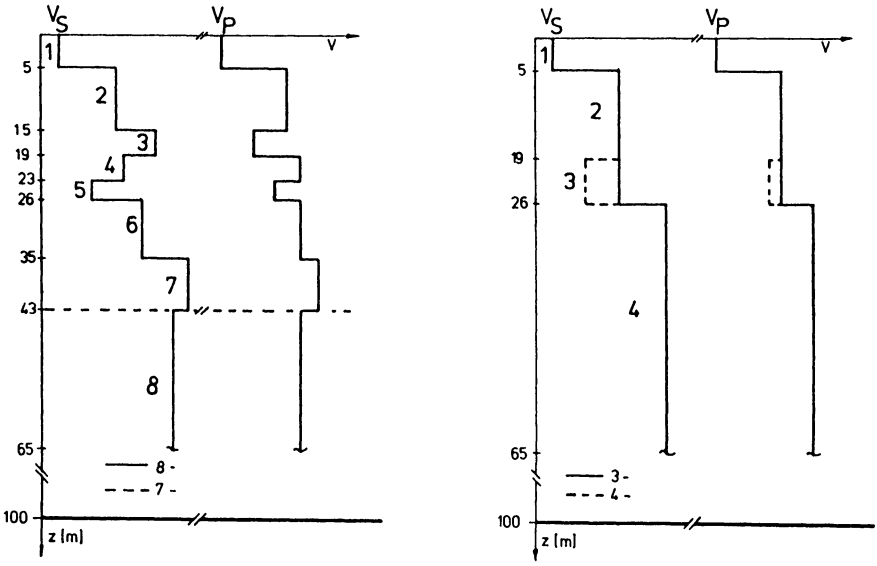

layer	v_s [m/s]	v_p [m/s]	ρ [g/cm³]	ξ_s = ξ_p [%]			layer	v_s [m/s]	v_p [m/s]	ρ [g/cm³]	ξ_s = ξ_p [%]
1	200	1000	1,8	10	10	20	1	200	1000	1,8	10
2	550	2000	2,1	10	5	10					
3	800	1500	2,3	10	5	10	2	600	2000	2,1	10
4	600	2200	2,1	10	5	10					
5	400	1800	2,0	10	10	15	(3)	400	1800	2,0	10
6	700	2200	2,2	10	5	10					
7	1000	2500	2,3	10	2	4					
8	900	2200	2,2	10	2	5	4	900	2500	2,2	10
	2000	3400	2,5	0,1	0,1	0,1		2000	3400	2,5	0,1

Figure 5. Simplified Velocity Profiles for the Forgaria Site From

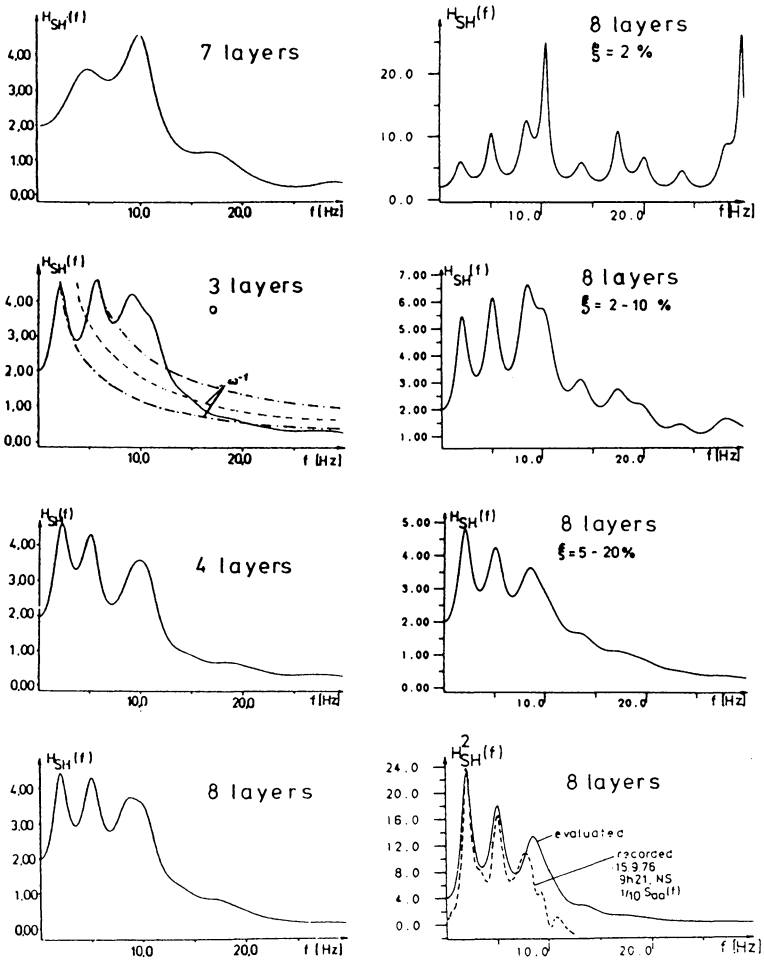

Figure 6. Transfer Functions of the Forgaria Site for a Normal Incidence of S-Waves

The sensitivity analysis of the transfer function of the layered soil clearly shows that the second corner frequency is the highest dominant resonance frequency. It is a function of the soil damping and the velocity profile. Moreover, the whole spectral shape is mainly determined by the local site conditions. This also supports the foregoing results that the power spectrum of the bed rock acceleration is an approximately white noise spectrum. It means that the amplification effects of the deposit are so dominant that the spectral shape of the acceleration in the bed rock can be neglected.

The importance of the spectral shape in the determination of the structural damage is demonstrated in (Scherer, 1985).

4. CONCLUSIONS

Using the strong motion records obtained during the Friuli Earthquake Sequence 1976, it is shown that the frequency pattern of the acceleration on the surface of the earth is mainly determined by the local site condition, whereas the power spectrum of the acceleration on bed rock* is approximately a white noise spectrum with an upper cut off frequency of more than 20-25 Hz. The time shape of the acceleration during the part of the direct body waves, which in most cases represents the strong motion duration, is mainly determined by the source mechanism. This is demonstrated by comparing the records of two greater aftershocks with nearly equally located epicenters but different source mechanisms.

* Bed rock means compact, non-weathered rock situated sufficiently deep under the surface.

5. ACKNOWLEDGEMENT

The valuable suggestions by Dr. Gebrande and Prof. Angenheister, Institute of Geophysics, University of Munich, are deeply appreciated. The helpful discussions with Prof. Schueller, Institute of Mechanics, University of Innsbruck, and Prof. Grundmann, Institute of Mechanics, Technical University of Munich are gratefully acknowledged.

6. REFERENCES

Scherer, R.J.(1984), The Importance of Surface Waves in Structural Damage, Proc. Conference on Structural Analysis and Design of Nuclear Power Plants, Porto Alegre, Brazilian, Oct. 3-5, 1984.

Scherer, R.J.(1984), Modelling of the Transient Structural Excitation from Seismic Waves Utilizing the Theory of Stochastic Processes, (Ph.D.thesis in German), Berichte zur Zuverlassigkeitstheorie der Bauwerke, Heft 73, 311 pp, Techn. Univ. München, 1984

Papageorgiou A.S., Aki K.(1983), A specific Barrier Model for the Quantitative

Description of Inhomogeneous Faulting and the Prediction of Strong Ground Motion, I. Description of the Model, II. Application of the Model, Bull. Seism. Soc. Am., Vol. 73, pp 693-722, pp 953-978, 1983

Aki, K., Richards P.G.(1980), Quantitative Seismology, Theory and Method, Vol.1, Vol.2, Freeman & Co., San Francisco, 1980

Scherer, R.J., Schuëller G.I.(1976), Records and Power Spectra of Corrected and Integrated Strong Motion Earthquake Data, Vol. I: Friuli Earthquake Sequence of 1976
Part A : Theoretical Background of Data Processing, p 75
Part B : Graphical Representation of Data, 620 pp TU München/Univ. Innsbruck, June 1984

Hanks T.C.(1982), f_{max}, Bull. Seism. Soc. Am., Vol.72, pp 1867-1879, 1982.

Cipar J.(1981), Teleseismic Observations of the Friuli Region from Strong Motion Acceleration Spectra, Bull. Seism. Soc. Am., Vol.71, No.6, pp 1981-1991, Dec. 1981

Fontanive A ., Gorelli V., (1981), Indagini Geotesiche Sui Terreni Sottostant Gli Accelerografi di Forgaria - S. Rocco E. Forgaria - Cornina, in : Contributo Alla Caratterizzazione Della Sismicita Del Territorio Italiano. Comissione ENEA-ENEL, March, 1981

Scherer, R.J., Schuëller G.I.(1985), Uncertainties in Current Aseismic Desig Concepts, 4th Int. Conference on Structural Safety and Reliability, Kobe, Japan, May 1985

SOIL STRUCTURE INTERACTION EFFECTS ON STRONG GROUND MOTION

Mustafa Erdik
Earthquake Engineering Research Center
Middle East Technical University
Ankara, Turkey

ABSTRACT. Dynamic interaction of soils and structures during dynamic excitation or earthquakes are of concern for the design of structures and foundations and also for the proper interpretation of the strong motion data recorded on the ground floor or basements of structures. In this paper a three-degree-of-freedom (3-D.O.F.) model for the soil-structure interaction problem will be studied on the basis of the sub-structure approach and the results will be applied to obtain the transfer function between the free field ground and structure-ground level motions during an earthquake.

1. INTRODUCTION

It is well known that, under certain conditions, soil structure interaction effects may cause significant difference between the basement and free-field motions. In fact, it has recently been shown that (Werner and Agbabian, 1984), the motions indicated by the El-Centro record of the 1940 Imperial Valley Earthquake, which has a world wide use as free-field seismic input for the design of structures, may be up to 100% below that of free field for frequencies above 1.5 Hz.

Through the use of finite element procedures the soil-structure interaction problem can be analysed in one step as a site-response problem in the frequency domain (Lysmer et al., 1975), or in the time domain (Bayo and Wilson, 1983). However a better physical understanding of the problem can be gained and the cases, where the interaction effects can be substantial, can be identified by breaking the total problem into seperate parts dealing with the structure, soil and interface conditions. This is known as the sub-structure approach.

In this study a three-degree-of-freedom (3.D.O.F.) model for the soil-structure interaction problem will be studied on the basis of the sub-structure approach and the results will be applied to obtain the transfer function between the free field ground and structure-ground level motions during an earthquake.

M. O. Erdik and M. N. Toksöz (eds.), Strong Ground Motion Seismology, 559–580.
© 1987 by D. Reidel Publishing Company.

2. SUB-STRUCTURE FORMULATION

The sub-structure formulation is essentially based on the determination of the total motions by superposing the free-field and interaction motions obtained on the basis of seperate analysis. The formulation given here follows that given by Gutierrez and Chopra (1978) and Kausel et al., (1978).

The structure-soil system is treated as two sub-structures shown in Fig.1. The compatibility of the displacements and the forces are satisfied by assigning the same displacements but opposite forces at the structure-soil interface.

The equations of motion for the finite element model of the structure alone can be written as :

$$[M_c]\{\ddot{r}_c\} + [C_c]\{\dot{r}_c\} + [K_c]\{r_c\} = \{R_c\} - [M_c]\{a\} \tag{1}$$

or

$$[M_c]\begin{Bmatrix}\ddot{r}_s\\ \ddot{r}_b\end{Bmatrix} + [C_c]\begin{Bmatrix}\dot{r}_s\\ \dot{r}_b\end{Bmatrix} + [K_c]\begin{Bmatrix}r_s\\ r_b\end{Bmatrix} = \begin{Bmatrix}0\\ R_b\end{Bmatrix} - [M_c]\{a\} \tag{2}$$

where :

$\{r_c\}$: vector of relative displacements (with respect to the free-field displacements at the structure-soil interface) at the degrees-of freedom (D.O.F.) associated with the structure

$\{r_s\}$: vector of relative displacements at the D.O.F. associated with the structure less those associated with the interface

$\{r_b\}$: vector of relative displacements at the D.O.F. associated with the interface

$\{R_b\}$: vector of forces due to soil-structure interaction at the D.O.F. associated with the interface

$\{a\}$: is a vector related to the free-field accelerations at the D.O.F. associated with the interface and to the pseudo-static deformations at the D.O.F. associated with the structure (less those associated with the interface)

and $[M_c]$, $[C_c]$ and $[K_c]$ are respectively the mass, damping and stiffness matrices.

The vector $\{a\}$ can be expressed in terms of the free-field accelerations at the D.O.F. associated with the structure-soil interface $\{\ddot{r}^o_f\}$ through the use of pseudo-static influence coefficient vector, $[V]$ (Clough and Penzien, 1975).

$$\{a\} = [V]\{\ddot{r}^o_f\} \tag{3}$$

Where the superscript "o" identifies free-field quantities. In the frequency-domain Eqn.2 can be given as :

$$\left[-\omega^2 \left[M_c\right] + i\omega\left[C_c\right] + \left[K_c\right]\right] \begin{Bmatrix} \hat{r}_s \\ \hat{r}_b \end{Bmatrix} = \begin{Bmatrix} 0 \\ \hat{R}_b \end{Bmatrix} - \left[P_c\right] \{\hat{\ddot{r}}_f^o\} \tag{4}$$

where ω is the excitation frequency, $\{\hat{r}_s\}$, $\{\hat{r}_b\}$,$\{\hat{R}_b\}$ and $\{\hat{\ddot{r}}_f^o\}$ are the Fourier Transforms of the respective time-domain quantities, and $\left[P_c\right]$ is given by :

$$\left[P_c\right] = \left[M_c\right]\left[V\right] \tag{5}$$

For the soil substructure the relationship between the forces and the displacements at the D.O.F. associated with the interface can be given in terms of the so-called impedance matrix ($\left[S_f\right]$),

$$\{\hat{R}_f\} = \left[S_f\right] \{\hat{r}_f\} \tag{6a}$$

or through compatibility relatinships

$$\{\hat{R}_b\} = -\left[S_f\right] \{\hat{r}_b\} \tag{6b}$$

Substituting Eqn.6b in Eqn.4 and re-arranging one can obtain :

$$\left[-\omega^2 \left[M_c\right] + i\omega\left[C_c\right] + \left[K_c\right] + \left[\begin{array}{c|c} 0 & 0 \\ \hline 0 & \left[S_f\right] \end{array}\right]\right] \left\{\begin{array}{c} \hat{r}_s \\ \hline \hat{r}_b \end{array}\right\} = -\left[P_c\right]\{\hat{\ddot{r}}_f^o\} \tag{7}$$

Solution of Eqn.7 requires first, the analysis of the soil substructure to obtain the free-field earthquake accelerations at the interface nodes, $\{\hat{\ddot{r}}_f^o\}$, under the existing seismic regime, and second, the determination of the impedance matrix $\left[S_f\right]$. The former analysis is also known as the "scatter" or "kinematic interaction" problem. In general both of these analysis require discrete, finite element type treatment. However for simple geometries and other restrictive assumptions closed form solutions have been developed.

Assuming planar rigid-body motion at the structure- soil interface $\{\hat{r}_f^o\}$ can be expressed as:

$$\{\hat{r}_f^o\} = \begin{Bmatrix} \hat{x}_f^o \\ \hat{y}_f^o \\ \hat{\psi}_f^o \end{Bmatrix} = \begin{Bmatrix} \hat{x}_b^o \\ \hat{y}_b^o \\ \hat{\psi}_b^o \end{Bmatrix} \tag{8}$$

Where $\hat{x}_b^o$, $\hat{y}_b^o$ and $\hat{\psi}_b^o$ are the free-field displacements at the rigid interface respectively along the x, y and ψ directions as shown in Fig.2. Assuming that the equations of motion for the vertical response can be decoupled,for seperate treatment, from that of the lateral-rocking $\{\hat{r}_f^o\}$ will be:

$$\{\hat{r}_f^o\} = \begin{Bmatrix} \hat{x}_b \\ \hat{\psi}_b^o \end{Bmatrix} \tag{9}$$

For a lumped-mass model of the structure with one lateral degree-of-freedom at each node, as indicated in Fig.3, the matrices in Eqn.7 can be derived and rearranged as follows :

$$[M_c] = \left[\begin{array}{c|cc} [M_s] & [M_s]\{I\} & [M_s]\{h\} \\ \hline \{I\}^T [M_s] & \{I\}^T [M_s]\{I\} + m_b & \{I\}^T [M_s] \{h\} \\ \{h\}^T [M_s] & \{I\}^T [M_s]\{h\} & \{h\}^T [M_s]\{h\}+I_t \end{array}\right] \tag{10}$$

$$[C_c] = \left[\begin{array}{c|cc} [C_s] & 0 & 0 \\ \hline 0 & 0 & 0 \\ 0 & 0 & 0 \end{array}\right] \quad ; \quad [K_c] = \left[\begin{array}{c|cc} [K_s] & 0 & 0 \\ \hline 0 & 0 & 0 \\ 0 & 0 & 0 \end{array}\right] \tag{11}$$

$$[P_c] = \left[\begin{array}{c|c} [M_s]\{I\} & [M_s]\{h\} \\ \{I\}^T [M_s]\{I\} + m_b & \{I\}^T [M_s]\{h\} \\ \{I\}^T [M_s]\{h\} & \{h\}^T [M_s]\{h\}+I_t \end{array}\right] \tag{12}$$

where $[M_s]$, $[C_s]$ and $[K_s]$ are the conventional mass, damping and stiffness matrices for the structure obtained on the basis of fixed base assumption. $\{I\}$ is the unit vector, $\{h\}$ is the vector of vertical distances of the structural nodes from the interface, m_b is the mass of the base of the structure and I_t is the sum of the moments of inertia of the lumped masses about their own centroidal axis of rocking and that of the base mass about the axis of rocking at the interface level.

The displacement vector becomes :

$$\left\{\begin{array}{c} \hat{r}_s \\ \hline \hat{r}_b \end{array}\right\} = \left\{\begin{array}{c} \hat{u} \\ \hline \hat{x}_b \\ \hat{\psi}_b \end{array}\right\} \tag{13}$$

where $\{\hat{u}\}$ is the vector of relative lateral displacements at the lumped masses and $\hat{x}_b$ and $\hat{\psi}_b$ are respectively the base relative lateral displacement and rocking angle.

For proportional damping assumption in the structure, where the so-called Rayleigh condition:

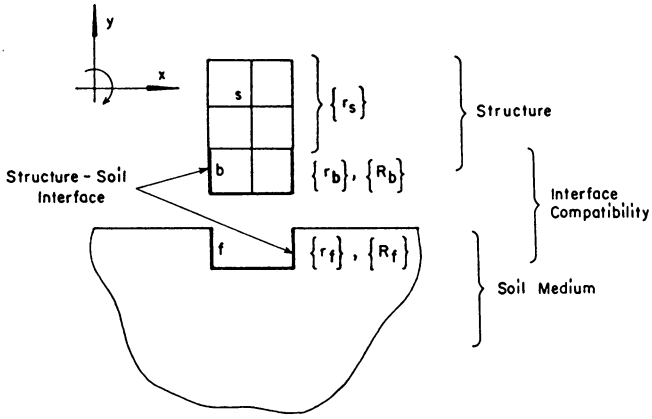

Figure 1. Substructure Representation of the Structure - Soil System.

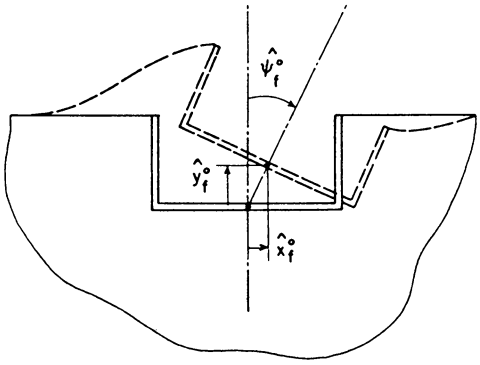

Figure 2. Planar Rigid Body Motion at the Structure - Soil Interface.

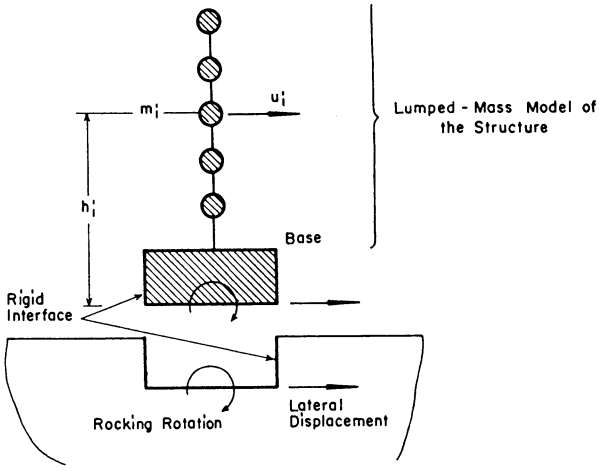

Figure 3. Soil-Structure Interaction Model Structure Modeled With Lumped Masses and Rigid Base

$$[C_c] = \alpha_1 [M_c] + \alpha_2 [K_c] \tag{14}$$

is satisfied, it follows that the modal damping ratios ξ_i of the i th fixed base structural mode are related to α_1 and α_2 by the following equation

$$\xi_i = \frac{\alpha_1}{2\omega_i} + \frac{\alpha_2\ \omega_i}{2} \tag{15}$$

Where ω_i is the natural circular frequency associated with the i th fixed-base normal mode of vibration. In practice α_1 and α_2 are chosen in such a way that the damping ratios agree for the first two modes of the structure. It is also a common practice to assume only stiffness proportional damping, yielding :

$$[C_c] = \alpha_2 [K_c] = \frac{2\xi_1}{\omega_1} [K_c] \tag{16}$$

Thus Eqn.7 can be written as :

$$\left[-\omega^2 [M_c] + \left(1+2i\xi\left(\frac{\omega}{\omega_1}\right)\right)[K_c] + \left[\begin{array}{c|c} 0 & 0 \\ \hline 0 & [S_f] \end{array}\right]\right] \left\{\begin{array}{c} \hat{r}_s \\ \hline \hat{r}_b \end{array}\right\} = -[P_c]\{\hat{\ddot{r}}_f^o\} \tag{17}$$

2.1. Foundation Impedance Matrix

Impedance matrices for simplified cases can be evaluated through analytical and numerical procedures and can be given in closed form expressions The harmonic forced vibration of a massless rigid cylindirical foundation in a homogenous soil halfspace has been studied by several researcher (Richart et al., 1970). In general the impedance matrix of such a foundation is of the following from :

$$\left\{\begin{array}{c} \hat{F}_b \\ \hat{M}_b \end{array}\right\} = [S_f] \left\{\begin{array}{c} \hat{x}_b \\ \hat{\psi}_b \end{array}\right\} \quad ; \quad [S_f] = \begin{bmatrix} K_{xx} & K_{x\psi} \\ K_{\psi x} & K_{\psi\psi} \end{bmatrix} \tag{18}$$

Where $\hat{F}_b$, $\hat{M}_b$, $\hat{x}_b$ and $\hat{\psi}_b$ are respectively the amplitudes of harmonic force and moment and the corresponding lateral translation and rocking rotation at the base of the foundation. The complex stiffnesses functions: K_{xx}, $K_{x\psi}$, $K_{\psi x}$, and $K_{\psi\psi}$ can be given by (Kausel et al., 1978):

$$K_{xx} = \bar{K}_{xx}\ (k_{11} + i\ a_o\ c_{11})(1 + 2i\beta) \tag{19}$$

$$K_{\psi x} = K_{x\psi} = \bar{K}_{x\psi}\ (k_{12} + i\ a_o\ c_{12})(1 + 2i\beta) \tag{20}$$

$$K_{\psi\psi} = \bar{K}_{\psi\psi}\ (k_{22} + i\ a_o\ c_{22})(1 + 2i\beta) \tag{21}$$

Where $i = \sqrt{-1}$, $a_o = \omega R/V_s$ is the normalized frequency, R is the radius of the foundation and V_s is the shear wave velocity. $\bar{K}_{xx}$, $\bar{K}_{x\psi}$, $\bar{K}_{\psi\psi}$, are the static (i.e. $\omega = 0$) stiffnesses, k_{ij}, c_{ij} are the frequency dependent coefficients and β is the hysteretic damping ratio of the soil media. K_{xx}, $K_{x\psi}$, $K_{\psi\psi}$, k_{ij} and c_{ij} have been provided by several authors (e.g. Johnson et.al., 1975; Richard et al. 1970; Veletsos and Wei, 1971; Kausel et al., 1978; ATC, 1978) as a function of G (Shear modulus), E(depth of embedment), H(depth to bedrock), ν(Poisson's ratio), R and ω.

The coeffient k_{ij} and c_{ij} are provided as plots against a_o in Fig.4 after Veletsos and Wei (1971).

Kausel et al.(1978) provides the following approximate expressions for the static stiffnesses :

$$\bar{K}_{xx} = \frac{8G\,R}{2-\nu}\left(1+\frac{1}{2}\,\frac{R}{H}\right)\left(1+\frac{2E}{3R}\right)\left(1+\frac{5}{4}\,\frac{E}{R}\right) \tag{22}$$

$$\bar{K}_{x\psi} = \bar{K}_{xx}\,R\left(\frac{2}{5}\,\frac{E}{R} - 0.003\right) \tag{23}$$

$$\bar{K}_{\psi\psi} = \frac{8G\,R^3}{3(1-\nu)}\left(1+\frac{1}{6}\,\frac{R}{H}\right)\left(1+2\,\frac{E}{R}\right)\left(1+0.71\,\frac{E}{H}\right) \tag{24}$$

These expressions are also included in ATC (1978).

For foundations that are different from a circle in plan, the effective radius can be defined for the translational motion as $\sqrt{A_o/\pi}$ and for the rocking motion as $\sqrt[4]{4I_o/\pi}$ where A_o is the area of the foundation and I_o is the area moment of inertia of the foundation about the centroidal rocking axis (ATC, 1978).

The first column of the complex impedance matrix in Eq.17 defines the set of forces and moments which are needed to displace the rigid foundation laterally by a unit amount without rocking, and the second column defines the set of forces and moments required to rock the disk by a unit amount without translation. The real parts of these quantities represent force quantities in phase with the motion, whereas the imaginary parts represent force components which are 90° out of phase as shown in the following equation.

$$\left\{\begin{matrix}\hat{F}_b\\ \hat{M}_b\end{matrix}\right\} = \begin{bmatrix}Re(K_{xx}) & Re(K_{x\psi})\\ Re(K_{\psi x}) & Re(K_{\psi\psi})\end{bmatrix}\left\{\begin{matrix}\hat{x}_b\\ \hat{\psi}_b\end{matrix}\right\} + \begin{bmatrix}Im(K_{xx}) & Im(K_{x\psi})\\ Im(K_{\psi x}) & Im(K_{\psi\psi})\end{bmatrix}\left\{\begin{matrix}\hat{x}_b\\ \hat{\psi}_b\end{matrix}\right\} \tag{25}$$

It is convenient to think of the forces represented by real parts of Eqn.25 as being due to as set of linear springs, and of the forces represented by imaginary parts as being due to a series of dashpots (Veletsos and Wei, 1971). In this representation the spring elements account for the combined effect of restraining action of the supporting medium and the inertia forces, whereas the dashpots account for the effect of energy dissipation by radiation as given by the following time-domain equation.

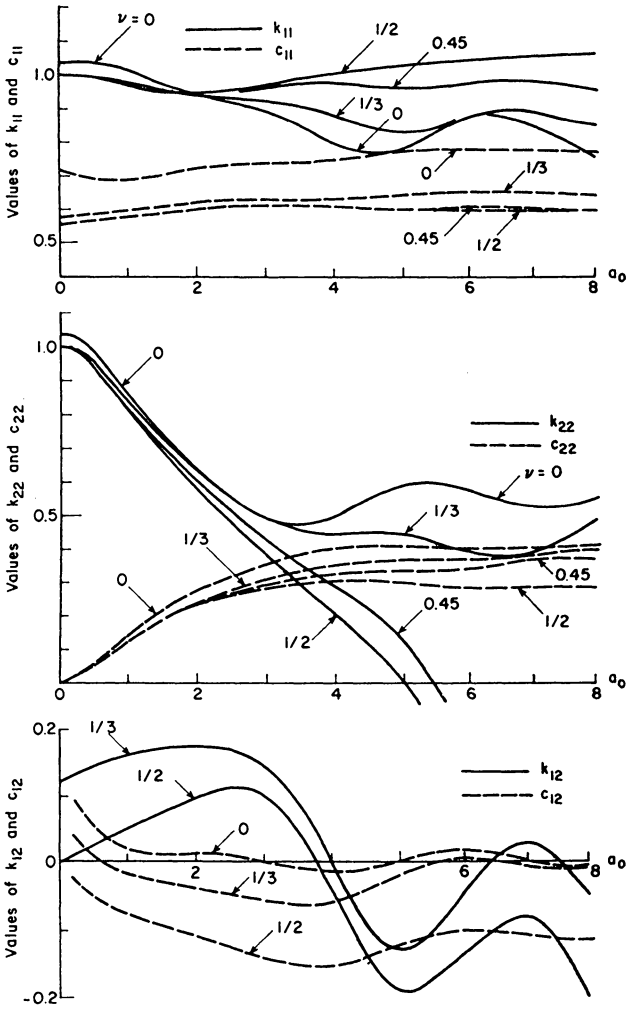

Figure 4. Half-space Impedance Function Coefficients (After Veletsos and Wei, 1971)

$$\begin{Bmatrix} F_b \\ M_b \end{Bmatrix} = \begin{bmatrix} k_{xx} & k_{x\psi} \\ k_{\psi x} & k_{\psi\psi} \end{bmatrix} \begin{Bmatrix} x_b \\ \psi_b \end{Bmatrix} + \begin{bmatrix} c_{xx} & c_{x\psi} \\ c_{\psi x} & c_{\psi\psi} \end{bmatrix} \begin{Bmatrix} \dot{x}_b \\ \dot{\psi}_b \end{Bmatrix} \tag{26}$$

The first matrix of Eqn.26 will be referred to as the foundation stiffness matrix and the second matrix will be referred to as the foundation damping matrix. The stiffness and damping coefficients respectively constitute the elements of these matrices. On the basis of these stiffness and damping coefficients, the foundation of the structure can be modeled by springs and dashpots in coupled and in uncoupled models as indicated in Fig.5. The stiffness and damping matrices for the uncoupled foundation models can be given as follows :

$$\begin{Bmatrix} F_B \\ M_B \end{Bmatrix} = \begin{bmatrix} k_{xx} & k_{x\psi} \\ k_{\psi x} & k_{\psi\psi} \end{bmatrix} \begin{Bmatrix} x_b \\ \psi_b \end{Bmatrix} + \begin{bmatrix} c_{xx} & c_{x\psi} \\ c_{\psi x} & c_{\psi\psi} \end{bmatrix} \begin{Bmatrix} \dot{x}_b \\ \dot{\psi}_b \end{Bmatrix} \tag{27a}$$

$$\begin{Bmatrix} F_A \\ M_B \end{Bmatrix} = \begin{bmatrix} k_x & 0 \\ 0 & k_\psi \end{bmatrix} \begin{Bmatrix} x_b + z\psi_b \\ \psi_b \end{Bmatrix} + \begin{bmatrix} c_x & 0 \\ 0 & c_\psi \end{bmatrix} \begin{Bmatrix} \dot{x}_b + z\dot{\psi}_b \\ \dot{\psi}_b \end{Bmatrix} \tag{27b}$$

The uncoupled stiffness coefficients k_x and k_ψ of the uncoupled model can be determined on the basis of the equilibrium of forces and moments :

$$F_A = F_B \quad \text{and} \quad M_B = M_A + F_B . z \tag{28}$$

Yielding :

$$k_x = k_{xx} \quad \text{and} \quad k_\psi = k_{\psi\psi} - k_{xx} z^2 \tag{29}$$

and

$$c_x = c_{xx} \quad \text{and} \quad c_\psi = c_{\psi\psi} - c_{xx} z^2 \tag{30}$$

where $z = k_{x\psi}/k_{xx}$ (31)

Practical findings indicate that z can be taken to be equal to E/3, where E is the depth of embedment.

3. KINEMATIC INTERACTION

In several applications of the soil-structure interaction problem the kinematic interaction is either neglected or treated on an approximate basis. For example in the lumped mass formulation of the soil-structure interaction problem adopted in Masao et al.(1980) the kinematic interaction is approximated by assigning the free-field values of the displacements obtained at the foundation level of the structure as input motions to the model as indicated in Fig.6. In the lumped mass model used by

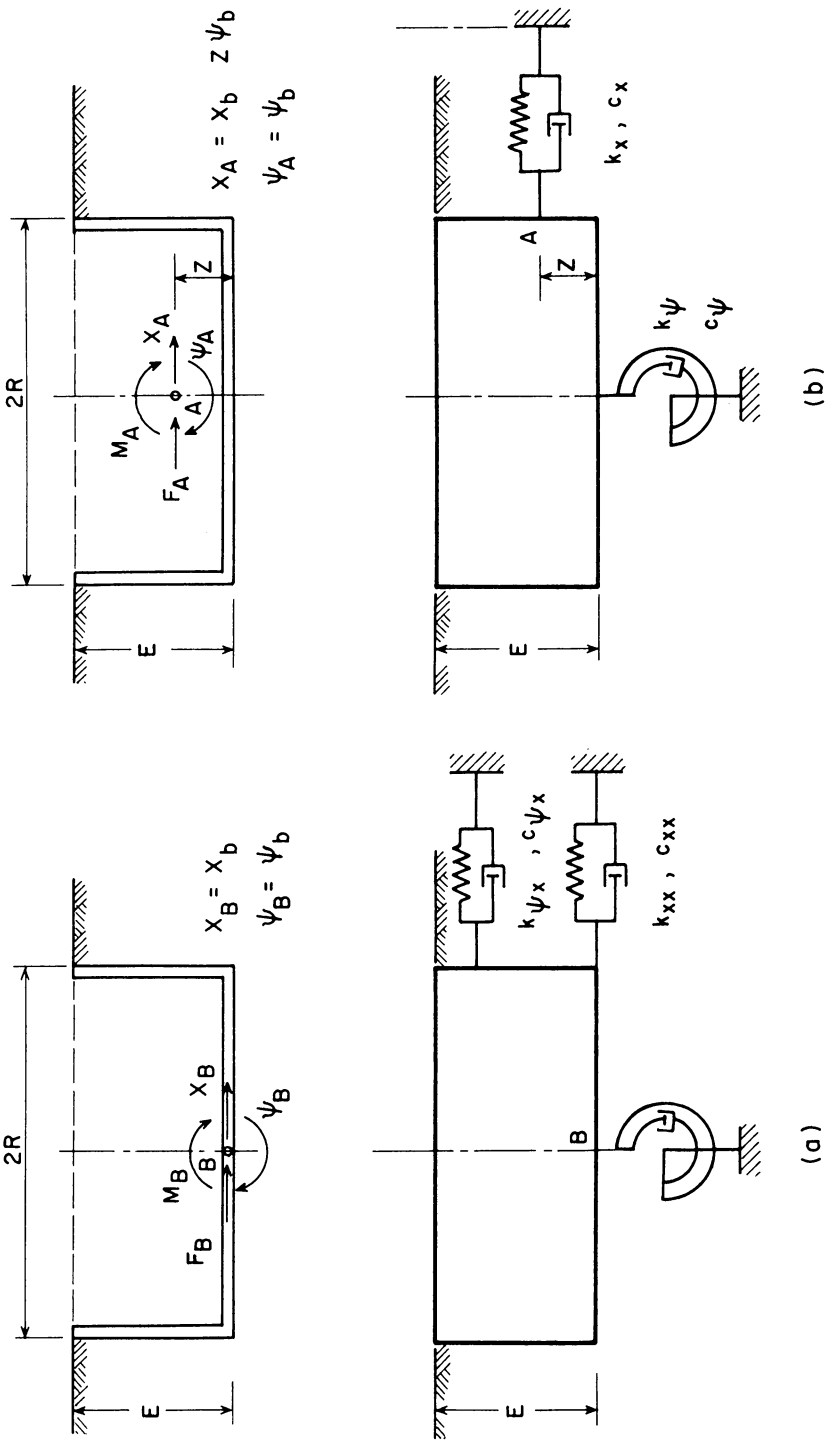

Figure 5. Coupled and Uncoupled Foundation Models.

Hall et al. (1975), shown in Fig.7, the kinematic interaction is accounted through the use of masses m_1 and m_2, representing the free field soil inertia and the springs K_1 and K_2.

The motion of the rigid-massless cylindirical foundation in a uniform soil media has been investigated through theoretical and experimental means. Kausel et al. (1978) has reported the results of a theoretical investigation of the problem, for a foundation located in a homogenous layer overlying a half space, for different embedment layer thickness values, assuming vertically propagating SH-waves. The findings indicate that the translation of the rigid-massless foundation is similar to the free-field translation at the embedment depth in the low frequency regions. However it is smoother in the higher frequency regions and does not show any pronounced absence of the certain frequency components. The transfer function between the translation at the embedment depth of the rigid-massless foundation and the free-field ground-translation (control motion) is approximated by :

$$|T_x| = \frac{|\hat{x}_b^o|}{|\hat{x}_g^o|} = \begin{cases} \cos\left(\frac{\pi}{2}\,\frac{f}{f_1}\right) & \text{for } f < 0.7\,f_1 \\ 0.453 & \text{for } f > 0.7\,f_1 \end{cases} \tag{32}$$

Where $\hat{x}_b^o$ and $\hat{x}_g^o$ are respectively the Fourier Transforms of the free-field lateral motions at the bottom of the rigid-massless foundation and at the free ground surface and f_1 is the shear beam fundamental modal frequency of the soil column with thickness equal to the embedment depth (E), and shear wave propagation velocity equal to V_s.

$$f_1 = \frac{V_s}{4E} \tag{33}$$

Eqn.10 can also be written as :

$$\frac{|\hat{x}_b^o|}{|\hat{x}_g^o|} = \begin{cases} \cos\left(\frac{\omega E}{V_s}\right) & \text{for } \frac{\omega E}{V_s} < 1 \\ 0.453 & \text{for } \frac{\omega E}{V_s} > 1 \end{cases} \tag{34}$$

As it has been reported in Kausel et al. (1978) the rocking motion experienced by the massless-rigid cylindirical foundation is found to be related to the difference of the free-field displacements between the two locations of the soil corresponding to the top and bottom levels of the foundation divided by the embedment depth. The transfer function between the Fourier Transform of the rocking motion of the rigid-massless foundation ($\hat{\psi}_b^o$ R) and the Fourier transform of the free-field lateral ground motion (control motion) ($\hat{x}_g^o$) is approximated by :

$$|T_\psi| = \frac{|\hat{\psi}_b^o|\,R}{|\hat{x}_b^o|} = \begin{cases} 0.257\ (1-\cos\frac{\pi}{2}\ \frac{f}{f_1}) & \text{for } f < f_1 \\ 0.257 & \text{for } f > f_1 \end{cases} \tag{35}$$

or expressed differently, by :

$$\frac{|\hat{\psi}_b^o|\,R}{|\hat{x}_b^o|} = \begin{cases} 0.257\ (1-\cos\frac{\omega E}{V_s}) & \frac{\omega E}{V_s} < 1 \\ 0.257 & \frac{\omega E}{V_s} > 1 \end{cases} \tag{36}$$

It has been noted that the rotational component may significantly decrease in foundations with flexible walls.

Ishii et al.(1984) has proposed the following empirical expression for the transfer function given in Eqn.32 and 34.

$$\frac{|\hat{x}_b^o|}{|\hat{x}_g^o|} = \begin{cases} \frac{\tilde{f}}{\pi f}\ \sin(\frac{\pi f}{\tilde{f}}) & \text{for } f < 0.71\,\tilde{f} \\ 0.35 & \text{for } f > 0.71\,\tilde{f} \end{cases} \tag{37}$$

$$\tilde{f} = \frac{1.408}{2.19(\frac{E}{V_s}) + 0.117}$$

Eqns.32, 36 and 37 behave essentially as low-pass filters.

4. STRUCTURAL CONSIDERATIONS

The overturning moment and the base shear created by the inertial forces of the structure are the main contributors to the soil-structure interaction phenomena. Both the base overturning moment and the shear are controlled by the first mode vibration behavior of the structure and the contribution of the higher modes can be assumed to be negligible for most engineering structures. Within the range of parameters that are of interest for the earthquake resistant design of structures the soil-structure interaction affects substantially only the response components associated with the fundamental mode of the structure. Accordingly the use of only the first fixed base mode shape of the structure is common in engineering practice for the assessment of the soil structure effects (ATC,1978). The higher modes of the structure are not essentially affected by the soil-structure interaction since the base overturning moment and the shear in these modes are comparatively quite low.

The representation of the structural matrices by the generalized fundamental mode characteristics can be found in structural dynamics books (e.g. Clough and Penzien, 1975). With such a representation the $[M_c]$, $[K_c]$ and $[P_c]$ matrices of Eqn. 10, 11, 12 and 16 can be given as follows :

$$[M_c] = \left[\begin{array}{c|cc} \bar{m} & \bar{m} & \bar{m}(\bar{h}+E) \\ \hline \bar{m} & \bar{m}+\bar{m}_b & \bar{m}(\bar{h}+E) \\ \bar{m}(\bar{h}+E) & \bar{m}(\bar{h}+E) & \bar{m}(\bar{h}+E)^2+I_t \end{array}\right] \tag{38}$$

$$[K_c] = \left[\begin{array}{c|cc} \bar{k} & 0 & 0 \\ \hline 0 & 0 & 0 \\ 0 & 0 & 0 \end{array}\right] \tag{39}$$

$$[P_c] = \left[\begin{array}{c|c} \bar{m} & \bar{m}(\bar{h}+E) \\ \bar{m}+\bar{m}_b & \bar{m}(\bar{h}+E) \\ \bar{m}(\bar{h}+E) & \bar{m}(\bar{h}+E)^2 + I_t \end{array}\right] \tag{40}$$

In these matrices E is the depth of embedment of the base and the first mode effective mass, $\bar{m}$, height, $\bar{h}$, and stiffness, $\bar{k}$, can be given in terms of the fixed base fundamental mode shape $\{\phi_1\}$ and frequency ω_1 by the following equations :

$$\bar{m} = \frac{(\{\phi_1\}^T [M_s]\{I\})^2}{\{\phi_1\}^T [M_s]\{\phi_1\}} \tag{41}$$

$$\bar{h} = \frac{\{h\}^T [M_s] \{\phi_1\}}{\{\phi_1\}^T [M] \{I\}} \tag{42}$$

$$\bar{k} = \bar{m}\, \omega_1^2 \tag{43}$$

For uniform building type structures $\bar{m}$ can be taken equal to the 70% of the total mass of the super-structure and $\bar{h}$ can be taken equal to the 70% of the height of the super-structure (ATC, 1978).

The displacement vector of Eqn.7 will have the following shape:

$$\left\{\begin{array}{c} \hat{r}_s \\ \hline \hat{r}_b \end{array}\right\} = \left\{\begin{array}{c} \hat{u}_1 \\ \hline (\hat{x}_b)A \\ \hat{\psi}_b \end{array}\right\} \tag{44}$$

Where $\hat{u}_1$ is the relative generalized first mode displacement of the super-structure with respects to the base, $\hat{x}_b$ is the relative lateral displacement of the base with respect to the free-field base displacement, $\hat{x}_b^o$, and $\hat{\psi}_b$ is the relative base rocking angle (rotation) of the base with respect to the free field base rocking angle (rotation), $\hat{\psi}_b^o$.

Soil-structure interaction models of this type are called three-degree-of-freedom models (two D.O.F. at the base, one at the super structure). Such a model is indicated in Fig.8.

Through re-arranging and normalizing the frequency domain equation of motion for such a 3.D.O.F. system can be given as follows :

$$\begin{bmatrix} \left[-1+\left(\frac{\omega_1}{\omega}\right)^2+2i\xi_1\left(\frac{\omega_1}{\omega}\right)\right] & -1 & -\frac{\bar{h}_c}{R} \\ -1 & \left[-1-\left(\frac{m_b}{\bar{m}}\right)+\frac{k_x+i\omega c_x}{\bar{m}\omega^2}\right] & -\frac{\bar{h}_c}{R} \\ -\frac{\bar{h}_c}{R} & -\frac{\bar{h}_c}{R} & \left[-\left(\frac{\bar{h}_c}{R}\right)^2-\frac{I_t}{\bar{m}R^2}+\frac{k_\psi+i\omega c_\psi}{\bar{m}R^2\omega^2}\right] \end{bmatrix} \begin{Bmatrix} \hat{u}_1 \\ (\hat{x}_b)_A \\ R\hat{\psi}_b \end{Bmatrix}$$

$$= -\begin{Bmatrix} 1 \\ 1+\frac{m_b}{\bar{m}} \\ \left(\frac{\bar{h}_c}{R}\right) \end{Bmatrix} (\hat{x}_b^o)_A + -\begin{Bmatrix} \left(\frac{\bar{h}_c}{R}\right) \\ \left(\frac{\bar{h}_c}{R}\right) \\ \left(\frac{\bar{h}_c}{R}\right)^2+\frac{I_t}{mR^2} \end{Bmatrix} \hat{\psi}_b^o R \qquad (45)$$

Where $\bar{h}_c = E+\bar{h}$, ω_1 and ξ_1 are respectively the first mode frequency and damping ratio of the fixed base structure, and $(\hat{x}_b^o)_A$ can be determined in terms of the free-field rigid body motion components of the foundation.

5. NON-DIMENSIONAL PARAMETERS

The non-dimensional parameters for the solution of the set of equations given by Eqn.45 can be determined to be as follows for an embedded structure on a homogenous half space. (Başaran, 1985):

Transfer Function : $TF = |\hat{x}_B|/|\hat{x}_g|$

Where $\hat{x}_B$ and $\hat{x}_g$ are respectively the Fourier Transforms of absolute lateral displacements at the ground level of the structure (Point B of Fig.8) and at the free field ground level.

Non-Dimensional Frequency : $a_o = \frac{\omega R}{V_s}$

Where V_s is the shear wave propagation velocity of the homogenous half-space

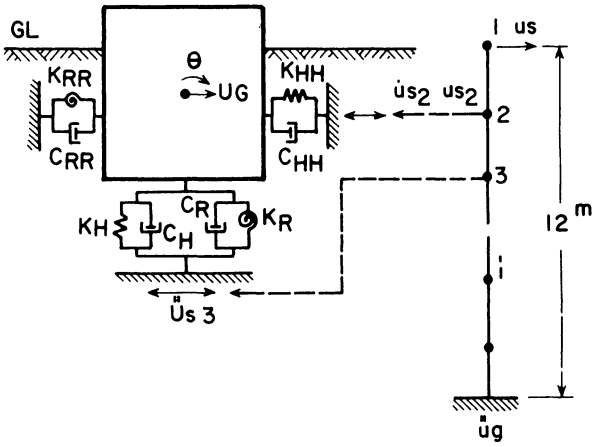

Figure 6. Lumped Parameter Model of Masao et al., (1980)

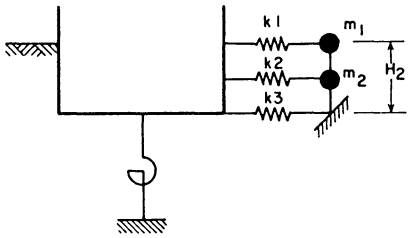

Figure 7. Lumped Parameter Model of Hall et al., (1975)

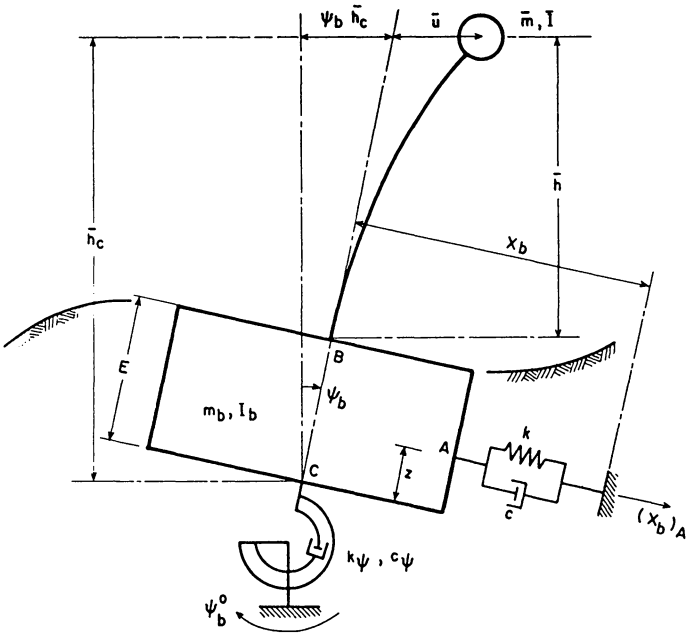

Figure 8. Three-Degree-of-Freedom Lumped-Mass-Spring Mode

Non-dimensional First Mode Frequency : $a_1 \frac{\omega_1 R}{V_2}$

Where ω_1 is the first mode vibration frequency of the fixed base super structure.

Mass Ratio : $m_1 = m_b/\bar{m}$

Relative Density Ratio : $n_2 = \alpha/\rho$ (Where α is the gross density of the structure (i.e.mass divided by gross volume) and is the density of the half-space. n_2 is defined in a similar way in ATC-3-06 (1978) an average value of $n_2 = 0.15$ is suggested for practical applications).

Non-dimensional Height : $n_3 = \bar{h}_c/R$

Non-dimensional Embedment : $n_5 = E/R$

For structures founded on a soil layer of depth H to bedrock n_4 and n_6 can be defined as R/H and E/H. For structure founded on half-space N_4 and N_6 become zero.

Structure Damping Factor : ξ_1

Poisson's Ratio of the Half-Space : ν

Figures 9, 10 and 11 depict the behaviour of the transfer function $TF = \hat{x}_B / \hat{x}_g$ for different values of these non-dimensional parameters as indicated on each figure. As it can be assessed the motion at the ground level of the structure can be up to 80% above or below of that of the motion recorded in the free field ground level depending on the frequency range. For typical accelerograph stations utilized in the United States as indicated in Figure 12 (Crouse, 1983) one can determine the dimensionless parameters to be : $m_1 = 2\text{-}4$, $a_1 = 1\text{-}2$, $n_2 = 0.15$, $n_3 = 1.25$, $n_5 = 0.3$ and $\nu = 0.45$. The transfer function between the motions at the accelerograph location and the free field are indicated in Figure 13 on the basis of these non-dimensional parameters. As it can be seen the recorded motion may be about 50% above or under the free field motion depending on the frequency range. Similar findings have been reported by Crouse (1983) and Crouse et.al.(1984).

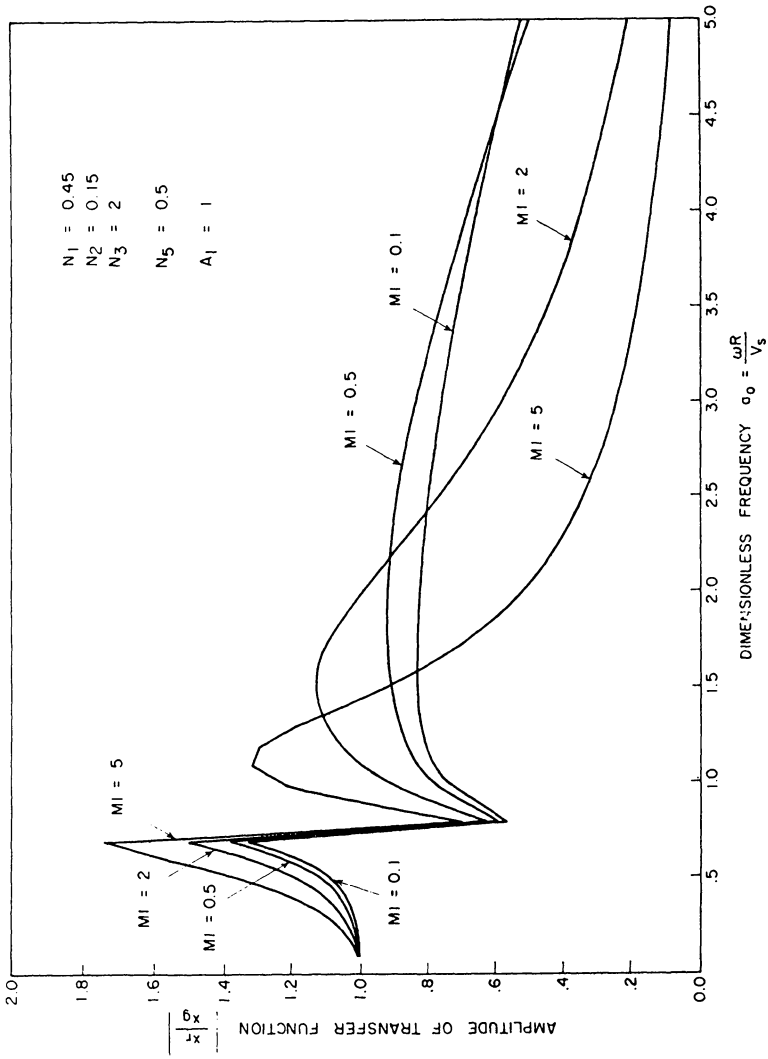

Figure 9. Transfer Function Between Structural and Free Field Motions for Structures on Half Space

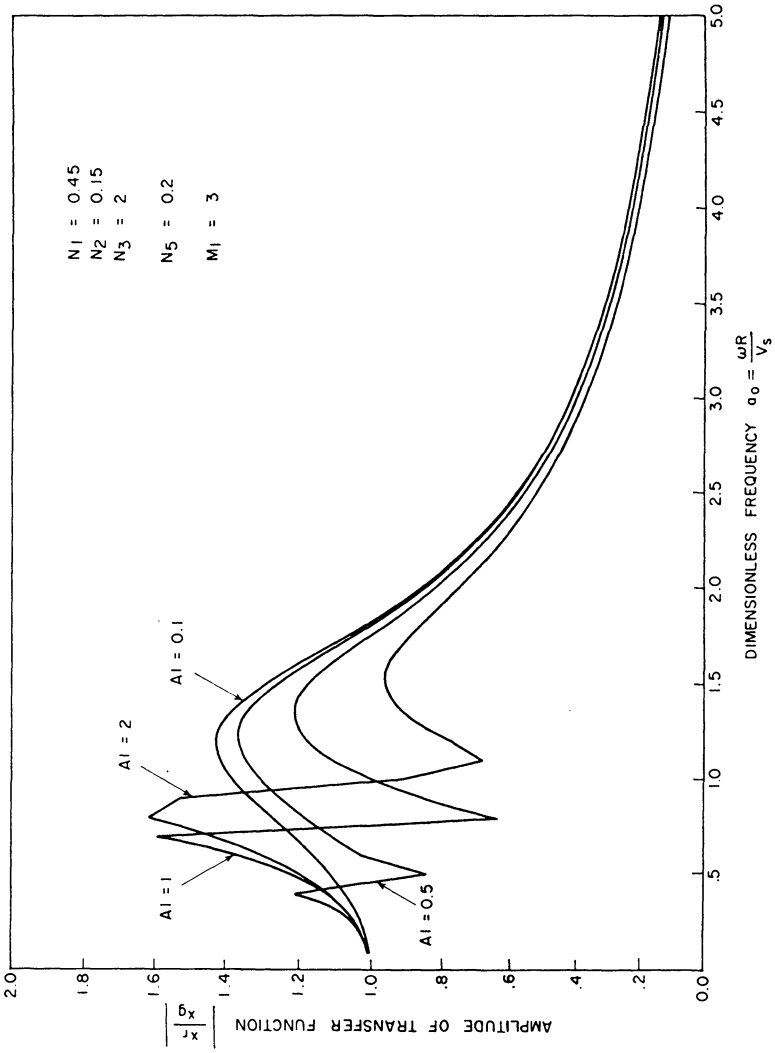

Figure 10. Transfer Function Between Structural and Free Field Motions for Structures on Half-Space

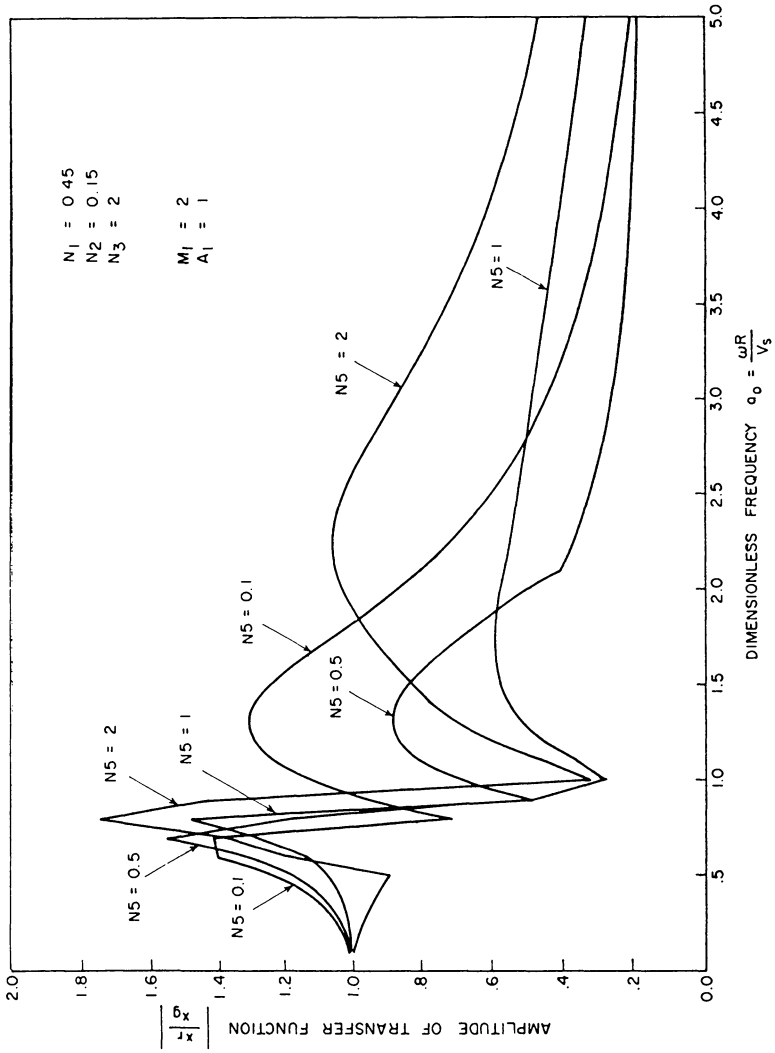

Figure 11. Transfer Function Between Structural and Free Field Motions for Structures on Half-Space

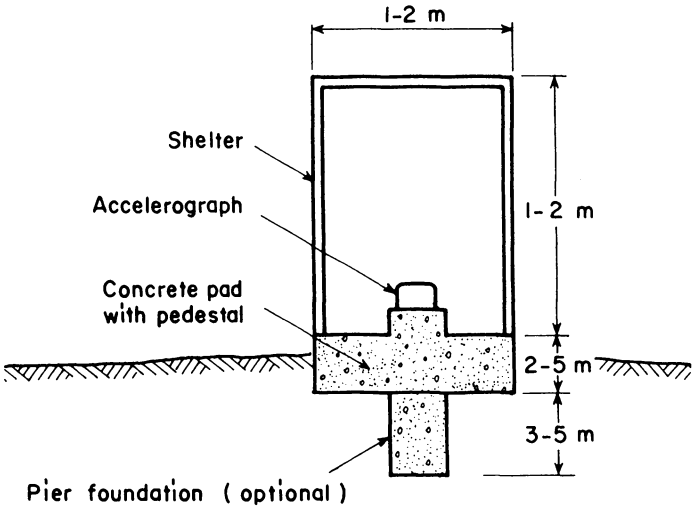

Figure 12. Typical Accelerograph Station (After Crouse, 1983)

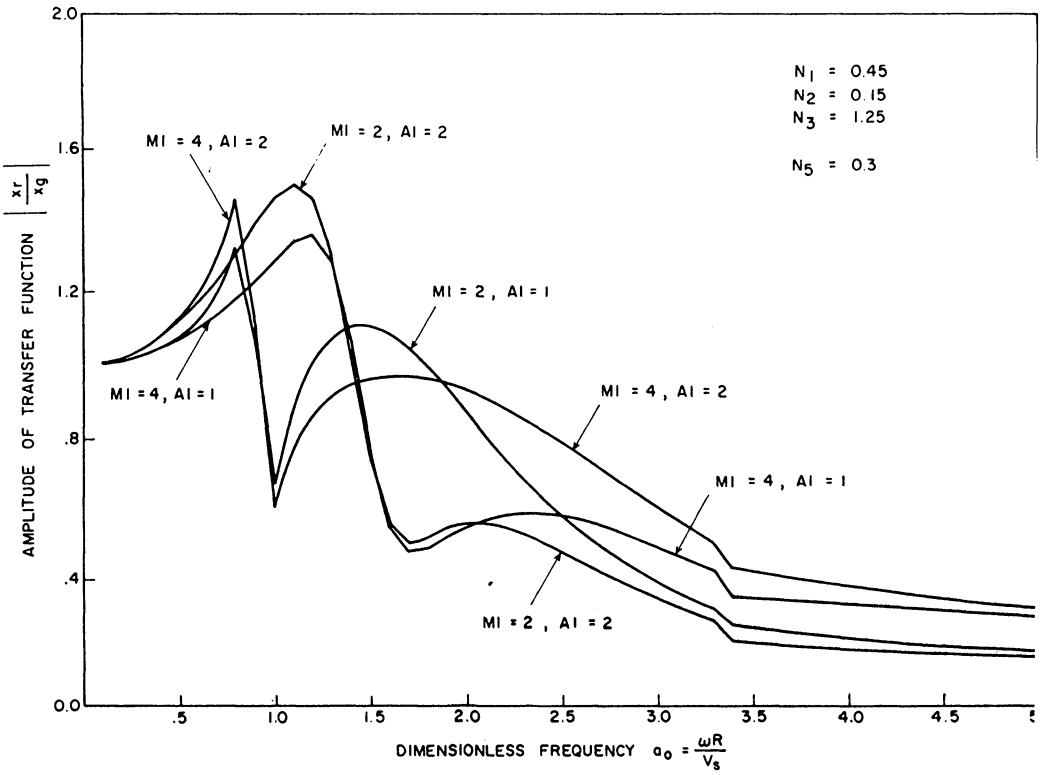

Figure 13. Transfer Function Between Structural and Free Field Motions

REFERENCES

ATC-3-06 (1978), Tentative provisions for the Development of Seismic Regulations for buildings, Applied Technology Council, U.S. Government Printing Office, Washington, 1978.

Başaran, C. (1985), Effects of Soil-Structure Interaction on Strong Ground Motion, M.S.Thesis, Dept. of Civil Engineering, Middle East Technical University, Ankara, Turkey.

Bayo, E. and E.L.Wilson (1983), Numerical Techniques for the Evaluation Soil-Structure Interaction Effects in the Time Domain, Report No: EERC/ 83-04, Earthq. Engrg. Res. Center, Univ.of Cal., Berkeley, CA.

Clough, R.W. and J.Penzien (1975), Dynamics of Structures Mc.Graw Hill Book Co., 1975.

Crouse, C.B.(1983), Soil-Structure Interaction Effects at Accelerograph Stations, Proc. of Conference XXII-a Workshop on "Site-Specific Effects of Soil and Rock on Ground Motion and the Implications for Earthquake-Resistant Design", U.S.G.S:, Reston, Virginia, USA.

Crouse, C.B., G.C.Liang and G.R.Martin (1984), Amplification of Earthquake Motions Recorded at an Acclerograph Station, Proc.8th. World Conf. on Earthq.Engrg., San Francisco, CA., USA.

Gutierrez, J.A. and A.K.Chopra (1978), A Substructure Method for Earthquake Analysis of Structures Including Structure-Soil Interaction, Earthq. Engrg. and Struct. Dyn., v.6, pp.51-69.

Hall, J.R.Jr., J.F.Kissenpfenning and P.C.Rizzo (1975), Continuum and Finite Element Analyses for Soil-Structure Interaction Analysis of Deeply Embedded Foundations, Proc.3rd. Int. Conf. on Struct. Mech. in Reactor Technology, London.

Ishii, K., T.Itoh and J.Suhara (1984), Kinematic Interaction of Soil-Structure System Based on Observed Data, Proc. 8th. World Conf. on Earthq. Engrg. San Francisco, California, USA.

Johnson, G.R., P.P. Christiano and H.I.Epstein (1975), Stiffness Coefficients for Embedded Foundations, Proc.ASCE, Vol.101, No.GT8, Aug.1975.

Kausel, E., R.V.Whitman, J.P.Morray and F.Elsabee (1978), The Spring Method for Embedded Foundations, Nucl.Engrg. And Des., 48, pp.377-392.

Lysmer, J., T.Udaka, C.Tsai and H.B.Seed (1975), "FLUSH-A Computer Program for Approximate 3-D Analysis of Soil-Structure Interaction Problems", Report No: EERC 75-30, Earthq. Engrg. Res. Center, Univ. of Cal., Berkeley, CA.

Masao, T. et.al.,(1980), Earthquake Response of Nuclear Reactor Buildings Deeply Embedded in Soil, Nucl. Engrg. and Des., 58, 393-403.

Richart, F.E.Jr., J.R.Hall and R.D.Woods (1970), Vibration of Soils and Foundations, Prentice Hall, New Jersey, 1970.

Veletsos, A.S. and Y.T.Wei (1971), Lateral and Rocking Vibration of Footings, Proc.ASCE, SM9, September, 1971.

Werner, S.D. and M.S.Agbabian (1984), Soil/Structure Interaction Effects at El-Centro, California Terminal Substation Building, Proc. 8th. World Conference on Earthq. Engrg., San Francisco, CA.

Wong, H.L. and J.E. Luco (1985), Tables of Impedance Functions For Square Foundations on Layered Media, Soil Dynamics and Earthquake Engineering, v.4, pp.64-81.

ENGINEERING USES OF STRONG MOTION DATA

Polat Gülkan
Faculty of Engineering
Hacettepe University, Ankara
and
Earthquake Engineering Research Center
Middle East Technical University, Ankara

ABSTRACT. This paper is divided into two principal parts. In the first set of subsections we deal with features of the ground motion, and existing methods for arriving at the design response spectrum which is its most prevalent engineering use. In the second part we look at some specific forms of strong motion data obtained from structures and their engineering utilization.

1.INTRODUCTION

Much has been accomplished by the earthquake engineering research community toward improving procedures in analysis, design and construction of buildings and other facilities with reliable resistance against severe ground motions caused by earthquakes. Against the rather broad scope suggested by the title of this paper we wish to state that in most of what follows our attention will be rather selective, and will be confined primarily to "conventional" structures. The engineering approach to the seismic design of such structures varies in the detail with which the three stages of engineering involvement are implemented when compared with more exotic edifices: nuclear plants, long-span bridges, very tall buildings and the like. A sobering reminder needs to be appended here: loads represented by strong ground motion constitute a rather narrow band within the spectrum of effects for which structures are commonly designed. Extreme environmental effects such as tornadoes and earthquakes are recognized as being postulated infrequent occurrences, and the way they are handled in codes and regulations reflects this reasoning. It is helpful to place the earthquake design process in perspective with the overall process of building design and construction. An engineer s association with this overall design effort can be broken down into the sectors shown in the pie chart in Fig.1. With regard to structural analysis a balanced consideration should be given to the effects of dead and live loads, wind loads, hydrostatic and lateral earth pressures, thermal effects, time dependent phenomena, stability and deformation criteria in addition to seismic forces (Poland,1980) The following is a list of items to check during the seismic design of important structures (ASCE,1980).

M. O. Erdik and M. N. Toksöz (eds.), Strong Ground Motion Seismology, 581–604.
© 1987 by D. Reidel Publishing Company.

- Gross motion of the structure
- Stability under dynamic effects
- Torsional motion
- Hydrodynamic effects
- Settlement
- Differential displacements
- Strain level effects on material response
- Uncertainties in material properties
- Motion of appurtenant parts

PART A: FEATURES OF GROUND MOTION

1. PURPOSES OF STRONG MOTION INSTRUMENTATION

The main utilization of strong motion records for engineering purposes in the determination of appropriate design criteria for future construction. Understanding the ground motion record and the resulting structural response made possible by a record of the structural acceleration is essential for structural design, and assessment of whether codes specify earthquake forces for safe design. The mushrooming network of strong motion instruments in the world insures a wealth of records with a wide spectrum of characteristics (magnitude, distance, site geology, location on structure) available for analysis and interpretation. With the increase of records obtained under very different conditions, our confidence grows in empirical models of earthquake effects on buildings.

The most obvious purpose for instrumenting a ground site is to obtain hard evidence will be in establishing a data bank of earthquake activity at the site which may be under consideration for an important installation or where seismic activity has been frequently observed in the past. The proximity of that site to a known active fault makes it invaluable from the point of view of collecting records. Any information from this site would be used by the structural engineering profession for the design of structures located on geologically similar sites.

Another purpose for instrumenting a particular location for ground motion data is to verify, identify or generate mathematical models of dynamic soil behavior either "free-field" or adjacent to structures. In this case the intent may be to ascertain in an experimental environment the validity of some mathematical description of the dynamic behavior of the site so that similar models may be utilized to predict accurately the ground motion at some other location. The response of a column of soil above bedrock, or the spatial variation of the motion may be the items under scrutiny, and these add to our capacity to produce balanced designs for our future needs.

Ground motion studies for the purpose of evaluating the seismicity of a site typically involve at least one triaxial package of accelerometers at the site in question; the exact location may be at the surface or at some depth below grade.

Acceleration records (sometimes called "time histories") are recorded in three mutually perpendicular directions. Companion papers have been concerned with widely differing characteristics of the infor-

mation contained in these records which invariably require some preprocessing in their raw form so that upon integration they represent the variation of velocity and displacement of the ground with accuracy These records are of great value as input motions for dynamic analysis of structures. Although simple characterizations of records such as peak acceleration, duration of strong-motion, the number of peaks larger than some threshold value, "dominant" period are sometimes used by the design profession, these are ordinarily of limited usefulness.

For purposes of earthquake analysis, the response of continuous structural systems can be represented by the equations of motion of approximate models. There are levels of complexity for this purpose (ASCE, 1980; Gates, 1977; Fintel,1974). Most structural arrangements can be modeled through expressions for shells, shear walls, frames and combinations of these. Once the model has been selected for the main structural system numerous techniques are available to determine their response to earthquake motions. A frequently used technique is that of defining the structure in terms of its natural frequencies, mode shapes and damping. Direct integration techniques are also available when nonlinear properties are taken into account. Sometimes, though rarely, static analysis is an acceptable alternative to handle seismic effects.

In the direct integration method of dynamic analysis, the input ground motion, usually recorded during some strong motion earthquake is prescribed as a function of time. The qualification "direct" implies that the equations of motion for the assembly of finite elements are not transformed into some other form before integration begins. This method can be used in both linear and nonlinear formulations of structural behavior, but in this paper we shall not belabor the machine solution strategies of such formulations.

In most design situations something is known about the bedrock motion and the soil characteristics of the overlying burden. Then from fundamental principles one can calculate the modifications of the bedrock motion when seismic waves reach the surface. If we denote

$X(\omega)$ = Fourier transform of the bedrock motion $x(t)$
$Y(\omega)$ = Fourier transform of the surface motion $y(t)$

then

$$H(\omega) = Y(\omega)/X(\omega) = \text{transfer function} \tag{1}$$

if soil behavior is assumed as linear. Then, once this transfer function is obtained, projections can be made of other records taken under similar conditions. Clearly the range of validity of this approach is determined by that of its underlying assumption of linearity.

Another purpose of collecting data regarding soil structure dynamics is to determine the spatial variation in ground motion over a large area. Ground motion is typically represented by three accelerations at a given point. It is then implicitly assumed that the entire site experiences the same motion at all points. This assumption may not be valid for areas with dimensions of the order of wavelength or for multiply supported structures such as bridges. Rotational components of ground motion are small in horizontally homogenous soil layers, and are commonly ignored for design requirements.

3. THE DESIGN SPECTRUM

The design spectrum and the response spectrum from which it is derived are basic items in earthquake resistant design. They are used as input in the dynamic analysis of structures; in an implicit way the relationship between the lateral force coefficient for a building and its period is a reflection of some design spectrum. Conventional wisdom in arriving at estimates of the design spectrum is to estimate first some characteristic index value of the design earthquake and then to use this value for scaling some normalized standard shape such as that given in Ref. Raggett,1980 and Newmark et al., 1973. This procedure is valid only to the extent that the shape at the recording site (Joyner and Boore, 1982). The earlier standard shapes recommended by Newmark,(1969) depended on peak velocity and displacement as well as on peak acceleration, and thus partially avoided this deficiency.

It is important to recognize the distinction between a response spectrum and a design spectrum. The former, an example of which is shown in Fig.2, is a plot showing the maximum responses of a series of differen oscillators to a given acceleration record. In this sense it is a particular description of the earthquake motion in a particular direction recorded at a particular site. The design spectrum, which does not have the jagged look of a response spectrum (see Fig.3) is a specification of the intended resistance or capacity of a particular structure as a function of its fundamental period and damping. The shape of the design spectrum is determined from the general shapes of a collection of response spectra by smoothing out the jagged features but the difference between the two is still more than skin deep. In this and the next few subsections we will review the state-of-the-art concerning design spectra

An additional difference between response and design spectra is that the implications of the latter are broader. While the response spectrum applies to the linear response of an oscillator, the level of force prescribed by the design spectrum is associated with a particular level of material strength, typically corresponding to allowable stresses or displacements. The result thus becomes the specification of the elastic resistance of the structure and its elements. When material resistance is formulated in terms of allowable inelastic deformations, the design spectrum should be interpreted as the specification of ductility to be build into the structure. From this discussion also it should be obvious that other factors govern the suitability of earthquake design criteria in addition to the level of the design spectrum. These are: (1) the level of designated spectral damping, (2) permissible stresses or strains, (3) duration of the expected seismic event that governs design, and (4) the method used for determining the building period. Combination of these factors may have as significant an effect as the force level specified in the design spectrum.

3.1. Modification of the Shape of the Design Spectrum

The shape of the design spectrum should reflect the relative intensities of ground motion expected at different frequencies so that the capacity of the structure can be expressed in a consistent manner. The different

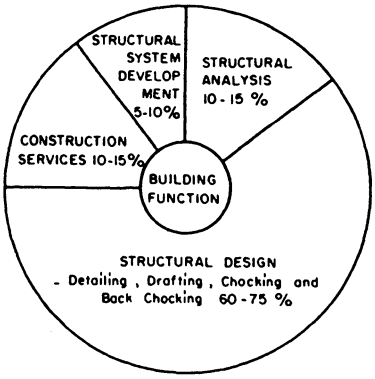

Figure 1. Utilization of the Engineer's Time in the Overall Design Effort (Poland, C.D.,1980).

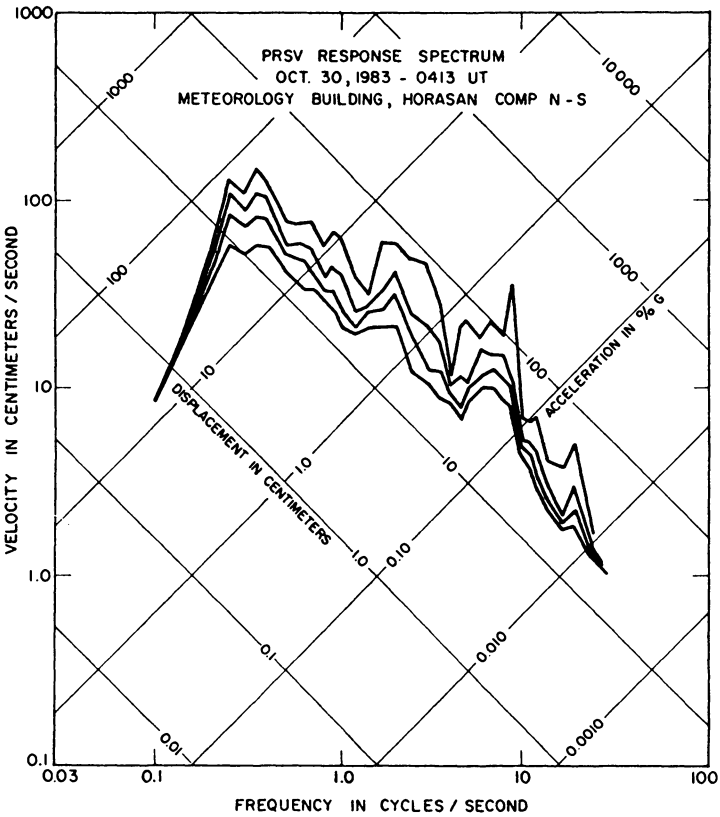

Figure 2. Response Spectrum for the October 30, 1983 Earthquake Recorded at Horasan. The Curves Are for Damping Values of 0.5, 2, 5, and 10 Percent.

frequency ranges of the design spectrum may be controlled by different magnitude and distance earthquakes. When this is the case the standard shape of spectra given in Fig.3 serves only as a beginning before a more site specific spectrum is developed. Most current thinking in this regard is in conformity with the belief that it is not meaningful to go into great detail in tailoring the shape of the spectrum because the present state-of-the-art does not warrent or justify this. It is best to limit all modifications in spectrum shapes to simple and easily understood minor changes (Housner,1982).

A problem that arises more frequently than adjusting the shape to accommodate different magnitude events at different distances is associated with the effort to adjust the shape with regard to different geological conditions. While theoretical predictive models are developed for this purpose (Joyner and Boore, 1982; Trifunac, 1978) there is a dearth of good data which has been embedded into the solution, and such models should be used with caution.

3.2. Site Spectrum: An Example Case

A significant feature of the response spectrum shapes contained in Newmark et al.1973 which were adopted by the U.S.Nuclear Regulatory Commission in its Regulatory Guide 1.60 (USNRC,1973) relates to the recommendation that these be used only for "general" site conditions. In support of this statement it is suggested that for sites judget to be "significantly" responsive to ground motion components with frequencies less than about 2 Hz the shapes in (USNRC,1973) should not be used without "appropriate" modifications. By extrapolation it may be argued that these shapes do not reflect the influences of near-by events.

Categorization of response spectra obtained from records made in different geological environments has been a vigorous research area. Statistically significant modifications occur because of the vibratory characteristics of the underlying starata. and the epicentral distance (Joyner and Boore, 1982 ; Seed et al., 1976 ; Mohraz,1976). Strong arguments, again from the statistical point of view, against placing disproportionate emphasis on local geology are given in (Trifunac,1980).

Current thinking in relation to design response spectra determination is that the peak ground acceleration is a reasonable basis for moderately distant sources. For nearer events it appears that this procedure does not work, judging from the spectra of near field earthquakes and from lack of damage consistent with measured peak acceleration values. Examples of such earthquakes are the Pacoima Dam, Parkfield, Melendy Ranch and the Ancona records.

The smoothed spectrum in Fig.3 has been constructed according to the simple rules given in (Newmark et al.,1973): amplification factors for various control points (typically corresponding to 0.25, 2.5, 9, and 33 Hz) are multiplied by the design acceleration or displacement values, and the polygonal shaped spectrum for a given damping ratio is determined There exist minor differences between the frequency control points for the horizontal and the vertical directions. The amplification factors employed in Fig.3 are based on the mean-plus-one-standard deviation or 84.1 percentile level for the lognormally distributed ordinates.

Among the first systematic analysis of the influence of local soil conditions on the shapes of response spectra are the studied in (Seed et al.(1976) and Mohraz (1976). In the former study the results are unfortunately given in terms of 5 percent damping only, and this diminishes the usefulness of data. In Mohraz (1976) similar data is given at the mean and the 84.1 percent confidence levels for a greater number of damping values in the three orthogonal directions of motion. We present a set of design spectrum curves (for rock sites and for the component with the larger horizontal acceleration) in Fig.4. In comparisons between Figs.3 and 4 it should be noted that only three out of the five values of damping match. The procedure suggested for drawing the spectra in Fig.4 is based upon "spectrum bounds" rather than on "amplification factors" which forms the basis of Fig.3. The spectral bound for displacement, velocity and acceleration are drawn parallel to the corresponding axes between small frequency values and the limiting value of 8 Hz. At 33 Hz the bounds for different damping values coalesce into a single line equal to the maximum ground acceleration which is taken as 1 g in Fig.4. Between 8 and 33 Hz the variation of acceleration bounds is assumed to be linear. In general the design spectra in Figs.3 and 4 agree closely for frequencies larger than about 3.5 Hz. In the medium frequency range (0.3 to 2 Hz) the R.G. 1.60 curves are considerably more conservative than the curves in Fig.4.

In making estimates of site-specific spectra according to the concepts embodied in Fig.4, one needs to estimate peak ground velocity and displacement as well. The mean v/a ratio for rock sites is given as 69 $cm.s^{-1}/g$ in Mohraz(1976) while the data studied in Seed et al.(1976) indicates a range of 59 - 74 $cm.s^{-1}/g$. The agreement is noteworthy. Estimation of maximum ground displacement (d) is based on the dimensionless ratio $a\,d/v^2$ which is a rather sensitive parameter because it is influenced by earthquake magnitude and distance to the zone of energy release as well as local geology. For rock sites a mean value of 7 is indicated although for close events it may be somewhat less.

The last important item to consider in determining a specific design spectrum is the possible modification due to near-field events. There are several considerations concerning this point. The first is the relative abundance of high-frequency components of motion which normally filter out rapidly for more distant sites. The second relates to our earlier observation that the large acceleration peaks do not seem to cause significant damage. An extended duration of strong shaking coupled with large acceleration peaks characterizes destructive earthquakes while records with several high-frequency large peak pulses correspond to short-duration nearby events. The final evaluation should consider the comparison between the response spectrum derived for a particular site and those of records obtained under as similar conditions to the postulated event as possible. While it is not the objective to make the design spectrum enclose those of the actual events for all frequency ranges, a degree of conservatism should be attained. In most cases the selected accelerograms will not have been recorded under circumstances identical to those of the design event, and it will become necessary to adjust their spectra. This adjustment consists of multiplying by a scaling factor of the spectral ordinates; the scaling factor is commonly

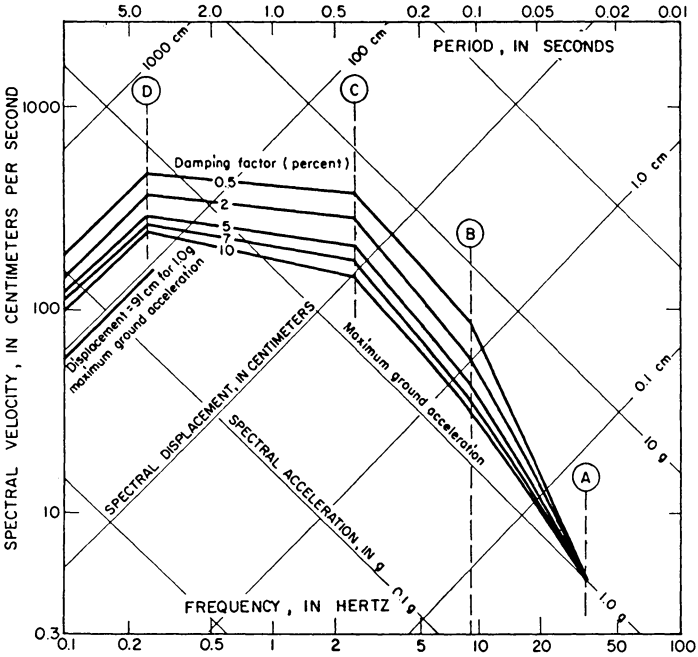

Figure 3. USNRC RG 1.60 Standard Design Spectrum Shapes

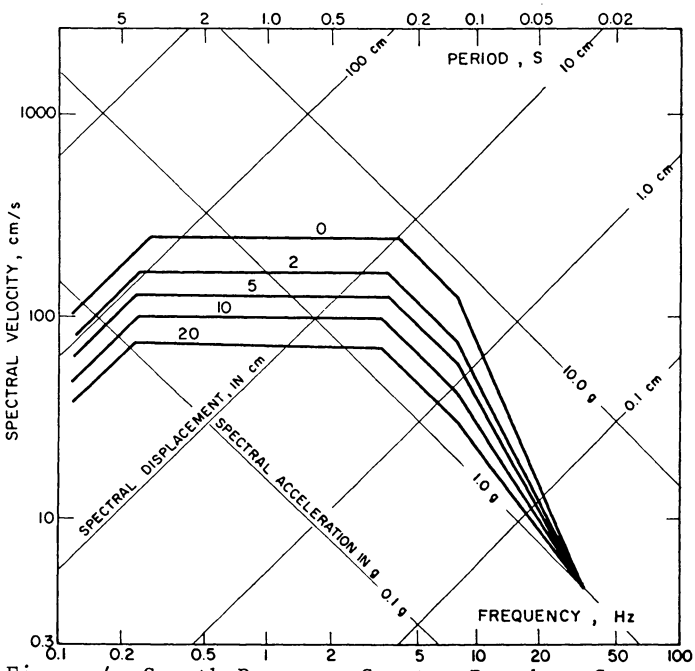

Figure 4. Smooth Response Spectra Based on Spectrum Bounds (Mohraz, B., 1976).

determined by dividing the peak acceleration that corresponds to the distance and magnitude of the design event by the acceleration which corresponds to the distance and magnitude of the accelerogram whose spectrum is being scaled. Such an operation is an approximate practice, and it is desirable to keep it to a minimum. It should be emphasized that whatever form of acceleration attenuation is used, it is intended to serve only as a tool for measuring the severity of the ground motion relative to some arbitrary yardstick, and not as an absolute predictor of the peak acceleration. Our view is that slight modifications in the overall spectrum shapes given by the procedure in Newmark (1969) or Mohraz (1976) is to be preferred over the raw NRC shapes (Newmark et al.,1973) because careful analysis of existing data corroborates this. This view is also expressed by Joyner and Boore (1982).

3.3. Final Remarks on Design Spectra

From discussions of the shape of the design spectrum it is clear that professional opinion regarding the preparation of such curves has reached a consensus: efficient ways need to be incorporated into the methodology so that influences associated with event size, distance and local site conditions are embedded into the final product. The results of regression analyses conducted on spectral ordinates reported in Joyner and Boore, (1982) or Trifunac and Lee, (1978) are two examples of work in this direction.

The study reported by Joyner and Boore (1972) is restricted to shallow earthquakes recorded in western North America with magnitudes larger than 5. A two-stage regression procedure is employed in fitting the spectral ordinate data with the expression

$$\log y = \alpha + \beta(M-6) + \gamma(M-6)^2 - p \log r + br + cS \qquad (2)$$
$$r = (d^2 + h^2)^{1/2}$$

In terms of the original notation y is the response spectrum ordinate at a given period, M is the (moment) magnitude, S is a binary variable assuming a value of 1 for soil sites and 0 otherwise, d is the closest distance from the recording site to the projection of the rupture surface. The parameters α, β, γ, p, b, c, and h are determined for each period by the regression analysis.

In Fig.5, taken from the original work, we show the predicted spectra for rock and soil sites for magnitudes equal to 5.5, 6.5, and 7.5. A large effect of magnitude on spectral shape is indicated in these curves. This fact supports the argument that the common practice of using peak acceleration to scale normalized spectra with a fixed shape may lead to substantial error for large magnitude events. The scaling procedure suggested by Newmark and Hall (1969) largely avoids this error because it uses the peak velocity for scaling spectral ordinates in the middle part of the diagram (periods ranging from 0.25 to 2 s). Figures 6 and 7 indicate the shapes for fixed magnitudes of 6.5 and 7.5, respectively, for a range of d values. It is observed that there are significant differences between the shapes of spectra for 0 and 10 km, but the alteration of shape is much less pronounced for distances larger than 10 km.

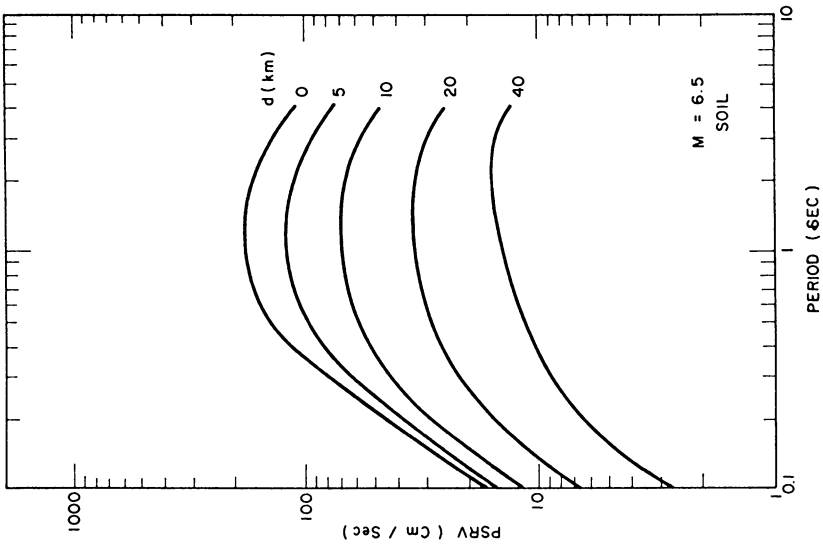

Figure 6.
Predicted PSRV Spectra for 5 Percent Damping at Soil Sites for M=6.5 and Range of d Values (Joyner,W.B., and D.M.Boore, 1982).

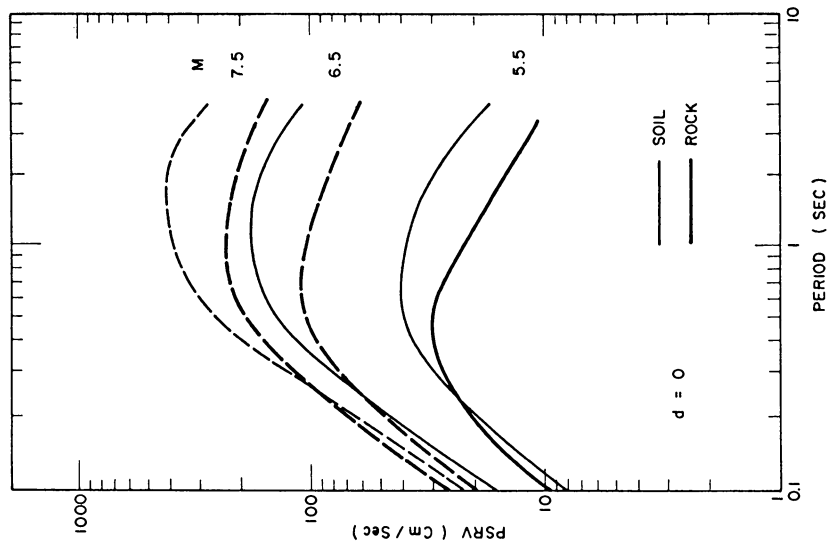

Figure 5.
Predicted PSRV Spectra for 5 Percent Damping at Rock and Soil Sites for d=0 and for the Larger Horizontal Component (Joyner, W.B., and D.M.Boore, 1982).

Regression analysis of a different population of records followed by scaling Fourier amplitudes by means of the equation

$$\log y = M + \log A_o(R) - bM - c - dh - ev - fM^2 - gR \qquad (3)$$

is reported in Trifunac and Lee (1978). In Eqn. 3 y represents the Fourier amplitude spectrum at the period considered T, M is the magnitude, h is the depth of soil sediments in km, v equals 0 for horizontal and 1 for vertical motion, and R is the epicentral distance in km. The expression $A_o(R)$ is the empirical amplitude attenuation relation, and b, c, d, e, f, and g are the regression coefficients, all of which also depend on the period. In Fig.8 we present the coefficients' variation in solid lines enclosed by their 95 percent confidence intervals. The prediction of Fourier spectrum ordinates via Eq. 3 for the two horizontal components of the motion recorded at Pacoima Dam during the 1971 San Fernando event is shown in Fig.9. In this figure p denotes the confidence interval for the ordinates.

The role of regression analyses appears likely to grow in importance as our library of records continues to grow. However, the predictive capacity of such equations can not be expected to assume the elusive all-seeing characteristics that they are sometimes purported to have. We cite as an example the record made at the township of Horasan at an epicentral distance of 20-25 km for the October 30,1983 earthquake near Erzurum, Turkey. The east-west component of the corrected accelerogram with its velocity and displacement traces is shown in Fig.10. When data concerning magnitude (M = 7.2), epicentral distance and p are substituted into Eq. 3 we determine the comparative curves in Fig.11; the lack of conservatism in the narrow bands centered around 0.2 Hz and 8 Hz is noteworthy.

PART B: SOME ADDITIONAL FEATURES OF ENGINEERING USES OF STRONG-MOTION DATA

4. PRESENT METHODS OF PRESCRIBING DESIGN EARTHQUAKES

The objective of this part of the paper is to review the overall problem of establishing design earthquakes in what should be the end product of geophysical, seismological or soil dynamics points of view. Difficulties in the application of analytical tools to seismic analysis arise from uncertainties regarding the details of a particular ground motion, and the important effects these details may have on overall response. An estimate of the economic losses likely to be incurred in case of failure is required to obtain optimum design. The word "failure" is used in this context to define any undesirable limit state which makes the structure unfit for use (Bertero,1977) The main design aspects which the structural engineer considers are listed in the flow diagram in Fig.12.

From a conceptual point of view the design earthquake should be the ground motion which drives the structure into its critical response state. Establishment of the design earthquake for purposes of analysis using direct integration techniques is similar to the determination of the mechanical properties of materials so that their behavior under various effects can be predicted. When such analysis is considered two limiting

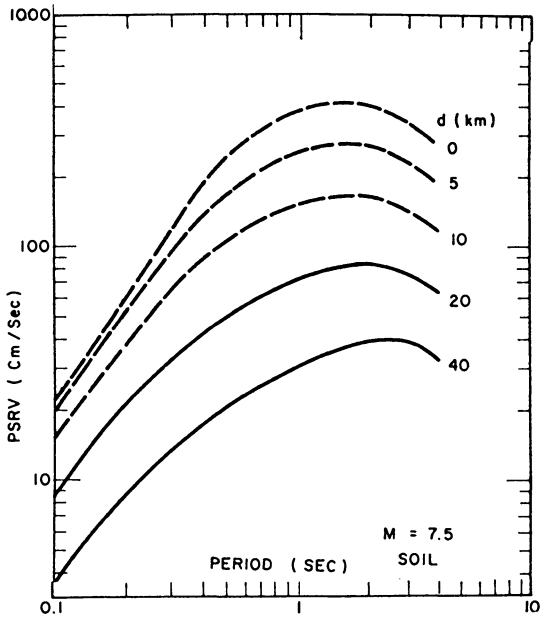

Figure 7. Predicted PSRV Spectra for 5 Percent Damping at Soil Sites for M=7.5 and Range of d Values. Curves Are Dashed Where Not Constrained by Data (Joyner,W.B., and D.M.Boore, 1982).

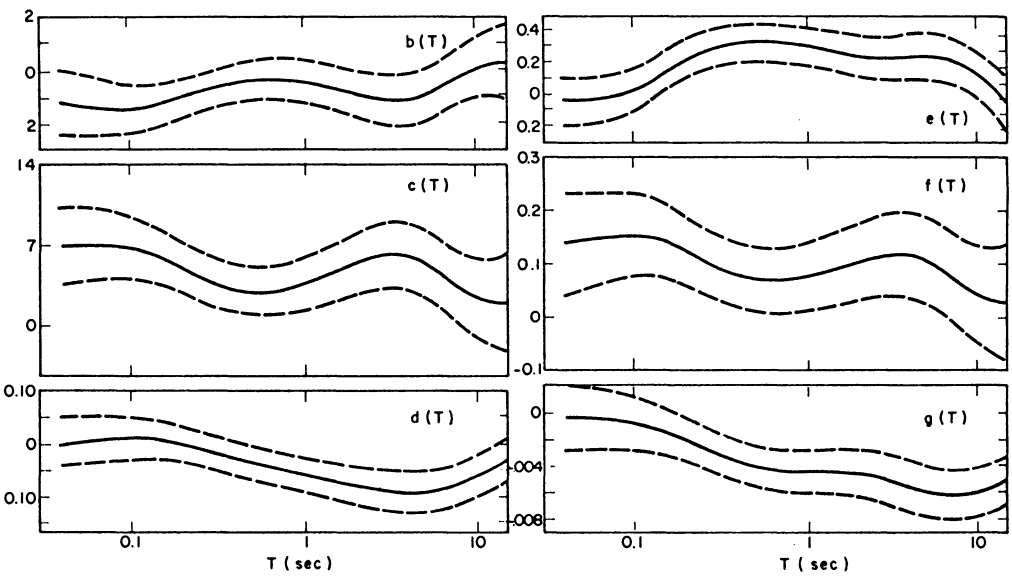

Figure 8. Coefficients' variation in solid lines enclosed by their 95 percent confidence intervals (Trifunac and Lee, 1978)

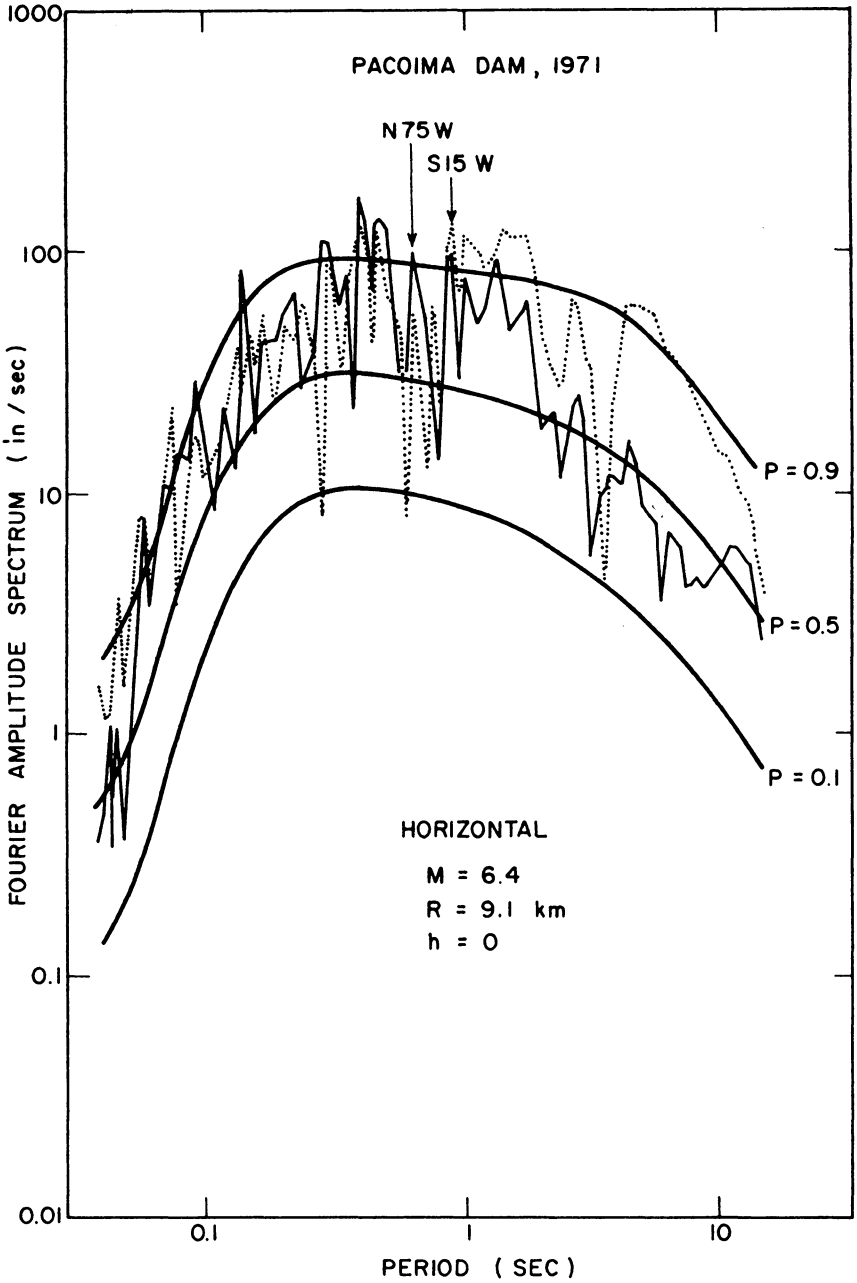

Figure 9. Comparison of Predicted and Compited Fourier Amplitude Spectra for the Pacoima Dam Record (Trifunac, M.D., and V.W.Lee, 1978).

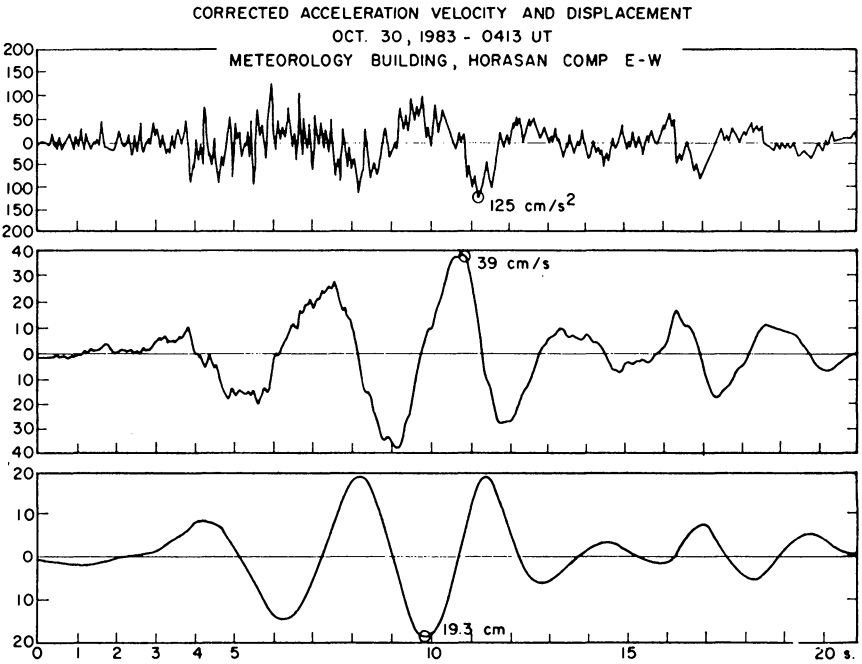

Figure 10. Corrected Accelerogram for the Erzurum Earthquake

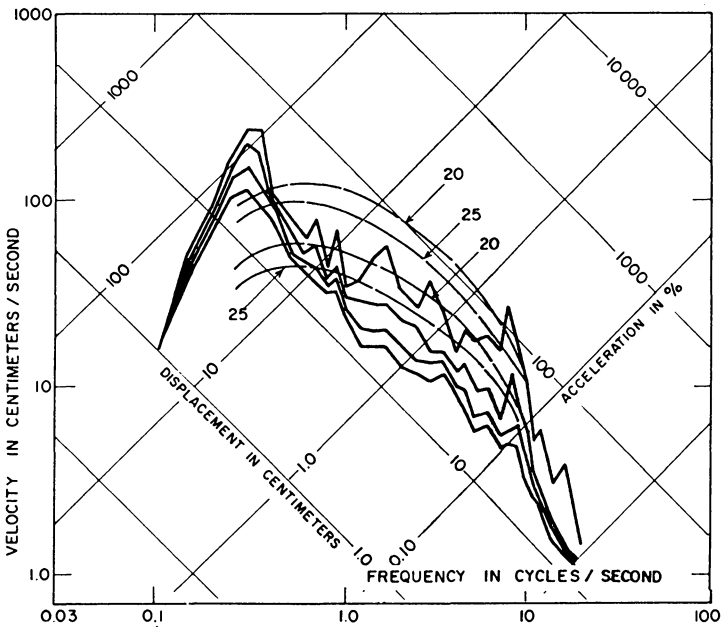

Figure 11. Comparison of the Response Spectrum of the Record in Fig.10 with Predictions Based on Eq.(3). The Two Sets of Curves Are for d=20 or 25 km and for Mean and Mean + 1 Standard Deviation.

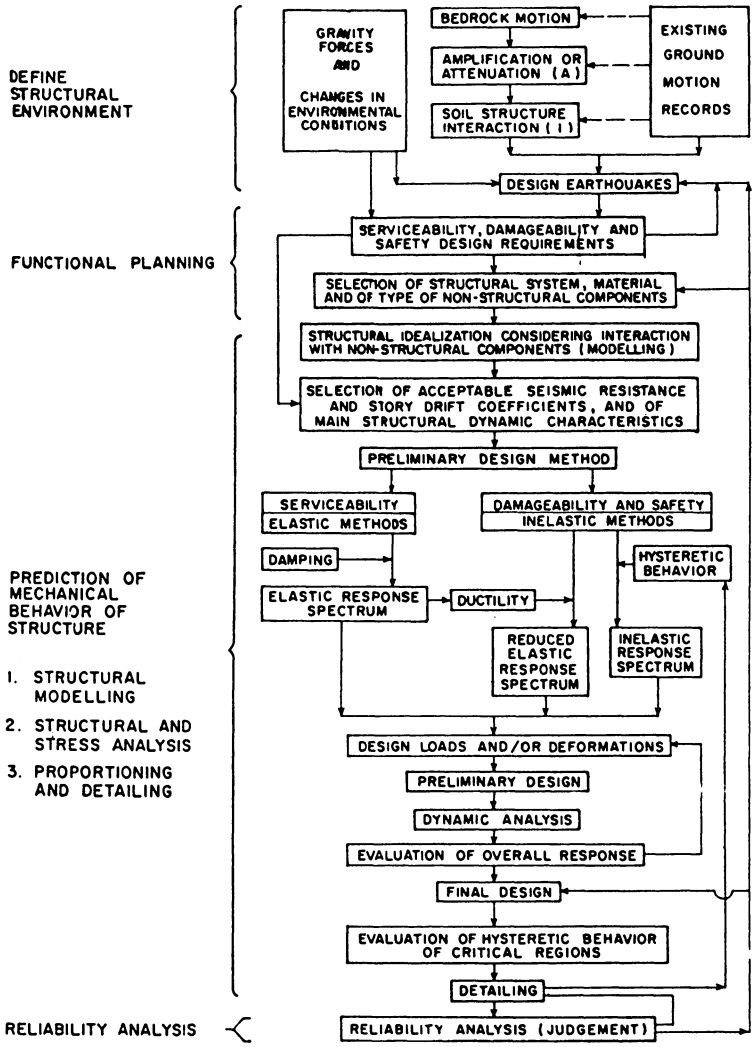

Figure 12. General Aspects and Features Involved in Seismic Design (Bertero, V.V., 1977).

cases should be established. The first corresponds to the limit of serviceability, and the second of strength. In the former state the structure is understood to remain in its linear range of behavior with little or no loss of function, and in the latter inelastic large displacements up to the point of incipient collapse are controlled and tolerated. These limit states are quite disparate, and attempts at describing a damageability limit have the objective of bridging the two (Bertero,1977)

4.1. Serviceability

For structures located at moderate distance to the earthquake zone the most convenient form of specifying the design earthquake is through the smooth design spectrum. One difficulty associated with this approach lies in the combination of the modal maxima; summing the squares of the sum (SRSS) works only when there is no modal coupling or closely spaced modal frequencies. Methods exist for avoiding the consequent difficulties (Amin, 1971 ; Wilson et al.,1981).

The use of a specific record of ground motion appears attractive but for design purposes several records need to be input, and details of response may obscure the true statistical nature of the limit displacements.

4.2. Ultimate Limit State

In general it is not feasible or even possible to design buildings close to zones of energy release for the forces indicated in the smooth design spectrum. Accepting the premise that they are inavoidable inelastic deformations still need to be kept within allowable limits in order to avoid collapse. One of the most pressing requirements of the structural engineer involved in design is the development of reliable and practical procedures based on inelastic behavior which considers the damageability and ultimate limit states. These procedures would of course depend strongly on the development of reliable design basis earthquake records because only the direct integration approach offers reasonable prediction of the response of actual structures in the inelastic range. Code procedures based on the equivalent static force (and the implicitly understood elastic analysis) are unsatisfactory. Problems in using time history motions as input include the difficulty of establishing reliably the true hysteretic behavior of components, and the computational effort that is required. Again, the variability of response requires that many different input motions be tried.

One improvement over the simple code procedure is the expedient of specifying the design earthquake for the ultimate limit state through the use of inelastic design response spectra from whic preliminary design loads can be derived by evaluating the nonlinear dynamic response of actual models with realistic hysteresis idealizations. Yet simpler methods which modify the elastic spectra by using factors based on various forms of inelastic behavior have been advanced (Newmark and Hall, 1982).

A method which approximates the response of inelastic systems driven into their limit state by the response of an elastic substitute system is given in Gülkan and Sozen (1974). The method is not empirical,

but is based on experiments on reinforced concrete frames subjected to very intense one-directional base motions. Its applicability to multi-degree structures and use as a design tool have been demonstrated (Shibata and Sozen, 1976).

The use of design spectrum, elastic or otherwise, requires two key ingredients: a characteristic frequency (or a period) and a characteristic damping value. The shape of the hysteresis loops for reinforced concrete frame elements under static forces suggests that they may be approximated by a vibrating linear system with "equivalent" viscous damping. Quantitative values for this fictitious or substitute damping were obtained from tests on the premise that energy input from the base motion is dissipated entirely by a viscous damper associated with the mass. In Fig.13 we show the values of the substitute damping ratio β_s plotted against the ratio μ of maximum absolute displacement to yield deflection of the test frames. Data from different tests with different base motions and different specimen sizes are not strictly comparable but there is a definite discernible trend with the ductility ratio for the substitute damping. If we assume that β_s has a threshold value of 0.02 at $\mu = 1$, Eq.4 may be used to define the data in Fig.13:

$$\beta_s = 0.02 + 0.2\,(1 - \frac{1}{\sqrt{\mu}}) \qquad (4)$$

Using the concept of reduced stiffness and substitute damping, a procedure based on linear response can be used to estimate the effects of inelastic response for reinforced concrete structures which can be idealized as simple systems. The procedure involves the following steps:

(1) Assume an admissible value of μ
(2) Calculate stiffness on the basis of cracked section
(3) Determine the natural period T
(4) Calculate β_s corresponding to μ from Eq. 4 or Fig.13
(5) Obtain base shear and maximum displacement by entering the elastic response spectrum with the increased period $T\sqrt{\mu}$ and β_s from the previous step

A series of direct integration analyses were made for simple systems with hysteretic response representative of reinforced concrete. Each oscillator was subjected to the two particular horizontal base motions indicated in Table 1 which shows the maximum attained values of μ with those required by the approximate method. The approximate substitute damping was used iteratively to obtain the required value of μ.

The favorable comparison between the exact and the approximate values of μ suggests that the substitute damping method may be used successfully in the domain covered by the former. In design applications the design spectrum curves corresponding to the limit event should be smoothed (Housner and Jennings, 1982 ; Newmark and Hall, 1982). A safety factor may be intrdoduced in selecting the smooth curves by modifying β_s in Eq. 4 or explicitly at the end of the design process. This procedure reduces drastically the number of input motions required for analysis.

TABLE 1. COMPARISON OF CALCULATED DUCTILITIES (Gülkan and Sozen, 1974)

Period s	Base Shear (1) Coeff.	Values of Ductility Ratio			
		El Centro 1940, N		Managua 1972, E	
		Exact (2)	Approx. (3)	Exact	Approx.
0.15	0.16	28.5	26	28.8	26
	0.32	4.1	10	13	10
	0.48	3.3	5	5.2	6
0.5	0.16	8	6	5.6	6
	0.32	2.9	3	2.8	3
	0.48	2	2	2	2
1.0	0.08	4.9	6	5.6	6
	0.16	2.5	2	3	2
	0.24	1.5	1.5	1.3	1.5
2.0	0.04	4.6	5	4.5	4
	0.08	2	3	1.9	2
	0.12	1.5	2	1.4	2

(1) Lateral yield force divided by weight of the structure
(2) Attained in response history analysis
(3) Required by iterations using the substitute-damping concept

5. PARAMETER AND SYSTEM IDENTIFICATION

The major part of our concern until now has been the use of strong motion records for purposes of analysis and design. The next, and perhaps more sophisticated, level of information gathered from records of structural response is model verification. This may be defined by means of the following steps:

(1) Assume that a complete record of the ground motion is obtained at what may be regarded as the base of the structure, i.e. the input,
(2) Concurrently at least one time correlated record of the response is made, i.e. the output at some other point,
(3) A mathematical model of the structure is formulated,
(4) This model is subjected to the recorded input motion,
(5) The response of the model is compared with the known response of the physical structure. If the measured and the computed responses match, then the mathematical model represents the structure accurately, otherwise the need is indicated for one or more of the parameters that comprise the model to be varied. This

process of iteratively reducing the difference between predicted and observed response constitutes parameter or systems identification.

The most important item for a parameter identification scheme to succeed is that the entire input be known even though there may be only one output record available. If the input record is incomplete and this fact is not fully recognized the only information that one could expect to obtain are peak values, natural frequencies for some modes, and approximate mode shapes. At the most sophisticated level of gathering after-the-fact information from strong motion records is model or system identification. The difference between identification and verification is that the model is identified by relating the known output to the known input according to some goodness-of-fit criterion (Udwadia and Marmarelis, 1976 ; Hart and Yao, 1977 ; Kaya, and McNiven, 1978).

System identification procedures promise a good deal of useful information regarding the way structural systems are modeled and the way they behave, although the results of such analyses are sometimes hard to generalize. This fact has motivated much research McVerry (1979). Strong motion data recorded on structures permit force levels to be determined on time correlated traces through the simple expedient of applying Newton's second law; searching for the optimum number and location of instruments is considered in Hart and Rojahn (1979). In the next section we will consider a hypothetical bridge instrumented by accelerographs; relatively few strong motion instruments may be required for the verification of mathematical models, but they may be insufficient for the calculation of force levels in the structure. It is important to determine whether there are adequate instruments for force determinations; if there are not then the mathematical model needs to supplement the physical records.

6. EXAMPLE: A BRIDGE STRUCTURE

For a typical bridge deck it may be assumed that all significant horizontal distortions can be described in terms of the four modes of vibration shown in Fig.14. Let us assume that the instruments located on the bridge as well as the vicinity are as in Fig.15. Corresponding to the assumed deflected shapes generalized accelerations can be expressed in terms of the measured accelerations by means of the relations

$$\ddot{\alpha}_1(t) = \frac{1}{3}\left[\ddot{u}_1(t) + \ddot{u}_2(t) + \ddot{u}_3(t)\right] - \ddot{u}_{yg}(t) \tag{5}$$

$$\ddot{\alpha}_2(t) = \left[\ddot{u}_3(t) - \ddot{u}_1(t)\right]\frac{1}{L} \tag{6}$$

$$\ddot{\alpha}_3(t) = \ddot{u}_2(t) - \frac{1}{2}\left[\ddot{u}_1(t) + \ddot{u}_3(t)\right] \tag{7}$$

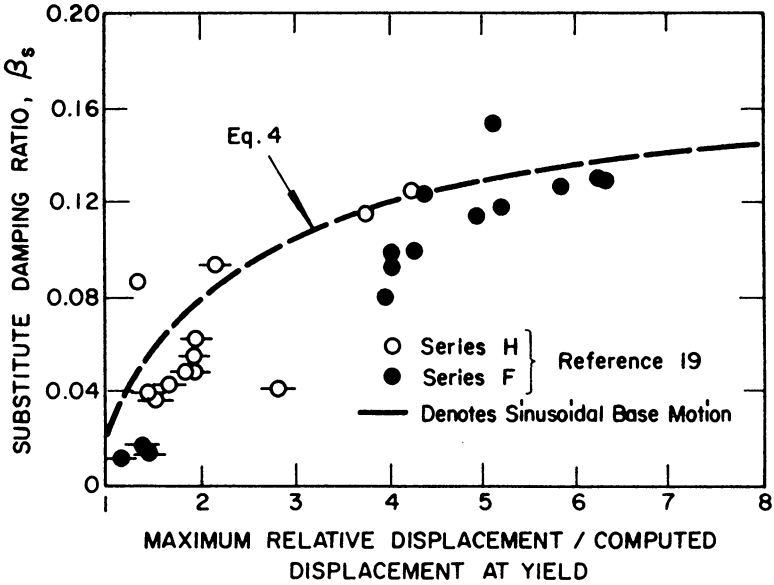

Figure 13. Variation of the Substitute Damping Ratio with the Ductility Ratio (Gülkan,P., and M.A.Sozen,1974).

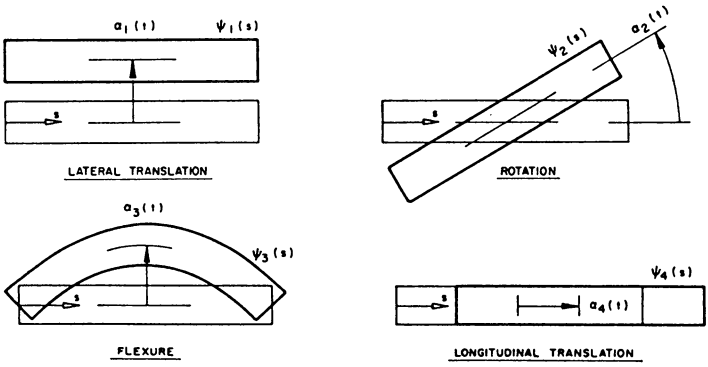

Figure 14. Possible Modes of Vibration for a Bridge

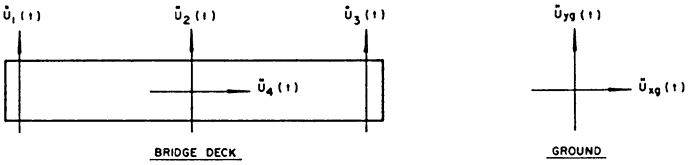

Figure 15. Location of on and around the Bridge (Raggett, J.D., and C.Rojahn, 1978).

$$\ddot{\alpha}_4(t) = \ddot{u}_4(t) - \ddot{u}_{xg}(t) \tag{8}$$

These equations are equivalent to backtransforming from the physical to the generalized coordinates $\alpha(t)$ (Raggett and Rojahn, 1978). The generalized accelerations can be used to determine force levels in the bridge associated with the four modes in Fig.14.

A general approach to the computation of force levels in a bridge has the following steps:

(1) Computation of the inertia forces
(2) Computation of the reactions to these forces
(3) Computation of the internal actions from known external and reactive forces

Inertia forces acting on a particular bridge can be obtained from lumped mass models described in physical coordinates. At any time t the inertia force acting on the i'th mass is

$$F_i(t) = M_i \ddot{u}_i(t) \tag{9}$$

When deformations are expressed in terms of generalized coordinates determination of inertia forces is somewhat more involved. With M(x) denoting the mass of the bridge structure per unit length the inertia force per unit length at coordinate ξ on the bridge deck at time t is given by

$$F(\xi,t) = M(\xi)\, \ddot{u}(\xi,t) \tag{10}$$

where $\ddot{u}(\xi,t)$ is the absolute acceleration. When these absolute accelerations are expanded in terms of ground accelerations

$$\underline{\ddot{u}}(\xi,t) = \sum_{i=1}^{n} \underline{\Phi}_i(\xi)\, \ddot{\alpha}_i(t) + \ddot{u}_{xg}(t)\vec{i} + \ddot{u}_{yg}(t)\vec{j} + \ddot{u}_{zg}(t)\vec{k} \tag{11}$$

Substitution of Eq.(11) into Eq.(10) yields the inertia forces from which the reactive forces may be obtained by any of the standard procedures of structural analysis. Finding a maximum reaction, or a maximum internal action, may require a trial and error approach, but visual examination of the records is often helpful in this regard.

With regard to the problem of identifying the mathematical model from strong motion records it is reasonable to obtain model properties in normal coordinates where each mode of vibration is characterized by (Clough, 1975).

$$\ddot{\eta}_i + 2\zeta_i\omega_i\dot{\eta}_i + \omega_i^2\eta_i = \gamma_{xi}\, \ddot{u}_{xg} + \gamma_{yi}\, \ddot{u}_{yg} + \gamma_{zi}\, \ddot{u}_{zg} \tag{12}$$

In Eq.(12) the notation is standard (γ denotes the participation factor); the total relative displacement vector is a combination of the modal responses

$$\underline{\ddot{u}}(\xi,t) = \underline{\emptyset}_1(\xi)\ddot{\eta}_1(t) + \underline{\emptyset}_2(\xi)\ddot{\eta}_2(t) + \ldots \tag{13}$$

where $\emptyset_i(\xi)$ are the normal modes of vibration. In most cases little data will exist for ω_i, $\emptyset_i$ and γ_{xi} etc. This can be avoided in lightly damped

systems by noting that the total distortion of the system can be found by considering only a few of the lower modes:

$$\underline{u}(\xi,t) = \underline{\emptyset}_1\alpha_1(t) + \underline{\emptyset}_2(\xi)\alpha_2(t) + \ldots + \underline{\emptyset}_m(\xi)\alpha_m(t) \qquad (14)$$

where $m \ll n$. If the properties of only a few of the lower modes can be found the general features of the response of the bridge can be determined with little error.

7. FINAL REMARKS

Uses of strong motion data for structural engineering purposes constitute a mixed bag of activities. By far the most prevalent use of records is in the definition of the seismic input for future structures in the design stage. The state-of-the-art here is not perfect but much has been accomplished toward the definition of the event for which an engineer is to design his structure. At the simplest level this is the code base shear. With increasing levels of complexity we encounter the design response spectrum, and prescribed ground input motions. Records of instruments placed on structures may be used to unravel the physical characteristics of the mechanical systems, and assist in understanding their actual behavior in case of strong ground motion.

REFERENCES

Poland, C.D. (1980), "Utilization of Strong-Motion Records in Building Design," Proceedings of the Workshop on Interpretation of Strong-Motion Earthquake Records Obtained in and/or near Buildings, UCLA Report No.8015, April, 1980.

ASCE, (1980). Structural Analysis and Design of Nuclear Plant Facilities, 1980.

Gates, W.E. (1977), "The Art of Modelling Buildings for Dynamic Seismic Analysis," Proceedings of the Workshop on Earthquake-Resistant Reinforced Concrete Building Construction, V.V.Bertero, Editor, University of California, Berkeley, June, 1977.

Fintel, M. (1974), Handbook of Concrete Engineering, Van Nostrand, 1974, (Chapter 12).

Raggett, J.D. (1980), "Information Obtained from Strong Motion Records," Proceedings of the Workshop on Interpretation of Strong-Motion Earthquake Records Obtained in and/or Near Buildings, UCLA Report No.8015, April, 1980.

Newmark, N.M. (1973), J.A.Blume, and K.K.Kapur, "Seismic Design Spectra for Nuclear Power Plants," Journal of the Power Division, ASCE, Vol.99, No.PO2, Nowember, 1973, pp.287-303.

Joyner, W.B., and D.M.Boore (1982), "Prediction of Earthquake Response Spectra," USGS Open File Report No.82-977, 1982, 16 pp.

Newmark, N.M., and W.J.Hall, (1969), "Seismic Design Criteria for Nuclear Reactor Facilities," Proceedings of the Fourth World Conference on Earthquake Engineering, Santiago, Chile, 1969.

Housner, G.W., and P.C.Jennings (1982), Earthquake Design Criteria, Earthquake Engineering Research Institute Monograph, Berkeley, California, 1982.

Trifunac, M.D., and V.W.Lee (1978), "Dependence of the Fourier Amplitude Spectra of Strong Motion Acceleration on the Depth of Sedimentary Deposits," USC Department of Civil Engineering Report No.78-14, 1978.

U.S.Nuclear Regulatory Commission (1973), "Design Response Spectra for Seismic Design of Nuclear Power Plants," Regulatory Guide No.1.60, 1973.

Seed, H.B., C.Ugas, and J.Lysmer (1976), "Site-Dependent Spectra for Earthquake Resistant Design," Bulletin of the Seismological Society of America, Vol.66, No.1, February, 1976, pp.221-243.

Mohraz, B. (1976), "A Study of Earthquake Response Spectra for Different Geological Conditions," Bulletin of the Seismological Society of America, Vol.66, No.3, June, 1976, pp.915-935.

Trifunac, M.D. (1980), "Effects of Site Geology on Amplitudes of Strong Motion," Proceedings of the Seventh World Conference on Earthquake Engineering, İstanbul, Turkey, 1980.

Bertero, V.V. (1977), "State-of-the-Art in Establishing Design Earthquakes," Proceedings of the Workshop on Earthquake-Resistant Reinforced Concrete Building Construction, V.V.Bertero, Editor, University of California, Berkeley, June, 1977.

Amin, M., and I.Güngör (1971), "Random Vibration in Seismic Analysis-an Evaluation," ASCE National Structural Engineering Meeting Preprint No. 1409, April, 1971.

Wilson, E.L., A.Kiureghian, and E.P.Bayo (1981), "A Replacement for the SRSS Method in Seismic Analysis," International Journal for Earthquake Engineering and Structural Dynamics, Vol.9, 1981, pp.187-194.

Newmark, N.M., and W.J.Hall (1982), Earthquake Spectra and Design Earthquake Engineering Research Institute Monograph, Berkeley, California, 1982.

Gülkan, P., and M.A.Sozen (1974), "Inelastic Responses of Reinforced Concrete Structures to Earthquake Motions," Journal of the American Concrete Institute, Vol.71, No.12, December, 1974, pp.604-610.

Shibata, A., and M.A.Sozen (1976), "Use of Linear Models in Design to Reflect the Effect of Nonlinear Response," Proceedings of the Review Meeting, U.S. - Japan Cooperative Research Program in Earthquake Engineering with Emphasis on the Safety of School Buildings, Japan Society for Earthquake Engineering Research Promotion, IISEE, Tokyo, 1976.

Udwadia, F.E., and P.Z.Marmarelis (1976), "The Identification of Building Structural Systems, I: The Linear Case," Bulletin of the Seismological Society of America, Vol.66, No.1, February, 1976, pp.125-151.

Hart, G.C., and J.T.P.Yao (1977), "System Identification in Structural Dynamics," Journal of the Engineering Mechanics Division, ASCE, Vol.193, EM6, December, 1977.

Kaya, I., and H.D.McNiven (1978), "Investigation of the Nonlinear Characteristics of a Three-Story Steel Frame Using System Identification," Earthquake Engineering Research Center Report No.UCB/EERC-78/25, University of California, Berkeley, December, 1978, 93 pp.

McVery, G.H. (1979), "Frequency Domain Identification of Structural Models from Earthquake Records," Earthquake Engineering Research Laboratory Report No.79-02, California Institute of Technology, Pasadena, 1979.

Hart, G.C., and C.Rojahn (1979), "A Decision Theory Methodology for the Selection of Buildings for Strong Motion Instrumentation" International Journal for Earthquake Engineering and Structural Dynamics, Vol.7, 1979, pp.579-586.

Ragett, J.D., and C.Rojahn (1978), "Use and Interpretation of Strong Motion Records from Highway Bridges," Federal Highway Administration Report No.FHWA-RD-78-158, October, 1978.

Clough, R.W., and J.Penzien (1975), Dynamics of Structures, McGraw Hill, 1975.

INDEX

Acceleration,
    corrected, 321
    peak, 110,116,143,421,429
    RMS, 143,428
Acceleration time shape, 550
Accelerograph, 252
Active fault, 462
Analog to digital conversion, 252, 286
Apparent stress, 343
Arias intensity, 428
ARMA process, 337
Asperity source model, 41,43
Attenuation, 29,121,143,145,146, 225,235,364,441,444
Autocorrelation function, 437

Backus-Gilbert theory, 99
Barrier source model, 41,43
Baseline, 320
Baseline correction, 321,356
Bodywave, 25
Brune model, 343
Boundary elements, 496

Caldiran earthquake, 72
Caltech
    data set, 280
    procedure, 227
Capable fault, 462
Central Japan Sea Earthquake, 376
Codawaves, 227
Coherence function, 438
Colombia earthquake, 72
Constitutive model,
    elasto-plastic, 539
    endochronic, 540
    hyperbolic, 518
    hysteretic, 516
    nonlinear elastic, 536
    Ramberg-Osgood, 519,536
    relationships, 535
Continuum formulation, 483
Corinth earthquake, 58
Corner frequency, 28,89,123,342, 547
Corrected acceleration, 321
Correlation coefficient, 437
Coyote Lake earthquake, 193
Cross power spectrum, 437

Damping matrix, 560
Data acquisition, 251
Design spectrum, 584
Differential motions, 199
Digitization, 286,356
Digitizer table, 291
Dip-slip, 168,179,185,196,203
Directivity effects, 144,209
Discrete methods, 491
Double couple source model, 145
Ductility, 587
Duration of motion, 429

Effective stress, 18
Elasto-plastic relations, 539
Empirical prediction, 109
Endochronic model, 540
Equivalent linear method, 494,513, 522

Fault
    mechanics, 28
    plane, 43,45
    rupture, 110
Folding frequency, 288
Forward modeling technique, 209
Fourier
    spectrum, 297
    transform, 100,426,495,561,583
Foundation impedance matrix, 564
Frequency domain analysis, 89
Fruili earthquake, 85,146,158,282, 545

Gazli earthquake, 66
Gediz earthquake, 58
Geometrical spreading, 211,225
Green's function, 8,10,210,221
Guatemala earthquake, 72,193

Hardin-Drnevich model, 536
Harmonic response function, 495
Haskell's model, 5,347
Heterogenous fault plane, 10,18
Historical seismicity, 405
Hyperbolic constitutive model, 518
Hysteretic constitutive model, 516
Hypocentral distance, 120

Idaho earthquake, 58
Impedance
    matrix, 564
    ratio, 487
Imperial Valley earthquake, 50
Instrumental seismicity, 411
Intensity, 369
Intensity scale,
    JMA, 384
    MSK, 386,393
Irpinia earthquake, 282
Isoseismal map, 369

JMA intensity scale, 384

Kanai's transfer function, 507
Kinematic
    model, 5
    interaction, 567

Laterally heterogenous structure, 210
Love waves, 199,485
Lysmer-Kuhlemeyer boundaries, 496

Macroearthquake, 462
Macroseismic data, 446,462
Magnitude, 110,416
Mass matrix, 560
Microearthquake, 462
Modal superposition, 494
Morgan Hill earthquake, 58
MSK intensity scale, 386,393

New Hampshire earthquake, 355
Nonlinear
    elastic relationships, 536
    site response, 517
Numerical simulation, 185
Nyquist frequency, 288

Occurence models, 413
Off-Urakawa earthquake, 372
Ormsby's filter, 327,362

Q-factor, 146,155,173,227
Questionaire for intensity, 371

P-waves, 44,235,483
Parabolic baseline, 321
Paraxial ray tracing, 212
Parkfield earthquake, 189
Patheffects, 379
Peak
    acceleration, 110,116,143,421, 429
    velocity, 110,421,429
Plate tectonic models, 467
Point source, 44,99,145
Positioning error, 310
Power Spectral density, 435,547, 554
Processing of accelerograms, 320
Propagation medium, 41
Propagator matrix, 483
Pseudo velocity response spectrum, 428

Radiation pattern, 144,209,221
Ramberg-Osgood model, 519,536
Ray, 211,221
Rayleigh
    condition, 562
    wave, 199,483
Regionalization, 461
Response spectrum, 123,129,426,584
Risetime, 15,89,155,168
RMS acceleration, 143,428
Rotational component, 203,439,583
Rupture
    front, 13,189
    mechanism, 86
    propagation, 44
    velocity, 13,189,193

S-wave, 4,196,483
San Fernando earthquake, 46,199

Scaling law, 23,25,125
Scattering, 228,239
SH-wave, 44,89,196,479,554
Seismic
    albedo, 229
    hazard, 109,396,461,462
    intensity, 370
    moment, 110,120,144,155,343
    source regionalization, 461
    risk, 396,462
    zoning, 462
Seismicity
    historical, 405
    instrumental, 411
Seismotectonic maps, 465
Serviceability, 596
Simulation of time series, 456
Site
    effects, 144,380,545
    response, 144,479
Slip
    average, 15
    distribution, 15,76
    uniform, 8
    velocity, 18,21
Snell's law, 486
Soil-structure interaction, 559
Source
    effects, 379,545
    mechanism, 41,89,196,235
    parameters, 15,85
    spectra, 23,35
Source model,
    asperity, 41,43
    barrier, 41,43
    double couple, 145
Spectral
    content, 120
    parameters, 89
Spectrum,
    design, 584
    pseudo velocity response, 428
    response, 123,129,426,584
Spectrum intensity, 362
Stiffness matrix, 485,560
Stochastic
    models, 10,405
    process, 405
Strike-slip, 168,179,185
Strong motion
    seismology, 3,4
    instrumentation, 263
Stress drop, 18,21,86,89,94
Subfault method, 44
Substructure formulation, 560
SV-wave, 44,89,196,479,554
Synthetic accelerogram, 146,158

Theoretical prediction, 116
Timedomain analysis, 87,126
Timing system, 272
Transducer, 272
Transfer
    function, 435,554,583
    matrix, 483
Trigger system, 272
Truenonlinear methods, 517,519

Uniform slip, 8
Ultimate limit state, 596

Voight model, 486,513
Vulnerability, 391

Wave
    Coda, 227
    Love, 199,485
    P-, 44,235,483
    Rayleigh, 199,483
    S-, 44,,196,483
    SH-, 44,89,196,479,554
    SV-, 44,89,196,479,554
Waveform inversion, 43,85